CARL VON OSSIETZKY universität OLDENBURG

Rare Earth Oxide Thin Films from Solution Based Inorganic Precursor Deposition as Potential Candidates for Insulators in Advanced Gate Stacks

–

Deposition Mechanism and Performance Studies

Der Fakultät für Mathematik und Naturwissenschaften der
Carl von Ossietzky Universität Oldenburg zur Erlangung des Grades und Titels
eines

Doktors der Naturwissenschaften
Dr. rer. nat.

angenommene

Dissertation

von
Frau Dipl.-Chem. Maraike Ahlf
geboren am 24.01.1984 in Hamburg

The present thesis has been carried out in the Institute of Pure and Applied Chemistry at the *University of Oldenburg* and the School of Materials Science and Engineering at the *Nanyang Technological University Singapore* under supervision of Prof. Dr. Katharina Al-Shamery and Assoc. Prof. Dr. Pooi See Lee from July 2008 to October 2012.

1. Reviewer:	Prof. Dr. Katharina Al-Shamery
2. Reviewer:	Prof. Dr. Mathias. S. Wickleder
3. Examiner:	apl.Prof. Prof.h.c. Dr. Dr.h.c. Manfred Neumann

Day of disputation: 16.11.2012

The important thing in science is not so much to obtain new facts
as to discover new ways of thinking about them.
Sir William Bragg

Nichts auf der Welt ist so mächtig,
wie eine Idee, deren Zeit gekommen ist.
Victor Hugo

Abstract

In the present work, the mechanism of a new, specially developed wet chemical deposition technique of rare earth oxide thin films on silicon, germanium and germanium silicon semiconductor substrates has been investigated. Ultra thin films could be generated by an application of the, in organic solvents dissolved, precursor molecules on previously cleaned, passivated H-terminated surfaces. The oxide layer was formed by the thermolytic decomposition of the inorganic precursor molecules on the surface. The coating thickness was maintained by adjusting the concentration of the precursor solution. As the deposition from solutions is limited by differing factors than conventionally thin film deposition techniques the initial mechanism and therefore interface formation was detected to be completely different.

Based on literature known, wet chemical etching procedures a surface cleaning was implemented to remove the native formed oxide layers, whereby the successful removal of the oxide was confirmed by XPS analysis. The choice of the solvent, was done according to criteria of the optimum wetting of the cleaned surfaces and the solubility of the precursors used. The application method was determined by testing a drop-cast, spray injection into the vacuum and a dipping process. In terms of film quality and process compatibility, it could be restricted to dip-coating.

In collaboration with the AG Wickleder a precursor data base, of crystallographic and thermolytical completely characterized molecules, has been developed, whereas the selection of the metal centers and the respective ligands leads to tunable decomposition temperatures. The decomposition of the precursors to the oxide can be realized under mild, sputter free heating conditions in nitrogen flow or UHV. All decomposition temperatures are far below the desorption temperature of the H-passivation of the cleaned substrates, therefore an unwanted reoxidation of the underlying substrate or intermediate layer formation during the formation of the rare earth oxide, is suppressed.

For film deposition the aqueous solvates of the nitrates of La and Nd have been used to start a systematic investigation of the wet chemical deposition technique of the group of the rare earth elements. For the first time the powder trinitrate-hexahydrate precursors of La and Nd as well as possible formed intermediates on the surface have been characterized by XPS.

In the initial state after the precursor deposition the films exhibit a salt like, free-hovering behavior. The thermolytically generated Nd_2O_3 and La_2O_3 films are carbon free and in the initial state after the thermolysis completely amorphous. XPS was utilized to investigate the elementary composition of the precursor films after deposition and the oxide films after decomposition and the corresponding surface species. Topography analyses with AFM, STM and SEM facilitated by roughness and structure studies to restrict the solution concentration with respect to a preferred film formation towards spontaneous nucleation from the solution. The concentration dependent film thickness was determined by HRTEM. It was found that the roughness of the generated films correlates with the roughness of the underlying substrates and the solution concentration.

With respect to a potential application as gate oxides in MOSFETs the generated films were electrically characterized by means of current-voltage, and capacitance-voltage characteristics the dielectric constant and leakage rates have been determined. Temperature dependent current-voltage analysis enabled the determination of participating leakage current conduction mechanisms. Applied annealing processes demonstrated the possibility of the optimization of the films regarding the dielectric properties. Significantly low leakage current rates with high dielectric constants could be determined, in particular for atomically smooth *Si(111)* substrates. As the deposition techniques is controlled by the crystallization process, substrates are enabled to be used for microelectronic devices, which show an increased number of dangling bonds resulting in a high amount of unwanted traps and charges at the oxide/semiconductor interface with conventionally used deposition techniques. Generated multilayer systems of Nd_2O_3 and TiO_2, deposited with the novel wet-chemical approach and atomic layer deposition, opened the path for the applicability of thermodynamically in direct contacts with silicon unstable oxides (such as TiO_2). In addition, a compatibility of the developed technique with conventional deposition methods could be demonstrated. The wet chemical application of the oxide films on germanium and silicon-germanium mixed compounds allowed to show that the method is a simple, and energy efficient technique, which provides the general possibility of high quality oxide thin film deposition from a variety of materials on different types of substrates.

Due to the dielectric properties and the analyzed film thicknesses the generated films are feasible for MOSFET or even DRAM devices in the sub 22 nm node.

Zusammenfassung

Im Rahmen dieser Arbeit wurde der Mechanismus eines eigens entwickelten nasschemischen Abscheidungsverfahrens von Selten-Erd-Oxid Dünnschichten auf Silizium, Germanium und Silizium-Germanium Halbleitersubstraten untersucht. Durch Aufbringung des in organischen Lösungsmitteln gelösten Precursors konnten Ultradünnschichten auf den zuvor gereinigten, H-terminierten Oberflächen erhalten werden. Die Oxidschicht wurde durch die thermolytische Zersetzung der anorganischen Precursormoleküle auf der Oberfläche erzeugt. Eine Schichtdickenkontrolle erfolgte über die Einstellung der Konzentration der Precursorlösung. Die Abscheidung aus Lösungen der Vorläufermoleküle verläuft nach einem Komplett anderen Mechnanismus als herkömmliche Abscheidungsverfahren, da der initiale Kristallisationsprozess an der Substratoberfläche essentiell ist.

Auf Basis literaturbekannter, nasschemischer Ätzverfahren erfolgte die Oberflächenreinigung zur Entfernung nativ gebildeter Oxidschichten, wobei die erfolgreiche Präparation mit XPS Analysen bestätigt wurde. Die Auswahl des Lösungsmittels erfolgte nach Kriterien der optimalen Benetzung der gereinigten Oberflächen und der Löslichkeit der verwendeten Precursoren. Das Aufbringungsverfahren konnte durch Testen der Aufbringung in Tropfenform, als Spray-Einspritzung ins Vakuum und einem Tauchverfahren hinsichtlich der Filmqualität und der Prozesskompatibilität auf das Tauchverfahren eingeschränkt werden.

In Zusammenarbeit mit der AG Wickleder konnte eine Precursordatenbank kristallografisch und thermolytisch vollständig charaktersierter Verbindungen erstellt werden, bei der durch die Auswahl der Metallzentren und der Liganden eine Einstellung der Zersetzungstemperatur des Precursors möglich ist. Die Zersetzung der Precursoren zum Oxid erfolgt unter milden, sputterfreien Heizbedingungen im Stickstoffstrom oder UHV. Alle Zersetzungstemperaturen liegen unterhalb der Desorptionstemperatur der H-Passivierung der gereinigten Substrate, daher wird eine ungewollte Reoxidation oder Zwischenschichtformation während der thermolytischen Bildung des Selten-Erd-Oxids unterdrückt.

Zur Filmabscheidung wurden die wässrigen Solvate der Nitrate von La und Nd verwendet, um eine systematische Untersuchung der nasschemischen Abscheidung der Reihe der Selten-Erden zu eröffnen.

Erstmals konnten die Pulver der Nitrat-Hydrat Precursoren von *La* und *Nd* sowie mögliche auf der Oberfläche gebildete Zwischenprodukte mittels XPS eindeutig charakterisiert werden.

Bei der Generierung der Nd_2O_3 und La_2O_3 Filme bildet sich zunächst ein freischwebender, Salzfilm des Precursors, der in der initialen Phase nach der thermolytischen Zersetzung zum kohlenstoffreien Oxidfilm amorph ist. Die Precursor- und Oxidfilme wurden mittels XPS auf ihre elementare Zusammensetzung und entsprechende Oberflächenspezies untersucht. Ferner ermöglichten topografische Analysen mit AFM, STM und SEM durch Bestimmungen der Rauhigkeiten und Struktur der Filme die Einschränkung der Lösungskonzentration hinsichtlich einer präferierten, homogenenen Filmformation gegenüber einer spontanen Nukleation aus der Lösung. Die Konzentrationsabhängige Schichtdicke wurde mittels HRTEM bestimmt. Die Rauhigkeit der erzeugten Filme korreliert mit der Rauhigkeit der unterliegenden Substrate und der Lösungskonzentration.

Hinsichtlich einer potentiellen Anwendung als Gate-Oxid in MOSFETs wurden die erzeugten Oxidfilme elektrisch charakterisiert und mittels C-V und I-V Kennlinien die Dielektrizitätskonstanten und Leckstromraten ermittelt. Temperaturabhängige I-V Analysen ermöglichten eine erste Abschätzung der jeweiligen Leckstrommechanismen. Angewendete Ausheilprozesse zeigten die Möglichkeit der Optimierung der Filme hinsichlich ihrer dielektrischen Eigenschaften. Signifikant niedrige Leckstromraten in Kombintaion mit durchschnittlichen Dielektrizitätskonstanten konnten insbesondere für atomar glatte *Si(111)* Substrate ermittelt werden. Durch die kristallisationskontrollierte Abscheidung werden Substrate zugänglich, die aufgrund erhöhter Anzahl an freien Oberflächenbindungen bei herkömmlicher Dünnfilmaufbringung drastisch schlechtere dielektrische Eigenschaften zeigen. Anhand erzeugter Mehrschichtensystemen aus Nd_2O_3 und TiO_2, abgeschieden mit dem neuartigen nasschemischen Ansatz und Atomlagenabscheidung, konnte die Anwendbarkeit von thermodynamisch im direkten Kontak mit Silizium instabilen Oxiden (wie TiO_2), ausserdem eine Kombinierbarkeit des entwickelten Prozesses mit herkömmlichen Verfahren demonstriert werden. Die Aufbringung der Oxidfilme auf Germanium und Silizium-Germanium Substraten ermöglichte zu zeigen, dass das Verfahren eine einfache, energieeffiziente, generelle Möglichkeit bietet, oxidische Dünnschichten aus einer Vielzahl an Materialien auf verschiedensten Substraten in hoher Qualität abzuscheiden.

Aufgrund der ermittelten dielektrischen Eigenschaften und Schichtdicken kommen die erzeugten Filme für Anwendungen in MOSFETs oder DRAMs im sub 22 nm Bereich in frage.

Acknowledgments

During this work I have collaborated with many colleagues for whom I have great regard, and I wish to extend my thanks to all those who have helped me with my work.

Firstly I want to thank *Prof. Dr. Katharina Al-Shamery* for providing me the interesting and challenging scientific question of the present doctoral thesis, the supervision throughout the entire work and for supporting me in my personal development.

I am deeply grateful to *Assoc. Pr. Dr. Pooi See Lee* from the NTU Singapore for an expert scientific and personal supervision and support, for excellent measurement conditions and guidance during twelve wonderful and successful month in Singapore as well as for encouraging me to believe in my abilities.

Prof. Dr. Mathias Wickelder is gratefully acknowledged for numerous fruitful scientific discussions and the second examination of the present thesis.

I owe thanks to *Prof. Dr. Manfred Neumann* from the University of Osnabrück for scientific discussions regarding the XPS analysis and the possibility to attend synchrotron measurements at the University of California ALS Berkeley as well as the third examination of the thesis.

I wish to express my warm and sincere thanks to *Jörg Stöver* for uncountable hours of common work and (non-)scientific discussions, for being a fabulous colleague and for "ensuring that the beer is never empty".

I am grateful to *Dr. Mareike Ahlers* and the *AG Wickleder* for an excellent project collaboration, the precursor synthesis and supply.

Lars Schütte and *Peter Clawin* are gratefully acknowledged for their mathematical assistance.

Dr. Du Anyan and *Dr. Zhou Yong Kai* from Global Foundries Singapore are gratefully acknowledged for scientific and technical assistance in HRTEM imaging.

My special thanks goes to *Meng Meng Vanessa Chong* from the Nanyang technological University for an excellent scientific collaboration, for contributing and supporting my work during my overseas stay in Singapore and for the AFM measurements. Thank you for making my stay in Singapore an scientifically successful and personally awesome experience.

I thank *Dr. Eugene Khoo* for the organizational assistance during the stay in Singapore.

Many thanks to *Nadine Jacobs* and *Jan Schlemminger* for correcting this exceptionally long manuscript and their outstanding patience.

Mr. Bug is gratefully acknowledged for a reliable function during the critical parts of the experimental work.

Especially, I thank the colleagues of the *AG Al-Shamery* and *Prof. Lee's group* in Oldenburg and Singapore, who were very helpful in providing information during countless fruitful scientific discussions and for an excellent, creative working environment.

Sincere appreciation to *Filza Aslam* and *Dr. Heiko Aydt* for the warm welcome, support and for an unforgettable time in Singapore.

The financial support through the granted PhD scholarships of the *Fond of Chemical Industry (FCI)*and the *Heinz-Neumüller-Stiftung* as well as the *German Academic Exchange Service (DAAD)* for the granted full time overseas scholarship for PhD students, which made my stay in Singapore possible, is gratefully acknowledge.

Meinen Eltern danke ich ganz herzlich ich für die Geduld, die immer anwährende, unerschütterliche, bedingslose Unterstützung sowie den Rückhalt während meines gesamten Studiums und der Promotion.

Contents

List of Abbreviations xxiii

List of Symbols xxvii

1. Motivation 1

2. Surface Analysis Techniques 5

2.1. X-Ray Photoelectron Spectroscopy: XPS 5

2.2. Scanning Probe Microscopy: SPM 16

2.2.1. Scanning Tunneling Microscopy: STM 16

2.2.2. Atomic Force Microscopy: AFM 21

2.2.3. Film Roughness 23

2.3. Electron Microscopy: EM 23

2.3.1. Transmission Electron Microscopy: TEM 25

2.3.2. Scanning Electron Microscopy: SEM 30

2.4. Focused Ion Beam: FIB 31

2.4.1. Cross sectional TEM (XTEM) Specimen Preparation . . 33

2.5. Energy Dispersive X-Ray Spectroscopy: EDX 35

2.6. X-Ray Diffraction: XRD 36

3. Basics & Analysis of Semiconductor Devices 41

3.1. Semiconductor Devices 41

3.1.1. Metal Oxide Semiconductor: MOS Capacitors 42

3.1.2. Transistors 50

3.2. MOS Component Characterization 58

3.2.1. Experimental Setup 58

3.2.2. Capacitance Voltage Measurements: C-V 59

3.2.3. Current Voltage Measurements: I-V 62

3.2.4. Temperature Dependent I-V Characteristics: Leakage Current Conduction Mechanisms in Insulating Films . . 63

3.3. Equivalent Oxide Thickness: EOT 68

4. Crystallization & Film formation **69**
4.1. Nucleation from Solutions 69
4.2. Crystallization in Films 72

5. State Of The Art **77**
5.1. Alternative Gate Stack Materials 78
5.2. Limitations for Different Device Applications 79
5.3. Gate Stack Tailoring: Multi Layer Systems 79
5.4. Interfacial Structure 80
5.5. REO Systems 80
5.5.1. Rare Earth: Elemental Abundance, Extraction and Political Influence 81
5.5.2. Thermodynamic Stability of Rare Earth Oxides in Contact with Silicon 82
5.5.3. Lattice Constants and Physical Parameters 84
5.6. Process Compatibility and Deposition Techniques 85
5.6.1. Atomic Layer Deposition 87
5.7. Non-Silicon Devices 89

6. Experimental Setup & Data Processing **91**
6.1. The UHV-Chamber 91
6.1.1. The Sample Holder 93
6.1.2. Exchange/Transport Module 94
6.2. Additional Analytical Equipment 95
6.2.1. Surface Analysis 95
6.2.2. Electrical Characterization 96
6.3. Technical Equipment 97
6.4. Software 98
6.5. XPS Data Processing and Curve Fitting 98

7. Experimental Thin Film Deposition **101**
7.1. Wet Chemical Deposition Process 102
7.1.1. Precursor Application 103
7.1.2. Choice of Solvent 106
7.1.3. Precursor Decomposition 108
7.1.4. Annealing Conditions 108
7.2. Experimental Conditions: Remarks 108

8. Substrates **111**
8.1. Basics on Silicon and Germanium . . . 112
8.1.1. The *100* Surface . . . 113
8.1.2. The *111* Surface . . . 113
8.1.3. Lattice Constants . . . 114
8.2. Silicon Substrates . . . 114
8.2.1. Wet Chemical Cleaning of Silicon . . . 115
8.2.2. Atomically Smooth *Si(111)*: Additional Etching . . . 117
8.2.3. Recipe for *Si* Cleaning . . . 118
8.3. Germanium and Silicon-Germanium Substrates . . . 119
8.3.1. Wet Chemical Cleaning of *Ge* and *SiGe* . . . 119
8.3.2. Recipe for *Ge* and *SiGe* Cleaning . . . 120

9. Precursor System & Powder Reference Data **123**
9.1. Survey of Systems . . . 124
9.1.1. Synthesis . . . 124
9.1.2. Decomposition Behavior . . . 125
9.1.3. Crystallographic Data . . . 128
9.2. Elementary Powder Analysis:
XRD and XPS . . . 131
9.2.1. Summary of XPS Reference Data . . . 149

10. Film Topography, Structure & Thickness **151**
10.1. Topography: SEM . . . 152
10.1.1. Highly Concentrated Solutions . . . 152
10.1.2. Transition - Crystallization to Film Formation . . . 153
10.1.3. Substrate Orientation Influence: SEM . . . 156
10.2. Topography *La*: STM . . . 157
10.3. Topography *Nd*: AFM . . . 158
10.3.1. Substrate Orientation Influence . . . 158
10.3.2. Film Stability . . . 162
10.3.3. Annealing Influence . . . 167
10.4. Film Thickness and Structure: HRTEM . . . 169
10.5. Topography Alternative Substrates . . . 172
10.5.1. Germanium . . . 173
10.5.2. Silicon-Germanium . . . 175
10.6. Discussion Topography and Film Thickness . . . 176

11. Elementary Thin Film Analysis: XPS **185**
11.1. *La*-based Films on *Si(111)* . . . 186
11.1.1. The *Si2p* and *O1s* Signal . . . 188
11.1.2. Carbon Content: The *C1s* signal . . . 193
11.1.3. The *La3d* Signal . . . 194
11.1.4. Thermal Stability of the Interface . . . 196
11.2. *Nd*-based Films on *Si(111)* and *Si(100)* . . . 200
11.2.1. The *Nd3d* Signal . . . 203
11.2.2. The *Si2p* and *O1s* Signal . . . 206
11.3. *Nd*-based Films on *Ge(100)* . . . 214
11.3.1. The *Nd3d* signal . . . 215
11.3.2. The *Ge3d* and *O1s* Signal . . . 216
11.4. *Nd*-based Films on *SiGe(111)* . . . 221
11.4.1. The *Nd3d* signal . . . 223
11.4.2. The *Si2p Ge3d* and *O1s* Signal . . . 224
11.5. Conclusion XPS Analysis . . . 231

12. Electrical Characterization **235**
12.1. Electrical Properties: Experimental Part . . . 236
12.2. MOS Capacitor Fabrication . . . 238
12.3. Silicon Substrates . . . 239
12.3.1. C-V Characteristics . . . 239
12.3.2. I-V Characteristics . . . 247
12.3.3. Temperature Dependent I-V Analysis . . . 253
12.3.4. Conclusion Electrical Characterization of Silicon . . . 260
12.4. Alternative Substrates . . . 270
12.4.1. Germanium . . . 270
12.4.2. Silicon-Germanium . . . 274
12.4.3. Conclusion and Discussion Alternative Substrates . . . 278

13. Multilayer Gate Stacks on Silicon Substrates **281**
13.1. ALD Deposition of Titanium Dioxide . . . 282
13.2. Topography and Film Thickness of the Bilayer System . . . 283
13.2.1. Topography: AFM . . . 283
13.2.2. Film Thickness: HRTEM . . . 285
13.3. Electrical Characterization: Bilayer Systems . . . 287
13.3.1. C-V and I-V Characterization: Bilayer . . . 288

13.3.2. C-V and I-V Characterization: Reverse Bilayer 297
13.4. Conclusion and Discussion of the Bilayer Analysis 306

14. Discussion & Conclusion **315**

15. Outlook **327**

Bibliography **346**

List of Figures **361**

List of Tables **367**

Appendix **368**

Curriculum Vitae **I**

Scientific Work **III**

Statement of Authorship **VII**

List of Abbreviations

Abbreviation	Meaning
AC	Alternating Current
AES	Auger Electron Spectroscopy
Ag	Silver
AFM	Atomic Force Microscopy
Al	Aluminum
amu	atomic mass unit
ALD	Atomic Layer Deposition
ARXPS	Angle Resolved X-ray Photoelectron Spectroscopy
Au	Gold
AVD	Atomic Vapor Deposition
B	Boron
BFD	Bright Field Detector
BSD	Back Scattered Detector
BZ	Brillouin Zone
C	Carbon
CCI	Constant Current Imaging
Ce	Cerium
CHA	Centric Hemispherical Analyzer
CHI	Constant Height Imaging
Cl	Chlorine
CMOS	Complementary Metal Oxide Semiconductor
Cu	Copper
CVD	Chemical Vapor Deposition
DC	Direct Current
DFD	Dark Field Detector
DRAM	Dynamic Random Excess Memory
Dy	Dysprosium
EDX	Energy Dispersive X-ray Spectroscopy
EELS	Electron Energy Loss Spectroscopy
EOT	Equivalent Oxide Thickness
Er	Erbium

ESCA	Electron Spectroscopy for Chemical Analysis
Eu	Europium
eV	electron Volt
F	Fluorine
FESEM	Field Emitting Scanning Electron Microscopy
FIB	Focused Ion Beam
FWHM	Full Width Half Maximum
Ga	Gallium
Ge	Germanium
Gd	Gadolinium
GID	Gracing Incident Detection
GIS	Gas Injection System
H	Hydrogen
HAADF	High Angle Annular Dark Field
He	Helium
Hf	Hafnium
Ho	Holmium
HREM	High Resolution Electron Microscopy
HRTEM	High Resolution Transmission Electron Spectroscopy
IC	Integrated Circuit
IETS	Inelastic Electron Tunneling Spectroscopy
IR	Infrared
Ir	Iridium
ITRS	International Roadmap for Semiconductors
La	Lanthanum
LDOS	Local Density of States
LEED	Low Energy Electron Diffraction
LMIS	Liquid Metal Ion Source
Lu	Lutetium
MBE	Molecular Beam Epitaxy
Mg	Magnesium
Mo	Molybdenum
MOCVD	Metal Organic Chemical Vapor Deposition
MOSFET	Metal Organic Semiconductor Field Effect Transistor
MS	Mass Spectrometry
N	Nitrogen

Na	Sodium
Ne	Neon
Nd	Neodymium
O	Oxygen
P	Phosphorus
PID	Proportional Integral Derivative
Pr	Praseodymium
Pt	Platinum
PVD	Physical Vapor Deposition
QUAD	Quadrupol (Mass Spectrometer)
RBS	Rutherford Backscattering
RCA	Radio Corporation of America
REO	Rare earth oxide
RMS	root mean square
Sc	Scandium
SEM	Secondary Electron Multiplier
SEM	Scanning Electron Microscopy
Sm	Samarium
SNOM	Scanning Nearfield Optical Microscope
SOFC	Solid Oxide Fuel Cell
SPM	Scanning Probe Microscopy
SPV	Surface Photovoltage Technique
STEM	Scanning Transmission Electron Microscopy
STM	Scanning Tunneling Microscopy
S	Sulfur
Si	Silicon
SiGe	Silicon-Germanium
Tb	Terbium
TDS	Thermal Desorption Spectroscopy
TPD	Thermal Programmed Desorption
TEM	Transmission Electron Microscopy
THF	Tetrahydrofuran
Tm	Thulium
ToF-SIMS	Time-of-Flight Secondary Ion Mass Spectrometry
UHV	Ultra High Vacuum
UPS	Ultra Violet Photoelectron Spectroscopy

UV	Ultra Violet
W	Tungsten
XPS	X-ray Photoelectron Spectroscopy
XRD	X-ray Diffraction
XRR	X-ray Reflectivity
Y	Yttrium
Yb	Ytterbium
Zr	Zirconium

List of Symbols

Abbreviation	Meaning
a	lattice constant
$a,\ b,\ c$	real basis vectors
$a^*,\ b^*,\ c^*$	reciprocal basis vectors
A	area of the capacitor
	Richardson(-Dushman) constant
$A,\ B,\ C,\ D,\ E,\ F$	constants of integration
$\vec{B}$	magnetic field
c	speed of light
C	capacitance
c_1	constant which includes the electron density
	of tip and sample
c_2	constant, dependent on the work function
	of tip and sample
C_{Acc}	capacitance in accumulation
C_{Dep}	capacitance in depletion
C_{Inv}	capacitance in inversion
C_{Ox}	capacitance of the oxide
C_{p-n}	capacitance of the p-n junction
d	distance between tip and sample
	horizontal length of the scanned line
	thickness of the insulator
D	horizontal image width of the full image
e	electric charge of electrons
E	total energy of the particle
	energy level
	electric field
E_a	energy level of acceptor atoms
E_A	energy of core level electrons
E_{ABC}	energy of an Auger electron for the transition ABC
E_{ads}	energy of the adsorption
E_B	binding energy of electrons

	energy of outer shell electron
E_B^F	binding energy of electrons in solid state relative to E_F
E_C	energy of second shell electron
	energy of the conduction band
E_d	activation energy of desorption
	energy level of donor atoms
E_{eff}	effective binding energy
E_F	Fermi energy
$E_{F,n}$	Fermi energy in n-type substrate
E_i	intrinsic Fermi energy
E_{Vac}	vacuum energy level
E_{Gap}	band gap energy
E_{kin}	kinetic energy
E_{Ox}	electric field within the insulating oxide
E_{pot}	potential energy
E_S	electric field within the semiconductor
E_V	valence band energy
E_{VZ}	retarding potential
e_χ	electron affinity
g	degeneration
$g(E)$	density of states per volume and unit energy
$g_c(E)$	density of states at the bottom of the conduction band
h	Planck constant
i	$\sqrt{-1}$
I	current
I_E	base current of a bipolar transistor
I_{Depl}	depletion current
I_n	electron current
I_p	hole current
I_t	tunneling current
j	total angular momentum
J_{HC}	tunneling current hopping conduction
J_{PF}	tunneling current Poole-Frenkel emission
J_{SE}	tunneling current Schottky emission
J_{TAT}	tunneling current trap assisted tunneling
$k_{x,y,z}$	space component in x, y, z direction

$\vec{K}$	lattice vector
$\vec{k}$	specific wave vector
$\vec{k_e}$	wave vector of the electron
$\vec{h_h}$	wave vector of the hole
k	wave number
	Boltzmann constant
k_m	frequency factor
k_α	X-ray α lines emitted from K shell
L	side length of a cube
l	orbital angular momentum
m	mass
	slope
m^*	effective mass of the electron
m_e	electron mass
m^{eff}	effective mass
m_e^{eff}	effective mass of the electron
n	quantum number
	refractive index
	integer
N	concentration of adsorbed particles per surface area unit
	number of points within the given area
N_A	density of the ionized acceptor atoms
N_D	density of the ionized donor atoms
N^*	number of critical nuclei
n_0	electron density
N_C	effective density of states within the conduction band
n_i	intrinsic carrier density
N_V	effective density of states within the valence band
p	particle momentum
	dipole moment
p_0	hole density
q	electronic charge
p_v	vapor pressure
q	electronic charge
Q	charge
Q_{IT}	total interfacial traps per unit area of the gate

Q_M	total ionic charge per unit area of the gate
Q_F	fixed charge per unit area of the gate
r	radius
	inter atomic spacing
R	resistance
r_0	distance of minimum energy
r_c^*	critical nucleus radius
r_{2D}^*	critical radius in 2D
s	spin quantum number
S	saturation state
t	thickness of the insulating layer
	thickness of the generated layer from crystallization
t_{Ox}	physical thickness of the oxide layer
$t_{Ox,eff}$	effective physical thickness of the oxide layer
T	temperature
	absolute temperature
	transmission coefficient
U	voltage
U_b	acceleration voltage
U_t	bias between tip and sample
$U_{x,y,z}$	voltage applied to x, y, z direction piezo crystals
V	volume of the unit cell
	voltage
V_A	voltage applied the anode
V_0	energy of the potential barrier
V_B	voltage applied to the bulk/back contact
V_{BS}	voltage applied between bulk (back contact) and source
V_{CB}	base collector voltage
V_{DS}	voltage applied between drain and source
V_{EB}	base emitter voltage
V_{FB}	flatband voltage
V_G	voltage applied to the gate
	voltage applied to the real device
V_G'	voltage applied to the ideal device
v_g	group velocity
V_{GS}	voltage applied between gate and source

V_{TH}	threshold voltage
$V(x)$	position dependent potential curve
x	coordinate of space
X	element symbol
x_D	width of the depletion layer
$x_{D,T}$	width of the depletion layer when inversion is initiated
x_p	depletion layer width within the p-type semiconductor
x_n	depletion layer width within the n-type semiconductor
y	sub shell
z	atomic number
Z_{ave}	average height value within the given area
Z_i	current height value within the given area
α	half aperture angle
$\mathring{A}$	Angstrom
$\varnothing$	diameter
$\hbar$	reduced Planck constant
β	desorption rate
χ	electron affinity of the semiconductor
δ	resolution of the microscope
ΔE	energy difference in XPS peaks
ΔE_{ac}	activation energy of electrons
ΔG_C	free Gibbs enthalpy for spherical clusters
ΔG_V	bulk dependent free Gibbs enthalpy
ΔG_σ	surface dependent free Gibbs enthalpy
$\Delta G*$	critical free Gibbs enthalpy
$\Delta G_\Theta*$	corrected critical free Gibbs enthalpy
ϵ	permittivity
	electric field
ϵ_0	permittivity of free space
ϵ_{Ox}	permittivity, dielectric constant, of the insulator
ϵ_{Vac}	electric field induced due to difference in vacuum energies
ϵ_S	dielectric constant of the semiconductor
$\in$	energy of the upper valence edge
$\in_n$	energy of the hole
$\in_e$	energy of the electron
κ	dielectric constant

κ_{Ox}	dielectric constant of the oxide
λ	wave length
ν	frequency of radiation
θ	contact angle
Θ	Bragg angle
ϕ_i	built in potential of a p-n junction
ϕ_B	interface barrier height
ϕ_{PF}	Poole-Frenkel barrier height
Φ_M	work function of the metal
Φ_{MS}	work function difference between metal and semiconductor
Φ_S	work function of the semiconductor
Φ_{Sam}	work function of the sample
Φ_{Spe}	work function of the analyzer
η	ideality factor
ρ	resistivity
$\rho_{ion}(x)$	ionic charge distribution within the oxide
ρ_m	mol density
$\rho_{Ox}(x)$	charge distribution within the oxide
$\rho(x)$	electric charge density
σ	surface tension
σ_{BC}	surface energy of the substrate-crystal interface
σ_{CS}	surface energy of the crystal-solution interface
σ_{SB}	surface energy of the solution-substrate interface
Ψ	wave function

1. Motivation

The current development in microelectronic industries leads to the need of a further decrease of microelectronic components while simultaneously increasing the performance of semiconductor devices. In transistors (metal oxide semiconductor field effect transistors: MOSFETs), in integrated circuits (ICs), silicon dioxide (SiO_2) is currently used as gate oxide. The gate oxide insulates the source-electrode from the drain-electrode. An increasing miniaturization of gate dielectrics below 20 nm causes a required oxide thickness of below 1 nm, which leads to fundamental limits of SiO_2 based devices. With SiO_2, at this film thickness, electrons tunnel through the thin layer due to a quantum mechanical tunneling effect resulting in a high leakage current, which rises exponentially with increasing miniaturization. Besides unwanted high Joule heating, this leads to intolerable switching errors in MOSFETs. The high Joule heating results in overheating and in the worst case in the destruction of the device, in either case to a loss effect concerning the impressed voltage. This is relevant in the view of functional reliability as well as for economic aspects and therefore unacceptable for microelectronic applications.[1] [2]

To improve the performance and avoid the high leakage currents by applying equal gate-source voltages, the SiO_2 layer has to be replaced by a physical thicker layer of alternative gate oxide materials, as the capacitance of the device is given by:

$$C = \frac{A\epsilon_0\kappa}{t} \tag{1.1}$$

A: capacitor area
t: thickness of the insulator
ϵ_0 permittivity of free space
κ dielectric constant of the insulator

It can be seen that materials which are eligible for the replacement of SiO_2 need to have higher dielectric constants (κ) than SiO_2 ($\kappa = 3.9$), which can be deposited on semiconductor substrates (conventionally used silicon (Si)) in

adequate thin layers. Oxides with high κ values are also referred to as "high-κ oxides".[3]

Oxides which come into consideration to replace SiO_2 further, need large band gaps (above 1 eV) between the conduction- and valence band. With Si high quality, perfectly defined oxide/silicon interfaces, which exhibit low defect densities, have to be formed. Besides the formation of silicides with Si has to be avoided. These conditions necessitate either amorphous insulators or insulating materials, or materials where, by the formation of interfacial layers of e.g. one or two monolayers of SiO_2, coincident lattice structures can be generated.[4] [5]

Candidates as alternative gate oxide materials, which meet these requirements, are rare earth oxides (REOs). They have a high resistivity ($\rho = 10^{12}$-10^{15} Ωcm), high dielectric constants (κ = 7-20) and large band gaps (E_g = 4-6 eV).[6] The recrystallization temperatures are quite high. That is important in order to avoid changes in the structure during high temperature production of ICs. Their high thermodynamic stability in contact with Si is a further advantage of REOs.[7] For semiconductor industries in the sub 22 nm node layer thickness below 10 nm of the REOs are in the point of interest, since the Equivalent Oxide Thickness (EOT) in this range assumes values, which afford further miniaturization of MOSFET devices. The EOT allows a comparison of the performance of high-κ MOS-Gates with SiO_2 MOS-Gates. The values specify the potential oxide thickness of alternative gate-oxide materials in proportion to SiO_2 to reach the same gate capacity as with SiO_2.[8]

Some techniques are already used industrially, to deposit ultra thin REO films with defined layer thickness and structures. The Metal Organic Vapor Deposition (MOCVD) is one of the currently most promising approach for thin film deposition. In MOCVD metal organic , evaporated precursors are used to deposit the thin films. The Atomic Layer Deposition (ALD) is a MOCVD technique which enables a successful preparation. In this process in two temporal separated half reactions a monolayer of the relevant REO is deposited on a respective substrate.[9]. However, precursors for MOCVD are mostly toxic, hardly volatile and instable at high process temperatures.[10] The technical complexity to use those materials is remarkable. Some problems of MOCVD can be obviated by Atomic Vapor Deposition (AVD) techniques as the precursors are stored at room temperature in organic solutions and than heated to the process temperature in a specialized nozzle.[11] Further known methods for

deposition of REO thin films are the oxidation of metallic mirrors and cathodic sputtering of REO targets as well as physically controlled and laser based techniques (physical vapor deposition (PVD) and pulsed laser deposition (PLD)) where the films are grown epitaxially or crystalline.

MOCVD techniques suffer from problems such as carbon impurities in the deposited films caused by the organic precursor molecules. The reaction of precursors demands the use of additional oxygen in the process, which leads to the formation of undefined SiO_2 interfacial layers between the Si substrate and the deposited thin film. Both effects have negative influence on the dielectric properties of the deposited oxide layer. Physical methods are highly time consuming and therefore inapplicable for mass productive industrial applications. Technical difficulties like gaseous impurities during ion sputtering, high process temperatures, which result in unwanted side reactions, demanded energy costs and dissociation of oxides out of the formed REO thin films and the resulting destruction of structure, cause the necessity to develop new techniques for an effective thin film deposition.[12]

Besides the use in transistors, REO thin films are in current interest of applications for opto electronics due to their high transparency from UV- until IR-region.[13] In heterogeneous catalysis certain REOs are used as coating- or supporting materials in amorphous structures in context with their potential for oxygen transport as promoters for metal catalyzed reactions.[14] [15] Furthermore, they are promising candidates as mediator materials in several industrial processes due to the possibility to bridge deviating lattice parameters and thermal extension coefficients in coating ceramics and metallic components, e.g. in turbines. Within the scope of the commercialization of Solid Oxide Fuel Cells (SOFCs) REO thin films are a matter of particular interest to decrease material costs, whereas besides reduced operational costs an improvement of cell efficiency is expected. In the future thin layers of various rare earth mix-oxides like praseodymium oxide, neodymium oxide, cerium oxide or lanthanum silicon oxides shall be used as electrolyte materials, based on established nickel/yttrium stabilized zirconium oxide anodes.[16] [17]

New, alternative, simplified techniques for thin film deposition are required to generated thin REO layers in the nm range. To avoid carbon impurities the synthesis of new, carbon free precursors is essential. In the present thesis a new, highly innovative integrated inorganic dip-coating method should be introduced, to decrease the instrumental based effort of conventionally used

methods for thin film application and to elude the mentioned drawbacks. For the deposition process the specially developed precursors have to be stable in air and ultra high vacuum for certain applications. In order to prevent residues on the substrate, the precursors should form gaseous decomposition products under mild, sputter free heating conditions. For an easy application out of solutions the precursors should be easily dissolvable in the used solvents. The choice of solvent has to be realized under criteria of optimized wetting of the substrate and minimal impurities in the formed films. The native formed SiO_2 needs to be removed prior to the thin film deposition, to inhibit the formation of undefined interfacial layers. Under economic points of view the process has to be designed eminently energy efficient, therefore low decomposition temperatures and fast application procedures are necessary. Si and Ge based industrially applicable semiconductor substrates shall be combined with REO films of La and Nd in order to open a systematic investigation and to achieve an assessment of the invented techniques as a general method for REO thin film depositions.

The deposited films will be mainly analyzed regarding the film thickness using high resolution transmission electron microscopy (HRTEM), topography and roughness studies will be performed by atomic force microscopy (AFM) and scanning tunneling microscopy (STM). Binding properties and elementary composition will be investigated by X-ray photo electron spectroscopy (XPS) to achieve a rather detailed insight into the film and interface formation.[18] In order to estimate the potential of the films for an effective application as gate stacks in MOSFET devices typical current voltage (I-V) and capacitance voltage (C-V) measurements reveal the leakage current densities and mechanisms as well as the respective κ values. Furthermore detailed studies of precursor powders and respective decomposition products will be shown.

2. Surface Analysis Techniques

Surface science in general deals with fundamental and high end experimental and analytical studies to understand the physics and chemistry of a tremendous range of surfaces and interfaces of solids, polymers, biomaterials, nanostructures, liquids, gases or vacuum.

In the following chapter a short introduction into the used measurement techniques, theoretical basics and the respective aspects for data analysis should be given subdivided by spectroscopic, topographic, microscopic and diffraction techniques. Contemplated are issues relevant for this thesis.

2.1. X-Ray Photoelectron Spectroscopy: XPS

X-ray Photoelectron Spectroscopy is a versatile non destructive atomic spectroscopic technique based on the photoelectric effect and capable of providing atomic and molecular information regarding the surface of the material.

The photoelectric effect was discovered in 1887 by Heinrich Rudolph Hertz and explained in 1905 by Albert Einstein who was honored with the Nobel Prize in 1921. It is elucidated as the emitting process of electrons as a consequence of their absorption of energy from electromagnetic radiation (e.g. visible light, ultra violet (UV)- or X-ray). XPS itself was investigated by Kai Siegbahn in 1957[19] referring to the technique as Electron Spectroscopy for Chemical Analysis (ESCA), since every element shows a characteristic set of peaks. Chemical shifts of core levels appear, depending on the chemical environment of the atom which is ionized, enabling the chemical constitution, environment and oxidation state to be determined. XPS spectra are obtained by irradiating a material with a X-ray beam while simultaneously measuring the kinetic energy and number of electrons that escape from the surface. Hence, X-ray radiation is energy rich, particularly core level electrons are effected. Beside XPS, UPS (Ultraviolet Photoelectron Spectroscopy) is used complementary. In this technique UV-radiation is utilized, investigating the outer shell electrons due to the lower energy of the incident excitation beam. In general XPS requires ultra high vacuum (UHV) conditions and can be performed, applying

commercially or individually built systems using monochromatic or non monochromatic X-ray sources. Most commonly used are Mg- or Al-K_α lines. For more detailed and precise analysis synchrotron based light sources are applied. The first XPS synchrotron experiment has been performed in 1974 at *Stanford Synchrotron Radiation Project* by Lindau et al.[20]. In the present thesis only a short introduction into theory and data collection should be given, a detailed explanation of XPS can be found e.g. in[21].

Content of Analysis

XPS is an effective method to determine the qualitative elementary composition of surfaces since the energy of the emitted electrons and peak intensity/ratio is element specific. By analyzing the shifts of specific signals in the spectra the binding state and electronic structure of the prevailing element can be determined in detail. Additionally it is possible to analyze the quantitative ratio of different elements related to each other under consideration of the sensitivity factors, as the number of emitted electrons is proportional to the number of atoms on the surface. Sensitivity factors take into account that the different elements exhibit different emission probabilities. Due to the limited mean free path of electrons, XPS is surface sensitive. With state of the art equipment also spatial resolved analysis is possible. Non destructive layer profiles of samples can be investigated by the variation of the angle between sample and analyzer (Angle Resolved XPS (ARXPS)). ARXPS is widely used for in depth analysis of very thin films due to the restrictions of conventional used techniques, like sputter depth profiling where physical effects on the surfaces are investigated.[22]

Theoretical Background

In XPS X-ray photons which were generated by an X-ray source are accelerated to the sample. Thereby inner shell electrons from the sample are emitted with a defined kinetic energy (E_{kin}) and can be detected energy selectively.

Figure 2.1. shows the different relevant energy levels and differences in XPS analysis schematically .

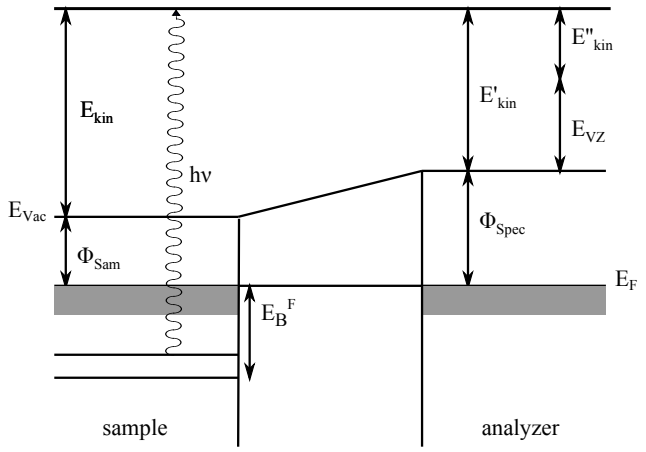


Figure 2.1.: Schematic XPS energy diagram. E_{kin} is the energy of the electrons at emission from the sample, E'_{kin} is the energy in access to the analyzer, E''_{kin} is the detected energy of the electrons at the detector (after[23]).

The respective variables are :

h: Planck constant
ν: frequency of radiation
E_B^F: binding energy of electrons in solid state related to Fermi energy E_F
Φ_{Sam}: work function of the sample (Difference between vacuum energy level E_{Vac} and Fermi energy E_F)
Φ_{Spec}: work function of the analyzer
E_{VZ}: potential of retarding

Under assumption of the Koopmanns' theorem the kinetic energy E_{kin} has to fulfill:

$$E_{kin} = h\nu - E_B^F - \Phi_{Sam} \tag{2.1}$$

The Koopmans' theorem states that in closed-shell Hartree-Fock theory, the first ionization energy of a molecular system is equal to the negative orbital energy of the highest occupied molecular orbital (HOMO). This theorem is named after Tjalling Koopmans and was published in 1934.[24]

In XPS analysis sample and analyzer are in conducting connection, thus their Fermi levels are identical. A difference of the spectrometer Φ_{Spec} and sample Φ_{Sam} work function results in a change of E_{kin} of the emitted electrons:

$$E'_{kin} = h\nu - E_B^F - \Phi_{Sam} - (\Phi_{Spec} - \Phi_{Sam}) = h\nu - E_B^F - \Phi_{Spec} \tag{2.2}$$

Equation 2.2 indicates that the detected E_{kin} is dependent on the work function of the spectrometer, however not on the work function of the sample. For data analysis Φ_{Spec} is already taken into account, by calibration and respective software settings while data collection, and does not have to be considered in detail for final data processing.

In solid state samples all energies are related to the Fermi energy E_F. Thus for correct interpretation of spectral data it is essential to determine E_F exactly. Due to the fact that the Fermi energy level is equivalent with the HOMO in metal components, E_F of metals can be easily deduced from the XPS spectra, since the signal at highest kinetic energy belongs to the electrons emitted from the valence edge. The signal at highest kinetic energy in the spectra depends on surface states or adsorbates of the surface. To investigate E_F therefore reference samples of pure metals are analyzed.

Binding states of the respective elements can be investigated by XPS, since the effective charge distribution, located at the centered atom which is dependent on the chemical environment, is detected during the measurement as the effective binding energy E_{eff}. The effective binding energies are dependent on several terms e.g. static and dynamic effects.

The surface sensitivity of XPS can be explained by the mean free path of the emitted photoelectrons which is identical with the mean emission depth in solid state materials. The mean free path of electrons is dependent on the kinetic energy and therefore in XPS on the emitting material. A minimum of the mean free path of the electrons in most solid materials is observed around 100 eV due to the fact that in this range energy consuming processes like plasmons can be initiated. X-ray excited electrons, with energies between 20 and 1500 eV, exhibit a short mean free path in the range of two to three mono layers and therefore a penetration depth of 1 to 10 nm. Thus, the sensitivity of XPS is dependent on the excitation source, the respective excitation energy and the material.

Excitation Processes As XPS is generally based on the interaction of solid matter and radiation. Beside the photoelectric effect, different excitation processes need to be understood for a detailed comprehension of XPS analysis.

Photoemission processes can be generally divided into primary and secondary processes. A schematic overview of the excitation processes can be found in figure 2.2.

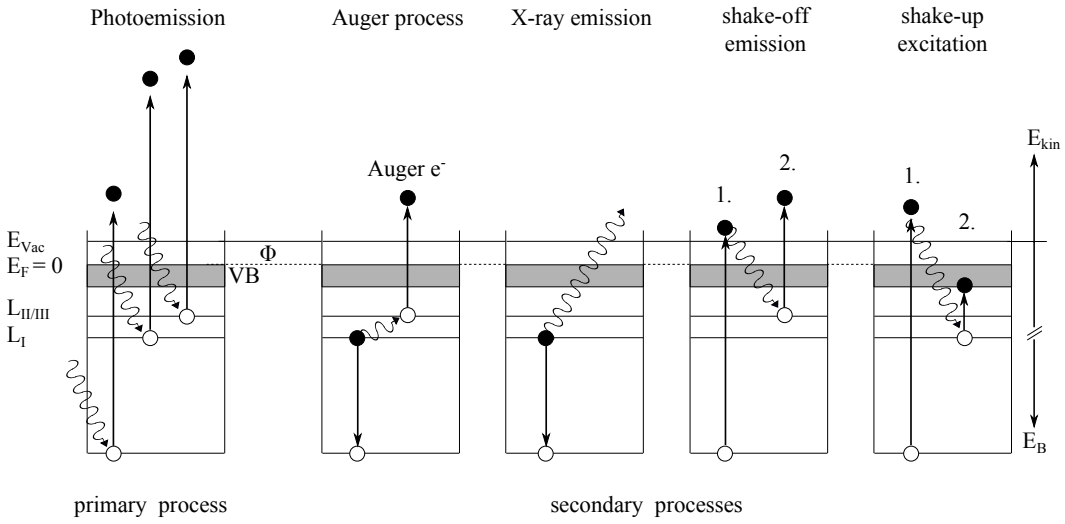


Figure 2.2.: Primary and secondary electron excitation processes during interaction of matter with radiation.

Initially a photoelectron is emitted, resulting from excitation by X-ray photons creating a hole in the atom collective (Photoeffect). The kinetic energy of the photoelectron can be described as:

$$E_{kin} = h\nu - E_B \tag{2.3}$$

E_B: binding energy of the electron

Primary photoelectrons, which are excited to significant higher energy levels or emitted, create electron holes within the atomic structure, which exhibits a major discrepancy of the electronic equilibrium, resulting in so called secondary electron processes.

Secondary processes can be divided into specific and unspecific excitation processes. Specific secondary processes are characterized as processes, where a defined amount of energy is converted into a second excitation process. For

unspecific processes an unspecific energy loss is characteristic. A radiant specific secondary process is X-ray emission, non radiant are plasmon, Auger as well as shake-off and shake-up excitations.

For *X-ray emission* an electron hole is created by a primary process (not necessary photoemission). In consequence the hole is filled by an electron, initially located at a higher energy level, emitting the difference in energy as characteristic X-ray photons (s. experimental setup). The photon energy is material specific and independent from the excitation source for the primary electron emission process.

Plasmons are collective oscillations of the free electron gas density caused by an energy transfer from the passing, emitted electron to the electron collective. Plasmon oscillations are quantized and therefore plasmon signals are detected in characteristic signal spacings.

The *Auger effect* is a secondary electronic process in excited atoms resulting from the inter- and intrastate transitions of electrons. The hole, created due to the primary photoemission, can be filled by an outer shell electron, loosing the energy amount equal to the difference in orbital energies. The transition energy can be transmitted to a second outer shell electron, which will be emitted from the atom if the transferred energy is larger than the orbital binding energy. The emitted electron is the so called Auger electron.[21] [25] [26] In contrast to the emitted photoelectrons the energy of detected Auger electrons is independent from the excitation energy. The nomenclature for Auger transitions follows the rule for ordinary X-ray transition like AB_xC_y (e.g. KL_1L_{23}). Where A is the energy level of the incident primary electron, B the level of the relaxing electron and C the level where the respective Auger electron is emitted from. The capital letters denominate the electron shells (K, L, M etc.) and the indexes the respective orbitals (1 (s-orbitals), 23 (p-orbitals), 45 (d-orbitals), 67 (f-orbitals)).

In approximation the kinetic energy of an Auger electron for the transition ABC can be estimated as:

$$E_{ABC} = E_A - E_B - E_C \tag{2.4}$$

E_A: energy of core level electron
E_B: energy of first outer shell electron
E_C: energy of second outer shell electron

As the binding energy of electrons in the presence of core close holes is increased compared to the same level in a neutral atom, E_{kin} of the Auger electron for an atom with the atomic number z can be written as:

$$E_{ABC} = E_A(z) - \frac{1}{2}[E_B(z) + E_B(z+1)] - \frac{1}{2}[E_C(z) + E_C(z+1)] \qquad (2.5)$$

Emission of inner valence electrons results additionally in *plasma oscillation* as well as *shake-off* and *shake-up* processes especially for heavier elements. The shake-off and up secondary processes are sample dependent and caused by a defined excitation of a second electron during the photoemission process. Thus, the respective photoelectron is emitted with accordingly lower kinetic energy. If the second electron is likewise emitted the process is called shake-off. In shake-up processes the second electron is excited to a higher orbital and remains bound in the electron collective.

The XPS Spectrum

In XPS spectra the counting rate (intensity) of detected electrons is plotted versus the kinetic/binding energy. For comparable results usually E_B is plotted in literature. In the range of low binding energies characteristic signals for binding states close to the solid state occur caused by photoemission of electrons from the valence band. Inner valence signals are detected at higher E_B in the spectra.

The number, position, character and order of signals is sample specific. The line width in the spectra is dependent on the natural line width of the elements, the line width of the radiation source and the resolution and setup of the analyzer. Besides the characteristic photoemitted electrons the different secondary processes generate characteristic signals within the spectrum. The background of the spectra is affected by inelastic scattering of electrons, resulting in an energy loss accordingly altering the detected energy of electrons or by photoelectrons which were excited by Bremsstrahlung. These processes result in a background of counts that derive from electronic states other than the element specific lines. The shape of the background can be determined by the probability distribution for electrons with a given kinetic energy undergoing some modification to their initial value. Unfiltered X-ray sources include photons from Bremsstrahlung excitation of electronic states out of the reach of monochromatic sources. Thus, the background intensity of a XPS spectrum

is typically lower when monochromatic sources are used. Figure 2.3. shows exemplary a schematic structure of a XPS spectrum and the assignment of the respective underlying excitation processes.

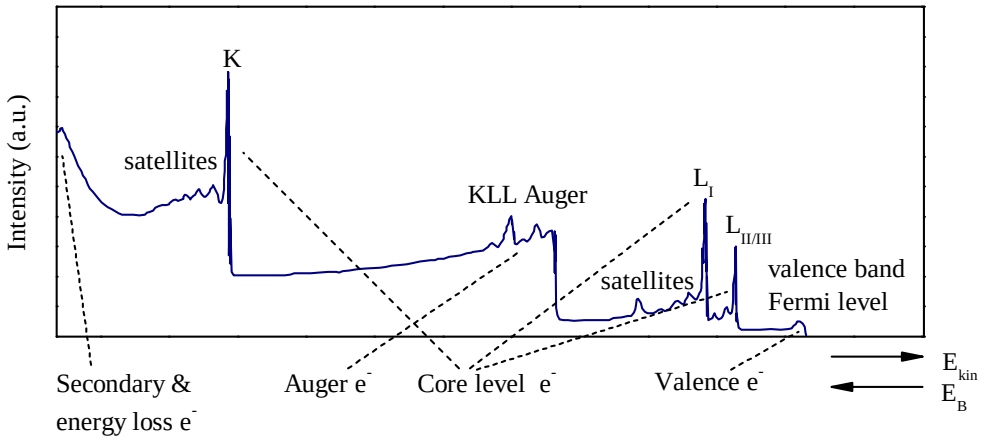


Figure 2.3.: Schematic XPS survey spectra to illustrate the different signals.

Besides the sample dependent secondary signals as Auger and satellites (plasmons, shake-up and off) processes, sample independent satellite peaks are detected. The so called spikes result e.g. from non monochromatic excitation radiation or contaminated anode materials.

Peak-Structure of Core Level Signals Spin-orbit coupling is the interaction of the electron spin magnetic moment with the magnetic moment due to the orbital motion of the electron. A consequence of spin-orbit coupling is the intermixing of zero-order states of different multiplicity. This effect may result in a fine structure of inner valence signals from p-, d- and f-orbitals in doublets and is called spin-orbit splitting. Descriptively the explanation can be carried out with a semi classical model. Depending on the orientation of the electron spin to the orbital angular momentum two different energy states can be adopted.

The orientation of spin can be described by the total angular momentum j:

$$j = l \pm s > 0 \tag{2.6}$$

with l: orbital angular momentum and s: spin quantum number.

The total orbital momentum of paired electrons is zero, thus in this case the spin-orbit coupling is irrelevant. Caused by photoemission, electrons are emitted and therefore removed from the electron collective. Due to spin-orbit coupling the remaining and emitted electrons can both exist in two different energy states and therefore the emitted photoelectron causes a doublet in the spectrum. Splitting of signals is characteristic and dependent on the atomic number. Within one group in the periodic table of the elements it increases at a constant orbital angular momentum from top to bottom. Examining one element the splitting decreases with increasing orbital angular momentum. Hence, the peak intensity is consistent with the ratio of degeneration. The intensity ratio of the peaks of a doublet can be predicted with help of the degeneration g:

$$g = 2j + 1 \tag{2.7}$$

Labeling of inner valence signals consists of the element symbol (X), the main quantum number (n), the symbol of sub shell (y) and the total angular momentum j: Xny_j (e.g. $Au4f_{5/2,7/2}$).

Experimental Setup

UHV conditions are required during XPS measurements to enable the emitted photoelectrons to be analyzed without interference from collisions in the gas phase. Therefore the experimental setup has to be installed in an UHV-System with a μ metal shielding and an optimal working pressure below 10^{-10} mbar during measurement performance.

Further components of the system are the X-ray source, the electron analyzer to separate electrons of different kinetic energy and a detector. Since the energy of the photoelectrons is dependent on the energy of the incident X-rays, the X-ray source has to be monochromatic or at least unwanted undefined X-rays need to be removed by special filters.

X-rays itself were discovered and described by Wilhelm Conrad Röntgen in 1896 who was honored by the first Nobel Prize in Physics in 1901.[27] They are generated in a X-ray tube by targeting an electrode with high accelerated electrons. X-rays are electromagnetic radiation with a wavelength of 10^{-8} m to 10^{-10} m and energies in the range from 1 keV to 250 keV depending on the electrode materials. For XPS relatively soft X-rays in the range of 200 - 2000 eV are applied.

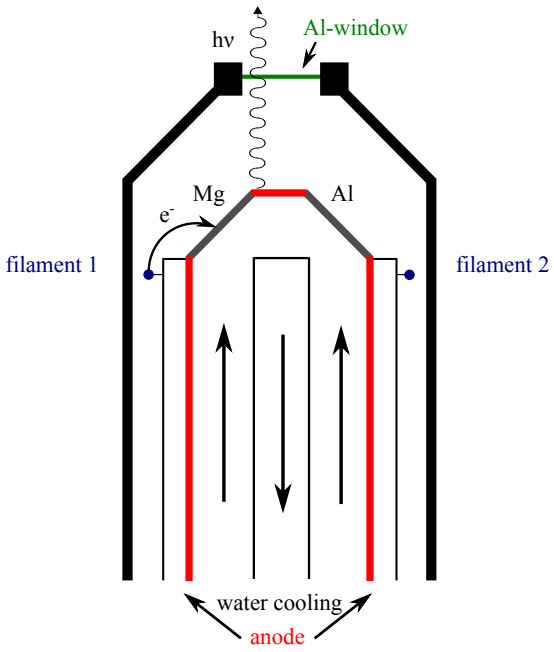


Figure 2.4.: Assembly of a dual Mg/Al anode X-ray tube for XPS incident beam generation (after[23]).

In X-ray tubes electrons, which are emitted from an incandescent cathode, are accelerated to the anode at ground potential by applying a high voltage of 10 to 15 kV between anode and cathode. By the interaction of the accelerated electrons and the anode materials electrons are slowed down, sending out the difference in energy as continuous Bremsstrahlung with the intensity being dependent on the acceleration voltage. Besides the Bremsstrahlung, characteristic radiation is generated by electrons, which hit the anode target, emitting one electron from the target while leaving an electron hole behind (photoemission). These vacancies can be filled by a relaxing electron from a higher energy level and emission of the difference in energy as characteristic X-rays. X-ray lines are element and shell specific and therefore dependent on the anode material. Due to the high intensity of the transition from L- to K shell, K_α lines are used for XPS analysis.

The most common used anode materials for XPS are magnesium (Mg) (K_α : 1253.6 eV) and aluminum (Al) (K_α : 1486.7 eV) in dual Mg/Al anode X-ray tubes. A thin Al-window prevents secondary and back scattered electrons to reach the sample and to reduce the unwanted Bremsstrahlung. Prism, grating or single crystal monochromators are applied using the Bragg reflexion

to get highly monochromatic beams depending on the application and type of equipment. Due to the high heat loss during the X-ray generation the tubes are cooled with an internal water circulation (s. figure 2.4.).

Analyzers which are used for electron spectroscopy are concentric spherical analyzers (CHA). They consist of two concentric precision hemispheres with an inner and outer hemisphere. The incoming electrons are focused to an entrance slit by electromagnetic lenses. By applying a negative potential to both hemispheres, the electrons, entering the analyzer, are focused to an exit slit due to the resulting electric field. The electric field is tuned by the applied voltage. Therefore electrons with different kinetic energies leave the analyzer energy-selective for subsequent detection. Most frequently used are channeltron and Faraday detectors combined with secondary electron multipliers (SEM), where the incident electrons are initially multiplied to amplify the resulting signal. Computer software is utilized for signal processing and data analysis. A general scheme of a XPS setup is shown in figure 2.5.

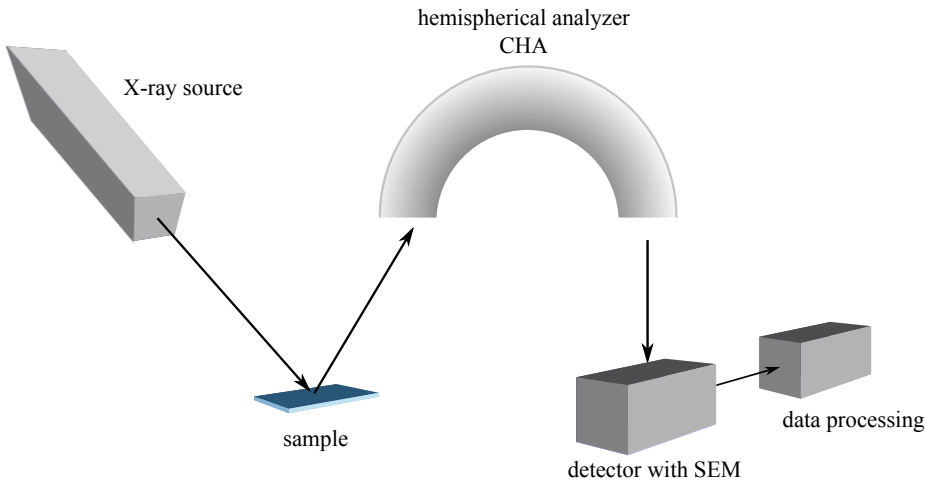


Figure 2.5.: Experimental setup of the different components for XPS.

Non monochromatic X-rays: X-Ray satellites Besides the main core level signals excited by $K_{\alpha_{1,2}}$, low intensity peaks can be detected caused by non monochromatic X-ray excitation which is given in the present thesis referred to as X-ray satellites. Those less probable transitions result in X-ray satellites at defined energies in ratio to the main signal and defined area ratios.

The known satellite positions of the different excitation sources are given in table 2.1.

Table 2.1.: High energy X-ray satellite lines.[21]

	Separation from main signal (eV) (relative intensity (%))	
X-ray line	*Mg*	*Al*
$K_{\alpha'}$	4.5 (1.0)	5.6 (1.0)
K_{α_3}	8.4 (9.2)	9.6 (7.8)
K_{α_4}	10.0 (5.1)	11.5 (3.3)
K_{α_5}	17.3 (0.8)	19.8 (0.4)
K_{α_6}	20.5 (0.5)	23.4 (0.3)
K_{β}	48.0	70.0 (2.0)

2.2. Scanning Probe Microscopy: SPM

Scanning Probe Microscopy is a category of several techniques which are all based on the mechanical scanning of respective specimens, line by line with an extremely sharp tip in the near field of the sample and the probe. The meaning of near field is different for the different SPM techniques. With SPM techniques imaging of the topography, in 3D on a fine scale, down to atomic resolution, is possible directly in real space. When the tip moves in proximity to the investigated object, interaction forces between the tip and the surface influence the movement of a cantilever which is detected by a sensor and converted into a topographic information. Depending on the technique, information about the physical surface structure, electronic structure or magnetic and electrical properties can be obtained. Thus, resolutions down to the atomic range are possible.

The most common routine scanning probe techniques are Scanning Tunneling Microscopy (s. section 2.2.1.). and Atomic Force Microscopy (s. section 2.2.2.).

2.2.1. Scanning Tunneling Microscopy: STM

The Scanning Tunneling Microscopy is theoretically based on the tunnel effect of quantum mechanics. The distance dependent tunnel current is measured

between a rastering sharp tip and the sample to gain information about the electronic structure of the substrate. It was invented by Gerd Binnig and Heinrich Rohrer in 1981 and awarded with the Nobel Price in Physics as an outstanding technique for surfaces analysis in 1986. The invention of STM opened the way for the development of several SP techniques.

Content of Analysis

With STM determination of nano structured surfaces as well as monitoring of dynamic processes is possible. As no unbound electrons are incorporated in the experiments analysis in air, liquids and within the vacuum are possible. Conducting and semi conducting samples can be scanned. Besides surface analysis STM is often utilized for in-situ electrochemical experiments. STM is a complete non destructive technique as the tip and sample are never in contact during the measurements, which is one of the main advantages.[28] [29] Single atoms and molecules can be examined. Perpendicular to the surface resolutions down to the pm range can be achieved. Lateral resolutions extend typically the sub Å range. Surface defects as well as ordered or non ordered structures can be observed. By STM a local mapping but no general survey of the sample can be obtained. Even if the scan range of STM leads into the μm range, it is not possible to gather information about the complete sample from the collected data of the respective part. Interpretation of STM images is not trivial and should be accomplished by quantum mechanical calculations for completely unknown samples. With STM local densities of states (LDOS) at the Fermi level are detected instead of direct topographical information. With positive bias the tip is operating as cathode, therefore the anti bonding density of states is analyzed, with negative bias the tip acts as anode and the bonding density of states are visualized. STM is often combined with other analysis techniques to identify the chemical species on the surface.

Theoretical Background

The tunnel effect of quantum mechanics is the basic principle of STM. This effect allows particles with small mass and size (e.g. electrons) to exceed space and energy barriers with a finite probability due to their wave character. In classical mechanics particles with a total energy smaller than a potential barrier which needs be exceeded are reflected. In quantum mechanics the

mathematical solution of the wave function within and behind the barrier is unequal to zero, hence the particle can surmount a potential barrier even though the total energy is smaller than the energy of the barrier. In the following only electrons should be considered as tunneling species.

In STM a tunneling voltage U_t is applied between a metal tip and a conductive sample. The distance between sample and tip is the potential barrier which can be exceeded by the tunneling electrons. Due to the tunneling effect a tunnel current, I_t, in the range of 1 nA, can be detected, which is exponentially dependent on the distance between tip and sample. The electrons tunnel elastically from the occupied states of the cathode to the unoccupied states of the anode.[28]

For planar electrodes and free electrons the tunneling current can be approximately defined as:

$$I_t = c_1 \cdot U_t \cdot e^{-c_2 d\sqrt{\phi}} \tag{2.8}$$

I_t: tunneling current
c_1: constant, which includes the electron density of sample and tip
U_t: bias between tip and sample
c_2: constant, dependent on work function ϕ of tip and sample
d: distance between tip and sample

A quantitative description of the tunneling process can be given by solving the Schrödinger equation for the region prior, behind and within two potential barriers.

The fraction of the particles which tunnel through the potential barrier is described by the transmission coefficient. The tunneling probability increases with increasing energy of the particle and decreases with increasing height and width of the potential barrier and mass of the particle.[30]

The high resolution of STM results from the exponential dependency of the tunneling probability from height and width of the potential barrier and therefore the distance between the sample and tip.

For STM different tunneling models in 3D and 2D can be utilized using different parameters and models to describe the sample-tip tunneling system and behavior. An overview of different tunneling models in STM can be found in e.g.[28],[29],[31] or[32].

Experimental Setup and Operation Modes

The central unit of a STM is the sharp metal tip (mostly platinum-iridium $PtIr$ or tungsten W), which is in ideal case as sharp as a single atom at the apex. The tip is connected to a piezo electric element, which enables the precise 3D movement of the tip in the sub nanometer regime. For STM analysis a bias U_t of several mV is applied between sample and tip. If the tip is approached down to a few Å to the sample, a tunnel current I_t in the dimension of 1 nA can be detected. To scan the surface the tip is moved raster like, line by line over the sample. Figure 2.6. shows schematically the experimental setup of a STM.

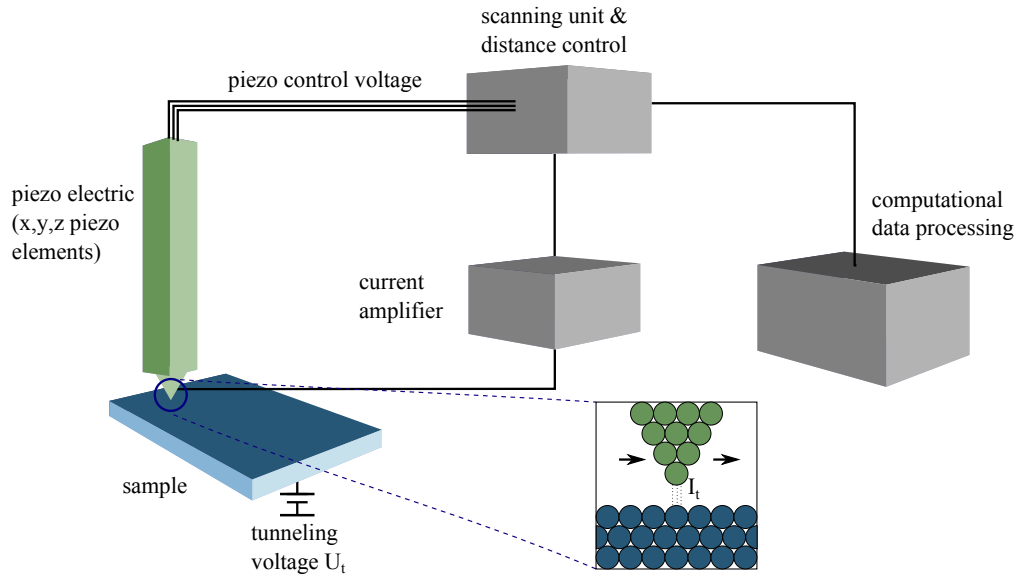


Figure 2.6.: Experimental STM system setup.

Vibration damping and shielding against electromagnetic radiation are crucial factors of STM equipment design. Due to the high resolution, STM requires an adequate vibration damping (passive and active), since the distance between sample and tip may need to be maintained constant at approx. 0.1 pm. Interferences can be minimized by the choice of the right site and respective materials for the experimental setup. Piezo corrections can be applied for active vibration damping.

Different operating modes are deployed with respect to the required information and specimens to be determined. Constant Current Imaging (CCI) is the most applied mode in STM. In CCI mode, the tunnel current between sample and tip is maintained at a constant value by a feedback loop. The z-shift is controlled by the appropriate voltage U_z at the piezo electric actuators. x- and y- coordinates can be controlled by U_x and U_y. Detected is the deflection of the z-piezo element as a function of the position $z(x,y)$, which can be translated into the sample "topography". Due to the constant distance between the sample and the tip, relatively rough samples can be analyzed in CCI mode. The scan speed is limited by the feedback loop, which is a major drawback of CCI. Constant Height Imaging (CHI) mode, where the tip scans the sample in a constant height, is applied for atomically smooth samples, which can be rastered with a faster scan speed.

To achieve atomic resolution, the response of the preamplifier needs to be faster than the scanning speed, as the tunnel current has to be modulated with respect to the sensitivity of the exponential dependency. The tunnel current is detected by recording the probe-surface interaction as a function of the position. The scan speed for CHI is much faster than for CCI, since the feedback loop ceases to apply. In CHI images only atomically smooth specimen can be analyzed, hence for rough samples the tip can crash into the samples, causing sample and tip damaging on the one hand and loss of the tunnel current, due to an oversized distance between sample and tip, on the other.

A major drawback of STM are the very sensitive tips, which structure change during measurements. Interaction between sample and tip can cause changes on the determined surface. Moreover the voltage can vary during imaging. The piezo elements can cause further errors like piezo bow, hysteresis, non linear expansion or creeping of materials. Therefore, the reproducibility of STM images is demanding.[33]

Beside the experimental difficulties the exact shape of the tip is rarely known in the experiments, so that the quantum mechanical modeling can not be executed correctly. Inelastic tunneling transactions cause further problems in STM, but can be used in other techniques (Inelastic Electron Tunneling Spectroscopy) for specific excitation of adsorbates by tunnel electrons.[29]

2.2.2. Atomic Force Microscopy: AFM

In Atomic Force Microscopy, the short range forces between the tip and the samples are analyzed alternatively to the distance dependent tunnel current in STM, while screening a sample surface to gain for topographic information. AFM was developed by Binnig et al. in 1986 as a result of the detectable mechanical forces during conventional STM analysis.[34] The determination of mechanical forces under very low contact pressure instead of electrical interactions opened the road to investigate electrically non conductive samples. In AFM, the force of interaction depends on the sample/tip distance, the appearance and topography of the sample. Topographic as well as local analysis of cohesiveness and adhesion can be performed with AFM. A short conclusion of the AFM basics and principles from[35], [29] and[36] is given in this paragraph.

Theoretical Background

For AFM analysis the tip is connected to a bending cantilever. While scanning the surface, the force of distortion of the moving cantilever is detected. The distortion of the cantilever is based on Hooks law. Under consideration of the spring constant of the cantilever, the effective force can be measured and converted into a topographic image of the scanned surface.

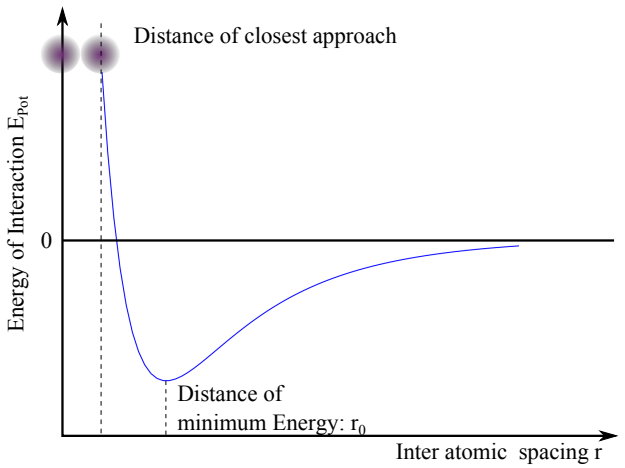


Figure 2.7.: Atrractive and repulsive forces in dependency on the inter atmoic spacing between two atoms, Lennard Jones potential.

Short range forces between sample and cantilever are attractive van der Waals and repulsive electrostatic interactions. The tip-sample interaction can be described by the Lennard-Jones potential (s. figure 2.7.). The Lennard-Jones potential is a mathematically simple approximation, which describes the interaction of neutral atoms or molecules depending on their distance. For distances of 10^{-7} to 10^{-8} m attractive van der Waals forces are dominant. Within a distance of several Å the electrostatic, repulsive forces are dominant.

Experimental Setup and Operation Modes

A basic AFM consists of a cantilever with a sharp tip, typically made of silicon or silicon nitride (depending on the sample type), which interacts with the surface to be investigated. The respective bending of the cantilever due to the mechanical forces is measured with a laser beam, which is deflected by the top surface of the cantilever. The so formed optical signal can be detected by a position sensitive array of photo-diodes (photo detector). The accuracy of the measurement of the cantilever bending is crucial for the accuracy of the analysis. Piezo elements are applied for the exact cantilever positioning. Different tip geometries and materials are utilized for respective analysis.

As in STM, different operating modes are applicable in AFM measurements. In contact mode, which is the most commonly used scanning mode, the cantilever is in direct mechanical contact to the sample. It can be divided into constant force and constant hight imaging. With constant height imaging the cantilever is moved in constant distance to the sample and the force is measured. In constant force mode the force is the constant parameter which can be regulated by a control loop. As in STM the regulated technique is speed limited due to the switching speed of the control loop. Tapping mode is another alternative scanning technique for AFM. In this case, the cantilever is set under oscillation by a high frequent AC voltage applied to the piezo elements. Due to interactions between the tip and the sample, the amplitude of oscillation varies in dependency on the surface topography. Other operating modes like pulsed force or lateral force mode are described e.g. in[37].

In AFM attractive or repulsive forces between 10^{-9} to 10^{-6} N can be measured. High resolution top end equipment enables detections down to 10^{-13} N. The resolution of the AFM is limited by the curvature radius of the tip, which is typically in the range of 10 to 20 nm. AFM does not need to be based on a can-

tilever, in Scanning Near-field Optical Microscopes (SNOMs) tapered etched optical fibers are used as styluses and the damping of the fiber is detected while, the stylus oscillates parallel to the surface. Magnetic, electrical e.g. and other characteristic forces can be measured with other force microscope types.

2.2.3. Film Roughness

The film roughness parameter used in the present thesis is the root mean square roughness (RMS), which can be calculated after:

$$RMS = \sqrt{\frac{\sum_1^N}{(Z_i - Z_{ave})^2} N} \tag{2.9}$$

Z_i: current height value within the given area
Z_{ave}: average height within the given area
N: number of points within the given area

In commercial AFM systems, as applied in the present thesis, the RMS values can be extracted directly from the measurement software.

2.3. Electron Microscopy: EM

The development of science led to new imaging techniques for increasingly smaller structures, which are much more efficient than conventionally used light microscopes. The resolution of a microscope is limited by the Rayleigh criterion (s. eq. 2.11.). To visualize small structures with high resolution, particles with a de Broglie wavelength shorter than the structure are necessary. To obtain resolutions in μm range, electrons as particles are eligible.

In general there are two types of electron microscopes, which are totally different in analysis methods. In Transmission Electron Microscopy (TEM, s. section 2.3.1.), transmitted light is used to generate an electron image of ultra thin samples. In Scanning Electron Microscopy (SEM, s. section 2.3.2.), 3D images of determined samples are generated in reflection mode. The different techniques exhibit a slight variance of resolution, enabling to investigate many types of samples. Electron Microscopy techniques are in the first place used to illustrate and analyze nano structures and defects up to atomic resolution.

By the combination of imaging and analysis techniques e.g. Energy Dispersive X-ray Analysis (EDX, s. section 2.5.), the local constitution and elementary distribution can be quantified up to the nanometer scale. Detailed analysis on 3D structures and bulk volume can be implemented by electron tomography. To achieve better resolved images, High Resolution Electron Microscopy (HREM) is implemented. HREM is a powerful tool for unraveling the structural features specifically in non-stoichiometric compounds. It is able to give an insight into the real structure and therefore overcomes problems like multi domains. HREM opens the possibility to obtain diffraction data in the back focal plane and images showing the projection of the atoms arrangement of a structure at atomic scale simultaneously.[38]

With respect to the required information, the different techniques are utilized. EDX is used for elemental mapping, morphology can by analyzed with SEM. If the composition of a materials is in the focus of research, EDX and EELS (Electron Energy Loss Spectroscopy) are the methods of choice and for structural investigations (HR)TEM, Scanning TEM (STEM) and diffraction techniques are appropriate analysis methods.

Theoretical Background

In electron microscopes, electrons instead of light are used to image nano scaled samples. The wavelength of electrons can be described based on the idea of wave particle duality by the de-Broglie equation:

$$\lambda = \frac{h}{p} = \frac{h}{\sqrt{2m_e E_{kin}}} \tag{2.10}$$

λ: wavelength
p: particle momentum
m_e: electron mass

The resolution of microscopes, δ, can be described by the Rayleigh criterion:

$$\delta = 0.61 \frac{\lambda}{n \sin \alpha} \tag{2.11}$$

Where λ is the wavelength of incident light, n the refraction index of determined medium and α is the half aperture angle of the objective.

The term '$n \sin \alpha$' is the numerical aperture of an optical system. It is a dimensionless number that characterizes the range of angles over which the system can accept or emit light. At $\lambda \approx 400$ nm (in the visible) it correlates to a resolution of 244 nm. Wavelength of electrons can be calculated according to equation 2.10 referred to their respective kinetic energy depending on the acceleration voltage.

If an electron is accelerated with an acceleration voltage U_b, the following correlation shall apply:

$$E_{kin} = eU_b = E_{pot} \tag{2.12}$$

E_{pot}: potential energy
e: electric charge of electrons

Introducing the kinetic energy E_{kin} into equation 2.10 the wavelength can be described depending on the acceleration voltage:

$$\lambda = \frac{h}{p} = \frac{h}{\sqrt{2m_e U_b e}} \tag{2.13}$$

Considering the relation between λ and U_b, it is evident that by increasing the acceleration voltage and therefore the velocity (kinetic energy) of the electrons a decrease of electron wavelength is obtained. Thus, better resolution can be achieved. At high acceleration voltages (>100 kV), a relativistic term including the speed of light, c, has to be respected additionally:

$$\lambda = \frac{h}{p} = \frac{h}{\sqrt{2m_e U_b \left(1 + \frac{eU_b}{2m_e c^2}\right)}} \tag{2.14}$$

2.3.1. Transmission Electron Microscopy: TEM

Content of Analysis and Sample Requirements

Analytical Transmission Electron Microscopy provides the facility to determine the structure, morphology and composition of solid state materials in ultra thin layers from the micrometer to the nanometer regime with high spatial resolution. The first TEM was built by Max Knoll and Ernst Ruska in 1931. Nowadays, TEM is applied in the first place to determine the structure and

chemical constitution of scientific samples. Defect and damage analysis and furthermore quality assurance is performed with TEM, too.

In TEM analysis electron absorption leads to significant heating of the sample. Therefore the sample thickness is limited to 100 nm resulting in complex, time consuming sample preparation techniques especially for solid state materials. In the present thesis, cross sectional samples of the prepared thin films on the respective substrates were analyzed with the TEM to determine the film thickness and structure of the different oxides. Cross sections were prepared using the focused ion beam (s. section 2.4.). Cross sectional imaging should be mentioned as XTEM in the following.

Apparatus

The TEM operates analogous to the optical microscope with a system of vertical aligned magnifying lenses. An electron beam is focused by electromagnets. The magnets generate an inhomogeneous magnetic field, which bundles and directs the beam. To avoid scattering of electrons and interactions with unwanted molecules from air, the column is evacuated to high vacuum. The electron beam is generated by the filament cathode (normally made from W or LaB_6), a current carrying and thereby heated hair pin shaped coil. A potential gradient, which results from an applied high voltage, accelerates the electrons in the direction of the anode. Usually acceleration voltages from 80 kV (TEM) to 300 kV (HRTEM) are used, depending on the required resolution of the captured images.

Field emission electron guns (FEG) allow imaging in higher resolution due to a bright (100 times higher than LaB_6 tips), narrow, highly stable and well defined electron beam. In FEGs the electrons are emitted due to an applied high voltage of several kV to the cathode and the resulting potential gradient to an internal anode within the gun instead of heat emission. A detailed description of the operation mode of a FEG can be found in[39]. The incident electron beam interacts with the sample and an image can be formed from collected transmitted electrons. Electrons are deflected depending on the sample material. The deflection increases with increasing atomic weight and is therefore element specific. Detected images can be magnified and focused by the projective (a second lens system) onto an imaging device such as a fluorescent screen or a CCD camera.

Figure 2.8. illustrates the alignment of the different components inside the TEM column (a) and the specific beam path in bright field mode (b).

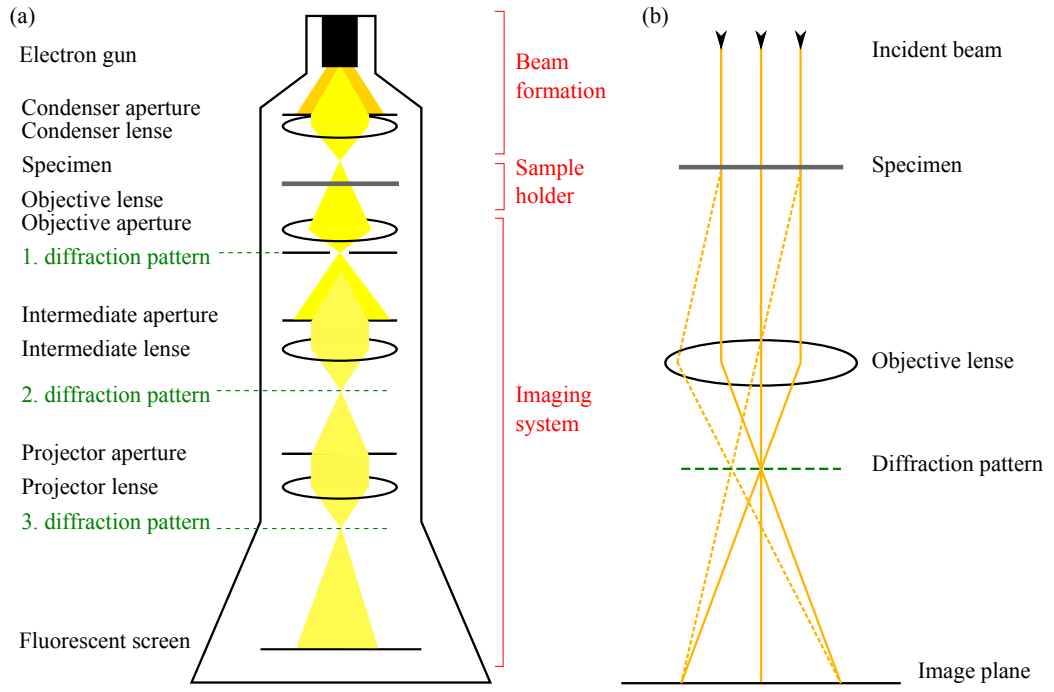


Figure 2.8.: Alignment scheme and beam path inside the TEM column (a). Beam diagram in bright field (BF) mode (b).

TEM images are black-and-white shots, whereas the gray level is dependent on the electron density and therefore of the material composition on the respective sample position. Theoretically the resolution of the TEM is limited by the acceleration voltage of the electrons. Experimentally the lens and sample quality confine the highest possible resolving power. Due to lens aberration e.g. spherical aberration, astigmatism and Boersch-Effect the final magnifications are limited up to 300000, although theoretically much better resolutions are applicable. Therefore the quality and correct alignment of the lens system is one of the main aspects for high quality imaging.

High Resolution TEM: HRTEM High Resolution TEM is an imaging mode of TEM that allows the determination of crystal structures of samples at the atomic scale.[40] Due to the high resolution, HRTEM is a precious technique to study nano scale properties of different crystalline materials. In HRTEM

mode, higher acceleration voltages up to 1 Mio. Volts, in the majority of cases 200 kV, are utilized to get higher resolution. Resolution up to 0.08 nm are possible with high end microscopes like the One-Ångstrom-Microscope at Berkeley Lab.[41] With low acceleration voltages, the thickness of the sample is limited to approx. 100 nm because of aberration. With acceleration voltages up to 10^6 Volts samples up to a thickness of 1 μm can be determined.[42]

Scanning TEM: STEM In Scanning Transmission Electron Microscopy, a supplement mode of TEM, the samples are rastered spot by spot by a tiny, convergent focused electron beam. The interaction between electron beam and the specific spot of the sample generates signals of emitted, backscattered and secondary electrons as well as X-rays as in TEM. Characteristic signals are detected and combined to a full image of the sample. By converting the signals into a contrast image, information about alignment, structure and topography can be determined. Additionally diffraction patterns can be recorded for crystallographic analysis. Different detectors give discriminate analysis contents, so that both quantitative and qualitative information can be investigated.

The resolution of STEM is dependent on the ratio of the image and scan width:

$$M = \frac{D}{d} \tag{2.15}$$

D: horizontal image width of the full image
d: horizontal length of the scanned line

The smallest possible resolution is limited by the smallest spot of the sample which can be imaged, and therefore by the probe spot diameter. With FEGs, high resolutions down to 0.2 nm are achievable.

Due to the punctual signal detection in STEM, different types of detectors can be used, which allow more detailed analyses of the samples than with conventional TEM. The different detector types in STEM facilitate more efficient utilization of the beam and sample interaction. In figure 2.9. the alignment of the different detectors within the TEM column is illustrated.

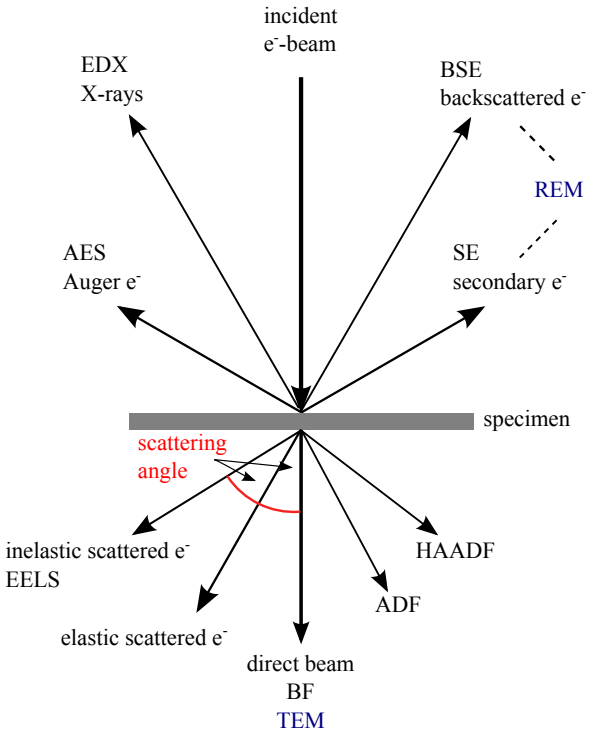


Figure 2.9.: Alignment of detectors for different electron/matter interactions to be determined.

Bright Field (BF) detectors detect the transmitting beam and the direct intensity from the spot of the specimen analogous to TEM. Parts of the scattered beam can be detected by Annular Dark Field (ADF) detectors, where the measured contrast mainly results from electrons diffracted in crystalline areas, but is superimposed by Rutherford scattering. With BF and ADF detectors crystalline areas, defects and grain boundaries, phases, and particle sizes can be determined. z-contrast can be achieved by using High Angle Annular Dark Field (HAADF) detectors, which detect electrons emitted in higher angles and almost only incoherent Rutherford scattering contributes to the image. It opens the way to visualize structures and defects, small clusters or even single atoms of a heavy metal in a matrix of light elements can be observed. Additionally EDX and EELS detectors are used for elementary analysis, hence the combination of analytical methods with STEM is a main application in practical work. Further detector types and their functionality can be found in[39] and[43] .

2.3.2. Scanning Electron Microscopy: SEM

Content of Analysis and Sample Requirements

Scanning Electron Microscopy is utilized to illustrate surfaces of conductive samples by rastering the sample with a high energetic electron beam. The first SEM image was obtained by Max Knoll in 1935. In SEM, the samples are scanned in a raster scan pattern by a primary electron beam, resulting in the emission of secondary electrons, which give information about the topography of the determined sample. Furthermore back scattered electrons, characteristic X-rays, cathodoluminescense, specimen current and transmitted electrons are induced by the electron beam. The different types of electrons can be analyzed by different detector types. Most commonly used in SEM are back scattering detectors. The detected signals result from the interaction of the incident beam and the atomic sample surface and are dependent on the slope of the surface.

SEM is a surface sensitive technique for topography analysis in high resolution down to revealing details with less than 1 nm. The resolution of a SEM is generally much lower than the resolution of a TEM, but a far better depth of field can be achieved. Thus, SEM is particularly suitable for analysis of rough surfaces.

Compared to TEM, sample preparation for SEM is simple, since no transmission is necessary and no thin layers are needed. Samples for SEM are obliged to be conductive, therefore non conductive samples need to be coated by a conducting layer (e.g. Au) prior to SEM analysis.

Apparatus

In SEM, the electron beam is generated analogous to TEM with acceleration voltages between 300 V and 30 kV. The electron beam is focused by a condenser lens system to one spot of the sample and moved raster like by deflecting coils. As mentioned above, the incident beam interacts with the surface atoms of the samples, resulting in characteristic emission effects. Emitted secondary back scattered electrons are collected with a detector and transformed into a SEM image on a computing monitor. The number of detected electrons relates to the intensity of the signals on the monitor, like in TEM analysis. Magnification results, as in STEM, from the ratio of the dimensions of the raster and the raster on the monitoring device itself. EDX (s. section 2.5.) detectors are

added for chemical elementary analysis in the micrometer regime and phase composition by detecting the characteristic emitted X-rays. Field emitting sources can again be utilized for higher resolution imaging.

2.4. Focused Ion Beam: FIB

Content of Analysis

As already mentioned in section 2.3., particles with a de-Broglie wavelength shorter than the structure are necessary to visualize small structures with good resolution. As it can be seen from the name, in the Focused Ion Beam (FIB), ions are used to image structures in the nm range. FIB columns can either be used as stand alone single beam instruments or in combination with other analytical components. The most common way is the FIB/SEM dual-beam system.

FIB offers a wide range of sample preparations for numerous analytical techniques. It has expanded to applications in different parts of material science, biology and pharmaceuticals.[44] FIB has become an essential tool in semiconductor analytical laboratories due to the possible reduction in the probe size and reliable and fast analysis capabilities of virtually any region of interest.[45] Magnifications up to 100 000 times with a very good depth profile field are available.[46] Additionally the FIB can be used for micro structuring and revolutionized the area of TEM specimen preparation.

Experimental Setup

The basic FIB instrument consists of a vacuum chamber, an ion column, the liquid metal ion source (LMIS), a detector and the sample stage. For image generation, different detectors are installed, depending on the type of FIB system. For structuring and deposition experiments, a gas system with different precursors e.g. for Pt or C (carbon) deposition is integrated. The whole system is controlled by a computer set up. Figure 2.10. shows a scheme of the FIB column as well as the LMIS.

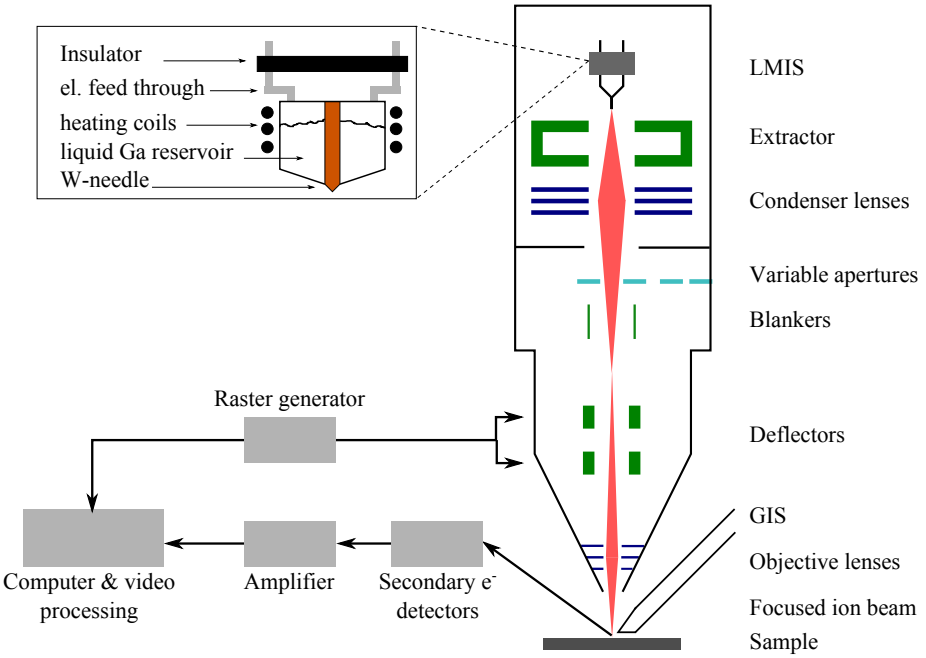


Figure 2.10.: Schematic illustration of a typical FIB column including the resulting ion beam and a detailed image of the LMIS.

In general, a FIB instrument looks like a SEM, except that in the FIB an ion beam instead of the electron beam is used to scan the sample. In both microscope types, the intensity of secondary produced electrons at each raster position is displayed to create an image of the sample. In FIB additionally the secondary ions are detected. Gallium (Ga) ions are most commonly used to generate the ion beam. Alternative materials are helium (He) or neon (Ne). Ga is preferentially used because of the low melting point and the availability in liquid state near room temperature, which minimizes any reaction or inter diffusion between the liquid and the W-needle substrate. In addition, Ga can be focused to a probe size below 10 nm in diameter. To generate the ion beam, a LMIS is used to wet a sharp W-needle. Therefore, a reservoir with liquid Ga is positioned in contact to the W-needle to wet the needle and flow to the W-apex. By passing through a strong electric field, on the tip Ga^+-ions are generated, due to a field emitting process and accelerated down the FIB column towards the sample. Typical acceleration voltages in FIB are between 5 and 50 kV. A system of different electrostatic lenses focuses the ion beam on the sample. Stigmators generate a circular beam-profile, which shows a Gaussian shape in cross section. Due to their high mass, the towards

the sample accelerated ions generate a sputter process at the surface, which results on the one hand in excavation of material and in Ga-ion implantation into the sample and on the other hand in amorphization of the surface layers. This aspect has to be taken into account for FIB analysis and patterning.

Another feature of the FIB is ion beam assisted chemical vapor deposition. It is widely used for Pt deposition for TEM sample preparation in order to protect the top surface of interest from damages, due to the sputter processes of the ion beam. Therefore, a precursor is evaporated and injected by a gas injection system (GIS), which is equipped with a precursor reservoir and a gas injection needle. The needle is brought close to the surface after injecting the gaseous precursor and the molecules adsorb on the surface. By rastering the sample with the Ga^+ ion beam, the precursor molecules decompose to the metal layer and gaseous decomposition products, which are removed from the chamber by the vacuum system. Beside Pt, also other metals and insulators can be deposited with the GIS, generating nano structures on different substrates. Thus, FIB is also known as an instrument for constructive material deposition.

2.4.1. Cross sectional TEM (XTEM) Specimen Preparation

To locally investigate the internal micro structure and the assembly of different layers at high resolution, the sample has to be cut from the top perpendicular to the surface (s. figure 2.11.). For analysis in transmission with the TEM and HRTEM, cross sectional specimens, called lamellas, with thicknesses below 100 nm are required.

As already mentioned, the FIB is excellent for side-specific TEM lamella preparation. How to prepare TEM cross sectional with the Focused Ion Beam is generally known and has already been reported given first by Stevie et al. in 1995.[47] In just a couple of hours uniformly thin, high quality TEM specimens of a wide range of materials and composites can be prepared. For TEM lamella preparation dual beam FIB/SEM instruments are preferentially used, as they allow sample preparation, imaging and analysis in one tool.

In the following paragraph the general procedure of TEM specimen preparation should shortly be elucidated and supplemented by the scheme in figure 2.11.

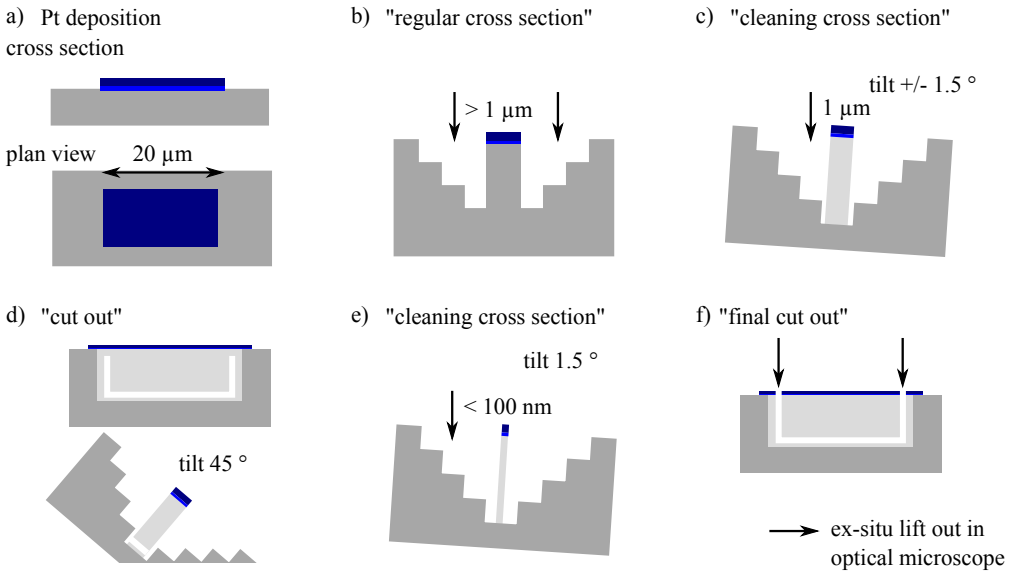


Figure 2.11.: Schematic XTEM specimen, lamella, manufacturing with FIB.

First of all, the sample has to be arranged in an eucentric position to the ion- and electron-beam under high vacuum conditions in the microscope chamber. To protect surface layers from damages due to sputter processes of the ion beam, the preparation starts with an e-beam induced Pt-layer deposition, followed by an i-beam Pt-layer deposition (a) to create a stable Pt-protection film. All processes can be observed in situ with a back scattering detector. The next step in preparation is the formation of a step structure profile using high beam current to remove material on both sides of the protection layer, forming a relatively thick lamella (thickness > 1 μm), which is still connected to the bulk material (b). Next steps of preparation are different milling procedures while continuously decreasing the beam current and milling the lamella on alternate sides of the sample, respecting the Gaussian profile of the beam, by tilting the sample until the lamella is thinned to ≈ 1 μm (c). Subsequently the sample is tilted perpendicular to the e-beam to separate the lamella from the bulk without damaging the material by amorphization and ion implantation (d), leaving only two small connections to the bulk to be stabilized for further thinning. Further milling steps with extremely low beam currents are implemented until a final lamella thickness of $<$100 nm (e) is reached. For the lift out, the two connections to the bulk are severed vertically to the top of the sample with the i-beam and low beam current, leaving a free standing

lamella inside the bulk sample (f). The used FIB facility allows no in-situ lift-out. Therefore, the samples are transferred from the FIB chamber and the lift out of the lamella to TEM grids is done with quartz needles in an optical microscope and micro manipulation components.

The generated lamellas are supposed to show the same structure as the investigated sample material (amorphous, crystalline etc.) and can be determined in HRTEM. A detailed list of steps of the specimen preparation, as well as SEM images of the different states during preparation can be found in appendix A.

2.5. Energy Dispersive X-Ray Spectroscopy: EDX

Content of Analysis

In Energy Dispersive X-ray Spectroscopy (EDX) the existence, amount and distribution of elements in investigated samples can be analyzed by detection of the emitted X-rays. EDX relies on the interaction between an incident electron beam and matter and is a likewise applicable technique to determine the elemental distribution of microscopic samples.

Theoretical Basics

Characteristic X-rays are generated by irradiating the sample with an incident electron beam. Inner shell electrons of the surface atoms are excited and ejected from the shell while creating an electron hole pair. The inner shell holes are filled by electrons from outer shells like in X-ray tubes. Since the energy differences between the shells are element specific , elementary analysis, by detecting the energy of emitted X-rays, is possible.

Experimental Setup

For detection of X-rays, a lithium-doped Si crystal is implemented, which is protected by a beryllium window. To absorb non linear and reflected electrons a collimating lens, containing C coated walls, is positioned in front of the detection crystal. The S/N ratio is optimized by a field effect transistor.

Outside the vacuum a X-ray analyzer, containing an impulse processor, analog digital converter and a four channel analyzer converts the voltage/current pulse, which is send by the detection crystal into a computer signal. In EDX spectra the number of pulses is plotted versus the detected energy and the number of counts. As the number of counts is proportional to the quantity of the detected element, quantitative analysis of the different elements can be performed besides the qualitative, by calculating the peak area of the signals. As the mean free path of X-ray photons is relatively low, in EDX averaged results of depth of approx. 1 μm are determined and bulk characteristics are investigated.[48] [49] EDX analysis are possible for elements with atomic number z of 8 - 99. Elements with a low atomic number show a high absorption at the detector window due to the low kinetic energy of the emitted X-ray photons, therefore analysis from atomic number 11 (sodium, Na) upwards are advisable. Alternative window materials as plastics or diamond are available for the analysis of elements down to the atomic number of 5 (boron, B). However, those materials have serious drawbacks, as fragility and capacity overload of the detector for samples with high amounts of C, N, and O therefore usually beryllium detector windows are utilized. A spacial resolution down to 5 μm with a detection limit of 0.08 % is achievable. EDX detectors are often combined with SEM, (HR)TEM or STEM analysis systems.[42]

2.6. X-Ray Diffraction: XRD

Content of Analysis

X-ray Diffraction is a non destructive method for structural analysis of crystalline materials and atomic arrangements in amorphous materials. It is one of the most commonly used techniques to identify unknown substances and the relative abundance and purity of compounds. Single crystal XRD establishes the possibility to solve the complete structures of crystalline materials. X-ray powder diffraction is a strongly used technique to determine crystallographic structure and structural properties such as preferred orientation, crystallite and grain sizes, strains, epitaxy, lattice constants, phases, geometry and defect structures in crystalline materials.

To analyze preferred orientation and crystallographic structure in thin films, grazing incidence and thin film XRD can be used. Inorganic solids, more

complex macromolecules or proteins can be investigated by XRD techniques. Laboratory based XRD spectrometers facilitate surface sensitivities down to 50 Å. Synchrotron radiation allows the characterization down to mono atomic layers due to its much higher intensity.[50]

Only powder analysis have been performed during the experimental work for the present thesis. Therefore only a short description of these experimental setups should be summarized in this paragraph. A detailed description of XRD can be found in e.g.[51],[52],[53],[54] or[55].

Theoretical Background

In XRD, incident monochromatic X-ray beams are used to investigate the crystallographic structure due to characteristic diffraction of the X-rays by the crystal lattice. The wavelength of X-ray radiation is within the order of magnitude of lattice constants in crystalline compounds. Therefore the incident X-ray beam, which is irradiated to a crystal with a periodical order of atoms (the sample), causes interference and diffraction phenomena.

The interference of the crystal lattice and the incident beam (s. figure 2.12.) is based on Bragg's diffraction. Bragg's diffraction was first demonstrated by William Lawrence Bragg and his father William Henry Bragg in 1913, who were honored with the Nobel price in 1915 "for their services in the analysis of crystal structure by means of X-rays"[56] and can be described by Bragg's law:

$$n\lambda = 2d \sin \Theta \tag{2.16}$$

n: integer
λ: wavelength of incident X-ray
d: spacing between lattice planes
Θ: angle between incident X-ray and scattering plane, Bragg angle

The conditions for constructive interference and therefore a maximum of scattered intensities are given at:

$$n\lambda = 2\delta \tag{2.17}$$

with δ as difference in the path length of the interfering beams.

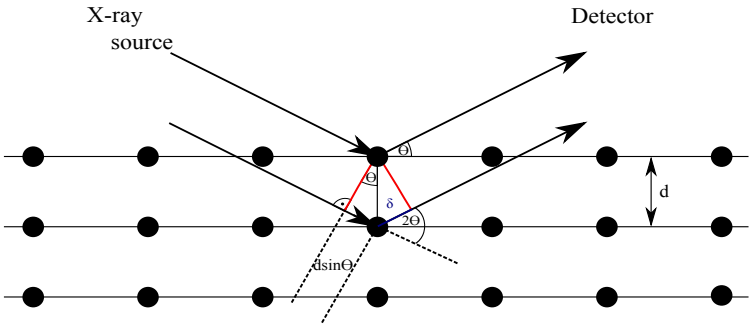


Figure 2.12.: Schematic demonstration of the diffraction, Bragg interference, of an incident beam on a periodically ordered crystal lattice (after[57]).

An equivalent way to describe diffraction on crystal lattices are the Laue equations, which are named after Max von Laue.

Reciprocal systems are introduced for interpretation of crystallographic data. The reciprocal lattice represents the Fourier transformation of the spatial function of the real lattice. Reciprocal vectors are perpendicular to the respective vectors in real space and can be defined as:

$$a^* = \frac{b \times c}{V}; b^* = \frac{a \times c}{V}; c^* = \frac{a \times b}{V} \tag{2.18}$$

a^*, b^*, c^*: reciprocal basis vectors
a, b, c: real basis vectors
V: volume of the unit cell

A graphical, geometric construction for the compliance of Bragg's law is the Ewald sphere. For the Ewald construction Bragg's law can be written as:

$$\sin\Theta = \frac{1/d}{2/\lambda} \tag{2.19}$$

In a circle with the radius $r = 1/\lambda$, a right angled triangle with the hypotenuse $2r$ is constructed. The opposite leg has the length 1/d. d can be substituted by the reciprocal scattering vector d^* ($d^* = K/d$) and for $K = 1$ the following is obtained to construct the Ewald circle (s. figure 2.13.).

$$\sin\Theta = \frac{\lambda}{2} d^* \tag{2.20}$$

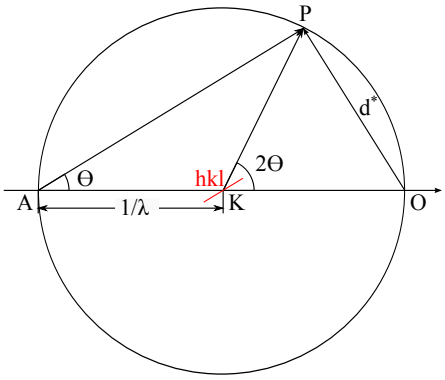


Figure 2.13.: Construction of the Ewald circle.

In 3D, the construction results in a spherical depiction where K is in the center position. The variable O in figure 2.13 is considered as the origin of the reciprocal lattice. The reciprocal lattice points, which are positioned at the end of d^*, fulfill the Bragg condition for reflexion. In X-ray diffractometers the Ewald sphere assembly is implemented for the experimental setup. Waves scattered at atoms in different crystallographic positions reach the detector angle dependent, with a relative phase shift, depending on the respective interference. Therefore, the measured intensities yield information about the relative atomic positions. The intensity of the diffracted X-rays is sample specific. Peak broadening is caused by instrumental factors, the presence and differences of defects and strains in grains as well as the size of crystallites. Therefore, particle size distributions can be extracted from XRD analysis in addition to the crystallographic data. Collected data can be compared to crystal databases for sample and phase identification.

To identify the different atomic structures, atomic planes can be uniquely distinguished by Miller indices, which were introduced by William Hallowes Miller in 1839. A unit of lattice planes is characterized by the three integers h, k and l (hkl), the Miller Indices, which are the reciprocal intercepts of the lattice plane with the $a-$, $b-$ and $c-$axes. Negative integers are by convention written as $\bar{h}$. All indices are reduced to the smallest integers having the same number.

The lattice spacing d of a crystal is labeled as d_{hkl} and for a simple cubic system it is given by:

$$d_{hkl} = \frac{a}{\sqrt{h^2 + k^2 + l^2}} \tag{2.21}$$

a: lattice constant

Experimental Setup and Sample Requirements

A XRD spectrometer generally consists of a X-ray source and monochromator, goniometer, specimen holder, different slits to bundle the X-ray beam and a detector (incl. multiplyer). Depending on the technique, data analysis is done via computer software or photo film generation.

The incident X-rays for XRD are generated by using a conventional X-ray tube like described in section 2.1. Typically copper (Cu) or molybdenum (Mo) are used as anode Materials for XRD with wavelength of Cu-K_α = 0.154 nm and Mo-K_α = 0.071 nm. To observe the reflection of the sample, the detector must be positioned in a way that the diffraction angle is 2Θ and the normal of the analyzed crystal is coplanar with the incident and diffracted beam. Consequential, the angle between the diffracting plane and the incident beam is identical with the Bragg angle.

For different diffraction modes appropriate spectrometer setups need to be installed. The different types are focusing geometry in Bragg-Brentano- and Seemann-Bohlin-, parallel beam: Debye-Scherrer-, single crystal: Laue-, rotating crystal-, panning- and Weissenberg- configuration. For thin film analysis a grazing incidence (GID) setup is utilized. Typically "white" and monochromatic X-rays are used as incident beams, depending on the XRD technique.

For powder analysis, a Bragg-Brentano setup with monochromatic X-rays is most commonly used. In this configuration the incident and emergent angles to the sample are identical, hence it is synonymously called $\Theta - 2\Theta$ method. Detector and sample are rotated simultaneously. In the detected spectra, the intensity is plotted versus 2Θ.

For high quality XRD screening, the powder X-ray diffraction patterns can only be collected from samples consisting of very fine particles not arranged in special patterns. To yield a statistical intensity distribution in the Bragg reflection, a sufficient high number of crystalline particles is required. The powder, pellet, plate, sheet or fiber samples need to be fixed on/in a glass or aluminum specimen holder.

3. Basics & Analysis of Semiconductor Devices

The electrical characterization of semiconductor devices is essential to evaluate their potential significance for future applications. Furthermore, under aspects of basic research, the basic principles of conduction mechanisms, charging and discharging, defect structures, and their influence on the electrical performance need to be understood in general. In the following chapter an introduction into oxide containing semiconductor devices, especially metal oxide semiconductor (MOS) devices, will be given, followed by a detailed elucidation of the different leakage current conduction mechanisms in insulating films. Subsequently, the necessary fundamentals to measure and calculate characteristic relevant variables such as leakage current and dielectric constants for insulating oxide layers will be introduced. More detailed elaborations as well as the derivations of the different characteristic variables can be found in e.g.[58],[59] and[60]. The basic fundamentals of semiconductors are summarized in appendix B.

3.1. Semiconductor Devices

For a basic understanding of the functionality of semiconductor devices, charge carrier transport processes in the vicinity of different interface structures need to be elucidated. Changes in the band structure affect the local distribution of the charge carrier densities in structures where the semiconductor is in contact with vacuum, a metal or in contact with another semiconductor with different charge carrier types.

For semiconductor devices, typically four different types of electrical contacts need to be understood. The direct interface of different doping in a semiconducting single crystal is known as the p-n transition or homo junction, while the interface between two differently grown epitaxial semiconductors is referred to as hetero junctions. Schottky diodes or ohmic contacts are interfaces between two different materials like metal-semiconductor or metal-vacuum. Interfaces between three types of materials (metal/oxide/semiconductor, MOS)

are known as MOS junctions. In the following, semiconductor and MOS structures should be elucidated in detail since those are essential for the subsequent device analysis in the present thesis.

The functionality of semiconducting devices is mostly based on charge carrier transport, which is attributed to the position dependent characteristics of the potential energy in direct proximity to the interface. Due to space charges, the course of the potential curve is position dependent. Formally the correlation of the potential and the density of electrical charge carriers can be explained by the Poisson-Equation of electrostatics:

$$\frac{\delta V(x)}{\delta x^2} = -\frac{1}{\epsilon\epsilon_0}\rho(x) \tag{3.1}$$

$V(x)$: position dependent potential curve
ϵ: permittivity
$\rho(x)$: electric charge density
ϵ_0: permittivity of free space

3.1.1. Metal Oxide Semiconductor: MOS Capacitors

To investigate the electrical properties of dielectric materials and to understand the basic principle of operation for MOSFETs, the most powerful structure is the metal insulator metal (MIM) or the metal insulator semiconductor (MIS) structure. In the case that the insulating layer is formed by an oxide, the devices are frequently referred as MOS structures. The metal and semiconductor or metal are conductive, the insulators (most common an oxide) are dielectrics. A typical setup for an nMOS capacitor is illustrated in figure 3.1.

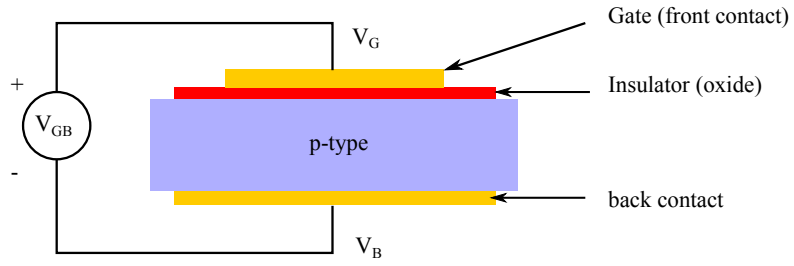


Figure 3.1.: Schematic cross section of a nMOS capacitor. V_G is supposed to be the gate voltage whereas V_B is the voltage at the back contact.

Three different bias voltages need to be contemplated, the voltage at the gate V_G, the flat band voltage V_{FB} (no surface potential at the semiconductor) and the threshold voltage V_{TH}, which is the voltage where inversion takes place. The flat band voltage can be calculated from the difference of the work function of the metal and the semiconductor, whereas the threshold voltage is defined as the voltage where the density of minority charge carriers equals the density of the dopant atoms. The three bias regimes are named as accumulation, depletion and inversion mode of device operation. The charge distributions are shown in figure 3.2.

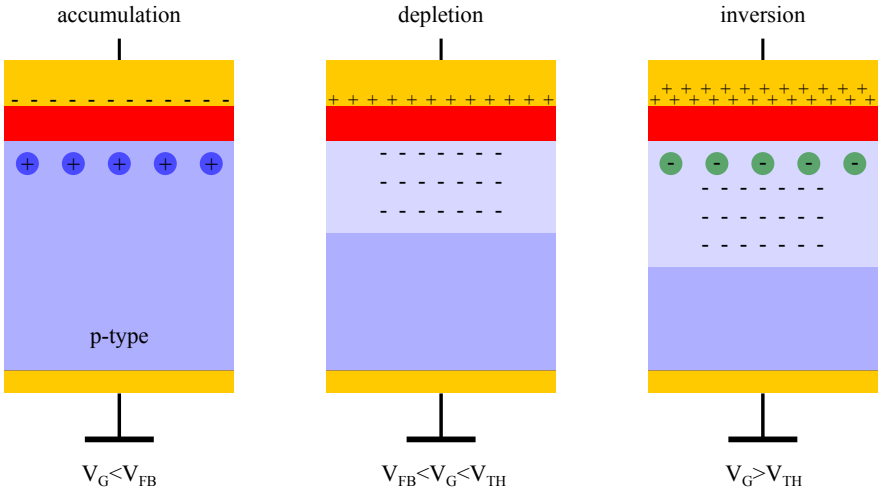


Figure 3.2.: Charge distributions for a p-type substrate in accumulation, depletion and inversion operation mode of MOS devices (after[59]).

The operation modes of the MOS device should be discussed under flat band conditions, where the energy band diagram of the semiconductor is considered to be flat and no charges are existent within the substrate. The flat band voltage of a device can be determined when the applied gate voltage is equal to the difference in work functions of the metal gate and the semiconductor.

Accumulation: $V_G < V_{FB}$
For negative biasing, majority charge carriers are accumulated at the oxide semiconductor interface, since the negative charge on the gate attracts holes from the substrate. The accumulation charge can be built by marginal band bending, therefore nearly all potential variation occurs within the insulating

layer and in accumulation mode the capacitance of the insulating layer (oxide) can be determined as:

$$C_{Acc} = C_{Ox} \tag{3.2}$$

Depletion: $V_G > V_{FB}$

For positive biasing, mobile majority charge carriers are pushed into the substrates, resulting in the formation of a space charge region from ionized dopant atoms. Initially this charge is caused by the depletion of the semiconductor starting from the oxide-semiconductor interface. The width of the so called depletion layer further increases with increasing gate voltage. In depletion mode the capacity of a series connection of the insulator capacity and the capacity of the depletion layer is analyzed:

$$C_{Dep} = \frac{1}{\frac{1}{C_{Ox}} + \frac{x_D}{\epsilon_S}} \tag{3.3}$$

with ϵ_S as dielectric constant of the semiconductor.

The width of the depletion layer x_D is dependent on the dopant concentration and increases with increasing dopant concentration:

$$x_D = x_p + x_n = \sqrt{\frac{2\epsilon_S}{q}\left(\frac{1}{N_A} + \frac{1}{N_D}\right)(\phi_i - V)} \tag{3.4}$$

where $x_{p(n)}$ is the depletion layer width in a p-(n) type semiconductor, q is the electronic charge, ϕ_i is the built in potential of a p-n junction and V is the applied voltage. The built-in potential equals the difference between the Fermi energies of the n- and p-type regions divided by the electronic charge. It also equals the sum of the bulk potentials of each region, since the bulk potential quantifies the distance between E_F and E_i. With increasing dopant concentration, x_D is decreased.

The accumulation and depletion region are separated by the so called flat band voltage.

Inversion: $V_G > V_{TH}$

By applying an even higher voltage than in depletion mode, an increase of the potential within the semiconductor beyond as twice the bulk potential leads to the generation of a negatively charged layer of minority charge carriers (inversion layer) at the semiconductor-insulator interface, attracted by the

positive gate voltage, additionally to the depletion layer. Increases in the gate voltage have almost no effect on the depletion layer width, since the charge in the inversion layer increases exponentially with the surface potential. The capacity, which can be calculated in inversion mode, refers to the series connection of the insulator (oxide) capacity and depletion layer in maximum extension:

$$C_{Inv} = \frac{1}{\frac{1}{C_{Ox}} + \frac{x_{D,T}}{\epsilon_S}} \tag{3.5}$$

where $x_{D,T}$ is the width of the depletion layer when the inversion is initiated.

Deviation from Ideal Case: Traps and Charges

The considerations in the previous paragraph are based on the assumption that the structures show ideal characteristics. In real devices, perceptible deviations from the ideal behavior can be observed from electrical characterization. Non-ideality in real MOS structures is based on identified or suspected physical phenomena, causing a variety of abnormalities in the C-V and I-V characteristics (s. section 3.2.). Prevalent abnormalities observed are negatively or positively shifts of several tens of Volts in the C-V characteristics compared to theoretical values, as well as severe device instability during bias temperature stressing, which is a standard device testing procedure, where the devices is heated under biasing to accelerate the device degrading process. The shifts always show reverse bias behavior. Uncontrollable changes in C-V characteristics lead to unreliable devices, therefore a detailed understanding of the effects causing the abnormalities are required.

For the ideal case, it is assumed that the work function of the metal Φ_M and the semiconductor Φ_S are equal. In real devices the energy difference between E_F and E_{Vac} is unlikely to be the same and therefore:

$$\Phi_M \neq \Phi_S = e_\chi + (E_C - E_F)_{FB} \tag{3.6}$$

with e_χ as electron affinity of the semiconductor.

This *difference in the work function* has to be taken into account to modify the theory of the ideal device. Due to the difference in the vacuum energies of the two materials, an electrical field ϵ_{Vac} develops between the two components and modifies the relation between the semiconductor surface potential and the applied gate voltage. Thus, it changes the device characteristics. Additionally

band banding occurs inside the semiconductor. Both effects are increasing, since the components are further approached to each other. The insertion of the oxide layer between the semiconductor and the metal lowers the surface barrier energies and therefore reduces the electric field in the contact region. The difference in the work function leads to the fact that the flat band voltage is contrary to the ideal device unequal to zero. This results in a required negative voltage to be applied for nMOS devices to achieve flat band conditions. Under flat band conditions, ideal and real devices show identical behavior, concluding that due to a difference in the work function of the metal and the semiconductor in the graphical examination, the entire C-V characteristics will be shifted by the value of the required additional voltage to be applied (difference in work functions) Φ_{MS} along the voltage axis.

$$\Phi_{MS} = \Delta V_G = (V_G - V_G')|^{same\ \Phi_S}_{(for\ same\ C)} \tag{3.7}$$

V_G: voltage applied to the real device V_G': voltage applied to the ideal device

The work function difference does not strongly effect the ideality, thus it is predictable and incapable of causing device instabilities. Another more significant influence is caused by *oxide charges*, which can be fixed charges, mobile ions, interfacial traps or induced charges as schematically shown for a $SiO_2 - Si$ structure in figure 3.3.

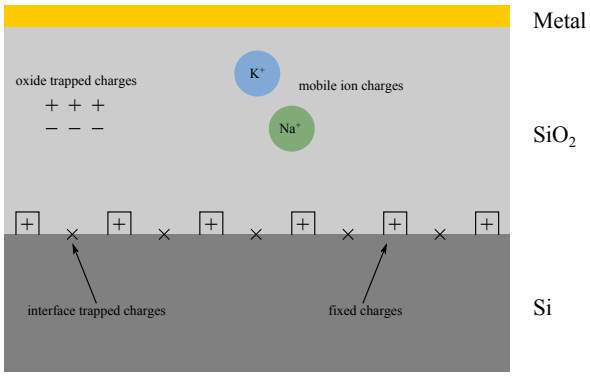


Figure 3.3.: Nature and location of charge centers in thermally grown $SiO_2 - Si$ structures (after[60], ©1980 IEEE).

The effect of oxide charges, can be explained by the postulation of a charge distribution $\rho_{Ox}(x)$, which varies randomly across the oxide width. The voltage translation for oxide charges can be written as:

$$\Delta V_{G,oxide\ charges} = (V_G - V_G')|_{same\ \Phi_S} = -\frac{1}{\kappa_{Ox}\epsilon_0}\int_0^{x_0} x\rho_{Ox}(x)dx \tag{3.8}$$

where κ_{Ox} is the dielectric constant of the oxide, ρ_{Ox} is the charge density within the oxide and ϵ_0 is the permittivity of free space ($8.85 \times 10^{-14}\ Fcm^{-1}$).

As fabricated MOS devices, show a large shifting and device instability, which can be attributed to the mobile ions inside the oxide. Including the ionic charge distribution $\rho_{ion}(x)$ in the total ionic charge within the oxide per unit area of the gate

$$Q_M = \int_0^{x_0} \rho_{ion}(x)d(x) \tag{3.9}$$

the voltage translation for ionic charges can be summarized as:

$$\Delta V_{G,mobile\ ions} = -\frac{1}{\kappa_{Ox}\epsilon_0}\int_0^{x_0} x\rho_{ion}(x)dx \tag{3.10}$$

It has to be indicated that theoretically positive ions attribute to a rise of the negative shift in C-V curves, as observed from experiments and negative ions of positive shifts in contrast to experimental results. Furthermore, the voltage translation is dependent on the exact position of the ions, therefore a critical interpretation is essential. Ionic charge effects can be minimized, by counterion (in most cases chlorine) treatments and a concomitant neutralization of the ionic charge carriers. The existence of ionic charges can be analyzed under bias stressing testing.

Another type of charges, the *fixed charges*, show totally reproducible voltage shifts towards negative bias relatively to the theoretical ideal characteristics. Fixed oxide charges are assumed to result from excess ionic Si close to the $Si - SiO_2$ interface, when the oxidation process is abruptly abandoned. The ΔV_G shift for fixed charges is caused by a charge residing close to the $Si - SiO_2$ interface, a quasi interface charge which is stable under bias temperature stressing and therefore referred to as fixed charges. The voltage shift can be described as:

$$\Delta V_{G,fixed\ charge} = -\frac{Q_F}{C_{Ox}} \tag{3.11}$$

with Q_F as fixed charge per unit area of the gate. And a resulting positive fixed oxide charge to account for the negative translation voltage which can be observed experimentally. Fixed charges are independent of the oxide thickness, the doping type and concentration of the semiconductor. Furthermore it varies as a function of the surface orientation and is strongly dependent on the oxidation conditions. As the excess reactants can be reduced by annealing and therefore the number of charges per unit area of the gate, the voltage shift can also be influenced significantly. $\Delta V_{G,fixed\ charge}$ can always be reduced to a minimum amount by inert gas annealing.

In vicinity to the surface of a material, the most influencing nonidealities in MIS structures are affected by the so called *interfacial traps*, which are also referred to as surface states or interfacial states. Interfacial traps cause diminished slopes in C-V curves. All bulk centers, donors, acceptors as well as recombination generation centers introduce additional permitted levels within the band gap close to E_C, E_V and rarely also above and below E_C and E_V leading to a distribution of permitted states within the band gap. Based on the assumption that all interfacial traps are unoccupied, all energy levels above E_F are empty whereas all below are occupied. For donor like states (positive charge for empty states and neutral for electron occupied states) the net charge rate for the interfacial traps Q_{IT} can be assumed to be positively charged. For depletion, inversion and accumulation bias different occupation states can be observed (s. figure 3.4.) as the interfacial traps charge and discharge as a function of the applied bias and thereby affect the charge distribution inside the respective device.

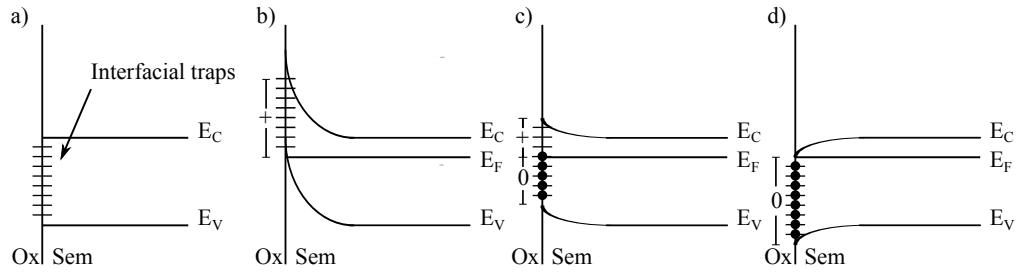


Figure 3.4.: Electrical modeling of interfacial traps, as allowed electronic levels at the oxide-semicondcutor interface (a), filling of the interfacial levels under inversion(b), depletion (c) and accumulation (d) biasing in n-type devices (after[60]).

As the interfacial traps are located directly at the semiconductor-oxide interface, the voltage translation can be written analogous to the fixed charges:

$$\Delta V_{G,interfacial\ traps} = -\frac{Q_{IT}(\phi_S)}{C_{Ox}} \tag{3.12}$$

indicating that the charge translation associated with the interfacial states is dependent on the surface potential of the semiconductor. The C-V curves show on the one hand, while processing in depletion towards accumulation, a decrease of translation which is supposed to continue once passing accumulation according to theoretical considerations. In contrast an increasing positive shift can be observed for increased bias experimentally which can be explained by the donor like assumptions for the theoretical discussions whereas in real devices the upper half of the band gap shows supposably acceptor like characteristics. Thus, roughly around the flat band voltage the net charge rate of the interfacial traps becomes significantly negative due to an increasing number of electrons within the upper energy states of the band gap.

The physical origin of interfacial traps is not completely clarified but experimental results allow the assumption that they result from dangling bonds, which are unsatisfied bonds at the surface of the semiconductor. Dangling bonds result from abruptly terminated Si surfaces and the following formation of the SiO_2 which satisfies not all surface bondings, the remaining dangling bonds become the interfacial traps within the semiconductor-oxide structure.

The concentration of interfacial traps and the effect on the device characteristics is strongly sensitive to device production and varies from device to device. A trend which has been observed for the interfacial trap density is that the concentration of the fixed oxide charge shows a maximum for *Si(111)* substrates and a minimum for *Si(100)*. The ratio of the mid gap states is approximately 3:1. This can be correlated with the available surface bonds per unit area on the respective surface.[61] [62] Interfacial states can be annihilated partially, by post metalization or hydrogen-ambient annealing. However, inert gas annealing does not reduce them.

Induced charges are caused by radiation effects or bias instabilities. A multi step process leads to the formation of radiation induced charges which are fixed charges as well as high concentrated interface traps. Primarily the incident ionizing radiation generates an electron-hole pair within the oxide, followed by immediate recombination as well as separation of the electrons and holes by

the electric field inside the oxide layer. The electrons are highly mobile and can easily be swept out of the material, whereas the holes tend to be trapped at their place of generation and they are transported by a hopping mechanism through the localized bulk states to the Si/SiO_2 interface, where they either recombine with present electrons or become trapped as deep level sites. Fixed at the interface they mimic fixed charges. The radiation induced charges have destructive impact on the device performance, which is a fatal aspect for space applications. Trapped hole charges can be removed or controlled by special annealing procedures. A high negative bias applied to the device causes a stressing of the material, leading to an increasing concentration of the apparent fixed charge as well as interface trap concentration and a distortion of the C-V characteristics. The change in the voltage for the C-V curve is opposite to the shifting, caused by alkali ion charges. The negative bias instability is ascribed on a hole injection from the Si to the oxide and a subsequent trapping of the generated holes at deep level sites near the Si/SiO_2 interface. Hydrogen annealing close to 373 K is the most common way to reduce the negative bias instability.

3.1.2. Transistors

For a precise understanding of the MOS based transistors, an introduction into p-n junctions and the functionality of transistors should be given in the following.

Transistors in general are semiconductor based electrical devices to switch and amplify electronic signals and power. They consist of at least three connections. Today transistors are embedded in ICs. The working principle of the transistor is based on a change of an incident current or voltage applied to one connection region, while flowing through the other connection.

Bipolar Junction Transistor and p-n Junction

The bipolar junction transistor (BJT) was the first solid-state amplifier element, invented by Bardeen, Brattain and Shockley at Bell Laboratories in 1948 to replace vacuum tube components by solid state devices. The invention of planar semiconductor processing, which is a special technique for device setup, yielded the first integrated circuits on chips. Within the 1960s the BJT based

devices were the engine for semiconductor circuit design development. The invention of the MOSFET displaced the BJT almost completely for logic circuits, microprocessors and memory chips, so that it is only applied for ultra high speed devices. Nevertheless, in the following a short introduction to the functionality of the idealized BJT, containing of two p-n junctions which are all contacted, should be given for integrity reasons after introducing the p-n junctions.

p-n junctions are p-type and n-type semiconductors brought together in close contact (s. figure 3.5.), creating a depletion region. The importance of this contact is the creation of a region between the p- and n-doped regions, where p-type holes can recombine with n-type free electrons, producing light, such as in light emitting diodes (LEDs).

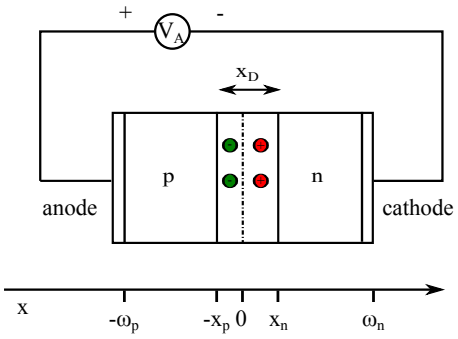


Figure 3.5.: Cross section of a p-n junction, showing the respective depletion layers x_p and x_n in each region, with $\omega_{n(p)}$ as the width of the n-(p)type region.

Under equilibrium conditions, when no bias is applied, the Fermi energies of the two phases must become equal, which occurs by charge transfer (carrier diffusion) between p- and n-type charge regions due to a gradient between the two doping regions within the p-n junction of the density of donor (N_D) and acceptor (N_A) atoms. Holes and electrons move to the opposite doping sites, accumulating the excess charge in a so called space charge region, which creates an electric field, resulting in carrier drift that antagonizes the carrier diffusion. In the so created dynamic equilibrium, the diffusion and drift current compensate each other establishing the equilibrium state.

In forward active biasing mode (positive applied voltage, V_A to the anode), electrons from the n-type region and holes from the p-type region are pushed

towards the junction, resulting in a reduced depletion layer width and a reduction of the barrier potential. Due to the positive voltage electrons are forced to flow from the n- to the p-substrate. For forward bias the width of the depletion layer and therefore the potential gradient becomes narrow enough that the electrons are enabled to cross the junction to be injected to the p-type component. The flowing current is limited by the recombination from electrons and holes. The flow of electrons from n- to the p-type region equals the flow of holes from p- to the n-type region. Thus, the electron flow is compensated by the hole flow in the opposite direction. The overall current flows I_n and I_p are directed in the same way, since electrons and holes are oppositely charged.

For reverse active biasing (negative applied voltage to the anode), the potential across the semiconductor increases, resulting in an increase of the depletion layer width, analogous to the decrease in width, with positive applied voltages. The high potential barrier causes a reduction of the electrical flow to a minimum and a resistive functionality of the p-n junction. By increasing the applied voltage to a critical value, the depletion zone breaks down and the current starts to flow under break down conditions, which can be used in special diode types.

The characteristic modes of a p-n junction, depending on the applied voltage, are shown in figure 3.6.

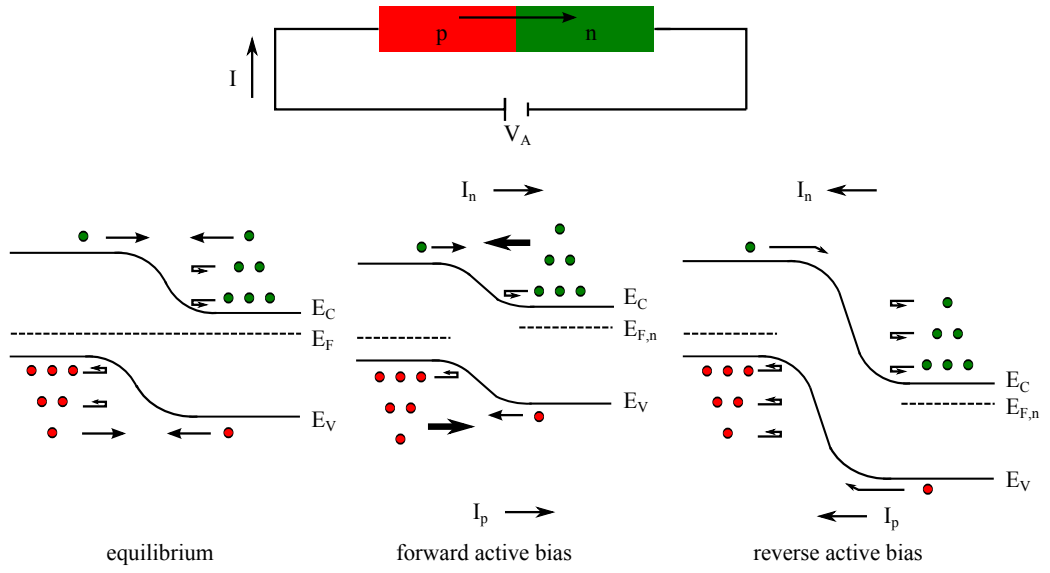


Figure 3.6.: p-n junction energy band diagrams for equilibrium, forward and reverse bias conditions (compare[60]).

As in diodes, a current, generated by an applied voltage, can flow easily in one direction (forward biasing), but is blocked in the other (reverse biasing). Therefore, p-n junctions are used as switching components, which are a basis for digital electronics. p-n junctions are powerful devices, since they can additionally be used e.g. as rectifier packages, voltage dependent capacitors, photo diodes or in solar cells.

One of the most famous examples for p-n junctions is the semiconductor-semiconductor diode which was at first described by W. Schockley in 1949. Beside the implementation in BJTs, they are essential parts of the MOSFET.

The p-n junction shows a rectification effect and exhibits diode properties. The I-V characteristics for the p-n junction can be calculated after the drift diffusion model:

$$I = I_{Depl}(e^{\frac{eV}{\eta kT}} - 1) \tag{3.13}$$

I: current
η: ideality factor
I_{Depl}: depletion current

The capacitance C_{p-n} of the p-n junction can be calculated from the change of charges per voltage change:

$$C_{p-n} = \frac{\epsilon_S}{x_D} \tag{3.14}$$

In the BJT, the two outer regions are referred to as the emitter and collector, where the inner region is called the base. The term bipolar results from the operation mode, which involves electrons and holes.

As in simple p-n junctions, quasi-neutral regions and in between depletion regions are existent. Two characteristic ways of switching are possible: basic and emitter circuits. In basic circuits two specific conditions can be examined. If the applied emitter voltage to the base is $V_{EB} > 0$ (forward active bias), a huge number of holes is induced into the base and therefore a resulting base current I_E can be measured. As a consequence a diffusion of minority charge carriers to the interface between base and collector is induced.

In the case that the base collector voltage is $V_{CB} < 0$ (reverse active bias), the minority charge carriers at the base-collector contact are extracted by the

electric field, resulting in a high forward current despite the base-collector contact blocks. Concluding that the voltage dependent collector current $I_C(V_{CB})$ is controlled by the base current.

MOS Field Effect Transistor: MOSFET

Field effect transistors in general are unipolar transistors where only one charge carrier type participates to the conduction transport. The concept of the FET predates the BJT, since it was first invented in 1925 by Julius E. Lilienfeld, though it was not physically implemented until the early 1950s due to the limitations of semiconductor materials and a concomitant retarded development.

The essential technological problems were based on the control and reduction of field blocking surface states. The field effect is referred to as the process where the conductivity of a semiconductor is modulated by an electric field, which is applied normal to the surface of the semiconductor itself.

MOSFETs, where an insulating oxide layer separates the substrate from the gate, were first proposed by Kahng and Atalla in 1960.[63] The introduction of the MOSFET solved the problem of surface states, which blocked electric fields from penetrating into the semiconductor material by a thermally grown SiO_2 layer. The reduced surface states enabled the production of microelectronic devices which do not have a conducting channel unless a voltage is applied (enhanced mode). Enhanced mode MOSFET based ICs are recently the predominant technology in microelectronic industries. MOSFETs enable a current and voltage gain in one device, which is highly desirable under technological and economic aspects. The current gain capability in MOSFETs results from the fact that no gate current is required to maintain the inversion layer and the resulting drain-source current. The voltage gain can be explained by a current saturation at higher drain-source voltages inducing a large drain voltage variation by a small incident drain current variation. Physically the MOSFET is a MOS capacitor with two p-n junctions placed directly adjacent to the semiconductor controlled by the MOS gate.

In the following, the nMOSFET should be shown exemplary. An n-type MOSFET consists of two identical, highly conducting n-type semiconductor regions, source (S) and a drain (D), which are insulated from the p-type substrate by reversed-biased p-n diodes. The gate, mostly made from metal or poly-crystalline materials, covers the region between source and drain. It is

separated from the semiconductor substrate by the gate oxide. The applied voltage determines which of the n-type regions provides the electrons (source) and which receives the electrons becoming the drain. The applied voltages between the drain and source V_{DS}, gate and source V_{GS} and substrate, bulk (via back contact) and source V_{BS} are referred to the source potential.

Figure 3.7. shows a schematic cross section of a MOSFET device.

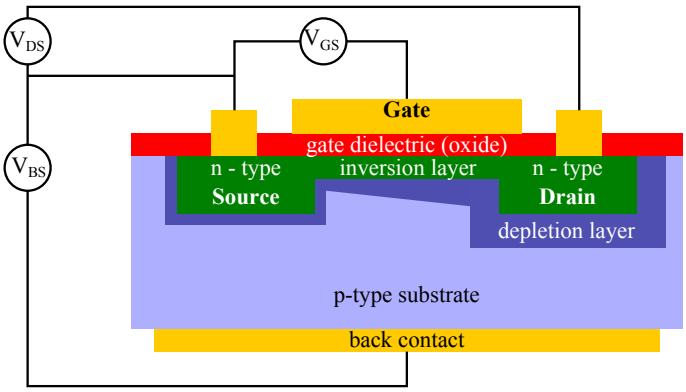


Figure 3.7.: Schematic illustration of a nMOSFET in saturation mode with respective applied voltages, the inversion and depletion layer regions which are formed during device operation are shown additionally.

The flow of electrons from the source to the drain is controlled by the voltage which is applied to the gate (V_{GS}). If a positive voltage is applied to the gate, electrons are attracted to the oxide-semiconductor interface, forming the conducting inversion layer, which is of the same type (in the nMOSFET case n-type) as the source and drain and therefore provides a channel through which the current can pass.

A variation of the applied voltage leads to a modulation of the inversion layer and its respective conductivity. It therefore controls the current flow between source and drain. If the applied gate voltage is below the threshold voltage of the transistor, the channel is barely populated and therefore only a so called subthreshold current can flow between source and drain.

The threshold voltage for nMOSFETs increases with higher doping concentrations, while pMOSFETs show contrary behavior. Oxide charges influence the flat band voltage. Positive charges effect a reduction of V_{TH}. Furthermore, the threshold voltage is influenced by the applied voltage V_{BS}, since the width and

charge of the depletion layer is changed and therefore also the voltage across the oxide. The threshold voltage is given by:

$$V_{TH(nMOSFET)} = V_{FB} + 2\phi_F + \frac{\sqrt{2\epsilon_S q N_A (2\phi_F + V_{BS})}}{C_{Ox}} \tag{3.15}$$

$$V_{TH(pMOSFET)} = V_{FB} + |2\phi_F| + \frac{\sqrt{2\epsilon_S q N_D (2\phi_F + V_{BS})}}{C_{Ox}} \tag{3.16}$$

$$\tag{3.17}$$

with V_{FB} and ϕ_F

$$V_{FB,p/n} = \Phi_{MS} - \frac{Q_f}{C_{Ox}} - \frac{1}{C_{Ox}} \int_0^{t_{Ox}} \frac{x}{x_{Ox}} \sigma_{Ox}(x) dx \tag{3.18}$$

$$\phi_{F,p} = V_{TH} \ln \frac{N_A}{n_i} \tag{3.19}$$

$$|\phi_{F,n}| = V_{TH} \ln \frac{N_A}{n_i} \tag{3.20}$$

and

$$\Phi_{MS,p} = \Phi_M - \Phi_S = \Phi_M - (x + \frac{E_{Gap}}{2q} + \phi_F) \tag{3.21}$$

$$\Phi_{MS,n} = \Phi_M - \Phi_S = \Phi_M - (x + \frac{E_{Gap}}{2q} + |\phi_F|) \tag{3.22}$$

ϕ_F: bulk potential and t_{Ox}: oxide thickness

The modulation of modern MOSFET systems requires complex mathematical models, depending on the parameters taken into account and the respective device design. Physical effects, like limited carrier transport or lowering of current barriers, have to be considered. Therefore, at this point only a short description of the operation modes should be given renouncing a detailed mathematical elucidation, since equations from simple models become inaccurate for state of the art devices.

Depending on the voltages applied, the operation modes of an enhancement-mode nMOSFET can be described, as follows:

Cut-Off, subthreshold mode: $V_{GS} < V_{TH}$
In the basic threshold model for the case that the transistor is switched off,

no conduction between drain and source is possible. Effectively some of the electrons are allowed to enter the channel due to higher energies given by the Boltzmann distribution of the energy of the electrons (concept of the electron gas), causing a subthreshold current, which is exponentially dependent on the function of the voltage between gate and source. Therefore, in ideal case for the turned-off device, the current between drain and source should be zero, but a marginal inversion current can be measured, the subthreshold leakage.

The manufacturing of the device strongly influences the current voltage behavior in the subthreshold regime. For long channel devices, the drain voltage is independent of the current, whereas for short channels a device geometry dependency is introduced.

Ohmic mode, linear region: $V_{GS}>V_{TH}$ and $V_{DS}<(V_{GS}-V_{TH})$
In the Ohmic mode, the transistor is switched on. The conductive channel has been created, since a strong inversion region is present and a current is enabled to flow between the drain and the source.

The device operates like a resistor, controlled by the gate voltage relative to the source and drain voltages.

Active, saturation mode: $V_{GS}>V_{TH}$ and $V_{DS}>(V_{GS}-V_{TH})$
In active saturation mode, the transistor is switched on. The conductive channel has been created like in Ohmic mode. The electrons spread out due to a higher drain than gate voltage and the conduction is realized through a broad (2 or 3D) current distribution, extending from the semiconductor-insulator interface deeper into the substrate contrary to a narrow channel in the Ohmic mode. The onset of the channel is referred to as pinch-off to indicate the lack of a channel region near the drain.

In this case, the drain current is hardly dependent on the drain voltage and can be controlled by the gate-source voltage.

3.2. MOS Component Characterization

As the present thesis is focused on the deposition mechanisms and the film quality of deposited oxides and therefore insulating layers, which can be used as gate oxides in MOS devices, it is essential to determine the electrical behavior of the generated films in order to evaluate the quality of the films with respect to a future application in microelectronic devices. In the following section, the analysis techniques as well as equations and the specific content of the analysis should be introduced. The quality of the dielectric layer between the metal (top or gate electrode) and the semiconductor substrate (bottom electrode) and the respective generated interfacial system in MIS structures can be determined by applying a varying voltage between the two electrodes, analyzing the current or capacitor response in the I-V and C-V curves. The current flow from the electrode into the insulating layer and the mechanisms, involved inside the dielectric films, defines the current voltage characteristics.

From the C-V and I-V characteristics, several parameters of the dielectrics are accessible, e.g. the dielectric permittivity and the leakage current can be determined. Furthermore, detailed analysis of the conduction mechanisms inside the dielectric layer can be performed. Electrical breakdown phenomena can be shown by the response under high applied voltage. Doping profiles and concentrations are additionally accessible. Hysteresis behavior, changes in slopes, and the course of the curve give information about the built up of the previously explained traps and charges within the structure and the electrical defects localized in the insulator layer or at the semiconductor/insulator interface.[64] The current conduction mechanism in insulating films can be determined by I-V analysis. Basic conduction mechanisms and their dependencies upon the applied voltage and varying temperature in insulators will be discussed in the following.

3.2.1. Experimental Setup

To determine the C-V and I-V characteristics of the insulating films, MOS capacitor structures are generated by depositing top and back contacts from Pt or Au e.g. to built a MOS capacitor system like shown in figure 3.1.

The measurement itself is performed by using an automated equipment as schematically illustrated in figure 3.8.

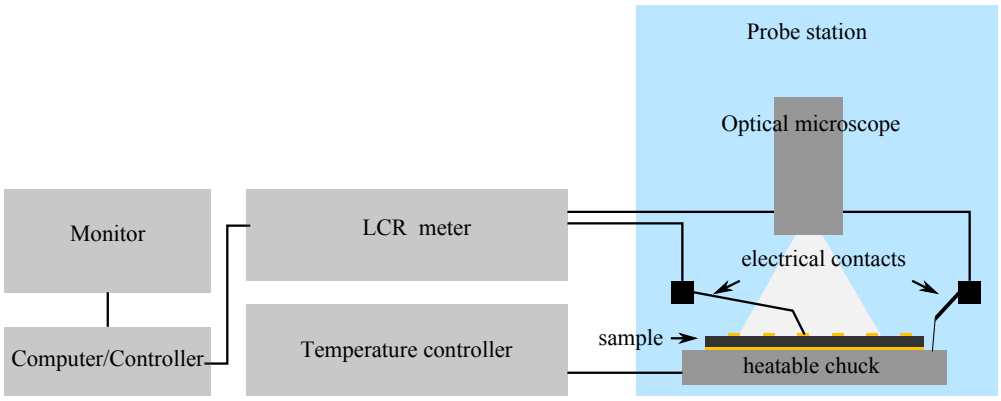


Figure 3.8.: Schematic illustration of a C-V/I-V measurement system.

The LCR meter is the main component of the system. Different capacitance ranges can be adjusted as well as specific frequencies for the biasing DC current. Data processing is realized by a connected computer with specific software components.

The sample is placed on a heatable chuck, which provides the electrical back contact. The complete sample set up is placed within a probe chamber which can be darkened and isolated from outer influences. Top electrodes are contacted by a probe. The probe contacts are positioned precisely utilizing an optical microscope.

3.2.2. Capacitance Voltage Measurements: C-V

Capacitance voltage characteristics open the way to determine the dielectric properties, doping concentrations, amount and structure of traps and charges as well as characteristic system voltages for the dielectric and for the semiconductor itself, though for the present thesis only the characteristics of the dielectric and the interface structures are matter of interest.

For C-V measurements a small AC signal is superimposed to an applied DC voltage to the MOS-Capacitor structure placed on the chuck, detecting the resulting AC current, which flows through the determined device. C-V characteristics are generally measured at 100 kHz (high frequency) or at variable frequencies between 1 kHz to 1 MHz. By varying the DC bias at the gate, quasi-continuous C-V characteristics can be observed.

The desired measured variable, the capacitance, can be calculated from:

$$C = \frac{Q}{U} \tag{3.23}$$

The capacitance varies with the applied voltage, since the charge inside the MOS structures responds to the applied AC signal and the DC bias is systematically changed from accumulation through depletion to inversion. Therefore, in C-V diagrams the capacitance per area is plotted versus the applied voltage. Depending on the frequency of the implied AC signal, different C-V characteristics can be observed in the designated low and high frequency limits (s. figure 3.9.).

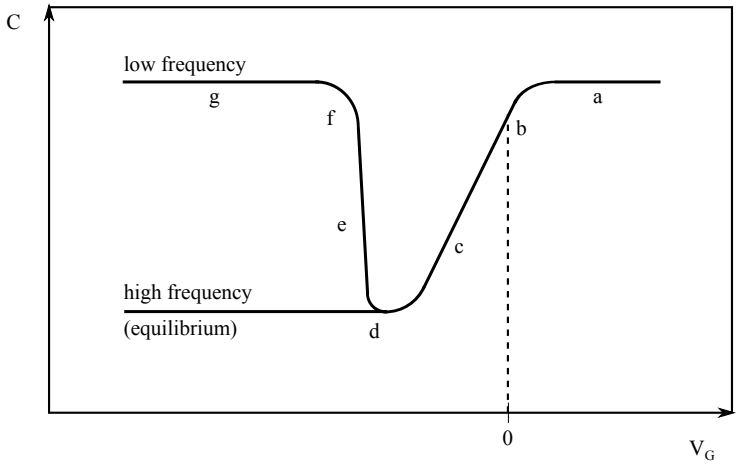


Figure 3.9.: C-V characteristics of a nMOS structure in dependence on the applied gate voltage V_G for high and low frequency measurements.

The C-V curve in figure 3.9. shows the response of the device in accumulation (a), under flat band conditions (b) depletion (c), transition (d) and in inversion (e-g). p-type substrates show a reverse curve progression. In most of the cases, C-V measurements are performed to determine the behavior of the tested device in accumulation, depletion or inversion.

Figure 3.10. shows schematically the AC charge fluctuation inside a nMOS capacitor under DC biasing and the respective circuit models.

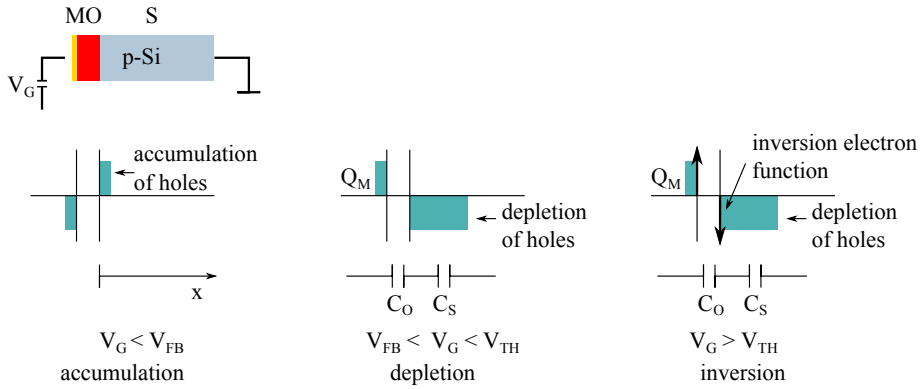


Figure 3.10.: Charge fluctuation inside the nMOS capacitor under DC biasing conditions in accumulation, depletion and inversion (similar to[60]).

The respective equations to calculate the capacitance are given in eq. 3.2, 3.3 and 3.5. The AC charge response is depending on the frequency, resulting in different characteristic C-V curve structures. For low frequencies, the electrons are able to respond to the AC voltage and minority carriers can be generated or annihilated in response to the applied signal, resulting in time varying AC states which are mainly caused by DC states.

Therefore, in inversion for low frequencies, the capacitance equals the capacitance in accumulation, analogous to two parallel plate capacitors in series. For high frequency biasing, the recombination generation process is relatively slow and no supply of minority carriers occurs in response to the applied AC signal. This results in a fixed amount of charge at the DC value. The situation is similar to two parallel plate capacitors connected in series.

If the voltage is ramped at high rates, a special case occurs, since no inversion layer is formed and no equilibrium can be achieved. This state is called deep depletion. Under deep depletion conditions, the inversion layer thickness will increase, excessing the thickness at the threshold voltage. The gate capacitance increases. As in accumulation, the measured capacitance equals the capacitance of the oxide C_{Ox} (s. eq. 3.2) the dielectric constant of the dielectric (oxide), κ, from the value of the capacitance in accumulation can be calculated after equation 1.1. As for high frequencies, the formation of the space charge region differs from the low frequency regions, the high frequency dielectric constant, ϵ_{Ox}, of the dielectric material (e.g. oxide) is given by:

$$\epsilon_{Ox} = n^2 \tag{3.24}$$

n: refractive index

3.2.3. Current Voltage Measurements: I-V

Like mentioned in the motivation of the present thesis, apart from the device design the dielectric layer in MOSFETs becomes critical and more important as the size and performance limiting component due to leakage current conduction caused by quantum mechanical tunneling within the in principle insulating the layers.

To determine the I-V characteristics the samples are biased by a chosen voltage to investigate the leakage current for the respective voltage for the analyzed device. Based on the Thévenin theorem [1], complex electrical systems consisting of voltage sources and resistors like solar cells, accumulators, diodes or transistors, can be modulated as a bipolar electrical device.

The leakage current characteristics are analyzed by applying stepwise varying different voltages to the device (e.g. -10 to 10 V) and detecting the resistance (in resistor mode). For the present thesis, only gate biasing was utilized to determine the leakage currents for the insulating oxide layer. All contacts within the device are assumed to be Ohmic, so that the insulating layer characteristics can be determined by detecting the resistance (R) of the device under different voltage biasing (U) and calculating the current for the respective resistance value (I) by:

$$I = \frac{U}{R} \tag{3.25}$$

If the resistance within the device is Ohmic, linear I-V characteristics can be observed, which is the simplest type of I-V curves. For more complex systems, varying I-V curve types can be detected. A typical I-V curve of MOS structures is shown in figure 3.11.

[1] The Thévenin theorem states that every electrical connection between voltage and current sources and resistors is equivalent to a connection in series of a voltage source and a resistor.

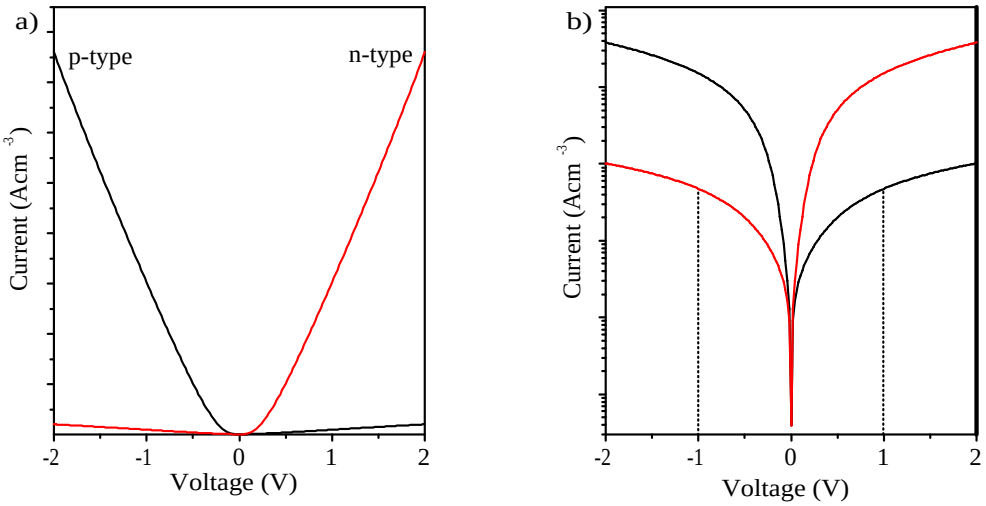


Figure 3.11.: I-V curves for p- and n-type substrates. Shown are the linear scale for the ordinate in (a) and the typical logarithmic scale in (b).

As leakage currents are commonly compared in current per area, the calculated leakage current needs to be divided by the respective electrode area. It is obvious that the off and on state characteristics for p- and n-type substrates show a contrary curve set as also shown for the C-V curves. From the linear current scale in (a), the off and on state regions can be easily identified, since the current is almost zero up to the threshold voltage. After exceeding the threshold voltage, the current increases exponentially. As the conductance increases with increasing voltage, the device can not be considered to be Ohmic. The off state leakage currents at 1 V for p-type substrates or -1 V for n-type substrates are usually considered for comparison of different devices.

3.2.4. Temperature Dependent I-V Characteristics: Leakage Current Conduction Mechanisms in Insulating Films

For a given dielectric material different conduction processes may dominate in certain temperature and electric field ranges and they may not be completely independent from each other.[58] Therefore, different conduction models exist to describe the leakage conduction, depending on the mechanism which dom-

inates the electron transport. To separate the different current components responsible for the leakage current, temperature-dependent I-V measurements within the activation energy of the leakage current need to be performed, since trapping processes are temperature dependent. Characteristic linear dependencies within certain voltage ranges in various plots of the response to the applied electric field are used to identify the respective leakage conduction mechanisms in the corresponding temperature and voltage range. At this point, the different mechanisms should be introduced briefly, including the linearity conditions If generated defects have an effect on the I-V characteristics, but no changes in C-V curves can be observed, the defects should be neutral.[65] [66] With the equations, specified in the following paragraph, characteristics of thin films from 6.5 nm to 30 nm have been analyzed and calculated based on the displayed mathematical issues.[64] As no further limitations are known for the derivation of the equation systems, it is concluded that the equations can be applied for films within this thickness region, even though it might be possible that for thinner films the formation of the space charge region differs and therefore a change in parameters might become be necessary.

The following listed parameters are used consistently to describe the leakage current conduction mechanisms:

d: insulator thickness
E: electric field
E_{Ox} electric field within the insulating oxide
E_S electric field within the semiconductor
h: Planck constant
k: Boltzmann constant
m^*: effective mass of the electron
q: electronic charge
T: temperature
V: applied Voltage
ϵ_0: permittivity of free space
ϵ_{Ox}: permittivity (dielectric constant) of the insulator
ϵ_S: permittivity of the semiconductor
ϕ_B: interface barrier height

For real MOS capacitor structures, the conductance of the insulating film can not be assumed to be zero like in ideal MOS structures, since they show

marginal carrier conduction when the applied electric field or respective temperature is sufficiently high. Under the assumption of negligible oxide charges, a small flat band voltage and band bending compared to the applied voltage, E_{Ox} can be calculated as:

$$E_{Ox} = E_S \left(\frac{\epsilon_S}{\epsilon_{Ox}} \right) \approx \frac{V}{d} \tag{3.26}$$

Tunneling Tunneling processes resulting from quantum mechanics (s. section 2.2.1.) are the most common conduction processes in insulators. Different tunneling mechanisms can be taken under consideration: *The field assisted tunneling: FAT* is strongly dependent on the applied voltage, but independent from the respective temperature. Another direct tunneling mechanism is the *Fowler-Nordheim tunneling: FN*, where the charge carriers only tunnel through a partial width of the barrier during a one step excitation process.

The Fowler-Nordheim tunneling current is given by:

$$J_{FN} = \frac{q^2}{8\pi h \phi_B} E_{Ox}^2 \exp\left[\frac{-8\pi (2m^* q)^{1/2}}{3hE_{Ox}} \phi_B^{3/2} \right] \tag{3.27}$$

$$\Rightarrow J_{FN} = A E_{Ox}^2 \exp\left[(-B/E_{Ox}) \phi_B^{3/2} \right] \tag{3.28}$$

with $A = \frac{q^2}{8\pi h \phi_B}$ and $B = \frac{8\pi (2m*q)^{1/2}}{3h}$

$$\Rightarrow ln(J_{FN}/E_{Ox}^2) = \ln A + (-B/E_{Ox}) \phi_B^{3/2} \tag{3.29}$$

B can be extracted from the slope (m) of the graph as:

m = $-B\phi_B^{3/2}$

and the y-intercept gives A after:

y-intercept = $\ln A$

For FN leakage current conduction the barrier hight ϕ_B is tabulated if the effective mass m^* is known.

A better understanding of trap participation for temperature independent processes can be extracted from measurements at very low temperatures, since for

those temperature regions, all temperature activated processes are suppressed and only temperature independent processes operate.

At low electric fields, *Trap Assisted Tunneling: TAT* can occur, where defects in the dielectric layer give rise to tunneling processes. Different complex models are known to model the TAT characteristics.

The tunneling current is given by:

$$J_{TAT} = A \ \exp\left[\frac{-8\pi(2m^*q)^{1/2}}{3hE_{Ox}}\right]\phi_B^{3/2} \tag{3.30}$$

$$\Rightarrow \ln J_{TAT} = \ln A + (-B/E)\phi_B^{3/2} \tag{3.31}$$

according to this relation, ϕ_B can be found from plot of $\ln J_{TAT}$ vs. $1/E_{Ox}$, with $B = \frac{8\pi(2m^*q)^{1/2}}{3h}$ and the slope m $= -B/\phi_B^{3/2}$.

A can again be calculated from the y-intercept (y-intercept = ln A).

Schottky Emission: SE Currents which are caused by electrons crossing above the potential barrier at the surface of a metal or semiconductor are called Schottky currents. They are associated with the thermionic emission across the metal/insulator or the metal/semiconductor interface due to a lowering of a Coulomb potential barrier under the applied electric field.[58] [64]

The current density-electric field relation for the Schottky emission is given by the Schottky-Richardson relation:

$$J_{SE} = A^*T^2 \exp\left[\frac{-q(\phi_B - (qE_{Ox}/(4\pi\epsilon_0\epsilon_{Ox}))^{1/2})}{kT}\right] \tag{3.32}$$

$$\Rightarrow \ln(J_{SE}/T^2) = \left[\frac{(q^3E_{Ox}/(4\pi\epsilon_0\epsilon_{Ox}))^{1/2}}{kT}\right] + \left[\ln A - \frac{q\phi_B}{kT}\right] \tag{3.33}$$

with $A = \frac{2qm^*k^2}{(2\pi)^2h^3}$, A^* as Richardson(-Dushman) constant and ϕ_B as interface barrier height.

For the Schottky emission the graphical relations are as followed:

Plot I	$\ln(J_{SE}/T^2)$ vs. $1/E_{Ox}^{1/2}$
Slope m $= (q^3/4\pi\epsilon_0\epsilon_{Ox})^{1/2}/kT$	y-intercept $= \ln A - q\phi_B/kT$
Plot II	$\ln(J_{SE}/T^2)$ vs. $1/T$
Slope m $= ((q^3E_{Ox}/4\pi\epsilon_0\epsilon_{Ox})^{1/2} - \phi_B)/k$	y-intercept $= \ln A$

Poole-Frenkel: PF The Poole-Frenkel emission can be referred to as the thermal excitation of trapped electrons into the conduction band of the dielectric.[58] [67] Electrons are generally trapped in localized states and associated to a single atom, but thermal fluctuation will occasionally lead to the effect that these electrons transport out of the localized states, move to the conduction band and are able to move through the crystal lattice, before relaxing into a different localized state.

In high electric fields, electrons do not require as much thermal energy to get unlocalized, since a part of the energy is contributed by the electric field and the fluctuations occur more frequently. The field dependent behavior of the field enhanced electron emission from Coulomb donor like centers or holes from acceptor centers, can be described by the standard quantitative expression for the Poole-Frenkel effect:

$$J_{PF} \propto E_{Ox} \exp\left[\frac{-q(\phi_B - (qE_{Ox}/(\pi\epsilon_0\epsilon_{Ox}))^{1/2}}{kT}\right] \tag{3.34}$$

$$\ln(J_{PF}/E_{Ox}) = \left[\frac{(q^3E_{Ox}/\pi\epsilon_0\epsilon_{Ox})^{1/2}}{kT}\right] + \left[\ln B - \frac{q\phi_B}{kT}\right] \tag{3.35}$$

For the graphic analysis the following plots need to be evaluated.

Plot I	$\ln(J/E_{Ox})$ vs. $E_{Ox}^{1/2}$
Slope m $= (q^3/\pi\epsilon_0\epsilon_{Ox})^{1/2}/kT$	y-intercept $= \ln B - q\phi_B/kT$
Plot II	$\ln(J/E)$ vs. $1/T$
Slope m $= (q^3E_{Ox}/\pi\epsilon_0\epsilon_{Ox})^{1/2}/kT) - \phi_B/k$	y-intercept $= \ln B$

where B is the constant conductivity at low fields and ϕ_B the barrier height.

For low voltages and high temperatures, the current results from thermally excited hopping electrons between different isolating states. The mechanism hopping conduction[67], is considered to show Ohmic characteristics under those

conditions and is therefore dependent on the activation energy of the electrons ΔE_{ac}:

$$J_{HC} \propto E_{Ox} exp\left(\frac{\Delta E_{ac}}{kT}\right) \tag{3.36}$$

Other leakage mechanisms Increased tunneling current at low bias is called *Stress-Induced Leakage Current (SILC)*, which is caused by inelastic trap assisted tunnel transitions. The traps are created by the high electric field stress during writing and erasing processes in non volatile memory devices. SILC is mainly responsible for the degradation of the retention in the devices.[68] [69] [70]

Phonon Assisted Tunneling: PhAT is a defect assisted, inelastic two step tunneling process of an electron from a cathode to the anode via a trap. The electrons are captured by the cathode, relax to the energy level of a trap by emitting one or more phonons and are afterwards emitted to an anode.

Space charge limited type current: SCLC results from carriers injected into the insulator, where no compensating charge is present.[58]

As these mechanisms are not relevant for the standard testing method, they should not be elucidated in detail at this point.

3.3. Equivalent Oxide Thickness: EOT

To evaluate the quality and performance, especially the leakage current values of alternative gate oxides in comparison to conventionally used SiO_2 gates, the equivalent oxide thickness is introduced. The EOT indicates how thick a SiO_2 layer is to achieve the same effect as the alternative gate material used. The EOT can be calculated after:

$$EOT = \frac{\kappa_{SiO_2}}{\kappa_{Ox}} t_{Ox} \tag{3.37}$$

κ_{SiO_2}: dielectric constant of SiO_2 (3.9)
t_{Ox}: physical thickness of the alternative gate oxide

For materials with higher dielectric constants, increasing film thicknesses are possible to be implemented in MOS devices (s. eq. 1.1) while achieving the same or better performances than MOS structures with SiO_2 gate oxides.

4. Crystallization & Film formation

The film deposition techniques introduced in the present thesis are solution based. Therefore, the mechanism of film formation is strongly dependent on the crystallization behavior. In the following chapter an introduction into hetero- and homogeneous nucleation should be given, based on the drop formation model after Volmer for supersaturated vapors.[71] Different film formation mechanisms should be introduced in conclusion. The detailed analysis of crystallization processes in complex systems is challenging, since a compatible model for the respective process needs to be found to describe the process theoretically and in most of the cases, the respective variables are not or insufficiently accessible experimentally.

Processes, where the crystallization happens within the respective phase without the influence of an external interface based on statistical variations of the density and kinetic energy, are referred to as homogeneous, whereas processes initiated by an external interface (molecules or surfaces) are so called heterogeneous crystallization processes. A crystallization process is always initiated by the formation of a submicroscopic nucleus, followed by the growth to a macroscopic nucleus with a characteristic shape, dependent on the material and growth conditions. The dynamics of phase transitions from over saturated solutions to crystalline solids are mostly explained by a change of the "solution structure", like melts or soluted aggregates of clusters.[72]

4.1. Nucleation from Solutions

In solutions, agglomerations of the dissolved molecules are statistically distributed. Clusters are unstable due to a release of phase transition energy and the resulting attempt to convert into another state. The energy, which is required to built a new interface, ΔG_σ, counters the trend to dissociate. Based on the classic nucleation theory, spherical clusters are generated with the radius r and the surface energy can be expressed by the surface tension σ.

Therefore, the free Gibbs enthalpy, ΔG_C, for the crystallization of spherical clusters can be written as:

$$\Delta G_C = \Delta G_V + \Delta G_\sigma = \frac{4}{3}\pi r^3 \Delta G_v + 4\pi r^2 \sigma \tag{4.1}$$

with ΔG_σ as surface dependent factor and ΔG_V as bulk factor. In growing systems, the difference is increasing and therefore the systems are unstable, resulting in a dissociation of the clusters. As ΔG_V and ΔG_0 depend differently on the radius of the cluster, for small nuclei an energy input is required to initiate and continue the growth process.

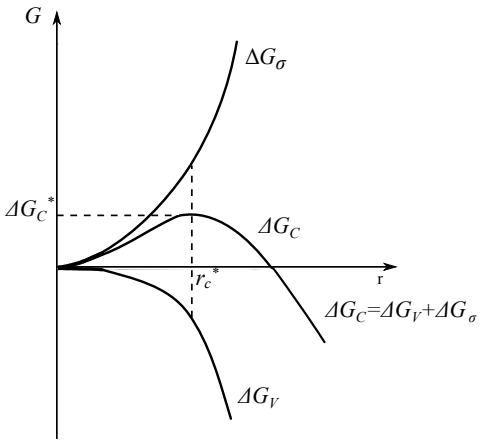


Figure 4.1.: Free Gibbs enthalpy of crystallization in dependency on the nuclei radius r (after[73]).

Figure 4.1. shows the enthalpy versus nucleus radius. At the critical nucleus radius r_c^*, the free Gibbs enthalpy shows a maximum. The slope of the energy benefit, caused by the phase transition, exceeds the required energy to form a new interface and the cluster remains stable.[73]

The critical radius is dependent on the supersaturated state, S, temperature, T, and the mol density, ρ_m :

$$r_c^* = -\frac{2\sigma}{\Delta G_v} = \frac{2\sigma}{2\rho_m RT \ln S} \tag{4.2}$$

The required free Gibbs enthalpy to achieve the critical radius is given by:

$$\Delta G_C^* = \frac{16\pi\sigma^3}{3\Delta G_V^2} \tag{4.3}$$

The distribution of nucleus sizes can be described by the Boltzmann statistic. Therefore, the number of critical nuclei N^* can be calculated from[74]:

$$N^* = Ne^{\left(-\frac{\Delta G_C^*}{kT}\right)} \tag{4.4}$$

The critical free Gibbs enthalpy of nucleus formation is exponentially connected to the supersaturation of the solution, causing a strong tendency of nuclei formation at a particular high solution concentration, resulting in spontaneous crystallization, the homogeneous crystallization.

The different concentration based states of the crystallization lye in dependency on the temperature are illustrated in figure 4.2.

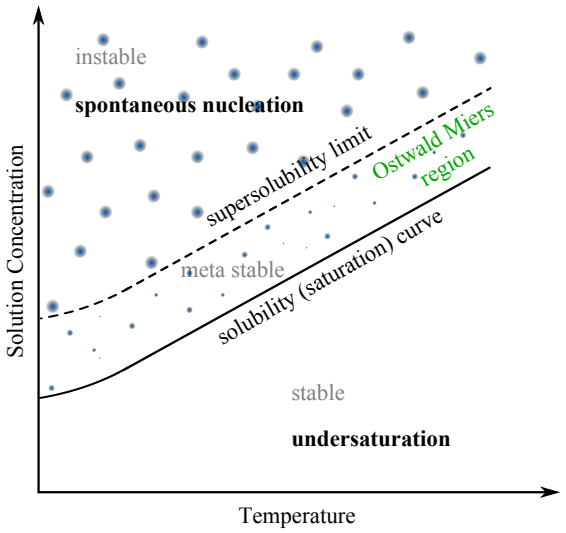


Figure 4.2.: Saturation regions in solutions.

Shown are the regions of saturation, undersaturation and the meta stable threshold range between the over saturation limit and solubility curve, called Ostwald Miers region. In the Ostwald Miers region, the solubility product is exceeded, however the nuclei are still solvable due to a gain of entropy by the formation of a large number of small nuclei and non homogeneous crystallization is initiated. The solution is meta stable and sensitive to external influences. In the labile region of supersaturation, the Ostwald ripening occurs, where huge nuclei sizes are the preferred formed crystallites.

4.2. Crystallization in Films

Referring to figure 4.2., film formation from solutions due to crystallization can only occur above the solubility curve and therefore at certain solution concentrations. Within the Ostwald Miers region, the system is considered to be meta stable and can be easily influenced by outer effects. Foreign particles like dust, reaction vessel walls as well as crystalline or non crystalline substrates can cause a decrease of the critical free enthalpy and therefore an initiation of the crystallization process. The described process is called heterogeneous crystallization, which is the preferred mechanism for film deposition and nuclei formation on substrates from solutions. The process needs to be initiated by a particle diffusion towards the surface to exceed the solubility limit in vicinity of the surface. The elementary reaction steps which proceed simultaneously and are temporarily superimposed, can be described as particle supply and adsorption, nuclei formation, film growth and ripening as illustrated in figure 4.3. Therefore, the reaction rate for the heterogeneous reaction is limited by the diffusion and adsorption processes.

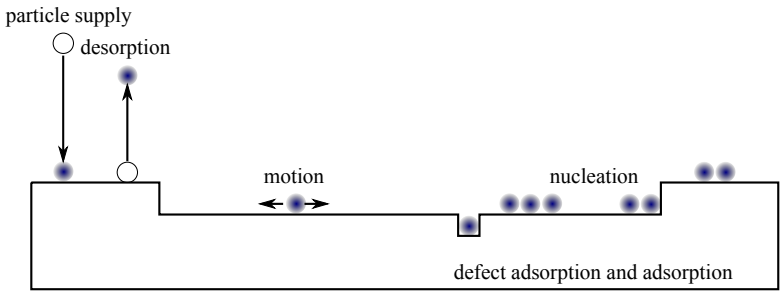


Figure 4.3.: Heterogeneous crystallization process for substrate supported layer formation (compare[75]).

Cluster formation during film growth processes needs to be described in 2D models. For film formation the critical radius r^*_{2D} can be written as:

$$r^*_{2D} = \frac{\sigma}{\rho_m RT \ln S} \tag{4.5}$$

and the respective critical enthalpy:

$$\Delta G^*_{2D} = \frac{\pi \sigma^2 t}{\rho_m RT \ln S} \tag{4.6}$$

where t is the thickness of the generated layer, which equals the lattice constant. On surfaces, the nuclei formation is additionally dependent on the wetting behavior, described by the contact angle θ between the substrate and the solvent used. The basic precedent for heterogeneous crystallization is the general wetting ability of the droplet on the supported external substrate. The critical Gibbs enthalpy needs to be corrected by $f(\theta)$:

$$f(\theta) = \frac{(2 + \cos\theta)(1 - \cos\theta)^2}{4} \tag{4.7}$$

$$\Delta G^*_\theta = \Delta G^*_C f(\theta) \tag{4.8}$$

The nuclei formation is primarily influenced by the energy of the interface between crystal and solution. Nevertheless, the relation between the interface energy of the substrate-crystal (σ_{BC}), the crystal-solution (σ_{CS}) and solution-substrate (σ_{SB}) defines the character of the film formation, since they affect the contact angle after Young as following:

$$\cos\theta = \frac{(\sigma_{SB} - \sigma_{BC})}{\sigma_{CS}} \tag{4.9}$$

Figure 4.4. shows the wetting of a droplet of the mother lye on the substrate. Droplets with circular shapes are formed due to the attempt to achieve a min-

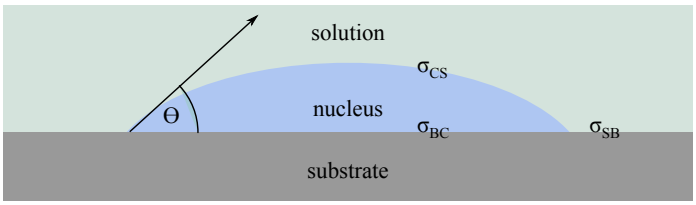


Figure 4.4.: Contact angle in heterogeneous nucleus formation on dissimilar substrates.

imum of energy in the system, which can be maintained by minimizing the forces affecting the molecules of the respective substance. By maximizing the surface area, a minimum energy is realized due to a deficiency of forces taking effect on the boundary layer molecules. The nucleus formation in heterogeneous crystallization is therefore essentially ruled by the inter atomic forces between the particles within the mother lye and the underlying substrate.

The energy of the adsorption is composed by the different interface energies:

$$E_{ads} = \sigma_{BC} + \sigma_{SB} + \sigma_{CS} \tag{4.10}$$

which is similar to the adsorption of metals on oxides.[76]

Different models are applied to describe the film growth mechanisms, leading to discriminate film structures depending on the type of interaction (cohesion, adsorption) between the film and the substrate (s. figure 4.5.).

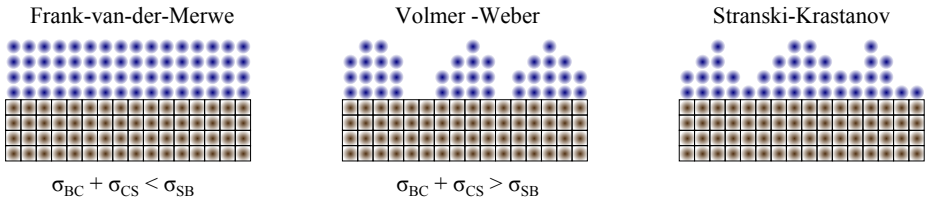


Figure 4.5.: Schematic illustration of different film growth types in dependency on the interface energy.

Uniform films are formed by subsequent 2D monolayer formation if the substrate-crystal interaction force is lower than the interaction force with the surface (Frank-van-der-Merwe). Island growth leads to 3D growth on the surface if the interaction between the substrate and the solution is stronger (Volmer-Weber). Stranski-Krastanov growth is a mixture of the previously mentioned mechanisms, where after the growth of one or more mono layers islands are formed. Furthermore, the varying interaction forces lead to completely different transition regions which are shown in figure 4.6.

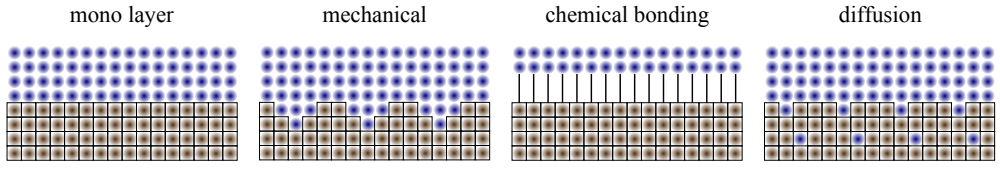


Figure 4.6.: Possible interfacial structure formations from crystallization processes on dissimilar substrates.

Concluding, that the film formation characteristics are, besides the concentration dependency, strongly influenced by the structure and roughness of the

underlying substrate, adhesion and cohesion forces as well as diffusion and chemical bonding energies. Substrate and solution temperature are other sensitive factors, which lead to different types of film formation.

5. State Of The Art

In order to full fill the mentioned requirements of the semiconductor roadmaps ITRS[1] 2011 for device scaling of decreased device sizes down to the future sub 22 nm node and improved stable electrical performance one of the promising approaches besides completely new transistor structures is the high-κ material application. High-κ materials enable the integration of physical relatively thicker gate oxide layers and yet achieve the same capacitance as SiO_2, in other words: high-κ materials will be physically thicker at a respective EOT and therefore exhibit desired lower leakage currents.

Based on the previous ITRS 2005 less than 3.9 nm oxide thickness is required for DRAM and 1.9 nm for low power transistor applications in the recent sub 65 nm node. Sub 65 nm node devices show intolerable increased leakage currents due to the physical limitation of pure SiO_2 gate stacks leading to direct quantum mechanical tunneling.

The choice of the precursor materials, the semiconductor surface and the surface and film preparation plays a significant role for the tailoring of the properties of the high-κ gate stacks.[77] Besides the dielectric constants and the resulting increased possible oxide thickness, the maintenance of the band gap of the dielectric material in order to minimize the appearing leakage currents, is another adjustable variable by gate stack tailoring.

In the following chapter alternative gate stack materials should be introduced including the concomitant interface requirements. REOs should be elucidated with respect to a potential SiO_2 replacement describing the thermodynamic stability in contact with Si, the respective physical properties and a short introduction about basic chemistry and the recent political discussion about the availability of RE based resources will be given. The chapter terminates with an exposition of the importance of the process compatibility and a short introduction of conventional deposition techniques including their advantages and problematic aspects.

[1] International Technology Roadmap for Semiconductors made by SIA (Semiconductor Industry Association in Collaboration with Japan, Europe, Korea and Taiwan)

5.1. Alternative Gate Stack Materials

Several high-κ materials are in discussion for SiO_2 replacement. The properties of a selection of widely used alternative gate stack materials is listed in table 5.1.[78]

Table 5.1.: Alternative materials as high-κ replacement, κ values, band gaps and crystal structures.[79] [78] [80]

Dielectric Material	κ	**Bandgap (eV)**	**Crystal Structure**
SiO_2	3.9	8.9	amorphous
Si_3N_4	7	5.1	amorphous
Al_2O_3	9	8.7	crystalline $>$ 1173 K
Y_2O_3	15	5.6	
CeO_2	26	5.5	
Ta_2O_5	26	4.5	crystalline $>$ 873 K
La_2O_3	30	4.0	crystalline $>$ 870 K
TiO_2	20-80	$\approx$ 3.5	crystalline $>$ 673 K
HfO_2	25	5.7	crystalline $>$ 723 K
ZrO_2	25	5.8	
$SrTaO$	20-100	4.5-4.8	crystalline $>$ 973 K
$HfSi_xO_y$	15-25	6	
$ZrSi_xO_y$	15-25	6	

Some of the high-κ materials, which are in the current focus of research including tantalum pentoxide (Ta_2O_5) and TiO_2 show enormous high dielectric constants ranging from 10 up to 80 but are not thermally stable in direct contact with silicon. Low temperature crystallization issues for thermally stable compounds such as hafnium dioxide (HfO_2) or zirconium dioxide (ZrO_2) lead to segregation of Si into the oxide layer and unwanted silicate formation. HfO_2 and Ta_2O_5, are the most investigated materials as they have already been integrated into Dynamic Random Access Memory (DRAM) and transistor devices.[81] [82] A review on high-κ dielectrics for microelectronic applications can be found in[79]. According to Chau et al. high-κ dielectrics attribute their high dielectric constants to the polarizable metal oxygen bonds.[83]

As the present thesis is mainly focused on the investigation of a new inorganic RE based technique for thin film generation, in the following the details are focused on RE materials.

5.2. Limitations for Different Device Applications

Different application types require different limits in maximum leakage current densities. Lo et al. showed an overview of the required values in dependency on the oxide thickness.[3] [84]

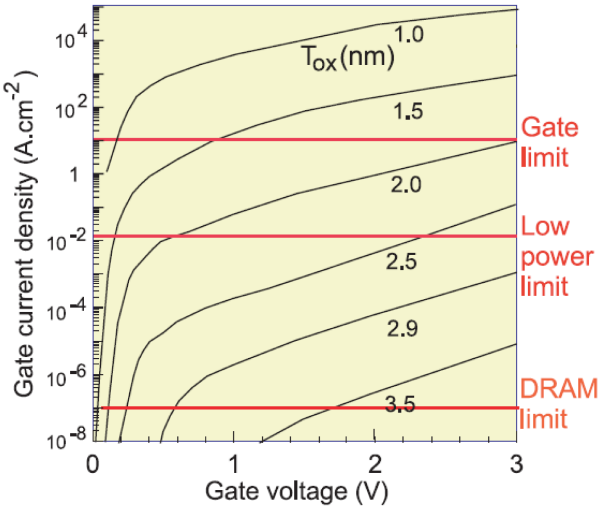


Figure 5.1.: Leakage currents vs. voltage for various thicknesses of SiO_2 layers (from[84]).

According to the shown results the lower leakage current density limits for gates are $< 10\ Acm^{-2}$, in low standby power CMOS $< 1.5 \times 10^{-2} Acm^{-2}$ and for high quality DRAM capacitors $< 10^{-7}\ Acm^{-2}$.

5.3. Gate Stack Tailoring: Multi Layer Systems

Besides single layer systems of new materials a great effort is put into the development of engineered multi layer high-κ systems merging the best properties of each material in a multi layered gate stack. The combination of two or more

dielectrics enables a leakage current reduction by increasing the energy band gap. Combinations of e.g. *Ta*-oxides with *Al*, intermixed *Hf-Al* oxide films or laminates of *Al*, *Hf* and *Ta* have been reported in the literature.[85] [86] [87] [88] In the present work a new approach will be presented combining a wet chemical deposited RE based film with an ALD deposited high-κ TiO_2 film.

5.4. Interfacial Structure

Besides the dielectric layer itself, the interface quality and therefore the number of traps and charges is crucial for the final electrical performance of the gate stack. For conventionally used techniques, the formation of SiO_2 or other metal/silicate interfacial layers occurs during the deposition process or during further annealing steps, which are necessary for dopant activation. Moreover intended interfacial buffer layers of SiO_2 are suggestively integrated to avoid chemical reactions between thermodynamic unstable alternative gate stack materials and the *Si* substrates.

However, the formation of those low permittivity materials lead to a limitation of the final electrical performance for a dielectric gate stack, as the highest possible capacitance or equivalently the lowest achievable EOT is decreased (analogous to the tailored multi layer stacks).

Hence, an effective physical oxide thickness can be defined as:

$$t_{ox,eff} = t_{ox} + \frac{\epsilon_{ox}}{\epsilon_{high-\kappa}} \tag{5.1}$$

It is particularly important to mention that additional layers introduce additional interfaces between the dielectrics, which serve as potential sources of undesired electron traps and charging within the films. Therefore, the interface formation needs to be controlled precisely in order to generate high performance gate stacks.[89]

5.5. REO Systems

Several high-κ materials do not fulfill the requirements of alternative gate oxides as they show small band gaps or no band offset from silicon. REOs

emerged as promising alternative materials for SiO_2 gate stack replacement due to their excellent electrical properties such as wide band gaps (4-6 eV), reasonable high dielectric constants (7-30) and a high resistivity (10^{12}-10^{15} cm). Additionally the diffusion coefficient of oxygen is controllable depending on the structure, which is important regarding interfacial reaction avoidance.

High recrystallization temperatures provide a high thermal stability and no changes in the structures during high temperature IC processing. The thermal and kinetic stability in contact with *Si* prevents an unwanted reoxidation of the substrates.[6]

However, there are certain associated problems with the REOs such as potential interaction of the film with the *Si* surface at high temperature deposition or annealing, which leads to silicide formation or a thin SiO_2 layer due to segregation of the oxide into the metal and oxygen. REOs show stoichiometry dependent dielectric constants.

New gate stacks require new top electrode materials. Moreover, some of the REOs are highly hygroscopic even though they show excellent electrical properties. This leads to the need of in situ top electrode covering and makes scientific evaluations of the films more complicated as the complete characterization has to be performed under air exclusion. Despite the mentioned problems, research on these oxides remains popular due to their promising dielectric behavior.[90] In dependency on the electronic configuration different oxides are known from the different RE elements.

With respect to an inorganic wet chemical approach there are also other advantageous relevant aspects of importance as the RE materials are easy to handle and they show a similar inorganic chemistry which makes precursor synthesis simple and a large number of compounds available for thin film deposition.

5.5.1. Rare Earth: Elemental Abundance, Extraction and Political Influence

The designation RE-elements is generally related to scandium, yttrium and the row of the 15 lanthanides (lanthanum to lutetium).

Within the group of the lanthanides the ionic radius decreases with increasing atomic number. The so called lanthanide contraction is caused by the effect that the shielding impact of the *4f* orbitals is not sufficient to compensate

the increasing nuclear charge with increasing atomic number. All lanthanides exist in the oxidation state +III. Crystallographic similarity leads to common occurrence of the RE minerals, which are not embedded into other element mineral systems due to high ionic radii of the f elements.

Chemically the RE are rather similar which makes a separation from the multi RE minerals difficult and cost intensive. Technically the RE elements are commonly extracted by fluid-fluid-extraction whereby the different solubility depending on the ionic radius are exploited.[91] [92]

Whereupon the name rare earth is misleading since the elements of the scandium group are not rare but as abundant as e.g. lead or zinc but they are less enriched in mineral deposits. Mineral deposits of RE compounds are known at several places worldwide e.g. China, Australia, Greenland, USA, India, Brazil or Malaysia.[93] Due to the low costs the commercial excavation to date is essential dominated by China.

The "monopoly position" of China in the RE excavation business, caused by the high excavation costs at other countries and missing production permissions for other production sites, lead to political problems regarding the RE excavation as China limited the export rates of the REs at the beginning of 2011, in order to preserve the development of key technologies within the country.[94] A dispute arising about increased export duties or even export prohibitions resulted in a complaint against China by the USA and EU in March 2012 to the WTO.[95] In response China established a trade association in April 2012 with the intended aim to develop a coordinated resource processing combined with a reasonable pricing mechanism. According to many critics this might be just another mechanism in order to achieve a full control of the RE market.

For a full integration of RE materials into commercial semiconductor industries these political restrictions or extraction limitations needs the be regulated in order to ensure a possible low cost device production.

5.5.2. Thermodynamic Stability of Rare Earth Oxides in Contact with Silicon

As mentioned previously the thermodynamic stability of alternative gate-oxide materials in contact with Si is one of the essential criteria regarding the choice of the metal oxide for gate applications in MOSFETs. Insufficient stable ma-

terials lead to unwanted extensive inter diffusion or chemical reactions that degrade the properties of the oxide layers and the underlying *Si*. Interfacial formed phases e.g. silicates often result in a lack of lattice matching or epitaxy. Those phases as well as unwanted SiO_2 layers, formed due to reoxidation processes, lead to drastically degraded leakage behavior and concomitant joule heating which ends up in intolerable switching errors of the devices. Many of the possible high-κ candidates react with *Si* forming a SiO_x interfacial layer which is detrimental to the dielectric thickness due to lower dielectric constants. Inter diffusion between the film and the oxide layer results in the uncontrolled formation of poor quality silicate or oxide layers.[96]

In the following section an overview on the thermodynamic stability of the ternary REO in contact with *Si* should be given based on reference[97]. The thermodynamic stability of the REO and RE-silicides at 1000 K (typical deposition temperature for epitaxial oxide growth with conventional methods) were investigated focusing on high potential candidates as alternative gate oxides.

The interesting REO candidates to replace SiO_2 as gate oxide due to positive Gibbs free Energy at 1000 K (ΔG_{1000}) for the reaction $Si + MO_X \rightarrow M + SiO_2$ (balanced appropriately), as according to thermodynamic data the formation of silicides and interfacial oxides is unfavorable, are listed in table 5.2.

From the shown free Gibbs Enthalpy values it is obvious that except from *Eu*-oxide modifications all sesquioxide oxides show positive ΔG_{1000} values around 100 kcal/mol indicating a high thermodynamic stability and an unlikely SiO_2 formation at the interface to the *Si* substrate. Therefore the shown compounds are appropriate candidates as alternative gate oxides with respect to the thermodynamic data.

As within the present thesis a completely new deposition technique is introduced and shall be analyzed regarding the deposition mechanism and the influence of the new pure inorganic precursor materials on the film formation a precise selection of elements has been made for the experimental work. The thermodynamic stable sesquioxide compounds *La* and *Nd* have been chosen to open a systematic investigation starting from the first element in the row of the lanthanides, *La* and continuing with the second which forms exclusively the sesquioxide and is stable under air exposure, *Nd*.

Table 5.2.: Thermodynamically stable and therefore interesting RE candidates for SiO_2 replacement and the respective ΔG_{1000} values.

Binary Oxide		ΔG^*_{1000} **(kcal/mol)**	**Reference**
Sc_2O_3	+	123.105	[98] [99]
Y_2O_3	+	116.823	[98]
La_2O_3	+	98.470	[98] [99]
Ce_2O_3	+	104.946	[98] [99]
CeO_2	+	36.290	[98] [99]
Pr_2O_3	+	105.768	[98] [99]
Nd_2O_3	+	101.692	[98] [99]
Sm_2O_3	+	103.941	[100]
EuO	+	33.238	[100]
Eu_2O_3	+	61.901	[100]
Gd_2O_3	+	101.549	[98]
Tb_2O_3	+	114.762	[98] [99]
$TbO_{1.72}$	+	38.273	[98] [99]
Dy_2O_3	+	112.435	[100]
Ho_2O_3	+	118.450	[100]
Er_2O_3	+	122.030	[100]
Tm_2O_3	+	116.654	[100]
Yb_2O_3	+	103.830	[100]
Lu_2O_3	+	116.965	[100]

5.5.3. Lattice Constants and Physical Parameters

All sesquioxides of the lanthanides show a polymorphism resulting in temperature dependent transformations to different coordination states. Five different states are known, which are basically existent below and above 2273 K. As for the lighter RE materials only one low temperature modification is known. The working conditions for the present thesis are far below the transformation temperature of 2273 K. Therefore only one modification is expected for *La* and *Nd*.

The sesquioxides La_2O_3 and Nd_2O_3 are found to form hexagonal structures of the space group P32/m with one formula per unit cell.[101] [102] They show a seven fold coordination with four oxygen atoms closer than the other three.[103] [104]

According to[105] and[106] the four closer oxygen atoms are bound to five metal atoms, whereas the other three are bound to additional four metal atoms.

The lattice parameters of the sesquioxides are listed in table 5.3.

Table 5.3.: Lattice parameters of the "low temperature modifications" of the lanthanide sesquioxides.[104]

	a (nm)	**c (nm)**
La_2O_3	0.39372	0.61295
Nd_2O_3	0.38293	0.59970

The ionic radii are listed as $Nd^{3+} = 98$ pm and $La^{3+} = 106$ pm[107] showing a rather similar ionic size and therefore expected similar characteristics with respect to solubility and deposition behavior.

During deposition and device processing it is important that the thermal expansion mismatch between the oxide and the Si substrate needs to be minimized to prevent cracking caused by thermally induced strains during cooling after the film growth. Strains caused by the low expansion coefficient of Si lead to tension inside the oxide films and subsequently in erroneous loss of electrical quality.

5.6. Process Compatibility and Deposition Techniques

For high cost efficiency, it is important that deposition techniques can be easily integrated into device production. Low temperature approaches are desirable as well under economic as under environmental aspects.

In order to obtain and maintain excellent electrical characteristics, as low leakage currents and high-κ values, the generated gate dielectrics need to remain stable during post-generation treatments in the semiconductor processing. It is discussed contradictory in literature if amorphous or crystalline structures are better candidates. Crystalline structures offer the main advantage of good lattice matching in the case of similar lattice constants and resulting good interface qualities but amorphous structures reduce the number of grain boundaries which may serve as high leakage path.

Anyway, from our point of view it is desirable to generate an amorphous structure since they can be transformed into crystalline species by specific annealing treatments, whereas crystalline structures can hardly be processed into amorphous. As many alternative oxides crystallize at respectively low temperatures, this aspect is a main challenge in high-κ material implementation.[89]

Many techniques have been suggested for thin film deposition within the range of 100 down to 1 nm. Among these, conventional sputtering, physical vapor deposition (PVD), molecular beam epitaxy (MBE) and chemical vapor deposition (CVD) including atomic layer deposition (ALD) are noteworthy as they provide the possibility of a precise control of the film composition. PVD, MBE and simple forms of CVD do not guarantee film smoothness and accurate thickness control, whereas ALD ensures a layer-by-layer growth and thereby an ensured conformal film thickness.[108] Recently pulsed laser deposition (PLD), which is a precise form of PVD, came into the focus of research. All techniques in common are required vacuum conditions and therefore a complex and cost intensive process integration.

Typical PVD is used as a general designation to describe thin film deposition methods which are based on the condensation of a vaporized precursor onto various substrates. PVD is a physically based technique, including the high temperature vacuum evaporation with subsequent condensation, or plasma sputtering of the precursors. Oxides are generated by oxygen gas dosage. PVD is cost inefficient due to high evaporation temperatures, furthermore the precursors are unavoidably deposited on the entire deposition chamber which induces a high number of impurities in case of multiple batch production.

If laser components are integrated into the PVD process in order to vaporize the precursor targets, the technique is referred to as PLD. Crucial factors for the film quality during PLD deposition are the laser parameters, surface temperature and the remaining background pressure of oxygen, as a too low oxygen pressure effects the stoichiometry of the formed oxides, therefore the nucleation density and subsequently the film quality.[109]

MBE allows to deposit relatively pure epitaxial layers. Solid sources of the precursors in ultra-pure form are sublimed separately in so called quasi-Knudsen effusion cells. Films are deposited by the condensation of the gaseous elements on the wafer substrates, where a possible reaction of the different components is induced. MBE is limited by the mean free path of the evaporated precursor

atoms and therefore highly time consuming, which prevents it from being the method of choice for major industrial processes, even though it enables the purest films to be deposited. However, it was found that for films deposited from MBE, unwanted and the electrical performance negatively influencing, silicide formation might occur in the initial state of the deposition which is another major drawback of MBE.[110] The applicability of MBE is limited by the lattice matching of the substrate and the desired film. Due to the epitaxial growth mechanism, a lattice mismatch lead to elastic energy accumulation within the generated films, leading to cracked island structures instead of homogeneous films.

In contrast, CVD is based on the chemical reaction or decomposition of one or more volatile precursors on the substrate surface to generate the desired film material. A gas flow trough the chamber removes eventually formed gaseous products. Numerous types of CVD are known. CVD enables to deposit mono crystalline, polycrystalline, amorphous and epitaxial structures of various materials. The volatile precursors are mostly toxic organic compounds, leading to high impurity rates within the deposited films. Again a relatively high energy consumption is caused by high evaporation temperatures. The classification of different CVD processes is based on the pressure conditions, vapor characteristics and resulting injection mode or type of precursor molecules. A special type of CVD is the metal organic CVD (MOCVD), where metal organic precursors are applied. Particular type of MOCVD is atomic layer deposition, which is the only technique integrated into commercial real device production up to date.[111] Due to the significance of ALD and since it has been applied for bilayer generation in the present work, a more detailed explanation is given in the following.

5.6.1. Atomic Layer Deposition

Atomic layer deposition (ALD) is a high potential thin film deposition technique which has become the method of choice for semiconductor industry to process ultra thin films with high uniformity onto large area substrates. It was invented by Suntola and Antson in 1977[112] initially to meet the requirements for thin film based electroluminescent displays. The basic ALD process consists of four characteristic steps (referred to collectively as one cycle), where the precursor molecules react with the surface in two separated reactions. Initially,

a typical organometallic, evaporated precursor is exposed to the substrate inside an ALD chamber, whereas the precursor molecules react with the surface terminated substrates (1.). In the second step, the reaction chamber is purged with an inert gas flow to remove the non reacted precursor and the gaseous reaction products (2.), followed by the exposure and reaction of the second precursor or activating reactants (e.g. plasma) to prepare the surface for the second surface reaction (3.). The process is completed by another purge of the reaction chamber (4.).

The experiments are typically conducted at a certain temperature, the so called ALD window, where the reaction is limited by the precursor condensation. Sometimes, no precise ALD window can be observed if the deposition rate is dependent on the number of available reactive sites.[113] For ALD no homogeneous reactant flux is required, as the reactions are self limited and surface controlled. Deposited films show excellent conformity, they are dense and pinhole free. A defined precise thickness control down to the Å regime is provided by the choice of the number of cycles.

ALD has bee successfully applied for high-κ material deposition and is already integrated into device production[114] [115] and was mentioned as probably the only suitable technique for oxide gate stack deposition.[116]

However, despite the numerous advantages of ALD, the process suffers from severe problems such as availability of precursor compounds at reasonable prices or simply incapability of adequate precursor synthesis. Even though the problem of insufficient volatility, which is essential for the ALD process has been recently overcome for some new precursor materials[117], the criteria of non toxicity and safe handling of the materials is frequently not satisfied.[118] Another major drawback is the usage of organic precursor molecules containing carbon and other components which result in serious chemical impurities within the deposited films. Those impurities have a strong negative influence of the final electrical performance of the deposited films, which is a serious issue for the integration of high-κ thin film materials into electrical MOS devices. Besides thin film deposition, ALD became recently a key technology for surface modifications and coatings of nano structured materials.[119] [120] [121]

5.7. Non-Silicon Devices

To enable further high-performance transistors built up alternative high-mobility materials such as Ge, carbon nanotubes or III-V semiconductors are in discussion additionally to Si based transistors.[83]

The first transistors were fabricated in 1947 in Bell laboratories using Ge as bulk material and the inventors Bardeen, Brattain and Schockley have been awarded with the Nobel Price in Physics for their research on semiconductors and the discovery of the transistor effect in 1956.[122] In the 1950s and early 60s, Ge was the predominant material for solid-state devices, but has been replaced by Si after MOSFETs became technologically significant, due to the outstanding advantage of the high quality native oxide SiO_2 and a larger band gap of Si, resulting in lower leakage currents. Currently in the 45 and sub 45 nm node those advantages are neglected due to tunneling currents at an oxide thickness below 1.5 nm. Therefore, Ge is back in interest since the much higher electron and hole mobilities and the high solubility limits for p-type doping of Ge compared to Si can be exploited by using Ge instead of Si.[66] [123] Furthermore, the development of high-κ dielectrics with Ge seems promising, which overcomes the problem of insufficient stable native oxide formation of Ge.[124] [125]

Ge wafers are commercially available in standardized sizes from 50 to 300 nm diameter. The wafers are highly fragile and thinner than conventionally used Si wafers, requiring a careful wafer handling. Technically the major drawback about the reintegration of Ge as transistor material, are the extensive material costs for Ge (600 USD/kg) compared to bulk Si (54 USD/kg), which is a significant objection regarding mass production of transistor devices. Moreover, Ge shows a much higher density than Si (5.32 g/cm^3 vs. 2.33 g/cm^3). This implies that tool sharing for both substrates is not possible which is a challenging issue for wafer handling (robots etc.).

To combine both advantages and to ensure the feasibility of the commercial built wafer production lines alloys of Si and Ge, $SiGe$ are recently under discussion to replace pure Si substrates, as they offer the significant advantage of lower costs and higher mechanical strength provided by the usage of Si combined with the greater electron hole mobility and larger band gaps of Ge.[126] [127]

The crucial aspect for a possible implementation of high-κ gate dielectrics for Ge based devices is the development of a successful and reliable surface cleaning method. The problem of Ge segregation into the films itself needs to be overcome prior to a technical implementation of high-κ dielectrics on Ge.[77]

6. Experimental Setup & Data Processing

In the following chapter, the scientific instruments used for the experimental analysis and handling of chemicals in the present thesis are shortly introduced. The utilized software for data plotting and analysis is listed. For XPS analysis, extensive peak fitting is necessary for data processing. Therefore, the peak fit parameters should be elucidated additionally.

6.1. The UHV-Chamber

Figure 6.1. the UHV system which has been used for the surface analysis in the present thesis. System design and installation were done during the work of U. Leist and S. Neuendorf.[128] [129]

The system comprises a main recipient for sample preparation and analysis as well as an STM section (*STM VT STM H LN2 XA by Omicron*). Available analysis methods in the main recipient are XPS (X-ray source: *XR 50 Specs*, analyzer: *EA-10P Leybold-Heraeus*, high voltage supply: *HV-XR 20 Leybold-Heraeus*, secondary electron multiplier: *PSEV 10 Leybold Heraeus*, software: *SPECTRA Windows V.8.0-A-1 Scientific Instrument Consultants*), UPS (non operative during the present thesis), Low-Energy-Electron-Diffraction (LEED, *OCI Vacuum Micro engineering BDL800 IR-LMX-ISH Specs*) and mass spectrometry in combination with TPD analysis (MS, *Pfeiffer Vacuum Prisma^{TM}QMS 200 M2*, software: *Quadstar 422*).

Additionally, the samples can be indirectly cooled with liquid nitrogen and heated with a filament by applying low and high voltages, depending on the required temperatures. The temperature regulation is done using a *BesTec controller* with an *Eurotherm module* equipped with a K-type thermo couple (chromel/alumel).

Main- and STM-recipient are under UHV ($p < 10^{-9}$ mbar) pressure conditions. The chamber is featured with a load lock for easy and fast sample exchange.

A parking station, where three samples can be stocked within the vacuum, is installed. Both parts are under HV (p $\approx 10^{-8}$ mbar) pressure conditions. For sample transfer between the different parts of the chamber within the vacuum a 360° turnable, gear wheel operated transfer arm is integrated. The specific parts can be separated by shutter valves.

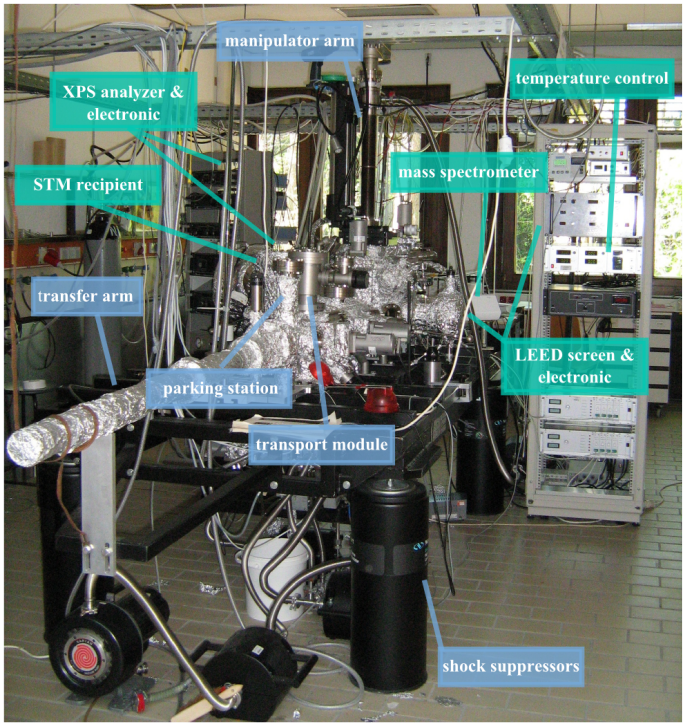


Figure 6.1.: Photograph of the utilized UHV chamber for surface analysis. Shown are the analytical parts (green) and the constructional specifics (blue).

The pump system of the chamber contains the essential elements required to obtain UHV conditions using oil free pumps including different turbo molecular pumps, a titan sublimation pump and an ion getter pump for UHV generation and single/tri scroll pumps for pre-vacuum generation. A detailed description of vacuum generation can be found in[130] e.g.

A detailed description of the chamber, the in the following explained exchange module and sample holder system, can be found in[128] [129] and[131] i.a.

6.1.1. The Sample Holder

The mobile, modular sample holder system was designed in collaboration with the mechanical workshop, by U. Leist, A. Winkler and S. Neuendorf. It contains of the holder slot at the manipulator in the main recipient of the UHV chamber, the sample holder itself and the movable transfer arm. The components can be connected with a plug in system. The sample holder includes a slot for the standardized built-in sample slid of *Omicron*. In chamber views of the sample holder arrangement are shown in figure 6.2.

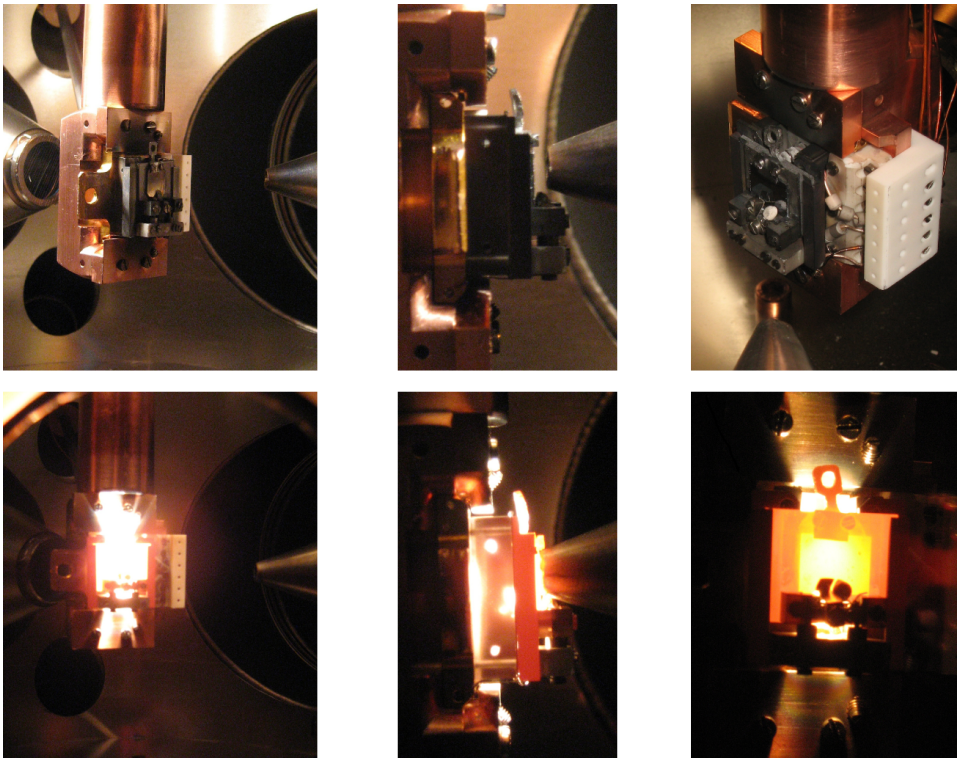


Figure 6.2.: Sample holder with mounted sample within the chamber at room temperature (top), while heating (bottom) in front of the analyzer entrance slit (left), sample holder with approached Feulner cup snorkel of the mass spectrometer (middle) and left side view of the sample holder showing the Macor® contact slit (right).

The sample holder itself (s. figure 6.3.) contains a filament for temperature regulation and contacts for temperature control to install the K-type thermo couple, which is covered with ceramic adhesives for good heat conduction. Sample and thermo couple are fixed by small screws and fixing boards.

Electrical contacting of the sample holder is implemented by a contact strip, which can be connected to the manipulator by pins for the thermo couple, grounding and filament.

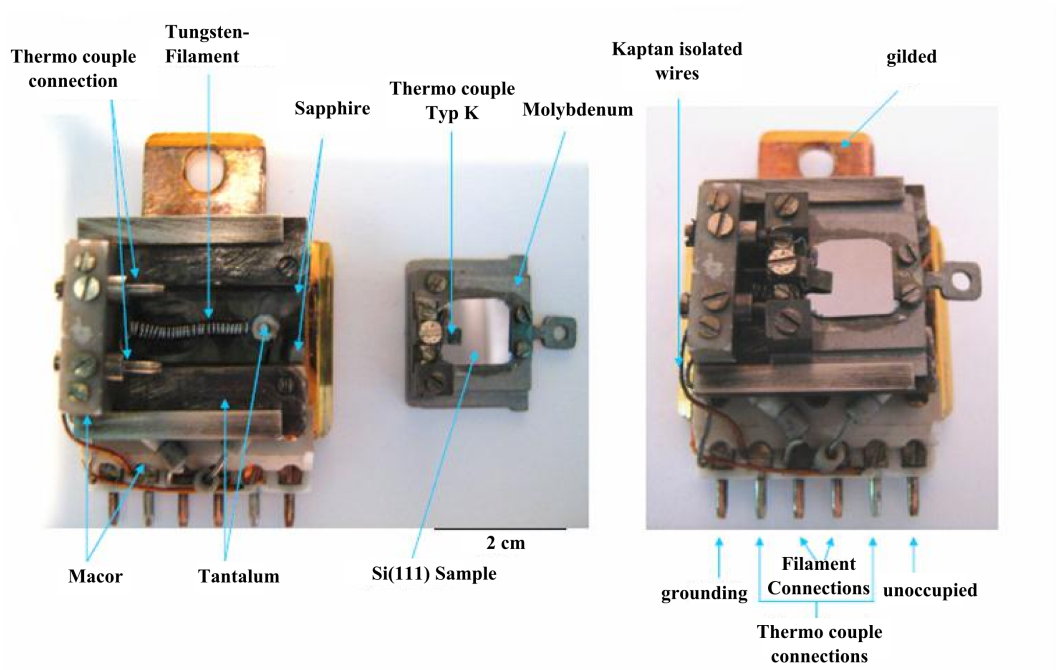


Figure 6.3.: Photograph of the sample holder with sample mounting.

Vacuum feed troughs connect the contacts in the UHV with the respective control unit. Connecting wires on the sample holder mostly consist of tantalum. The contact strip consists of Macor®. Screws are made of tantalum or stainless steel. Due to possible easier low-cost machining, the Macor® parts were replaced by aluminum oxide during the experimental work for the thesis.

6.1.2. Exchange/Transport Module

Figure 6.4. shows the exchange, respectively transport module, which can be mounted to the load lock of the chamber. The module includes a slit to be combined with the sample holder to do the load lock of the samples into the UHV chamber. The sample holder height can be finely adjusted by a screw thread. The transport module can be evacuated or operated under inert gas atmosphere, opening the possibility to load air sensitive or unstable samples into vacuum without air exposure.

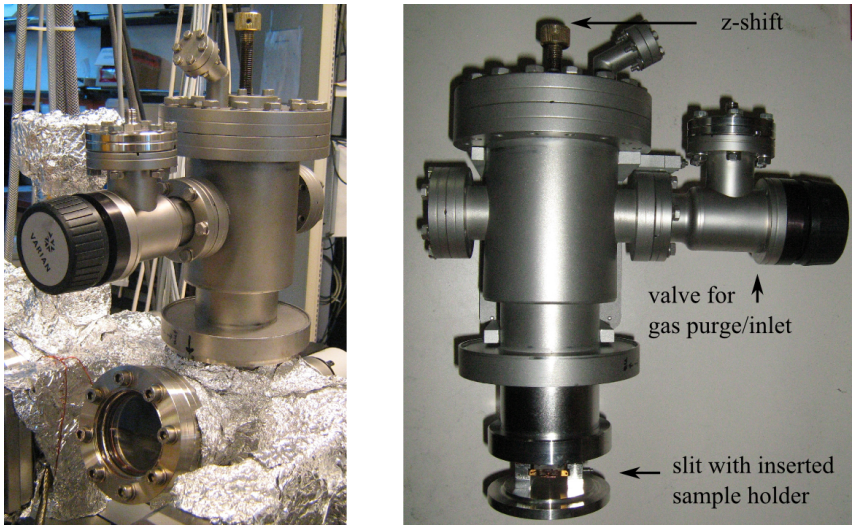


Figure 6.4.: Exchange module adjusted to the chamber (left) and with inserted sample holder prior to sample load (right).

6.2. Additional Analytical Equipment

In the following paragraphs, the instruments which were utilized additionally to the UHV chamber are listed.

6.2.1. Surface Analysis

AFM Topographical analysis under atmospheric conditions were done with the *AFM Digital Instruments, DI 3100 with a NCH-W POINTPROBE - silicon sensor* at NTU Singapore and University of Oldenburg.

FIB and SEM XTEM sample preparation and SEM analysis have been executed with a dual beam unit including an electron and ion beam *QUANTA 200 3D* at the University of Oldenburg and *Nova Nanolab 600 both by FEI™ Company* at NTU Singapore.

TEM For film thickness and composition examinations, the following TEMs have been deployed: *Tecnai F20 S-Twin of FEI™ Company with EDX detector and STEM attachment* at IFAM (Institut für Fertigungstechnik und Materialforschung) Bremen, *HRTEM JEM-2010F by JEOL™* equipped with FEG,

STEM and EDX in FACTS (Facility for Analysis, Characterization, Testing and Simulation) Laboratory at NTU Singapore both working at 200 kV acceleration voltage. The highest resolution was achieved with *Titan G2 60-300 TEM by FEI*^{TM} *Company* at 300 kV with point resolution 0.9 Å at Global Foundries Singapore.

XRD A *XRD Shimadzu-6000* was implemented for crystallographic analysis. Thin films were analyzed using *Shimadzu-6000 with thin film measurement attachment THA 1101*. Data processing has been done with *MATCH software*.

6.2.2. Electrical Characterization

I-V and C-V Measurements The electrical characterization of the fabricated metal-insulator semiconductor devices were performed using the *semiconductor characterization system KEITHLEY 4200 SCS* I-V and *precision LCR meter AGILENT E4983A* (s. figure 6.5.) for C-V measurements in NTU Singapore.

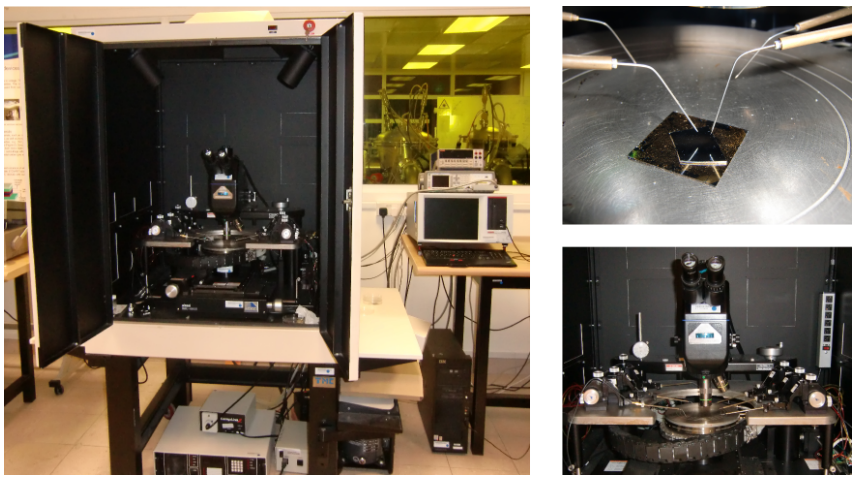


Figure 6.5.: *KEITHLEY 4200 SCS* and LCR meter for semiconductor analysis.

Electrode deposition for electrical characterization was done, using a physical sputtering mask in a high vacuum system at 10^{-6} mbar. High quality top electrodes were formed from pure Au and Cr targets. The bottom of the Si substrates were mechanically polished prior to back contact deposition. Back contact made of pure Au (90 nm) were prepared in *sputter coater EMITECH K575* at 10^{-3} mbar in a class ISO 5 clean room (s. figure 6.6.).



Figure 6.6.: Sputter coater for back contact deposition (left) and high vacuum sputtering equipment for front electrode deposition (right).

6.3. Technical Equipment

Glove Box Air sensitive precursors and powder substrates were handled under air exclusion in nitrogen atmosphere in a glove box for hydrolysis and oxidation sensitive substances. The box is equipped with a precision balance and a polarization microscope. Two differently sized exchange modules can be utilized to transfer chemicals and glass wares into the box. The UHV exchange module explained in section 6.1.2. can be brought into the glove box to enable direct sample transfer from nitrogen atmosphere into vacuum without air exposure.

Rapid Thermal Annealing Rapid Thermal Annealing was performed in *ULVA-RIKO MILA-5000* with K-type thermo couple (s. figure 6.7) at the MSE/NTU Singapore.



Figure 6.7.: RTA equipment with N_2 and O_2 annealing gas supply.

Atomic Layer Deposition Atomic Layer Deposition for bilayer samples was done using a commercial ALD system fabricated by BENEQ (s. figure 6.8.) of the SPMS/NTU Singapore.



Figure 6.8.: *Beneq TFS 200* operated with *Intouch Wonderware by Invensys software.*

6.4. Software

General Data Processing and Illustration All plots and regressions in the present thesis are generated by *Origin 8G SR5*. Simple data set calculations were done with *Microsoft Excel 2010*. Graphic illustrations are generated with *Inkscape 0.48*.

6.5. XPS Data Processing and Curve Fitting

For a detailed understanding of XPS-analysis, a peak fitting of the analyzed complex spectra including multiplots of different signals is required to determine the elementary composition. The detected spectra need to be unfolded using mathematical fit and background correction functions.

The raw data were not smoothed and taken as detected for the peak fitting. A suitable background subtraction has been performed with a Shirley type background, an iterative processing, which particularly considers the increasing scattering background, caused by inelastic scattered electrons, generated by the photoelectron excitation process itself.[132] Further applicable background

types are e.g. linear, constant or Tougaard background correction, which are explained in[131] or[133].

Core level signals arise in different types of shapes, due to the underlying physical effects during the measurement process. As an idealized model the peak shape has been described by a combined Gaussian/Lorentzian function, since the Gaussian fit function considers measurement based influences as the X-ray line shapes, Doppler and thermal broadening and the Lorentzian fit function concerns broadening caused by uncertainty principle related lifetimes.[134] According to[135], experimental studies showed that for low binding energies a Gaussian/Lorentzian ratio between 90:10 and 80:20 is recommendable, whereas for binding energies $>$ 700 eV a 70:30 ratio is more suitable.

XPS peak analysis has been realized using Software *Casa XPS Version 2.3.15*, which enables the definition of the absolute peak position and FWHM as well as the definition in relation to other detected signals. Different back ground types, curve fitting functions as well as asymmetry parameters can be chosen within the software. For peak fitting, the number of required signals and satellites has been determined roughly followed by the definition of FWHM limits for the respective elements.

Parameters, chosen for the XPS measurements are listed in table 6.1.

Table 6.1.: Measurement parameters for XPS analysis.

	Survey Spectra	**Detail Spectra**
Number of Scans	10	20
Step range	0.5 eV	0.1 eV
Pass Energy	50 eV	50 eV
Dwell	0.1 s	0.1 s

The selected step ranges limit the maximum resolution of the detected spectra as $\pm$0.1 eV for the detail and $\pm$0.5 eV for the survey scans.

All spectra have been calibrated with the *C1s* signals mainly resulting from adventitious carbon considered to appear at 284.6 eV as charge reference.

7. Experimental Thin Film Deposition

Thin film deposition and different deposition techniques are, as already mentioned, increasingly investigated due to the broad applicability of thin film materials. Sundry applications require varying film qualities and parameters to be tuned by the deposition technique. In semiconductor industries most common are techniques where the film growth is controlled by the crystal structure of the substrate like MBE or by self controlled/limited surface reactions (ALD/CVD), where the solid, in the majority of cases organic carbon containing and less volatile precursors are evaporated to generate the thin film itself during a gas-phase/surface reaction. Those conventional techniques suffer from problems such as high energy consumption due to high evaporation temperatures of the precursors, carbon impurities within the generated films, which lead to inferior final electrical performance or unwanted interfacial layer formation by reoxidation of the substrate or interface reactions resulting in undefined interfaces (s. chapter 5.).

Within the present thesis an unconventional, alternative, solution processible approach using purely inorganic precursors in organic solvents to deposit REOs on semiconductor substrates should be presented. The solution based technique is expected to show a completely different deposition and crystallization behavior than conventionally used processes, since the method is based on the crystallization from solution in initial state, resulting in a specific chemical and physical anchoring of the oxide molecules on the substrates. The process has been basically invented during our previous work[136] in collaboration with H. Schnars[137] and should be particularly optimized in the present thesis concerning the thin film quality with respect to an application in semiconductor devices such as MOSFETs or DRAM. Additionally, a basic mechanistic understanding of the film and interface formation should be acquired to open up the possibility of a precise tuning of the film characteristics in future work.

In the following, the general deposition process should be elucidated, followed by a detailed description of the individual process steps and the precise conduction of the experiment.

7.1. Wet Chemical Deposition Process

The solution based, wet chemical technique can be basically described by a three step process which is schematically illustrated in figure 7.1.

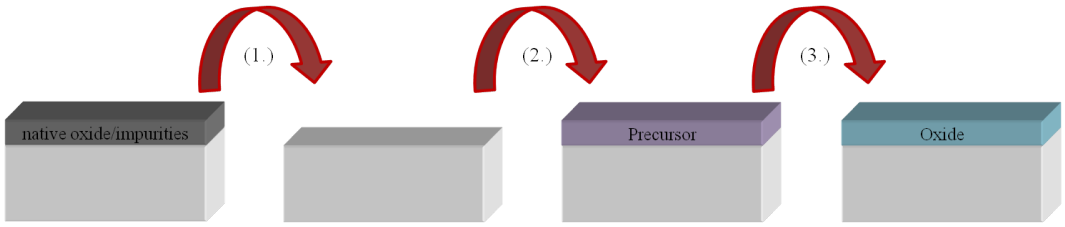


Figure 7.1.: Process flow of the deposition technique, surface cleaning (1.), precursor deposition (2.) and oxide formation (3.).

In order to obtain high quality thin films regarding the purity, interface quality and the resulting final electrical performance with respect to a future application in semiconductor devices, the initial step of the deposition is a surface cleaning (1. in figure 7.1). It is required to result in a highly smooth, chemically clean, oxide free and thermodynamically stable surface to avoid unwanted impurities and interfacial reactions during the deposition process. The process is substrate dependent and will be explained in chapter 8. The cleaning process is followed by the precursor deposition (2. in figure 7.1). As the presented method is solution based, standard, formally known application techniques can be tested. The choice of the deposition technique is essential for a closed and extended film formation. Therefore, different techniques and parameters are shown and evaluated in section 7.1.1. The last and most critical step of the process is the conversion of the precursor molecules to the oxide (3. in figure 7.1). In the presented technique purely inorganic precursors are decomposed thermolytically, whereby the decomposition temperature is maintained carefully by the precursor design, to avoid unwanted reoxidation and interfacial layer formation in contact with the substrate.

In the present thesis, the inorganic RE precursors, $La(NO_3)_3 \times 6H_2O$ and $Nd(NO_3)_3 \times 6H_2O$ have been applied for film deposition. A detailed description of the precursor system is shown in chapter 9. To assess and investigate a more general applicability of the technique *Si(100)*, *Si(111)*, *SiGe(111)* and *Ge(100)* semiconductor substrates have been tested, which are introduced in chapter 8.

The deposited films are analyzed regarding the critical solution concentration for preferable thin film formation, the respective topography of the films and the dependency of the film thickness of the solution concentration which will be discussed in chapter 10. Furthermore, the chemical constitution of the films, substrates and the chemical interaction between the films and the substrates, including possible interfacial reactions are analyzed with XPS measurements (s. chapter 11.). As this work is mainly motivated under the aspect to find an alternative way to deposit high quality alternative gate oxides, the deposited REO films are analyzed regarding the CMOS characteristics (s. chapter 12.).

Besides the wet chemically deposited single layer of the REOs, bilayer systems have been synthesized using the wet chemical approach in combination with conventional ALD to deposit an additional layer of TiO_2 and also characterized with respect to the film thickness, topography and electrical performance (s. chapter 13.).

7.1.1. Precursor Application

The deposition of substances on surfaces out of solutions is formally known and a rather simple process based on the affinity between the substrate and the used solution. The precursors can be applied by dip-coating, drop-casting, spray-coating or spin-coating.

Overview of Application Techniques

During dip-coating, the sample is dipped into a precursor solution under a certain angle and the film is formed during removal and evaporation of the solvent. Drop-casting is initiated by a dropping of the precursor solution on top of the surface, where the residual solvent evaporates. Spin-coating is a widely used technique in micro fabrication to deposit oxydic thin films with film thicknesses below 10 nm.[138] [139] During spin-coating, an excess amount

of the precursor solution is applied onto the substrates, followed by a rotation of the substrate at high speed in order to spread the fluid by centrifugal forces. The film thickness is controlled by the rotation speed. The spray-cast (Liquid Injection Dosing: LiDo) is a home built, vacuum based technique which has been explained in detail already in the preliminary work.[137][136] Higher injection pressures could solve this problem. However, this approach was not investigated further here. The precursor solution is injected into the load lock of the UHV system by a magnetically operated valve. The injection is based on the pressure difference between the outer atmosphere and the load lock of the chamber.

Choice of Application Technique

In our previous work it has been shown from AFM, STM and SEM analysis that drop-cast and dip-coat applications show good results regarding the extension and uniformity of film formation. The LiDo could be eliminated as deposition method of choice in the initial state of the experiments, since only brittle, crusty and nonuniform structures have been deposited caused by the lack of a fine droplet distribution, which arrives at the surface in a sufficient number to wet the surface.[136][137] With the spin-coating technique, highly uniform droplet structures could be created, but no uniform film formation has been achieved with a maximum of rotation speed and therefore also the spin-coating could be excluded as method of choice.

We have already shown in[140] that a common aspect of all techniques is that the critical factor to achieve uniformly flat thin films is the wetting of the substrate. Therefore, the choice of the right solvent is most essential and the application technique could be chosen under technical relevant aspects.

Dip-coating and drop-casting are comparable with respect to the experimental effort. Both techniques are formally known and widely investigated. A major and decisive advantage of the dip-coating is the easy compatibility with standardized wafer cleaning processes in commercial semiconductor production as surface cleaning procedures (s. chapter 8.) are conducted by several dip-coat baths. Since both techniques lead to comparable film qualities but the dip-coating shows the outstanding possibility for easy process integration it was selected as application technique in the present thesis.

The Dip-Coat In general, the dip-coat can be divided into different steps. During dip-coating processes, the substrate is at first immersed in the solution of the precursor or coating material preferably at a constant speed (start-up). Afterwards, the substrates remain in the solution for a defined period of time. While removing the substrate from the solution at a constant speed, the thin layer will be deposited on the surface (deposition), whereas the excess liquid will drain from the surface (drainage). Finally, the solvent evaporates leaving the thin layer behind (evaporation). The speed of evaporation depends on the used solvent and therefore the layer formation depends on the used components if the layer is already formed during the removal of the sample from solution or during the evaporation after removal.[141] Besides the solvent, the dipping angle effects the layer formation. In continuous processes, the steps are carried out directly after each other and multiple layer deposition is possible.

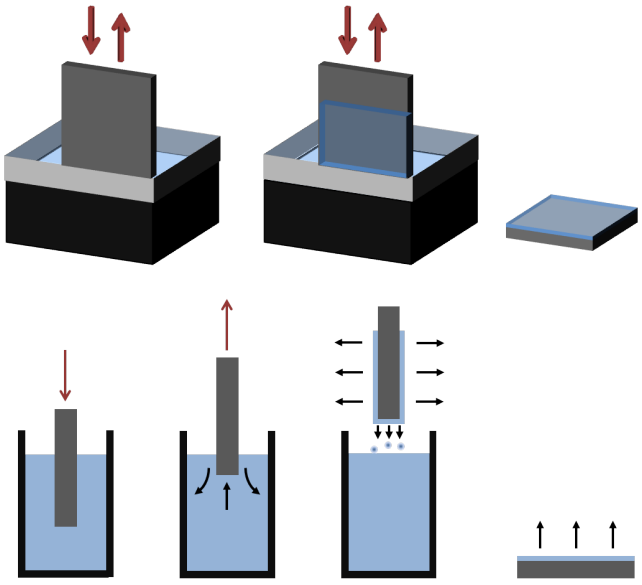


Figure 7.2.: Schematic illustration of the different steps within the dip-coating process (similar to[141]).

In the present thesis, the semiconductor substrates have been immersed in the precursor solution perpendicularly to the solution surface. For deposition, the sample has been removed immediately from the solution, placed horizontally and the evaporation of the residual solvent took place at room temperature, which is schematically shown in figure 7.2.

7.1.2. Choice of Solvent

As already mentioned, the wetting of the surface by the used solvent, is the determining factor for the solution based deposition technique. Other crucial factors for the choice of the solvent are the volatility, respectively the vapor pressure and the required solubility of the precursor powder in specific concentrations in the used solvent. As the precursor molecules show polar characteristics, they should be soluble in polar solvents.

It has been shown from contact angle measurements that cleaned Si containing, oxide free and hydrogen terminated surfaces show hydrophobic characteristics.[136] [142] Therefore, a compromise between solubility and wetting potential needs to be found with respect to a uniform film formation. Slow and homogeneous evaporation of the solvent is desirable to achieve closed films over large areas of the sample with an even distribution of the precursor molecules on top of the surface.

To be able to spread and wet the surface of a substrate by the liquid, the surface tension of the solid must be higher than that of the liquid, otherwise the liquid will be repelled. To achieve an overview of the different wetting and evaporation behavior, different types of solvents have been chosen under criteria of vapor pressure and surface tension.

The tested solvents are 1-Butanol ($C_4H_{10}O$), Isopropanol (2-Propanol, C_3H_8O) , n-Hexane (C_6H_{14}), Tetrahydrofurane (THF: C_4H_8O) and Toluol (C_7H_8). For comparison, characteristic values for water are shown additionally in the following. Solubility experiments discussed in[140] showed that the precursor molecules are soluble in these solvents in sufficient concentration for the following deposition experiments.

Experimentally, all substances except water showed strong spreading and fast evaporation. Therefore, no contact angle measurements were possible using standard conventional equipment and the wetting potential was tested by visual criteria.

Wetting experiments have been conducted at room temperature using 10 μL of the solvent on H-terminated *Si(111)* surfaces as reference substrate for all tested substrate types.

Table 7.1.: Results of the wetting experiments of different solvents on the *H-Si(111)* surface and the tabulated surface tension values γ, vapor pressures p_v and dipole moments p of the solvents at room temperature.

Solvent	γ [N/m]	p_v [143] [mbar]	p [$\times 10^{-30}$Cm]	**Wetting behavior**
1-Butanol	0.0242 [144]	6.67	5.84	good wetting, long duration (1 h)
Isopropanol	0.0212 [145]	43	5.54	good wetting, short duration (10 min.)
n-Hexan	0.0181 [146]	162	0	bad wetting
THF	0.0266 [147]	173	5.84	very bad wetting, droplet movement
Toluol	0.0279 [148]	29	1.43	bad wetting, droplet formation
Water	0.0720 [145]	23.4	6.07	no wetting

Discussion

According to table 7.1., all solvents except water show similar surface tension values, but different wetting characteristics. Therefore, the solvent needed to be chosen by the visual criteria. Only 1-butanol and isopropanol show acceptable extensive wetting of the prepared surfaces. They differ by the duration of the evaporation, which correlates with the vapor pressure. The vapor pressure is low for 1-butanol and higher for isopropanol, resulting in a preferred slow evaporation for butanol and a faster evaporation for isopropanol. As the vapor pressures are much higher (except for toluol) than for butanol, the bad wetting behavior of the other solvents apparently relates to a fast evaporation, suppressing a complete closed film formation on top of the surface. Even though it was expected that the wetting behavior could be related to the dipole moment and therefore the polarity of the tested solvents, no trends could be observed related to this aspect but it can be pointed out that the most promising candidates show quite similar values.

From the discussion above, it can be seen that 1-butanol is the most promising solvent for extensive high quality thin film deposition, which was also shown

experimentally, but not discussed in theory in[136]. Therefore, in the following all film depositions have been done using 1-butanol.

7.1.3. Precursor Decomposition

The REO oxides were as already mentioned, generated from the precursor molecules by thermal decomposition. Thermolysis conditions could be extracted from the TGA/DTA analysis, which have been performed for the precursor powders (s. section 9.1.2.). The temperature ramp was set to 0.5 K/s and a dwell of 20 min at the final decomposition temperature. The decomposition was realized in N_2 flow and under UHV conditions.

7.1.4. Annealing Conditions

With respect to a possible change in the electrical performance of the deposited films typical annealing processes for semiconductor devices have been performed for the oxide films from precursor thermolysis. Different annealing temperatures have been chosen in temperature ranges, where changes in the structure or significant influences on the substrates are expected. For a non oxidizing environment the annealing processes have been carried out in nitrogen flow. The duration of the annealing was set to 1 h.

Annealing at 673 K was performed as for this temperature no change in the crystal structure is expected, the second step was set to 1073 K, since *La*- and *Nd*- oxides are expected to crystallize above 850 K and significant changes especially in the electrical performance are possible. One further annealing step was performed for selected samples, to determine the maximum temperature for electrically stable films, at 873 K.

7.2. Experimental Conditions: Remarks

In the early stage of the studies, all samples have been prepared in dust-reduced standard laboratory environment at room temperature and roughly 60 % humidity. For advanced studies, a minimization of outer influences caused by impurity particles or different amounts of absorbed water was guaranteed by stable and cleaner experiment conditions inside the clean room at a constant

temperature of 292 K and a humidity of 50 %. The electrical, film thickness and topography analysis have been performed for samples prepared under clean room conditions whereas the elementary analyses were done for samples prepared under normal laboratory conditions and UHV environment.

8. Substrates

Si has been the mainly or even exclusively used substrate material for transistor fabrication within the past decades due to its low costs, the easy availability and the excellent electrical properties of the thermally grown native SiO_2 as gate oxides, since MOSFETs became technologically significant within the 1970s.

The recent requirements in semiconductor industries of aggressive scaling, resulting in gate oxide thicknesses below 2 nm lead to the already mentioned unwanted and intolerable high leakage currents due quantum mechanical tunneling through the SiO_2 gate oxides. Therefore, for Si based devices, new, much more cost intensive gate oxide materials are tested, but beside this aspect it needs to be considered that the main advantage of Si, the easy and cost efficient growth of high quality gate stack fabrication, is repealed within this range of scaling. Thus, other substrate types or even completely new approaches for transistor designs need to be taken into account for future device integration.

In the present thesis, different types of semiconductor substrates have been investigated using the wet chemical dip-coating of REOs to evaluate the potential of the invented technique to generate high quality insulating thin films with respect to different roughness, dangling bonds and stability against reoxidation. The substrates used, should be interesting for transistor applications. Experimental cleaning procedures to remove native formed unwanted oxide species should be formally known from the literature and the respective experimentally applied techniques just need to be adapted and repeated from literature known data.

Substrates which have been tested in the present work were *n-Si(111)*, *p-Si(100)*, *n-Ge(100)* and *n-SiGe(111)*. Both doping types show characteristic electrical performances. Specific details of the substrates can be found in appendix C.

In the following, a short introduction on the basic chemistry and physics of Si and Ge will be given, followed by the motivation and experimental surface cleaning procedures of the respective substrates.

8.1. Basics on Silicon and Germanium

Si as well as *Ge* are group IV elementary semiconductors. They exist in the diamond type crystal structure (s. figure 8.1.) where four valence electrons are complemented to a fully occupied electron shell by four closest neighbors.

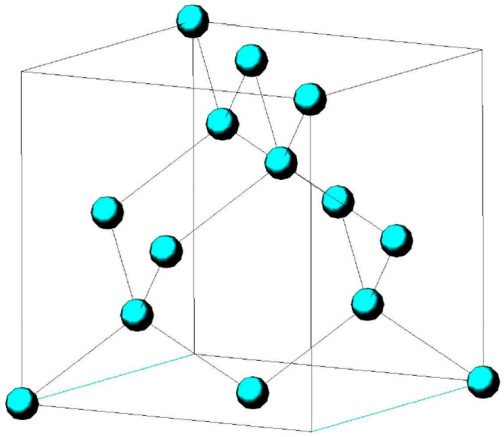


Figure 8.1.: Crystal structure of the diamond type crystal lattice. (see[149])

The strongly covalent bonding with tetrahedral spacial alignment caused by the sp^3-hybridization, is realized by two electrons with anti parallel spin. The fine structure of the valence edge results from spin-orbit coupling. Both materials show indirect semiconduction mechanisms. The energy of the indirect band gap for pure *Si* is 1.17 eV at 0 K and 1.11 eV at 300 K, whereas pure *Ge* shows lower band gap energies of 0.744 eV at 0 K and 0.66 eV at 300 K.[149] In both crystals, the valence edge in momentum space is located at $\vec{k} = 0$ and can be derived from the $p_{3/2}$ and $p_{1/2}$ states of the free atom. The energetically higher state $p_{3/2}$ is four times degenerated, whereas the $p_{1/2}$ state is two times degenerated. The holes close to the valence edge can be explained by two differing effective masses, a heavy and a light one, which are generated by the two bands from the $p_{3/2}$ level. Due to spin orbit coupling a third, from the $p_{1/2}$ level originating band is existent, which is separated from the $p_{3/2}$ band.

For intrinsic (doped) *Si* and *Ge* semiconductors, the number of electrons and holes equals. The concentration of electrons at 300 K for pure intrinsic conduction in *Ge* is $1.7 \times 10^{13}\ cm^{-3}$ and $4.6 \times 10^{9}\ cm^{-3}$ in *Si*. *Si* shows a resistance of $2.6 \times 10^5\ \Omega cm$ and *Ge* of 43 Ωcm.

8.1.1. The *100* Surface

The *100* surface can be constructed as the surface parallel to the surface of the cubic unit cell. On the surface, each atom can be attached to two dangling bonds due to the missing neighbors at the vacuum site. In order to achieve a minimum surface energy, dimers are formed by the two unsaturated bonds, whereby the direction is influenced by the orientation of the respective dangling bonds. Therefore, the number of dangling bonds is halfed and the surface unit cell doubles in the direction of the dimer axes compared to the 1×1 volume unit cell. The so formed structure is therefore named as 2×1 reconstruction.[150] A specific, simultaneous tilting of the dimers in combination with a charge transfer within the structure enables another energy gain as an almost empty s-like orbital with decreased energy is formed by the top dangling bonds and an occupied p-like orbital with increased energy is formed by the "down" dangling bond.[151] [152] This results in a higher energy difference between the surface HOMO and LUMO, whereby a lower surface energy is achieved.[152] [153] As different surface states are achieved, the process is referred to as asymmetric dimerization. The detailed dimerization process is described in[152] and[154]. A review on *Si(100)* and *Ge(100)* surface structures can be found in[150] and[151].

8.1.2. The *111* Surface

The *111* surface can also be basically characterized by a reconstruction of the metastable 2×1-surface. For *Si(111)* temperatures above 1143 K result in the $1 \times 1 - Si(111)$ reconstruction, below these temperatures the surface converts into a heavily corrugated 7×7 reconstruction, which involves the five top surface layers. The unit cell of the 7×7 reconstruction contains twelve adatoms as well as two triangular subunits, nine dimers and a deep corner hole that extends to the fourth and fifth layers. To describe the unit cell of the 7×7 reconstruction, the "dimer-adatom-stacking-fault" (DAS) model has been introduced, where the unit cell is divided into two triangular sub cell units to separate the shifted adatoms from the non shifted adatoms, in ratio to the bulk atom positions. The DAS model describes a much lower number of dangling bonds (19 vs. 49), which results in a significantly lower surface energy for the reconstructed surface.[155] [156] The structure of the 7×7 reconstruction could firstly be observed after the invention of the STM by Binnig et al.[157] In

SiGe(111) substrates the basic orientation is given by the bulk substrate (in the present thesis *Si(111)*).

8.1.3. Lattice Constants

The lattice constants are essential with respect to a film formation in direct contact to the underlaying substrate. The cubic unit cells exhibit side lengths (lattice constants) of 0.543 nm for Si and 0.566 nm for Ge and binding lengths of 235 pm (Si) and 245 pm (Ge).[149] [158] [159] The lattice constant of $SiGe$ alloys can be calculated by a linear extrapolation as a function of the respective composition.[160] For the $SiGe$ substrates, which have been used in the present thesis, the lattice constant needs to be determined in future analysis as for Ge coated Si substrates the lattice constants can not be easily calculated.

8.2. Silicon Substrates

Materials which are utilized in semiconductor industries need to meet the extremely high requirements with respect to purity and chemical composition. For instance, it is required that Si surfaces are atomically smooth, well ordered and particularly chemically clean. Si wafers are covered with a native formed oxide layer. As this layer is more or less irregular and for the sub 45 nm node, SiO_2 is an unsuitable oxide material, it needs to be removed completely initially to avoid unwanted interfacial layer structures during thin film deposition.

Production processes for applications in microelectronics, like ICs, are today dominated by a wet chemical sample pre-preparation to clean the surface from impurities and the unwanted native oxide layer.[161] Radio Corporation of America (RCA) wafer cleaning, which is described more detailed in[162], is used as a standard method to remove metallic and organic impurities from the Si substrates. In order to generate defined oxide layers and to remove all remaining impurities, the surfaces are chemically treated with a strong oxidation solution. The removal of the oxide layer is realized by an etching process with hydrofluoric acid (HF), remaining a hydrogen terminated, thermodynamic stable, pure Si surface.

8.2.1. Wet Chemical Cleaning of Silicon

In the present thesis, clean *H*-terminated *Si* surfaces shall be initially prepared, followed by the deposition of the REO films. Therefore, a wet chemical technique, analogous to the RCA wafer cleaning mentioned above, based on of Higashi et al. published method[163] has been developed and combined with standardized *HF* etching. Due to kinetic effects, the cleaning processes differ for *Si(111)* and *Si(100)* substrates. Experimental conduction of wet chemical preparation of *H*-terminated *Si* surfaces is basically done in a three step process. Initially, the native formed oxide layer on the *Si* sample is converted into a defined oxide layer by using a strong oxidizing solution while simultaneously removing metallic and organic particles applying standardized wafer cleaning 1 (SC1, alkaline, oxidizing) and 2 (SC2, acidic, oxidizing). The oxide layer is subsequently removed by etching with *HF*. It was successfully realized as RCA cleaning already in 1965 and published in 1970.[164]

The created surfaces are fully *H*-terminated, atomically flat and passivated against reoxidation for hours under air exposure. The success of the cleaning procedure has been proven with topography analysis (STM) and elementary analysis (XPS). The samples are carbon free in the range of the detection limit of XPS and do not contain SiO_2. Contact angle measurements showed that the surfaces are hydrophobic. A detailed description of the development of the cleaning process and the analysis of the samples is given in[136].

Discussion of Literature Known Mechanisms

Termination of *Si*-surfaces with hydrogen is specifically easy and effective due to the thermodynamic stability of the *Si*-*H*-bond. The mechanism has been determined considering quantum mechanical calculation and in-situ analysis.[165] At this point in-situ studies should be shortly elucidated to describe the etching process while methods of quantum mechanical calculations should no be explained.

Based on thermodynamic data by etching with *HF*, *F*-terminated surfaces are expected to be formed due to the fact that the *Si*-*F*-bond strength is higher than the strength of the *Si*-*H* bond (6.0 eV/3.5 eV). *F*-termination is accepted as last step of the reaction mechanism but by kinetic control anyways *H*-terminated surfaces are achieved. To understand the process, ab-initio

quantum mechanical calculations with transition state methods have been performed. Figure 8.2 summarizes the results of the calculations schematically.

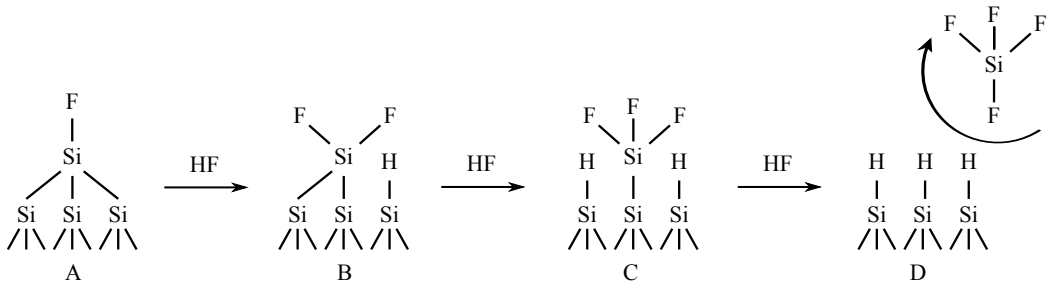


Figure 8.2.: Reaction scheme of *H*-termination with *HF*. (after[165])

Dangling bonds of the *Si*-surface are initially *F*-terminated (A) after the removal of the oxide layer. Caused by the fluorination, the *Si-Si* back bonding is highly polarized due to the significant difference in electronegativity between *Si* (EN = 1.7) and *F* (EN = 4.0). As a result of the polarization, it is possible to insert *HF* into the back bond (B), leading to a fluorination of surface *Si* atoms and hydrogenation of second layer *Si* atoms (C). The reaction is completed by SiF_4 elimination from the surface *Si*, leaving a fully *H*-terminated *Si* surface. After the termination, no dangling bonds are remaining, which is in agreement with empiric examinations, which verify a particularly low reaction rate.[166] [165] After removal of the oxide *F*-terminated surfaces and *Si-F* species in solution can be observed experimentally.[167]

For the model reaction

$$H_3Si - OH + HF \rightarrow \# \rightarrow H_3SiF + H_2O \tag{8.1}$$

activation energies of 0.55 eV have been calculated theoretically, whereas experimentally values of 0.35 eV for decomposition of SiO_2 in *HF* have been investigated. As the activation energies are very low the first reaction step, the *F*-termination of the surface is guaranteed. A further reaction with *HF* leads to a *H*- and *F*-terminated surface, depending on the different surface orientations.

The calculated activation energy for the reaction forming H-terminated surfaces is 1.0 eV. Additionally, the reaction is exothermic (1.8-2.0 eV) which results in a final elimination of SiF_4. The model reaction is published as:

$$H_3Si - Si - F_3 + HF \rightarrow \# \rightarrow SiH_4 + SiF_4 \tag{8.2}$$

The fluorination reactions proceed analogous:

$$FH_2Si - SiH_2F + HF \rightarrow \# \rightarrow SiH_2F_2 + SiH_3F \tag{8.3}$$

The activation energy for the fluorination has been calculated as ≈ 1.4 eV and the energy advantage is ≈ 1.6 eV. A comparison of both activation energies leads to the conclusion that the fluorination reaction can be neglected in this case, as it shows a much higher activation barrier.

Compared to the initially mentioned significant difference in EN between Si and F, the difference between H (EN = 2.1) and Si (EN = 1.7) is desperately lower, so that no polarization and consequently a passivation against new reaction with HF occurs. Due to relatively low activation energies, fluorination reactions remain possible, but the H-termination is under consideration of low etching rates of acidic HF-solutions still stable. The mechanism leads to the formation of mono-, di- and tri-hydrides on the surface, depending on the initial SiO_2/Si interface structure.

Conclusively it can be pointed out that F-terminated surfaces are thermodynamically more stable, but the reaction which leads to the H-terminated surfaces is significantly higher exothermic and therefore energetically preferred.

8.2.2. Atomically Smooth *Si(111)*: Additional Etching

Particularly with *Si(111)*-surfaces the samples are subsequently treated with alkaline, fluoride NH_4F solutions to smooth the surface as efficiently as possible. The anisotropic etching process promotes a selective formation of eminently atomically smooth surfaces.[168] [169] [170]

For ammonium fluoride solution with pH >5, molecular water is necessarily essential in order to generate dissociated F^--ions in solution. Therefore, the experiment was performed in aqueous solutions. The first, and because of the non-polarity of the *Si-H* bonding, the reaction rate determining process

step is the hydrolysis of *Si-H*-surface bonds at one *Si* lattice step, followed by the substitution of *Si-OH* surface bonds into *Si-F* bonds. Due to the fluorination the *Si-Si* back bonds are highly polarized as for the reaction with *HF*. The polarization favors the weakening of the back bonds, leading into the bonding of the negatively charged OH^- ion onto the positively polarized $Si^{\delta+}$ atom, which is bound onto the *F* atom. The hydrogen is bound onto the negatively polarized *Si* surface atom $Si^{\delta-}$, which leaves the surface and pass over into solution as $HSiF(OH)_2$. Meanwhile, *Si* is existent in the unstable oxidation state +II. Hydrogen ions are hydrolyzed in the solution forming another hydrogen molecule. If the substitution of *OH*-bonds into *Si-F* bonds occurs directly on the surface or after entering the solution, is dependent on the process kinetics. Reported XPS analysis showed *Si-F* bonds on the surface[167], whereas a detailed analysis of the other reaction steps is still in progress.[170]

The initial and final state of the reaction are in principal identical. They only differ in the removal of one crystallographic phase. *Si* atoms from different crystallographic phases show different activation energies for the discussed alkaline etching process, which is not diffusion- but etching-rate limited. *Si(111)*-phases are etching stops, in contrast *(100)* and *(110)* phases can be etched easily. Therefore, after the etching process a clean and atomically smooth surface can be observed only for *Si(111)* samples.[169]

8.2.3. Recipe for *Si* Cleaning

Silicon *(111)* and *(100)* substrates were experimentally cleaned in the following six step procedure, which has been developed according to the procedures reported in the literature[171] [172] [173] [123], taking into consideration the above mentioned aspects of the reaction mechanism as well as the requirements and set up of the present experiment. The success of the cleaning procedures will be discussed showing the respective XPS analysis in section 11.1. and section 11.2.

Preliminary to the etching process, the wafer samples which are laser cut to fit into the UHV sample holder as well as all required instruments are cleaned in an ultrasonic bath with acetone for 20 minutes.

1. Standard clean 1 (SC1): removal of particles and organic impurities NH_4OH, H_2O_2, DI-H_2O; 1:1:5 for 10 min at 353 K

2. Standard clean 2 (SC2): removal of metallic impurities
   HCl, H_2O_2, DI-H_2O; 1:1:6 for 10 min at 353 K
3. Etching: removal of SiO_2, Oxide Strip
   Dip in 5 % HF for 1.30 min
4. rinse with DI H_2O
5. *Si(111) special treatment: kinetically controlled etching*
   NH_4F (40 %), $(NH_4)_2(SO_3)$ (35 %); 15:1 for 7 min, (previous O_2 removal by N_2 purge of the solution for 20 min)
6. rinse with DI H_2O, drying in N_2 flow

8.3. Germanium and Silicon-Germanium Substrates

In the present thesis, *Ge(100)* and *SiGe(111)* have been tested for device integration alternatively to *Si* substrates, as they are potential candidates to replace *Si* as substrate material for microelectronic devices as described in section 5.7. The success of the cleaning procedures will be discussed showing the respective XPS analysis in 11.3. and 11.4.

8.3.1. Wet Chemical Cleaning of *Ge* and *SiGe*

As reported in the literature, cleaning of Ge substrates can be conducted analogous to Si with a wet chemical dip-based approach. However, due to differing bonding relations the precise etching conditions need to be tuned according to Ge.

For Ge and Ge containing substrates, the standardized SC1 and SC2 procedures to remove organic and metallic impurities are not suitable due to high etching rates even at room temperature.[123] Ge shows those significantly higher etching rates compared to Si, since Si forms a passivating SiO_2 layer in oxidizing solutions such as H_2O_2, which then limits the etch rate of SiO_2 in non HF etching solutions. As Ge forms GeO_2 which is water soluble, the simultaneous oxidation of the Ge and the etching of the GeO_2 results in a net like etching for Ge substrates with very high etching rates.[174] Therefore, for Ge containing substrates, the initial step of the surface cleaning is a treatment

with H_2O_2 to generate a defined oxide layer, which is subsequently dissolved in deionized water.

In order to generate passivated, carbon and oxide free surfaces another etching step with *HF* solutions is conducted, but as for the cleaning the etching needed to be adapted to the *Ge* substrates, as the *HF* concentration is much more critical than for *Si*. The etching of GeO_2 is possible with aqueous *HCl* and *HF* solutions. Whereas *HCl* leads to mono- and dichloride terminated surface, which is not feasible for our experiment due to *Cl* impurities. *HF* solutions generate *H*-terminated surfaces as known for *Si*. The concentration of the *HF* is much more critical, since the difference in electronegativity between *Ge* (EN = 2.0) and *F* (EN = 4.0) is lower than for *Si* (EN = 1.7) and therefore the *Ge-F* bonds, which are formed initially during *HF* treatment, are less strong and longer than the *Si-F* bonds. Due to the difference in electronegativity, the *Si-Si* back bonds are more polarized than the *Ge-Ge* equivalents and can therefore be easier attacked by the *HF* molecules.

Etching of *Ge* with 1:100 diluted 49 % *HF* like for *Si* leads to oxide residues and a high amount of carbon impurities. Therefore, the required concentration for a successful etching process has been intensively investigated in the literature, consulting STM and XPS analysis to determine the oxygen and carbon amount as well as the resulting surface roughness. It has been shown that a *HF* concentration of 1:3 diluted from the 49 % *HF* leads to the best results. As neither aqueous *HCl* nor *HF* etching alone leads to oxygen free low carbon containing surfaces, a final vacuum annealing step is required for *Ge* containing substrates.[171] Alternatively to the wet chemical etching, *Ar* ion sputtering was reported as a possible technique to remove unwanted impurities, but encountering high defect densities which makes this techniques less feasible for device production.[175]

The used p-*SiGe(111)* substrates have been generated from pure *Si(111)* wafers by Global Foundries Singapore by implementing 17 % of *Ge* into the *Si* wafers.

8.3.2. Recipe for *Ge* and *SiGe* Cleaning

Ge and *SiGe* substrates were experimentally cleaned in the following six step procedure, which has been developed according to the procedures reported in the literature[171] [172] [173] [123]. The above mentioned aspects regarding the experimental requirements have been taken into consideration for the set up

of the etching experiments after a cleaning in an ultrasonic bath with acetone for 20 minutes.

1. Preparation of defined oxide: Dip in H_2O_2 10% for 30 s
2. Rinse with DI H_2O
3. Etching: Dip in 1:3 diluted 49 % HF for 10 min
4. Rinse with DI H_2O, drying in N_2 flow
5. Anneal at 873 K to remove remaining surface carbon

9. Precursor System & Powder Reference Data

Recently, inorganic RE compounds including thermo-labil complex anions have been applied as precursor materials for the synthesis of REOs[176] e.g. in catalytic active nano particles. In the present thesis, RE precursors are utilized for electronically applicable thin films, which is innovative as well under the point of the usage of new precursor materials for thin films as well as for the application of the mentioned molecules. New inorganic precursors avoid unwanted, the final electrical performance limiting, carbon impurities within the electronic thin films. This is one of the main disadvantage besides the hard volatility and toxicity of conventionally used precursors for thin film deposition.

Precursor synthesis for different RE metals is rather easy due to their similar chemistry and the ensuing simple and equal synthesis steps. The different elements form different types of oxides. Most common and interesting for applications in MOSFETs are the sesqui- and dioxides. For the first time M. Ahlers from the group of M. Wickleder has succeeded to show a systematic investigation of the synthesis and thermal as well as crystallographic characterization of different inorganic complex RE systems.[177] By introducing different types of ligands, a variety of chemical structures and resulting crystallographic and thermal decomposition behavior can be achieved, which can be tuned by the choice of the RE center and the respective ligands. In the following chapter the precursor system should be described with respect to the chemical and crystallographic structure, decomposition behavior and products.

The precursors for REO thin film deposition of the present thesis have been synthesized and characterized in in the inorganic chemistry group of M. Wickleder at the University of Oldenburg, applying XRD and thermogravimetric/differential thermal analysis (TGA/DTA). A detailed description of the synthesis and characterization can be found in the work of M. Ahlers.[177] [178]

Elementary analysis of the pure precursor powders (nitrates-hydrates), the expected decomposition products (oxides) and the respective hydroxide by

XPS will be shown, as for complex film-substrate analysis reliable reference data of the pure compounds are essential.

9.1. Survey of Systems

From synthesis perchlorate and nitrate-solvate compounds of different rare earth metals are available which can be decomposed to the REO by thermolysis. Due to the high explosiveness of the perchlorates, they are not applicable for REO thin film deposition and only the nitrate-solvates are subsequently used and will be elucidated in the following.

Synthesis of aqueous nitrate compounds and their thermolysis behavior have been shown by Gamal et al. in 2001.[179]

The nitrate compounds have the general structure:

$$RE(NO_3)_3 \times \mathrm{x}S \tag{9.1}$$

By varying the RE metal and solvent molecules (S), a diversity of different chemical structures and properties of the precursors can be achieved as mentioned above.

9.1.1. Synthesis

Aqueous compounds of the RE metals are synthesized as hexahydrates from the oxides. For synthesis of the RE-nitrates-hexahydrates 1 g of the REO (purity > 99.999 %) is dissolved in 15 mL nitric acid (65 %). Subsequently the acid is evaporated and the residues are dried for 12 h at 333 K in a drying cabinet. Organic solvent ligands are introduced into the system by substituting the water molecules of the hydrate compounds with the respective solvent molecules by a simple ligand exchange. The detailed synthesis steps are explained in[177].

Precursors including water (H_2O), 1,2-dimethoxy-ethane (DME: $C_4H_{10}O_2$), ortho-formic-acid-trimethyl-ester ($CH(OCH_3)_3$) and tetrahydrofurane (THF: C_4H_8O) as solvate molecules have been synthesized. The used REO educts are the sesqui oxides of lanthanum (La), praseodymium (Pr), neodymium (Nd), samarium (Sm) and europium (Eu). Except for the H_2O compounds, all molecules are sensitive to air and need to be handled under inert conditions.

In the present thesis experimentally only the nitrate-hydrates of *La* and *Nd* should be applied as precursor molecules for thin film generation, to start a systematic investigation on the deposition behavior and to get an understanding of the film formation mechanism in an incipiently state.

Figure 9.1. shows the molecule structure of the trinitrate-hexahydrate.*Nd*-nitrate hexahydrate crystallizes in light purple whereas the *La*-nitrate-hexahydrate forms white/colorless crystals.

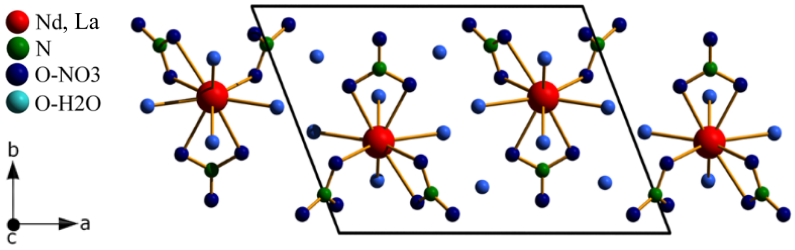


Figure 9.1.: Molecule structure of the *La* and *Nd* trinitrate-hexahydrate.

In the following $[RE(NO_3)_3(H_2O)_4] \times 2\ H_2O$ and $RE(NO_3)_3(H_2O)_6$ are used synonymic for the trinitrate-hexahydrates.

The reference systems of the oxides of *La* and *Nd* have been synthesized from the precursor powders. Oxides are generated by the thermolysis of the nitrates-hydrates, whereas the hydroxide has been measured as delivered by the supplier.

9.1.2. Decomposition Behavior

With respect to a low temperature, energy efficient, non chemically aggressive approach to deposit the REO thin films on the chosen semiconductor substrates the desorption temperature of the protective hydrogen termination (810 K[180]) needs to be above the final decomposition temperature of the precursor applied to avoid unwanted interfacial layer formation during decomposition.

Figure 9.2. shows an overview of the tunability of the decomposition temperature by the respective element and solvate ligand of the nitrate-solvates.

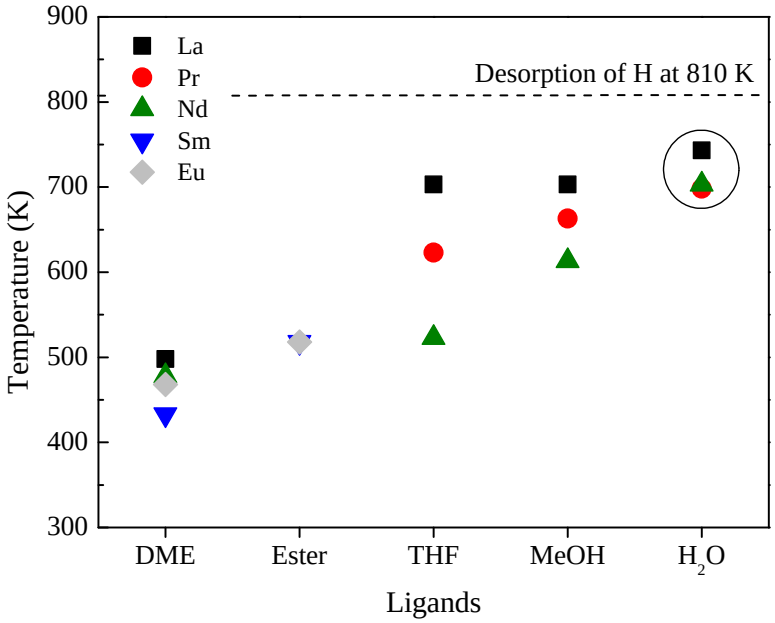


Figure 9.2.: Dependency of the decomposition temperature of the RE-nitrate-solvates from the respective solvate and RE center.

It can be shown that all final decomposition temperatures of the precursors are below the desorption temperature of the *H*-passivation.

The thermal decomposition of the nitrate-hydrates to the REOs has been already reported in 1960 by Wendlandt et al. and in direct collaboration to the presented project by M. Ahlers in 2007.[178] It is an endothermic multi-step process, which is described in the following.

TGA/DTA analysis, where the weight loss of the initial weight of the substance is detected temperature dependent, have been performed to investigate the decomposition behavior of the powders and to obtain the required temperature ranges for the decomposition to the REO after precursor film deposition. In the following, only data for *La/Nd* nitrate-hydrates are shown. *La* and *Nd* aqueous precursors are used in the present thesis are used as a "worst case study" with respect to a substrate/precursor interaction during the film deposition process, since they exhibit the highest decomposition temperatures. For *La* and *Nd*-trinitrate-hexahydrate complexes, the general decomposition mechanism is formally known and given by:

1. $[RE(NO_3)_3(H_2O)_4] \times 2\ H_2O \rightarrow RE(NO_3)_3\ +\ 6\ H_2O \uparrow$
2. $RE(NO_3)_3 \rightarrow REO(NO_3)\ +\ 2\ NO_2 \uparrow\ +\ 1/2\ O_2 \uparrow$
3. $REO(NO_3) \rightarrow RE_2O_3\ +\ NO_2 \uparrow\ +\ 1/4\ O_2 \uparrow$

TGA and DTA data of the synthesized *La*- and *Nd*-trinitrate-hexahydrate are shown in figure 9.3.

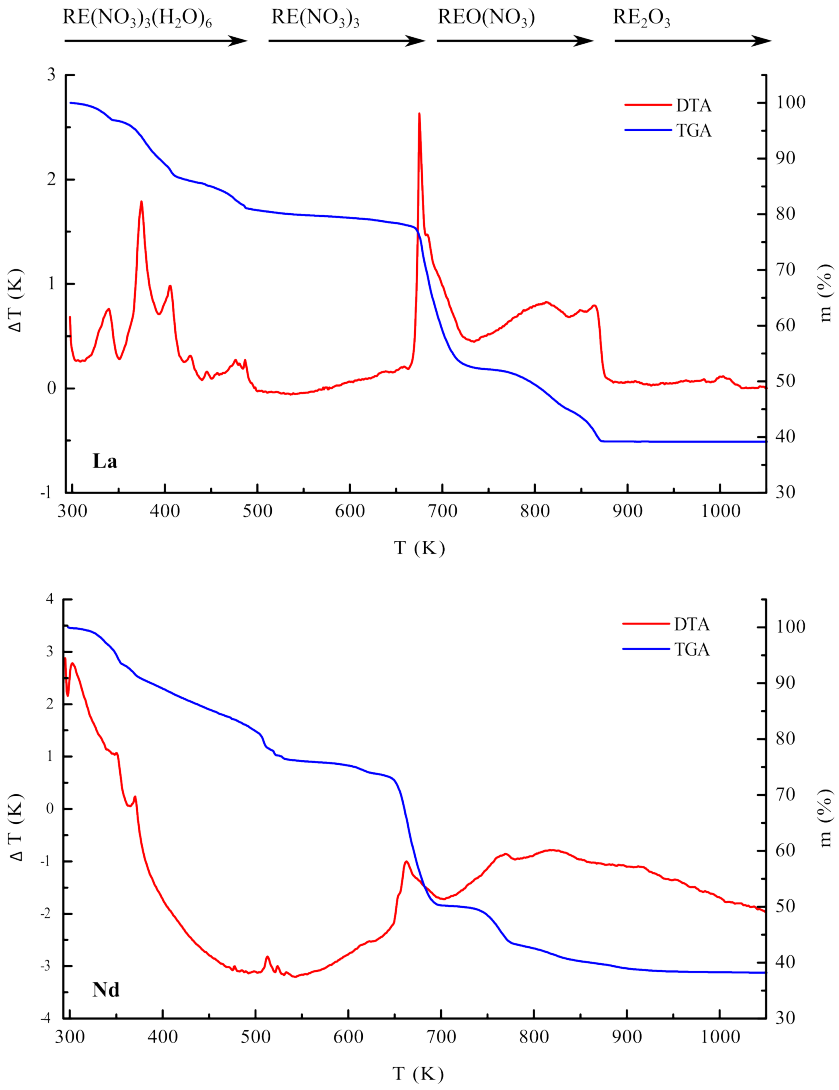


Figure 9.3.: DTA/TG-diagrams of $La(NO_3)_3(H_2O)_6$ (top) and $Nd(NO_3)_3(H_2O)_6$ (bottom).

Thermal decomposition of the nitrate-hydrate produces slight inflections in TGA/DTA analysis due to stepwise dehydration while $RE(NO_3)_3$ formation, which has been reported several times e.g. in[181]. Those intermediate stages are usually not observed due to a considerable tendency to decompose to the oxynitride $REO(NO_3)_3$.[182][183] It has been shown that pure anhydrous $RE(NO_3)_3$ can be isolated by very careful heating of hydrated nitrates under vacuum conditions.[184]

Respective decomposition temperatures are summarized in table 9.1. T_i is the temperature when the decomposition is initiated and T_f is the temperature where the decomposition is concluded and no further weight loss can be detected.

Table 9.1.: Thermal decomposition temperatures in K of $RE(NO_3)_3(H_2O)_6$ with RE=La, Nd[178].

Step		**1.** -$6H_2O$	**2.** -$2NO_2$, -$1/2O_2$	**3.** -NO_2, -$1/4O_2$
La	T_i	313.15	663.15	763.15
	T_f	513.15	743.15	873.15
Nd	T_i	323.15	643.15	733.15
	T_f	543.15	703.15	933.15

9.1.3. Crystallographic Data

To achieve a minimum of interfacial traps and ensure a good interface quality within the aspired thin films, preferably high lattice matching between the coating top layer and the substrate should be given. The lattice constants of available precursor compounds, extracted from single crystal XRD analysis by M. Ahlers[177] and known from literature[185], are listed in table 9.2.

Table 9.2.: Available lattice parameters of the ligand-metal combinations. All lattice spacings are given in pm.

	H_2O	**Ester**	**THF**	**DME**
La	a = 893.4 b = 1071.4 c = 665.7 α = 78.86° β = 77.91° γ = 87.90°	-	-	a = 1049.22 b = 1513.8 c = 1136.91 β = 92.423° monoclinic
Pr	a = 923.9 b = 1178.2 c = 679.4 α = 91.10° β = 110.67° γ = 69.68°	-	a = 778.5 b = 1371.2 c = 946.1 β = 95.96° monoclinic [185]	no isolation of single crystals possible
Nd	a = 931.6 b = 1175.3 c = 677.84 α = 91.11° β = 112.23° γ = 109.16°	-	a = 781.11 b = 1374.04 c = 946.09 β = 96.33° monoclinic	a = 1038.4 b = 1506.7 c = 1138.4 β = 92.467° monoclinic
Sm	-	a = 1042.74 b = 1425.71 c = 1285.82 β = 91.994° monoclinic	a = 774.5 b = 1368.8 c = 942.3 β = 95.75° monoclinic	a = 1032.5 b = 1502.0 c = 1134.6 β = 92.53° monoclinic
Eu	-	a = 1042.61 b = 1423.78 c = 1280.61 β = 91.834Đ monoclinic	a = 773.5 b = 1367.6 c = 941.3 β = 95.7° monoclinic [185]	a = 1033.1 b = 1504.3 c = 1136.4 β = 92.612Đ monoclinic

XRD powder analyses have been performed to confirm the structure and phase purity of the reaction products from the mentioned synthesis (s. section 9.1.1.) and the decomposition products.

In the following, for the reason mentioned above, detailed XRD scans only for the *La* and *Nd* nitrate-hydrates and the achieved decomposition products should be given.

The, in the final step, formed oxides exhibit lattice constants of a = 339.7 pm and c = 612.9 pm (La_2O_3)[186], whereas the lattice constants of the hexagonal type Nd_2O_3 are reported in the literature as a = 382.9 pm and c = 600.0 pm.[38] In comparison, *Si* substrates exhibit lattice constant of 543 pm and *Ge* of 566 pm (s. section 8.1.3).

As the differences in lattice constants between the substrate and the covering thin film is essential for the interface quality, the values are given in table 9.3.

Table 9.3.: Percentage difference of the lattice parameters of the $Ln(NO_3)_3 \times 6H_2O$ (*Ln* = *La* and *Nd*) to the *Si* and *Ge* substrates.

		$Ln(NO_3)_3 \times 6H_2O$		Ln_2O_3	
		Si	***Ge***	***Si***	***Ge***
La	a	39.2	36.7	37.4	40.0
	b	49.3	47.2	-	-
	c	18.4	15.0	12.9	8.3
Nd	a	41.7	39.2	29.5	32.4
	b	53.8	51.8	-	-
	c	19.9	16.5	10.5	6.0

It can be seen that from the calculated percentage differences, significantly high values are given for the initially deposited nitrate-hydrate precursor molecules. With respect to the oxides, a minimum of 8.3 % deviation can be achieved for the La_2O_3 and 6.0 % for Nd_2O_3 on *Ge*. The minimal deviations for *Si* substrates are even higher (12.9 % and 10.5 %).

The lattice similarity in crystalline structures is essential for the number of defects and resulting lattice strain at the interface. Bäumer et al. reported that several monolayers of *NiO* grown on *Ni* with a lattice mismatch of 16 % lead to tilted crystallite surfaces and drastically increased strain due to the high lattice mismatch.[187]

The lattice constants can depend on the film thickness, as for ultra thin films the lattice constants might differ from the values of bulk materials as reported in e.g.[77]. Furthermore, for crystalline films the grain sizes and therefore the number of grain boundaries is strongly influenced by the film growth and the final film thickness.

For electrical devices, defect density needs to be as low as possible. Thus, due to the relatively high lattice mismatch between the Si and Ge and the REO and in order to achieve a reduction of grain sites, which promote as faster electron conduction and therefore result in increased unwanted leakage currents, it is desirable to create amorphous films by a deposition mechanism of choice to avoid crystal lattice interaction effects on the interfaces.

9.2. Elementary Powder Analysis: XRD and XPS

For elementary analysis of the powders and to achieve reference data of the nitrate-hydrates, the decomposition and possible hydrolysis products, XPS measurements were done of $RE(NO_3)_3 \times 6H_2O$, RE_2O_3 and $RE(OH)_3$ ($RE = La, Nd$).

Reference data are essential for the following thin film analysis, since the film-substrate combination shows complex signal structures in XPS spectra which need to be understood in detail to enable the investigation of the film formation mechanism.

XRD analysis were done to control the phase purity of the analyzed nitrate-hydrate, oxide and hydroxide powders .

Figure 9.4. shows the XRD spectra of the La compounds. La_2O_3 is highly hygroscopic, leading to a direct formation of hydroxides under air conditions. Therefore, only the hydroxide spectra are shown after the decomposition process.

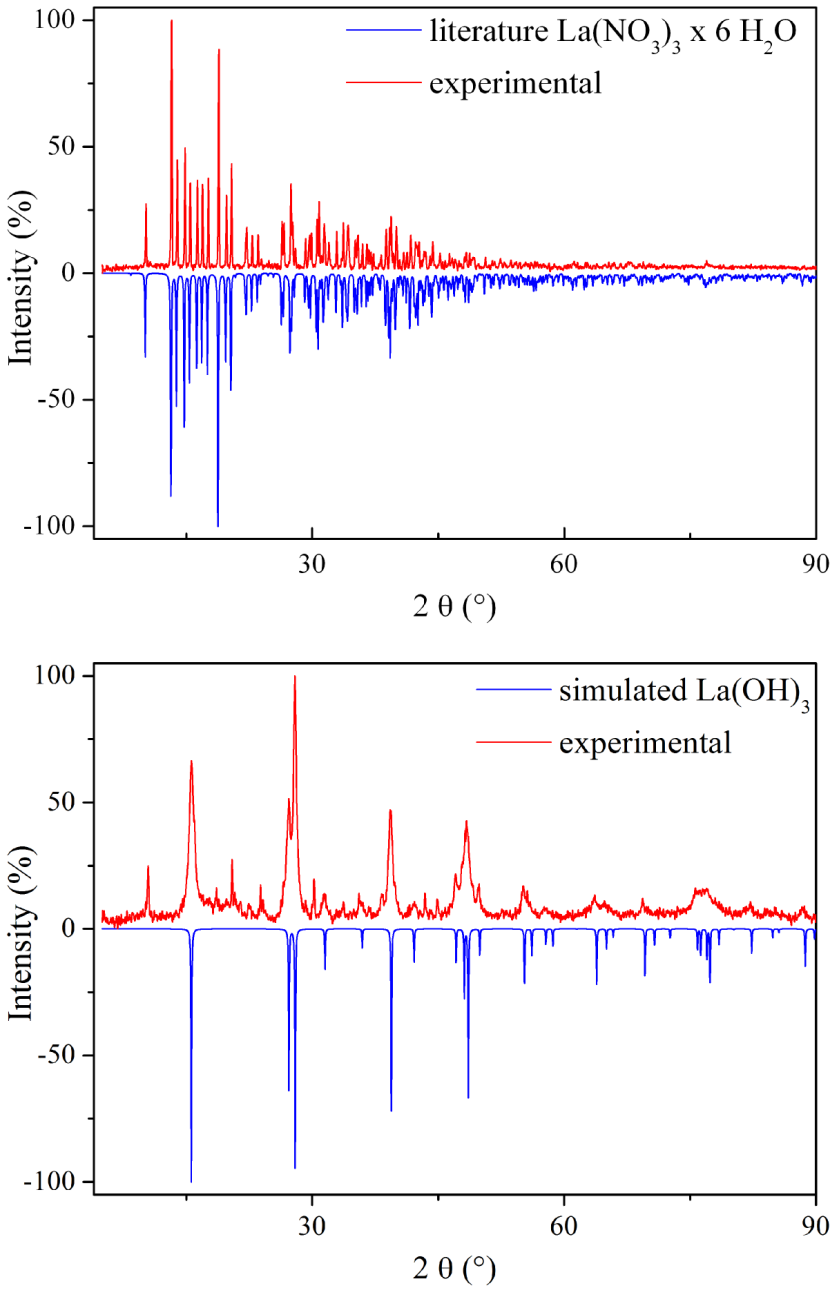


Figure 9.4.: XRD spectra of the precursor $La(NO_3)_3 \times 6\ H_2O$ (top) and the hydrolysis product $La(OH)_3$ (bottom) after thermolysis to La_2O_3 compared to measured[188] and simulated literature data[189].

The *Nd* compound has been analyzed analogous. Figure 9.5. shows the XRD data of $Nd(NO_3)_3 \times 6\ H_2O$ and Nd_2O_3.

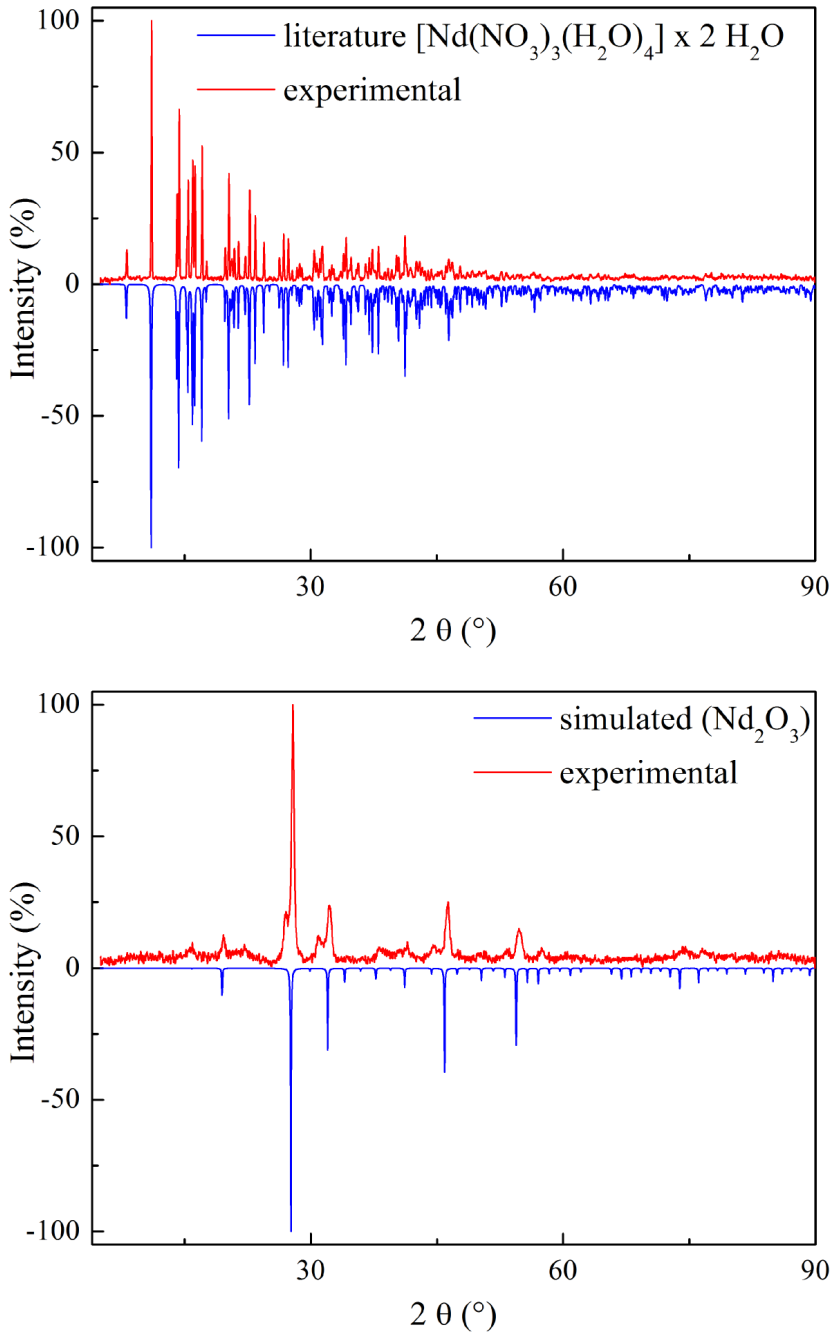


Figure 9.5.: XRD spectra of the precursor $Nd(NO_3)_3 \times 6\ H_2O$ (top) and the thermolysis product Nd_2O_3 (bottom) compared to measured[190] and simulated literature data[191].

From the XRD spectra, the phase composition of the powders could be verified as well for the *La* as for the *Nd* powders.

After an introduction about expected XPS signal structures and positions, survey and detail spectra of *La*, *Nd* and *O* should be discussed. Results for the *La* and *Nd* containing powders are shown separately in the following sections. All spectra have been measured at room temperature.

For all peak fits, a Shirley type background has been applied for background correction. Calibration of the energy scale was done assuming the *C1s* signals arising from the adhesive tape or surface contamination to be 284.6 eV.

For the experimental setup, the powders were attached to the sample holder (s. section 6.1.1) on *Si* substrates covered with double sided adhesive carbon tape. The sample mounting was done inside the glove box, followed by a direct transfer into the UHV chamber, applying the transport module (s. section 6.1.2.) to ensure necessary phase purity of the analyzed substances. The measurement parameters have been set according to the data listed in table 6.1.

Due to the adhesive carbon tape, the analysis of the *O1s* signals becomes more complex, as a variety of signals results from the adhesive itself. The adhesive consists of oxygen containing organic substances, which show variable peak positions depending on the piece and batch of tape. Detailed information regarding the chemical composition of the adhesive are kept as a secret by the manufacturer. Intensities of signals resulting from the tape are dependent on the thickness of the adhered powder layer. Therefore, during powder analysis different peak positions are expected from XPS analysis, which are not caused by the analyzed powders.

As chemical shifts in XPS spectra, result from effective binding energies caused by attraction of electrons by highly electronegative binding partners, the difference in electronegativity of the involved elements need to be considered for a theoretic examination of expected trends in signal structures. The respective electronegativities after Allred and Rochow are given by:

Table 9.4.: Electronegativities of the involved elements.[91]

La, Nd	$<$	*H*	$<$	*N*	$<$	*O*
1.1		2.2		3.1		3.5

For the complete binding partners NO_3^- in the nitrates, O^{2-} in the oxides and OH^- in the hydroxide the, from the electronegativity and bonding state, resulting tendency to attract electrons, can be compared additionally:



Figure 9.6.: Tendency of the electron affinity of the different binding partners.

High electronegativity values show a high electron attraction force, leading to a decrease of the electron density at the binding partner of the electronegative element. The decreased electron density causes a higher effective binding energy of the remaining electrons. This effect results in a chemical shift (change in detected binding energy) of the signals in XPS spectra relative to the signal of the pure elements. The theoretical expected tendency for the *RE3d* and *O1s* signal caused by the shown differences in electronegativity are illustrated in figure 9.7.

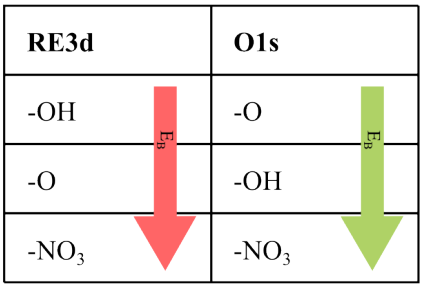


Figure 9.7.: Direction of chemical shifts of *RE3d* and *O1s* in dependency on the respective binding partners.

d-Orbital Core Level Signal Structure

During core level orbital analysis, the signals in XPS spectra are split into multiplet structures due to the spin-orbit coupling as already explained in 2.1. The *3d* orbitals of the *La* and *Nd* are equally effected. Since the orbital angular momentum l for *d*-levels is 2 and the spin is considered to be $\pm 1/2$, the total

angular momentum j can be calculated after eq. 2.6 as 3/2 and 5/2. This yields to an intensity ratio of the $3d_{3/2}$ to the $3d_{5/2}$ signals of 2:3.

Beside the spin-orbit coupling, unique satellite structures appear for the lanthanide compounds resulting from the electronic structure characteristic of the rare earth elements.[192] Thus, it can be observed that the two peaks are both additionally split into doublet structures.[193]

By applying the Anderson-Model of quantum mechanics this effect is caused by the hybridization of the $d10f0$ and $d10f1\underline{v}$ respectively $d9f0$ and $d9f1\underline{v}$ (for *La*, states in the initial and final state of photoemission). $\underline{v}$ specifies a hole in the band of a semiconductor with f symmetry.[194] The interaction causes a reduction of the quantum mechanically calculated energy exerted by a hole in the core to a free electron in the f-orbital. Thereby, a completely different energetic state of the whole atom is created and satellite signals can be detected additionally to the main peaks.

These satellite structures change depending on the occupancy of the f orbital and the resulting intensity of the interactions. Thus, for the different RE elements, individual signal structures are characteristic. For vigorous hybridization, strongly bonding and anti bonding states are created and the splitting of the peaks is less intensive.

For *La* ($4f^0$) compounds, typical intense satellite structures are observed shifted 3-6 eV to higher binding energies, which can be attributed to a charge transfer shake up from occupied ligand (L) orbitals to empty *4f* orbitals ($\mathrm{L} \rightarrow 4f$), whereas for the *Nd* compounds ($4f^4$), typical satellite structures with noticeably less intensity than for the *La*, shifted 3-4 eV to lower binding energies are detected. They are possibly caused by an energy gain by inter atomic shake up transition for molecules, where the molecular rearrangement can occur during core ionization.[192].

A detailed consideration of the *3d* peak splitting can be found e.g. in[195].

Lanthanum

All *La* powders have been measured applying Mg-K_α X-rays as excitation source. Figure 9.8. shows the survey spectra of the three powders.

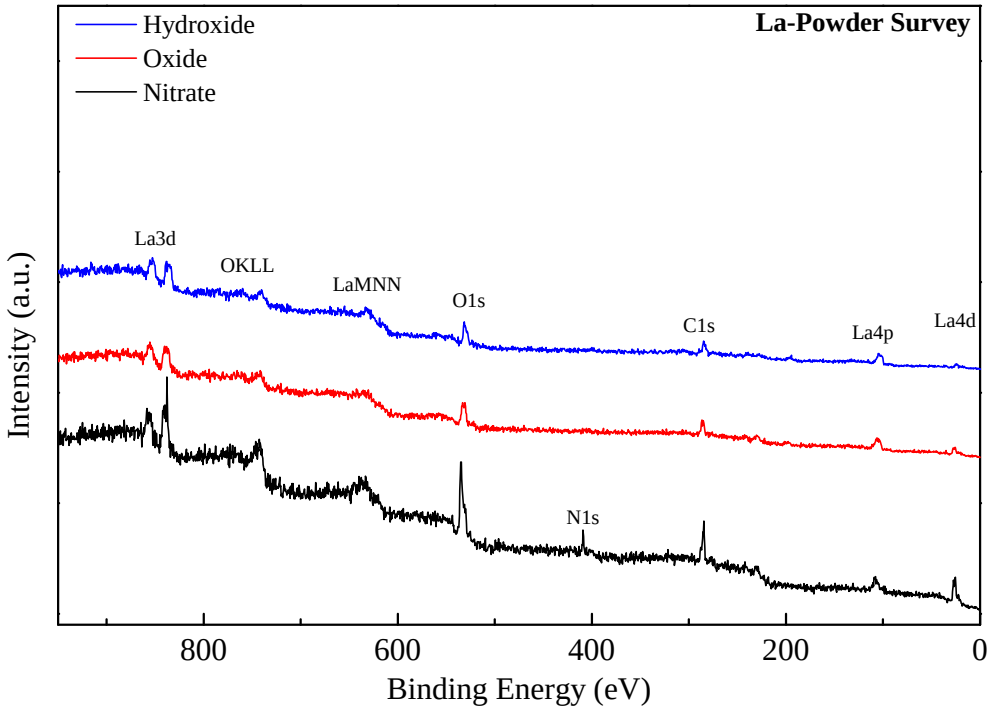


Figure 9.8.: *La* based powder survey spectra measured with Mg-K_α for $La(OH)_3$ (top), La_2O_3 (middle) and $La(NO_3)_3(H_2O)_6$ (bottom).

From the illustrated spectra, it can be seen that all expected significant signals can be observed. No unknown impurities can be detected assuming the purity of the analyzed substances. Specific signals of the *La* result from electrons in the *3d*, *4p* and *4d* orbital energy states. For oxygen, the *O1s* and *OKLL* Auger signals and for carbon the *C1s* are characteristic. For the nitrate powder, additionally the *N1s* peak can be observed. Precise analysis of the powders was possible by detecting detailed spectra of the *La3d* and *O1s* signal. In the following paragraph, the peak fits and comparison with literature based data should be shown to confirm the powder compositions. Difficulties arise from a deficiency of specific reliable literature values, particularly for the hydroxide and the nitrate. Therefore, data for elements with similar electronegativities like *Fe*, *Cr* and *Ba* are consulted for comparison.

The *La3d* Signal For oxydic *La* compounds, large satellite signals of the main peak can be observed for the *3d* orbitals. They arise on the high binding energy side of the *3d* peaks as expected. The expected intensity ratio of the main signal and the satellite is 0.70.[192] [196] Figure 9.9. shows the detail *La3d* spectra of the powders.

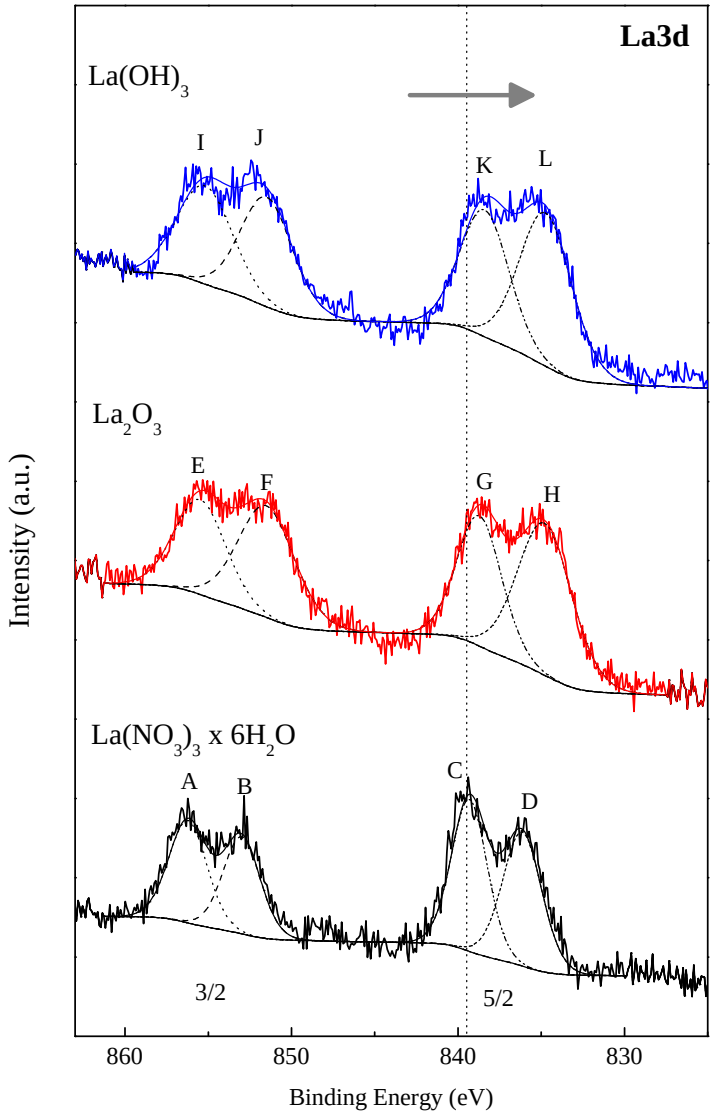


Figure 9.9.: Detail spectra of the *La3d* signal measured with Mg-K_α from the *La* based nitrate-hydrate (black), oxide (red) and hydroxide (blue) powders. The peak fit parameters are shown in table 9.5.

It can be seen that shifts to lower binding energies are observed for the *La3d* peak as expected from the theoretical considerations in figure 9.7. from the nitrate-hydrate to the oxide. In contrast to the theoretic assumptions, but in agreement with literature data, the oxide and hydroxide show equal peak structures and positions.

For curve fitting, a Gaussian/Lorentzian (GL) ratio of 70/30 was used according to guidelines in[135]. The detected peak positions and peak fit details Table are summarized in table 9.5.

Table 9.5.: Peak fit parameters and peak positions in eV for the *La3d* powder spectra of the nitrate, oxide and hydroxide.

Comp.	Pos.	FWHM	Area%	GL	Signal	Literature
$La(NO_3)_3 \times 6H_2O$			Region: 861.3-829.8 eV			
A	856.2	2.7	21.4	70/30	$d_{3/2\ sat}$	-
B	853.0	2.6	19.9	70/30	$d_{3/2\ main}$	-
C	839.3	2.5	29.8	70/30	$d_{5/2\ sat}$	-
D	836.1	2.8	28.9	70/30	$d_{5/2\ main}$	-
La_2O_3			Region: 861.3-827.5 eV			
E	855.5	3.6	19.1	70/30	$d_{3/2\ sat}$	855.0 La_2O_3[197]
F	851.5	4.0	25.0	70/30	$d_{3/2\ main}$	851.9 La_2O_3[197]
G	838.7	3.2	23.0	70/30	$d_{5/2\ sat}$	838.2 La_2O_3[197]
H	834.8	3.9	32.9	70/30	$d_{5/2\ main}$	835.1 La_2O_3[197]
$La(OH)_3$			Region: 859.5-824.6 eV			
I	855.2	3.9	21.3	70/30	$d_{3/2\ sat}$	854.9 $La(OH)_3$[192]
J	851.5	3.7	22.5	70/30	$d_{3/2\ main}$	851.8 $La(OH)_3$[192]
K	838.4	3.5	24.4	70/30	$d_{5/2\ sat}$	838.1 $La(OH)_3$[192]
L	834.7	3.7	31.8	70/30	$d_{5/2\ main}$	835.0 $La(OH)_3$[192]

Since no XPS literature data are available for the *La3d* signal in trinitrate-hexahydrates, the measured data can not be confirmed by comparison, but based on the previous XRD analysis and the thermodynamic stability in combination with the confirmation of the expected shift to lower binding energies, the four observed peak positions for $La(NO_3)_3 \times 6H_2O$ (A, B, C and D in figure 9.9) can be taken as basic data for comparison with future thin film

analysis. The existence of the nitrate has to be confirmed by the *O1s* peak analysis.

It can be seen from table 9.5. that the peak positions for *La*-III-oxide and -hydroxide are consistent with data reported in literature within the detector accuracy of approx. ±0.5 eV. No further precision of the oxide and nitrate can be found due to the equal peak positions. Therefore, the analyzed substances can not be identified with respect to the *La3d* signal and the interpretation of the *O1s* signals is essential.

Characteristic peak intervals (ΔE) between the main peak and the respective satellite could be calculated from the peak positions as 3.1 eV for the nitrate, 3.9 eV for the oxide and 3.7 eV for the hydroxide of *La* whereas the difference between the 3/2 and 5/2 doublet components are 16.9 eV (nitrate), 16.7 eV (oxide) and 16.8 eV (hydroxide). The intensity ratio of the satellite and the main peak in the $La3d_{5/2}$ of 0.70 were approximately confirmed for the oxide (G/H = 0.69) and the hydroxide powder (K/L = 0.76). The nitrate compound shows a different peak structure and the ratio could be measured as 0.97.

The theoretical expected area ratio of 2:3 for the $d_{3/2}$:$d_{5/2}$ could roughly be confirmed by 2.1:2.9 for the nitrate and 2.2:2.8 for the oxide and hydroxide.

***O1s* Signal of the Lanthanum Powders** *O1s* orbitals show a characteristic singlet structure. A critical examination of the *O1s* signal is necessary because of the variety of signals resulting from the underlying carbon sticky tape. Detected specified signals should be compared to literature data to confirm the results of the *La3d* analysis. Figure 9.10. shows the detected *O1s* signals and the curve fittings.

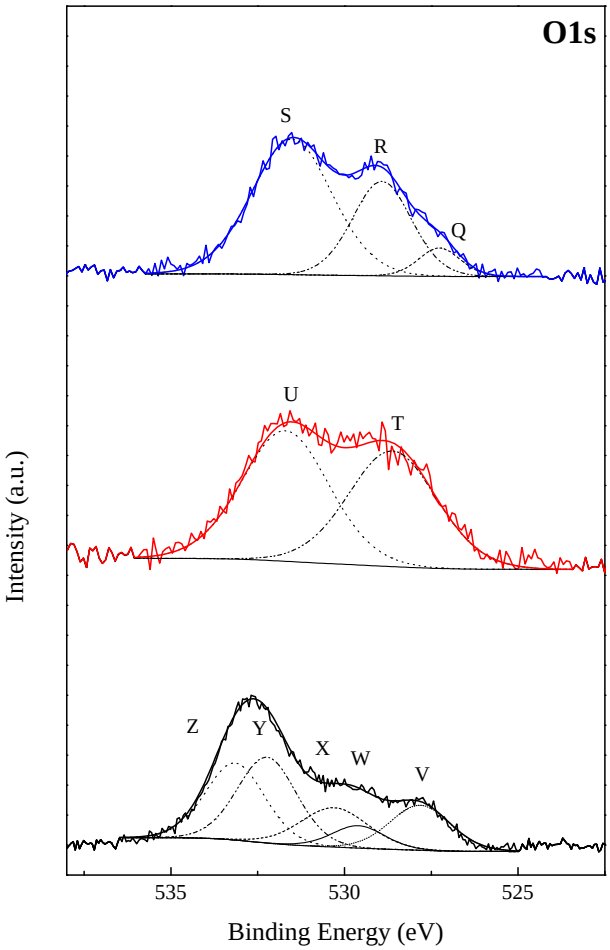


Figure 9.10.: *O1s* signal measured with Mg-K_α of the three *La* based powders (nitrate (black, bottom), oxide (red, middle), hydroxide (blue, top). Included are the peak fits, which are utilized for precise analysis.

For the nitrate powder several different $O1s$ signals could be identified from the illustrated curve fitting (s. table 9.6.). Peak fit parameters, peak positions and literature data are given in table 9.6.

Table 9.6.: Peak fit parameters and peak positions in eV for the $O1s$ powder spectra of the La nitrate, oxide and hydroxide.

Comp.	Pos.	FWHM	Area%	GL	Literature
$La(NO_3)_3 \times 6H_2O$	Region: 536.5-525.0 eV				
Z	533.2	2.0	28.1	80/20	533.3 crystal H_2O [198]
Y	532.2	2.0	31.3	80/20	532.7 $Ba(NO_3)$ [199]
X	530.3	2.3	16.4	80/20	carbon tape
W	529.6	1.8	7.3	80/20	carbon tape
V	527.8	2.1	16.9	80/20	carbon tape
La_2O_3	Region: 536.1-523.3 eV				
U	531.7	3.0	52.6	80/20	531.3 Fe or $Cr(OH)_3$ [192] [200]
T	528.6	3.0	47.4	80/20	528.6 La_2O_3 [201]
$La(OH)_3$	Region: 535.8-524.1 eV				
S	531.5	2.7	61.7	80/20	531.3 Fe or $Cr(OH)_3$ [200]
R	528.9	2.0	31.6	80/20	528.6 La_2O_3 [201]
Q	527.3	1.4	6.7	80/20	carbon tape

Signal Z in figure 9.10 (533.2 eV) with an area ratio of 28.1 % can be identified as $O1s$ in crystal H_2O by comparison with literature data from[198], whereas signal Y in figure 9.10 (532.2 eV) can be identified as $O1s$ in NO_3 and an area ratio of 31.3 % can be detected. Since no reference data for the $O1s$ signal in lanthanum-nitrates are available from the literature, the signal has been compared to barium-nitrate due to the similarity in electronegativity (EN barium = 0.89).

The expected area ratio of the two signals is 2:3, calculated from the number of atoms included in the molecule. In contrast to the expected quantity the measured ratio is 1:1, indicating that additional water species are adsorbed to the powder surface or the carbon tape during the measurement. Additional three peaks with lower intensity (X, W, V in figure 9.10) are detected, shifted to lower binding energies, which can not be identified as compound specific species.

Shifts to lower binding energies are caused by less electronegative binding partners and therefore the detected peaks are likely caused by the underlying carbon tape.

The oxide powder shows two different *O1s* signals. Signal U in figure 9.10 at 531.7 eV matches the data documented in the literature[192] for hydroxides, while signal V, detected at 528.6 eV, can be reliably identified as *O1s* in La_2O_3.[201]. The presence of hydroxide species can be explained by the reaction of the strongly hygroscopic La_2O_3 with absorbed water on the adhesive tape, which can not be avoided, even by handling under inertgas conditions.

Nevertheless, the initial goal to collect reference data for future thin film analysis has been fulfilled, although no phase free isolation of the La_2O_3 powder was possible. Three signals can be detected from the analyzed hydroxide powder. Similar to the oxide, peaks at 531.5 eV (S in figure 9.10) and 528.9 eV (R in figure 9.10) could be identified, indicating the presence of oxide and hydroxide species. As the hydroxide is synthesized from the pure oxide, detected oxide species can be explained by remaining oxide from synthesis. The additional third signal at 527.3 eV (Q) can again be assigned to the underlying carbon tape.

In accordance with the *La3d* analyzes, the *O1s* signals can be identified to result from nitrate, oxide and hydroxide species. The hydroxide and oxide could not be isolated phase free. Subsidiary signals of the *O1s* signals can be presumably assigned to result from the underlying adhesive tape or surface reactions.

Neodymium

All *Nd* powders have been measured applying Al-K_α X-rays as excitation source. Figure 9.11. shows the survey spectra of the three powders.

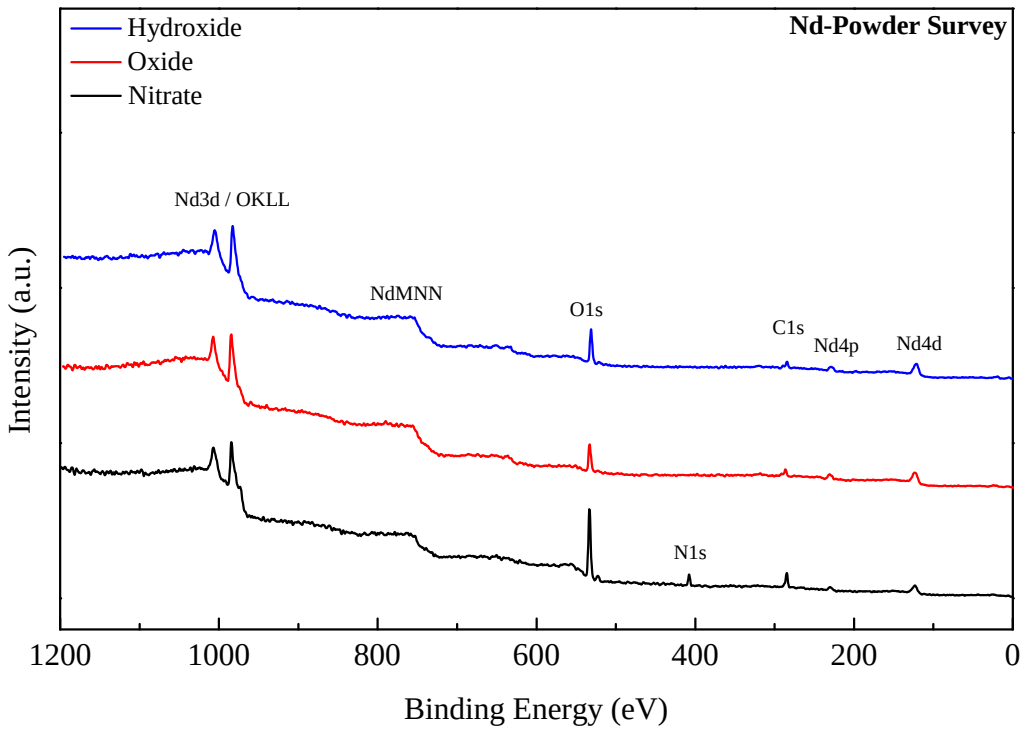


Figure 9.11.: *Nd* based powder survey spectra measured with Al-K_α for $Nd(OH)_3$ (top), Nd_2O_3 (middle) and $Nd(NO_3)_3(H_2O)_6$ (bottom).

It can be seen that as for *La*, all expected significant signals can be observed from the spectra. No unknown impurities can be detected, assuming the purity of the analyzed substances. Specific signals of the *Nd* are the signals resulting from electrons in the *3d*, *4p* and *4d* orbital energy states. For oxygen, the *O1s* signals and for carbon the *C1s* are characteristic. For the nitrate powder, additionally the *N1s* peak can be observed.

NdMNN Auger signals can be identified in the region around 800 eV. *OKLL* Auger peaks, where the main peak is expected to be detected at 948 eV[201], overlap with the intensive *Nd3d* signals for the Al-K_α excitation source which has been applied for technical reasons. The overlap structure will be interpreted as precise as possible.

The *Nd3d* Signal For the *3d* signal, the characteristic double peak structure caused by the spin-orbit coupling can be detected. In contrast to *La* for oxydic *Nd* compounds, satellite signals shifted to lower binding energies can be observed for the *Nd3d* orbitals. In the *Nd* case, the expected area ratio of the main peak and the satellite is 0.52 %.[192] [196]

Figure 9.12. shows the multiple plots of the *Nd3d* detail spectrum of the three powders.

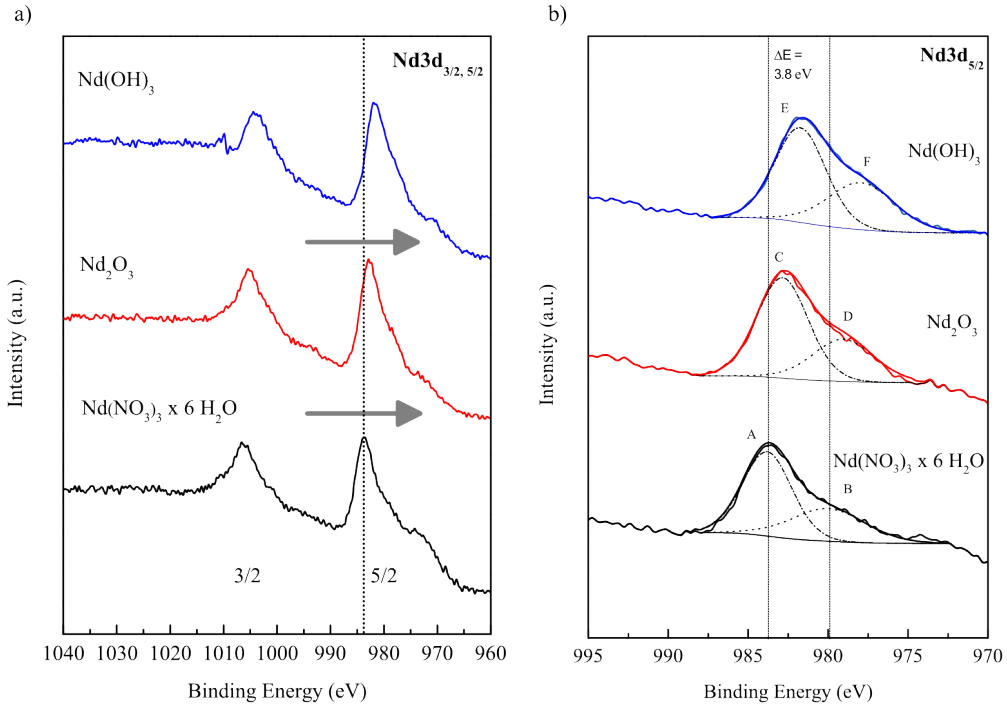


Figure 9.12.: Detail *Nd3d* spectra of the *Nd* based hydroxide, oxide and nitrate powder measured with Al-K_α, showing the binding energy shift tendency (a), fitted $Nd3d_{5/2}$ signal, shown are the specific peaks and energy difference (ΔE) of the nitrate, oxide and hydroxide powder (b) of the main peak ($Nd3d_{5/2}$) and the respective satellite.

The peak fit parameters of the adjusted curves in 9.12 b) are shown in table 9.7.

Table 9.7.: Peak fit parameters and peak positions in eV for the $Nd3d_{5/2}$ powder spectra of the nitrate, oxide and hydroxide.

Comp.	Pos.	FWHM	Area%	GL	Signal	Literature
$Nd(NO_3)_3 \times 6H_2O$			Region: 986.9-970.3 eV			ΔE = 3.8 eV
A	983.8	3.6	63.1	70/30	$d_{5/2\ main}$	-
B	980.0	5.5	36.9	70/30	$d_{5/2\ sat}$	-
Nd_2O_3			Region: 988.0-974.7 eV			ΔE = 3.8 eV
C	982.9	3.8	66.4	70/30	$d_{5/2\ main}$	982.9 Nd_2O_3[197]
D	979.1	4.6	33.6	70/30	$d_{5/2\ sat}$	978.4 Nd_2O_3[197]
$Nd(OH)_3$			Region: 986.9-970.3 eV			ΔE = 3.8 eV
E	981.7	3.8	60.5	70/30	$d_{5/2\ main}$	981.7 $Nd(OH)_3$[192]
F	977.9	4.6	39.5	70/30	$d_{5/2\ sat}$	E-3.8 $Nd(OH)_3$[192]

It can be seen that the peak positions for the *Nd*-III-oxide and -hydroxide are consistent with data reported in literature within the accuracy of the detector of ca. $\pm$0.5 eV. With respect to the *Nd3d* signal, the analyzed substances can be confirmed to be the expected compounds. No literature data are available for the $Nd(NO_3)_3 \times 6H_2O$, but as the compound has been characterized by XRD and is thermodynamically stable, it is unlikely to react under inert gas handling. Therefore, it can be assumed that the analyzed compound can be considered to be the pure $Nd(NO_3)_3(H_2O)_6$ and the measured peak positions can be utilized as reference data for the following thin film analysis.

Shifts to lower binding energies are observed as expected from the theoretical considerations in figure 9.7. The expected peak area ratio of the $3d_{3/2}$ and $3d_{5/2}$ orbital signals is 2:3 (s. section 2.1.). For the shown spectra, it is not possible to detect this ratio due to satellite structures within the background and the overlap with the *OKLL* Auger peaks, which were mentioned above. Therefore, only the $Nd3d_{5/2}$ signal is fitted in (b). Due to the overlap of signals, no asymmetric peak fitting was possible and a Gaussian/Lorentzian ratio of 70/30 was used as for *La*. Characteristic peak intervals between the main peak and the respective satellite could be calculated from the peak positions (ΔE) as 3.8 eV for the nitrate, oxide and hydroxide of *Nd*. Due to the overlap with the Auger signals no value for the $d_{3/2}$ and $d_{5/2}$ doublet components could be determined for the *Nd* powders. The area ratio between the main peak and the satellite could be calculated from the measurements as 0.58 (nitrate), 0.51

(oxide) and 0.65 (hydroxide). The data achieved from the *Nd3d* signal need to be confirmed by the *O1s* signals since all compounds additionally contain oxygen in a characteristic binding state.

The *O1s* Signal of the Neodymium Powders The following section includes the results of the *O1s* signal determined from the three *Nd* powder samples. Analogous to the *La* components, the specified signals should be compared to literature data to confirm the results of the *Nd3d* analysis. As for *La* difficulties arise from a deficiency of specific reliable literature values, particularly for the hydroxide and the nitrate and extra signals caused by the underlying carbon tape. Likewise, data for elements with similar electronegativities like *Fe*, *Cr* and *Ba* are consulted for comparison. Figure 9.13 shows the analyzed *O1s* signals. Additionally the curve fittings are shown. Peak fit parameters, peak positions and literature data for comparison are given in table 9.8.

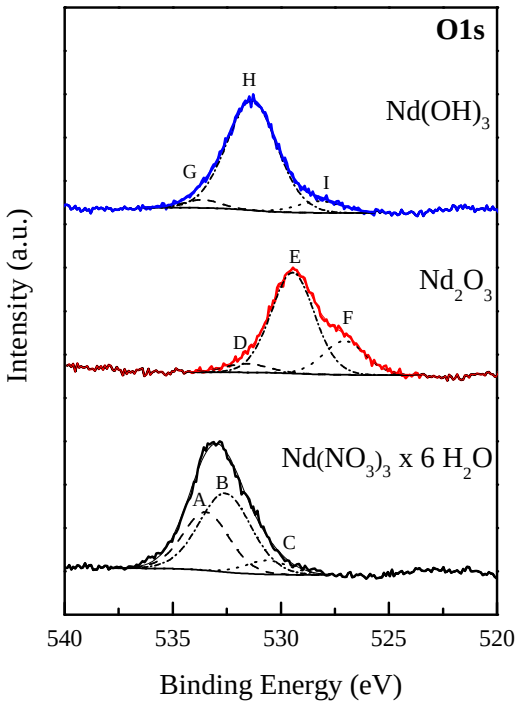


Figure 9.13.: *O1s* signal of the three *Nd*-based powders measured with Al-K_α. Included are the detailed peak fits.

Table 9.8.: Peak fit parameters and peak positions in eV for the *O1s* powder spectra of the *Nd*-based nitrate-hydrate, oxide and hydroxide.

Comp.	Pos.	FWHM	Area%	GL	Literature
$Nd(NO_3)_3 \times 6H_2O$			Region: 537.9-527.7 eV		
A	533.5	2.5	36.5	80/20	533.3 crystal H_2O [198]
B	532.6	2.8	55.2	80/20	532.7 $Ba(NO_3)_2$ [199]
C	530.6	2.4	8.3	80/20	carbon tape
Nd_2O_3			Region: 534.2-523.5- eV		
D	531.6	2.4	6.2	80/20	531.3 Fe or $Cr(OH)_3$ [200]
E	529.5	2.3	70.8	80/20	529.3 Nd_2O_3 [197], [202]
F	527.1	2.3	23.0	80/20	carbon tape
$Nd(OH)_3$			Region: 536.3-525.6 eV		
G	533.6	2.0	4.6	80/20	533.3 crystal H_2O [198]
H	531.3	2.7	87.0	80/20	531.3 Fe or $Cr(OH)_3$ [200]
I	528.2	2.5	8.4	80/20	carbon tape

For the nitrate powder, two main peak positions can be determined from the peak fits shown in figure 9.13. The signal at 533.5 eV (A in figure 9.13) can be identified as *O1s* in crystal H_2O by comparison with literature data in[198]. Since as for the *La*-nitrate, no reference data for the *O1s* signal in *Nd*-nitrates are available from literature, the second main signal at 532.6 eV (B in figure 9.13) has been compared to *O1s* in barium-nitrates. The area ratio of $O1s_{(H_2O)}$: $O1s_{(NO_3)}$ can be ascertained as 36.5 % : 55.2 % in agreement with the number of oxygen atoms contained in the compounds (6:9). The third signal, detected at 530.6 eV (C in figure 9.13), can not be identified as one of the expected oxygen species and is therefore considered to result from the underlying adhesive.

The analyzed oxide powder shows likewise three different *O1s* signals. The main signal at 529.5 eV (E) with an area ratio of 70.8 % matches the data, documented in the literature[197] [202] for *O1s* in Nd_2O_3, which confirms the composition of the powder as Nd_2O_3.

Small subsidiary signals can be observed, shifted to higher and lower binding energies. The signal at higher binding energies (531.6 eV, D in figure 9.13) can be identified as *O1s* in hydroxides, concluding that the thermodynamic slightly

unstable powder partially reacted with oxygen compounds from the adhesive, forming a thin surface layer of hydroxides. The third signal at 527.1 eV (F in figure 9.13) shows exceptional low binding energies, which may be suggestively explained by oxygen species bound to less electronegative elements as for *La*.

As the first two powders, the third analyzed substance shows three characteristic peak positions for the *O1s* signal as listed in table 9.8. Similarly to the nitrate, no direct reference data are available from the literature and the results have been compared to hydroxides from iron and chromium. The main signal (H in figure 9.13) with an area ratio of 87.0 % and a peak position of 531.4 eV can be identified as *O1s* from hydroxides whereas the signal (G) shifted to higher binding energies (533.3 eV, signal G in figure 9.13) results from remaining or absorbed water from synthesis.

Similar to the first two powders analyzed, a signal shifted to exceptional low binding energies (528.2 eV, signal I in figure 9.13) can be observed and assigned to the underlying adhesive. The differences in comparison to the detected peak positions of the $La(OH)_3$ and La_2O_3 can be explained by the initially mentioned varying composition of the adhesive.

In accordance with the *Nd3d* analyzes, the *O1s* signals can be identified to result from the nitrate, oxide and hydroxide. Subsidiary signals of the *O1s* signals can be presumably assigned to result from the underlying adhesive tape or products from surface reactions.

9.2.1. Summary of XPS Reference Data

From elementary XPS analysis, the characteristic peak positions for *O1s* and *Nd3d* in the nitrates, oxides and hydroxide have been shown in agreement with known literature data and theoretical considerations. Therefore, the determined peak positions can be utilized as reference data sets for the following film analyses. Table 9.9 shows the summery of the characteristic peak positions.

Table 9.9.: Summary of the collected XPS data showing the characteristic peak positions and distances in eV for the RE-nitrates, oxides and hydroxides (RE = *La, Nd*).

	La		***Nd***	
	$La3d_{5/2}$	O1s	$Nd3d_{5/2}$	O1s
Nitrate-hydrate	836.2	532.2, 533.2	983.8	532.6, 533.5
ΔE	3.1		3.8	
$\Delta E_{3/2-5/2}$	16.9		-	
Oxide	834.8	528.6	982.9	529.5
ΔE	3.9		3.8	
$\Delta E_{3/2-5/2}$	16.7		-	
Hydroxide	834.7	531.5	981.7	531.3
ΔE	3.7		3.8	
$\Delta E_{3/2-5/2}$	16.8		-	

10. Film Topography, Structure & Thickness

In the following, SEM, STM and AFM analysis of the deposited films will be shown to investigate the topography, roughness and the stability of the generated films. HRTEM was utilized to determine the film 6hickness and structure.

The principal aim of the topographic imaging is to determine the solution concentration range within the Ostwald Miers region, where film formation occurs preferred to spontaneous nucleation and a homogeneous film formation is ensured. Thus, images of films deposited from different concentrated solutions have been analyzed, regarding conditions for a homogeneous structure and low roughness (AFM data). Roughness studies are essential, since the low roughness values promote the final electrical performance, which is essential for future device integration.

SEM imaging has been utilized to obtain film structures for the oxide films after thermolysis under normal laboratory conditions, especially for high solution concentrations. Such films showed less homogeneous structures and therefore the films were not completely insulating, which made SEM imaging possible. In studies under clean room conditions, it was possible to create closed oxide films. The films showed insulating behavior and charging effects lead to impossible SEM characterization. Thus, the main focus for structural analysis was changed to AFM imaging.

La_2O_3 forms hydroxide species immediately under water or air exposure. Therefore, *La*-based films have been analyzed using UHV-STM.

Basic AFM studies on the deposition mechanism will be shown for the *H-Si(111)* and *H-Si(100)* substrates with respect to an influence of the substrate orientation (s. section 10.3.1. and 10.1.3.). The annealing dependent roughness of the films (s. section 10.3.3.) and the stability of the films (s. section 10.3.2.). Low roughness values are essential for the final electrical performance of deposited thin films as reported in[203], since a low roughness influences the tunneling current positively.

The solution concentration dependent film thickness has been firstly studied using HRTEM imaging for the solution based oxide deposition.

To investigate the film and interface structure and the dependency of the solution concentration on the film thickness, HRTEM analysis were done for the oxide films after precursor thermolysis. Three different solution concentrations, determined from the AFM analysis to be within the Ostwald Miers region, have been tested.

Due to the complexity of TEM sample preparation and imaging, representatively deposited films on *H-Si(111)* substrates are discussed to achieve a systematic overview on the film thickness control during solution processed deposition (s. section 10.4.). Due to the hygroscopicity of La_2O_3 and the possible undefined formation of $La(OH)_3$, La-based samples have not been determined by HRTEM.

Subsequently, the topography analysis results for the alternative substrates $SiGe$ and Ge are presented in section 10.5.

10.1. Topography: SEM

SEM analysis have been done for both precursor types ($La/Nd(NO_3)_3{\times}6H_2O$) on *Si(111)* and *Si(100)* substrates. As the analysis have been done both in NTU Singapore and University of Oldenburg two different types of SEM have been utilized (s. section 6.2.1).

10.1.1. Highly Concentrated Solutions

For high concentrated solutions, non uniform brittle structures were expected to be formed, as the spontaneous nucleation occurs, leading to salt agglomerations on top of the surface. It is known that solution concentrations above 0.4 M are considered to be much higher than suitable concentrations for homogeneous film formation.[140] Therefore, in the present thesis, analysis of 0.5 M $Nd(NO_3)_3 \times 6H_2O$ have been conducted to show the shape of the deposited brittle structures.

Figure 10.1. shows SEM images of the structures deposited from 0.5 M solution in four different magnifications (104x, 254x, 654x and 2710x). The current was set to 1.3 nA with an acceleration voltage of 30 kV.

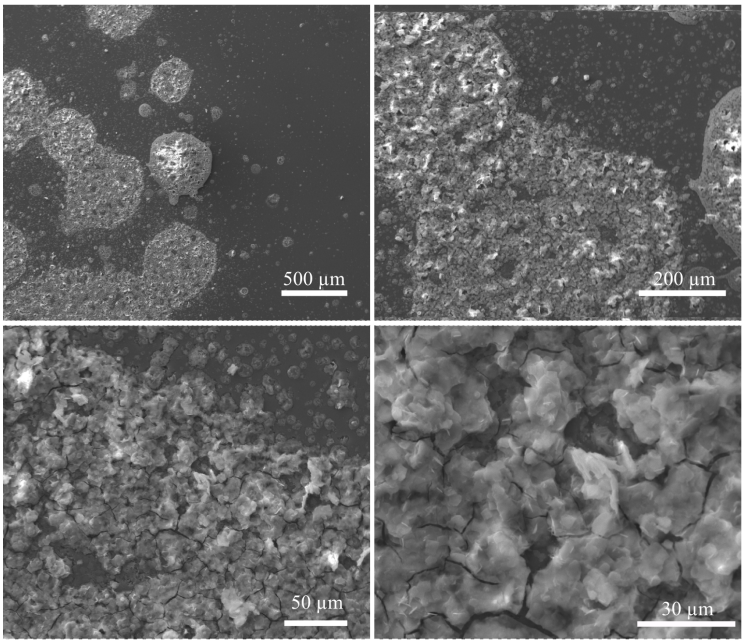


Figure 10.1.: SEM images of droppy and brittle structures deposited from 0.5 M $Nd(NO_3)_3 \times 6H_2O$ butanolic precursor solution on *H-Si(111)*. The images are taken with 1.3 nA beam current and 30 kV acceleration voltage.

Spotty and brittle, salt like structures can be observed, which are far away from a homogeneous, smooth and extensively uniform film formation. Thus, it can be shown as expected, that the Ostwald Miers limit for spontaneous nucleation is exceeded and the 0.5 M solution shows exemplary the structure formation within the range of highly concentrated solutions.

10.1.2. Transition - Crystallization to Film Formation

In order to determine the critical solution concentration, where homogeneous film formation occurs instead of crystal like structuring of the surface, serial dilutions in the range from 0.5 M down to 0.001 M of the *La* and *Nd* precursors have been tested.

$Nd(NO_3)_3 \times 6H_2O$ solutions show a characteristic light purple color down to 0.1 M precursor solution where the solution turns to colorless (s. figure 10.2.). $La(NO_3)_3 \times 6H_2O$ are colorless.

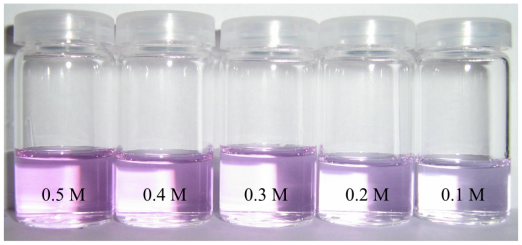


Figure 10.2.: Series dilution from 0.5 M to 0.1 M of the *Nd* precursor in 1-butanol.

In the following, only SEM images for concentrations below 0.01 M solution are shown, as all higher concentrated solutions show similar behavior to the presented structures in figure 10.1. and no uniform structures can be observed.

Figure 10.3. shows SEM images of films/structures which have been deposited from 0.01 M *Nd*-based solutions.

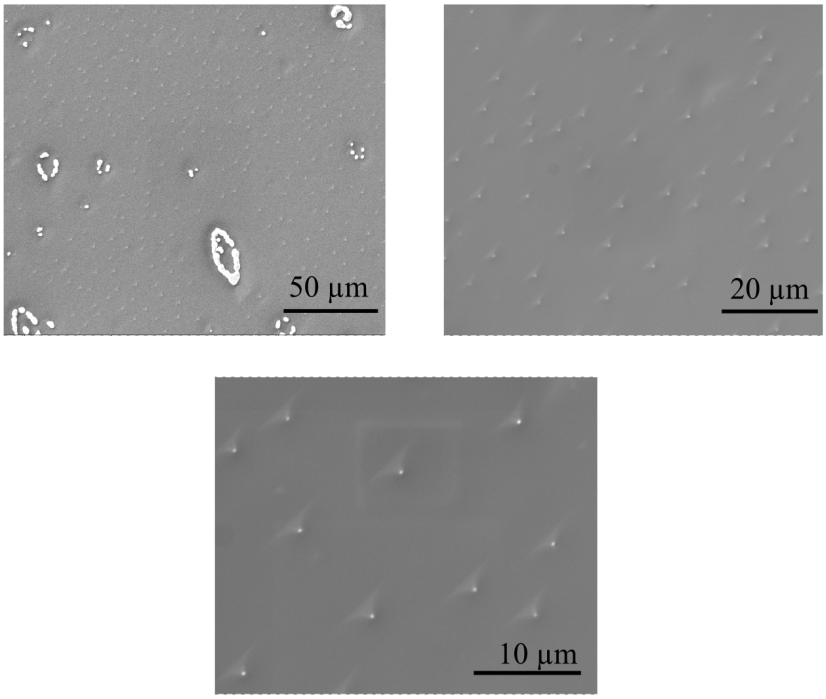


Figure 10.3.: SEM images of *Si(111)* samples coated with 0.01 M $Nd(NO_3)_3 \times 6H_2O$ precursor solution in 1-butanol. Homogeneously spread structures from nucleation centers are obvious. The images are taken with 0.88 nA beam current and 10 kV acceleration voltage.

From the images, shown in 1481x, 3805x and 8298x magnification, it can be seen that with respect to the precursor solution concentration, a characteristic number of spot like structures can be detected. These spot like structures can be interpreted as crystallization dependent nucleation centers. They are expected for solution concentrations which exceed the upper limit of the Ostwald Miers region.

Theoretically for exclusive film formation, a lower concentration or different experimental conditions are required, since the number of nucleation centers needs to exceed the limit for preferred film formation. Therefore, the concentration has been sensitively tuned to lower concentrations to determine the critical solution concentration for preferred film formation.

Scans of a 0.0096 M solution, which is just a slight change in concentration, show completely different appearance during SEM imaging, as shown in figure 10.4.

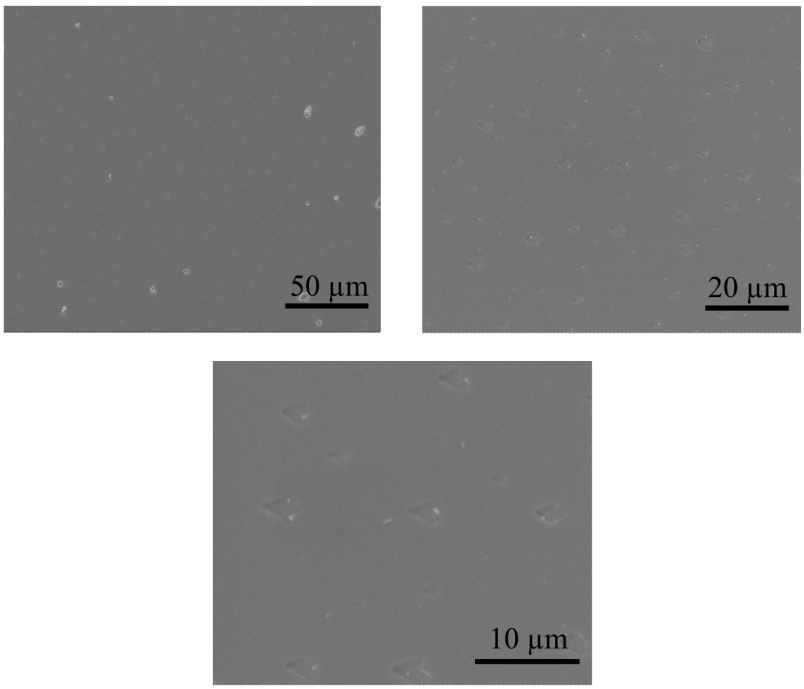


Figure 10.4.: SEM images of *Si(111)* samples coated with 0.0096 M $Nd(NO_3)_3 \times 6H_2O$. Changes are obvious from comparison with the 0.01 M samples as no spots can be observed anymore. The beam current was set to 0.88 nA and the acceleration voltage to 10 kV.

From the images in figure 10.4. (shown in 1290x, 3346x and 8257x magnification) it is obvious that the structure changed to homogeneous surfaces. Only small and irregular spreaded spots are detected, which can be referred to impurity based nucleation due to insufficient clean laboratory conditions outside the clean room. For improved film formation, the same solution has been tested under clean room conditions. After preparation in the clean room, charging effects made SEM imaging impossible, which allows to anticipate that the formed oxide films are closed and show insulating characteristics, which was one of the initial overarching objectives of the experimental work.

10.1.3. Substrate Orientation Influence: SEM

For the different substrates, different structures are expected, as the cleaning, which was described in chapter 8., leads to atomically smooth *H-Si(111)*, but relatively rough *H-Si(100)* surfaces due to kinetically controlled etching stops at the <111> lattice plane. The solution concentration, slightly above the Ostwald Miers limit (0.01 M), has been chosen for deposition in order to illustrate the significant differences.

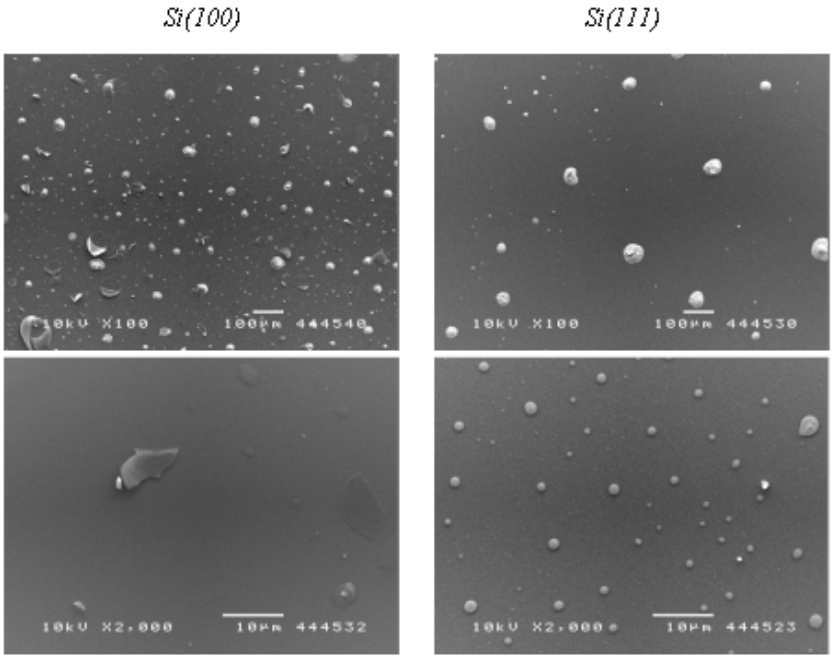


Figure 10.5.: SEM images of *Si(100)* (left) and *Si(111)* (right) substrates coated with 0.01 M $Nd(NO_3)_3 \times 6H_2O$ butanolic solution showing significant differences in deposition structures.

From the imaging shown in figure 10.5., it is obvious that for the prior to the deposition atomically smooth *H-Si(111)* substrates regular spread structures can be observed, whereas for the significantly rougher *H-Si(100)* substrates irregular formed shapes and spreading is characteristic. These findings are in agreement with the expected uniformity caused by the smoothness and the regularity of the underlying substrate. This aspect needs to be further investigated by more detailed AFM studies in the future.

10.2. Topography *La*: STM

In the initial state of the experiments, *La*-based films deposited from 0.001 M precursor solution have been analyzed, regarding the topography of the deposited structures. As La_2O_3 films are strongly hygroscopic, topography analyses under air exclusion have been necessary and performed under UHV conditions by STM.

The STM data, measured by myself, are already discussed in detail by H. Schnars in[137]. It has been demonstrated that structures deposited from the different application techniques show differing film topographies. Whereas drop-cast samples show strong island formation and higher roughness, homogeneous roughness values could be detected for films deposited from the dip-coat technique. It was suggested that for low precursor concentrations the films exhibit rougher surfaces, while the roughness decreases with increasing film thickness. No detailed root mean square roughness (RMS) values were given in[137].

As in further investigations the deposition technique of choice has been specified as dip-coat, in the following only an exemplary STM analysis of the films deposited from 0.001 M *La*-based solution by the introduced dip-coating technique (s. section 7.1.1.) is shown in figure 10.6.

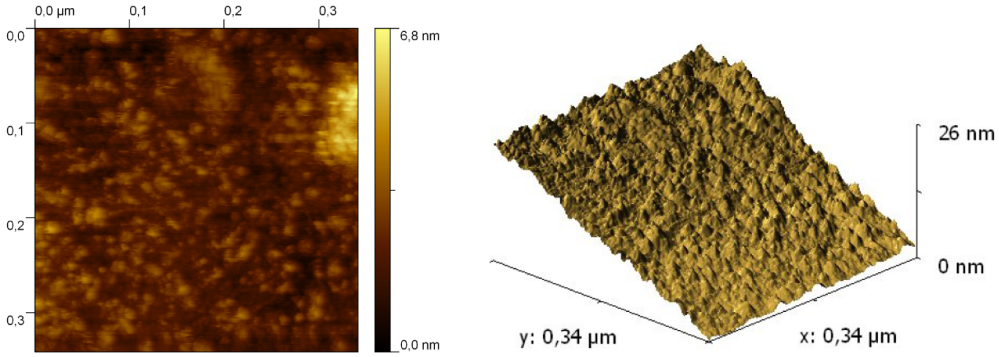


Figure 10.6.: STM images of films deposited from 0.001 M $La(NO_3)_3 \times 6H_2O$ butanolic precursor solution on *H-Si(111)*, exhibiting a RMS of 0.736 nm

The respective RMS could be obtained as 0.736 nm, which is within the range of RMS values achieved for *Nd*-based films, as it will be discussed in the following.

10.3. Topography *Nd*: AFM

As according to the shown SEM analysis, 0.0096 M solutions have been identified to meet the requirements of the Ostwald Miers region for homogeneous film formation, systematic investigation of the film roughness on the solution concentrations have been done, by using solution concentration below the limit (0.005 M and 0.001 M). To show the topographic changes in the deposited films, caused by exceeding the upper limit of the Ostwald Miers region, solution concentrations have been varied up to 0.01 M as a maximum concentration for deposition. Only *Nd*-based films have been analyzed due to the hygroscopicity and resulting instability of the La_2O_3 under ambient conditions during AFM imaging.

10.3.1. Substrate Orientation Influence

As indicated from the initial SEM analysis shown in 10.1.3., the deposition mechanism and the resulting film quality seems to be strongly dependent on the interaction between the precursor solution and the underlying substrate and

on the orientation of the substrate itself. Initially *H*-terminated *Si(111)* and *Si(100)* substrates have been prepared in one batch with identical precursor solution under exactly the same deposition and decomposition conditions in order to investigate the substrate influence more detailed.

For comparison, bare cleaned *H*-terminated substrates of *Si(111)* and *Si(100)* have been analyzed achieving a RMS of 0.45 nm for *H-Si(111)* and 1.36 nm for *H-Si(100)* (s. figure 10.7).

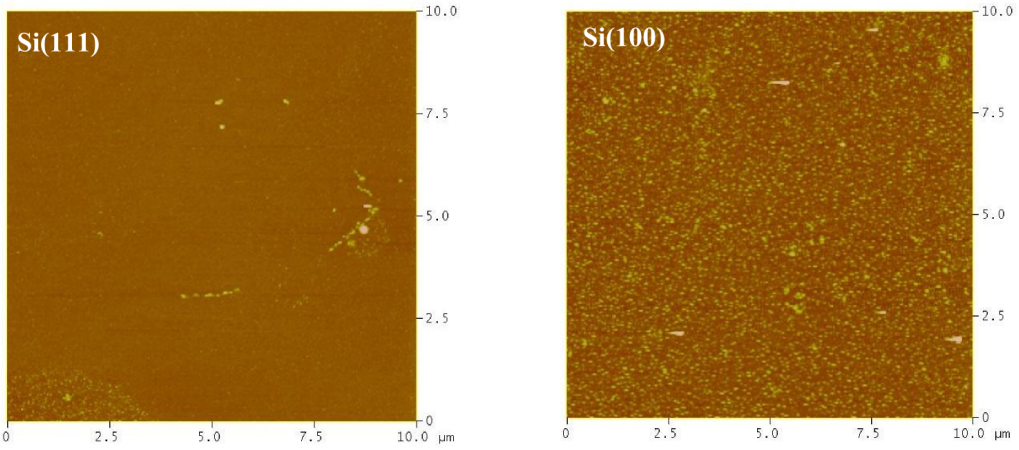


Figure 10.7.: Roughness studies using AFM tapping mode on bare cleaned *H-Si(111)* and *H-Si(100)*. Showing RMS values of 0.45 nm (*H-Si(111)*) and 1.36 nm (*H-Si(100)*).

The scan region was set to 10 × 10 μm with x = 0.2 μm/div and z = 50 nm/div.

It can be seen that *H-Si(100)* substrates show a three times higher RMS than *H-Si(111)* substrates, which is caused by the mechanism of the cleaning process, generating an atomically smooth *H-Si(111)*, but a relatively rough *H-Si(100)* surface due to the etching control on the <111> lattice plane (compare section 8.2.1).

The AFM measurements have been performed in non contact mode using the following parameters:

Size:	*Si(111)* $1 \times 1\ \mu m$, *Si(100)* $2 \times 2\ \mu m$
Angle:	$0°$
Scan rate:	Si(111) 1 Hz, *Si(100)* 2 Hz
Velocity:	$1\ \mu m$/s
Sample/Lines:	512

With the scaling parameters set to x = 0.2 μm/div and z = 50 nm/div for *H-Si(111)* and with x = 0.5 μm/div and z = 100 nm/div for *H-Si(100)* .

The achieved results are presented in figure 10.8. and summarized in table 10.1.

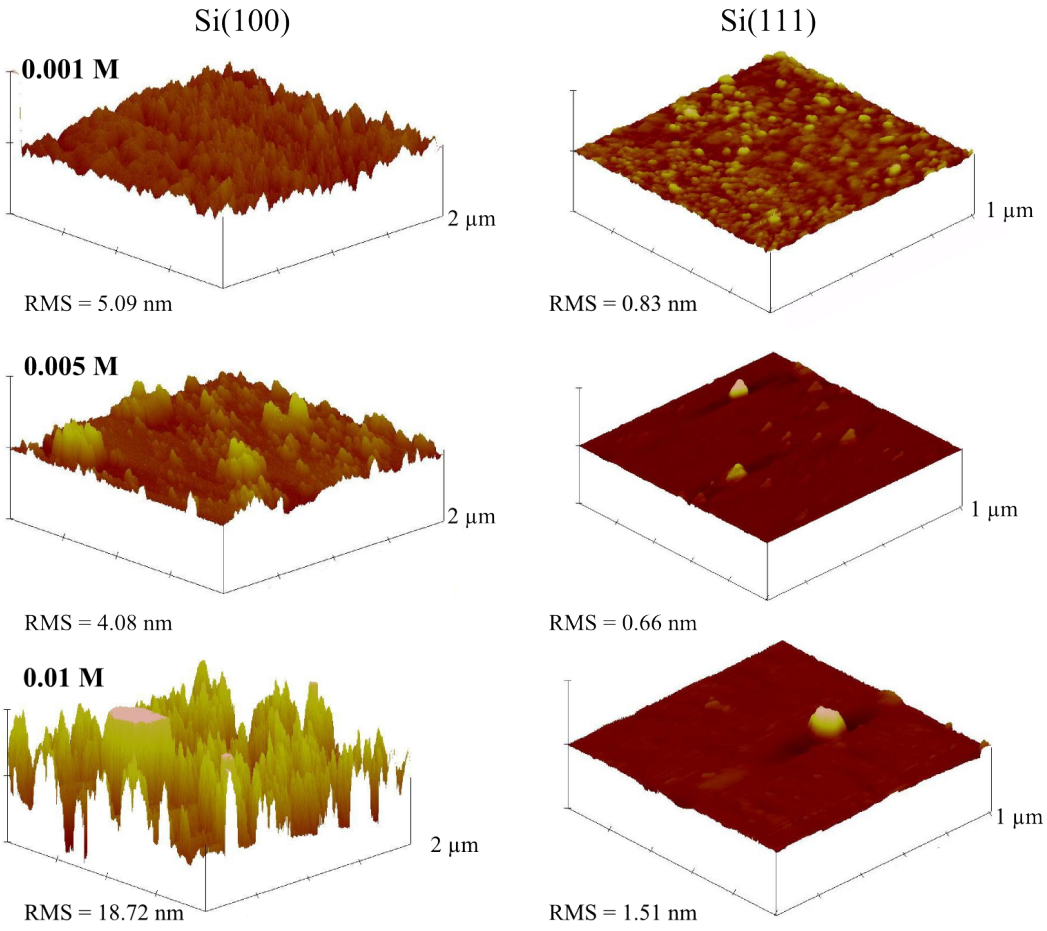


Figure 10.8.: AFM images taken in tapping mode and RMS values for oxide films after precursor thermolysis deposited from 0.001 M (top), 0.005 M (middle) and 0.01 M (bottom), $Nd(NO_3)_3 \times 6H_2O$ butanolic precursor solution on *H-Si(100)* (left) and *H-Si(111) (right)* substrates (*H-Si(111)*: x = 0.2 μm/div and z = 50 nm/div; *H-Si(100)*: x = 0.5 μm/div and z = 100 nm/div).

Table 10.1.: RMS and z-ranges in nm of the films illustrated in figure 10.8. and respective deviations between the two substrate types.

Conc.	***H-Si(100)***		***H-Si(111)***		**Deviation**
	z-range	RMS	z-range	RMS	
0.001 M	160.00	5.09	9.96	0.83	6.2:1
0.005 M	37.63	4.08	11.22	0.66	6.2:1
0.01 M	130.91	18.72	24.64	1.51	12.4:1

From the images in figure 10.8. and the summarized data in table 10.1., it can be seen that the films, generated from different concentrated solutions, show, as expected, a differing film roughness. Especially structures which are formed from solutions concentrated above the Ostwald Miers region (0.01 M) show a significant high roughness for both substrate types. Films deposited from 0.005 M and 0.001 M solution show similar low roughness values. For both cases the 0.005 M solution shows the lowest roughness, with a RMS value close to the RMS value of the 0.001 M solution. This indicates that both solution concentrations are within the Ostwald Miers region for homogeneous film formation.

As expected from the initial substrate roughness, *Si(100)* and *Si(111)* substrates show significant differences in the achieved roughness of the deposited films. Films deposited on *H-Si(100)* are 6.2 to 12.4 times rougher than films which have been deposited on *H-Si(111)*. Obviously, a rougher initial substrate leads to drastically increased final oxide roughnesses, whereas the increased roughness does not directly correlate with the initial substrate roughness values.

10.3.2. Film Stability

As the *Si(111)* substrates showed more homogeneous and less rough structures compared to *Si(100)*, the stability of the films has been studied on *Si(111)* substrates.

AFM imaging of the 0.001 M, 0.005 M and 0.01 M solution based films deposited on *H-Si(111)* directly after precursor deposition, after thermolysis of the precursor to the oxide and after 72 h of air exposure, has been performed to analyze the stability of the films by the change of roughness under outer influences (s. figures 10.9., 10.10. and 10.10.).

All images have been taken using the following settings:

Size:	$1 \times 1\ \mu m$
Angle:	$0°$
Scan rate:	1 Hz
Velocity:	$1\ \mu m/s$
Sample/Lines:	512

For the precursor films, the scan rate was modified to 2 Hz. The scales were set to x = 0.2 μm/div and z = 50 nm/div.

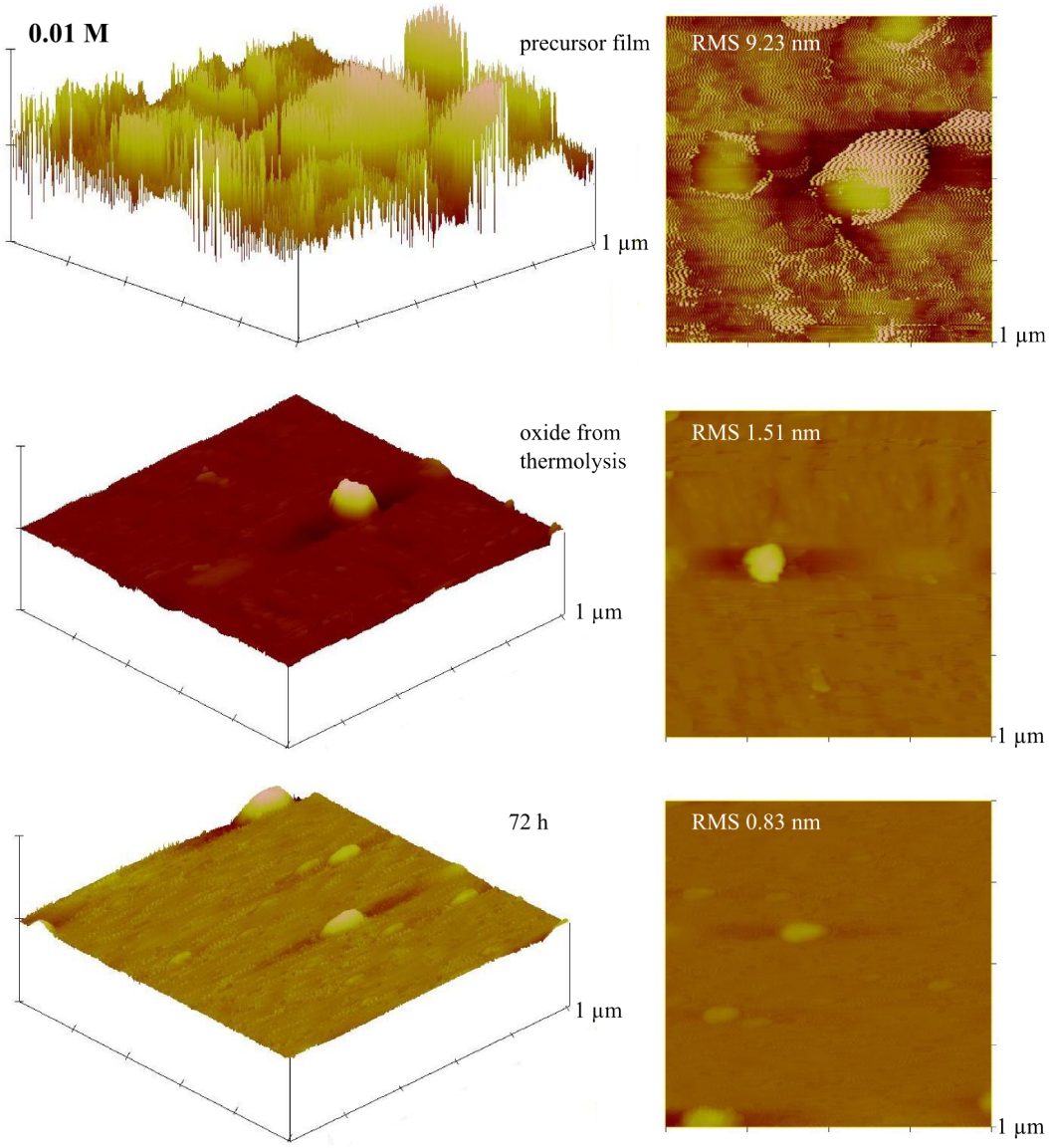


Figure 10.9.: AFM 3D and 1D images (tapping mode) of the films deposited from 0.01 M butanolic $Nd(NO_3)_3 \times 6H_2O$ precursor solution after deposition (top), decomposition (middle) and after 72 h of air exposure (bottom) on *H-Si(111)* (x = 0.2 μm/div and z = 50 nm/div).

The roughness studies of the precursor film prior to the thermolysis to the oxide show strong interferences within the detected image, which might be related to artifacts resulting from a rough and less smooth surface and difficulties in

a constant reliable tip/sample interaction. Therefore, the extracted RMS of 9.28 nm should be interpretated with caution.

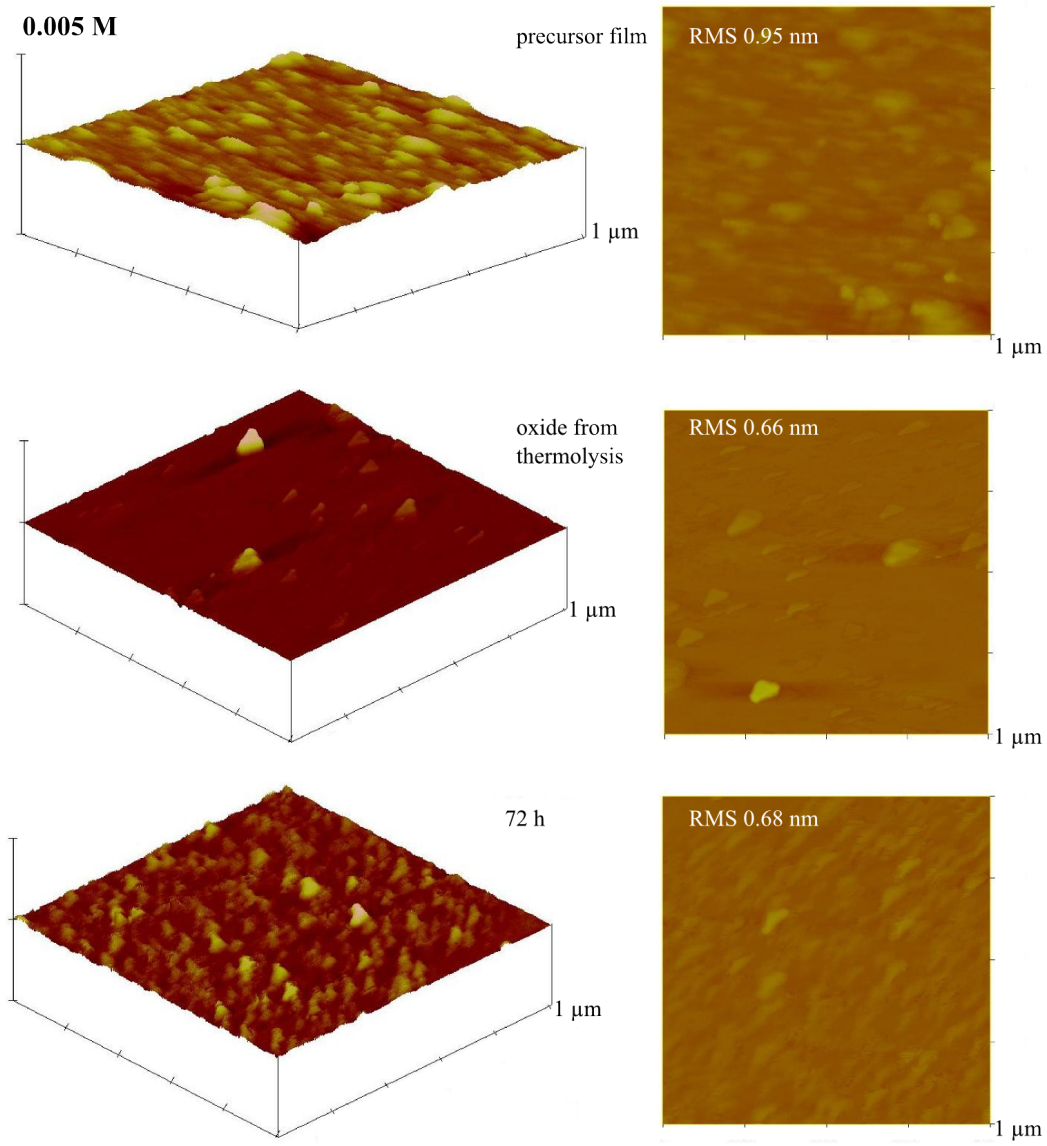


Figure 10.10.: AFM 3D and 1D images (tapping mode) of the films, deposited from 0.005 M butanolic $Nd(NO_3)_3 \times 6H_2O$ precursor solution after deposition (top), decomposition (middle) and after 72 h of air exposure (bottom) on *H-Si(111)* (x = 0.2 μm/div and z = 50 nm/div).

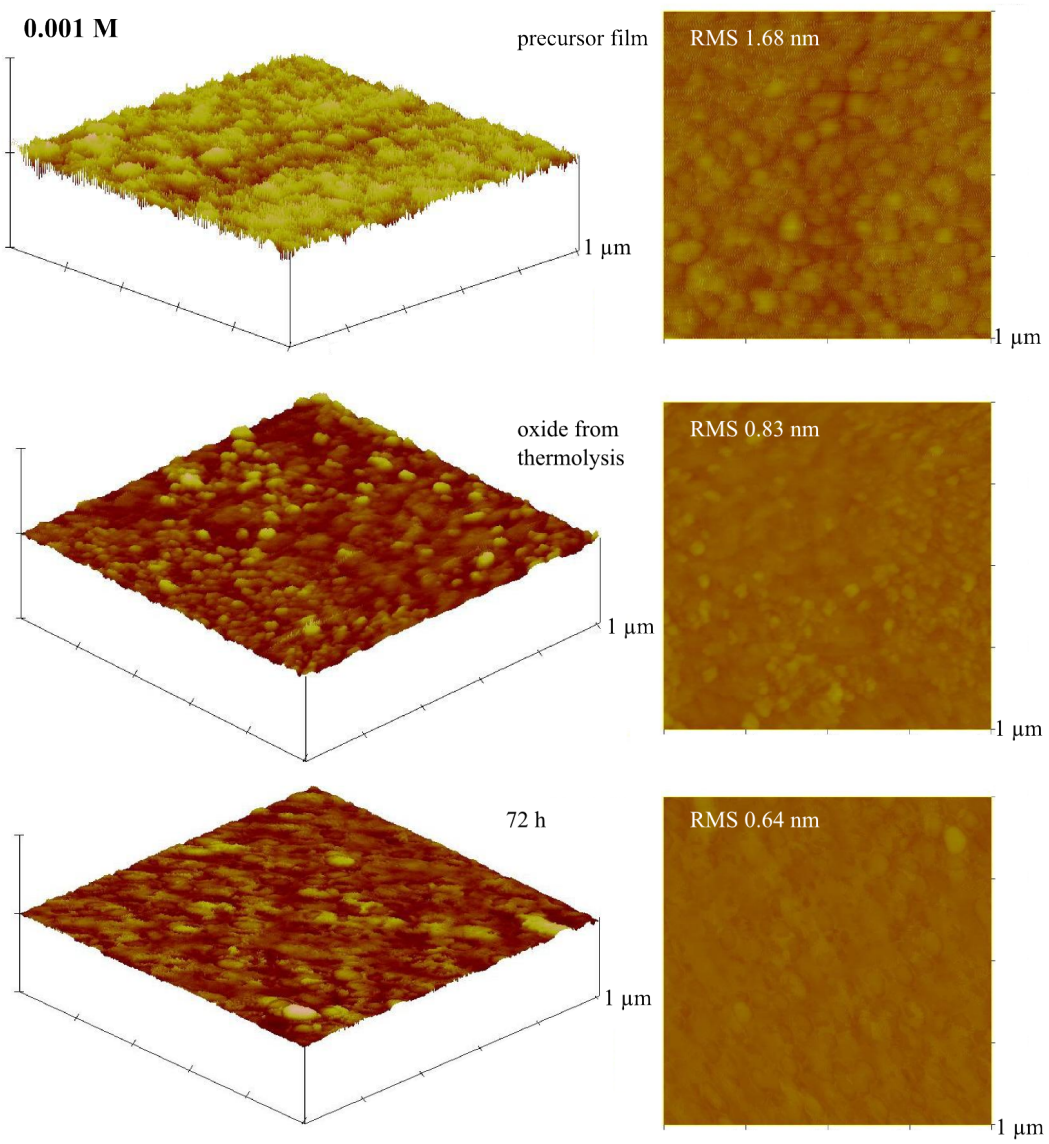


Figure 10.11.: AFM 3D and 1D images (tapping mode) of the films, deposited from 0.001 M butanolic $Nd(NO_3)_3 \times 6H_2O$ precursor solution on *H-Si(111)* after deposition (top), decomposition (middle) and after 72 h of air exposure (bottom) (x = 0.2 μm/div and z = 50 nm/div).

Table 10.2. concludes the determined RMS values and the z-ranges for the shown AFM images.

Table 10.2.: RMS values and z-ranges in nm, extracted from AFM measurements in tapping mode, for the films deposited from 0.001 M, 0.005 M and 0.01 M butanolic $Nd(NO_3)_3 \times 6H_2O$ precursor solution on *Si(111)* directly after precursor deposition, after decomposition to the oxide and after 72 h of air exposure.

Conc.	**precursor film**		**therm. oxide**		**72 h air exposure**	
	z-range	RMS	z-range	RMS	z-range	RMS
0.01 M	98.21	9.28	24.64	1.51	17.00	0.83
0.005 M	10.53	0.95	11.22	0.66	7.26	0.68
0.001 M	16.03	1.68	9.96	0.83	6.58	0.64

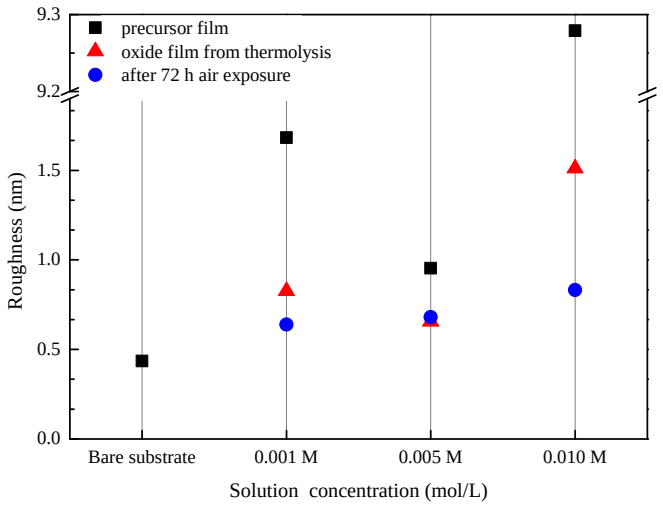


Figure 10.12.: Dependency of the film roughness on the $Nd(NO_3)_3 \times 6H_2O$ butanolic precursor solution, concentration and the step of the process. Shown are the determined roughness values from AFM analysis in tapping mode of samples after deposition (precursor film, black), after decomposition (oxide film from thermolysis, red) and after 72 h of air exposure (blue) on *Si(111)*. Additionally the roughness of the cleaned bare substrate is given for comparison reasons.

From the analysis shown above, it can be seen that for the films deposited from 0.01 M solution, a significantly high roughness of 9.28 nm can be detected for

the precursor film, which decreases after decomposition and the formation of the oxide film from thermolysis down to 1.51 nm. From the image of the oxide film a nucleation center like structure can be observed. This was not depending on different parts of the sample. Thus, it can be determined as a specific sample characteristic. The structure might be interpreted as one of the crystallization centers, which has already been observed from the SEM analysis shown in figure 10.3. After exposure to air, the film structure still shows nucleation spots and the roughness values decrease down to 0.83 nm. From the data it can be seen that obviously a change in the structure takes place after exposure to air and the films generated from the 0.01 M solution are relatively unstable, which was expected due to inhomogeneous film formation caused by the exceedance of the upper limit of the Ostwald Miers region.

Deposition from the 0.005 M solution also leads to a higher roughness for the precursor films, but with a value of 0.95 nm much lower than for the 0.01 M. The roughness value decreases after decomposition to the oxide film to 0.66 nm, showing small spots which disappear after 72 hours of air exposure, leaving a homogeneous flat surface with a similar roughness of 0.68 nm. Comparable results were achieved for the 0.001 M solution concentration where the precursor film shows a roughness of 1.68 nm with decreasing after the decomposition to the oxide film from thermolysis down to 0.83 nm and further to 0.63 nm after 72 h of air exposure. Due to the similar and low roughness values, 0.001 M and 0.005 M solution concentrations can be identified as concentrations within the Ostwald Miers region and can therefore be chosen for further detailed analysis of the film formation in 10.4.

10.3.3. Annealing Influence

For electrical studies, the films have been annealed at different temperatures in order to effect the film structure and roughness with respect to a better electrical performance. In the following paragraph annealing dependent AFM studies are presented on selected samples.

As the 0.005 M precursor solution showed the most stable RMS values, annealing dependent analysis have been performed on the stable 0.005 M solution deposited films. The analyzed films are the oxide after thermolysis, annealed at 873 K and 1073 K in nitrogen flow.

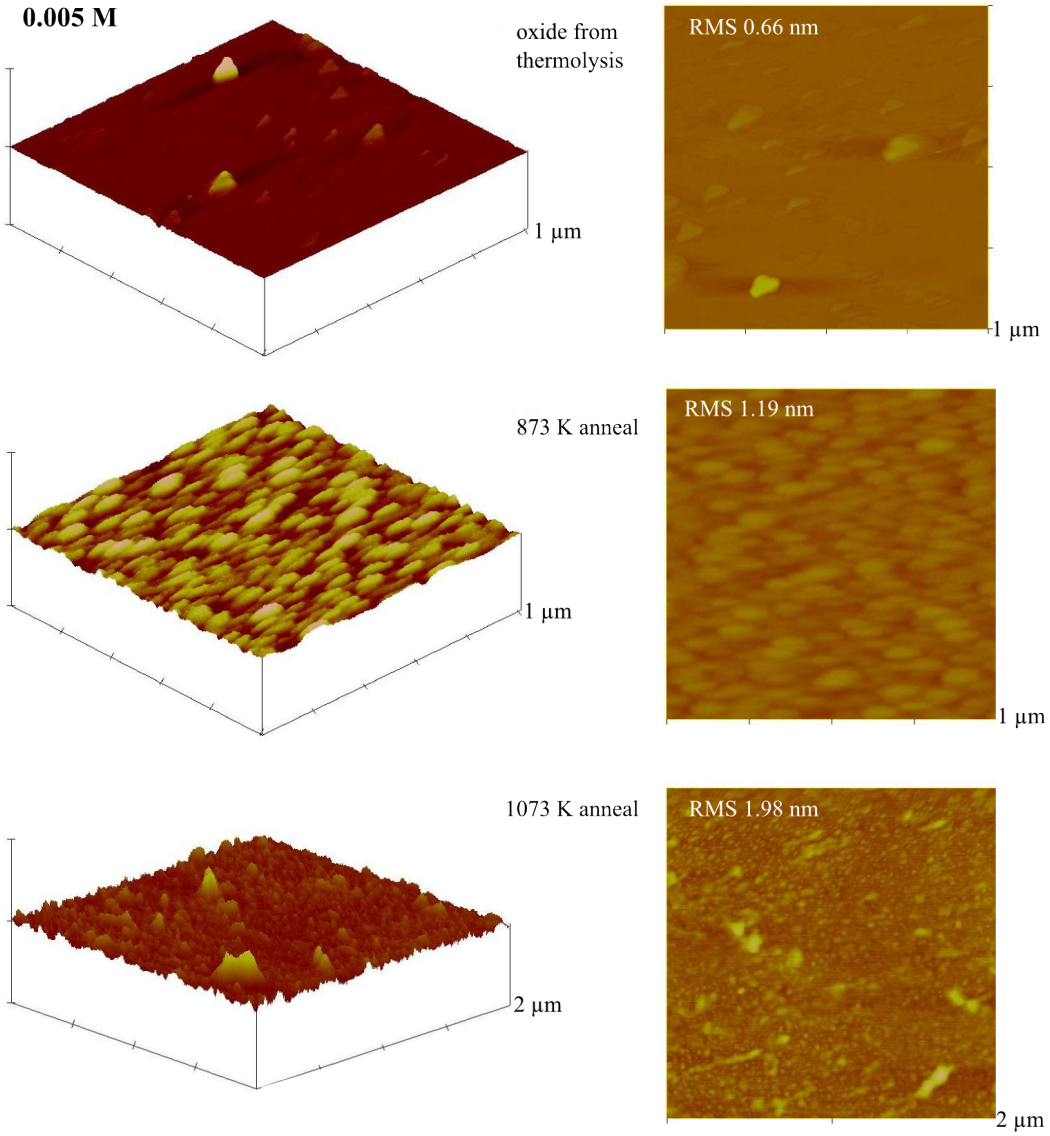


Figure 10.13.: Annealing dependent roughness measured with AFM in tapping mode of films, deposited from 0.005 M butanolic $Nd(NO_3)_3 \times 6H_2O$ precursor solution on *H-Si(111)*.

It can be seen from the images that an increase of the roughness (0.66 nm to 1.19 nm), but also an increase of homogeneity can be detected from the oxide film after thermolysis to the 873 K annealed sample. Annealing at 1073 K leads to a change in structure and a further increase of the roughness up to 1.98 nm. An explanation of the obvious change in the structure indicated by changes roughness values requires further analysis with respect to the precise elementary composition.

10.4. Film Thickness and Structure: HRTEM

In order to determine a precise dependency of the precursor solution concentration on the film thickness within the Ostwald Miers region HRTEM studies of the three characteristic precursor solution concentrations have been done. The HRTEM images are detected with 300 kV acceleration voltage at different magnifications to show the extension of the film as well as a precise detail image of the film structure. Figures 10.14., 10.15. and 10.16. show HRTEM images of the films, deposited from 0.0096 M, 0.005 M and 0.001 M $Nd(NO_3)_3 \times 6H_2O$ butanolic precursor solution on *Si(111)*, each in three different magnifications.

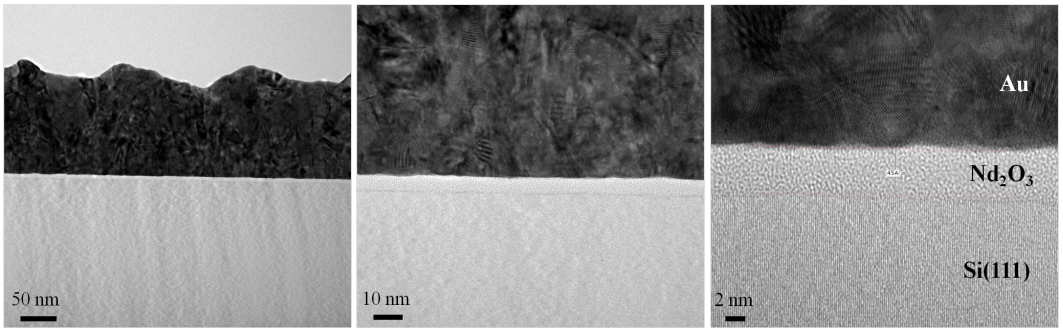


Figure 10.14.: HRTEM images of the oxide film from precursor thermolysis, deposited from 0.0096 M $Nd(NO_3)_3 \times 6H_2O$ butanolic precursor solution on *H-Si(111)*.

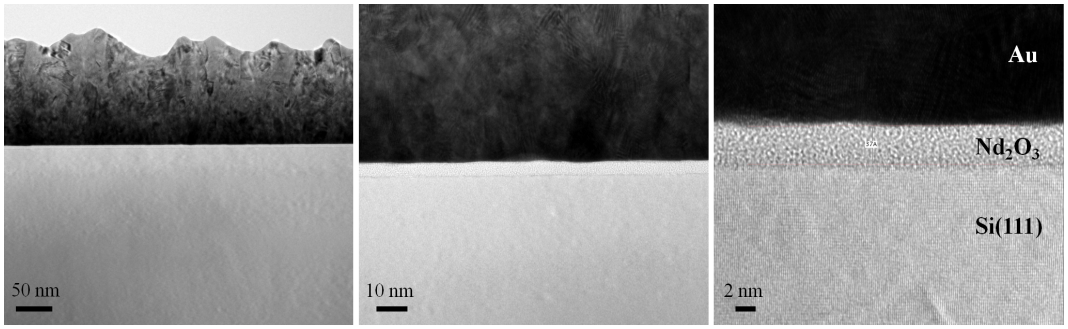


Figure 10.15.: HRTEM images of the oxide film from precursor thermolysis, deposited from 0.005 M $Nd(NO_3)_3 \times 6H_2O$ butanolic precursor solution on *H-Si(111)*.

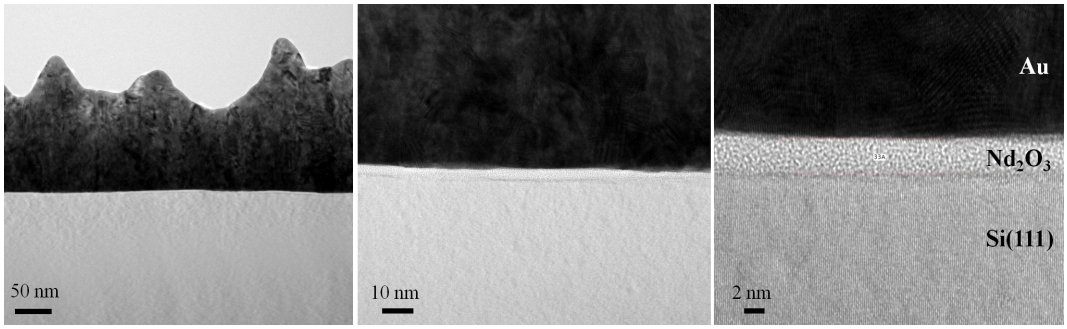


Figure 10.16.: HRTEM images of the oxide film from precursor thermolysis, deposited from 0.001 M $Nd(NO_3)_3 \times 6H_2O$ butanolic precursor solution on *H-Si(111)*.

The samples are coated with a protection layer of sputtered Au to avoid unwanted destruction of the oxide thin film caused by the FIB preparation.

It can be seen from the analysis that all precursor solution concentrations achieve a homogeneous film structure extended over large areas. In larger magnifications, the crystallinity of the Si substrates can be confirmed, but for all films no diffraction patterns can be detected, concluding that the deposited layers are completely amorphous after initial decomposition. The images show the crystalline Si substrate covered with an amorphous layer of the Nd_2O_3.

For a detailed study on the film thickness and the structure, considerably enlarged detail parts of the 2 nm images are shown in figure 10.17.

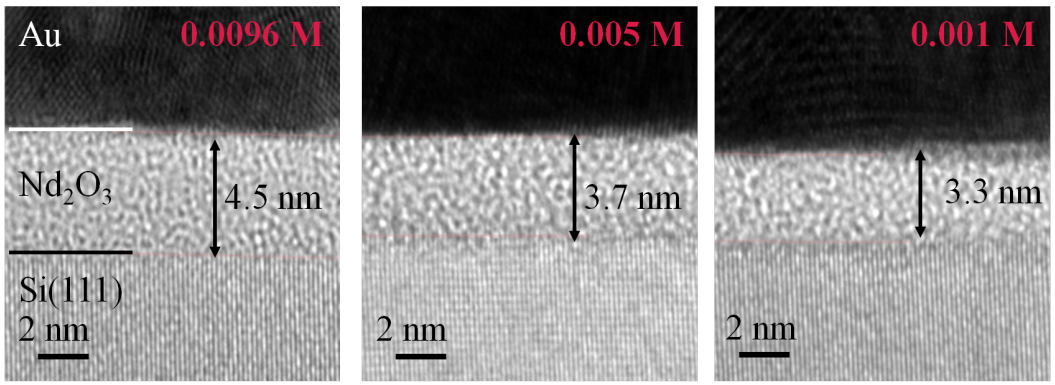


Figure 10.17.: HRTEM images of films deposited from 0.0096 M, 0.005 M and 0.001 M $Nd(NO_3)_3 \times 6H_2O$ butanolic precursor solution.

The enlarged views show in agreement with the previous illustrations that for all solution concentrations no significant interfacial layers are detectable in contact to the Si substrate.

The structure of the thin films are homogeneous. Different concentrations show different film thicknesses reaching from 3.3 nm for the 0.001 M, over 3.7 nm for the 0.005 M to 4.5 nm for the 0.0096 M $Nd(NO_3)_3 \times 6H_2O$ butanolic precursor solution.

Figure 10.18. shows the film thickness plotted versus the solution concentration and a direct fit of the measured data points.

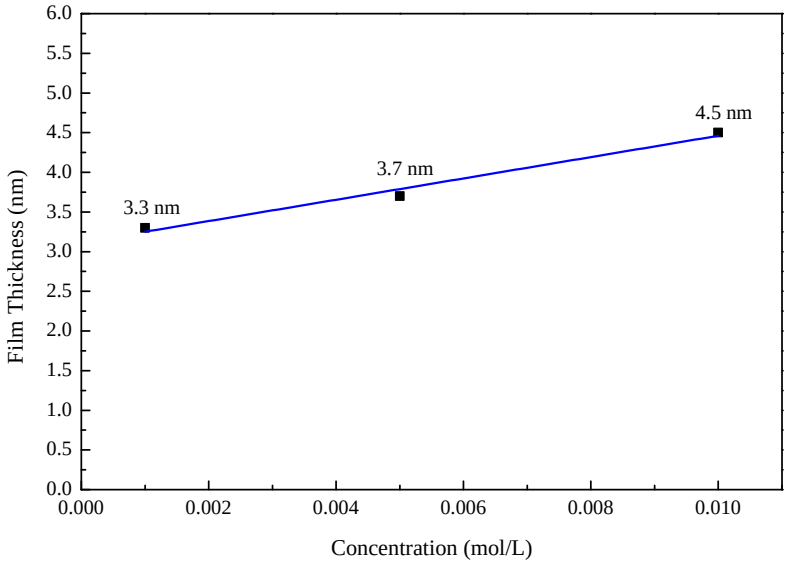


Figure 10.18.: Film thickness plotted vs. the $Nd(NO_3)_3 \times 6H_2O$ butanolic precursor solution concentration.

It can be seen that the detected film thicknesses show linear behavior within the tested concentration region, which does not intersect the y-axis at zero.

10.5. Topography Alternative Substrates

For *SiGe* and *Ge* samples, annealing temperature dependent AFM roughness analyses have been performed for the oxide films after thermolysis and different annealing temperatures. All films have been generated using the 0.005 M concentrated butanolic $Nd(NO_3)_3 \times 6H_2O$ precursor solution, since the lowest roughness values and most stable films were observed with this parameters for films deposited on *H-Si(111)*.

All images of the alternative substrates have been taken using the following settings:

Size:	$1 \times 1\ \mu m$
Angle:	$0°$
Scan rate:	1.96 Hz
Velocity:	$1\ \mu m$/s
Sample/Lines:	512

The scales were set to x = 0.2 μm/div and z = 100 nm/div.

10.5.1. Germanium

AFM images of the Ge substrates are shown in figure 10.19. For the two shown preparations, different sample spots are illustrated, each due to a large variety in the measured roughness.

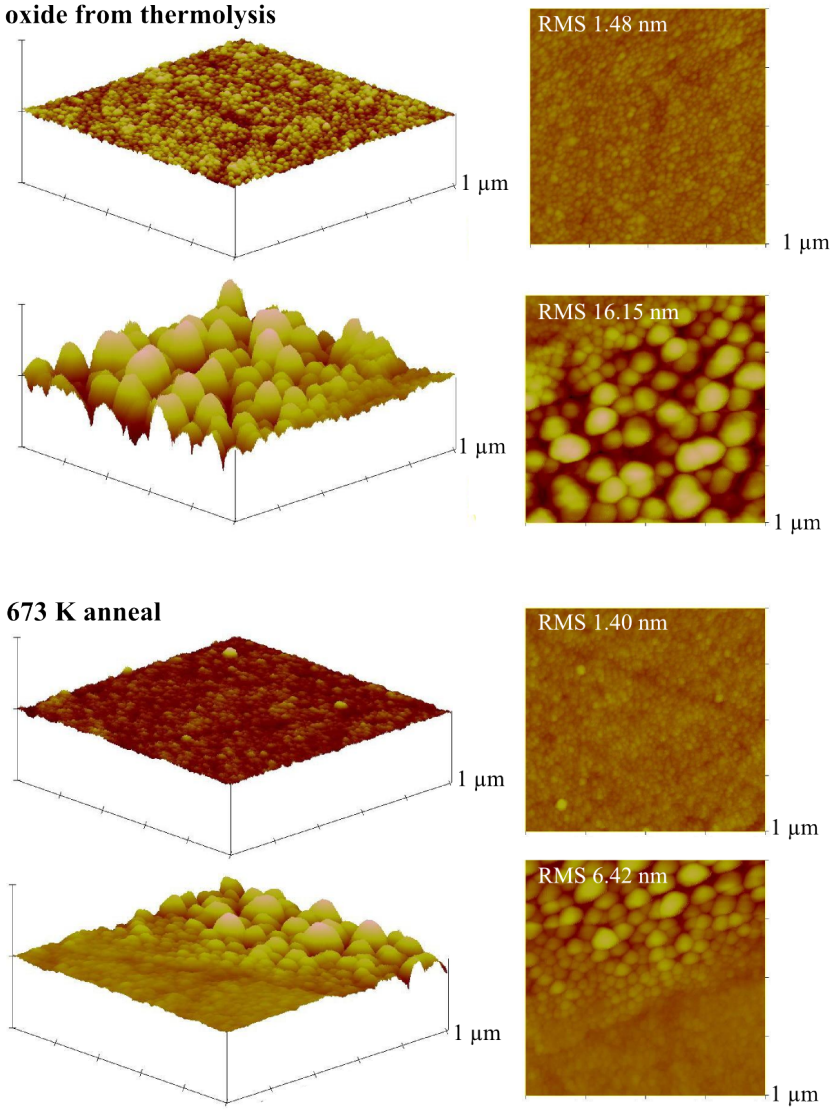


Figure 10.19.: AFM images of the Ge substrates coated with oxide films, deposited from 0.005 M butanolic $Nd(NO_3)_3 \times 6H_2O$ precursor solution. Shown are the topography and RMS for oxide films after thermolysis and annealed at 673 K. Two different sample spots are illustrated each due to a large variety in the roughness (with x = 0.2 μm/div and z = 100 nm/div).

Table 10.3. summarizes the detected RMS values.

Table 10.3.: RMS values of AFM tapping mode measurements and z-ranges in nm for the films deposited on *H-Ge(100)* from 0.005 M butanolic $Nd(NO_3)_3 \times 6H_2O$ precursor solution, of the oxide films from thermolysis, after 873 K and 1073 K anneal.

Sample	**z-range**	**RMS**
therm. oxide	11.415	1.48
	96.76	16.15
673 K	17.88	1.40
1073 K	61.91	6.42

The achieved roughness values differ for the oxide from thermolysis from 1.48 nm, which is relatively low, to 16.15 which is 4 times the expected film thickness. The samples annealed at 673 K exhibit the lowest roughness for the *Ge(100)* substrates with 1.40 nm whereas the RMS values of the films annealed at 1073 K could be detected as 6.42 nm.

10.5.2. Silicon-Germanium

AFM images (tapping mode) of the films, deposited from 0.005 M butanolic $Nd(NO_3)_3 \times 6H_2O$ precursor solution on *SiGe(111)* ,substrates are shown in figure 10.20. The measured RMS values are listed in table 10.4.

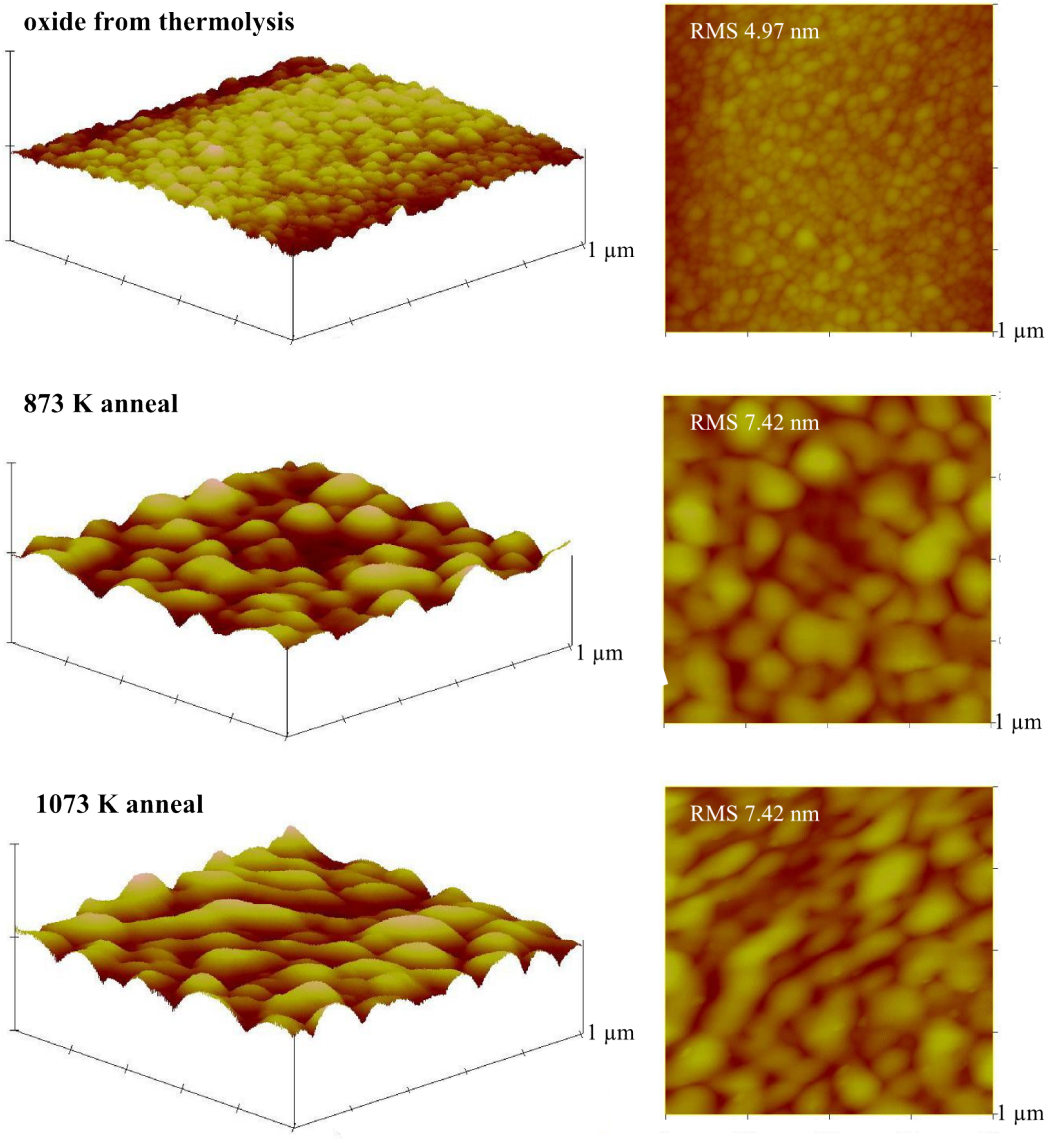


Figure 10.20.: AFM images of the *SiGe(111)* substrates, coated with oxide films, deposited from 0.005 M butanolic $Nd(NO_3)_3 \times 6H_2O$ precursor solution. The illustration shows topography and RMS for oxide films after thermolysis, at 873 K and 1073 K annealed samples.

Table 10.4. summarizes the detected RMS values.

Table 10.4.: RMS values of AFM imaging in tapping mode and z-ranges in nm for the oxide films deposited on *SiGe(111)* from 0.005 M butanolic $Nd(NO_3)_3 \times 6H_2O$ precursor solution after thermolysis, after 873 K and 1073 K anneal.

Sample	**z-range**	**RMS**
therm. oxide	34.06	4.97
873 K	44.89	7.42
1073 K	46.10	7.42

The achieved roughness for the oxide from thermolysis is with 4.97 nm lower than the roughness of the annealed films which show equal values of 7.42 nm.

10.6. Discussion Topography and Film Thickness

Silicon Substrates In the previous chapter, the topography and the structure of the films deposited from *La* and *Nd* based precursors have been determined utilizing SEM and AFM analysis techniques. The film thickness was analyzed from HRTEM imaging.

From the SEM analysis, the critical solution concentration for preferred film formation instead of spontaneous nucleation from solution could be determined with 0.0096 M. Since for 0.01 M, butanolic nitrate-hydrate solutions crystallization centers could be observed in a regular structure, spread over a wide surface area. Higher concentrated solutions, show brittle inhomogeneous salt like structures. Concentrations below the critical limit were not able to be investigated by SEM due to a closed film formation and the resulting insulating properties of the surfaces. Therefore AFM was used to achieve a more detailed view of the surface topography of the formed films.

As the AFM equipment is set up under ambient conditions only *Nd*-based films have been analyzed, since *La* is highly hygroscopic and forms hydroxide species immediately, which makes an analysis of the oxide structure impossible under ambient air. *H-Si(100)* and *H-Si(111)* samples covered with

0.01 M, 0.005 M and 0.001 M solution have been analyzed, regarding the influence of the concentration and underlying substrate on the film roughness. It was shown that rough *H-Si(100)* surfaces lead to rougher film structures than atomically smooth *H-Si(111)* substrates. 0.01 M solutions lead to extremely rough surfaces, which was expected due to the exceedance of the upper Ostwald Miers limit. The lowest roughness was observed for films deposited from 0.001 M solution. Stability studies showed massively rougher films instantly after deposition of the precursor nitrate films compared to the formed oxide films after thermolysis. Decomposition to the oxides lowers the roughness within an order of magnitude. Exposure to air for several days showed significant changes in the structure for the 0.01 M solution, which might be caused by a reoxidation of the inhomogeneously covered surface. Lower concentrated solutions showed an increased or mostly stable roughness value.

The stability studies showed that all precursor films from the deposited nitrate show a significantly higher roughness than the films after decomposition. In agreement with the SEM studies, crystallization centers can be observed for the 0.01 M solution. Films deposited from the 0.005 M and 0.001 M solution show a significantly low roughness down to 0.66 nm and 0.63 nm which is 17 % roughness for the 3.7 nm thin layer (0.005 M) and 19 % for the 3.3 nm thin layer (0.001 M). As for the 0.005 M solution, the roughness values are more or less constant and those film are considered to exhibit the most stable structures. Therefore, 0.005 M precursor solutions were utilized for the film deposition on alternative substrates.

Annealing dependent experiments showed an increase of the film roughness at higher annealing temperatures, which is contrary to conventional deposited films and strengthens the assumption of a completely different deposition mechanism and resulting binding state.

Comparison of the topography of films deposited different substrate types confirms the assumption that the deposition mechanism and film quality is strongly substrate dependent and the structure of the underlying substrate is essential for the roughness of the generated film.

As described in chapter 8. for *H-Si(111)*, atomically smooth structures can be achieved after the wet chemical etching, as the <111> lattice plane acts as an etching stop within the alkaline NH_4F etching solution. This advantage is not the case for *Si(100)*, which can be related to the detected increased roughness.

In the present chapter, results of the films deposited from *La*-based precursors on *H-Si(111)* have been presented shortly, showing a RMS of 0.736 nm during STM analysis in UHV. The basics on the topography on *La*-based films have been discussed previously in[137]. The detected roughness values for the *La* based films are within the same range as the shown results on *Nd* which indicates, that a similar deposition mechanism leads to the film formation for *La* and *Nd* precursors.

From HRTEM imaging, it has been shown that all deposited films show amorphous structures, opening the possibilities for film structure tuning by different annealing processes, since amorphous initial structures can be transformed into different types of crystal lattices, depending on the precise annealing conditions.

It was found that all films are amorphous after the initial decomposition of the precursors, no direct explanation of the film formation can be given by the common known crystallization mechanisms. But as the crystallization behavior is basically dependent on the interaction forces between the overlying molecules and the underlying substrates as well as inter molecular interactions are also responsible for molecule agglomeration within solutions, the film formation can be explained as a salt like deposition as reported for *NaCl*.[204]

A similar argument based on this theory can be given to explain the different dominating trends in film thicknesses. Apparently, the deposition mechanism changes if the concentration exceeds or falls below the Ostwald Miers limits (s. chapter 4.). For the case that the concentration falls into the region of stable under saturation and at a certain point the number of precursor molecules falls below a possible full coverage of the surface, by at least a mono layer, the interaction between the precursor molecules itself is dominated or superimposed by the interaction between precursor and solvent molecules or the solvent molecules itself. Therefore, an island formation without a full coverage of the substrate is expected, which leads to a deviation from the linear dependency.

For high concentrated solutions, the upper limit of the Ostwald Miers region is essential and spontaneous nucleation is preferred relatively to a possible film formation, which was determined to be the case for precursor solution concentrations ≥ 0.01 M for the present system. By exceeding the maximum concentration within the Ostwald Miers region, a homogeneous film formation

is suppressed by the spontaneous formation of crystallization centers from the solution, thus the dependency of film thickness and concentration should also be different. Extended and homogeneous films can be achieved below 0.0096 M precursor solution concentration, showing linear dependent film thicknesses reaching from 3.3 nm to 4.5 nm. The lowest tested concentration (0.001 M) was approx. one order of magnitude lower than the upper limit, still showing homogeneous film formation in linear dependency to the higher concentrated solutions. This indicates that the lower limit of under saturation has not been achieved with this concentration and it should be possible to generate even lower thicknesses by using lower concentrated solutions, which needs to be in the focus of future analysis.

It has been shown that the limits of the deposition technique are given by the concentration dependent structure formation. The upper limit for stable linear dependent, closed film formation could be determined as 0.0096 M solution concentration and for 0.001 M concentrated solutions homogeneous films can still be achieved for *Nd*-nitrate-hydrate butanolic solutions.

The discussed results are illustrated in figure 10.21.

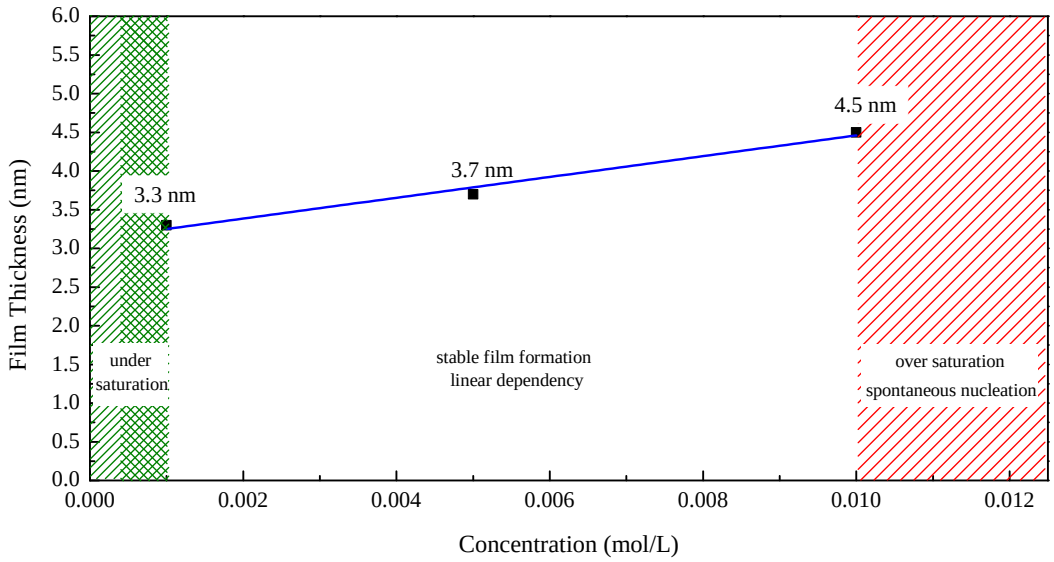


Figure 10.21.: Concentration dependent mechanistic regions for preferred film formation (white), spontaneous nucleation (red) and transition from stable film formation to under saturation, which is not determined precisely and therefore shown in crossed lines.

To evaluate the proposed dependency of solution concentration especially in the region of lower concentrations (green) and film thickness more data points are required in future experiments.

According to the detected HRTEM images, for all systems no significant interfacial layer formation can be detected, concluding that with the wet chemical deposition technique, high quality interfaces can be generated, which needs to be confirmed by XPS elementary analysis in chapter 11. Additionally, no domain boundaries are detected, indicating that a mono phase structure has been deposited. Sharp interfaces to the silicon substrates, which show a single phase, indicate, that no implementation of the oxides or silicides occurs during the oxide formation, which is one of the major issues for conventional MBE deposition.

In general, it has been shown with a high reproducibility that by the precursor solution concentration, a defined thickness control of the deposited material is enabled.

Different annealing temperatures influence the roughness of the films. For all analyzed films, an increased roughness could be detected after annealing, which is unusual and contrary to films which have been deposited with conventional deposition techniques.

A coherent view of the topographical and film thickness determinations opens the possibility to assess the obtained RMS values with respect to the film thickness and therefore to evaluate the actual quality of the films.

Table 10.5. summarizes the percentage roughness values of the oxide films after thermolysis of the precursors for the different solution concentrations.

Table 10.5.: Percentage of the measured roughness values of the oxide films on *Si(111)*, related to the respective film thickness.

Conc.	**RMS**	**Thickness**	**%**
0.01 M	1.51 nm	4.5 nm	33.6
0.005 M	0.66 nm	3.7 nm	17.8
0.001 M	0.83 nm	3.3 nm	25.2

Under the assumption, that the film thickness on *Si(100)* equals the thickness on *Si(111)* the roughness in percentages can be calculated as summarized in table 10.6.

Table 10.6.: Percentage of the measured roughness values of the oxide films on *Si(100)*, related to the respective film thickness.

Conc.	**RMS**	**Thickness**	**%**
0.01 M	18.72 nm	4.5 nm	416.0
0.005 M	4.08 nm	3.7 nm	110.3
0.001 M	5.09 nm	3.3 nm	154.2

For *Si(111)* substrates, the roughness values are within the range of min. 17.8 %, whereas *Si(100)* exhibits film roughnesses larger than the film thickness itself. This might be related to the initially conducted wet chemical cleaning procedure. *Si(111)* leads to atomically smooth step like structures due to the etching stop at the <111> lattice plane, which is not the case for *Si(100)* substrates. Thereby the highly ordered and homogeneously spread edges may serve as centers for the nucleation. This probably results in a better distribution of the nucleation centers and therefore in less rough structures.

From ALD, PLD or e-gun evaporation induced deposition, film roughnesses of REO on *Si* are reported in the literature. Spiga et al. discussed Yb_2O_3 and Lu_2O_3 films deposited by ALD using different organic precursor materials at 630 K, exhibiting a film thickness of 3-30 nm and a reported roughness of 0.3 nm in agreement with Myllymäki et al., who reported the same value for $GdScO_3$ (5-20 nm). $GdScO_3$ deposited from PLD and e-gun evaporation showed a minimal roughness value of 0.1 nm.[205] [206] Compared to the literature the films are relatively rough, as the lowest roughness in percentage is given by 10 % from the literature. But as the annealing conditions have been chosen in initial state and high influences on a decrease of the film roughness are expected by tuning the annealing conditions, this is one of the most promising future issues in order to achieve lower roughness values for the wet chemical deposition of ultra thin films.

Discussion Alternative Substrates According to the data concluded in table 10.3., the *Ge* samples do not show a homogeneous roughness which can be detected at different sample spots, therefore in figure 10.3. for two specific samples types, two roughness values which have been detected at one sample at different positions are given each. The trend which has been observed for

Si and *SiGe* that for higher annealing temperatures, higher roughness values are achieved can not be validated for the *Ge* substrates.

It can be seen that for the oxide films from thermolysis, RMS values of 1.48 nm as well as 16.15 nm are detected, showing a highly inhomogeneous structure which might be related to an unstable hydrogen termination after the *HF* cleaning or the already in chapter 8. mentioned remaining carbon impurities, which are a major issue during *Ge* cleaning. Undefined interfaces between the coating layer and the substrate could effect the final roughness of the film by an initial restructuring of the surface prior to film formation. As well during the precursor decomposition germanium oxides could be formed due to an easy reoxidation tendency of *Ge*.

Films deposited on *SiGe* surfaces from the 0.005 M solution show significant higher roughness values than the films which have been analyzed on pure *Si* substrates. Values from 4.97 nm to 7.42 nm could be measured from the oxide films after thermolysis, 873 K and 1073 K annealed samples, as shown in figure 10.20. and concluded in table 10.4. The annealed samples show a higher roughness as it was observed for the silicon samples, but no increasing trend can be observed related to the specific annealing temperature.

As both substrate types have not been in the major focus of research within the last decades, hardly any comparison data are available from literature for comparison.

Compared to the *Si* substrates, *SiGe* and *Ge* showed much higher roughness values. This is likely to be caused by a more critical cleaning procedure, which is not as effective as for the *Si* and initially rougher surfaces resulting from remaining impurities lead to a more inhomogeneous film formation. But from the topography analysis of the alternative substrates its was possible to show that a film formation is possible by the wet chemical inorganic dip-coating with improvement potential in different experimental steps. Furthermore, detailed analysis of the film thickness and structure are required in the future, as well as basic research on the substrate cleaning procedures.

The findings of the present chapter have been pioneering for the success of the invented thin film deposition technique, as it could be shown that extended homogeneous film formation is possible by tuning the solution concentration as expected from literature known mechanisms for crystallization from solutions, as introduced in chapter 4. Within the Ostwald Miers region, the film

thickness shows a linear dependency on the precursor solution concentration. Highly ordered substrates lead to ordered, homogeneous overlaying structures, whereas unordered substrates complement the formation of disordered films.

At this point, elementary analyses are essential to investigate the chemical constitution of the adsorbed precursor molecules and the resulting interface and surface structure and composition. Additionally, a deeper insight into the deposition mechanism and the explanation of changing roughness are required. Thus, in chapter 11. XPS analyses will be shown.

11. Elementary Thin Film Analysis: XPS

In order to achieve a detailed understanding of the interface and oxide layer formation, XPS analyses were performed under UHV conditions at room temperature. In the following sections, the different substrate types should be elucidated separately for the different single layer systems.

As for the powder measurements, for all peak fits a Shirley type background has been applied for background correction. Calibration of the energy scale was done assuming the *C1s* signals arising from adventitious carbon or surface contamination to be 284.6 eV as reference.

La-based films have only been analyzed on *H*-terminated *Si(111)* substrates due to their high hygroscopicity, whereas results for *Nd*-based films should be elucidated, presenting results on hydrogen terminated *Si(111)*, *Si(100)*, *SiGe(111)* and *Ge(100)*. For all films 0.005 M butanolic solution has been used fro XPS analyses, as the films are, according to the topography and stability analysis, most stable

For all samples, survey spectra will be shown. Detailed spectra of the significant core level signals are analyzed, fitted and discussed. The measurement parameters are listed under section 6.5. in table 6.1. Reasonable characteristic core level signals, which are considered to be discussed in detail are the *O1s*, *C1s*, $Si2p_{1/2,3/2}$, $Ge3d_{3/2,5/2}$, $La3d_{3/2,5/2}$ and $Nd3d_{3/2,5/2}$ peaks. Both excitation energies, Mg-K_α and Al-K_α, have been applied. For a detailed discussion of the results, the spectra have to be measured with the respective appropriate excitation source, as overlaps of core level and Auger signals need to be avoided for a precise analysis.

According to[201], the overlap of the *Nd3d* and *OKLL* signals during excitation with Al-K_α and *O1s* and *NdMNN* peaks while utilizing Mg-K_α are particularly critical. Therefore, on pure *Si* substrates, the *Nd3d* signals will be discussed, considering data measured with Mg-K_α, whereas the *O1s* signals will be discussed based on the measurements with Al-K_α as excitation source, as otherwise an overlap of the core level signal with the Auger peaks leads to

a possible misinterpretation of the peak structure. For *SiGe* substrates, the *Si2p* signal shows an overlap with the *Ge* Auger signals while utilizing Mg-K_α. Therefore, the *Si2p* spectra are shown measured with Al-K_α. On *Ge* and *SiGe* substrates, the *O1s* signal will be discussed based on measurements with Mg-K_α, as an overlap with the *NdMNN* Auger signals is considered to be preferred vs. a possible much more complex mixing with the *Ge* Auger structures.

Due to the complexity of the substrate-film systems, additionally to a given resolution of the measurement equipment, the *La3d* and *Nd3d* signals will be shown as raw data sets and no peak fits will be applied. The required information for a respective asymmetric Doniach-Sunjic peak fit, leads, with the given resolution and the number of fixed parameters, which are required to assess the desired information, to a lack of a possible output of information. Therefore, only trends in main peak positions, peak width and intensities shall be highlighted and discussed. A precise analysis of the peak structures requires HR XPS techniques or at least monochromatic excitation sources. However, it should be preliminary noted that the interaction of oxygen on *Si* surfaces has been one of the most intensively studied gas solid reaction systems in literature. Therefore, a large variety of comparison data for the *O1s* and the *Si2p* signals is available, which differs according to experimental conditions and respective data processing. Hence, it is of crucial importance to find reliable literature reports which have to be considered critically.

11.1. *La*-based Films on *Si(111)*

The survey spectrum multiplot in figure 11.1. shows the spectra detected from the *Si(111)* substrate with native oxide, *H*-terminated *Si(111)* as well as for the *La*-based nitrate precursor films and oxide film from thermolysis.

The spectra are normalized to the highest detected signal within each spectrum in order to illustrate the respective detected signal types. All spectra are measured with Mg-K_α.

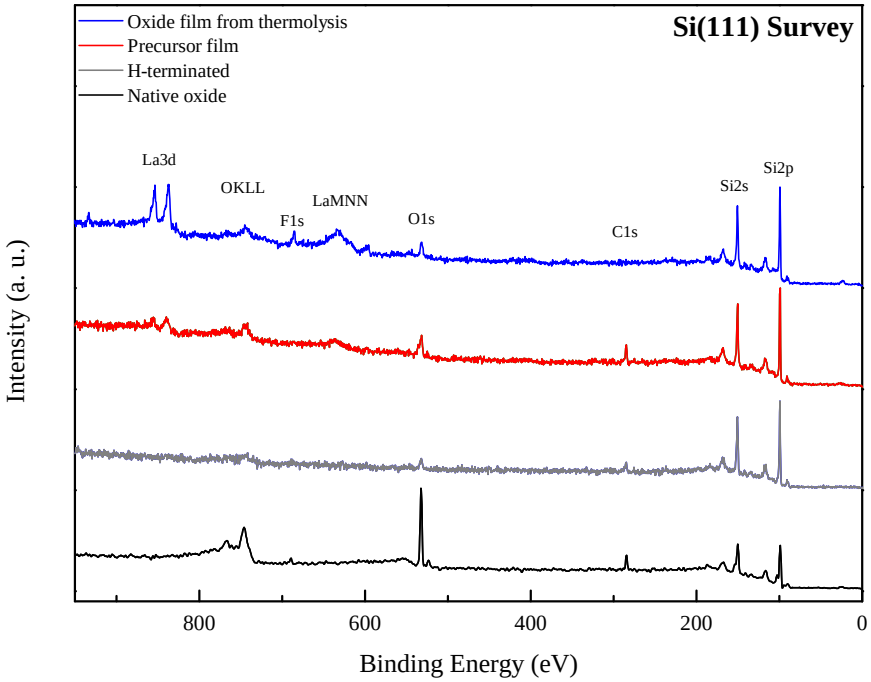


Figure 11.1.: Survey spectra measured with Mg-K_α of the native oxidized surface, the *H*-terminated samples, *La*-based precursor film and oxide film from thermolysis deposited from 0.005 M butanolic $La(NO_3)_3 \times 6H_2O$ precursor solution on *Si(111)*.

The illustrated spectra show all significant expected signals resulting from the *Si* substrates (*Si2p* and *Si2s*), oxygen (*O1s* and *OKLL*) as well as carbon (*C1s*) for the unheated samples. Due to different surface oxygen species and amounts, the intensity of the *O1s* peak varies substantially from sample to sample. The deposited films exhibit characteristic peaks of *La* (*La3d* and *LaMNN*). Remarkable is the significantly lower intensity of the *La* signals of the precursor films compared to the oxide films from thermolysis, which will be discussed in section 11.1.3. The detected *F1s* signal results from remaining chamber impurities which could be observed sample independently after heating procedures above 773 K and might be explained by an evaporation of parts of Teflon® containing gaskets during bake out procedures (compare internal standard survey spectra of the UHV chamber in appendix E). As the *F1s* signal can not be observed after the *HF* treatment, *F* contaminations caused by the cleaning procedure can be ruled out.

11.1.1. The *Si2p* and *O1s* Signal

The observed data of the *Si2p* and *O1s* signals detected from the surface as well as after the film deposition and decomposition are shown in figure 11.2.

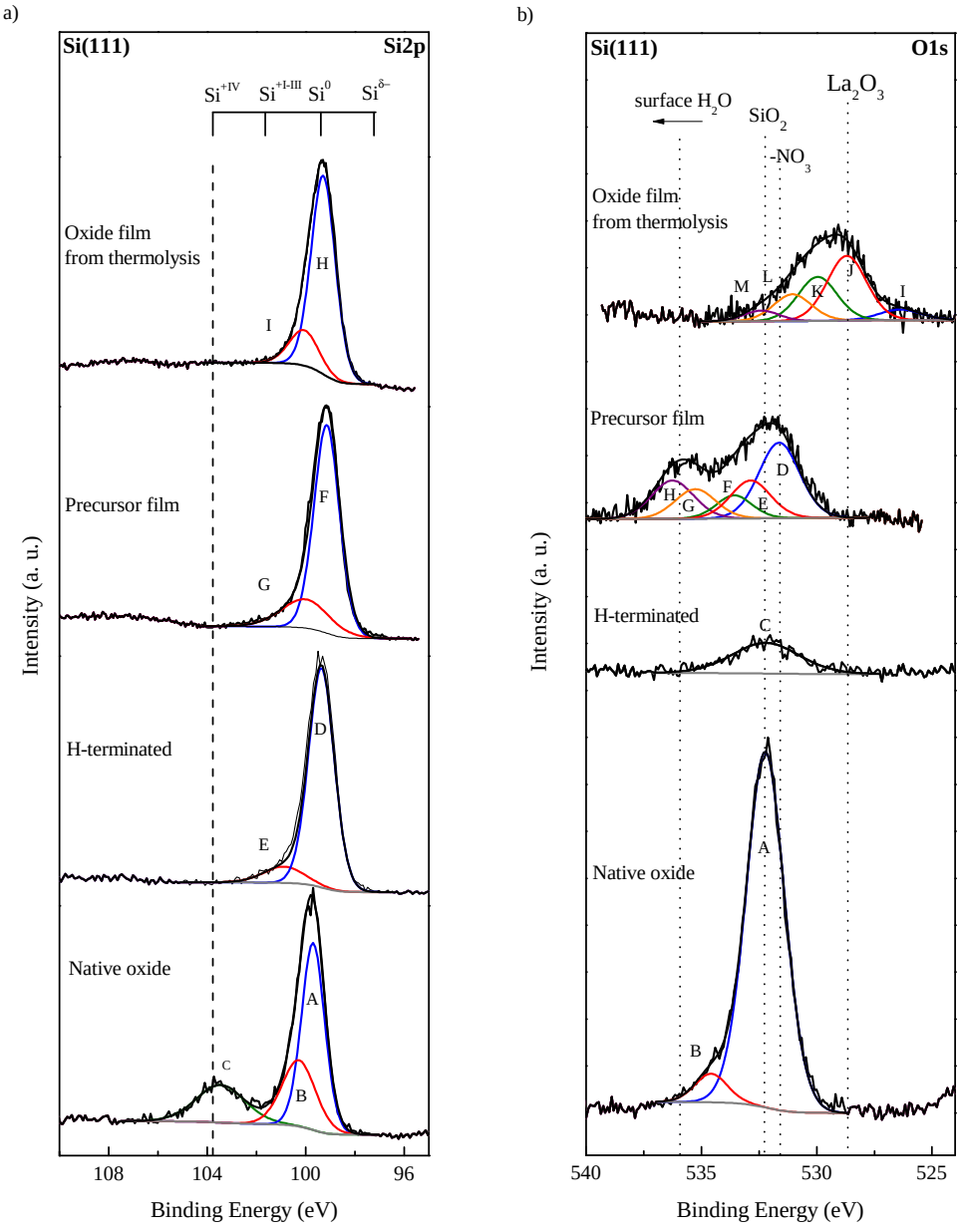


Figure 11.2.: *Si2p* (left) and *O1s* (right) spectra measured with Mg-K_α of the native oxidized the *H*-terminated samples, *La*-based precursor film and oxide film from thermolysis deposited from 0.005 M butanolic $La(NO_3)_3 \times 6H_2O$ precursor solution on *H-Si(111)*.

The respective peak positions, fit parameters and comparable literature data are summarized in table 11.1. ($Si2p$) and 11.2. ($O1s$) and discussed subsequently.

The *Si2p* signals are normalized to the highest peak within each spectra, whereas the *O1s* signal has been normalized to the maximum intensity of the signal resulting from the native oxidized sample in order to illustrate the significant changes in the intensity caused by the present oxygen species on the surface. This was possible, since a precise control and an exact matching of the measurement settings, lead to an equal background intensity, detected for all investigated samples.

Table 11.1.: Peak fit parameters and peak positions in eV for the *Si2p* signal of the native oxidized, *H*-terminated as well as *La*-based precursor films and oxide films from thermolysis deposited from 0.005 M butanolic $La(NO_3)_3 \times 6H_2O$ precursor solution on the *Si(111)* substrates.

Comp.	Pos.	FWHM	Area %	GL	Literature[207]
Native Oxide			Region: 107.6 - 97.0 eV		
A	99.7	1.1	51.5	80/20	99.2 Si^0
B	100.3	1.6	26.6	80/20	100.2 Si^{+I}
C	103.5	2.3	21.9	80/20	103.5 Si^{+IV}
H-Terminated			Region: 105.2 - 96.4 eV		
D	99.4	1.2	89.6	80/20	Si^0
E	100.9	1.9	10.4	80/20	100.6 Si^{+II}
Precursor Film			Region: 104.3 - 95.8 eV		
F	99.2	1.2	79.7	80/20	Si^0
G	100.0	2.2	20.3	80/20	Si^{+I}
Oxide Film from Thermolysis			Region: 104.2 - 97.2 eV		
H	99.3	1.2	82.1	80/20	Si^0
I	100.1	1.4	17.9	80/20	Si^{+I}

Table 11.2.: Peak fit parameters and peak positions in eV for the *O1s* signal of the native oxidized, *H*-terminated as well as *La*-based precursor films and oxide films from thermolysis deposited from 0.005 M butanolic $La(NO_3)_3 \times 6H_2O$ precursor solution on the *Si(111)* substrates.

Comp.	Pos.	FWHM	Area %	GL	Literature
Native Oxide				Region: 537.0 - 528.7 eV	
A	532.2	2.0	97.7	80/20	532.5 SiO_2/suboxides [208]
B	534.6	1.7	2.3	80/20	534.6 SiO_2/H_2O [209], ice on Re [210]
H-Terminated				Region: 537.1 - 527.2 eV	
C	532.2	3.4	100.0	80/20	SiO_2/suboxides [208]
Precursor Film				Region: 540.5 - 527.7 eV	
D	531.6	2.1	37.3	80/20	530.9/531.6 surface -OH [201] [211]
E	532.9	2.1	18.5	80/20	532.7 $Ba(NO_3)$ [199]
F	533.6	1.8	10.5	80/20	533.3 crystal H_2O [198]
G	535.3	2.1	14.6	80/20	loosely bound H_2O [210] [212]
H	536.3	2.2	19.6	80/20	loosely bound H_2O [210] [212]
Oxide Film from Thermolysis				Region: 535.0 - 524.1 eV	
I	526.4	2.17	7.4	80/20	-
J	528.7	2.01	41.7	80/20	528.6 La_2O_3 [201]
K	530.0	2.0	28.0	80/20	-
L	531.1	1.9	16.7	80/20	531.3 Fe or $Cr(OH_3)$ [192] [200]
M	532.4	1.8	6.2	80/20	532.2 SiO_2/suboxides [208]

The *Si2p* signals show a characteristic peak structure. With the given detector resolution, the $Si2p_{1/2}$ and $Si2p_{3/2}$ can not be separated. The second signal, fitted into the main peak, is not referred to the *2p* spin orbit splitting but to *Si* in different oxidation states. The native oxidized sample exhibits additionally a signal shifted to higher binding energies (signal C in figure 11.2.a) at 103.5 eV. Signals of the *H*-terminated, precursor film and oxide film from thermolysis show similar peak structures with the main signals positioned at the same binding energy within the spectrum.

According to Himpsel et al.[207], the different oxidation states of Si could be detected at 103.5 eV (Si^{+IV}), 101.9 eV (Si^{+III}), 101.0 eV (Si^{+II}) and 100.2 eV (Si^{+I}), whereas the Si-Si bonding and (Si^0) could be detected at 99.2 eV. The change in binding energies is based on an occurring charge transfer, caused by a change in the valence band population due to the bonding to oxygen. As oxygen is more electro negative than Si (EN = 3.5 vs. 1.8), the valence charge of Si moves to the O and an effectively higher binding energy for the Si in higher oxidation states can be detected, due to a higher repulsive force acting on every single electron.[213]

Surface Cleaning The success of the *HF* cleaning procedure can be proven by the shown signal of the H-terminated surface, since after the *HF* treatment the signal at $\approx$ 103.5 eV, resulting from Si^{+IV} (in SiO_2), is no longer observable. In agreement with STM and XPS data presented in relation to the present work in[136], the generated H-terminated Si surfaces can be considered to be SiO_2 free. The shoulder at approx. 100.2 eV (signal E, G and I in figure 11.2.a) indicates the existence of residual suboxides, which is unavoidable with the wet chemical cleaning procedure.

This can be confirmed by the measured $O1s$ peaks, as the native oxidized sample shows a signal characteristic for $O1s$ in SiO_x at 532.2 eV (signal A in figure 11.2.b). A drastically reduced peak intensity for the *HF* treated H-terminated sample at exactly the same peak position can be analyzed. The *O1s* signal of the H-terminated surface (signal C in figure 11.2.b) shows a significant peak broadening (FWHM 3.4 eV) compared to the average FWHM of 2.1 eV, but due to the expected low intensity of the signal caused by a low amount of remaining surface oxygen it was dissuaded from a more detailed peak fit. The peak broadening indicates the presence of several different oxygen species merged in one detected signal. Anyway, as reported in the literature[213] [214], the *O1s* peak position is dependent on the surface coverage and shifts to higher binding energies can be detected with increasing oxide coverage. Thus, the detected peak broadening can be explained by the existence of a certain amount of suboxides at the surface. Engstrom et al. showed shifts of 0.6 eV to higher binding for films from two monolayers up to 13.6 monolayers, which is in agreement with the findings of Namiki et al.[213], who demonstrated a shift of 0.8 eV for an oxide thickness increase from 0 to 12 Å. Whereby, for the *Si2p* signal for thin oxide layers, a mean shift to higher binding energies appears with

increasing coverage up to ten monolayers, approaching the expected values for ultra thin SiO_2 layers and the final oxidation state +IV.[213]

As from the *Si2p* signal it has been shown that suboxide species could be detected clearly, the findings of the *O1s* signal show a complete agreement. The detected data are consistent to findings from literature as discussed.It can be concluded that the *HF* cleaning procedure leads to a Si^{+IV} free surface. Detected *O1s* signals of the cleaned surfaces can be assigned to monolayers of suboxide species.

Lanthanum Deposition The analyzed precursor films exhibit the same *Si2p* structure as detected for the dioxide free surfaces, indicating that the wet chemical film deposition does not influence the underlying substrate. No re-oxidation or silicide formation can be detected according to the *Si2p* signal. An identical result can be observed for the oxide films directly after the decomposition. Only a small increase of the intensity of the suboxide shoulder can be observed, which indicates a slightly higher amount of suboxide surface species. The respective precursor and oxide species can be identified from the detected *O1s* signal.

After the peak fitting, five characteristic signals can be determined for the precursor film. Signals E (532.9 eV) and F (533.6 eV) in figure 11.2.b can clearly be identified to result from oxygen in nitrates (E)[199] and crystal water (F)[215]. With an area ratio of NO_3:H_2O as 1.7 :1, the expected ratio of 1.5 from the theory can not be confirmed. Contrary to the presented results of the *La*-nitrate-hexahydrate powder (s. section 9.2.) which showed a ration of 1:1, in the case of deposited films of the nitrate, obviously a lower amount of crystal water molecules is present after the deposition. This might also explain the high intensity and large area ratio of 37.3 % of signal D in figure 11.2.b) detected at 531.7 eV, which is related to surface -*OH* groups. A possible mechanistic explanation is the segregation of the water molecules to the upper surface, forming a high amount of surface species. This is in agreement with detected shifts to higher binding energies (signals G and H in figure 11.2.b), which show notably increased, atypical high binding energies for oxygen species. They are likely caused by water species, which are not strongly adsorbed or bound to the surface and might be explained as a surface covering ultra thin water layer.[210] [212]

After decomposition to the oxide film, also five signals can be analyzed. The main signal detected at 528.7 eV (signal J in figure 11.2.b) can be assigned to *O1s* in La_2O_3[201] and was confirmed by the powder spectra analysis (signal T in figure 9.10.), showing that the decomposition to the wanted oxide was successful. The signal at 531.1 eV (signal L in 11.2.b) results from hydroxide species formed at the surface due to the high hygroscopicity of the La_2O_3 as it was also discussed for the powders (signals U (531.7 eV) and S (531.5 eV) in figure 9.10 in agreement with literature.[192] [200]. The signal detected at 532.4 eV (signal M in figure 11.2.b) results from the increased amount of sub-oxide species resulting from the *Si* substrate.[208]

However, the origin of signal I in figure 11.2.b at significantly low binding energies is unknown at this point.

11.1.2. Carbon Content: The *C1s* signal

As for the following analyses, the *C1s* signal is required as a measurement standard within the spectra for calibration issues and is usually present within the spectra from remaining adventitious carbon special long term bake out procedures have been required, to investigate the carbon content of the films, which might result from organic solvents enclosed in the film during the drying and decomposition process, without interference.

Prior to the presented *C1s* analysis, the UHV chamber was baked out for ten days at an average temperature of approx. 400 K (dependent on the specific part and the temperature limits of the respective UHV components), until the residual gas pressure decreased to a minimum of 1×10^{-10} mbar and XPS analysis of internal *Cu* standards showed no indication of any *C1s* detection.

Figure 11.3. shows the *C1s* signal of the precursor film and the oxide film from thermolysis deposited from 0.005 M butanolic $La(NO_3)_3 \times 6H_2O$ precursor solution.

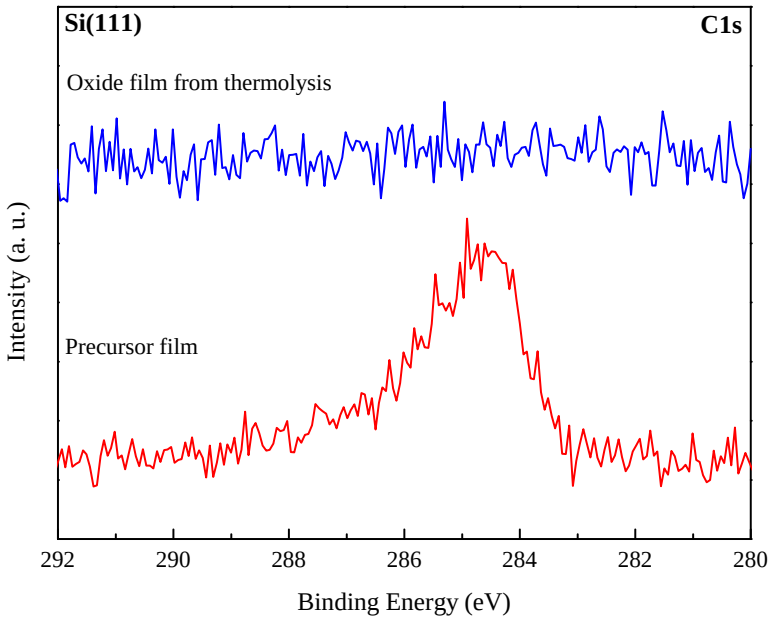


Figure 11.3.: *C1s* signal of the *La*-based precursor films and oxide films from thermolysis deposited from 0.005 M butanolic $La(NO_3)_3 \times 6H_2O$ precursor solution on *Si(111)* measured with Mg-K_α.

From the shown spectra it can be seen that for the precursor films, as expected, a characteristic *C1s* peak can be detected, resulting from adsorbed surface species and remaining solvent caused by the dip-coating process. After decomposition, no *C1s* signal can be observed and within the detection limit of the measurements and it can be concluded that the formed films are remaining carbon free on the substrates after the decomposition process.

11.1.3. The *La3d* Signal

Figure 11.4. shows the *La3d* signal detected from the precursor and the oxide film from thermolysis deposited on *Si(111)*. Both signals are normalized to the main intensity, observed from the oxide film from thermolysis.

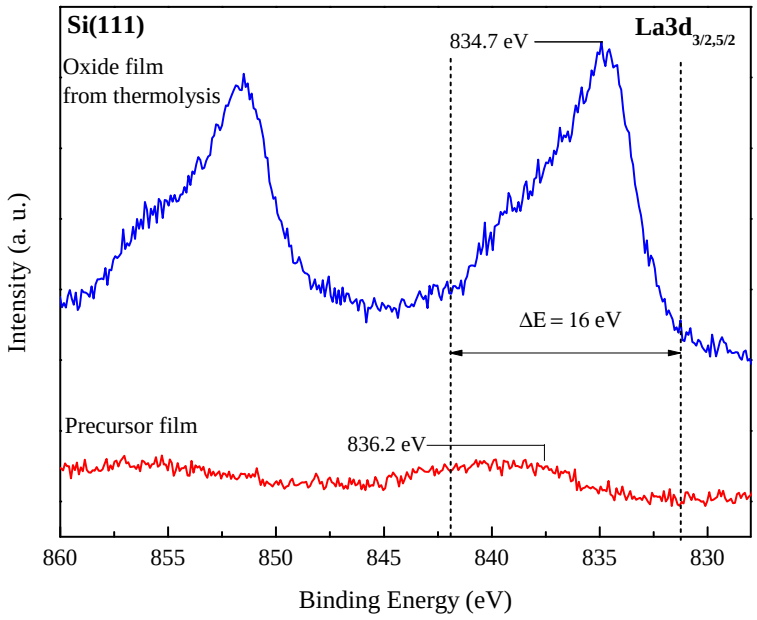


Figure 11.4.: *La3d* signal of the precursor film and the oxide film from thermolysis deposited from 0.005 M butanolic $La(NO_3)_3 \times 6H_2O$ precursor solution on *Si(111)* measured with Mg-K_α. Marked are the peak maxima and the peak width.

From the spectra, it is obvious that the precursor film shows a drastically decreased signal intensity compared to the oxide film from thermolysis, which can be explained by the surface carbon amount. It has been shown in section 11.1.2. that the precursor film exhibits, as expected, a defined *C1s* signal, which disappears after the heat treatment for precursor deposition. The carbon species on the surface lead to a shielding of the underlying substrate, resulting in lower signal intensities. The effect is much more significant for signals detected at higher binding energies (lower kinetic energies), as the depth of information increases with increasing kinetic energies. Therefore, the shielding effect can significantly be observed for the *La* peaks, whereas almost no changes in the signal intensity can be observed for the *Si2p* signals at low binding (high kinetic) energies (s. figure 11.1.).

After the precursor decomposition (induced by a heat treatment), the remaining carbon from the solvent as well as adsorbed adventitious carbon molecules can be desorbed, which leads to a much higher signal intensity of the *La3d* signal after the decomposition. The intensity ratio is dependent on the dwell

duration and therefore desorption time period within the UHV chamber, the remaining amount of solvent as well as the purity of the chamber itself.

Another observable aspect, especially in the signal structure detected from the oxide film from thermolysis, is a change in the peak/satellite intensity ratio compared to the powders which have been described in section 9.2. A precise analysis of the data of the precursor film is not possible due to the low signal intensity in combination with a poor S/N ratio.

The measured spectra of the oxide film from thermolysis show a significantly reduced signal intensity at higher binding energies, whereas the powders exhibited just a slight reduction of intensity which has been assigned to a characteristic satellite structure in agreement with data reported by Tatsumi et al.[192]. As La^{3+} exhibits an empty *4f* orbital and the satellite structure is characteristically influenced by a charge transfer shake up from occupied ligand orbitals to the empty *4f* orbitals (s. section 9.2.), the change in the signal structure might be explained by a change in the effect of the spin-spin coupling due to an interaction of the surface covering film and the substrate, which results in a slightly different ligand field.

A peak maximum for the $La3d_{5/2}$ signal of the oxide film from thermolysis can be detected at 834.7 eV and the respective satellite shoulder occurring at a binding energy of 838.9 eV. A peak broadening compared to the powder of 10 eV (powder) to 16 eV (film) can be observed, which indicates the formation of a multi component structure. The peak maximum of the precursor film could be identified at 836.2 eV. Both main peak positions are in agreement with the data collected for the powders, which have been discussed in agreement with findings from literature[197]. Thus, according to the *La3d* and *O1s* signal, the formation of the oxide from the nitrate can be confirmed.

11.1.4. Thermal Stability of the Interface

It has been shown in the previous paragraph that during the mild low temperature oxide generation process, no reoxidation and no silicide formation takes place at the *H*-passivated *Si* substrate. For high temperature IC processing, a limited temperature for reoxidation is required, and the investigation of the influence resulting from heat treatments, above the desorption of the passivating *H*-termination is essential. The reactivity between the metal oxide and the

substrate is believed to be related to the thermodynamic stability as discussed in chapter 5. from[97].

According to Ono et al.[216] silicates are formed after high temperature post deposition annealing for films which have been prepared under relatively mild pyrolysis conditions at 673 K. The formation depends on the ion radii of the rare earth elements. Post annealing at 873 K, 1073 K and 1173 K has been reported, showing increased numbers of *Si-O-Si* bonds as the annealing temperature increases.

Larger RE-ions showed significantly higher amounts of interfacial $LnSiO$, suggestively explained by an easier diffusion of *Si* from the substrate into the films. For the deposited films, the silicate formation at high temperatures is also likely, but due to a different expected interface structure caused by the wet chemical deposition technique, the bonding formation as well as characteristic temperatures for a possible reaction are likely to be different.

As it was introduced in section 5.5.2., La_2O_3 is considered to be thermodynamically stable in contact with *Si* up to a substrate temperature of 1000 K at least. In accordance to comparison data from[216]m heating temperatures of 1073 K and 1273 K have been chosen to investigate the effects of the annealing temperature on the reactivity and formation of interfacial layers.

Investigations of the thermal stability of the films XPS scans after flashing the sample up to 1073 K and 1273 K have been measured in order to investigate the thermal stability of the wet chemically deposited films, particularly the changes in the *Si2p* and *O1s* signal structure.

Figure 11.5. shows the *Si2p* and*O1s* signal measured with Mg-K_α. Illustrated are the signals of the native oxide, precursor film and the oxide films from thermolysis as well as oxide film samples heated up to 1073 K and 1273 K.

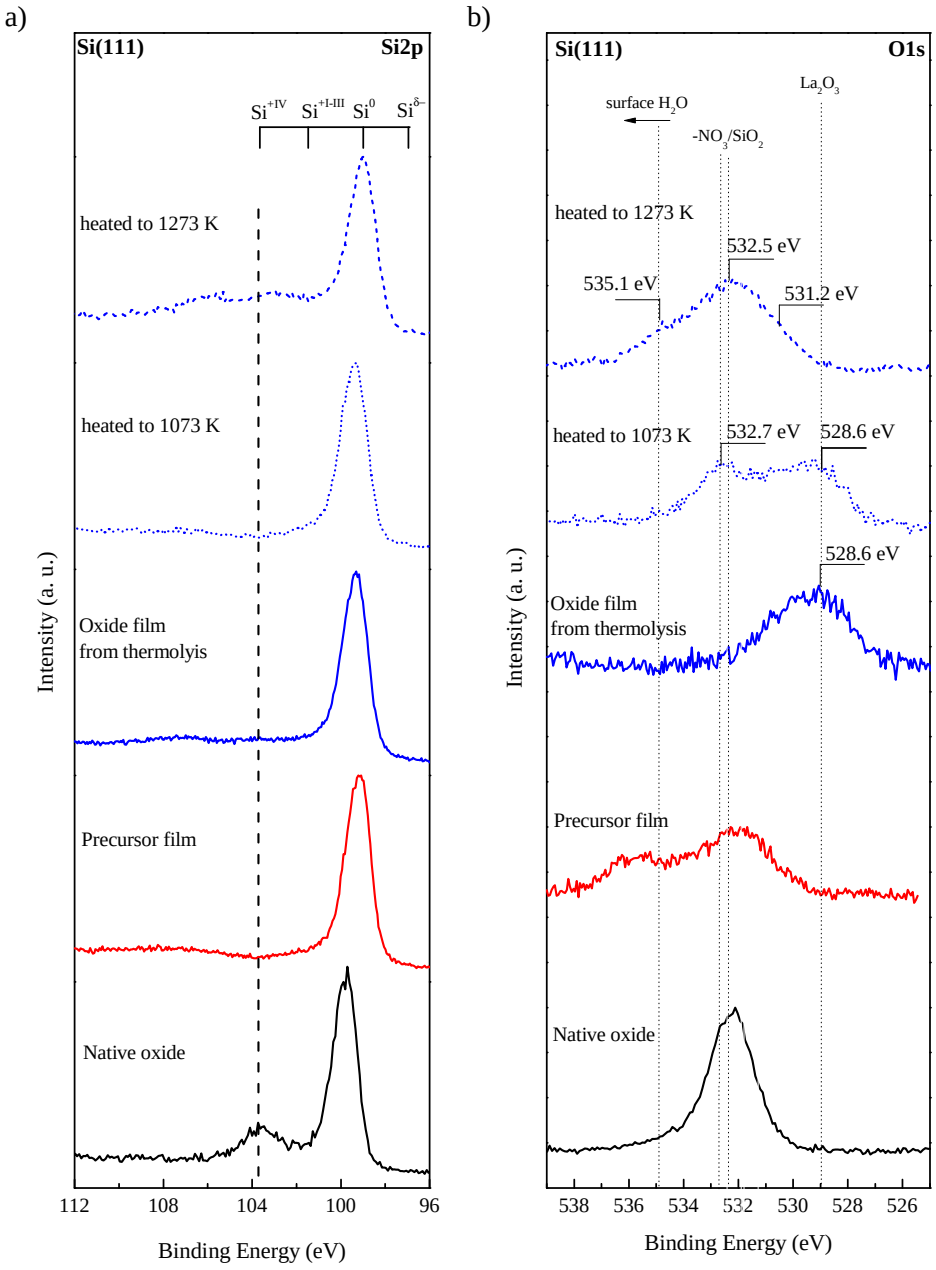


Figure 11.5.: Influence of the heating temperature on the interface formation respectively the influence on the Si substrate of the films deposited from 0.005 M butanolic $La(NO_3)_3 \times 6H_2O$ precursor solution on *Si(111)*, measured with Mg-K_α. Shown are the *Si2p* and *O1s* signal.

The *Si2p* signal shows no indication of a reoxidation or silicate formation after deposition and after decomposition to the oxide. After flashing the sample up

to 1073 K, again no changes appear within the $Si2p$ signal structure. Striking is an occurring broad shoulder structure, shifted to higher binding energies after heat treatment at 1273 K.

Severe changes in peak positions and structures can be observed within the $O1s$ signal. As it has been discussed in section 11.1.1., the precursor film and the oxide film from thermolysis show characteristic peaks for the nitrate-hydrate and the oxide, additionally to loosely adsorbed oxygen surface species. After heating the sample up to 1073 K, a split of the $O1s$ signal is indicated by a peak which shows two maxima, one in accordance with the main peak of the the oxydic La_2O_3 film from thermolysis (peak maximum at 528.8 eV) and the other one shifted to higher binding energies (peak maximum at 532.7 eV).

Even though the oxygen signal after the heat treatment at 1073 K detected at 532.7 eV might suggest a reoxidation of the Si substrate ($O1s$ in SiO_2 at 532.5 eV[215]), it can be concluded from the $Si2p$ signal that no unwanted reaction of the substrate happens at 1073 K. The changes in the $O1s$ signal structure can be suggestively explained by a change in the stoichiometry of the surface covering La_2O_3 layer or the formation of an oxygen containing topmost covering layer, containing relatively loosely bound oxygen species or surface hydroxy groups.

A different connection emerges after heat treatment up to 1273 K. The $O1s$ signal is significantly shifted to higher binding energies and no peak is observed at the characteristic binding energy for $O1s$ in La_2O_3 at 528.6 eV[217].

According to Hubbard et al., the free Gibbs energy data of the possible La-based silicates, La_2SiO_5 or $La_2Si_2O_7$ were not available. However, most of the silicate formations for RE-elements with similar atomic number as lanthanum show highly negative free Gibbs enthalpy values at 1000 K able for the reaction $Si + MO_x \rightarrow MSi_z + SiO_2$. A silicate formation is therefore most likely at annealing temperatures significantly above 1000 K. Characteristic $O1s$ signals for $LaSi_xO_y$ have been reported at 531.3 eV[218], which might be related to the right shoulder of the detected signal. A significant peak maximum can be observed at 532.5 eV in agreement with peak positions reported for $O1s$ ins SiO_2.[215] In this case, a reoxidation of the underlying substrate is also confirmed by the structure of the $Si2p$ signal which shows a clear signal at 103.5 eV (Si^{+IV} in SiO_2[207]) in agreement with the spectrum measured from the native oxidized surface. Additionally, a Si signal can be observed, shifted

to higher binding energies than Si^{+IV}, showing a peak maximum at >106 eV. *La4d* signals have been reported at 106.0 eV, but as for the precursor films, oxide films from thermolysis and oxide films annealed at 1073 K the *La4d* signal was not detectable within the given resolution and the *La3d* signal exhibits a comparable intensity after the different annealing steps. Therefore, it is highly unlikely that another annealing step leads to the appearance of the signal. Thus, no defined explanation could be found from literature but higher binding energies can indicate a binding partner, which shows a higher electronegativity than oxygen or a change in the stoichiometry of the oxide.

It can be concluded that obviously a substrate passivation is stable up to a temperature of 1073 K, as no changes in the structure of the *Si2p* signal are observed. According to the presented results, no significant interfacial reaction at the REO/*Si* interface takes place. Heat treatment at 1273 K leads to an obvious interaction of the substrate and the RE-containing toplayer. A silicide or silicate formation is most likely due to the documented negative free Gibbs enthalpy values. According to the shoulder structure of the *Si2p* signal, *Si* is existent in all oxidation states reaching from 0 to +IV, which indicates the presence of different binding partners.

However, the theoretical calculated data for the free Gibbs enthalpy must be considered carefully for the present case, as the calculation was based on a pre-deposition substrate temperature of 1000 K and gaseous oxide species. In the present work, the oxide and *Si* are in direct contact prior to the heat treatment, which might cause different surface processes, which are indicated by the change in the *O1s* structure after heat treatment at 1073 K. A resulting differing possible reaction between the substrate and the thin film in transition from the oxide into a mixed oxide or silicide compound, might be crucial for the thermodynamic stability. Nevertheless, the reported thermodynamic data can be used as guidance reference values in order to achieve the above suggested explanation for the substrate film interaction and reaction.

11.2. *Nd*-based Films on *Si(111)* and *Si(100)*

In comparison to the *La*-based films and in order to investigate the influence of the RE material systematically, the same analyses have been performed using

Nd-based precursors. Nd_2O_3 is more stable under ambient conditions than La_2O_3 and the system has been expanded to different substrate types.

The survey spectrum multiplot in figure 11.6. shows the data detected from the *Si(111)* substrate with native oxide, *H-Si(111)* measured with Mg-K_α, whereas the survey spectra of the precursor film and the oxide film from thermolysis are shown measured with Al-K_α, despite an overlap of the *Nd3d* and *OKLL* is significant due to technical reasons. For the same reason the spectra of the native oxidized substrate and the *H*-terminated surface have only been measured up to 1000 eV. However, at higher binding energies no significant signals are expected for those samples.

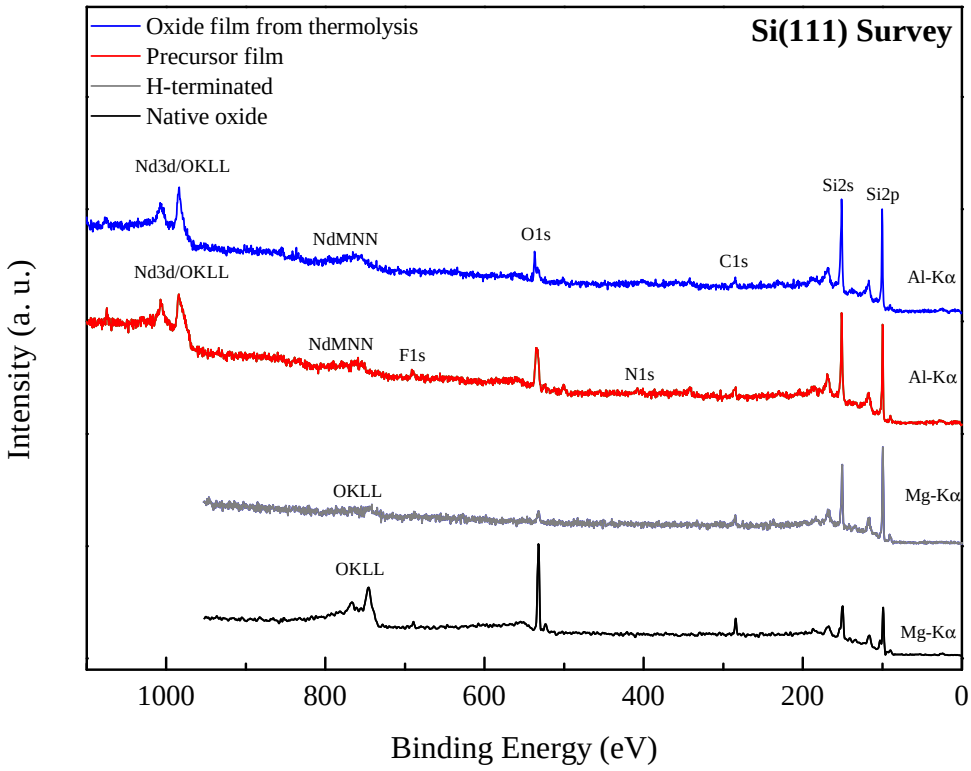


Figure 11.6.: Survey spectra measured with Mg- and Al-K_α of the native oxidized surface, the *H*-terminated samples, precursor film and oxide film from thermolysis deposited from 0.005 M butanolic $Nd(NO_3)_3 \times 6H_2O$ precursor solution on *Si(111)*.

The multiplot in figure 11.7. shows the survey spectra detected from the *Si(100)* substrate.

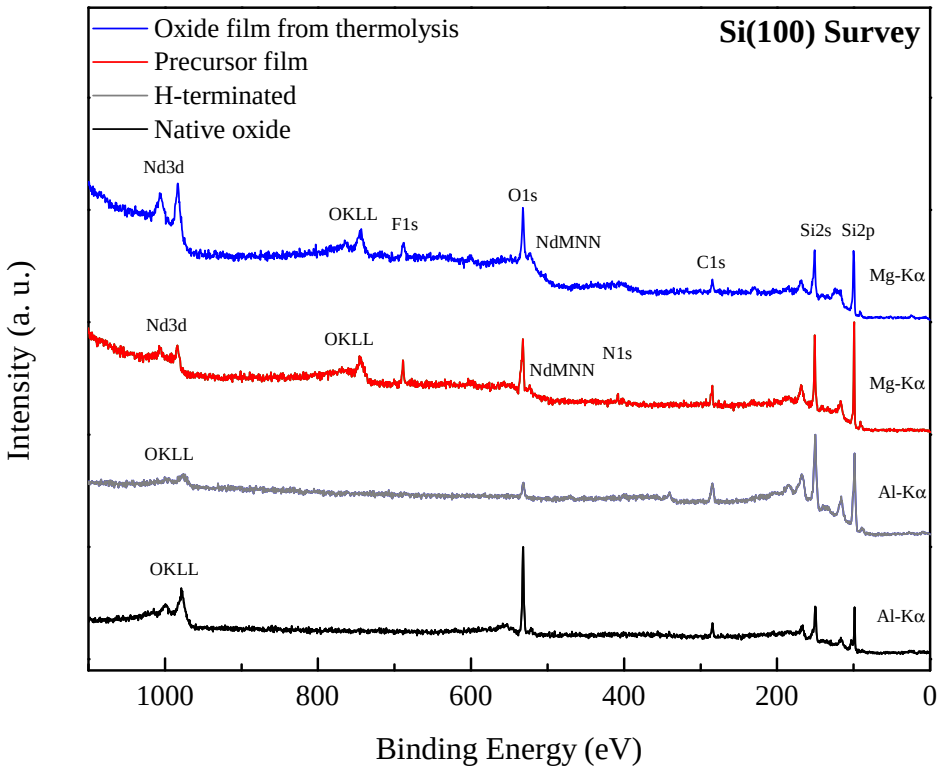


Figure 11.7.: Survey spectra measured with Mg-K_α and Al-K_α of the native oxidized surface, the H-terminated samples, precursor film and oxide film from thermolysis deposited from 0.005 M butanolic $Nd(NO_3)_3 \times 6H_2O$ precursor solution on *Si(100)*.

The native oxidized and H-terminated samples have been measured with Al-K_α, whereas the survey spectra of the precursor film and the oxide film from thermolysis are shown measured with Mg-K_α, as otherwise an overlap of the *OKLL* and *Nd3d* signal is observed. The spectra are normalized to the highest detected signal within each spectrum in order to illustrate the respective detected signal types. The detected *F1s* signal on *Si(100)* substrates can again be explained by remaining chamber impurities.

As for the *La*-based films, all expected significant signals can be observed for the *Si(111)* and *Si(100)* substrates. The native oxidized and H-terminated samples show the characteristic *Si* (*Si2p* and *Si2s*), *O* (*O1s* and *OKLL*) and *C* (*C1s*) peaks. The deposited films exhibit characteristic peaks of *Nd* (*Nd3d* and *NdMNN*). For the *Si(100)* substrates, a significantly lower intensity of the

Nd3d signals, resulting from the precursor film compared to the films after decomposition, can be observed as for the *La* based films on *Si(111)*.

11.2.1. The *Nd3d* Signal

Figure 11.8. and 11.9. show the *Nd3d* spectra of the precursor film and the oxide film from thermolysis on *Si(111)* and *Si(100)*. The extracted data are the binding energy of the peak with the highest intensity each, as emphasized in the spectra. This can be related to the main signal of the $Nd3d_{5/2}$, which has been discussed regarding the powders in 9.2.

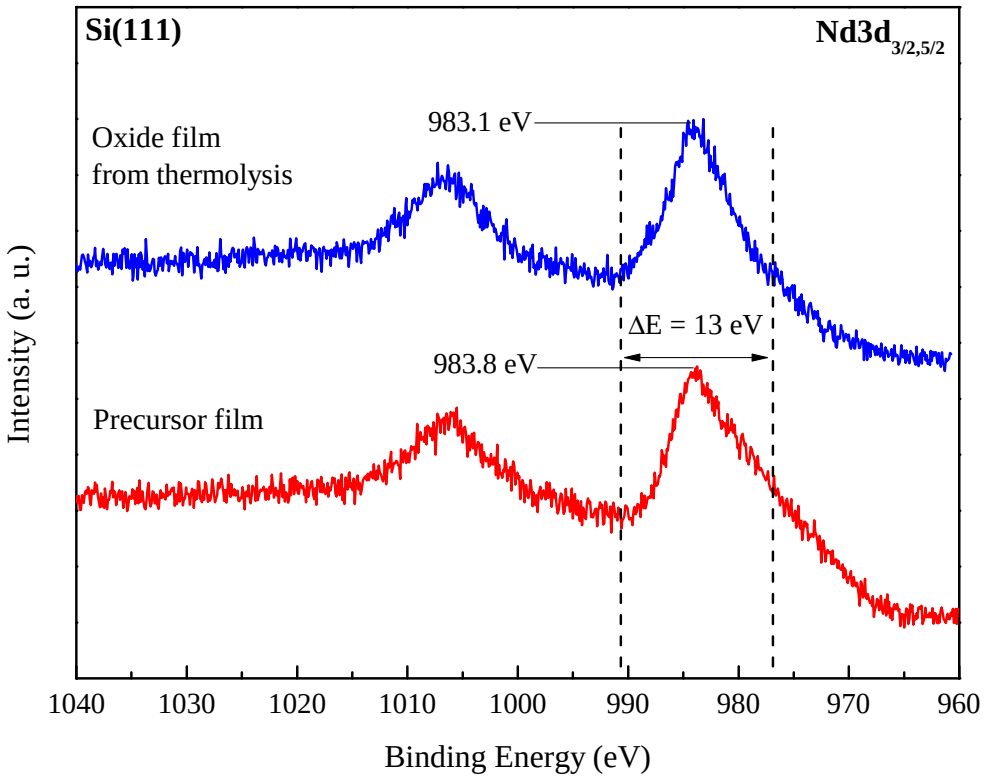


Figure 11.8.: *Nd3d* signal of the precursor film and the oxide film from thermolysis deposited from 0.005 M butanolic $Nd(NO_3)_3 \times 6H_2O$ precursor solution on *Si(111)* measured with Al-K_α. Notably is the overlap with the OKLL signal. Marked are the peak maxima and the peak width.

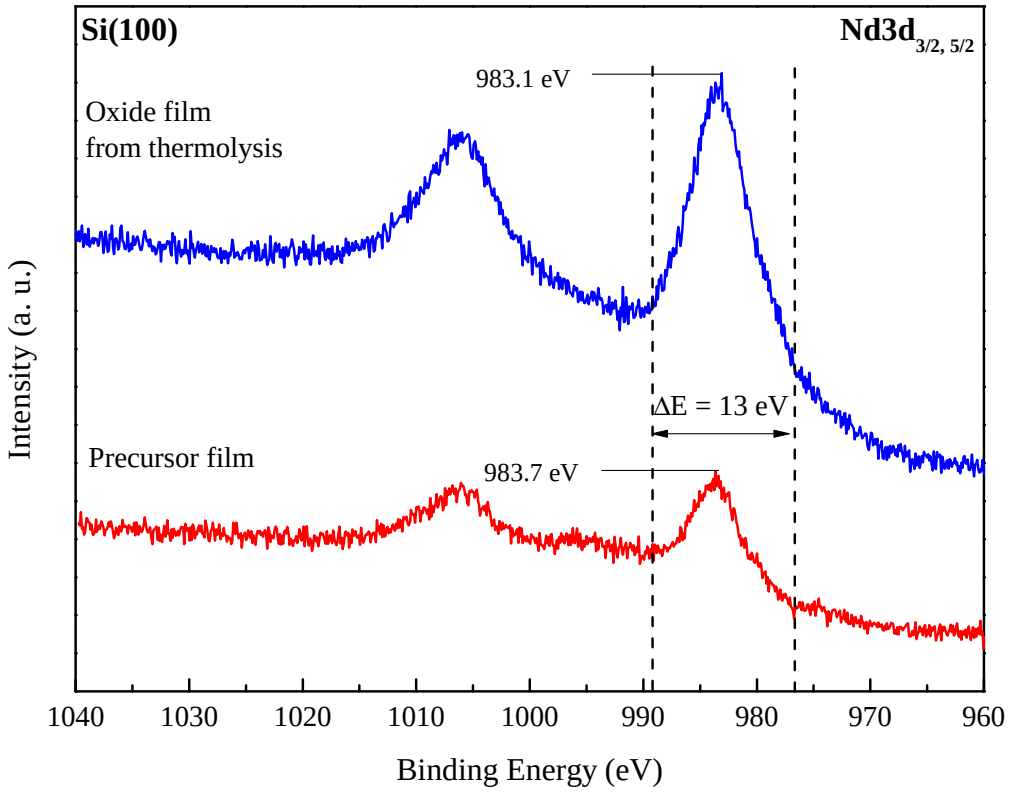


Figure 11.9.: *Nd3d* signal of the precursor and oxide film from thermolysis deposited from 0.005 M butanolic $Nd(NO_3)_3 \times 6H_2O$ precursor solution on *Si(100)* measured with Mg-K_α. Marked are the peak maxima and the peak width.

The signals detected from the *Si(111)* substrates have been measured applying Al-K_α exhibiting an overlap with the OKLL Auger structure. Therefore, a peak broadening is observed in comparison to the signals detected on *Si(100)*, which is not caused by the appearance of different *Nd* species.

Films deposited on *Si(111)* exhibit a peak maximum at 983.8 eV for the precursor film and 983.2 eV for the oxide film from thermolysis. *Si(100)* substrates result in peak maxima of 983.7 eV (precursor) and 983.1 eV (oxide from thermolysis). These values are in agreement with the presented data of the *Nd*-powders (s. 9.2.), summarized in table 9.7. It was presented that the main signal of the $Nd(NO_3)_3 \times 6(H_2O)$ could be identified at a binding energy of 983.8 eV (signal A in table 9.7.), whereas the oxides showed a characteristic

binding energy of 982.9 eV (signal C in table 9.7.) in agreement with data measured from Uwamino et al.[197].

The intensity ratio of the maximum peak of the oxide film from thermolysis and the precursor film can be calculated as 1.4:1 (*Si(111)*) and 1.9:1 (*Si(100)*), resulting from the surface covering carbon layer, which shields the surface prior to the heat treatment. The intensity is dependent on the remaining amount of carbon. Thus, the varying intensities are not caused by surface reactions. No peak broadening can be detected compared to the powders. Both substrate types exhibit a maximum peak width of roughly 13 eV, even though the *Nd* signal on *Si(111)* showed an overlap with the *OKLL*.

11.2.2. The *Si2p* and *O1s* Signal

Figure 11.10. shows the detected *Si2p* signals in direct comparison.

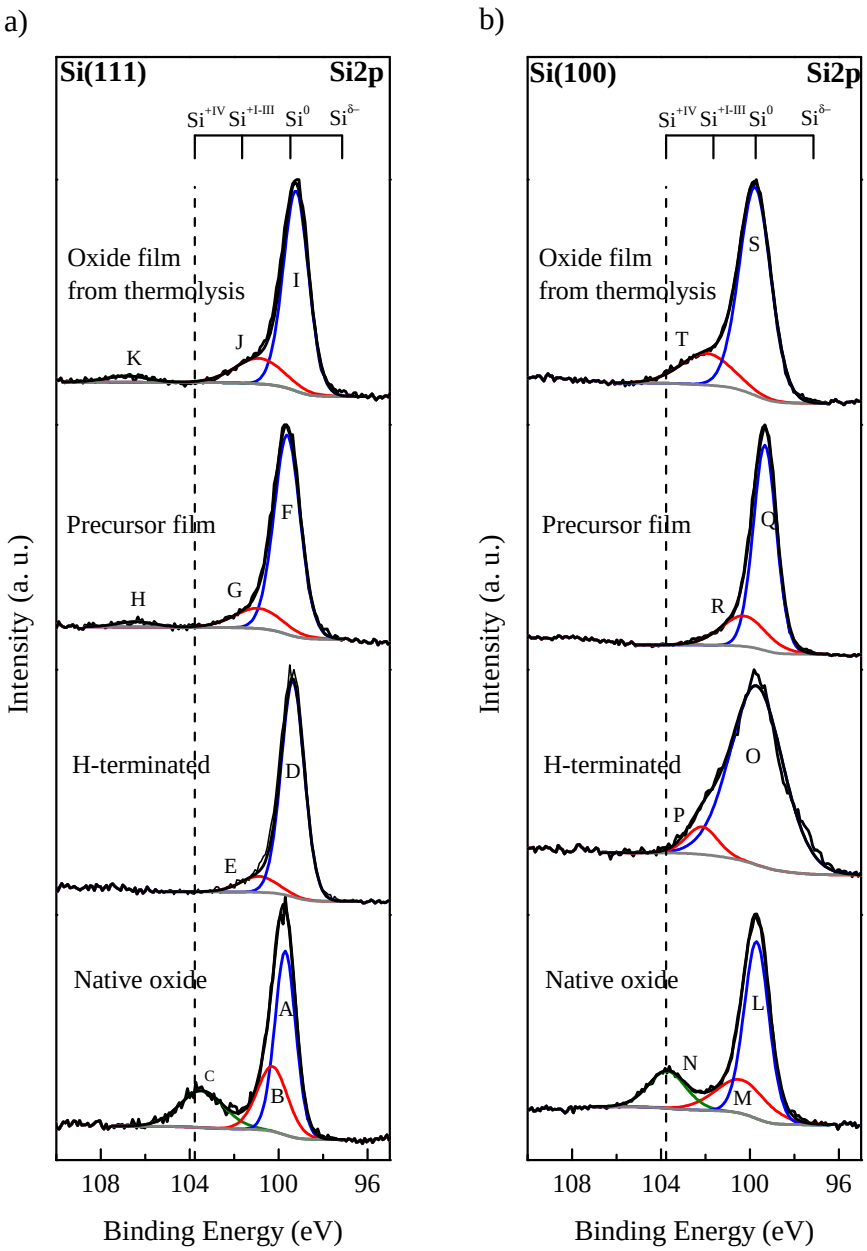


Figure 11.10.: *Si2p* spectra measured with Mg-K_α of the native oxidized surface, the *H*-terminated samples, *Nd*-based precursor film and oxide film from thermolysis deposited from 0.005 M butanolic $Nd(NO_3)_3 \times 6H_2O$ precursor solution on *Si(111)* and *Si(100)*.

Shown are, as for the *La*-based samples, the data detected of the native oxidized substrate, the *H*-terminated surfaces, precursor film and oxide film from thermolysis. The respective analyzed peak fit data are summarized in table 11.3. (*Si(111)*) and 11.4. (*Si(100)*).

Table 11.3.: Peak fit parameters and peak positions in eV for the *Si2p* signal of the *Nd*-based films on *Si(111)* substrates.

Comp.	Pos.	FWHM	Area %	GL	Literature[207]
Native Oxide				Region: 107.6 - 97.0 eV	
A	99.7	1.1	51.5	80/20	99.2 Si^{0}
B	100.3	1.6	26.6	80/20	100.2 Si^{+I}
C	103.5	2.3	21.9	80/20	103.5 Si^{+IV}
H-Terminated				Region: 105.2 - 96.4 eV	
D	99.4	1.2	89.6	80/20	Si^{0}
E	100.9	1.9	10.4	80/20	Si^{+I}
Precursor Film				Region: 108.7 - 97.0 eV	
F	99.6	1.4	81.8	80/20	Si^{0}
G	100.9	2.5	15.8	80/20	$Si^{+I/+II}$
H	106.4	2.0	3.2	80/20	-
Oxide Film from Thermolysis				Region: 109.0 - 96.0 eV	
I	99.2	1.3	78.0	80/20	Si^{0}
J	100.8	2.6	18.1	80/20	$Si^{+I/+II}$
K	106.8	2.2	3.9	80/20	-

Table 11.4.: Peak fit parameters and peak positions in eV for the *Si2p* signal of the *Nd*-based films on *Si(100)* substrates.

Comp.	Pos.	FWHM	Area %	GL	Literature[207]
Native Oxide				Region: 107.2 - 96.4 eV	
l	99.7	1.3	58.6	80/20	99.2 Si^{0}
M	100.5	2.7	22.8	80/20	100.2 Si^{+I}
N	103.7	2.0	18.6	80/20	103.5 Si^{+IV}
H-Terminated				Region: 105.8 - 94.2 eV	
O	99.7	2.8	91.8	80/20	Si^{0}
P	102.2	1.6	8.2	80/20	101.9 Si^{+III}
Precursor Film				Region: 105.2 - 96.5 eV	
Q	99.3	1.2	77.5	80/20	Si^{0}
R	100.2	2.6	22.5	80/20	Si^{+I}
Oxide Film from Thermolysis				Region: 106.2 - 96.5 eV	
S	99.7	1.7	80.2	80/20	Si^{0}
T	102.0	2.7	19.8	80/20	Si^{+III}

As for the *La*-based samples, the *Si(111)* substrates exhibit characteristic peak structures of the *Si2p* signals. The $Si2p_{1/2}$ and $Si2p_{3/2}$ are not separated due to the given resolution of the detector. The side signal (red) is referred to *Si* in different oxidation states. The sample cleaning has been explained in section 11.1.1. for the *Si(111)* substrate.

It can be seen from the spectra in figure 11.10., that for *Si(100)* substrates the appearance of the *Si2p* signal after the *HF* etching is slightly different, as a peak broadening up to a FWHM of 2.8 eV for the main signal (signal O in figure 11.10.) can be observed. This effect might be caused by the reduced number of dangling bonds on *Si(100)* substrates and a resulting polarization of the remaining bulk *Si* atoms, indicated by a δ^{-} charged *Si* species, which can be observed as a peak broadening shifted to lower binding energies.

Furthermore, due to the not present etching stop at the <111> lattice plane and the resulting more undefined etching process, the remaining number of oxide species after the *HF* cleaning is considered to be higher (s. chapter 8.), which is also confirmed by signal P in figure 11.10. at 102.2 eV.

As it has been discussed for the *La*-based films on *Si(111)*, no reoxidation can be observed after the film deposition or decomposition, as no characteristic signals for *Si* in oxidation state +IV are observable from the spectra. A slightly differing, but utmost important context can be determined for *Si(100)* substrates. The signals of the precursor films do not exhibit any changes within the *Si2p* structure compared to the oxide free surface, but after the decomposition, the precursor the broadening of the signal shoulder enters the region of *Si* in oxidation state +IV (compare the plotted perpendicular orientation line from the native oxidized surface in figure 11.10.) and therefore indicates an unwanted reoxidation of the surface after precursor decomposition. The consideration of the *O1s* signals is essential, as for the previous measurements, in order to achieve a detailed image of the present oxide species on the surface.

The *O1s* spectra have been measured with Al-K_α in order to avoid an overlap with the *NdMNN* Auger signal. The intensities are obtained from the respective peak areas and normalized with respect to the area of the *O1s* resulting from the native oxidized *Si(100)* and *Si(111)*. The respective data of the peak fitting are summarized in table 11.5. (*Si(111)*) and 11.6. (*Si(100)*).

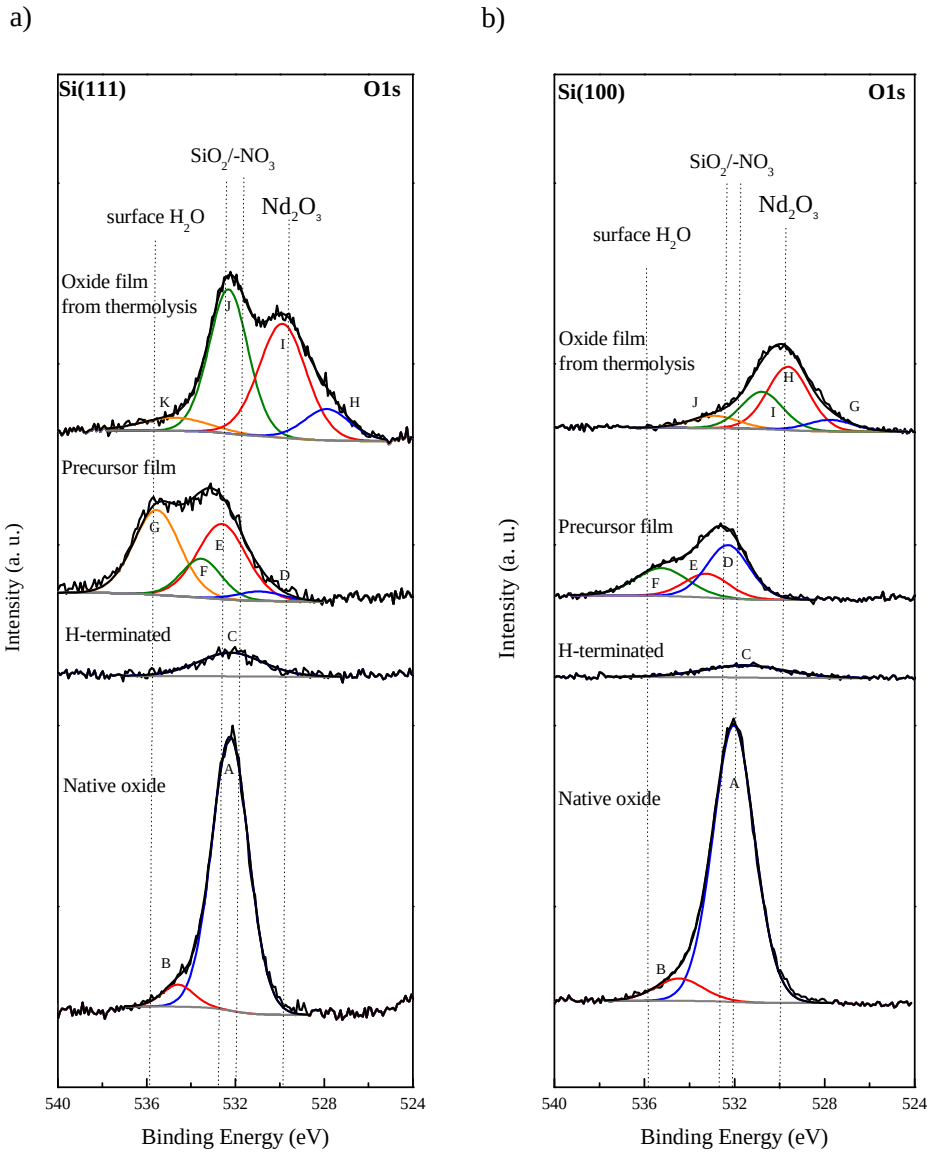


Figure 11.11.: *O1s* spectra measured with Al-K_α of the native oxidized surface, the *H*-terminated samples, *Nd*-based precursor film and oxide film from thermolysis deposited from 0.005 M butanolic $Nd(NO_3)_3 \times 6H_2O$ precursor solution on *Si(111)* (left) and *Si(100)* (right).

Table 11.5.: Peak fit parameters and peak positions in eV for the *O1s* signal of the *Nd*-based films on *Si(111)* substrates.

Comp.	Pos.	FWHM	Area %	GL	Literature
Native Oxide				Region: 537.0 - 528.7 eV	
A	532.2	2.0	97.7	80/20	532.5 suboxides/SiO_2 [208]
B	534.6	1.7	2.3	80/20	534.6 SiO_2/H_2O [209], ice on Re [210]
H-Terminated				Region: 537.1 - 527.2 eV	
C	532.2	3.4	100.00	80/20	SiO_2/suboxides [208]
Precursor Film				Region: 540.8 - 528.0 eV	
D	530.9	2.4	4.4	80/20	530.9/531.6 surface -OH, [201] [211]
E	532.6	2.6	38.4	80/20	532.7 $Ba(NO_3)$ [199]
F	533.5	2.1	16.3	80/20	533.3 crystal H_2O [198]
G	535.5	2.7	40.9	80/20	loosely bound H_2O [210] [212]
Oxide Film from Thermolysis				Region: 537.6 - 525.1 eV	
H	527.9	2.4	10.9	80/20	-
I	529.9	2.5	40.9	80/20	529.3 Nd_2O_3 [197] [202]
J	532.3	2.1	42.5	80/20	532.2 SiO_x [208]
K	534.3	2.6	5.7	80/20	adsorbed surface H_2O [210]

Table 11.6.: Peak fit parameters and peak positions in eV for the *O1s* signal of the *Nd*-based films *Si(100)* substrates.

Comp.	Pos.	FWHM	Area %	GL	Literature
Native Oxide				Region: 537.8 - 527.6 eV	
L	532.0	2.2	91.6	80/20	532.5 suboxides/SiO_2 [208]
M	534.5	2.5	8.4	80/20	534.6 SiO_2/H_2O [209], ice on Re [210]
H-Terminated				Region: 537.5 - 525.9 eV	
N	531.5	4.3	100.0	30	532.5 suboxides SiO_x [208]
Precursor Film				Region: 539.4 - 528.4 eV	
O	532.3	2.2	47.8	80/20	532.7 $Ba(NO_3)_2$ [199]
P	533.2	2.3	21.9	80/20	533.3 crystal H_2O [198]
Q	535.2	2.7	30.3	80/20	loosely bound H_2O [210] [212]
Oxide Film from Thermolysis				Region: 536.5 - 524.3 eV	
R	527.7	2.4	10.1	80/20	-
S	529.6	2.2	49.8	80/20	529.3 Nd_2O_3 [202] [197]
T	530.8	2.2	29.0	80/20	530.6 surface -OH [201]
U	532.9	2.5	11.1	80/20	532.5 suboxides SiO_x [208]

As the signals of the native oxidized and *H*-terminated surface of the *Si(111)* substrates have already been discussed in section 11.1.1., it should be omitted at this point.

Focusing on the *O1s* signals of the precursor and oxide film from thermolysis on *Si(111)*, it is obvious that both signals can be fitted with four signals each. The precursor film exhibits in agreement with the data detected for the *La*-based films characteristic signals for OH-surface species at 530.9 eV (signal D in figure 11.11.a) in addition to the main signals of *O1s* in NO_3 (signal E in figure 11.11.a) at 532.6 eV and *O1s* from crystal water at 533.5 eV (signal F in figure 11.11.a). The area ratio in this case constitutes 2.4:1 instead of the theoretically expected ratio of 1.5:1 for the *O1s* from the nitrate to the crystal water. An increased ratio of the O1s resulting from nitrate to the crystal water has been observed for the *La*-based films as well, explained by a segregation of the water molecules to the top surface, leaving the crystal collective within the UHV environment. As in the present case the ratio is even higher, it might be possible that almost the complete amount of crystal water leaves the crystal

collective, depending on the residence time inside the UHV. In agreement with the *La*-based films, a high amount of loosely bound water species can be detected, inducing signal G in figure 11.11.a at 535.5 eV, which can be associated with an oxygen adlayer with not strongly bound oxygen species, caused by a top-most covering water layer.

After the decomposition, the characteristic peak position of *O1s* in Nd_2O_3 can be observed at (signal I in figure 11.11.a) 529.9 eV in agreement with data from the literature[197] [202] and the nitrate powder measurements (s. section 9.2.). The remaining *Si* suboxides cause a signal at 532.3 eV (signal J in in figure 11.11.a) and again adsorbed water molecules can be detected at 534.3 eV (signal K in figure 11.11.a) in agreement with data shown in[210].

The *HF* surface cleaning of the *Si(100)* can, in agreement with the detected data for the *Si2p* signal and the discussion for the *Si(111)* surfaces, considered to be successful from the *O1s* signal. Signal L and M, resulting from the native oxidized sample in figure 11.11.b, can be assigned to oxygen from *Si* oxides or suboxides (signal L in figure 11.11.b at 532.0 eV)[208] and adsorbed surface H_2O (signal M in figure 11.11.b at 534.5 eV)[210]. Whereas for the *H*-terminated surfaces, a relatively broad peak at 531.5 eV (signal N in figure 11.11.b) can be assigned to suboxide species. As the FWHM of 4.3 eV is even higher than the value detected for *Si(111)*, it can be assumed, in agreement with the findings of the analysis of the *Si2p* signal, that a higher amount suboxide species can be detected compared to the *Si(111)* substrates. On *Si(100)* the precursor films exhibit three *O1s* signal types after the peak fitting. As for the previous analysis, the precursor film shows characteristic signals for *O1s* from nitrates (signal O in figure 11.11.b at 532.3 eV)[199] as well as crystal water (signal P in figure 11.11.b at 533.2 eV), as expected. The area ratio can be calculated as 2.2:1, contrary to theoretical calculated and measured data from the powders, which is similar to the values detected for *Si(111)*. After decomposition to the oxide film, the Nd_2O_3 can clearly be identified by the characteristic main signal at 529.6 eV with an area of 49.8 % (signal S in figure 11.11.b). The signal U (in figure 11.11.b) at 532.9 eV confirms the presumption considered from the *Si2p* signal that a slight reoxidation of the *Si* substrate to oxidation state +IV occurs after the decomposition.[208] The signal T in figure 11.11.b, detected at 530.8 eV, can not be assigned uniquely, but results very likely from the detected suboxides. As for the previous analyzed oxide films a small signal arises at 527.7 eV which can not be assigned in detail.

11.3. *Nd*-based Films on *Ge(100)*

Figure 11.12. shows the survey spectra of the pure *Ge(100)* samples as received with the native oxide, after the *HF* oxide strip, after precursor deposition (precursor film) and after decomposition to the oxide film analogous to the data shown on *Si*.

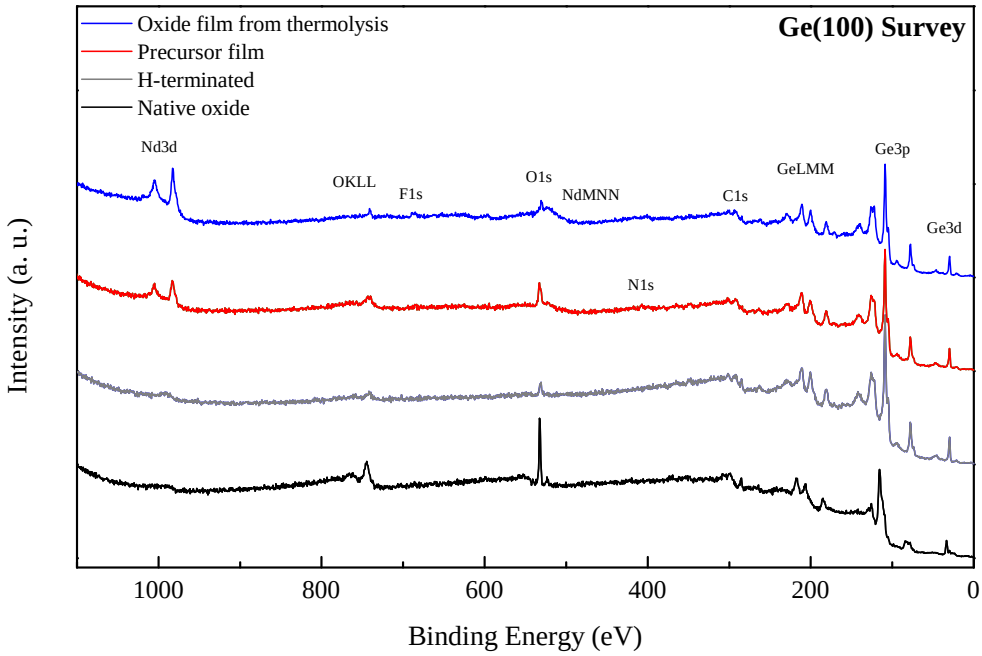


Figure 11.12.: Survey spectra measured with Mg-K_α of the native oxidized surface, the H-terminated samples, precursor film and oxide film from thermolysis deposited from 0.005 M butanolic $Nd(NO_3)_3 \times 6H_2O$ precursor solution on *Ge(100)*.

The spectra are measured with Mg-K_α and normalized to the highest detected signal within each spectrum in order to illustrate the respective detected signal types.

All expected significant signals can be observed for the *Ge(100)* substrates as it was observed for *Si*. The native oxidized and H-terminated samples show the characteristic signals of germanium (*Ge3p* and *Ge3d*), oxygen (*O1s* and *OKLL*) as well as a slight indication of carbon (*C1s*), which is covered by the germanium *GeLMM* Auger structure. The deposited films (precursor and ox-

ide from thermolysis) exhibit characteristic peaks of *Nd* (*Nd3d* and *NdMNN*). The detected *F1s* signal can again be explained by remaining chamber impurities.

11.3.1. The *Nd3d* signal

The detected *Nd3d* signals of the precursor film and oxide film from thermolysis on *Ge(100)* are shown in figure 11.13.

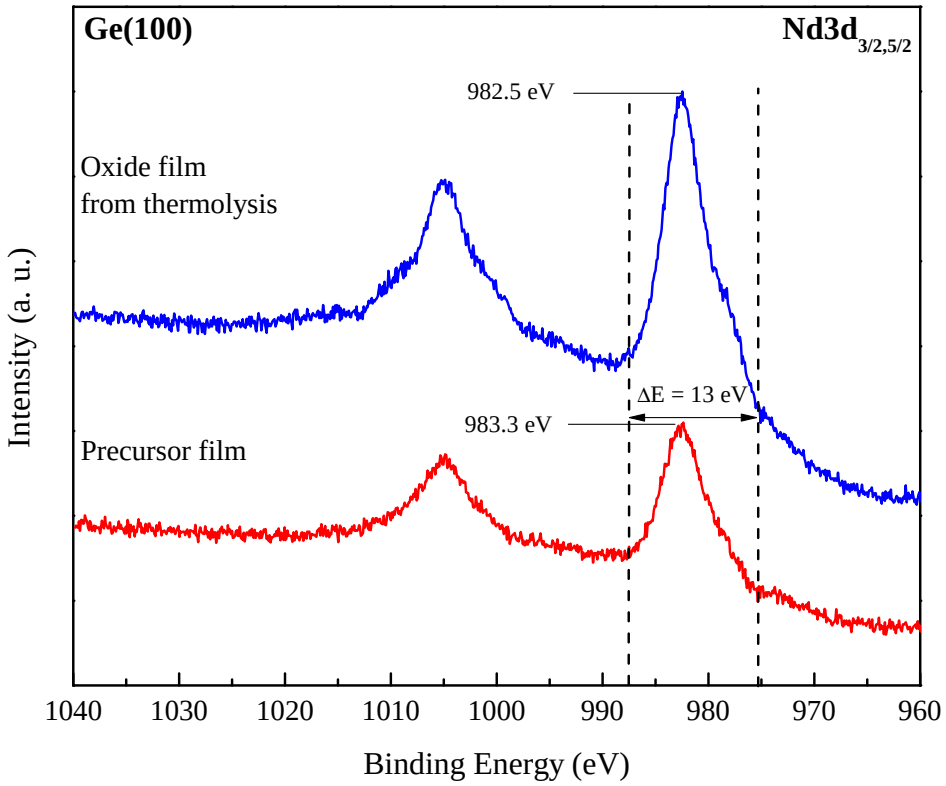


Figure 11.13.: *Nd3d* signal of the precursor and oxide film from thermolysis deposited from 0.005 M butanolic $Nd(NO_3)_3 \times 6H_2O$ precursor solution on *Ge(100)* measured with Mg-K_α. Marked are the peak maxima and the peak width.

As for the *Si* substrates, the peak position of the precursor and oxide films from thermolysis can be compared to the data detected from the pure powders. The precursor film exhibits a peak maximum at 983.3 eV, which is comparable to the detected 982.9 eV for the pure *Nd*-nitrate-hexahydrate (signal A in table

9.7.), whereas the detected maximum of the oxide film from thermolysis film at 982.5 eV shows a binding energy in agreement with the from Umwamino et al.[197] reported and measured value of 982.6 eV for $Nd3d$ in the Nd_2O_3 powder (compare section 9.2.). The detected intensity ratio of the precursor and oxide film from thermolysis can in this case be calculated as 1.6:1. It can be concluded that the *Nd3d* signal indicates the presence of the expected nitrate and oxide species, which needs again to be confirmed by the analysis of the *O1s* signals.

11.3.2. The *Ge3d* and *O1s* Signal

The detected spectra of the *O1s* and *Ge3d* signals are shown in figure 11.14. The peak fit data are summarized in table 11.7. (*Ge3d*) and 11.8. The *Ge3d* signals are normalized to the highest detected peak intensity, whereas the *O1s* is normalized according to the approach used for *Si*.

Due to the high amount of peaks to be fitted, the peak labels for the *Ge3d* signals are structured as follows. *X* for the oxidized samples, X′ for the *HF* treated samples, X″ for the precursor films and X‴ for the oxide films from thermolysis.

According to table 2.1., X-ray satellites of the $Ge3d$ signal, caused by non monochromatic Mg-K_α excitation radiation, can be detected at approx. +11 eV compared to the main signal with an intensity ratio of 10 %. Thus, the respective signals have been fitted accordingly. As the *Ge3d* peak shows an overlap with the *O2s* signal, respective additional peaks have to be taken into account. The results and respective peak fits of the *Ge3d* and *O1s* signal are summarized in figure 11.14.

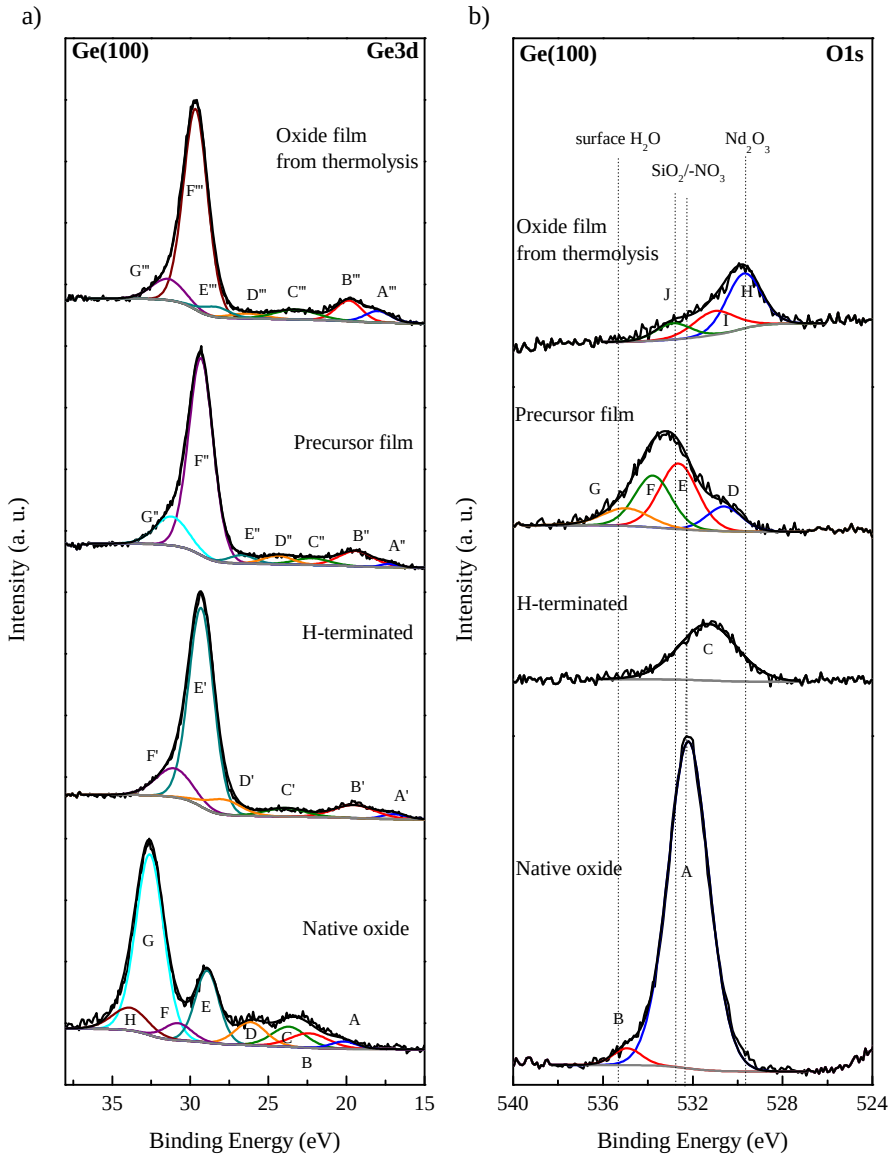


Figure 11.14.: *Ge3d* and *O1s* spectra measured with Mg-K_α (*O1s*) and Al-K_α (*Ge3d*) of the native oxidized surface, the *H*-terminated samples, *Nd*-based precursor film and oxide film from thermolysis deposited from 0.005 M butanolic $Nd(NO_3)_3 \times 6H_2O$ precursor solution on *Ge(100)*.

Due to a large amount of individual signals compared to *Si*, a more complex structure can be observed for the *Ge3d* peaks (s. table 11.7).

Table 11.7.: Peak fit parameters and peak positions in eV for the *Ge3d* signal of the *Nd*-based films on *Ge(100)* substrates measured with Al-K_α.

Comp.	Pos.	FWHM	Area %	GL	Literature[219]
Native Oxide				Region: 38.6 - 14.7 eV	
A	20.2	1.9	1.8	80/20	X-ray satellite of E
B	22.4	2.9	5.5	80/20	X-ray satellite of G
C	23.7	2.6	6.7	80/20	*O2s*
D	26.1	2.3	7.1	80/20	*O2s*
E	28.9	1.8	16.7	80/20	*Ge3d* 29.1 Ge^0 [219]
F	30.8	2.1	4.7	80/20	shake off satellite of E/ *Ge3d* suboxides of Ge [219]
G	32.6	2.1	49.7	80/20	*Ge3d* 32.5 Ge^{+IV} [219]
H	33.9	2.7	7.9	80/20	shake off satellite of G
H-Terminated				Region: 36.9 - 14.4 eV	
A′	16.9	1.8	1.5	80/20	-
B′	19.5	3.2	7.2	80/20	X-ray satellite E′
C′	23.9	3.0	4.5	80/20	*O2s*
D′	27.9	2.7	7.2	80/20	*O2s*
E′	29.3	1.9	65.8	80/20	*Ge3d* 29.1 Ge^0 [219]
F′	31.1	2.7	13.9	80/20	shake off satellite of E′ *Ge3d* suboxides of Ge [219]
Precursor Film				Region: 36.5 - 15.3 eV	
A″	17.3	1.3	0.8	80/20	-
B″	19.4	2.6	7.5	80/20	X-ray satellite of F″
C″	22.2	2.6	3.3	80/20	*O2s*
D″	24.4	2.2	3.5	80/20	*O2s*
E″	26.7	2.07	3.1	80/20	*O2s*
F″	29.3	1.5	68.5	80/20	*Ge3d* 29.1 Ge^0 [219]
G″	31.2	2.5	13.3	80/20	shake off satellite of F″ *Ge3d* suboxides of Ge [219]
Oxide Film from Thermolysis				Region: 36.6 - 13.8 eV	
A‴	18.0	1.9	4.1	80/20	-
B‴	19.8	1.9	7.4	80/20	X-ray satellite of F‴
C‴	23.2	3.2	5.8	80/20	*O2s*
D‴	26.3	2.6	2.3	80/20	*O2s*
E‴	28.4	2.1	4.0	80/20	*O2s*
F‴	29.7	1.8	67.0	80/20	*Ge3d* 29.1 Ge^0 [219]
G‴	31.5	2.4	9.5	80/20	shake off satellite of G‴ *Ge3d* suboxides of Ge [219]

Native oxidized *Ge(100)* samples exhibit eight characteristic signals in the measured region from 38 to 15 eV. GeO_2 causes a major signal at 32.6 eV (signal G in figure 11.14.a) in agreement with[219], exhibiting a characteristic X-ray satellite at 22.4 eV (B). The same peak structure can be detected for Ge^0 (main signal E in figure 11.14.a at 28.9 eV) from the underlying substrate, showing an X-ray satellite at 20.2 eV (signal A in figure 11.14.a). From literature[219], Ge^0 is characteristically detected at 29.1 eV. Signal D and E in figure 11.14.a can be assigned to *O2s* peaks, resulting from the suboxide and dioxide, which has been confirmed by two detected species from the *O1s* signal. As the effect of the ligand or binding partner surrounding of each atom, a defined shift of the *O2s* signal can not be given by the shifting or peak positions of the *O1s* signal. Thus, no further specification should be done at this point. For oxydic structures, often shake off satellites shifted to higher binding energies are observed, which can also be seen in the present spectra detected at 30.8 eV (signal F in figure 11.14. (satellite of Ge^0)) and 33.9 eV (satellite of Ge^{+IV}). Besides the assigned satellite structure signal F in figure 11.14 might also result from suboxide species of the *Ge*. Similar to the observed shoulder discussed for *Si* substrates the Ge_xO_y species have to result in characteristic signals between the positions of the *Ge3d* from Ge^0 (29.1 eV) and Ge^{+IV} (32.5 eV).

The success of the oxide strip, with respect to a complete removal of the GeO_2 can be confirmed by the signal structure change detected for the cleaned surfaces. As it can be seen in the spectra and from the peak fits, no significant signal can be detected at 32.5 eV after the cleaning procedure, indicating that all Ge^{+IV} species have been removed and no GeO_2 is observable. Again, a characteristic signal of the Ge^0 species can be detected at 29.3 eV (signal E′ in figure 11.14.a) and the shake off satellite of E′/suboxide of *Ge* (signal F′ in figure 11.14.a) at 31.1 eV, whereas the respective X-ray satellite can be observed at 19.5 eV (signal B′ in figure 11.14.a).

The two signals detected at 23.9 eV (signal C′ in figure 11.14.a) and 27.9 eV (signal D′ in figure 11.14.a) are, as for the native oxidized samples, assigned to result from the remaining oxygen species as *O2s*. The detected signal F′ in figure 11.14.a indicating the presence and amount of remaining suboxide species at the *Ge(100)* surface, is in agreement with expected data from literature as a complete passivation and deoxidation of the *Ge*surface is most unlikely (s. section 8.3.1).

After the deposition of the precursor film, no significant changes can be detected in the *Ge3d* signal structure, as it has been observed for *Si* substrates. Obviously no interaction of the covering thin film layer and the substrate occurs after the deposition. The number of detected *O2s* signals increases, which is expected due to the additional nitrate and water species on top of the *Ge* surface. Signals A″, B″, F″ and G″ are in a close agreement with A′, B′, E′ and F′ in figure 11.14.a.

The decomposition to the Nd_2O_3 does not lead to a reoxidation of the *Ge(100)* surface to GeO_2 as no changes in the *Ge3d* structure can be observed after the film deposition and signals A‴,B‴,F‴ and G‴ in figure 11.14.a are in agreement with the data for the *HF* treated sample.

Table 11.8.: Peak fit parameters and peak positions in eV for the *O1s* signal of the *Nd*-based films on *Ge(100)* substrates.

Comp.	Pos.	FWHM	Area %	GL	Literature
Native Oxide				Region: 538.3 - 526.9 eV	
A	532.2	2.1	96.5	80/20	532.2 suboxides/GeO_2 [198] [220]
B	534.5	1.5	3.5	80/20	surface H_2O
H-Terminated				Region: 536.3 - 527.1 eV	
C	531.3	3.0	100.0	80/20	530.9 suboxides of Ge [198] [220]
Precursor Film				Region: 539.6 - 526.8 eV	
D	530.6	1.8	14.1	80/20	suboxides of Ge
E	532.6	2.0	40.9	80/20	532.7 $Ba(NO_3)_2$ [199]
F	533.8	1.9	31.3	80/20	533.3 crystal H_2O [198]
G	535.0	2.5	13.7	80/20	loosely bound H_2O
Oxide Film from Thermolysis				Region: 535.9 - 526.1 eV	
H	529.7	1.8	55.0	80/20	529.3 Nd_2O_3 [197] [202]
I	531.0	2.2	28.4	80/20	530.9 suboxides of Ge
J	532.9	1.9	16.6	80/20	532.6 $Ba(NO_3)_2$ [199]

As for the *Si* samples, the native oxidized *Ge(100)* in GeO_2 exhibits a characteristic *O1s* signal at 532.2 eV (signal A in figure 11.14.b) for Ge^{+IV}, which is in agreement with literature data of Nefedov et al.[198]. Furthermore, adsorbed water species can be detected, indicated by the observed signal at 534.5 eV (signal B in figure 11.14.b). After the *HF* oxide strip, a peak with a drasti-

cally reduced intensity can be detected at 531.3 eV (signal C in figure 11.14.b), which can be assigned to remaining suboxide species as the presence of GeO_2 can be eliminated from the analyses of the *Ge3d* signal. After deposition of the precursor film, four characteristic peaks can be identified. First of all, it is notable that again the characteristic signal for *O1s*, resulting from nitrate compounds, can be measured with an area of 40.9 % at 532.6 eV (signal E in figure 11.14.b).

The expected signal of the crystal water could be confirmed at 533.8 eV (signal F in figure 11.14.b). In agreement with the results achieved for Si suggestively loosely bound surface water species are observed according to signal G in figure 11.14.b, detected at 535.0 eV. The ratio of the crystal water and the nitrate can in this case be calculated as 1.3:1 which is relatively close to the theory of 1.5:1 but indicates the adsorption of water species as the area ratio of *O1s* resulting from nitrates is too low.

After the decomposition of the precursor the characteristic signals of $O1s$ in Nd_2O_3 can be confirmed by signal H in figure 11.14. at 529.7 eV. Furthermore, two extra signals can be observed. Signal I is assigned to suboxide species of Ge which can be confirmed by the *Ge3d* analysis and signal J in figure 11.14. which might result from remaining nitrate species as the presence of Ge^{+IV}, which shows a signal at the same peak position, can be excluded from the *Ge3d* analysis.

11.4. *Nd*-based Films on *SiGe(111)*

As for the pure Si and Ge substrates XPS analyses were performed for the samples based on $SiGe$ substrates.

Figure 11.15. shows the survey spectra of the pure *SiGe(111)* samples as received with the native oxide, after the *HF* oxide strip, after precursor deposition and after decomposition to the oxide film from thermolysis.

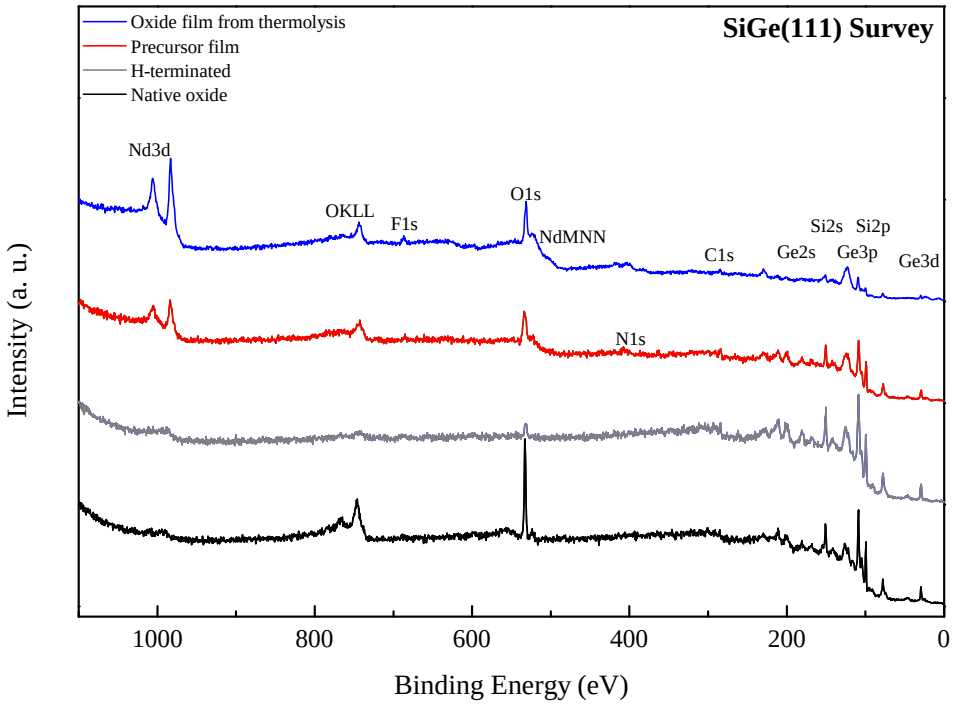


Figure 11.15.: Survey spectra measured with Mg-K_α of the native oxidized surface, the *H*-terminated samples, precursor film and oxide film from thermolysis, deposited from 0.005 M butanolic $Nd(NO_3)_3 \times 6H_2O$ precursor solution on *SiGe(111)*.

The multiplot in figure 11.12. shows the survey spectra detected from the *SiGe(111)* substrate, analogous to the spectra taken for *Si*. The spectra are normalized to the highest detected signal within each spectrum.

As for pure *Si* and *Ge* substrates all expected significant signals can be observed for the *SiGe(111)* samples. The native oxidized and *H*-terminated samples show the characteristic signals of *Ge* (*Ge3p* and *Ge3d*) and *Si* (*Si2p* and *Si2s*), *O* (*O1s* and *OKLL*) as well as a slight indication of *C* (*C1s*) which is obscured by the *Ge GeLMM* Auger structure. The deposited films (precursor and oxide from thermolysis) exhibit additionally characteristic peaks of *Nd* (*Nd3d* and *NdMNN*). The detected *F1s* signal can again be explained by remaining chamber impurities. It is noticeable that the intensity of the signals resulting from the underlying substrate appear to show a much lower intensity than the ones which have been observed on pure *Si* and *Ge* after the film deposition.

11.4.1. The *Nd3d* signal

As for the already shown substrate types for *SiGe(111)* the *Nd3d* detail spectra have been analyzed, which are summarized in figure 11.16.

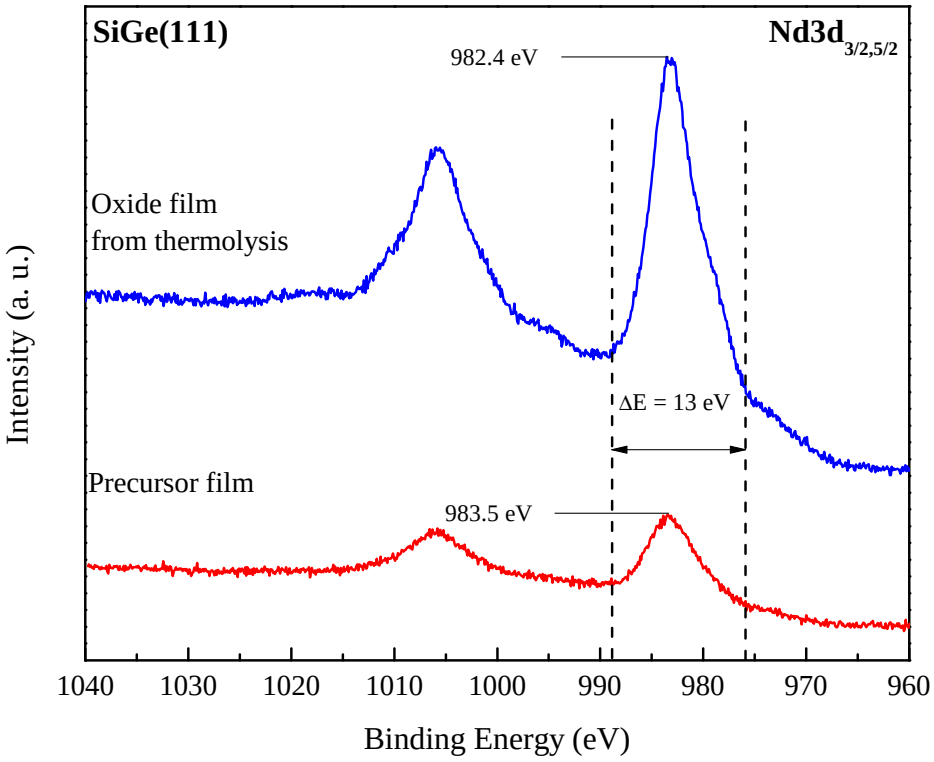


Figure 11.16.: *Nd3d* signal of the *Nd*-based precursor and oxide film from thermolysis, deposited from 0.005 M butanolic $Nd(NO_3)_3 \times 6H_2O$ precursor solution on *SiGe(111)*, measured with Mg-K_α. Marked are the peak maxima and the peak width.

It can be seen that again a decreased intensity for the precursor film is detected (ratio 2.5:1). As for the other substrate types, the detected peak maxima, show a good agreement with the data detected for the pure powders. A binding energy of 983.5 eV could be detected for the nitrate-hydrate and the oxide film from thermolysis exhibits the typical peak position for *Nd3d* resulting from *Nd* in Nd_2O_3 at 982.4 eV (s. table 9.7.).

As for the films on *Si*, a peak width of 13 eV is observed in agreement with the powder data.

11.4.2. The *Si2p Ge3d* and *O1s* Signal

The detail spectra of the *Si2p* and *Ge3d* signals are shown in figure 11.17.

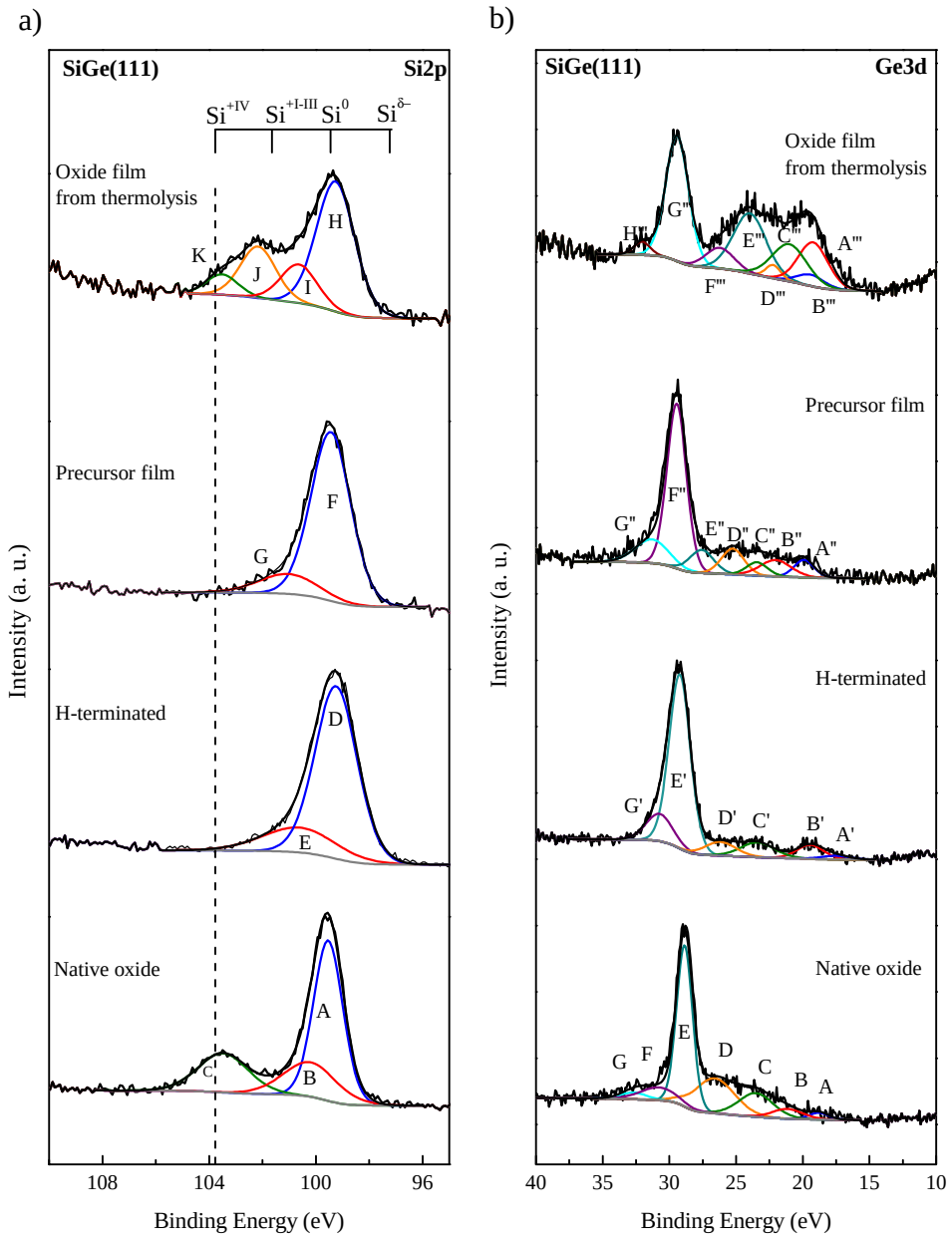


Figure 11.17.: *Si2p*(a) and and *Ge3ds* (b) detail spectra measured with Al-K_α of the native oxidized, *H*-terminated *SiGe(111)* surfaces and the respective *Nd*-based precursor films and oxide films from thermolysis deposited from 0.005 M butanolic $Nd(NO_3)_3 \times 6H_2O$ precursor solution.

The respective peak fit parameters and peak positions are summarized in table 11.9.

Table 11.9.: Peak fit parameters and peak positions in eV for the *Si2p* signal of the *Nd*-based films on *SiGe(111)* substrates.

Comp.	Pos.	FWHM	Area %	GL	Literature[207]
Native Oxide				Region: 107.2 - 96.1 eV	
A	99.5	1.3	56.1	80/20	99.2 Si^{0}
B	100.3	2.2	20.4	80/20	100.2 Si^{+I}
C	103.5	2.2	23.5	80/20	103.5 Si^{+IV}
H-Terminated				Region: 105.8 - 94.1 eV	
D	99.2	1.9	79.9	80/20	Si^{0}
E	100.6	3.2	20.1	80/20	Si^{+I}
Precursor Film				Region: 105.8 - 95.8 eV	
F	99.5	1.7	85.2	80/20	Si^{0}
G	101.0	2.6	14.8	80/20	Si^{+I}
Oxide Film from Thermolysis				Region: 104.8 - 95.7 eV	
H	99.3	1.7	56.1	80/20	Si^{0}
I	100.5	1.6	15.9	80/20	Si^{+I}
J	102.2	1.6	20.8	80/20	101.9 $Si^{+II/+III}$
K	103.5	1.4	7.3	80/20	Si^{+IV}

As summarized in table 11.9.a, the native oxidized samples of the *SiGe(111)* exhibit the same signal structure as it has been observed for the pure *Si(111)* and *Si(100)* substrates. A characteristic peak at 103.5 eV (C in figure 11.17.a) can be assigned to Si^{+IV} whereas the main signal of Si^{0} can be detected at 99.5 eV (signal A in figure 11.17.a). Again, a shoulder resulting from SiO_x species can be observed at 100.3 eV (signal B in figure 11.17.a). After the HF oxide strip, the characteristic peak for Si^{+IV} is not detectable. A signal broadening is caused by the δ^{-} charged Si surface atoms due to the relatively electropositive binding partner H as discussed for the *Si(100)* substrates.

The deposition of the precursor film leads likewise not to a destabilization of the Si passivation and no reoxidation of the Si is observable after the precursor film deposition, as only signals of Si^{0} and Si^{+I} can be observed (signals F and G in figure 11.17.a).

Differing from the previous results, the *Si* passivation is not stable. After the decomposition, the oxide, which is clearly observable from the *Si2p* structure as significant side signals, arise at binding energies characteristic for *Si* in higher oxidation states. Species of Si^{+I} (100.5 eV, signal I in figure 11.17.a), $Si^{+II/III}$ (102.2 eV, signal J in figure 11.17.a) and Si^{+IV} (103.5 eV, signal K in figure 11.17.a) could be identified, indicating a strong surface reaction during the precursor thermolysis to the oxide.

The peak positions and area ratios of the satellite signals of the *Ge3d* signals have been fitted according to the parameters listed in table 2.1.

Table 11.10.: Peak fit parameters and peak positions in eV for the *Ge3d* signal of the *SiGe(111)* substrates measured with Al-K_α .

Comp.	Pos.	FWHM	Area %	GL	Literature
Native Oxide				Region: 40.1 - 15.6 eV	
A	18.8	1.8	2.3	80/20	X-ray satellite of Ge^0
B	21.1	2.7	5.1	80/20	X-ray satellite of Ge^{+IV}
C	23.5	3.1	14.1	80/20	*O2s*
D	26.6	3.5	23.7	80/20	*O2s*
E	28.8	1.4	43.9	80/20	*Ge3d* 29.1 Ge^0 [219]
F	30.8	3.2	8.0	80/20	shake off satellite of E
					Ge3d suboxides of Ge [219]
G	32.6	2.3	2.9	80/20	*Ge3d* 32.5 Ge^{+IV} [219]
H-Terminated				Region: 37.6 - 14.6 eV	
A′	17.5	2.5	1.8	80/20	-
B′	19.4	2.4	6.4	80/20	X-ray satellite of E′
C′	23.4	3.0	8.6	80/20	*O2s*
D′	26.2	2.7	7.3	80/20	*O2s*
E′	29.2	1.9	63.3	80/20	*Ge3d* 29.1 Ge^0 [219]
F′	30.8	2.3	12.6	80/20	shake off satellite of E’
					Ge3d suboxides of Ge [219]
Precursor Film				Region: 37.3 - 15.2 eV	
A″	19.9	1.8	5.6	80/20	X-ray satellite of F″
B″	22.0	2.7	8.1	80/20	*O2s*
C″	23.4	1.9	4.6	80/20	*O2s*
D″	25.3	2.0	9.4	80/20	*O2s*
E″	27.6	2.1	9.0	80/20	*O2s*
F″	29.5	1.7	50.7	80/20	*Ge3d* 29.1 Ge^0 [219]
G″	31.3	3.0	12.7	80/20	shake off satellite of F″
					Ge3d suboxides of Ge [219]
Oxide Film from Thermolysis				Region: 35.5 - 14.1 eV	
A‴	19.2	2.6	15.0	80/20	-
B‴	19.4	2.4	3.6	80/20	X-ray satellite of G‴
C‴	21.0	3.1	14.9	80/20	*O2s*
D‴	22.2	1.3	2.3	80/20	*O2s*
E‴	24.0	2.9	22.6	80/20	*O2s*
F‴	26.2	2.5	6.7	80/20	*O2s*
G‴	29.4	2.0	32.6	80/20	*Ge3d* 29.1 Ge^0 [219]
H‴	32.1	1.4	2.4	80/20	*Ge3d* 32.5 Ge^{+IV} [219]
					shake off satellite of G‴

Native oxidized *SiGe(111)* samples exhibit seven characteristic signals in the measured region from 38 to 15 eV. GeO_2 causes a major signal at 32.6 eV (signal G in figure 11.17.b) in agreement with[219], exhibiting a characteristic X-Ray satellite at 21.1 eV (signal B in figure 11.17.b). As for pure *Ge*, the same peak structure can be detected for Ge^0 (main signal E at 28.8 eV in figure 11.17.) from the underlying substrate, showing an X-ray satellite at 18.8 eV (A). From literature[219], Ge^0 is characteristically detected at 29.1 eV. Signal D and E in figure 11.17.b can be assigned to *O2s* peaks, resulting from the suboxide and dioxide, which has been confirmed by two detected species from the *O1s* signal (s. figure 11.18.). For the reasons mentioned above no further specification should be done at this point. Signal signal F′ in figure 11.17.b detected at 30.8 eV can be assigned to a shake off satellite of Ge^0 or mentioned suboxide species of *Ge*. Whereby the amount of the oxydic *Ge* component is obviously drastically reduced compared to the pure *Ge* substrates. The signal shows a relative area of 2.9 %, whereas for pure *Ge(100)*, the amount could be measured as 49.7 %, which indicates that the main surface oxides are based on the integrated *Si* atoms within the atom collective.

After the deposition of the precursor film, no significant changes can be detected in the *Ge3d* signals structure, as it has been observed for pure *Si* and *Ge* substrates, indicating no chemical reaction after the film deposition. The number of detected *O2s* signals increases, which is expected due to the additional nitrate and water species on top of the surface. Signals A″, B″, F″ and G‴ are in a close agreement with A′, B′, E′ and F′ in figure 11.17.b.

The decomposition to the Nd_2O_3 leads besides the strong reoxidation of the *Si* species to a reoxidation to GeO_2 of the incorporated *Ge* in the *SiGe(111)* substrates, as signal H‴ in figure 11.17.b. is detected at the respective characteristic peak position for $Ge{+}IV$. Signals B‴, G‴ and H‴ in figure 11.17.b are in agreement with the data for the *HF* treated sample. The increasing peak intensity, which is observed at lower binding energies after the decomposition to the oxide film, can be explained by the higher amount of oxide species on the surface, as besides the formed oxide species, a reoxidation of the *Si* occurs according to the analyzed *Si2p* spectra in 11.4.2.

In order to achieve a more detailed view of the present oxygen species, the analysis of the *O1s* signal is essential the respective data curves are illustrated in figure 11.18. The peak fit data are summarized in table 11.11.

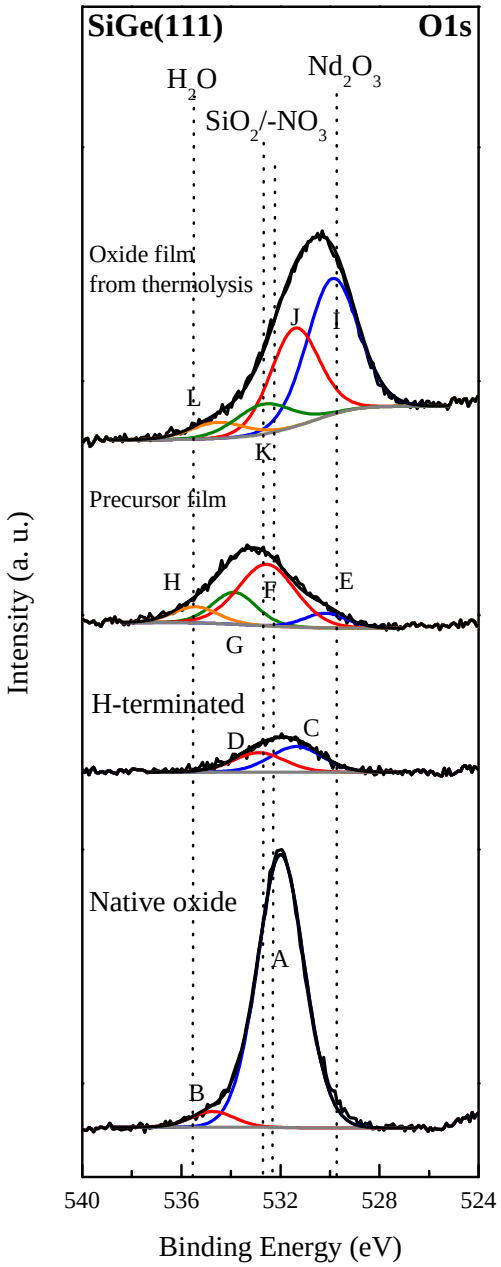


Figure 11.18.: *O1s* detail spectra measured with Mg-K_α of the native oxidized, *H*-terminated *SiGe(111)* surfaces and the respective *Nd*-based precursor films and oxide films from thermolysis deposited from 0.005 M butanolic $Nd(NO_3)_3 \times 6H_2O$ precursor solution.

Table 11.11.: Peak fit parameters and peak positions in eV for the *O1s* signal of the *Nd*-based films on *SiGe(111)* substrates.

Comp.	Pos.	FWHM	Area %	GL	Literature
Native Oxide				Region: 538.8 - 526.5 eV	
A	532.0	2.2	95.0	80/20	532.5 SiO_2/GeO_2
B	534.7	2.0	5.0	80/20	H_2O[209], ice on Re[210]
H-Terminated				Region: 537.5 - 527.0 eV	
C	531.5	2.5	57.1	80/20	suboxides/GeO_2[198][220]
D	532.9	2.5	42.9	80/20	suboxides/SiO_2[215]
Precursor Film				Region: 539.1 - 527.7 eV	
F	530.2	2.0	10.0	80/20	suboxides
G	532.5	2.7	56.2	80/20	532.7 $Ba(NO_3)_2$[199]
H	533.9	2.1	22.3	80/20	533.3 crystal H_2O[198]
I	535.4	2.1	11.5	80/20	loosely bound H_2O
Oxide Film from Thermolysis				Region: 538.9 - 525.2 eV	
J	529.9	2.4	48.6	80/20	Nd_2O_3[197]
K	531.4	2.3	33.5	80/20	suboxides Ge_xO_y[198][220] SiO_2[215]
L	532.7	2.7	11.7	80/20	suboxides of Ge[198][220] SiO_2[215] $Ba(NO_3)_2$[199]
M	534.5	2.6	6.1	80/20	loosely bound H_2O

A detailed peak fitting of the *O1s* signals, resulting from the native oxidized *SiGe(111)* surface, shows characteristic signals of Ge^{+IV} and Si^{+IV} at 532.0 eV (signal A in figure 11.18) and adsorbed water species at 534.7 eV (signal B in figure 11.18). After the oxide strip, remaining oxide species of *Ge* and *Si* can be detected (signal C and D in figure 11.18) in agreement with the data presented on *Si* and *Ge*. As it has been observed for all previous samples, the deposited precursor film exhibits the characteristic signal of *O1s* in nitrates (signal G in figure 11.18.) and crystal water (signal H in figure 11.17.b) with an area ratio of 2.5:1, indicating a high amount of desorbing water species, due to the deviation from the theoretically calculated value of 1.5:1. The signal I, detected at 535.4 eV, can be assigned to loosely bound surface H_2O. After the decomposition, the formation of Nd_2O_3 can be confirmed by the detection of signal J at 529.9 eV in agreement with[197]. The two signals detected at 531.4 eV and 532.7 eV can be assigned to oxides from *Ge* and *Si*, as indicated

by the *Si2p* and *Ge3d* signal. Surface top covering H_2O causes a signal at 534.5 eV, as observed for all other substrates.

11.5. Conclusion XPS Analysis

The shown XPS study of the different surface types illustrates that the oxide removal using HF and NH_4F solutions, according to the recipes explained in chapter 8, can be considered as successful. The analyzed *Si(111)*, *Si(100)*, *Ge(100)* and *SiGe(111)* are SiO_2 and GeO_2 free after the wet chemical etching, and H-terminated, passivated surfaces are generated.

From the XPS analysis it was possible to clearly identify surface species of the nitrate-hydrate after deposition and the oxide after decomposition according to the peak position of the *O1s*, *La3d* and *Nd3d* signal for all subrates types investigated. Thus, it can be concluded that during precursor thermolysis the targeted REO is formed from the nitrate based precursors.

La-based films showed a differing *La3d* signal structure compared to the results of the nitrate and oxide powders, discussed in section 9.2. This is explained by a possible influence of the substrate/film interaction on the spin-spin interaction within the *4f* orbitals. The detected structure of the *Nd3d* signal was congruent with the data discussed for the *Nd*-powders, with respect to peak positions and peak width. Independently of the substrate type, a surface covering loosely bound water film could be detected as discussed for the *O1s* peak analysis. Decreased *RE3d* signal intensities prior to the decomposition process are explained by a shielding effect, caused by adsorbed water and carbon species, which is also observable from the survey spectra.

The investigation of varying substrate types enabled a comparison of the substrate dependent stability of the passivation due to the H-termination, which was supposed to be created by the wet chemical cleaning procedure. The stability of the passivation was expected to be the critical factor for a possible interfacial layer formation due to surface reactions or reoxidation processes. Furthermore, the investigation of the influence of the covering precursor and oxide film on the underlying substrate provides significant information about the bonding of the film and the film/substrate interacation.

Detailed discussions of the *Si2p* signals demonstrated that a difference in *Si(111)* and *Si(100)* could be detected after the precursor decomposition, as

a slight reoxidation of the *Si(100)* substrate is observable, whereas *Si(111)* remains completely passivated. The effect can be explained by the influence of the surface roughness and the available number of dangling bonds. *Si(100)* shows a larger number of dangling bonds and does not form an atomically smooth *H-Si* surface after oxide removal, which opens the opportunity for an easier reoxidation of the surface compared to the atomically smooth *H-Si(111)* (s. chapter 10.). After the *HF* cleaning procedure of *Ge(100)* and *SiGe(111)*, no indication of Ge^{+IV}, but as for *Si* a slight indication of remaining suboxides was observable, which allows the conclusion of a successful passivation after the wet chemical cleaning procedure.

The stability against an unwanted reoxidation during the precursor deposition and thermolysis is one of the most crucial issues for the final film quality in order to avoid unwanted interfacial layer formation. From the analysis it was shown that *Si(111)* substrates exhibited the most stable surface as no change in the structure of the *Si2p* signal was detected during the generation of the oxide film. For *Si(100)* a similar behavior could be observed, but with a rather slight indication of the formation of oxide species during the heat treatment for precursor decomposition. *Ge(100)* was expected to show a strong reoxidation, as it is known from literature that the passivation does not remain stable under ambient conditions or during surface covering reactions. For the present case only a weak reoxidation to a larger amount *Ge* suboxide species was observable both for the pure *Ge(100)* and the *SiGe(111)* substrates after the precursor deposition. After precursor thermolysis no changes occurred in the *Ge3d* signal of the pure *Ge(100)* substrates which allows to anticipate a relatively stable substrate/oxide combination and a rather low influence of the oxide formation on the underlying substrate. *SiGe(111)* substrates showed a deviating individual behavior. According to the *Si2p*, *Ge3d* and *O1s* signal, a strong reoxidation of the *Si* to Si^{+IV} and a slight reoxidation to Ge^{+IV} occurs, which is obviously caused by the incorporation of the *Ge* atoms into the *Si* lattice. This might be explained by a lesser passivation after the *HF* treatment due to the material mixture of *Ge* and *Si* and the oxygen, available within the lattice due to the high reoxidation tendency of *Ge*.

The results achieved allow the conclusion that the precursor deposition has no or a very low influence on the underlying substrate and no reoxidation to the unwanted dioxides occurs for all tested substrate types. After the precursor thermolysis at 770 K (*La*) and 750 K (*Nd*) *Si(111)*, and *Ge(100)* does not show

a reoxidation according to the detected stable signals of *Si* and *Ge*, so that it can be concluded that the passivation of the substrates remains active during the thermolysis process and the formed oxides do not react with the underlying substrate under the mild decomposition conditions. For *Si(100)* the observed reoxidation was not significant, but however present. The situation is very different for the *SiGe(111)* substrates. Both for *Si* and for *Ge* characteristic signals of Si^{+IV} and Ge^{+IV} can be observed and therefore mixed and interfacial species are formed in conjunction with the REO formation. *SiGe(111)* substrates obviously do not offer the main advantage of an avoidance of interfacial reactions. The significance in terms of the final electrical performance needs to be investigated by an electrical characterization of the films as its was discussed that interfacial layers can both promote or worsen the electrical performances.

Exemplary studies on the thermal stability of *La*-based films showed that annealing up to 1073 K does not lead to the formation of silicides or unwanted reoxidation at the *REO/Si* interface. However, a change in the oxygen species is observable. In agreement with reported thermodynamic data[97], heating temperatures of 1273 k resulted in a change of the toplayer composition from the La_2O_3 to silicides or silicates. Ono et al. describe a dependency of the ionic size and the tendency of silicide formation.[216] As a result, larger ions showed a larger tendency of *LnSiO* formation, explained by the decreased steric interference for larger ions and an easier *Si* diffusion into the film. As *Nd* exhibits a smaller ionic radius, it is expected to show an even lower tendency of interfacial reactions. Further studies on the effect of different annealing temperatures and conditions need to be carried out in the future. These findings are in agreement with the determined changes in the film roughness presented in chapter 10, which might be caused by a reoxidation of the substrate due to desorption of the passivating *H*-termination during the heating process to 1073 K, resulting in an inhomogeneous uncontrolled, unwanted multi layer formation.

It has been shown, according to exemplary analysis of the carbon content, that the films, after the precursor decomposition, can considered to be carbon free within the detection limits of XPS. For a more detailed study, depth profiling via ToF-SIMS (Time of Flight Secondary Ion Mass Spectroscopy) is necessary.

As a key result it can be concluded that, with the wet chemical dip-coat, a free hovering salt like precursor layer is formed prior to the thermolysis to the oxide on *Si(111)*, *Si(100)*, *Ge(100)* and *SiGe(111)*. During thermolysis

the formed oxide films do not react with the underlying *Si(111)* and *Ge(100)* substrate. From the signal detected it can be concluded that no unwanted reoxidation or silicide formation on the substrates occurs. This is a major difference compared to conventional used thin film deposition techniques, as the substrate remains untouched and passivated. For *Si(100)* and *SiGe(111)* the passivation is not reliable, which can be concluded from detected signals indicating a reoxidation.The reoxidation for *Si(100)* is rather low compared to *SiGe(111)*.The within the detection limit of XPS, carbon free films are thermally stable up to temperatures above 1073 K.

Characteristic changes within the electrical performance are expected due to the findings from the XPS analysis. A detailed electrical analysis will be shown in the following chapter.

12. Electrical Characterization

The investigation of the final electrical performance of the generated films is one of the most essential steps within the characterization process to evaluate the quality of the films, regarding the possible potential of the invented deposition technique for future CMOS gate oxide replacement processing.

In the following, the C-V and I-V curves will be presented and analyzed regarding the κ values, respective EOTs and leakage current densities. The biasing during C-V analysis has been adjusted regarding threshold voltage of the respective samples. First in-depth studies of the leakage current conduction mechanism will be shown by measuring the leakage currents over increasing temperatures.

Different types of samples have been prepared for electrical analysis. The results will be shown and discussed after a short introduction about the experimental application (s. section 12.1.) of the electrical characterizing equations, which have been introduced in section 3.1.1., 3.2. and 3.2.4. and the MOS capacitor fabrication (s. section 12.2.). Detailed analysis of the Nd_2O_3 films on pure Si substrates (p-*Si(100)* and n-*Si(111)*) will be shown in section 12.3. Data for the films deposited from 0.001 M, 0.005 M and 0.01 M $Nd(NO_3)_3 \times 6H_2O$ precursor solution are available. La_2O_3 films have not been investigated with respect to the electrical performance due to their high hygroscopicity, as the measurements were done under ambient conditions.

Besides the results of the oxide films from precursor thermolysis, the annealing effects are studied by showing results of samples which have been annealed at 673 K, and 1073 K for 1 h in N_2 flow. Based on the achieved results during the measurement, additionally annealing at 873 K has been performed for the films deposited from the 0.005 M precursor solution.

Temperature dependent I-V measurements have been performed only for the films deposited from 0.005 M $Nd(NO_3)_3 \times 6H_2O$ butanolic precursor solution and are discussed with respect to detected tendencies within the measured temperature region.

Finally results of the alternative substrates, n-*Ge(100)* and p-*SiGe(111)*, should be elucidated in section 12.4. Films on p-*SiGe(111)* and n-*Ge(100)* substrates

have been analyzed using 0.005 M $Nd(NO_3)_3 \times 6H_2O$ butanolic precursor solution. The samples have been annealed at 673 K for n-*Ge(100)* and for *p-SiGe(111)* at 673 K, 873 K and 1073 K.

As for the electrical analysis the doping is essential for the detected data the doping types are included in the sample nomenclature for the electrical characterization experiments.

12.1. Electrical Properties: Experimental Part

The C-V measurements have been performed in the low frequency region at 100 kHz and 1 MHz. Frequency dispersion and hysteresis behavior allow to draw utilizable conclusions about the existence and typification of present traps and charges within the deposited dielectrics. κ values can be calculated from the measured capacitance in accumulation, typically at 100 kHz after transforming equation 1.1 into:

$$\kappa = \frac{Cd}{A\epsilon_0} \tag{12.1}$$

with $\epsilon_0 = 8.85418781762 \times 10^{-12}\ \frac{As}{Vm}$ and the electrode size $A = 270\ \mu m^2$.

The film thickness d, of the dielectric layer has been extracted from the HRTEM analysis in chapter 10. Respective EOT values can be calculated from equation 3.37.

Commonly leakage current values at ± 1 V at the off state side (positive for p-type substrates and negative for n-type) are compared in the literature, hence leakage current analyses are done for the samples at the negative bias for n-type substrates and positive voltage for p-type substrates, to determine the dominant leakage current conduction mechanism.

Possible detectable leakage current conduction mechanisms during temperature dependent measurements above 0 K are Poole-Frenkel and Schottky emission (s. section 3.2.4.), since those are the strongly temperature dependent leakage current components.

After transforming equations 3.33 and 3.34, the parameter dependencies for the Poole-Frenkel (field-enhanced thermal excitation of trapped electrons in the conduction band of insulators) and Schottky emission (thermionic effect

in which electrons are transported across the potential barrier at metal/oxide interface), can be written as:

Poole-Frenkel:

$$\ln(J_{PF}/E_{Ox}) = \left[\ln B - \frac{q\phi_B}{kT}\right] + \left[\frac{q\sqrt{\frac{q}{\pi\epsilon_0\epsilon_{Ox}}}}{kT}\right]\sqrt{E_{Ox}} \tag{12.2}$$

Schottky:

$$\ln(J_{SE}/E_{Ox}) = \left[\ln(AT^2) - \frac{q\phi_B}{kT}\right] + \left[\frac{\frac{1}{2}q\sqrt{\frac{q}{\pi\epsilon_0\epsilon_{Ox}}}}{kT}\right]\sqrt{E_{Ox}} - \ln E_{Ox} \tag{12.3}$$

with $q = 1.602176565\ \times 10^{-19}\ As$ and $k = 1.3806523\ \times 10^{-23} m^2 kg s^{-1} K^{-1}$.

It can be seen from equation 12.2 and 12.3 that both conduction mechanisms exhibit linear or approx. linear characteristics in $\ln(J/E)$ vs. $E^{1/2}$ plots as the term $-\ln E_{Ox}$ can be neglected for steep slopes and high electric fields.

The main difference between them are the slopes within the plots, which differ by a factor of two due to the interaction difference between carriers and traps. Poole-Frenkel mechanism shows a steeper slope because of the equal distance of escape from carriers to trapping centers. The two conduction mechanisms are related by the field lowering coefficient β[221] which can be written as:

$$\beta = \beta_{PF} = 2\beta_{SE} = \sqrt{\frac{q}{\pi\epsilon_0\epsilon_{Ox}}} \tag{12.4}$$

The field lowering coefficient β can be extracted from the slope x against q/kT as:

$$\beta = \frac{\text{x kT}}{q} \tag{12.5}$$

The calculated values for β from the graphically extracted slopes, can be compared with the theoretical values obtained from equation 12.4. For a precise analysis it has to be considered, that the theoretically calculated values are based on the accuracy of the determination of the ϵ_{Ox} from the C-V analysis.

As the generated films show a thickness of roughly 3 nm to 4 nm and the shown equations have only been proven for film thicknesses down to 6.5 nm, it has to be carefully considered that the expansion of the space charge region within the films might exceed the full film thickness in the present case and the leakage current conduction mechanism studies based on the literature known equations may lead to results which require further and more detailed investigations of the leakage current conduction mechanisms.

12.2. MOS Capacitor Fabrication

The experimental investigation of the electrical properties of the deposited films is realized by preparing a high quality MOS-Capacitor (s. section 3.1.1.).

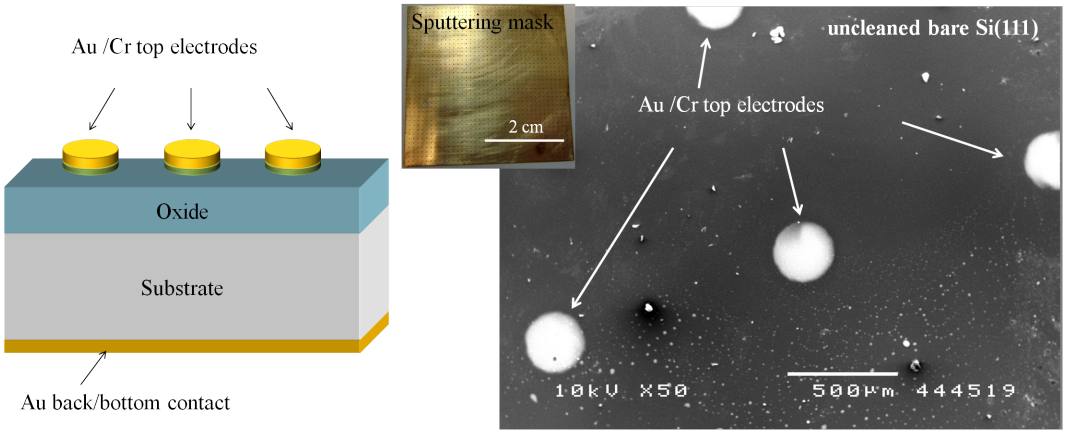


Figure 12.1.: Schematic MOS capacitor built by electrode deposition (size ratios are not in agreement with real samples) (left), photograph of the sputtering mask (middle), SEM image of the deposited electrodes confirming a diameter of 270 μm (right).

As the detected electrical behavior is sensitively dependent on the electrode quality the electrode deposition has been realized according to many years of extensive experience in semiconductor characterization in the group of Prof. Lee at the NTU Singapore.

Circular top and full covering bottom Au electrodes have been deposited on the substrate/thin film block. Due to a poor adhesion of Au on top of the REO, a Cr layer was integrated as adhesion promoter for top electrode deposition (s. figure 12.1).

The high quality top electrode deposition with a diameter of 270 μm (sputtering mask) has been conducted using a HV sputter coater at 10^{-6} mbar, depositing high purity (99.999 %) Cr (16 nm) as a contact layer between the REO and the Au electrode, followed by the 150 nm high purity Au deposition. As back contact, high purity Au (99.999 %) with a thickness of 300 nm was evaporated on the mechanically cleaned back of the sample with a sputter coater at 10^{-3} mbar to achieve good Ohmic contact behavior.

12.3. Silicon Substrates

In the following section, the results of the electrical characterization of Nd_2O_3 layers on n-*Si(111)* and p-*Si(100)* are shown and discussed. C-V analyses are shown in section 12.3.1., whereas I-V characteristics are illustrated in section 12.3.2., concluding with leakage current conduction mechanism studies in 12.3.3.

12.3.1. C-V Characteristics

Si(111)

Figures 12.2., 12.3. and 12.4. show the C-V curve data sets measured at 100 kHz and 1 MHz on the Nd_2O_3 films on n-*Si(111)*. 100 kHz is the typical frequency for the analysis of the κ values from the capacitance in accumulation. The influence of faster (1 MHz) excitations within the films reveals the appearance of slow traps and charges. The collected data are summarized in table 12.1.

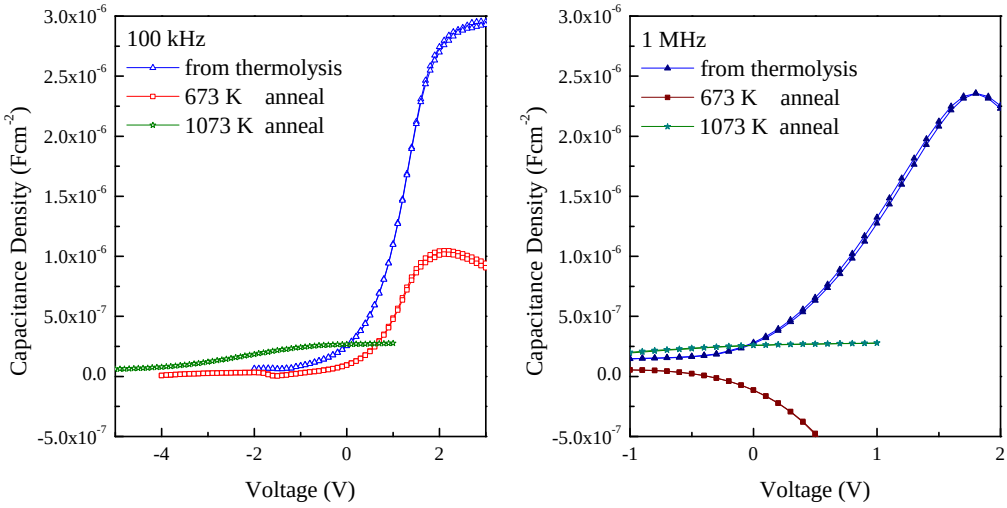


Figure 12.2.: C-V curves measured at 100 kHz (left) and 1 MHz (right) of the Nd_2O_3 films on n-*Si(111)*, generated from 0.01 M $Nd(NO_3) \times 6H_2O$ butanolic precursor solution. Shown are the analyses of the oxide from precursor thermolysis, at 673 K and 1073 K annealed samples.

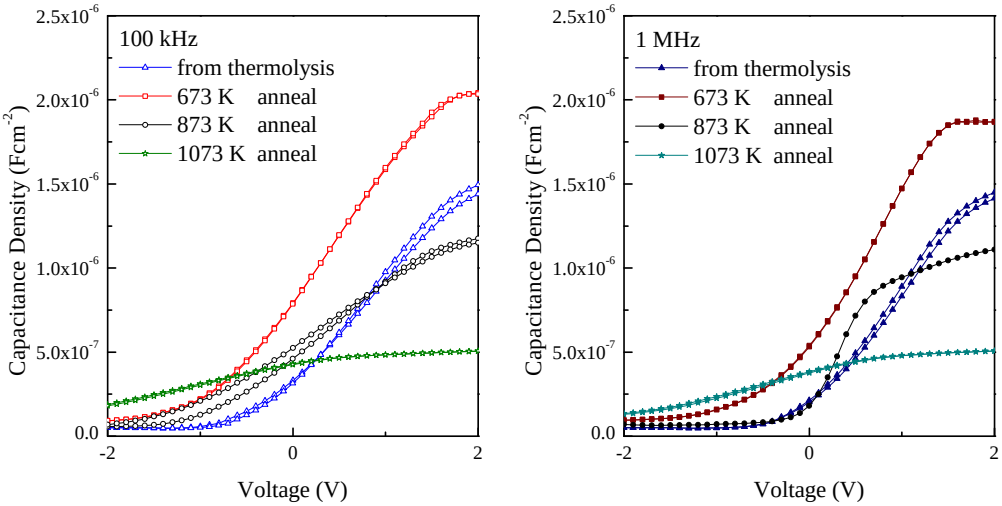


Figure 12.3.: C-V curves measured at 100 kHz (left) and 1 MHz (right) of the Nd_2O_3 films on n-*Si(111)*, generated from 0.005 M $Nd(NO_3) \times 6H_2O$ butanolic precursor solution. Shown are the analyses of the oxide from precursor thermolysis, at 673 K, 873 K and 1073 K annealed samples.

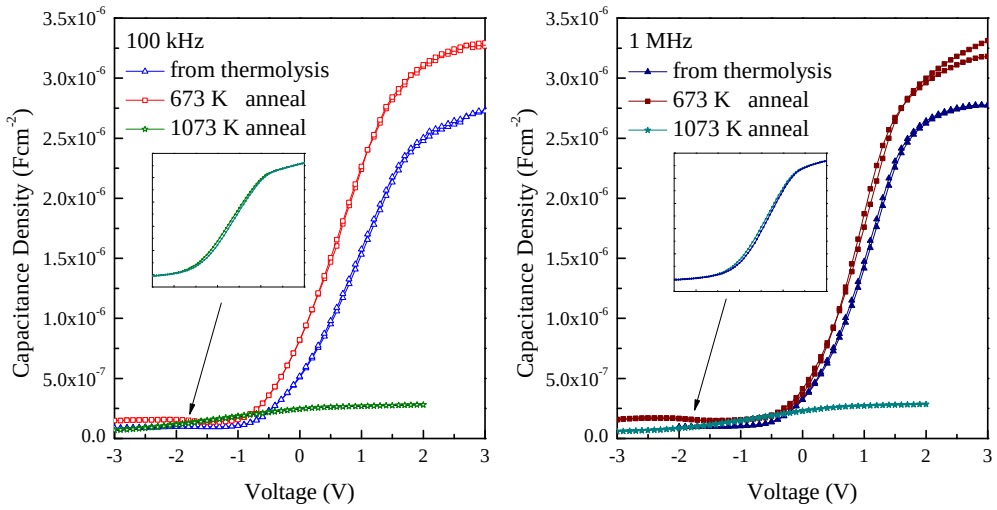


Figure 12.4.: C-V curves measured at 100 kHz (left) and 1 MHz (right) of the Nd_2O_3 films on n-*Si(111)*, generated from 0.001 M $Nd(NO_3) \times 6H_2O$ butanolic precursor solution. Shown are the analyses of the oxide from precursor thermolysis, at 673 K and 1073 K annealed samples.

All shown curves exhibit characteristic line shapes for typical C-V curves, showing a maximum of the capacitance at positive biasing, which is characteristic for n-type doped substrates. No hysteresis occurs for all samples, indicating a high quality of the deposited films. No significant differences in the final capacitance density in accumulation of the measurements at 1 MHz and 100 kHz is detected for each sample.

Capacity densities extracted from the measurements at 100 kHz shown in figure 12.2., 12.3. and 12.4. and the calculated κ and EOT values are shown in table 12.1. κ values have been calculated according to equation 1.1, taking the film thickness under consideration (compare chapter 10) and following from this the EOT after equation 3.37.

Table 12.1.: Summary of the extracted capacitance density values from the C-V measurements, calculated κ and EOT values for the Nd_2O_3/n-*Si(111)* samples.

Sample		**Capacitance Density** (Fcm^{-2})	κ	**EOT** (nm)
0.01 M	from therm.	2.93×10^{-6}	14.9	1.2
4.5 nm	673 K	1.05×10^{-6}	5.3	3.3
	1073 K	2.76×10^{-7}	1.4	12.5
0.005 M	from therm.	1.57×10^{-6}	6.6	2.2
3.7 nm	673 K	2.37×10^{-6}	9.9	1.5
	873 K	1.23×10^{-6}	5.1	2.8
	1073 K	5.06×10^{-7}	2.1	6.8
0.001 M	from therm.	2.73×10^{-6}	10.2	1.3
3.3 nm	673 K	3.31×10^{-6}	12.3	1.0
	1073 K	2.80×10^{-7}	1.0	12.3

In agreement with the previous topography and film thickness results, the structures deposited from 0.01 M precursor solution shows irregular behavior within the C-V analysis, which can especially be seen from the 1 MHz measurement for the 673 K annealed sample, exhibiting a theoretically impossible negative capacitance of the insulating layer which is probably a measurement artifact due to an extremely high leakage current of the device. Curves, detected from the oxide films after the precursor thermolysis, show a decrease of the capacitance density after reaching the maximum instead of a constant plateau, which results from increasing leakage currents and a subsequent collapse of the capacitance density. Films annealed at 1073 K, show a much lower capacitance density. The curve exhibits an increasing trend, but with a smoother slope, up to a maximum and constant capacitance density in accumulation.

Contrary to the film structures deposited from 0.01 M solution, 0.005 M and 0.001 M based films exhibit regular and repeatable electrical characteristics during C-V analysis in combination with a detectable constant maximum of capacitance density in accumulation.

0.005 M solution based films have been analyzed after annealing at three different temperatures and immediately after decomposition exhibiting different

final capacitance values. The resulting κ values could be calculated as 6.6 (from therm.), 9.9 (673 K), 5.1 (873 K) and 2.1 (1073 K). Respectively the EOT values are 2.2 nm (from therm.), 1.5 nm (673 K), 2.8 nm (873 K) and 6.8 (1073 K).

Two different annealing temperatures and the oxide films directly after the precursor thermolysis have been tested for films deposited from 0.001 M butanolic $Nd(NO_3)_3 \times 6H_2O$ precursor solution. Analogous κ values have been calculated as 10.2 (from therm.), 12.3 nm (673 K) and 1.0 (1073 K), thus the EOT values could be mentioned as 1.3 nm (from therm.), 1.0 nm (673 K) and 12.3 nm (1073 K).

For both concentrations it is notable that the capacitance increases for the 673 K annealed samples compared to the oxide from thermolysis and drops significantly after annealing up to 873 K. As for the 0.01 M solution a rapid decrease of the capacitance is observed in both cases for the films annealed at 1073 K.

Si(100)

Figures 12.5., 12.6. and 12.7. show the C-V curve data sets, measured at 100 kHz and 1 MHz of Nd_2O_3 films on p-*Si(100)*. As for the n-*Si(111)* substrates, two frequencies have been chosen to investigate the influence of 1 MHz treatment in order to show the appearance of slow traps and charges and metal insulator semiconductor structure formation (MIS, multi layer insulators from different materials) . The measured data are summarized in table 12.2.

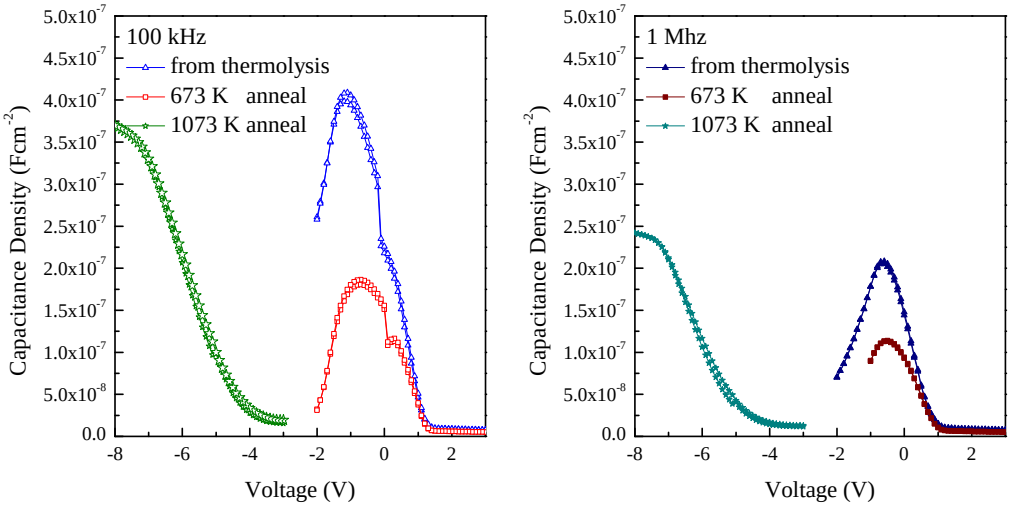


Figure 12.5.: C-V curves measured at 100 kHz (left) and 1 MHz (right) of the Nd_2O_3 films on p-*Si(100)*, generated from 0.01 M $Nd(NO_3) \times 6H_2O$ butanolic precursor solution. Shown are the analyses of the oxide from precursor thermolysis, at 673 K and 1073 K annealed samples.

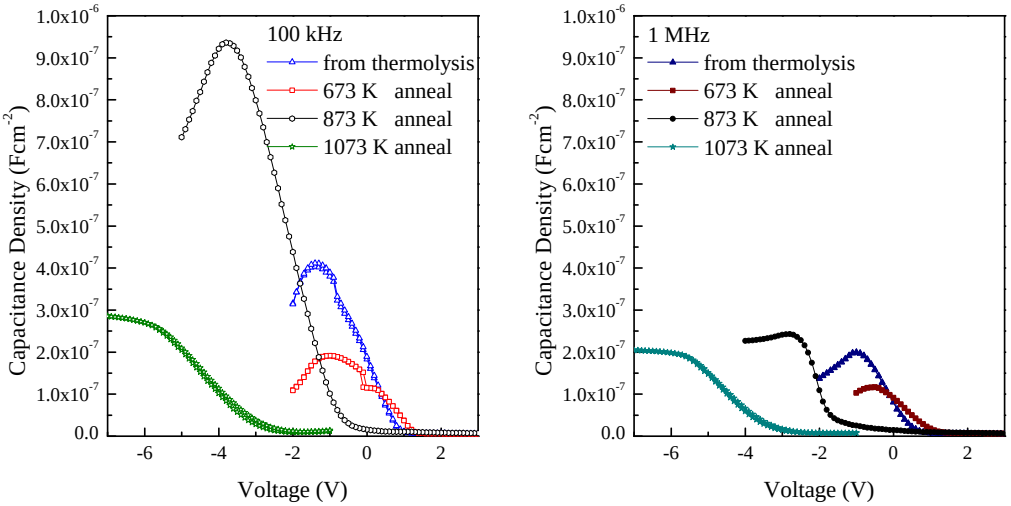


Figure 12.6.: C-V curves measured at 100 kHz (left) and 1 MHz (right) of the Nd_2O_3 films on p-*Si(100)*, generated from 0.005 M $Nd(NO_3) \times 6H_2O$ butanolic precursor solution. Shown are the analyses of the oxide from precursor thermolysis, at 673 K, 873 K and 1073 K annealed samples.

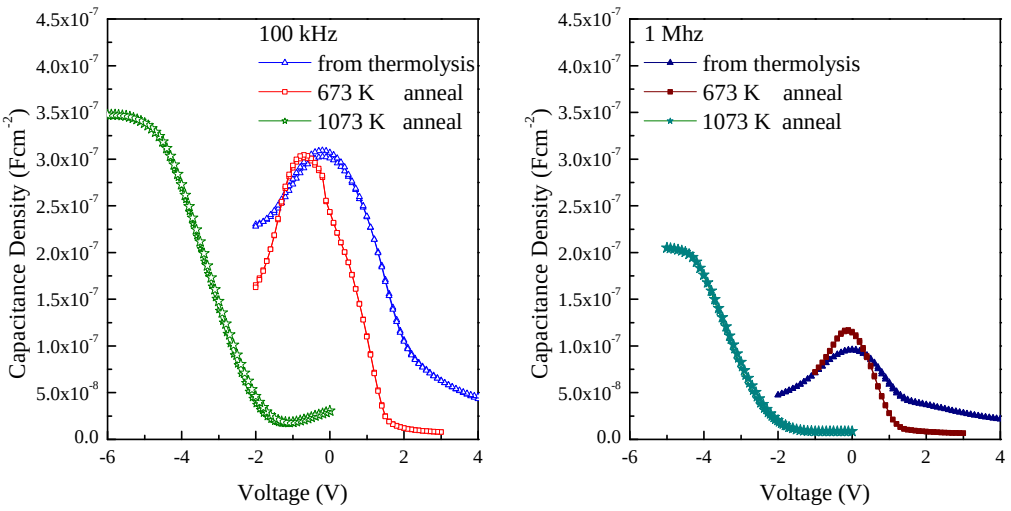


Figure 12.7.: C-V curves measured at 100 kHz (left) and 1 MHz (right) of the Nd_2O_3 films on p-*Si(100)*, generated from 0.001 M $Nd(NO_3) \times 6H_2O$ butanolic precursor solution. Shown are the analyses of the oxide from precursor thermolysis, at 673 K and 1073 K annealed samples.

As well as observed for n-*Si(111)*, all curves exhibit characteristic line shapes for typical C-V curves, but as p-type substrates have been measured, the maximum of the accumulation capacitance density occurs at negative biasing. As well as for the n-*Si(111)* substrates, no hysteresis can be observed for all samples. All curves show a steep drop of the capacitance density after reaching a maximum in capacitance density, except for the data of the samples which have been annealed at 1073 K . This indicates highly leaky structures, since no charge accumulation is possible up to a saturation limit. Additionally, the curves of the films deposited from 0.01 M and 0.005 M precursor solution show severe humps at high voltage stressing and samples prepared from all precursor solution concentrations exhibit a drastically reduced maximum of capacitance density during 1 MHz biasing compared to the 100 kHz.

Values for the respective film thickness, can again be extracted from chapter 10.

Capacity densities detected from the 100 kHz measurements in figure 12.5., 12.6. and 12.7. The calculated κ and EOT values are shown in table 12.1. and discussed below.

Table 12.2.: Summary of the extracted capacitance density values, calculated κ and EOT values for the $Nd_2O_3/Si(100)$ samples.

Sample		**Capacitance Density** (Fcm^{-2})	κ	**EOT** (nm)
0.01 M	from therm.	4.08×10^{-7}	2.1	8.4
4.5 nm	673 K	1.06×10^{-7}	0.9	18.6
	1073 K	3.72×10^{-7}	1.9	9.3
0.005 M	from therm.	4.11×10^{-7}	1.7	8.4
3.7 nm	673 K	1.91×10^{-7}	0.8	18.1
	873 K	9.36×10^{-7}	3.9	3.7
	1073 K	2.86×10^{-7}	1.2	12.1
0.001 M	from therm.	3.09×10^{-7}	1.2	11.2
3.3 nm	673 K	3.05×10^{-7}	1.1	11.3
	1073 K	3.48×10^{-7}	1.3	9.9

All solution concentration show a similar behavior on p-$Si(100)$ substrates. Thus, the dielectric constants are all within the same range between 0.8 and 2.1. The respective EOT values vary from 3.7 to 18.6 nm. As expected, the results from the 0.01 M solution are hardly repeatable and the humps within the curves are the largest, compared to the films from the 0.005 M and 0.001 M solution concentrations.

An outlier was detected for the 873 K additional annealing step on the Nd_2O_3 films deposited from 0.005 M $Nd(NO_3) \times 6H_2O$ butanolic precursor solution, showing an increased κ value of 3.9. Samples which have been annealed at 1073 K show a different behavior and low but rather constant capacitances in accumulation can be observed for all solution concentrations.

The flat band voltage of the samples annealed at 1073 K is significantly shifted to negative voltage, interfering that a different amount of positive charges is present within this case.[222]

12.3.2. I-V Characteristics

As the leakage current densities are the critical variables besides the κ values to estimate the performance of the deposited films with respect to their potential application as alternative gate oxides for microelectronic devices, in the following I-V analyses of the n-*Si(111)* and p-*Si(100)* substrates coated with a single layer of Nd_2O_3 are shown.

Leakage current densities measured from -1 to +1 V, depending on the solution concentration and annealing temperature are presented.

Si(111)

Figures 12.8., 12.9. and 12.10. show the measured I-V curves of the films deposited from 0.01 M (figure 12.8.), 0.005 M ((figure 12.9.) and 0.001 M (figure 12.10.) concentrated $Nd(NO_3) \times 6H_2O$ butanolic precursor solution measured at 298 K.

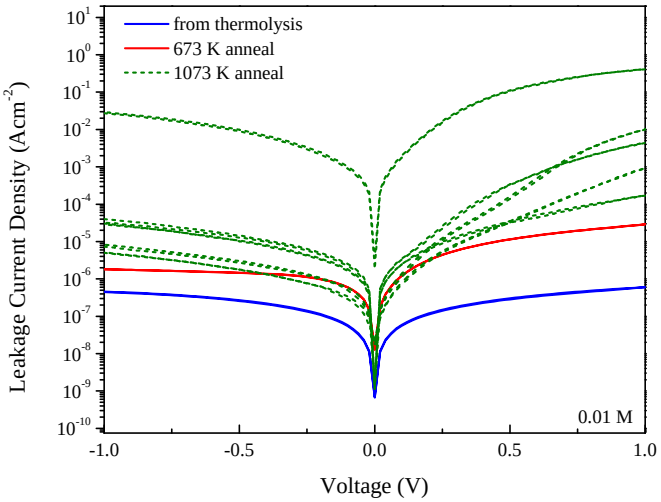


Figure 12.8.: I-V curves of the films deposited on n-*Si(111)* from 0.01 M $Nd(NO_3)\times 6H_2O$ butanolic precursor solution. Shown are curves of the oxide from precursor thermolysis, at 673 K and 1073 K annealed samples. Multiple curve shapes of the samples annealed at 1073 K have been detected.

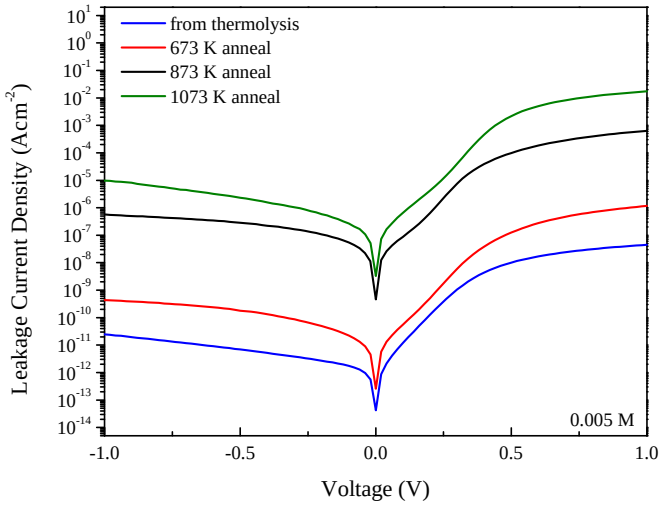


Figure 12.9.: I-V curves of the films deposited on n-*Si(111)* from 0.005 M $Nd(NO_3)\times 6H_2O$ butanolic precursor solution. Shown are curves of the oxide from precursor thermolysis, at 673 K, 873 K and 1073 K annealed samples.

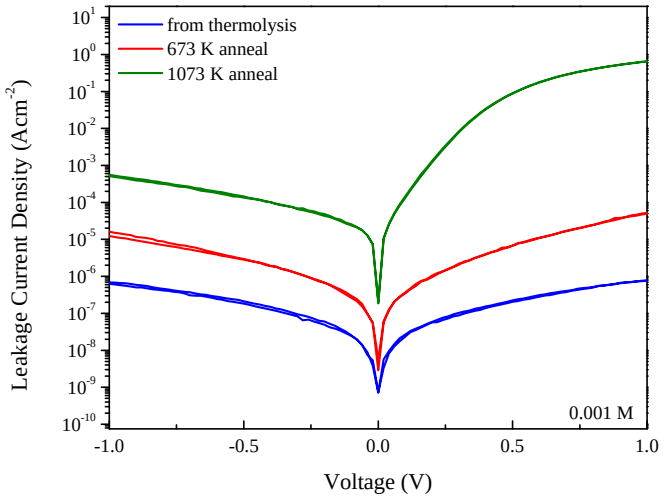


Figure 12.10.: I-V curves of the films deposited on n-*Si(111)* from 0.001 M $Nd(NO_3) \times 6H_2O$ butanolic precursor solution. Shown are curves of the oxide from precursor thermolysis, at 673 K and 1073 K annealed samples.

All measured curves exhibit a typical asymmetric shape for p-type doping with an increased maximum leakage current value at positive biasing. The measured off state leakage currents, measured at -1 V biasing are summarized in table 12.3.

Table 12.3.: Off state leakage current densities measured at -1 V for the Nd_2O_3 films deposited on n-*Si(111)*.

Leakage current (Acm^{-2})	**0.01 M**	**0.005 M**	**0.001 M**
from therm.	4.44×10^{-7}	2.47×10^{-11}	6.89×10^{-7}
673 K	1.80×10^{-6}	4.36×10^{-10}	1.61×10^{-5}
873 K	-	5.70×10^{-7}	-
1073 K	distribution	9.79×10^{-6}	5.17×10^{-4}

Leakage current densities within the range of 10^{-4} down to 10^{-11} Acm^{-2} could be detected. For all solution concentrations the leakage current density increases with the annealing temperature. Films deposited from different solution concentrations show different behavior and significantly different leakage current densities.

The best results have been observed for films deposited from 0.005 M precursor solution. For the oxide films from thermolysis, leakage currents down to 2.47×10^{-11} Acm^{-2} have been observed, which increased roughly three orders of magnitude per annealing step up to 9.79×10^{-6} Acm^{-2} for the samples, which have been annealed at 1073 K. 0.001 M precursor solutions lead to leakage current values of the film down to 6.89×10^{-7} Acm^{-2} for the oxide films from thermolysis increasing for higher annealing temperatures up to 5.17×10^{-4} Acm^{-2} for the samples annealed at 1073 K.

As for the film topography and C-V measurements, structures deposited from 0.01 M precursor solution are critical to analyze, since the results are unreliable due to instabilities and varying detected values during the measurements. Especially for the samples, which have been annealed at 1073 K, no specific leakage current value could be extracted due to a broad distribution of the measured curves.

Nevertheless, the lowest detected leakage current was achieved for the oxide films from thermolysis, like for the films deposited from 0.001 M and 0.005 M solution, exhibiting a value of 4.47×10^{-7} Acm^{-2}, clearly increasing for higher annealing temperatures.

Si(100)

Figures 12.11., 12.12. and 12.13. show the measured I-V curves of the films deposited from 0.01 M, 0.005 M and 0.001 M $Nd(NO_3) \times 6H_2O$ butanolic precursor solution on p-*Si(100)* substrates. According to the relatively low κ values and the drop in the capacitance in accumulation detected from the C-V analysis, much higher leakage current densities compared to the n-*Si(111)* substrates are expected for the p-*Si(100)* substrates, as severe humps and no charge accumulation have been observed from the C-V curves.

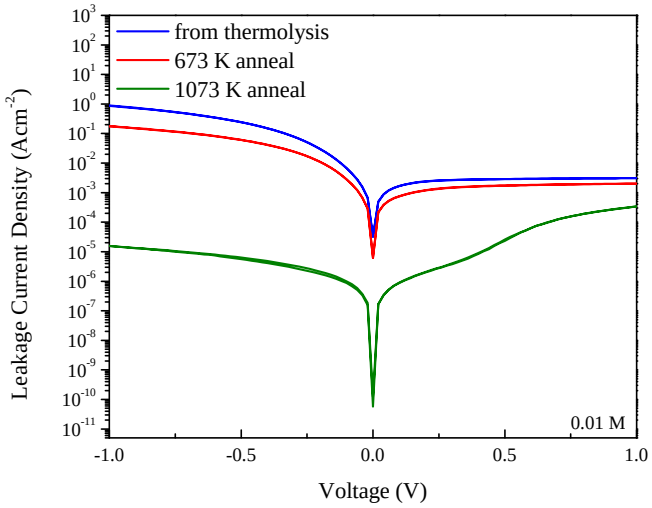


Figure 12.11.: I-V curves of the films deposited on p-*Si(100)* from 0.01 M $Nd(NO_3) \times 6H_2O$ butanolic precursor solution. Shown are curves of the oxide from precursor thermolysis, at 673 K and 1073 K annealed samples.

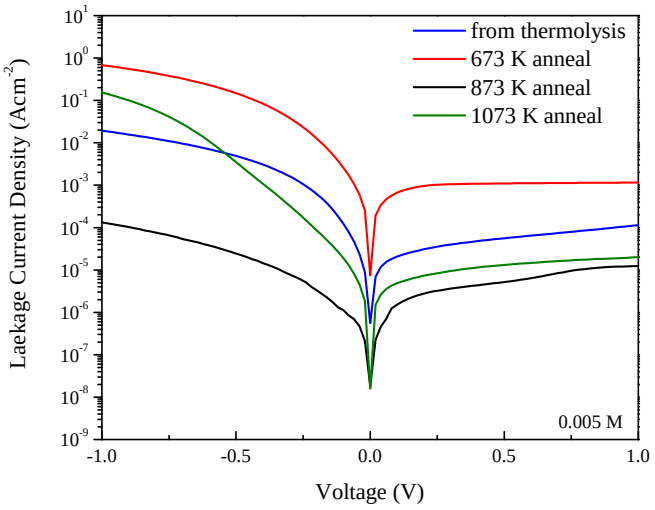


Figure 12.12.: I-V curves of the films deposited on p-*Si(100)* from 0.005 M $Nd(NO_3) \times 6H_2O$ butanolic precursor solution. Shown are curves of the oxide from precursor thermolysis, at 673 K, 873 K and 1073 K annealed samples.

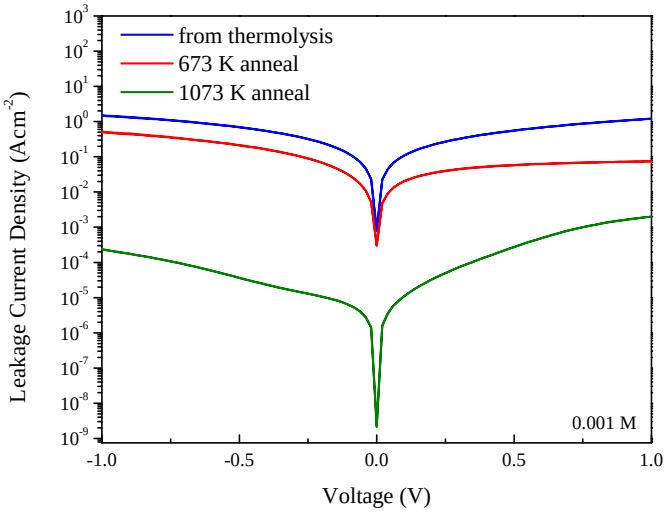


Figure 12.13.: I-V curves of the films deposited on p-*Si(100)* from 0.001 M $Nd(NO_3) \times 6H_2O$ butanolic precursor solution. Shown are curves of the oxide from precursor thermolysis, at 673 K and 1073 K annealed samples.

All measured curves exhibit an asymmetric shape, but not constantly with a typical progression for p-type doping. Most of the curves show, as expected, an increased maximum leakage current value at negative biasing. The I-V characteristics measured from the 0.001 M solution based films annealed at 1073 K exhibit line shapes, which are different from the expectations with a maximum of the leakage current density at positive biasing.

The measured off state leakage currents measured at +1 V biasing are summarized in table 12.4.

Table 12.4.: Off state leakage current densities measured at -1 V for the the Nd_2O_3 films deposited on p-*Si(100)*.

Leakage current (Acm^{-2})	**0.01 M**	**0.005 M**	**0.001 M**
from therm.	3.09×10^{-3}	1.14×10^{-4}	1.21×10^{0}
673 K	2.02×10^{-3}	1.15×10^{-3}	7.04×10^{-2}
873 K	-	1.23×10^{-5}	-
1073 K	3.41×10^{-4}	2.00×10^{-5}	2.10×10^{-3}

Leakage current densities within the range of 10^0 down to 10^{-5} Acm^{-2} could be detected. In agreement with the measured data of the films on n-*Si(111)* substrates, the films deposited from different concentrated $Nd(NO_3) \times 6H_2O$ butanolic precursor solution concentrations show different behavior and significantly different leakage current density values.

Films on p-*Si(100)* substrates exhibit higher leakage current densities for non or at low temperature annealed samples, which is contrary to results achieved of the films on n-*Si(111)* substrates.

The best results have again been observed for films deposited from 0.005 M precursor solution. For the 1073 K annealed films, leakage currents down to 2.00×10^{-5} Acm^{-2} have been observed, which increased up to 1.14×10^{-3} Acm^{-2} for the oxide films from thermolysis. 0.001 M precursor solutions lead to leakage current values of the films down to 2.10×10^{-3} Acm^{-2}, increasing up to 1.21×10^{0} Acm^{-2} for the oxide films from thermolysis.

I-V measurements of the structures deposited from 0.01 M precursor solution are, as expected from the C-V and topographic analysis, critical to analyze,

since the curve shapes are not consistent with the expected tendencies for n-type dopants. Especially for the samples which have been annealed at 1073 K, the shape was detected to be the other way around, showing a higher leakage current density value at the off state side. Thus, the detected data have to be considered carefully.

12.3.3. Temperature Dependent I-V Analysis

Temperature dependent I-V measurements are essential under two points of view. Mainly a stable leakage current also under higher processing temperature is important for electrical devices. As due to an increased joule heating during operation the requirement of a stable operation is not reliably fulfilled.

Furthermore, temperature dependent I-V measurements enable studies of different leakage current mechanisms participating in the resulting leakage current, which opens the path to tune the respective parameters for a further reduction of the leakage current.

Different mechanisms which may contribute to the leakage current have been theoretically introduced in section 3.2.4. The temperature dependent components Poole-Frenkel and Schottky emission can be investigated by biasing the samples at different temperatures and analyzing a possible linear behavior within the $\ln(J/E)$ vs. $E^{1/2}$ plot and the respective slopes.

Nd_2O_3 films on n-*Si(111)* on p-*Si(100)* substrates have been analyzed, which were prepared using the 0.005 M precursor solution and therefore a resulting film thickness of 3.7 nm.

The samples have been biased from -8 to +6 V at 298 K, 323 K, 348 K, 373 K and 398 K, as this is the typical temperature region of transistor performance incorporated in electrical devices.

Si(111)

Figure 12.14. shows the temperature dependent I-V curves of the samples generated from 0.005 M precursor solution on n-*Si(111)*.

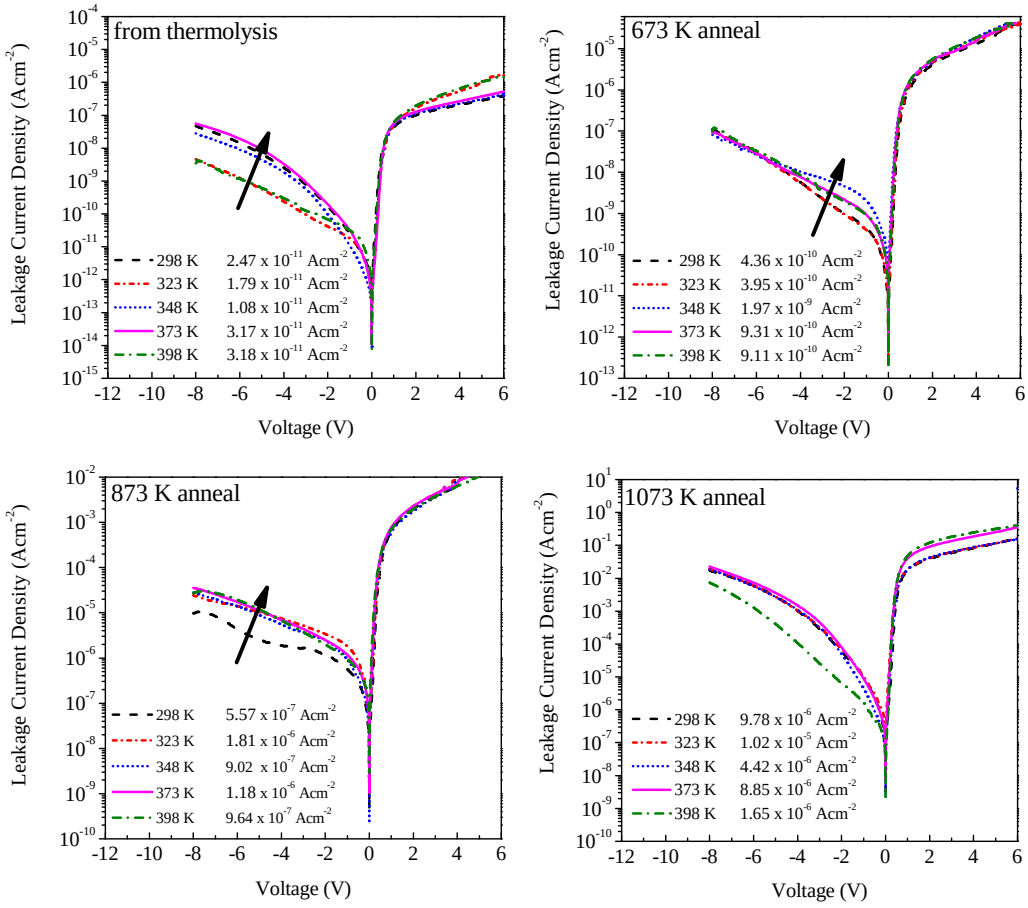


Figure 12.14.: Temperature dependent I-V measurements of Nd_2O_3 films, deposited from 0.005 M $Nd(NO_3) \times 6H_2O$ butanolic precursor solution on n-*Si(111)*, for different annealing temperatures.

All curves exhibit an asymmetric behavior with a slight temperature dependence in the off state and approx. no temperature dependence in the on state region. For all samples, increased leakage current densities can be detected for higher temperatures but no systematic trends are observed from the curves.

The increased leakage current densities are still within the same range as the samples measured at room temperature, considering a more or less stable leakage behavior even under high temperature conditions. Samples annealed at

1073 K show unsteady trends with varying leakage current densities over the measured temperature regime, but overall no significantly increased final leakage current. Besides, with the temperature, the differences in the leakage current densities vary with the applied electric field.

The low unsystematic temperature dependence indicates that both Poole-Frenkel and Schottky emission are not dominantly responsible for the leakage current conduction within the films and at this point the $\ln(J/E)$ vs. $E^{1/2}$ plots should be omitted, as according to the equations shown in section 3.2.4 both mechanisms result in a systematic increase of the leakage current density for higher processing temperatures.

Since approximately no temperature dependence is observed Poole-Frenkel and Schottky emission can be ruled out as dominant leakage current conduction mechanisms. The detected leakage currents need to be caused by processes which are temperature independent such as the different introduced tunneling processes. Therefore a precise assignment is not possible at this point and further investigations are required in the future work.

Si(100)

Temperature dependent I-V analyses have been performed analogous to the n-*Si(111)* substrates for the thin films on p-*Si(100)* substrates. The measured data are shown in figure 12.15.

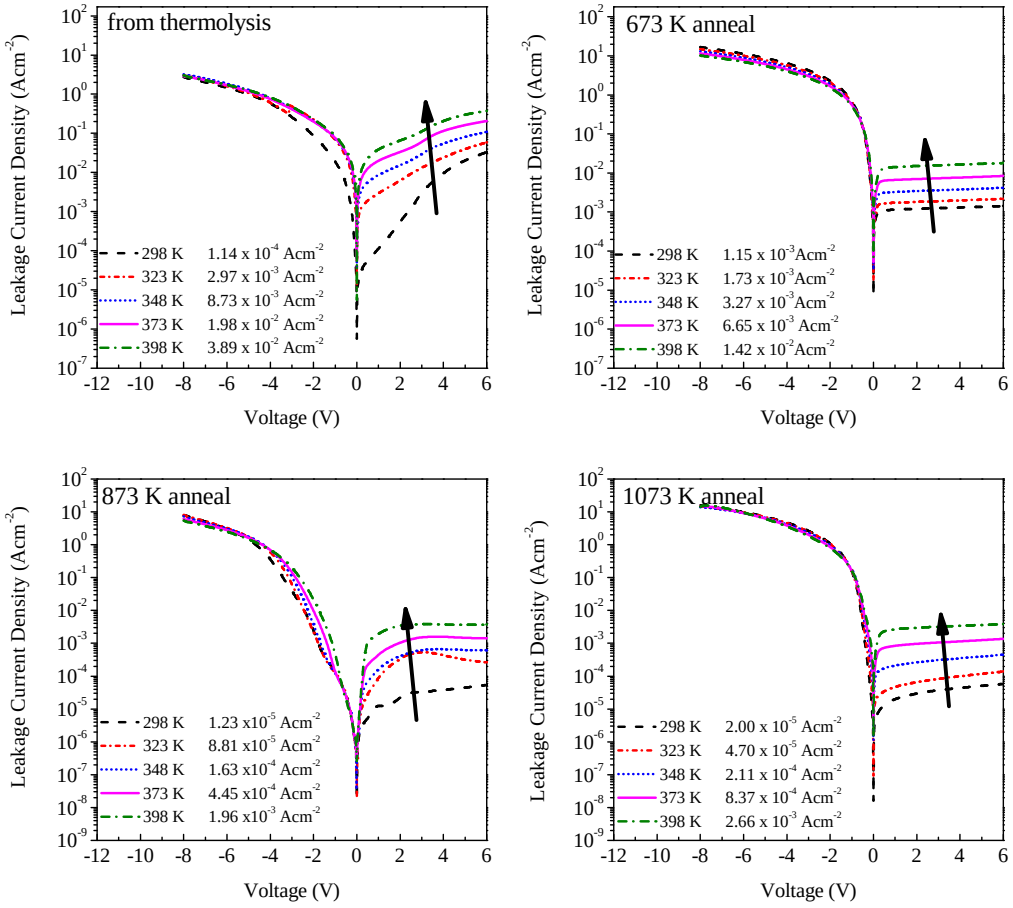


Figure 12.15.: Temperature dependent I-V measurements of films deposited from 0.005 M $Nd(NO_3) \times 6H_2O$ butanolic precursor solution on p-*Si(100)* for the samples annealed at different temperatures measured from 298 K to 398 K.

All curves exhibit an asymmetric behavior with a strong temperature dependence in the off state region. For all samples, increased leakage current densities can be detected for higher temperatures and systematic trends can be observed. Therefore the $\ln(J/E)$ vs. $E^{1/2}$ plots are shown in figure 12.16 in

order to identify the dominant temperature dependent leakage current conduction mechanisms from the extracted slopes.

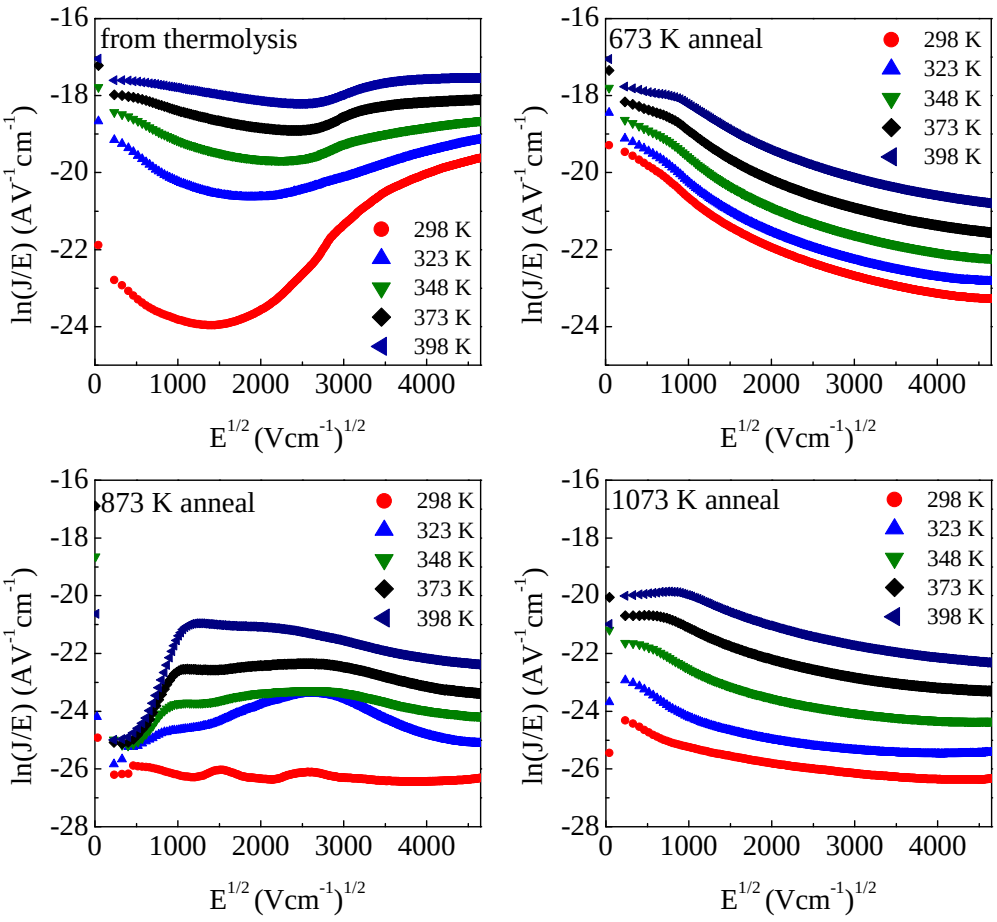


Figure 12.16.: $\ln(J/E)$ vs. $E^{1/2}$ plots over increasing temperatures of the Nd_2O_3 layers deposited from 0.005 M butanolic $Nd(NO_3)_3 \times 6H_2O$ precursor solution on p-*Si(100)* substrates (from thermolysis, annealed at 673 K/873 K and 1073 K). Shown are the data over the full measured electric field region.

It can be seen from the graphs that different courses of the curves are existent for different field regions depending on the type of sample. The oxide films from thermolysis and the films annealed at 873 K exhibit relatively unsteady curves with alternating positive and negative slopes. Samples annealed at 673 K and 1073 K exhibit steady trends with negative slopes over the full analyzed electric field region. All samples exhibit larger y-intercepts for higher processing temperature and linear trends can be observed at high electric fields. Linear

trends in accordance with increasing y-intercepts indicate the appearance of Schottky or Poole-Frenkel emission. For a more detailed study of the linear dependencies and the underlying leakage current conduction mechanism the linear regions are magnified in figure 12.17.

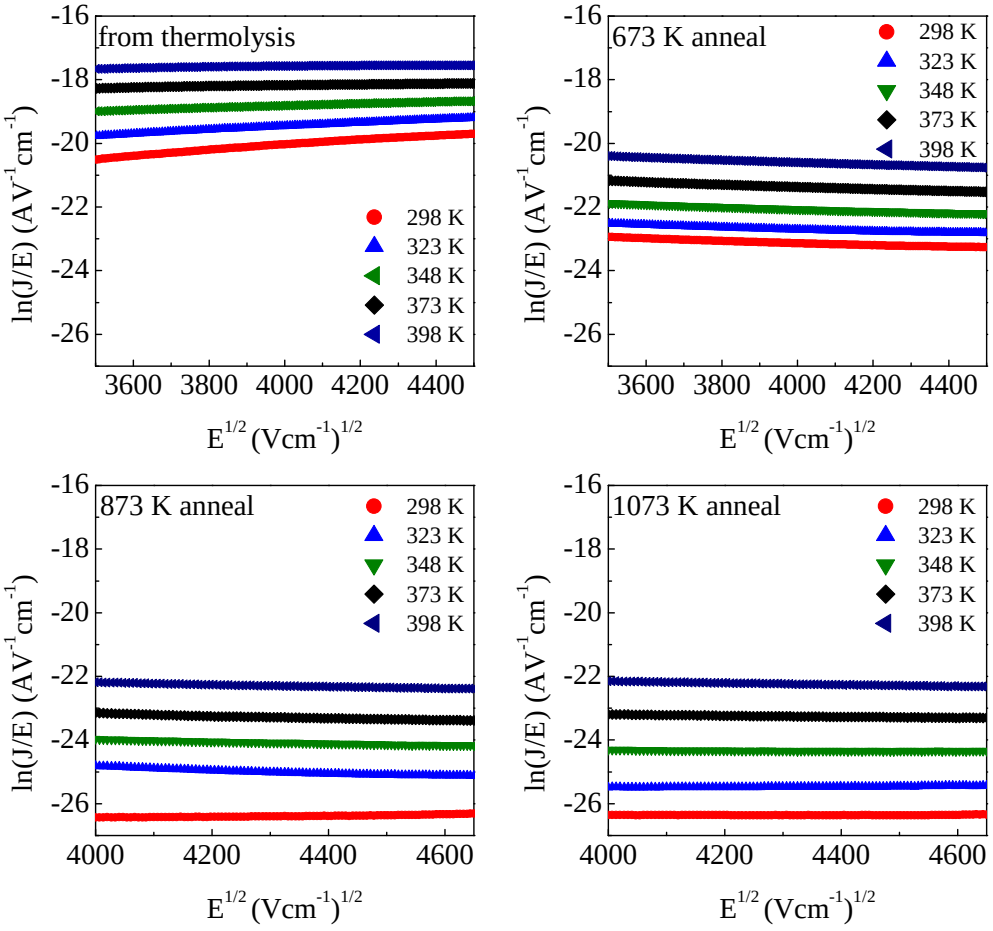


Figure 12.17.: $\ln(J/E)$ vs. $E^{1/2}$ plots over increasing temperatures of the Nd_2O_3 layers deposited from 0.005 M butanolic $Nd(NO_3)_3 \times 6H_2O$ precursor solution on p-*Si(100)* substrates (from thermolysis, annealed at 673 K/873 K and 1073 K). Shown are the data under linearity conditions at high electric field.

Based on the extracted slopes the β factors can be calculated according to equation 12.5. The results are summarized in table 12.5 whereby the absolute values of the slopes were used in the calculations.

Table 12.5.: Calculated β factors in $V^{1/2}cm^{1/2}$ from theory and determined from data of the 0.005 M $Nd(NO_3) \times 6H_2O$ butanolic precursor solution on p-*Si(100)* for the samples annealed at different temperatures measured from 298 K to 398 K.

Sample	β_{SE} $\frac{1}{2}\sqrt{\frac{q}{\pi\epsilon_0\epsilon_{Ox}}}$	β_{PF} $\sqrt{\frac{q}{\pi\epsilon_0\epsilon_{Ox}}}$	β plot	**Mechanism**
from thermolysis $\kappa = 1.7$				
298 K			2.05×10^{-5}	-
323 K			1.39×10^{-5}	-
348 K			9.00×10^{-6}	-
373 K			3.21×10^{-6}	-
398 K			3.43×10^{-6}	-
	2.91×10^{-4}	5.82×10^{-4}	$\overline{\beta} = 1.00 \times 10^{-5}$	
annealed at 673 K $\kappa = 0.8$				
298 K			1.03×10^{-5}	-
323 K			8.35×10^{-6}	-
348 K			1.20×10^{-5}	-
373 K			1.29×10^{-5}	-
398 K			1.37×10^{-5}	-
	4.24×10^{-4}	8.49×10^{-4}	$\overline{\beta} = 1.14 \times 10^{-5}$	
annealed at 873 K $\kappa = 3.9$				
298 K			2.57×10^{-6}	-
323 K			1.39×10^{-5}	-
348 K			9.00×10^{-6}	-
373 K			9.64×10^{-6}	-
398 K			1.03×10^{-5}	-
	1.92×10^{-4}	3.84×10^{-4}	$\overline{\beta} = 9.08 \times 10^{-6}$	
annealed at 1073 K $\kappa = 1.2$				
298 K			1.03×10^{-6}	-
323 K			1.95×10^{-6}	-
348 K			2.10×10^{-6}	-
373 K			6.43×10^{-6}	-
398 K			1.03×10^{-5}	-
	3.46×10^{-4}	6.93×10^{-4}	$\overline{\beta} = 4.36 \times 10^{-6}$	

From the listed data it can be seen that the graphically determined β factors are within the same region over the increasing operation temperature range for each sample. As the temperature dependence shows a systematic behavior and the slopes of the graph are equal, average values of β calculated from the graphs measured from 298 K up to 398 K are listed. But all determined values do not match with the β_{SE} and β_{PF} values calculated from theory and are actually within one order of magnitude lower than the theoretically calculated values.

The linear conditions indicate that one of the strongly temperature dependent mechanism is likely to be responsible for the detected increased leakage currents but obviously the initially mentioned concerns due to the width and extension of the space charge region and the origin of participating charge carriers comes into account for the present case of wet chemically deposited ultra thin oxide layers. This is also indicated by the negative slopes, which are observed from the $\ln(J/E)$ vs. $E^{1/2}$ plots and theoretically do not appear logically from the basic equations 12.2 and 12.3.

12.3.4. Conclusion Electrical Characterization of Silicon

In the following a short data summary should be given before the results are discussed with respect to the underlying mechanisms and literature known aspects.

For films deposited on n-*Si(111)* substrates no significant differences in the final capacitance density in accumulation for the 1 MHz and 100 kHz is detected. which suggests that no slow traps and charges are present within the deposited films or at the interface to the underlying substrate. According to Jiang et al.[223] irrespectively of the high-κ material in the stack for MOS structures (pure single layer of e.g. thermally grown SiO_2) no or very little dependence on the frequency can be observed while MIS structures of (e.g. slightly nitridated oxide and $SrTaO_6$ and $ZrSiO_4$) show rather strong frequency dependency. This leads to the conclusion that with the electrical characterization the formation of pure single layers of the Nd_2O_3 by the deposition process on n-*Si(111)* can be confirmed, which is in agreement with the shown HRTEM and XPS analysis in section 10. and 11.

C-V results of the films on *n-Si(111)* deposited from 0.01 M precursor solution, which is slightly above the Ostwald Miers limit for homogeneous film forma-

tion, show, as expected, irregular, not reliable and not repeatable results within the C-V characterization. The films seem to be leaky and especially detected "negative" capacitance lead to the conclusion that a detailed consideration of the calculated values is not representative, as obviously no homogeneous film structures are formed. Instead crystallization centers apparently might lead to a large number of grain boundaries, which results in a promotion of the charge transport within the films and diffusion across the boundaries. Therefore, the structures show highly leaky properties and no capacitance in accumulation could be measured.

Increased capacitance densities of the films deposited from 0.001 and 0.005 M on n-*Si(111)* after annealing up to 673 K can be observed. A significant drop after the annealing to 1073 K is detected. This leads to the conclusion that obviously a change in the structure or elementary composition occurs during annealing up to 873 K, which might be caused by the expected desorption of the *H*-passivation. Annealing at 673 K facilitates a reordering of the overlying oxide layer. Simultaneously the passivation of the substrates are kept active, which avoids a reoxidation and promotes the electrical performance. Above 830 K crystallization of the top covering Nd_2O_3 occurs[80], which leads to a decrease of the final capacitance density and therefore the κ value. Due to the crystallization of the Nd_2O_3 the effect of the lattice matching between the covering oxide and the underlying substrate comes into account for the electrical performance, as the deviation is rather high (s. chapter 8) and a lattice mismatch likely may lead to promoted electron conduction across the defect and strain rich interface. According to the XPS analysis shown in chapter 11. the passivation remains completely active during annealing up to 1073 K and therefore the changes in the capacitance density are likely to be caused by the crystallization process.

Compared to the conventional gate oxide material SiO_2 which features a dielectric constant of 3.9 especially the κ values for the 673 K annealed samples are significantly better by exceeding the values of the conventionally gate oxide material SiO_2 (κ=3.9) by maximally a factor of 2.5 to 3.

From the I-V analysis it was observed that the films deposited on n-*Si(111)* substrates exhibit leakage current densities down to 2.47×10^{-11} Acm^{-2} for the samples deposited from the 0.005 M precursor solution directly after thermolysis. Increased leakage current densities at higher annealing temperatures. This is untypical as it was expected that annealing leads to a reduction of the

present traps and charges within the films and a more ordered interface. A maximum leakage current density of $5.17 \times 10^{4-} Acm^{-2}$ has been detected for the samples deposited from 0.001 M precursor solution annealed at 1073 K. Temperature dependent I-V analysis revealed stable leakage current densities even at higher processing temperature.

Films deposited on p-*Si(100)* exhibited a drastically reduced maximum of capacitance measured at 1 MHz compared to the measured values at 100 kHz. This might result from a formed MIS, multi or mixed layer structure and therefore the measurement of different insulating layers in series.[223] This is in agreement with the previously shown XPS analysis, as the *Si* signals showed characteristic structures for other oxidation states than pure *Si* bulk material. Expected sufficiently lower κ values are detected. The unrepeatable results and severe humps within the detected C-V curves for the films deposited from 0.01 M precursor solution on p-*Si(100)* indicate the worst electrical properties for the films deposited from the highly concentrated precursor solution as observed for n-*Si(111)*. This is probably caused by an insufficient homogeneous coverage of the substrate.

Samples annealed at 1073 K showed a drastically reduced but stable capacitance in accumulation. Thus, the annealing process obviously leads to a change in the structure or the formation of interfacial layers which reduces the traps and charges within the films and at the interface and higher values for the accumulation capacitance can be achieved. These findings are in agreement with the XPS analysis shown in chapter 11. Annealing temperatures above 810 K lead to a depassivation of the substrate as the hydrogen termination desorbs and the surface remains reactive which was also shown from the XPS analyses (s. chapter 11.

Films deposited on p-*Si(100)* show decreased leakage current densities after annealing which is expected due to a reduction of the interface trap density in contrast to the observed results for n-*Si(111)* substrates. Maximum leakage current densities of 1.21×10^{0} Acm^{-2} have been measured for the films deposited from 0.001 M directly after precursor thermolysis and a minimum value could be detected at 1.21×10^{-5} Acm^{-2} for the films deposited from 0.005 M precursor solution annealed at 873 K. p-*Si(100)* substrates show strong temperature influenced increased leakage current densities during temperature dependent I-V measurements over increasing temperatures.

From a more general aspect it can be seen from the C-V analysis that films on n-*Si(111)*, where an atomically smooth, hydrogen passivated substrate, provides best basics for homogeneous film formation and avoids the reoxidation and interfacial layer formation, show the best performance for samples annealed at low temperatures. Annealing at temperatures above the desorption of the *H*-passivation and the crystallization temperature of the Nd_2O_3 obviously leads to reduced capacitances in accumulation and a break down of the dielectric according to the C-V analysis but unexpected simultaneously to a less leaky structure. In comparison, films deposited on p-*Si(100)* show bad electrical performances due to leaky films improving with annealing. This can be explained by an interfacial layer formation, which was confirmed by XPS measurements. Layers of SiO_2 or SiO_x with a thickness of a few atomic layers are in discussion to improve the final electrical performance of alternative gate oxide materials, as it offers the possibility to overcome problems of lattice matching and trap rich interfacial structures. Lower dielectric constants for p-*Si(100)* substrates compared to n-*Si(111)* have also been reported from the literature, but the drop of the capacitance was not detected.[222]

All detected dielectric constants are lower than the dielectric constant of bulk Nd_2O_3 material, where the dielectric constant has been determined as 13.6 - 15.4 for the cubic phase consistent with measurements on other RE_2O_3 oxides.[90] According to Busani et al., the dielectric constants differ in dependency on the crystallographic phase and the structure of the material. The authors attribute this to a possible lower density of the deposited amorphous phase of Nd_2O_3 and the formation of mixture or multilayer structures as compared to its crystalline phase.[90] [224] [225] Iuga et al. have shown that *Al* atoms in the crystalline phase are six-fold coordinated with oxygen, while in the amorphous phase, the coordination number decreases to four resulting in a lower density of the amorphous phase. The lowering of the dielectric constant in the less-dense amorphous phase can be explained according to the Clausius-Mossotti relation, which analyzes the relation of the dielectric constants of two different media and should not be further explained at this point.[226]

Therefore, the observed difference in the capacitance density of the generated films might be caused by a change of oxygen stoichiometry within the crystalline and amorphous phase. In future work, density values have to be determined via Rutherford Back Scattering (RBS) and X-ray Reflectivity (XRR)

measurements. Furthermore, experiments to investigate the oxygen stoichiometry are necessary.

From the I-V analysis it can be seen that on n-*Si(111)*, for all solution concentrations the leakage current density increases with the annealing temperature, while p-*Si(100)* substrates show contrary behavior and a decrease of the leakage current density with increased annealing temperature, as summarized in figure 12.18. Oxide films from thermolysis are considered to be treated at room temperature (298 K).

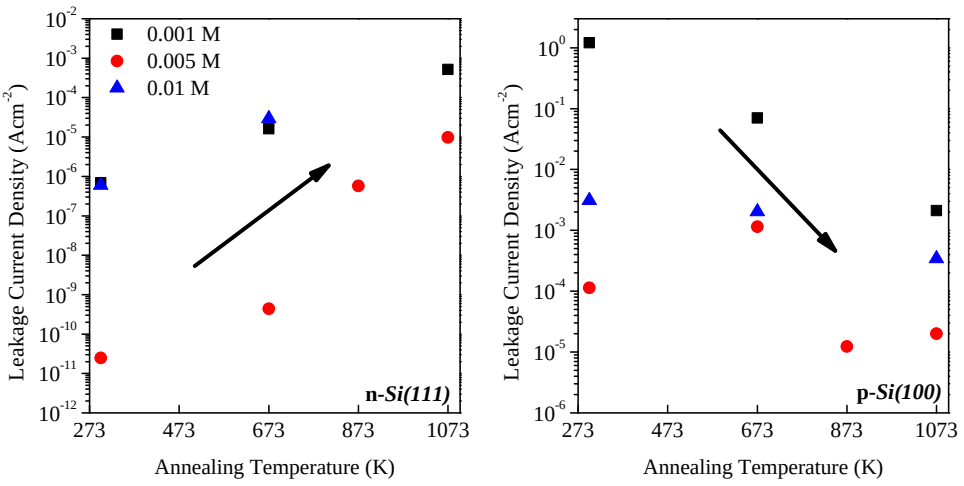


Figure 12.18.: Leakage current density values for the films deposited on n-*Si(111)* and p-*Si(100)* from different $Nd(NO_3) \times 6H_2O$ butanolic precursor solution concentrations plotted vs. the annealing temperature.

From figure 12.18. it is displayed clearly that the films deposited on n-*Si(111)* show leakage current densities which are orders of magnitudes lower than leakage current densities, which have been achieved for the p-*Si(100)* substrates. This was expected as the films on n-*Si(111)* showed also a much lower initial roughness (s. chapter 10.) and according to Hsu et al., low roughness values are essential for the final electrical performance of deposited thin films. A low roughness influences the tunneling current positively,[203] since films having a rougher surface and a larger conduction band offset cause a higher probability for trapping the charge carrier and the deep electron trap level in the film, which results in dramatically deteriorated electrical performances.[227]

Both substrate types have in common that a minimum of leakage current density could be observed for the films deposited from 0.005 M solution, which indicates that too high or too low solution concentrations lead to less homogeneous film formation. More electrically permeable structures result in high leakage current values, which might also be caused by higher densities of traps and charges.

The increased leakage current values for n-*Si(111)* after annealing are untypical and might be explained by a possible crystallization of the films during annealing.

In general the annealing leads to a higher influence of the amount of free dangling bonds. Furthermore, for crystalline films the lattice matching of the film and the substrate is a critical factor. The discussed lattice mismatch between the REO film and the substrate, leads to worsened leakage current characteristics to be observed. Additionally, high temperature treatment leads to the formation of interfacial structures, less homogeneous interfaces and a large amount of grain boundaries, reducing the advantage of the initially amorphous wet chemically deposited film, as grain boundaries possibly lead to increased charge carrier mobilities (extrinsic conduction) and subsequently higher leakage currents. For p-*Si(100)* annealing at higher temperatures results in an increase of the anyway formed interfacial $SiO_{2/x}$ layer leading to a reduced defect density at the direct semiconductor/insulator interface due to a better lattice matching of silicon oxides with the underlying silicon than with Nd_2O_3. Thus, lower leakage currents can be detected for the samples annealed at higher temperatures.

Besides the above mentioned differences between the two substrate types, it is known from literature that *Si* substrates with differing orientations show specific advantages and a characteristic electrical behavior.[222] It was found that the interface density of states differs with respect to the substrate orientation and the whole mobility.[228] [229] [230] [231] It has been reported for Gd_2O_3 deposited from MBE and an EOT of roughly 1 nm that *Si(111)* substrates show an increased leakage current compared to *Si(100)*. This is contrary to the determined results, showing that besides the substrate orientation the deposition process is responsible for the resulting electrical performance.[222]

To assess the real performance of the generated films, the measured leakage current density values have to be compared to alternative gate oxide materials

deposited from conventional deposition techniques or to SiO_2 gate dielectrics with the same or at least similar equivalent oxide thickness. Therefore, the results calculated in section 12.3.1. for the EOT need to be combined with the measured leakage current values as summarized in table 12.6.

Table 12.6.: Summary of the calculated EOT values and respective leakage current densities for the Nd_2O_3/n-*Si(111)* and Nd_2O_3/p-*Si(100)* samples.

Sample		κ	**EOT** (nm)	**Leakage Current** (Acm^{-2})
n-*Si(111)*				
0.01 M	from therm.	14.9	1.2	4.44×10^{-7}
	673 K	5.3	3.3	1.80×10^{-6}
	1073 K	1.4	12.5	distribution
0.005 M	from therm.	6.6	2.2	2.47×10^{-11}
	673 K	9.9	1.5	4.36×10^{-10}
	873 K	5.1	2.8	5.70×10^{-7}
	1073 K	2.1	6.8	9.79×10^{-6}
0.001 M	from therm.	10.2	1.3	6.89×10^{-7}
	673 K	12.3	1.0	1.61×10^{-5}
	1073 K	1.0	12.3	5.17×10^{-4}
p-*Si(100)*				
0.01 M	from therm.	2.1	8.4	3.09×10^{-3}
	673 K	0.9	18.6	2.02×10^{-3}
	1073 K	1.9		3.41×10^{-4}
0.005 M	from therm.	1.7	8.4	1.14×10^{-4}
	673 K	0.8	18.1	1.15×10^{-3}
	873 K	3.9	3.7	1.23×10^{-5}
	1073 K	1.2	12.1	2.00×10^{-5}
0.001 M	from therm.	1.2	11.2	1.21×10^{0}
	673 K	1.1	11.3	7.04×10^{-2}
	1073 K	1.3	9.9	2.10×10^{-3}

As low film thicknesses are required for future applications, in the following only the samples which exhibited low EOTs within the range of 1-2 nm shall be discussed. The high calculated EOT values for the *Si(100)* substrates are

outside the thickness region, where conventionally used SiO_2 shows extensive leakage currents due to quantum mechanical tunneling. Thus, for a precise discussion and comparison to literature data, the values achieved on n-*Si(111)* are considered.

Table 12.7. shows leakage current densities documented in literature for an EOT of 1.5 nm of SiO_2 and promising or already implemented high-κ materials.

Table 12.7.: Leakage current densities of alternative gate dielectrics from literature at EOT 1.5 nm and the detected minimum from the wet chemical deposited Nd_2O_3 film.

high-κ	**Leakage current** (Acm^{-2})	**Deposition Technique**	**Literature**
SiO_2	10^1	thermally grown	e.g.[232]
	10^0	low temp. vapor from HNO_3	[232]
HfO_2	10^{-6}	ALD	[2]
Al_2O_3	10^{-4}-10^{-5}	ALD	[2] [233]
SiO_2N	10^0		[3]
La_2O_3	10^{-6}-10^{-7}		[3]
Nd_2O_3	down to 10^{-11}	wet chemical dip-coat	own data

Films which showed EOT values within the range have been observed for n-*Si(111)* substrates with 0.001 M, 0.005 M and 0.01 M concentrated solutions for the oxide film from thermolysis and at 673 K annealed samples.

It can be seen from figure 12.19., which shows the leakage current density in dependency on the EOT, and table 12.7. that the measured leakage current densities from the wet chemical deposited films are within orders of magnitudes lower than conventionally generated films. The best results achieved are in the range of 10^{-10}-10^{-11} Acm^{-2}, which is in maximum eleven orders of magnitude lower than conventionally used SiO_2 and in minimum six orders of magnitude lower than values measured for alternative gate oxides deposited from ALD at respective EOTs of 1.5 nm.

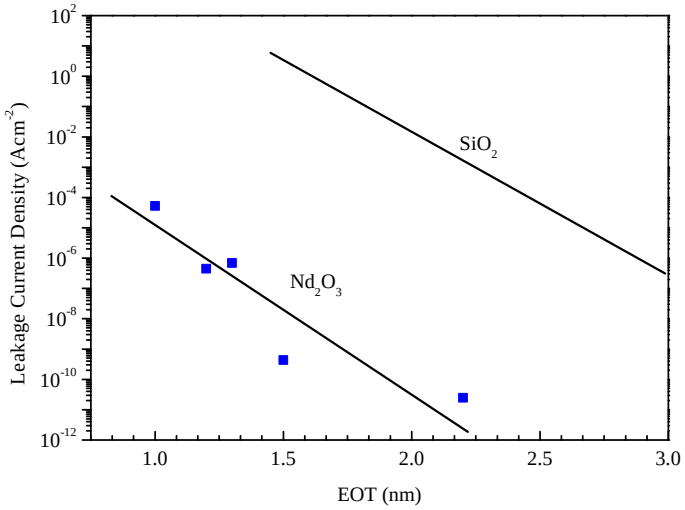


Figure 12.19.: Leakage current density vs. EOT for the deposited Nd_2O_3 films and SiO_2.

With respect to the investigated annealing temperatures it has been demonstrated that an annealing at approx. 700 K and 900 K leads to an average improved electrical performance whereas annealing at 1100 K results in detrimental electrical performances. As mentioned above the deterioration might be related to the crystallization of the generated oxide films, which is principally possible for temperatures above 830 K.[80] The formation of crystalline structures results on the one hand in strain in the lattice, due to differing lattice constants of the oxides and the underlying substrate (s. section 8) and on the other hand to the formation of grain boundaries which promote the electron conduction and lead to electrical discontinuities. Annealing below the crystallization temperature promotes the removal of impurities within the films and defects within the substrate and lead therefore to stable or improved electrical performances.

Temperature dependent I-V analysis lead to the major findings that the oxide films deposited on n-*Si(111)* show a stable leakage current behavior over increasing processing temperatures which is crucially important for real device applications as for device operation temperatures around 380 K, caused by the Joule heating, stable low leakage currents are desirable for a reliable device performance.

Contrary to that p-*Si(100)* substrates exhibited a relatively strong and systematic increase of the leakage current densities during higher processing temperatures and a less stable leakage behavior under high temperature conditions can be considered to be caused by a higher charge carrier mobility for p-*Si(100)* substrates. Preliminary calculations, to determine the participating leakage current conduction by specific linearity conditions, lead to the conclusion that Poole-Frenkel or Schottky emission have to participate in the conduction mechanism as characteristic systematics could be observed but according to the calculations a precise assignment was not possible.

The difficulty of a precise assignment might results from the appearance of the investigated films. For ultra thin films as in the present case the width of the generated space charge or depletion region is strongly dependent on the electric field and the materials. For film thicknesses lower than the depletion layer width the depletion layer may not be fully generated and a highly locally dependent electronic state is created, eventually leading to differing leakage current conduction behavior and an intermixing of different conduction mechanism. In the literature it is discussed that the mechanism is strongly dependent on the film thickness.[64] Furthermore, it has to be differentiated if bulk or interface charge carriers are mainly involved, which leads to experimentally introduced correction factors and changed current conduction.[64] The number of injected charge carriers, which are responsible for the Schottky emission, and the from the dielectric itself activated charge carriers are hard to estimate. Therefore in the present work no correction factors have been introduced.

In the future work measurements with alternating DC and AC current and at ultra low temperatures are required to achieve a detailed understanding of the participating temperature dependent and independent mechanisms and to clarify of which origin the charge carriers involved are.

In general it can be concluded from the detected temperature dependency that a direct connection exists between the conductivity, electric field and the temperature. Thereby a precise assignment of the respective mechanism is based on the accuracy of the determined κ values and therefore the homogeneous film thickness.

12.4. Alternative Substrates

In the following paragraph, the I-V and C-V measurements of the alternative substrates n-*Ge(100)* and p-*SiGe(111)* are presented. Those measurements are essential in order to estimate if the introduced technique is applicable to produce high quality thin films on different substrate materials, which opens an avenue for thin film technology development as a multifunctional, energy efficient technique, which is virtually applicable for several oxides and manifold smooth substrates.

All necessary basics for calculation and data extraction from C-V and I-V have been introduced within the previous paragraph about the *Si* substrates. Thus, the results of the films on the substrates other than *Si* are presented briefly and discussed at this point.

As mentioned previously, the wet chemical deposition technique has been tested on alternative substrate materials by using the 0.005 M $Nd(NO_3) \times 6H_2O$ butanolic precursor solution. For systematic studies the results on pure n-*Ge(100)* are shown prior to the results achieved from the p-*SiGe(111)* samples.

12.4.1. Germanium

Pure *Ge* samples are expected to show more critical electrical behavior due to the strong reoxidation tendency. But for the reasons mentioned in chapter 8., *Ge* is back in interest for transistor devices and therefore it is however beneficial to investigate if the wet chemical deposition technique is in general feasible for *Ge* materials. It has to be kept in mind that it was shown from the *Si* substrates that the initial substrate roughness has a strong influence on the final film roughness and therefore the electrical performance (s. chapter 10.), as the oxide films from thermolysis on n-*Ge(100)* exhibit a significantly higher roughness than *Si* substrates.

In order to investigate the dielectric constants and the EOT, C-V measurements have been done analogous to *Si*. The results are shown in figure 12.20.

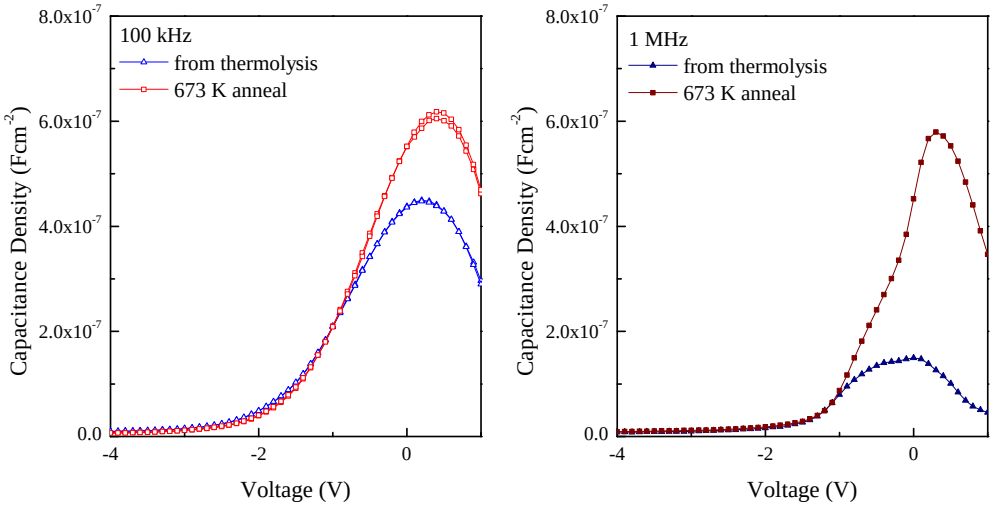


Figure 12.20.: Measured C-V curves of the samples deposited from 0.005 M $Nd(NO_3) \times 6H_2O$ butanolic precursor solution on n-*Ge(100)* at 100 kHz and 1 MHz.

The C-V curves show a characteristic shape for n-type substrates with a maximum in capacitance density at positive biasing. A significant drop of the capacitance, can be detected after passing the maximum value which has been used for the κ calculations. Therefore, the structures can be considered to be relatively leaky, which has to be investigated by I-V analysis in the following.

An increase of capacitance can be detected for annealed samples, indicating improved film quality caused by the annealing process. No hysteresis can be observed for both samples, whereas the changes between the 1 MHz and 100 kHz measurement differ for the not annealed and annealed samples. A significant drop of the capacitance in accumulation can be observed for the oxide films from thermolysis while comparing the measurements at 100 kHz to 1 MHz. This might related to a reoxidation of the *Ge* substrate caused by the easy tendency of oxide formation and the less stable hydrogen passivation compared to *Si*. An interfacial oxide layer involves slow traps and charges at the interface. Annealed samples do not show a drop in the capacitance during a change from 100 kHz to 1 MHz, indicating a higher film quality. The threshold voltage is equal for all measured curves.

For n-*Si(111)* the use of 0.005 M precursor solution resulted in a film thickness of 3.7 nm. If one assumes a similar film thickness, which necessitates a similar

wetting behavior, the dielectric constants can be calculated analogous to *Si*. The measured capacitance in accumulation, calculated κ and EOT values are listed in table 12.8.

Table 12.8.: Capacitance density in accumulation, κ and EOT values for Nd_2O_3 deposited from 0.005 M $Nd(NO_3) \times 6H_2O$ butanolic precursor solution on n-*Ge(100)*.

Sample	**Capacitance Density** (Fcm^{-2})	κ	**EOT** (nm)
from therm.	4.50×10^{-7}	1.9	6.2
673 K	5.79×10^{-7}	2.4	4.8

It can be seen that the measured κ values are not significantly high and as mentioned, the leakage current densities are the critical variables to estimate the potential of the deposition technique on n-*Ge(100)*.

The measured I-V curves, including the temperature dependent measurements to investigate the leakage current mechanism, are shown in figure 12.21.

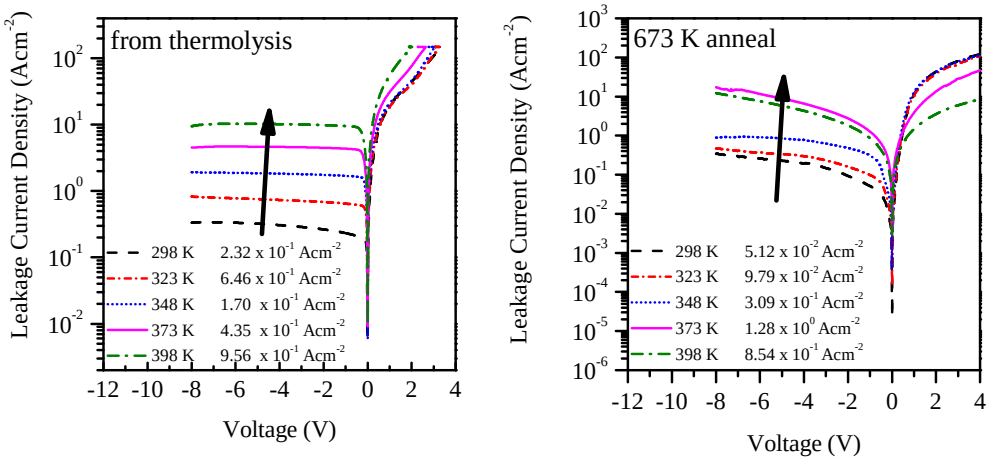


Figure 12.21.: Temperature dependent I-V curves of the samples deposited from 0.005 M $Nd(NO_3) \times 6H_2O$ butanolic precursor solution on n-*Ge(100)*. Shown are the oxide films from thermolysis (left) and at 673 K annealed samples (right).

Leakage current densities of 2.32×10^{-1} up to 9.56×10^{-1} Acm^{-2} could be measured for the oxide films from thermolysis and 5.11×10^{-2} up to $8.54 \times$

10^{-1} Acm^{-2} for the samples which have been annealed at 673 K. The leakage current densities are related to the EOT. In agreement with the κ values, annealed samples show a lower leakage current and therefore a better electrical performance than the oxide films from thermolysis. Both samples exhibit a strong temperature dependent leakage current increase up to one order of magnitude.

A strong systematic temperature dependency can be observed for the films on n-*Ge(100)*. The identification of the leakage current conduction mechanism attempts to be provided by the $\ln(J/E)$ vs. $E^{1/2}$ plots as the differing substrate type may lead to differing charging states. Therefore eventually a precise assignment of the respective leakage current conduction mechanism is possible in the present case.

The characteristic $\ln(J/E)$ vs. $E^{1/2}$ plots are illustrated in figure 12.22.

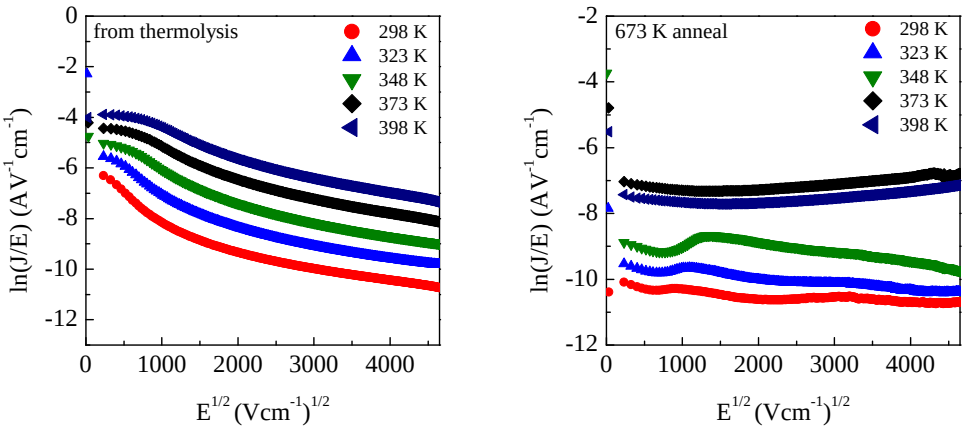


Figure 12.22.: $\ln(J/E)$ vs. $E^{1/2}$ plots over increasing temperatures of the Nd_2O_3 layers deposited from 0.005 M butanolic $Nd(NO_3)_3 \times 6H_2O$ precursor solution on n-*Ge(100)* substrates (from thermolysis and annealed at 673 K). Shown are the data over the full measured electric field region.

As observed for the films deposited on *Si* substrates the samples showed a systematic increase of the leakage current density, negative slopes can be extracted from the $\ln(J/E)$ vs. $E^{1/2}$ plots illustrated in figure 12.22. This is not explainable neither by Poole-Frenkel nor Schottky emission under theoretical consideration of equation 12.2 and 12.3. For this reason at this point no de-

tailed consideration of the β factors should be done. As for the Si samples the linear behavior in the $\ln(J/E)$ vs. $E^{1/2}$ plots indicates that Poole-Frenkel or Schottky emission are participating in the leakage current conduction but a systematic mixing of different mechanisms is present leading to untypical shapes of the analyzed graphs, which requires more detailed investigations in the future.

12.4.2. Silicon-Germanium

$SiGe$ compounds open the possibility to combine the advantages of Si and Ge in one substrate.

Due to the Ge implementation into the Si, a less passivated surface is expected to be formed after the HF etching according to the XPS analysis shown in chapter 11. Therefore distinct electrical performances are expected due to interfacial reactions and a reduced band gap of Ge compared to pure Si.

The measured C-V curves of the Nd_2O_3 films deposited on p-$SiGe(111)$ are shown in figure 12.23. C-V analyses have been performed for the oxide films from thermolysis as well as samples annealed at 673 K, 873 K and 1073 K.

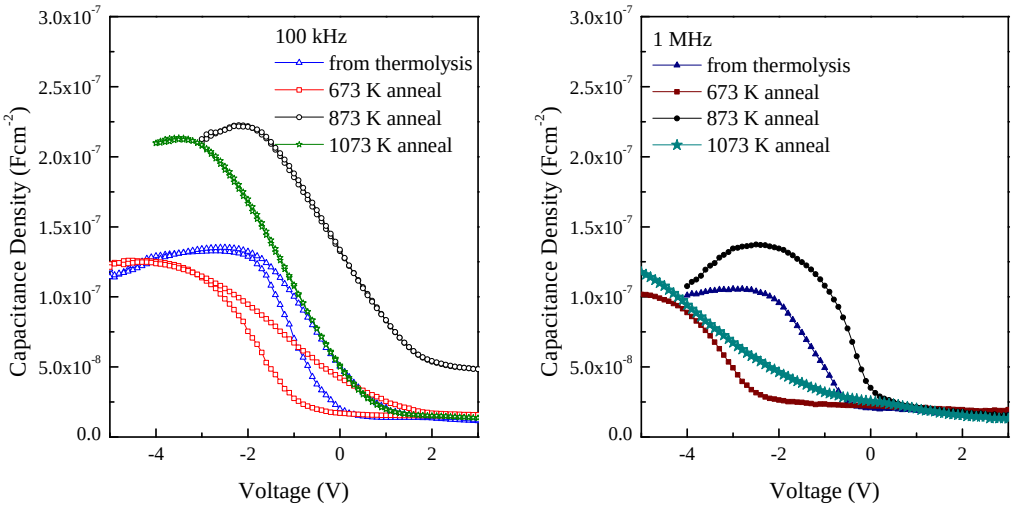


Figure 12.23.: C-V curves of the films deposited from 0.005 M $Nd(NO_3) \times 6H_2O$ butanolic precursor solution on p-$SiGe(111)$. Shown are data of the oxide from precursor thermolysis, at 673 K, 873 K and 1073 K annealed samples.

From the shape of the curves it can be seen that for both frequencies no hysteresis can be observed and for the measurements at 100 kHz a stable capacitance in accumulation can be detected. As for the p-*Si(100)* substrates a drop of the accumulation capacitance can be detected for the curves measured at 1 MHz compared to the slow excitation with 100 kHz.

By assuming that the film thickness equals the film thickness on Si substrates (3.7 nm) from the measured C-V curves, respective dielectric constants can be calculated analogous to the Si samples. The measured capacitance in accumulation and calculated κ values are listed in table 12.9. The EOT values are calculated analogous to the Si samples, to achieve comparable data.

Table 12.9.: Capacitance density in accumulation, κ and EOT values for Nd_2O_3 deposited from 0.005 M $Nd(NO_3) \times 6H_2O$ butanolic precursor solution on p-*SiGe(111)*.

Sample	**Capacitance Density** (Fcm^{-2})	κ	**EOT** (nm)
from therm.	1.35×10^{-7}	0.5	20.8
673 K	1.25×10^{-7}	0.5	22.4
873 K	2.22×10^{-7}	0.9	12.6
1073 K	2.12×10^{-7}	0.9	13.6

From the calculated values it can be seen that as expected, the κ values are significantly low and therefore extremely high EOT values have been calculated. Anyway, stable C-V curves could be detected. The detected threshold voltage is equal for all measured curves.

It is essential how the low dielectric constants influence the leakage current densities. The respective temperature dependent I-V curves and leakage current densities are shown in figure 12.24.

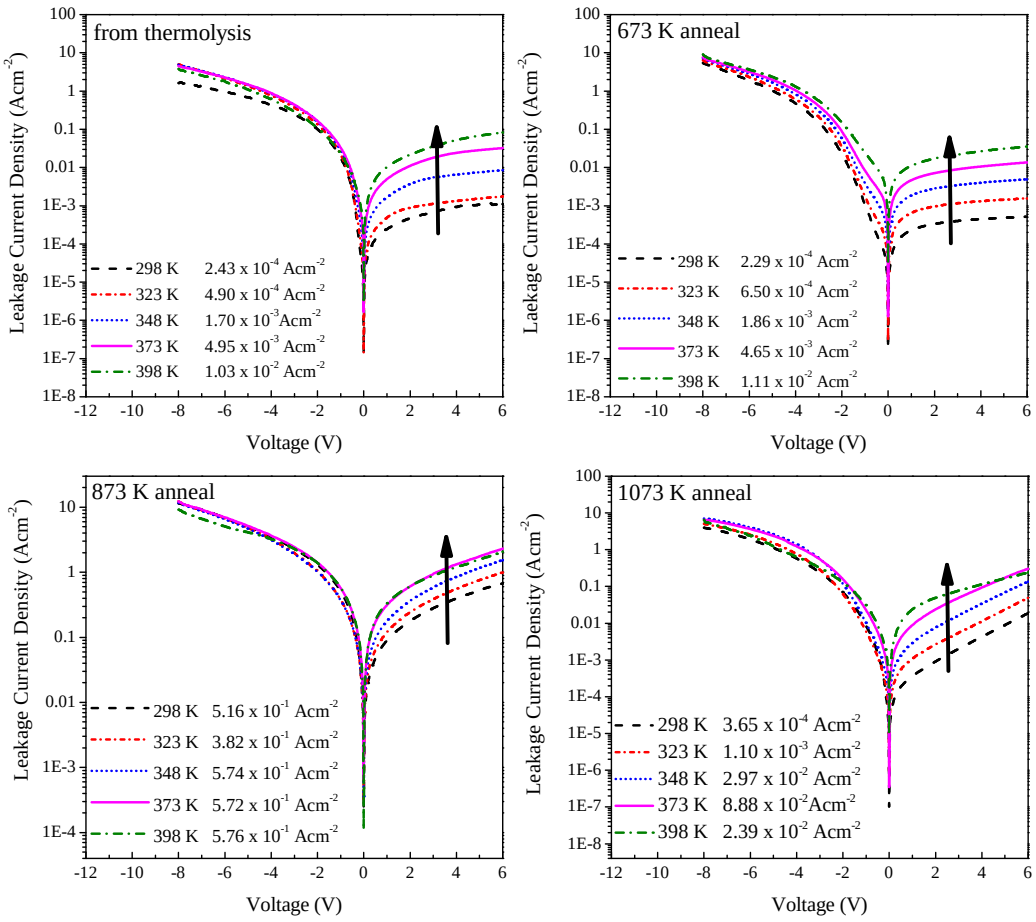


Figure 12.24.: Temperature dependent I-V measurements for the films deposited from 0.005 M $Nd(NO_3) \times 6H_2O$ butanolic precursor solution on p-*SiGe(111)*. The oxide film from precursor thermolysis, after annealing at 673 K, 873 K and 1073 K has been investigated.

It can be seen that all curves exhibit typical p-type shape with a relatively strong temperature dependence at off state biasing. The oxide film from thermolysis, at 673 K and 1073 K annealed samples show leakage current density within the range of 10^{-4} Acm^{-2}, whereas a much higher value of 10^{-1} Acm^{-2} can be detected for samples annealed at 873 K.

A systematic trend can only be observed for the samples annealed at 673 k and 1073 K and therefore at this point more detailed studies on the leakage current conduction mechanism are performed for these samples types. The characteristic $\ln(J/E)$ vs. $E^{1/2}$ plots are illustrated in figure 12.25.

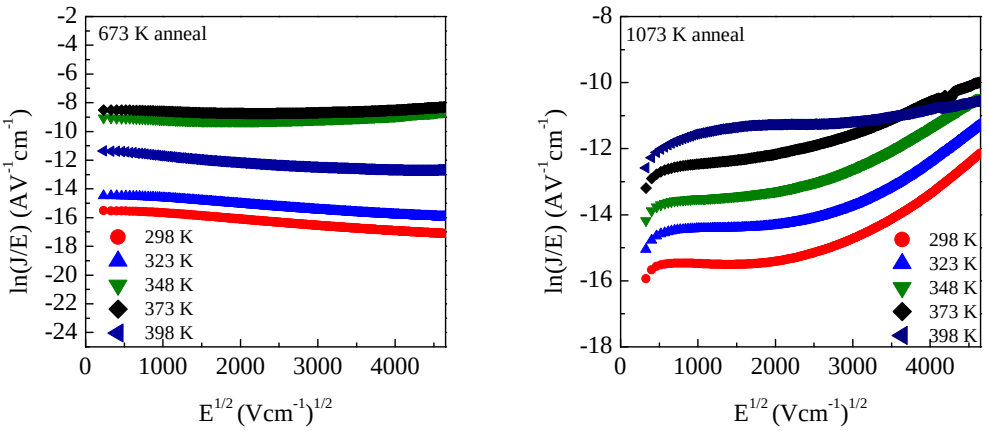


Figure 12.25.: $\ln(J/E)$ vs. $E^{1/2}$ plots over increasing temperatures of the Nd_2O_3 layers deposited from 0.005 M butanolic $Nd(NO_3)_3 \times 6H_2O$ precursor solution on p-*SiGe(111)* substrates (annealed at 673 K and 1073 K). Shown are the data over the full measured electric field region.

As observed for the *Ge* and *Si* samples the films deposited on p-*SiGe(111)* annealed at 673 K exhibit unsteady trends in the slopes and alternating positive and negative slopes over the measured temperature regime. The y-intercepts do not increase systematically and therefore a precise analysis of the respective leakage current conduction mechanism is not possible at this point. Samples annealed at 1073 K show a much more systematic behavior with linear positive dependency at high electric field except the outlier (398 K) which may be referred to measurement uncertainties. A detailed consideration of the graphs at high electric field leads to the in table 12.10 summarized β factors.

From the calculated factors it is obvious that again neither Poole-Frenkel nor Schottky emission can be identified from the $\ln(J/E)$ vs. $E^{1/2}$ plots as all experimentally determined factors are as for the *Si(100)* substrates within one order of magnitude lower than the according to equation 12.2 and 12.3 theoretically calculated values. The similarity intensifies the presumption that a mixture of differing leakage current conduction mechanism is responsible and that possibly different more complex factors need to be considered for a detailed understanding of the leakage current conduction mechanisms occurring in the deposited ultra thin films.

Table 12.10.: Calculated β factors in $V^{1/2}cm^{1/2}$ from theory and determined data of the 0.005 M $Nd(NO_3) \times 6H_2O$ butanolic precursor solution on p-*SiGe(111)* for the samples annealed at different temperatures measured from 298 K to 398 K.

Sample	β_{SE} $\frac{1}{2}\sqrt{\frac{q}{\pi\epsilon_0\epsilon_{Ox}}}$	β_{PF} $\sqrt{\frac{q}{\pi\epsilon_0\epsilon_{Ox}}}$	β plot	**Mechanism**
annealed at 1073 K $\kappa = 0.9$				
298 K			4.62×10^{-6}	-
323 K			4.73×10^{-5}	-
348 K			4.20×10^{-5}	-
373 K			3.21×10^{-5}	-
398 K			oulier	-
	4.00×10^{-4}	8.00×10^{-4}	$\overline{\beta} = 4.19 \times 10^{-5}$	

12.4.3. Conclusion and Discussion Alternative Substrates

In the previous section it was shown that Nd_2O_3 films deposited on n-*Ge(100)* substrates exhibit dielectric constants within the range of 2 whereas annealed samples exhibit higher dielectric constants. The drop in the capacitance in accumulation of the measurements at 100 kHz and 1 MHz is explainable by the formation of an interfacial layer formation in agreement with the shown XPS results in chapter 11. From I-V analyses leakage current densities in the range of 10^{-2} Acm^{-2} up to 10^{-1} Acm^{-2} have been detected.

Similar results have been achieved on p-*SiGe(111)*. From the C-V analyses dielectric constants from approx 0.5 to 1.0 were observed, whereby samples annealed at higher temperatures exhibit higher dielectric constants. I-V measurements demonstrated leakage current densities in the range of 10^{-4} Acm^{-2} at room temperature. An outlier was detected for the samples annealed at 873 K as a leakage current density of 10^{-1} Acm^{-2} was observed. The detected κ values of the films deposited on p-*SiGe(111)* are significantly low but stable C-V curves could be detected exhibiting a constant capacitance density in accumulation which indicates that the film formation was successful and the respective electrical properties need to be improved by specific annealing processes.

It is known from literature that despite the passivation concerns for Ge substrates compared to Si, high performing Ge-MOS devices are possible to be fabricated. However, gate stacks deposited on pure Ge wafers are expected to show relatively poor behavior, as it shows a large number of interface states near the conduction band.[234] Compared to Si independently from interfacial reactions higher leakage current densities are expected due to a lower band gap of Ge (1.12 (Si) vs. 0.66 eV (Ge)).[123] The theoretical considerations are in agreement with the achieved results for Ge and $SiGe$ substrates, as much lower κ values and higher leakage current densities have been detected. Anyway, especially the values detected for the $SiGe$ substrates are promising with respect to the applicability of the invented solution processable deposition technique, as leakage current values down to 10^{-4} Acm^{-2} are observed.

Chui et. al showed a successful integration of ultra thin pure ZrO_2 on pure Ge with EOT values of 5-8 Å, but significant hysteresis within the C-V curves.[235] It is discussed by the authors to analyze the Ge and $SiGe$ systems by considering a multiple layer capacitor model, since interfacial layer formation leads to layers with different dielectric properties each and the major goal is to eliminate the component with the worst dielectric properties.[236] Therefore, for the alternative substrate materials interfacial engineering is the essential factor to improve the electrical performance.[237] For $SiGe$, forming gas (mixture of H_2 and N_2) annealing should reduce the strain inside which is caused by the implantation of the Ge into the Si and therefore to improved electrical performance.[238] According to Mavrou et al., deposition at high substrate temperature and annealing in H_2 instead leads to improved capacitance densities.[127]

It has been shown that a deposition of REO films with the wet chemical deposition process is possible on on alternative substrate materials to Si but the dielectric films show improvable electrical behavior. Significantly better performances should be observed by tuning the annealing conditions to achieve a less oxygen rich atmosphere and therefore reduce the reoxidation of the substrate.

Temperature dependent I-V measurements revealed temperature dependencies of the final leakage currents but as for the films on silicon no precise assignment to literature known mechanisms was possible. Therefore further extensive investigations of the leakage current conduction mechanisms are required in the future work, for a more detailed understanding of the conduction process.

13. Multilayer Gate Stacks on Silicon Substrates

Bilayer or multilayer systems as SiO_2 gate stack replacements are particularly interesting for materials, which are thermodynamically unstable in direct contact with Si, but show significant high-κ values, like TiO_2. Protection layers between the non stable component and the substrate open the path to benefit from the excellent electrical behavior, while simultaneously overcoming the problem of unwanted interfacial reactions. According to Mavrou et al. bilayer systems are better scalable and easier to be engineered with respect to required properties, as the multi component system offers more starting points for performance improvement.[127]

To investigate the properties of promising bilayer structures and to achieve information about the potential to combine the invented technique with conventionally ALD, thin films of TiO_2 deposited by ALD, have been combined with the wet chemically deposited Nd_2O_3 films.

Systems with Nd_2O_3 and TiO_2 have been prepared on cleaned H-terminated n-*Si(111)* and p-*Si(100)* substrates. The TiO_2 was deposited on top of the Nd_2O_3, which was in direct contact with the substrate. The bilayer systems have been analyzed analogous to the single layer samples regarding the topography, thickness, structure and electrical performance. In order to investigate the stability of the synthesized gate stacks also reverse bilayer samples have been generated, whereas the thermodynamically instable at the Si interface instable TiO_2, was directly deposited on the substrate, followed by the dip-coat to prepare the Nd_2O_3 film. Additionally, ALD deposited TiO_2 single layers have been analyzed for comparison, which are shown in appendix F.

Due to the extensive measurement effort, only films deposited from the 0.005 M $Nd(NO_3)_3 \times 6H_2$ solution and TiO_2 ALD deposition have been investigated via HRTEM and AFM. The electrical characterization was done for the precursor solution concentrations within the Ostwald Miers region for homogeneous film formation (0.005 M, 0.001 M) and slightly above (0.01 M), in order to illustrate the differences in the electrical performance. As for the single layer, oxide films

after thermolysis and after 1 h annealing in N_2 flow at 673 K, 1073 K have been investigated.

The generated oxide bilayers are referred to as "as deposited" in the chapter, when directly investigated after thermolysis. Annealed samples are described by the respective annealing temperature.

13.1. ALD Deposition of Titanium Dioxide

$TiCl_4$ was used as metal and H_2O as oxygen source for the ALD TiO_2 deposition. The system has been chosen, since the precursors are also purely inorganic, similar to the wet chemical deposition, so that no carbon impurities are implemented into the films from the precursors used.

The scheme in figure 13.1. shows the ALD process for OH-terminated substrates. It has to be carefully considered and can not be directly transferred to differently terminated underlying substrates.

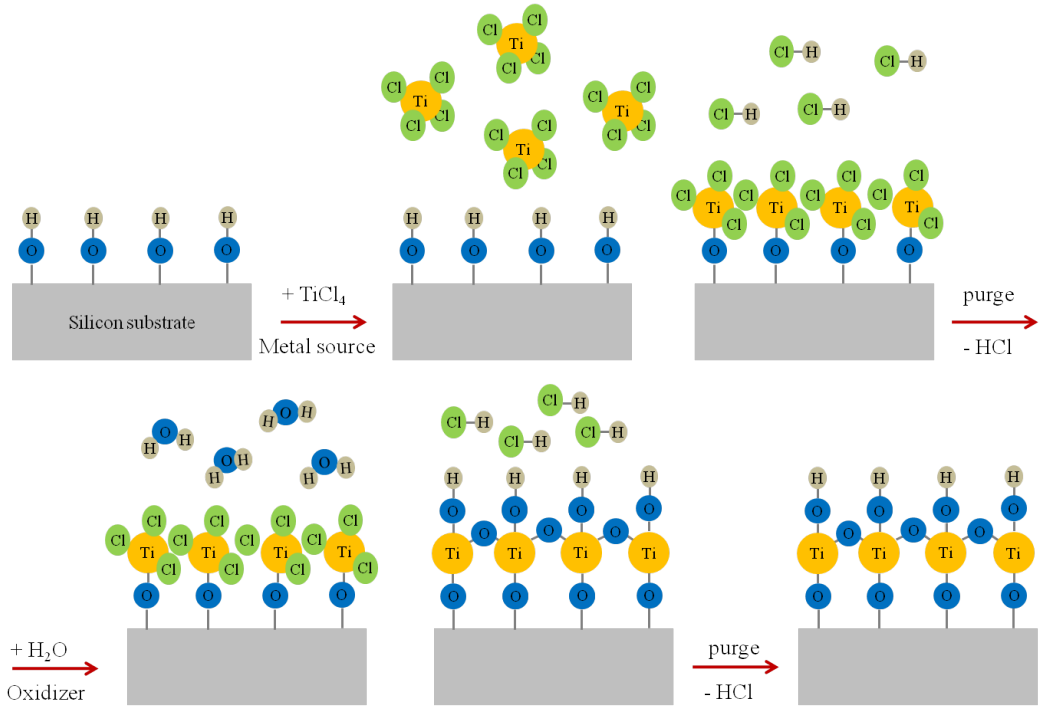


Figure 13.1.: Schematic ALD process to deposit TiO_2 on Si surfaces. $TiCl_4$ has been used as metal and H_2O as oxygen source.

The experiment was conducted using the commercial ALD system shown in section 6.8 at a substrate temperature of 373 K. Bilayer samples and reverse bilayer samples have been generated, using 50 cycles of ALD, resulting in an approx. 3 nm thick TiO_2 layer. To exploit the electrical characteristics of the generated TiO_2, 10 nm thin films of pure TiO_2 have been deposited using 150 cycles of ALD (s. appendix F).

13.2. Topography and Film Thickness of the Bilayer System

As for the single layer samples, initially the film topography has been determined by AFM measurements, in order to achieve a detailed analysis of the gate stack roughness. The bilayer gate stacks showed insulating behavior and therefore no SEM imaging was possible.

13.2.1. Topography: AFM

For AFM analysis films, deposited from 0.005 M butanolic $Nd(NO_3)_3 \times 6H_2O$-precursor solution and respective ALD cycles of of $TiCl_4$ and H_2O on *Si(111)* and *Si(100)* substrates in the as deposited state, after annealing at 673 K and 1073 K are compared and illustrated in figure 13.2. The images have been taken using the following settings:

Size:	$1 \times 1\ \mu m$
Angle:	$0°$
Scan rate:	1.00 Hz
Velocity:	$1\ \mu m$/s
Sample/Lines:	512

with respective scales of x = 0.2 μm/div and z = 50 nm/div for all samples, except the bilayer sample on *H-Si(100)* annealed at 673 K, which has been taken with x = of 0.2 μm/div and z = 20 nm/div.

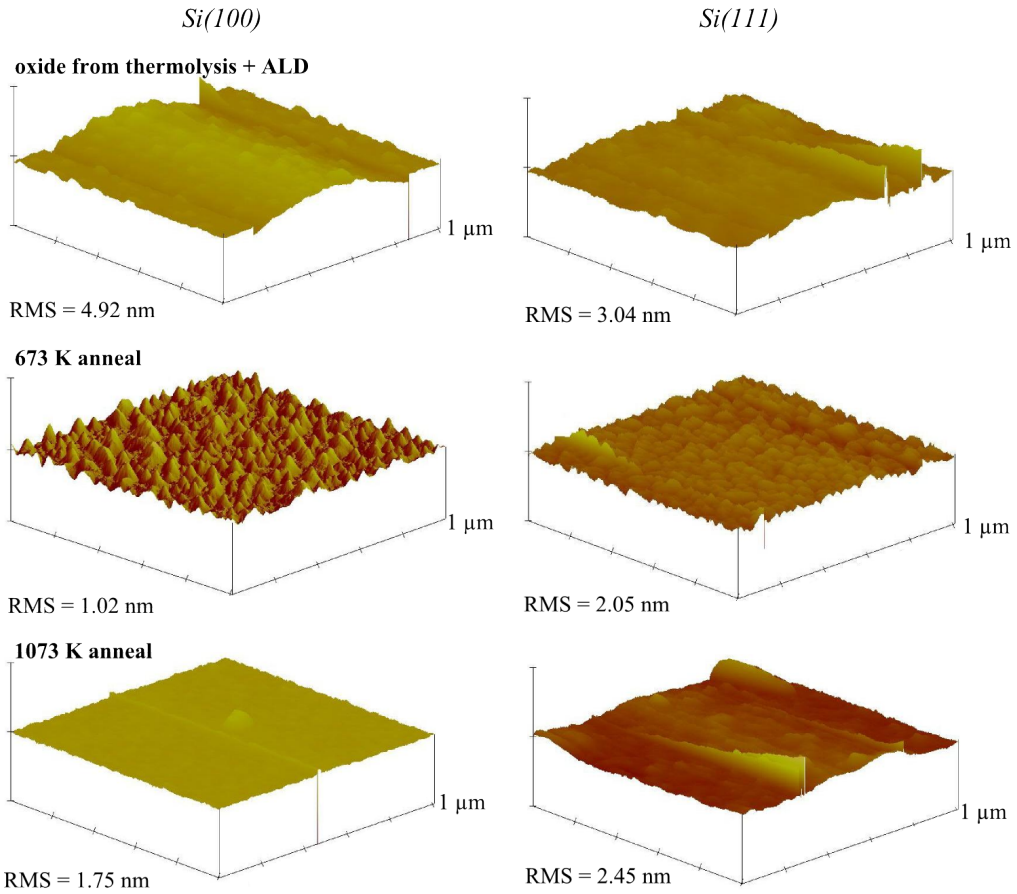


Figure 13.2.: AFM images of TiO_2/N_2O_3 bilayer films deposited from 0.005 M butanolic $Nd(NO_3)_3 \times 6H_2O$ precursor solution and 50 cycles of ALD on *H-Si(111)* and *H-Si(100)*, oxides as deposited, annealed at 673 K/1073 K (tapping mode, x = 0.2 μm/div and z = 50 nm/div).

The results are summarized in table 13.1.

Table 13.1.: RMS roughness values and z-ranges in nm of the oxide films illustrated in figure 13.2. and respective deviations between the substrate types.

Sample	***Si(100)***		***Si(111)***		**Deviation**
	z-range	RMS	z-range	RMS	RMS
as dep.	88.85	4.92	65.00	3.04	1.6:1
673 K	7.52	1.02	45.50	2.05	0.4:1
1073 K	70.04	1.75	74.53	2.45	0.7:1

It can be seen that RMS values reaching from 4.92 nm down to 1.02 nm, could be detected for the bilayer system on *Si(100)* substrates, whereas on *Si(111)* substrates RMS values from 3.04 nm down to 2.05 nm were achieved. Both substrate types have in common that the as deposited oxide films exhibit higher RMS values compared to the annealed samples. For each substrate type the RMS values for the films annealed at 673 K and 1073 K are equal. Compared to the single layer samples described in chapter 10. the actual RMS values are higher both on *Si(111)* and *Si(100)*.

13.2.2. Film Thickness: HRTEM

As for the single layers, HRTEM imaging has been utilized to determine the structure and thickness of the bilayer samples.

Figure 13.3 shows the HRTEM images of the bilayers on *Si(111)* and *Si(100)* in two different magnifications. The color bordered images are enlarged excerpts of the magnification shown in the middle.

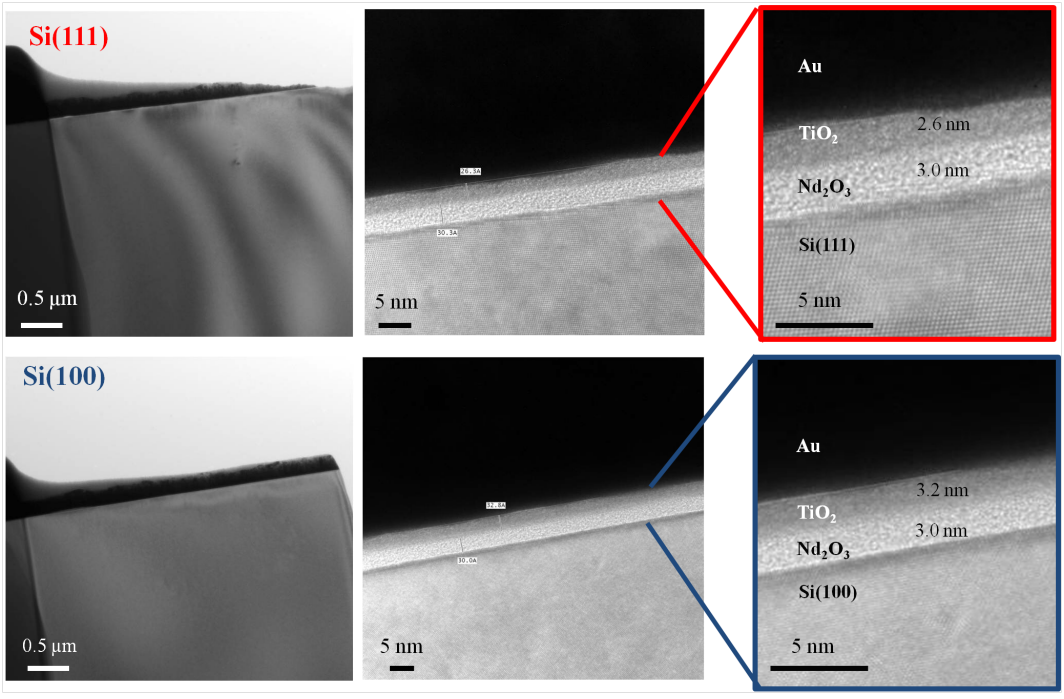


Figure 13.3.: HRTEM images of TiO_2/N_2O_3 bilayer films deposited from 0.005 M butanolic $Nd(NO_3)_3 \times 6H_2O$ precursor solution and 50 cycles of ALD on *H-Si(111)* (top) and *H-Si(100)* (bottom). (images are taken by Global Foundries®Singapore)

For both substrate types, a film thickness of the Nd_2O_3 layer of 3.0 nm was measured. But contrary to the expectations the thickness of the TiO_2 layer varies for the two samples although both samples have been prepared using 50 cycles of ALD to deposit the TiO_2. This indicates that in contrast to the presented wet chemical deposition technique the reliability of the thickness of the ALD deposited layers, is not given in the present experiment, which was also observed for other film depositions done by the used ALD system.[239]

As determined for the single layer samples, the layers are completely amorphous and they show a homogeneous structure over a wide area of the prepared samples. In comparison to the single layer of Nd_2O_3, the deposited films show a lower thickness of 3.0 nm instead of 3.7 nm, which has been analyzed for the single layer Nd_2O_3 films deposited from 0.005 M $Nd(NO_3)_3 \times 6H_2O$ butanolic precursor solution, even though a very good reproducibility of the detected film thicknesses for the single layers was shown and the Nd_2O_3 layers within the bilayer system were deposited under exactly the same deposition conditions with the same precursor solution. Therefore, the decreased film thickness of the Nd_2O_3 needs to be caused by the mechanism of the deposition of the covering TiO_2 layer or an interfacial reaction of the Nd_2O_3 with the underlying Si substrate or the TiO_2 overlayer.

The interfaces to the underlying substrate and between the TiO_2 and Nd_2O_3 seem to be relatively sharp for the bilayer deposited on *Si(111)*. On *Si(100)* a slightly darker region can be particularly observed at the direct interface of the Nd_2O_3 to the *Si(100)* substrate, indicating the formation of an interfacial layer with a differing elementary composition. The darker region exhibits a thickness of roughly 1.0 nm for the *Si(111)* substrates whereas a thicker layer of approx. 2 nm can be observed on *Si(100)*.

No XPS analysis were done for the bilayer samples because a non depth profiling analysis would only illustrate the top surfaces states and no overview of the whole structure can be given. Representatively one cross sectional EDX spectrum of the bilayer samples is shown in figure 13.4. to prove the composition of the coating layers to contain *Nd* and *Ti* on *Si*. Cross sectional TEM-measurements combined with local EDX or ToF-SIMS would reveal the exact layer structure and may have to be performed in the future.

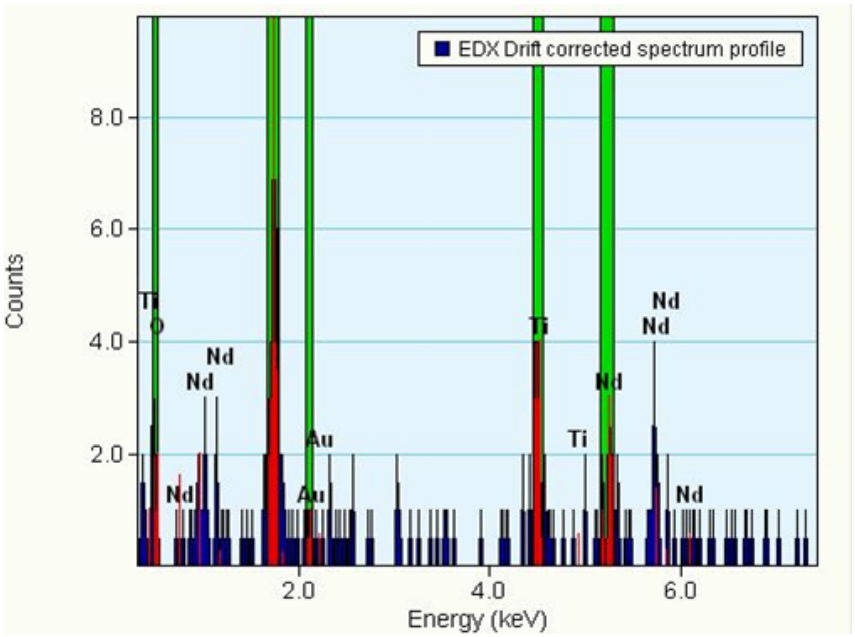


Figure 13.4.: EDX scan of the bilayer thin film on *Si(111)* deposited from 0.005 M $Nd(NO_3)_3 \times 6H_2O$ butanolic precursor solution and 50 cycles of ALD, confirming the oxide film to contain Ti and Nd.

13.3. Electrical Characterization: Bilayer Systems

In the following section, the synthesized bilayer system should be analyzed regarding the electrical performance. In order to investigate the influence of the thermodynamic stability of respective oxides with the substrates, results of the bilayer samples ($TiO_2/Nd_2O_3/Si$) are shown in section 13.3.1 whereas the results of the reverse bilayer ($Nd_2O_3/TiO_2/Si$) samples are summarized in section 13.3.2.

As the decomposition to the Nd_2O_3 requires temperatures almost up to 873 K for the reverse bilayer samples only as deposited (in this case already heated up to approx. 873 K) and samples annealed at 1073 K have been tested. Due to the thermodynamics for the reverse bilayer, an interfacial layer formation of SiO_2 is expected to be formed and depending on its thickness, improves or worsens the electrical properties. Thin SiO_2 layers of a few nm are expected to improve the lattice matching, whereas for thicker layers (>2 nm) the prop-

erties of the SiO_2 lead to severe increased leakage currents due to quantum mechanical tunneling.

The capacitance densities and leakage current densities have been measured, treating the bilayer system as a complete gate dielectric instead of two dielectrics in series. From the previous experiments it was not clear if the contact between the two layers can be assumed as Ohmic and the probability of a non Ohmic contact or mixed layer formation is much higher than pure Ohmic contacts in series. Therefore, in the following the dielectric constants are calculated after equation 12.1 from the detected capacitances in accumulation, equal to the single layers. The complete respective film thickness of the two layers has to be included.

For the sake of completeness however, in appendix G the equations for the calculations of dielectrics in series are elucidated.

Analogous to the single layer, initially the C-V analysis will be shown, including the calculations for κ and EOT values, followed by room temperature I-V analysis. Each part will be concluded with temperature dependent I-V leakage current conduction studies.

13.3.1. C-V and I-V Characterization: Bilayer

Figure 13.5. shows the measured C-V curves of the bilayer gate stacks deposited on *n-Si(111)*.

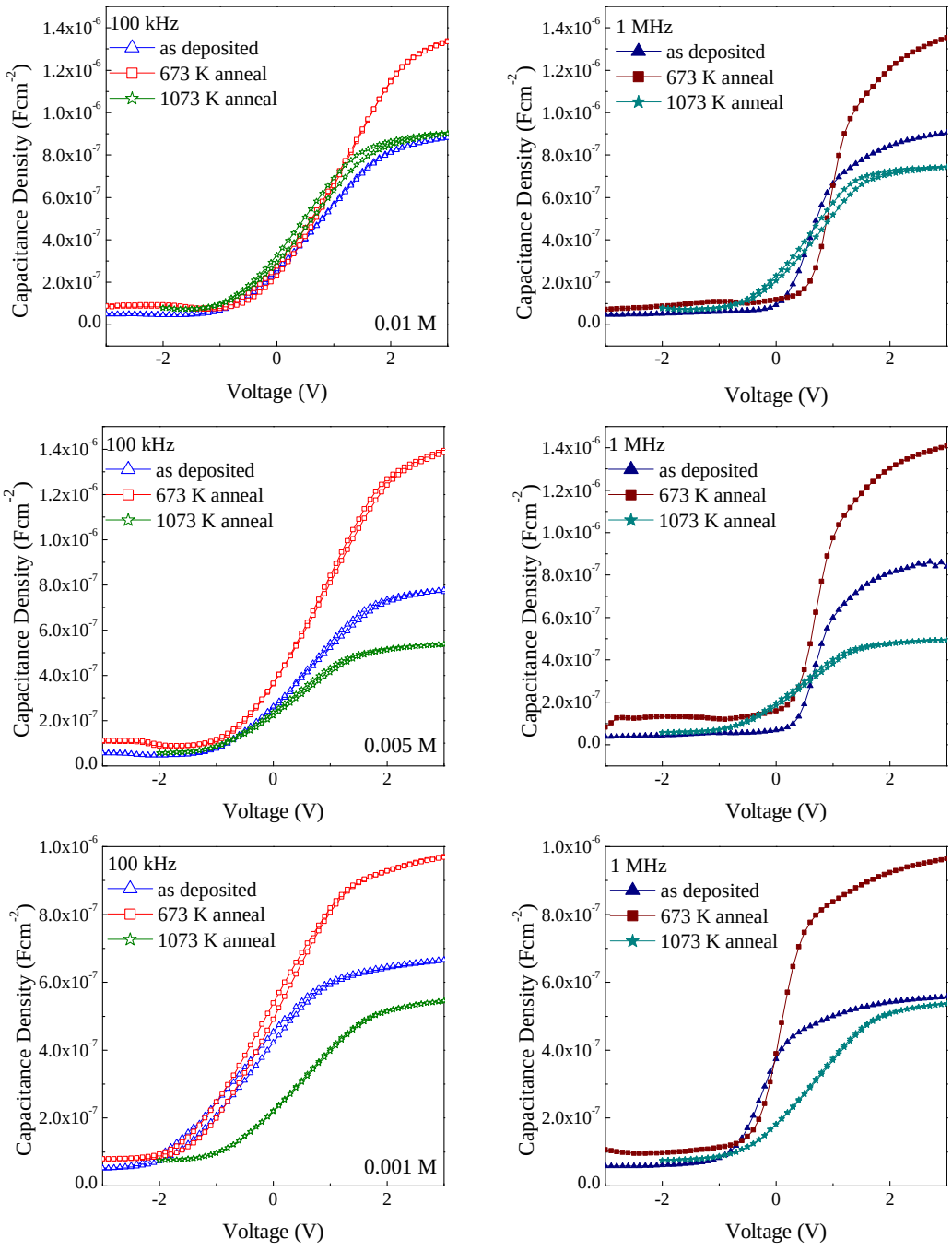


Figure 13.5.: C-V curves of the bilayer films ($TiO_2/Nd_2O_3/Si$) deposited on H-terminated *n-Si(111)* from 0.01 M (top), 0.005 M (middle) and 0.001 M (bottom) $Nd(NO_3)_3 \times 6H_2O$ butanolic precursor solution and ALD-TiO_2 (50 cycles). Shown are the results of bilayer oxide films as deposited and annealed at 673 K/1073 K measured with 100 kHz (left) and 1 MHz (right).

From the measured C-V curves it can be seen that in agreement with the *Nd*-based single layer samples on n-*Si(111)*, no hysteresis can be detected and stable capacitances in accumulation are observed both for 100 kHz and 1 MHz frequency measurements. For all solution concentrations, increased capacitance densities can be observed for the samples annealed at 673 K. Samples annealed at 1073 K exhibit a significant drop of the capacitance density as expected from the analysis of the single layer, since a similar interface reaction and crystallization process is expected due to identical deposition conditions for the initial substrate covering Nd_2O_3 layer.

Analogous the results achieved for p-*Si(100)* substrates are shown in figure 13.6.

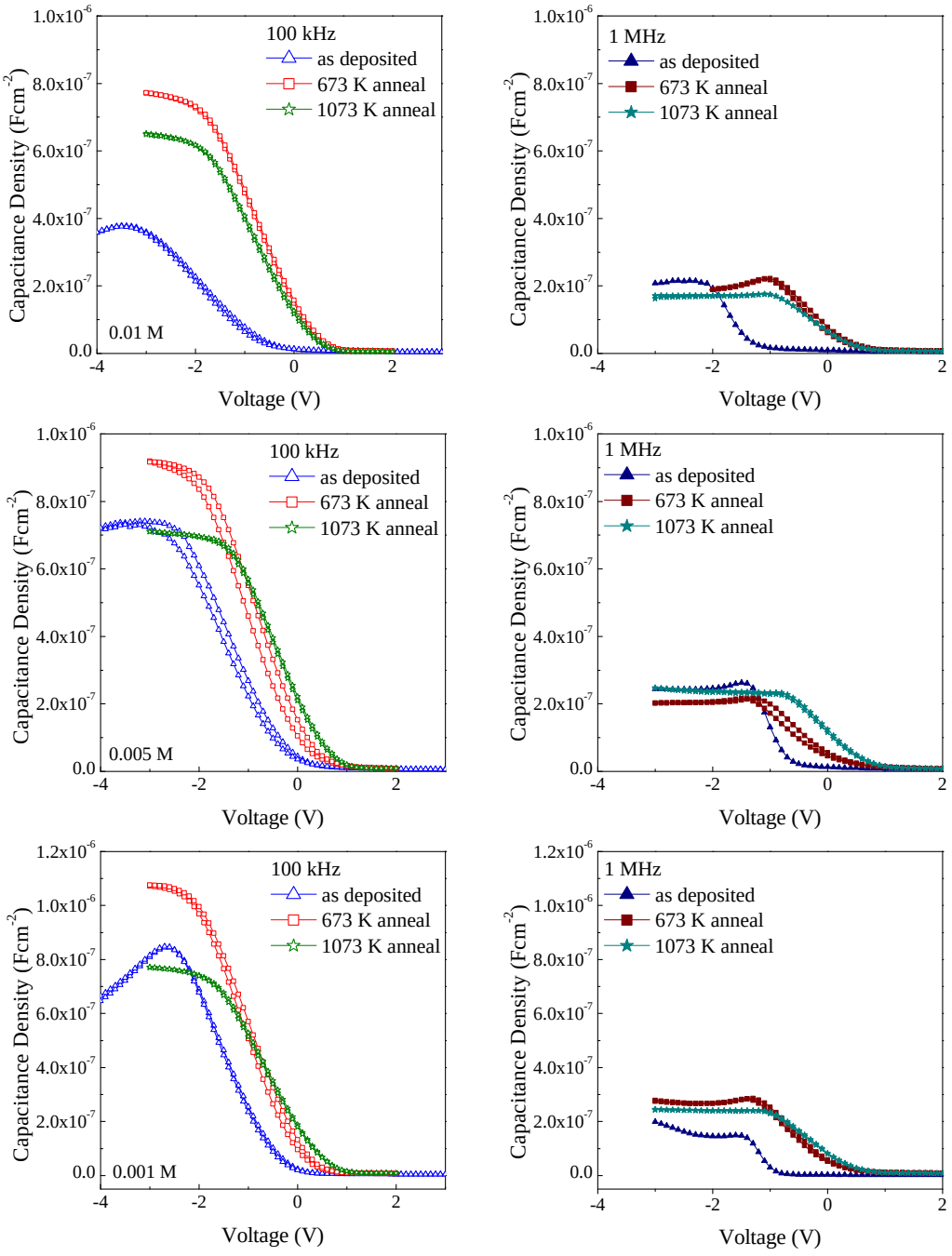


Figure 13.6.: C-V curves of the bilayer films ($TiO_2/Nd_2O_3/Si$) deposited on H-terminated p-$Si(100)$ from 0.01 M (top), 0.005 M (middle) and 0.001 M (bottom) $Nd(NO_3)_3 \times 6H_2O$ butanolic precursor solution and ALD-TiO_2 (50 cycles). Shown are the results of bilayer oxide films as deposited and annealed at 673 K/1073 K measured with 100 kHz (left) and 1 MHz (right).

As for the n-*Si(111)* substrates, the detected curves do not exhibit any hysteresis, which is contrary to the single layer films on p-*Si(100)*, indicating a low amount of traps and charges within the film and at the interface. In agreement with the single layer analysis, significant drops in the accumulation capacitance, while comparing measurements done at 100 kHz to faster measurements at 1 MHz, can be observed.

The measured capacitance densities at 100 MHz, calculated κ and EOT values are summarized in table 13.2. The respective film thickness has been determined, according to the results shown in chapter 10. As the films on both substrates types have been synthesized in batch production each, the film thickness of the TiO_2 layer can assumed to be equal for all samples (n-*Si(111)* = 2.6 nm; p-*Si(100)* = 3.2 nm). It has been shown from the HRTEM imaging that a decreased film thickness of the Nd_2O_3 layer in between the substrate and the covering TiO_2 can be observed (0.005 M: 3.7 nm vs. 3.0 nm) in comparison to the single layer system. As for the other solution concentrations no HRTEM analyses are available, the respective reduced film thickness has been calculated related to the determined linear dependency of the film thickness and the precursor solution concentration as 2.6 nm for the films deposited from the 0.001 M precursor solution and approx. 3.8 nm for the films deposited from the 0.01 M precursor solution.

It can be seen that both substrate types show the highest κ values for samples annealed at 673 K, whereas decreased values can be measured for the as deposited and at 1073 K annealed bilayer oxide films. The bilayer samples exhibit a maximum dielectric constant of 9.8 for the gate stack deposited from the 0.01 M precursor solution on n-*Si(111)* annealed at 673 K. Whereas the lowest calculated κ value is 3.3 for the samples generated from 0.001 M precursor solution on n-*Si(111)*. Films on p-*Si(100)* substrates exhibit maximum κ values of 7.2 for the films annealed at 673 K and deposited from the 0.001 M precursor solution and ALD. A minimum κ value of 2.9 for the films deposited from the 0.01 M precursor solution and ALD has been measured. EOT values of 2.4 up to 4.5 nm are achieved for the high-κ films. For films, which exhibit low κ values, EOT values between 6.4 nm and 9.1 nm could be calculated.

Table 13.2.: Capacitance densities measured at 100 kHz and the calculated κ and EOT values of the bilayer samples ($TiO_2/Nd_2O_3/Si$) deposited from ALD and 0.01 M, 0.005 M and 0.001 M $Nd(NO_3)_3 \times 6H_2O$ butanolic precursor solution on n-*Si(111)* and p-*Si(100)* (oxides as deposited, annealed at 673 K and 1073 K).

Sample		**Capacitance Density** (Fcm^{-2})	κ	**EOT**
n-*Si(111)*				
0.01 M	as dep.	8.82×10^{-7}	6.2	2.9 nm
6.4 nm	673 K	1.39×10^{-6}	9.8	2.5 nm
	1073 K	9.03×10^{-7}	6.3	3.8 nm
0.005 M	as dep.	8.06×10^{-7}	5.1	4.3 nm
5.6 nm	673 K	1.46×10^{-7}	9.2	2.4 nm
	1073 K	5.38×10^{-7}	3.4	6.4 nm
0.001 M	as dep.	6.64×10^{-7}	4.0	5.2 nm
5.2 nm	673 K	9.96×10^{-7}	5.0	3.5 nm
	1073 K	5.44×10^{-7}	3.3	6.9 nm
p-*Si(100)*				
0.01 M	as dep.	3.79×10^{-7}	2.9	9.1 nm
7.0 nm	673 K	7.72×10^{-7}	5.9	4.5 nm
	1073 K	6.52×10^{-7}	5.0	5.3 nm
0.005 M	as dep.	7.42×10^{-7}	5.2	4.7 nm
6.2 nm	673 K	9.14×10^{-7}	6.4	3.8 nm
	1073 K	7.10×10^{-7}	5.0	4.9 nm
0.001 M	as dep.	8.48×10^{-7}	5.7	4.1 nm
5.8 nm	673 K	1.08×10^{-6}	7.2	3.2 nm
	1073 K	7.71×10^{-7}	5.1	4.5 nm

To evaluate the achieved results, the leakage current densities of the films are essential, as already mentioned. I-V analyses measured at room temperature, are shown in figure 13.7.

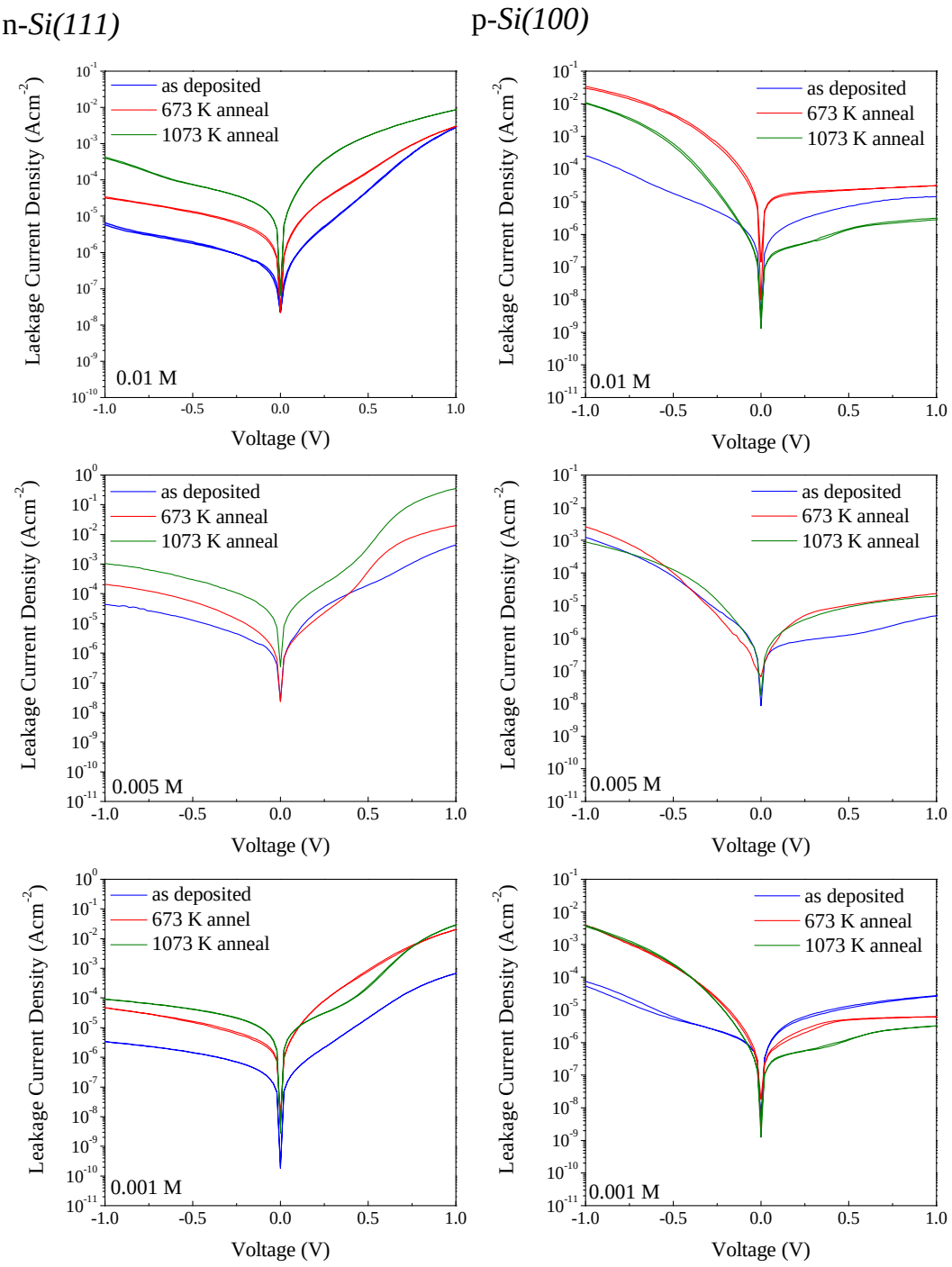


Figure 13.7.: I-V curves of the bilayer samples ($TiO_2/Nd_2O_3/Si$) generated from ALD-TiO_2 and wet chemical deposition from 0.001 M/0.005 M/0.01 M $Nd(NO_3)_3 \times 6H_2O$ butanolic precursor solution on n-*Si(111)* (left) and p-*Si(100)* (right).

All curves exhibit characteristic on and off state shapes for p- and n-type substrates. The achieved leakage current densities detected at ±1 V, are summarized in table 13.5.

Table 13.3.: Leakage current densities measured from the bilayer system ($TiO_2/Nd_2O_3/Si$) deposited on n-*Si(111)* and p-*Si(100)*.

Leakage current (Acm^{-2})	**0.01 M**	**0.005 M**	**0.001 M**
n-*Si(111)*			
as dep.	5.74×10^{-6}	4.39×10^{-5}	3.46×10^{-6}
673 K	3.40×10^{-5}	2.07×10^{-4}	4.56×10^{-5}
1073 K	4.26×10^{-4}	1.04×10^{-3}	8.89×10^{-5}
p-*Si(100)*			
as dep.	1.43×10^{-5}	4.87×10^{-6}	2.71×10^{-5}
673 K	3.14×10^{-5}	2.34×10^{-5}	1.22×10^{-5}
1073 K	3.13×10^{-5}	1.95×10^{-5}	5.45×10^{-6}

At room temperature a minimum leakage current density of 3.46×10^{-6} Acm^{-2} and a maximum of 1.04×10^{-3} Acm^{-2} could be detected for the bilayer system on n-*Si(111)* whereas the films on p-*Si(100)* exhibited a minimum value of 4.87×10^{-6} Acm^{-2} and a maximum of 3.14×10^{-5} Acm^{-2}. It can be seen that most of the detected leakage current densities are within the range of 10^{-5} Acm^{-2} - which is with respect to the EOT values - within the order of magnitude for conventionally used SiO_2 (compare table 12.7.). Increased leakage currents up to 10^{-3} Acm^{-2}, can be detected for annealed samples on n-*Si(111)* substrates. Films deposited on p-*Si(100)* again show a decreasing tendency except from the 0.01 M solution based samples, which anyway are expected to show non reliable results due to insufficient film formation. With respect to the shown κ values, the trend that films annealed at 673 K show the best electrical performance, can not be verified by the I-V analysis.

Temperature dependent I-V measurements, analogous to the single layer samples, show the leakage current behavior at increased temperatures. The temperature dependent I-V curves, measured from 298 K to 398 K of the bilayer systems deposited from 0.005 M $Nd(NO_3)_3 \times 6H_2O$ butanolic precursor solution and ALD of TiO_2, are shown in figure 13.8.

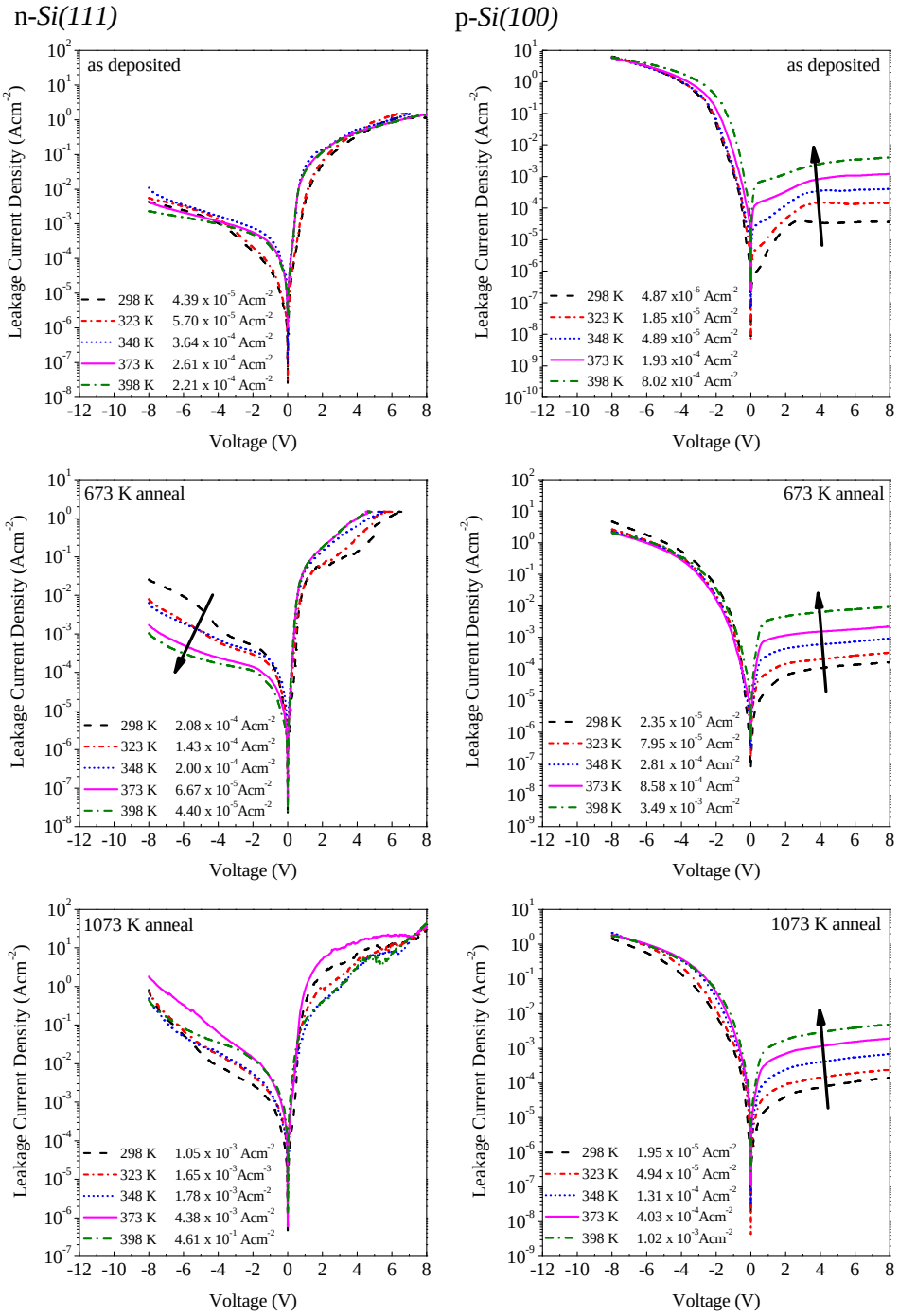


Figure 13.8.: Temperature dependent I-V curves of the bilayer $(TiO_2/Nd_2O_3/Si)$ system deposited from 0.005 M $Nd(NO_3)_3 \times 6H_2O$ butanolic precursor solution and ALD of TiO_2. The samples are the oxides as deposited and after annealing at 673/1073 K on n-*Si(111)* (left) and p-*Si(100)* (right).

In agreement with the single layer systems, highly temperature dependent leakage current densities can be detected for p-*Si(100)* substrates, whereas a systematic increase of the leakage current densities can be observed for higher operation temperatures. n-*Si(111)* substrates show just a slight change in the leakage current density for varying processing temperatures but no systematic increase. Differing from the expectations and the discussed results decreased leakage current densities can be observed for higher process temperatures for the bilayer films annealed at 673 K. That is unusual as for higher temperatures higher electron mobilities and therefore promoted electron conduction is anticipated.

As it has already been shown from the analysis of the wet chemical deposited single layer that a precise assignment of the leakage current conduction mechanism is probably not possible. This is caused by complex interface structures and resulting charge carrier transport. At this point the analysis of the $\ln(J/E)$ vs. $E^{1/2}$ plot shall be omitted as the direct interface between the substrate and the film is formed similarly to the single layer and the film thickness is again below the thickness of a formed depletion layer.

13.3.2. C-V and I-V Characterization: Reverse Bilayer

All measured C-V curves of the 0.001 M, 0.005 M and 0.01 M butanolic $Nd(NO_3)_3 \times 6H_2O$ precursor solution based Nd_2O_3 films deposited on top of 3 nm of ALD deposited TiO_2 (as deposited and annealed at 1073 K) on n-*Si(111)* are summarized in figure 13.9. The thickness of the TiO_2 needs to be assumed to be 3 nm from the settings of the ALD deposition. The concentration dependent film thickness of the Nd_2O_3 layer has been described in chapter 10. Therefore, in the following reverse bilayer films ($Nd_2O_3/TiO_2/Si$) deposited from 0.01 M $Nd(NO_3)_3 \times 6H_2O$ butanolic precursor solution covered with ALD-TiO_2 are considered to show a film thickness of 7.5 nm, from 0.005 M precursor solution of 6.7 nm and from 0.001 M precursor solution of 6.3 nm.

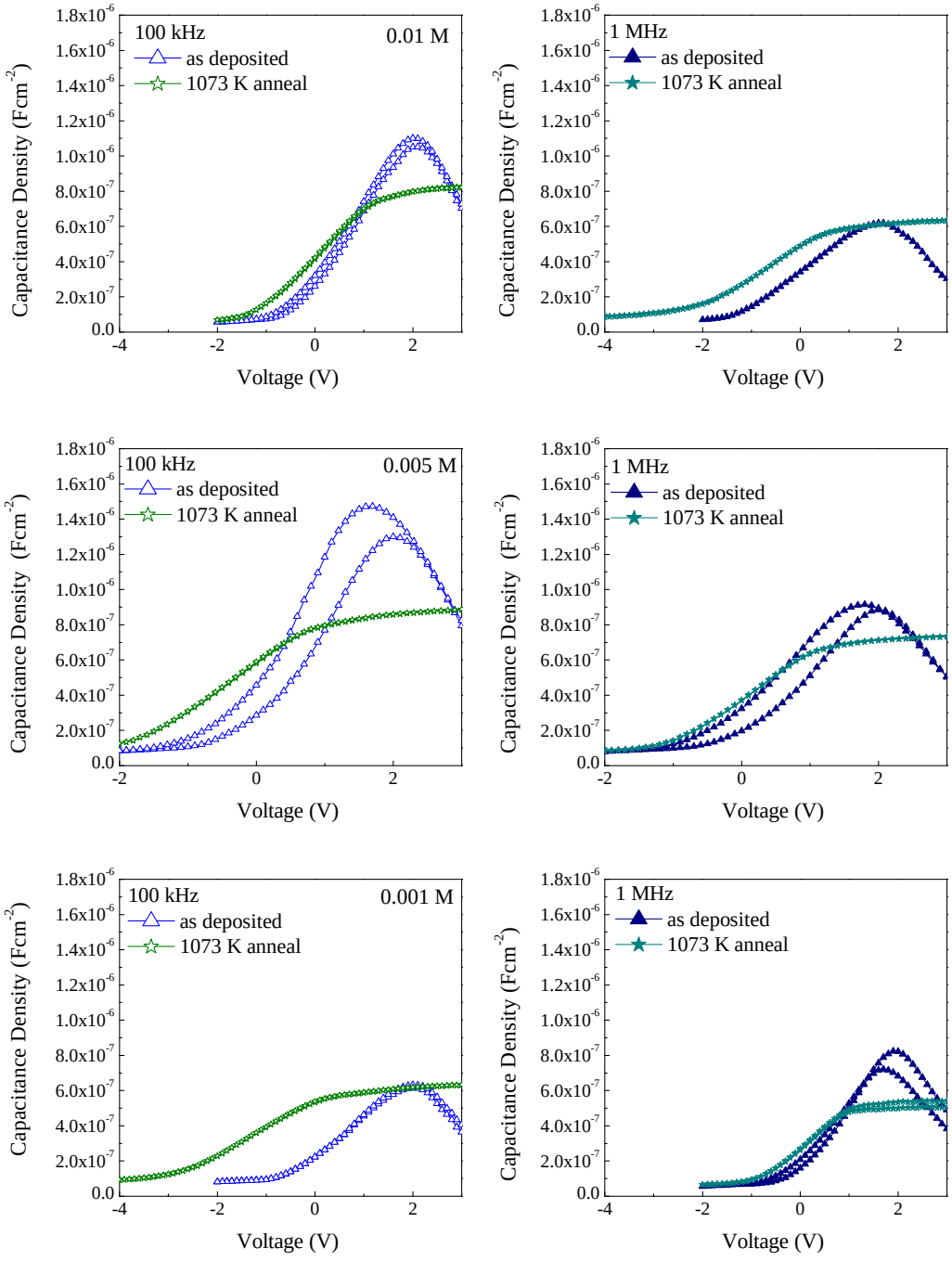


Figure 13.9.: C-V curves of the reverse bilayers Nd_2O_3/TiO_2 deposited on n-*Si(111)* for films deposited from 0.001 M, 0.005 M and 0.01 M $Nd(NO_3)_3 \times 6H_2O$ butanolic precursor solution and ALD of TiO_2 (50 cycles). Shown are data of the oxide films as deposited and annealed at 1073 K.

From the measured curves, it can be seen that the C-V characteristics of the reverse bilayer strongly differ from the normal bilayer and single layer samples as hysteresis appears in the measured curves for the as deposited samples during measurements at 100 kHz and 1 MHz. A significant characteristic change in the curves shapes appears from the as deposited to the annealed samples. All annealed samples show a low but stable accumulation capacitance, whereas as deposited samples show severe hysteresis additionally to a maximum within the curve and no constant capacitance in accumulation. For the samples deposited from 0.005 M and 0.01 M precursor solution, a drop in the capacitance can be detected for 100 kHz and 1 MHz measurements, possibly due to the formation of multi layer insulator and therefore interfacial oxide species. The detected maxima within the curves of the as deposited reverse bilayers might result from high leakage currents, which needs to be determined by I-V analysis.

Analogous all measured C-V curves of the oxides deposited from 0.001 M, 0.005 M and 0.01 M solution on top of 3 nm of ALD deposited TiO_2 (as deposited and 1073 K anneal) on p-*Si(100)* are summarized in figure 13.10.

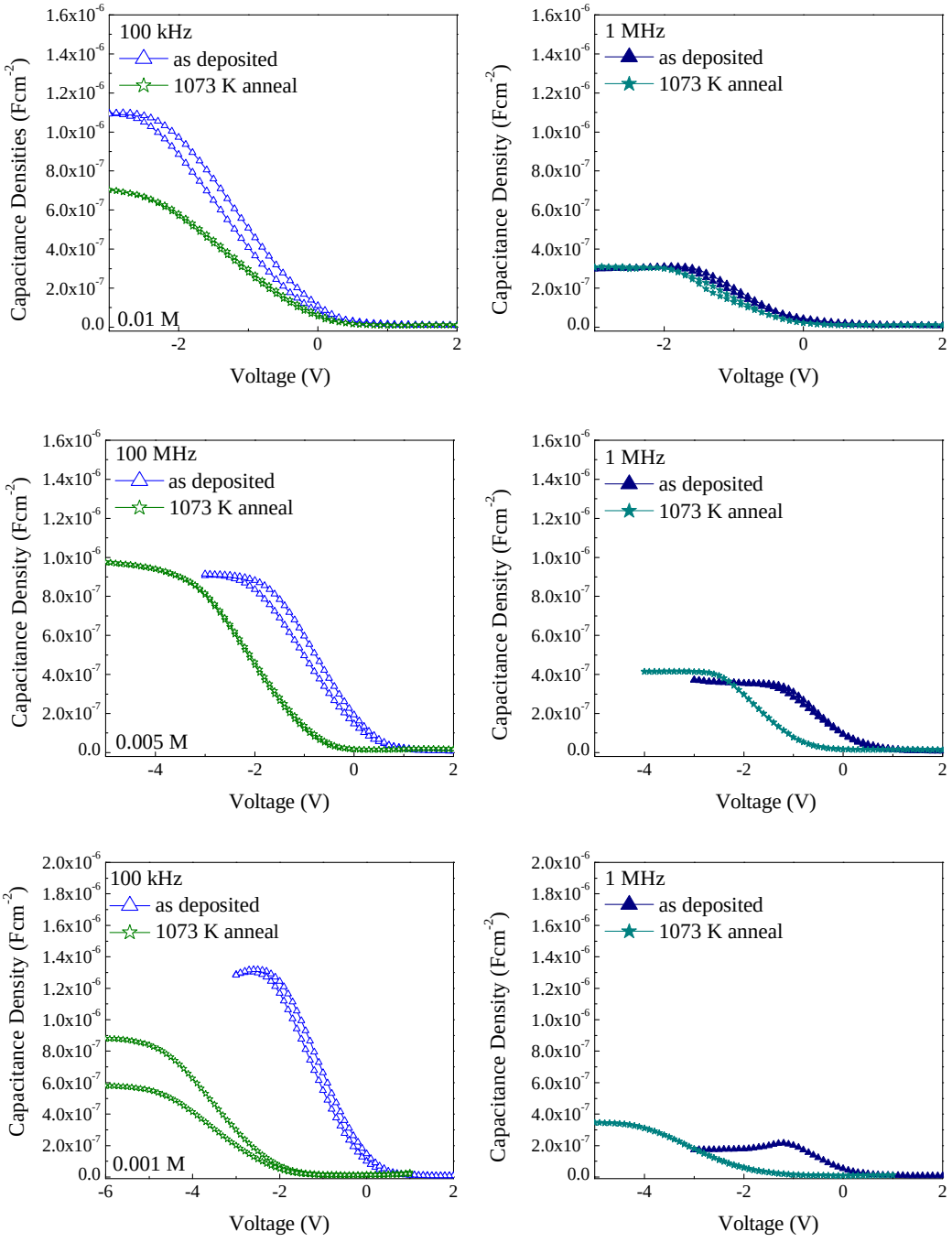


Figure 13.10.: C-V curves of the reverse bilayers Nd_2O_3/TiO_2 deposited on p-*Si(100)* for films deposited from 0.001 M, 0.005 M and 0.01 M $Nd(NO_3)_3 \times 6H_2O$ butanolic precursor solution and ALD of TiO_2 (50 cycles). Shown are data of the oxide films as deposited and annealed at 1073 K.

Reverse bilayer systems deposited on H-terminated p-*Si(100)*, exhibit smoother C-V curves than the reverse bilayer system on n-*Si(111)*. Slight hysteresis can be detected for as deposited samples measured at 100 kHz. A stable accumulation capacitance can be observed for as deposited and annealed samples. A huge drop in the capacitance density is detected from 100 kHz to 1 MHz frequency measurements, as it has been observed for the single layer samples. Samples deposited from 0.001 M show an outlying behavior measured at 100 kHz as different accumulation capacitances are measured for the forward and return biasing.

The respective capacitance densities, measured at 100 kHz and the calculated κ and EOT values, are listed in table 13.4.

Table 13.4.: Capacitance densities measured at 100 kHz and the calculated κ and EOT values of the reverse bilayer samples deposited from 50 cycles of ALD (TiO_2) and 0.01 M, 0.005 M and 0.001 M $Nd(NO_3)_3 \times 6H_2O$ butanolic precursor solution (as deposited and annealed at 1073 K).

Sample		**Capacitance Density** (Fcm^{-2})	κ	**EOT**
n-*Si(111)*				
0.01 M	as dep.	1.00×10^{-6}	9.3	3.1 nm
7.5 nm	1073 K	8.25×10^{-7}	7.0	4.2 nm
0.005 M	as dep.	1.48×10^{-6}	11.1	2.3 nm
6.7 nm	1073 K	8.86×10^{-7}	6.7	3.9 nm
0.001 M	as dep.	6.14×10^{-7}	4.3	5.6 nm
6.3 nm	1073 K	6.32×10^{-7}	4.5	5.5 nm
p-*Si(100)*				
0.01 M	as dep.	1.10×10^{-6}	9.3	3.1 nm
	1073 K	7.03×10^{-7}	6.0	4.9 nm
0.005 M	as dep.	9.14×10^{-7}	6.9	3.8 nm
	1073 K	9.75×10^{-7}	7.4	3.5 nm
0.001 M	as dep.	1.31×10^{-6}	9.3	2.6 nm
	1073 K	8.79×10^{-7}	6.3	3.9 nm

For n-*Si(111)* substrates, dielectric constants up to 11.1 could be achieved for the samples deposited from 0.005 M precursor solution. The lowest κ value has been detected for the films deposited from 0.001 M precursor solution with 4.3. The films deposited from 0.01 M and 0.005 M precursor solutions show higher κ values for as deposited than annealed samples, whereas 0.001 M solution lead to equal values for both samples. The EOT was determined as a minimum of 2.3 nm, whereas the lowest κ value lead to a maximum in EOT of 5.6 nm. For p-*Si(100)* substrates κ values up to 9.3 have been calculated including a minimum EOT of 2.6 nm. 0.001 M and 0.01 M solution based films show higher κ values for non annealed samples. Both substrate types show the tendency of decreased dielectric constants for the high temperature annealing.

The leakage current densities in dependency on the film thickness are shown in figure 13.11. All curves exhibit the respective typical shape for n-type and p-type substrates. It can be seen that decreased leakage current densities can be observed for the annealed samples, indicating a better interface and film quality for n-*Si(111)* substrates, whereas for the p-*Si(100)* substrates almost no change of the leakage current density in dependency on the annealing process, can be detected.

The decreased leakage current densities after annealing for the n-*Si(111)* substrates are in contrast to the detected dielectric constants, since as mentioned above in table 13.4., all as deposited reverse bilayer structure exhibit higher κ values from the C-V analysis.

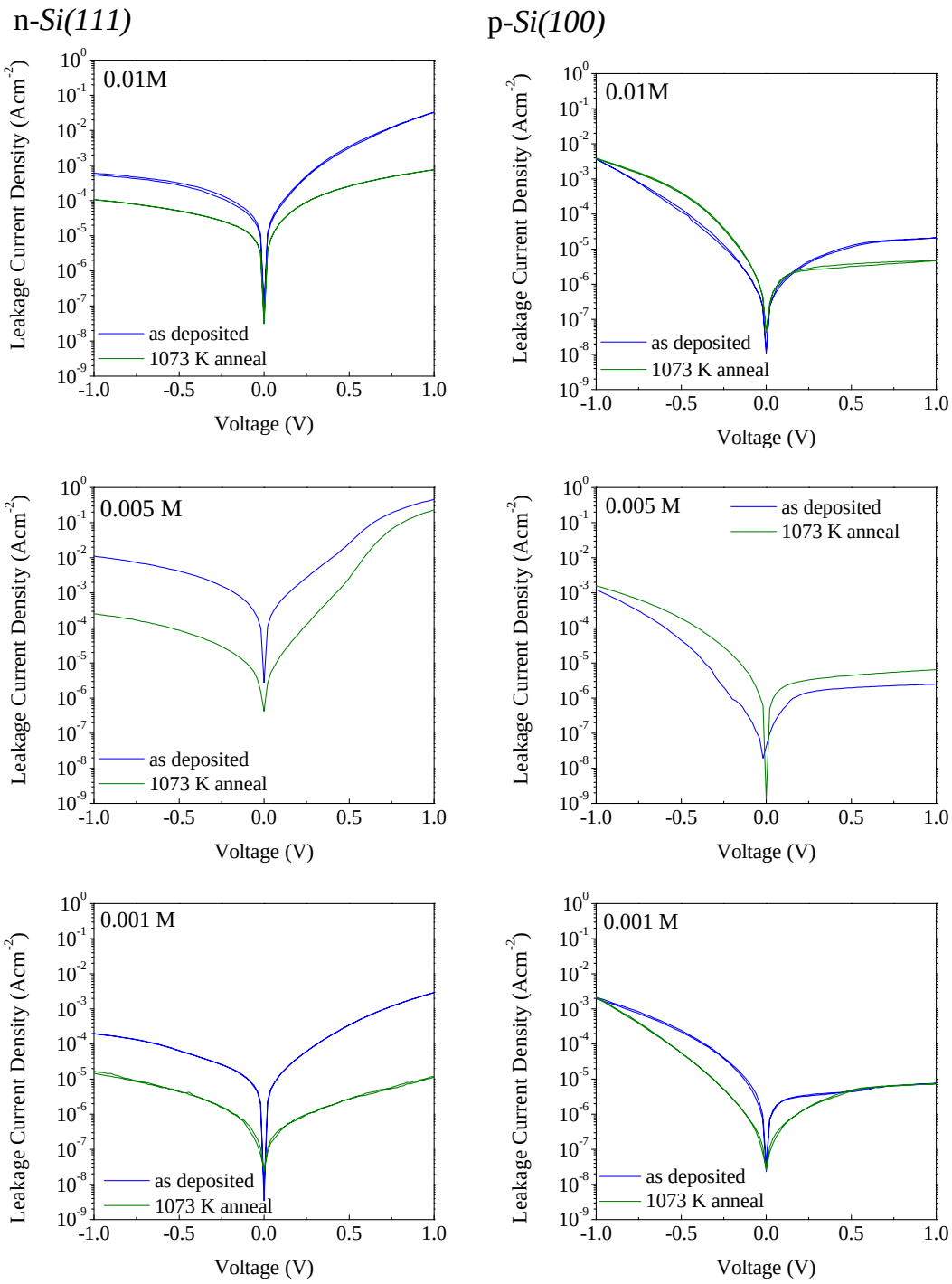


Figure 13.11.: I-V curves of the reverse bilayers films ($Nd_2O_3/TiO_2/Si$) generated from ALD of TiO_2 (50 cycles) and wet chemically deposited Nd_2O_3 from 0.001 M/0.005 M/0.01 M $Nd(NO_3)_3 \times 6H_2O$ butanolic precursor solution on n-*Si(111)* (left) and p-*Si(100)* (right).

The measured leakage current densities are summarized in table 13.5.

Table 13.5.: Leakage current densities measured from the reverse bilayer ($Nd_2O_3/TiO_2/Si$) system deposited on n-*Si(111)* and p-*Si(100)*.

Leakage current (Acm^{-2})	**0.01 M**	**0.005 M**	**0.001 M**
n-*Si(111)*			
as dep.	5.39×10^{-4}	1.19×10^{-2}	1.97×10^{-4}
1073 K	1.08×10^{-4}	2.57×10^{-5}	1.45×10^{-5}
p-*Si(100)*			
as dep.	2.11×10^{-5}	2.43×10^{-5}	7.56×10^{-6}
1073 K	4.69×10^{-6}	6.51×10^{-6}	7.32×10^{-6}

The measured leakage current densities of the reverse bilayer systems are, as expected, higher than the measured values for films, where the thermodynamic stable oxide Nd_2O_3 is in direct contact with the substrate. Reverse bilayer gate stacks deposited on p-*Si(100)* show lower leakage current densities than films deposited on n-*Si(111)*. Annealed samples reveal much lower leakage current densities than non annealed samples, which is contrary to the previously observed results of the bilayer. For reverse oxide films on n-*Si(111)* the lowest leakage current densities could be detected at 1.45×10^{-5} Acm^{-2} and a maximum value of 1.19×10^{-2} Acm^{-2} was observed. Films deposited on p-*Si(100)* showed a minimum leakage current density of 4.69×10^{-6} Acm^{-2} and a maximum of 2.43×10^{-5} Acm^{-2}.

Leakage current densities down to 10^{-6} Acm^{-2} (p-*Si(100)*, annealed at 1073 K) and up to 10^{-2} Acm^{-2} could be measured (n-*Si(111)*, as deposited) .

Even though it was expected from the results of the C-V measurements that reverse bilayers deposited on n-*Si(111)* substrates, show highly leaky behavior, the detected leakage current densities are, with respect to the minimal calculated EOT values, significantly lower than values detected for conventional SiO_2 and within the order of magnitude of the results achieved for the single layer systems on p-*Si(100)*.

The temperature dependent I-V curves are illustrated in figure 13.12., for the reverse bilayer deposited from 0.005 M $Nd(NO_3)_3 \times 6H_2O$ butanolic precursor

solution and 50 cycles of ALD deposition of TiO_2 on H-terminated n-*Si(111)* and p-*Si(100)* samples.

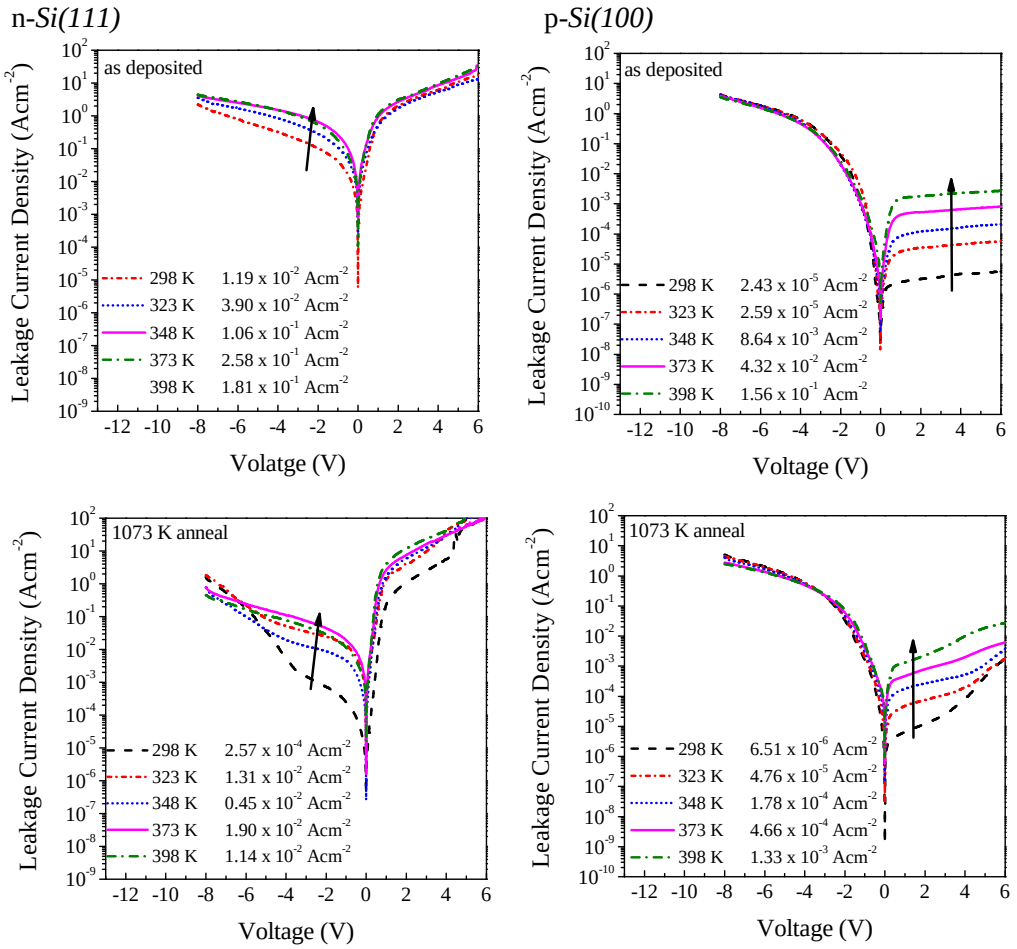


Figure 13.12.: Temperature dependent I-V curves of the reverse bilayer films ($Nd_2O_3/TiO_2/Si$) generated from ALD TiO_2 and wet chemical deposited Nd_2O_3 from 0.005 M $Nd(NO_3)_3 \times 6H_2O$ butanolic precursor solution on n-*Si(111)* (left) and p-*Si(100)* (right) (as deposited and annealed at 1073 K).

Reverse bilayer films on n-*Si(111)* exhibit leakage current densities down to 10^{-2} Acm^{-1} for the as deposited and 10^{-4} Acm^{-1} for the oxide layers annealed at 1073 K. Lower leakage current densities could be observed on p-*Si(100)* substrates, whereby the as deposited samples exhibited values down to 10^{-5} Acm^{-1} and the samples annealed at 1073 K of 10^{-6} Acm^{-1}. Thus for both substrate types better leakage current behavior is observed for samples annealed at higher temperatures. It can be seen that both substrate types ex-

hibit an increase of the leakage current density during a temperature increase at the respective off state biasing. Leakage current densities are detected down to 6.51×10^{-6} Acm^{-1} for the samples annealed at 1073 K. The measured final maximum leakage current densities are within the range of 10^{-3} Acm^{-2} for the annealed and 10^{-1} Acm^{-1} for the non annealed samples.

No strongly systematic temperature dependency is observable from the measurement and even though changes in the leakage current density occur during increased operation temperature for the reasons mentioned regarding the single layer systems at this point a precise analysis of the leakage current conduction mechanism is not possible without further measurements.

13.4. Conclusion and Discussion of the Bilayer Analysis

From the HRTEM imaging it was observed that within the bilayer system an equal film thickness on *Si(100)* and *Si(111)* can be observed, but the film thickness of the Nd_2O_3 layer decreased by 19 % compared to the single layer films, which exhibited a reproducible film thickness of 3.7 nm (s. chapter 10.).

For the ALD deposited TiO_2 layer, two differing film thicknesses are detected, although the number of deposition cycles was equal. This aspect has to be considered carefully, since ALD is expected to show exactly the same film thickness for the same number of cycles, as the process is surface limited. The deposited Nd_2O_3 layers are expected to show the same surface characteristics and therefore an identical surface reaction for the initially deposited single layer of Nd_2O_3. As for other experiments with the used ALD system, the film thickness has been variable for different runs of the deposition process, at this point the varying film thickness of the TiO_2 film is considered to be caused by an instability of the ALD system and not by the surface reaction process. Bilayer films deposited on *Si(100)* show, according to the HRTEM imaging a thin interfacial layer at the direct interface to the substrate.

XPS measurements of the pure Nd_2O_3 on *Si(100)* (s. chapter 11.) indicated a slight increase of the amount of suboxide species after the precursor deposition. However, this was not observed from the HRTEM imaging for the single layer but it obviously effects the formation of the bilayer system. For the bilayer

deposition, the samples are heated to 373 K during the ALD process, which could result in an increased amount of interfacial species detected by the TEM as a darker interfacial layer. Depth profiling is necessary in the future work in order to determine the precise elementary composition of the specific layers.

The film thickness of the Nd_2O_2 layer within the bilayer system has been identified to exhibit a lower film thickness than it was measured highly reproducible for the pure single layer of Nd_2O_3 (compare chapter 10.). A decreased film thickness can be caused by a surface reaction on the top surface of the Nd_2O_3, induced by the subsequent ALD deposition after the oxide generation from thermolysis. From the XPS analysis shown in chapter 11., it was demonstrated that the final Nd_2O_3 film from precursor thermolysis exhibits loosely bound surface H_2O species but no direct indication of a significant amount of surface *-OH* groups after the oxide formation and therefore no typical covalent anchoring of the $TiCl_4$ molecules from the initial ALD pulse is possible. A differing surface reaction might lead to a decrease of the Nd_2O_3 film thickness one the one hand due to a reaction of the top most surface species. On the other hand it can be suggested that the initial step of the ALD process, the anchoring of the $TiCl_4$, by a direct surface reaction, is not possible and the typical ALD surface controlled reaction mechanism is not given. Instead the $TiCl_4$ might be deposited as a salt like layer followed by a reaction with the H_2O as oxygen source in the second precursor pulse within the ALD chamber. The differing surface reaction is also indicated from the results of the topography studies as different roughness values have been observed (compare section 13.2.1. Another possible explanation is a chemical reaction with the underlying substrate due to increased process temperatures. Minor measurement inaccuracies caused by the alignment of the cross sectional lamella within the TEM column can not be ruled out.

From the AFM analysis it is notable that for both substrate types at 673 K, homogeneous structures can be observed with the lowest roughness detected at 1.02 nm for bilayer structures on p-*Si(100)*. Furthermore, for the annealed samples the bilayer structures show a lower roughness on *Si(100)* than on *Si(111)*, which is contrary to the single layer deposition.

The generated bilayer structure exhibits a higher film thickness, therefore detected higher roughness values need to be attempted to be related to the respective film thickness of 5.6 nm (on *Si(111)*) and 6.2 nm (on *Si(100)*) (s.

chapter 10.). Table 13.6. summarizes the percentage of roughness related to the film thickness.

Table 13.6.: Percentage of the measured roughness values of the oxide films related to the respective film thickness.

	Si(111)	***Si(100)***
as dep.	54.3 %	79.4 %
673 K	36.6 %	16.5 %
1073 K	43.7 %	28.3 %

With respect to the film thickness, the RMS results of the bilayer structures are comparable with the data detected for single layer on *Si(111)* substrates, but the net RMS values are much higher. The increased roughness at the top surface, could be related to differing interface structures reactions, caused by the ALD process and the underlying surface termination which was created from the wet chemical deposition process. The surface reactions obviously cause a more "bumpy" structure at the top surface. Rougher surfaces might lead to higher leakage current densities as the defects may serve as leakage path.

In the future, in situ studies of the ALD process are necessary, in order to achieve a more detailed image of the generation of the top covering second oxide layer. In situ ALD studies have been invented and introduced recently by Kolanek et al. in 2011.[240]

Results of the electrical characterization of bilayer gate stacks deposited from different techniques are rarely published in the literature. The system has been treated as a single gate stack formed of different materials. Therefore in the following the electrical performance of the shown samples should be discussed in comparison to single layer systems, deposited from the wet chemical approach and literature known data for conventional techniques.

For the bilayer films ($TiO_2/Nd_2O_3/Si$) deposited on n-*Si(111)* no hysteresis could be observed from the C-V analysis and no drop of capacitance from the 100 kHz to the 1 MHz measurements. Therefore, it can be concluded that the systems are of high quality with a low amount of traps and charges. A maximum κ value could be measured as 9.8 (EOT = 2.5 nm). The best results have been achieved for samples, which have been annealed at 673 K,

high temperature annealing lead to drastically decreased κ values, as it has also been observed for the Nd_2O_3 single layers, which might be related to an interfacial layer formation due to reoxidation of the substrate. Furthermore, the oxides might crystallize so that grain boundaries are formed. Leakage current densities down to 5.74×10^{-6} Acm^{-2} have been detected. The leakage current density is strongly dependent on the annealing treatment. For high annealing temperatures high leakage current densities could be detected for the bilayer films deposited on n-*Si(111)* substrates.

Bilayer films on p-*Si(100)* show with respect to the C-V analysis, comparable results as the bilayer oxide films on n-*Si(111)*, which is contrary to the single layer system. A slight hysteresis in the C-V curves indicates lower electrical performance, which is confirmed by a drop in the capacitance density from 100 kHz to 1 MHz frequency treatment. For bilayer p-*Si(100)* samples the maximum κ values achieved, has been calculated as 7.2, whereas the minimum leakage current density could be determined as 5.45×10^{-6} Acm^{-2}. The oxide bilayer on p-*Si(100)* shows contrary to the n-*Si(111)* substrates stable or decreased leakage current densities for higher annealing temperatures.

Most of the detected leakage current densities for both substrate types are within the range of 10^{-5} Acm^{-2}, which is, with respect to the EOT values (in the range of 2-3 nm), still within the order of magnitude for conventionally used SiO_2 (s. table 12.7.).

The reverse bilayer systems ($Nd_2O_3/TiO_2/Si$) must be treated as a multilayer system, due to the thermodynamic instability of the TiO_2 layer in direct contact with *Si*. Thus, a reactively formed interfacial oxide layer has to be included ($Si/SiO_x/TiO_2/Nd_2O_3$). This can be verified by the appearance of the C-V curves, measured at different frequencies, since the capacitance density in accumulation drops during 1 MHz biasing compared to the measurements at 100 kHz. The drop in the capacitance of the reverse bilayer intensifies the presumption that interfacial layers are formed as expected, due to the thermodynamic instability of TiO_2 in contact with *Si*. For the reverse bilayers as deposited samples showed improved electrical performance compared to samples, which have been annealed at 1073 K. The maximum κ values detected are 11.2 for n-*Si(111)* and 9.3 for p-*Si(100)* substrates. Hysteresis could be observed during C-V characterization of n-*Si(111)* substrates. The appearing hysteresis implies the appearance of an increased amount of interfacial traps

and charges within the films, which might also be caused by the expected interface reaction.

The minimum in leakage current density for the reverse bilayer systems could be measured as 1.45×10^{-5} Acm^{-2} for n-*Si(111)* and 4.69×10^{-6} Acm^{-2} for p-*Si(100)* substrates and EOT values down to 2.6 nm could be calculated. With respect to the low EOT values the measured leakage currents are still within two to three orders of magnitude lower than values detected for thermally grown SiO_2 at room temperature (s. table 12.7.). Therefore, the expectations that the formation of an ultra thin interfacial layer of SiO_2 might lead to improved electrical performances due to a better lattice bridging instead of destructive performances, can be confirmed.

Reverse bilayer systems exhibited leakage current characteristics contrary to all previously measured data as lower leakage current values were observed for annealed p-*Si(100)* substrates instead of *Si(111)*. This is notable, as for the reverse bilayer case, the initial anchoring of the gate stack on the substrate is caused by ALD instead of the wet chemical deposition technique and the initial interface structure is formed by a chemical reaction instead of the formation of a salt like layer of the precursor species. Since ALD is dependent on the available ordered surface sites, the role of the higher amount of dangling bonds comes into account for n-*Si(111)* surfaces leading to poorer electrical performances compared to p-*Si(100)*.

Compared to single layer systems of pure TiO_2 on Si substrates (summarized in appendix F.) which exhibited κ values up to 11.2 but with respect to the EOT significantly high and intolerable leakage current densities the shown results of the reverse bilayer systems are remarkably good. This leads to the conclusion that as expected the implementation of a second high-κ material opens the possibility to improve the electrical performance of the gate stack but the limits are set by the worst dielectrics within the gate stack - in this case the formed sub/dioxide layer at the interface to the underlying substrate.

From temperature dependent I-V analysis again non symmetric and mostly stable leakage current densities could be observed for the films deposited on n-*Si(111)*, whereas increased leakage current densities could be observed at higher processing temperatures for the reverse bilayer system on p-*Si(100)*.

In order to get an impression about the comparability of the synthesized gate stacks with literature reported data and the wet chemically deposited layers, the achieved data are concluded in figure 13.13.

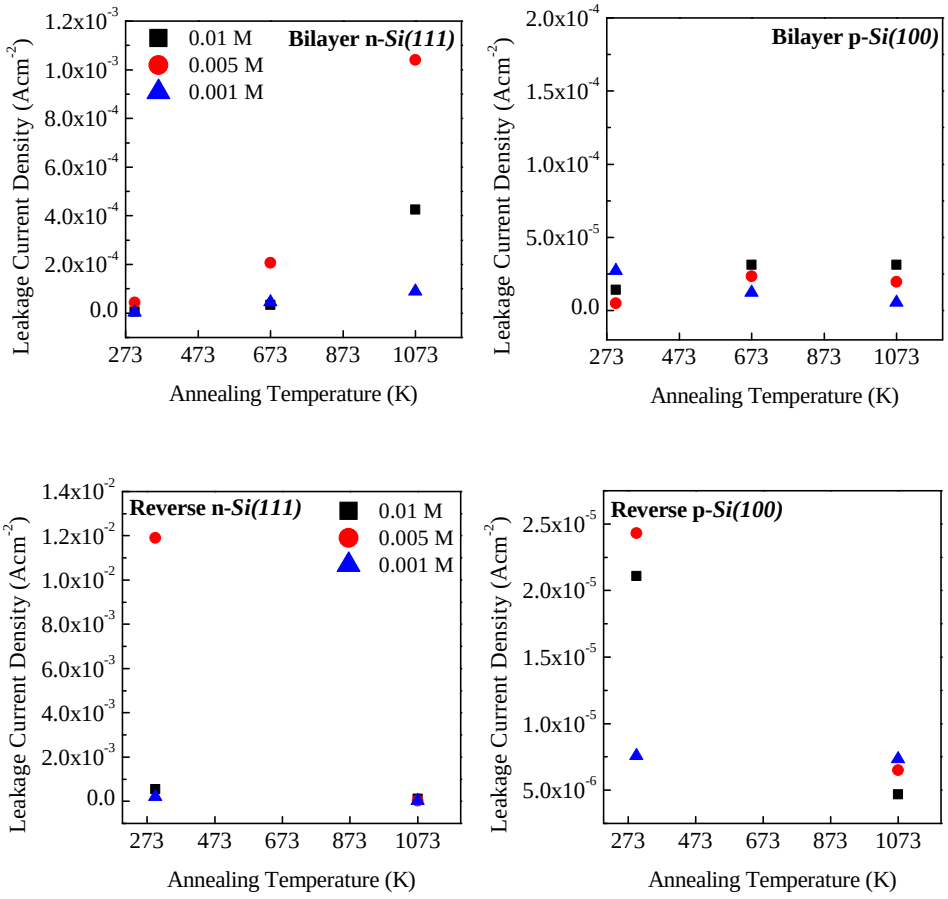


Figure 13.13.: Dependency of the leakage current density on the solution concentration of the Nd-based solution and the respective annealing temperature. Shown are bilayer ($TiO_2/Nd_2O_3/Si$) (top) and reverse bilayer ($Nd_2O_3/TiO_2/Si$) (bottom) samples deposited from 0.01 M, 0.005 M and 0.001 M $Nd(NO_3)_3 \times 6H_2O$ butanolic precursor solution and ALD generation of TiO_2 (50 cycles), after deposition, annealing at 673 K and 1073 K.

It can be seen that no obvious trends as for the single layer can be observed for the leakage current densities from all bilayer and reverse bilayer samples. The achieved values show a distribution within a major number of data points within the range of 10^{-4} to 10^{-6} Acm^{-2}.

As a general point it can be mentioned that obviously changes in the structure with respect to a possible crystallization of the films effect the electrical performances. TiO_2 and Nd_2O_3 are expected to crystallize at temperatures above 830 K. For crystalline structures the impact of the lattice matching of the substrate and the covering oxide layer comes into account for the electrical performance as defects, unordered vacancies and grain boundaries may lead to increased or changed electron conduction. For titanium oxides it is known form literature that interstitials are formed within the crystal lattice and therefore differing oxygen stoichiometries are expected at higher annealing temperatures.[241] For crystalline structures the interface structure is completely different to amorphous and detailed studies are necessary in future work in order to investigate the specific states within the films and at the interfaces.

The dielectric constant vs. EOT and the leakage currents vs. EOT values are shown in figure 13.14.

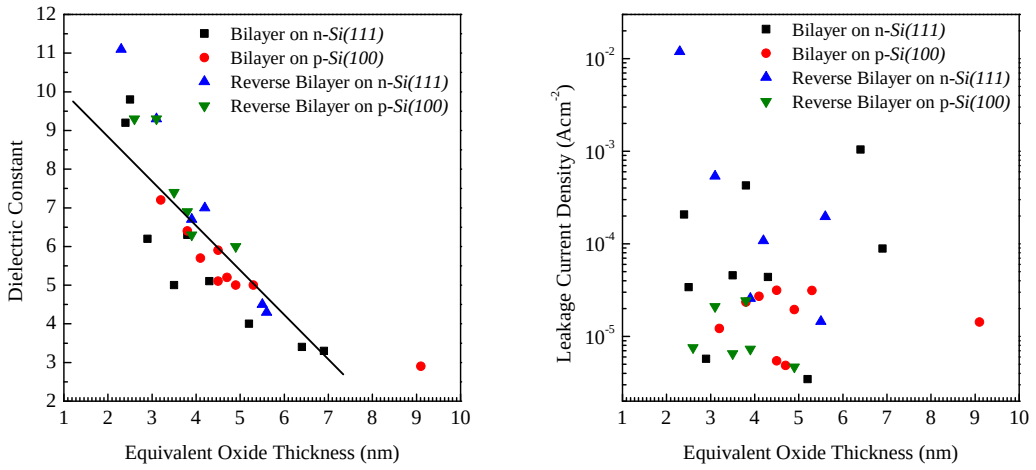


Figure 13.14.: κ values and leakage current densities in dependency on the respective EOT values for the generated bilayer ($TiO_2/Nd_2O_3/Si$) and reverse bilayer ($Nd_2O_3/TiO_2/Si$) gate stacks on *H-Si(111)* and *H-Si(100)*.

Again, a relatively broad distribution of leakage current densities is displayed (right image figure 13.14) and no linear dependency between the EOT and respective leakage current, could be detected, as it was observed for the single layers.

For all bilayer and reverse bilayer systems the temperature dependent I-V measurements have shown that depending on the type of sample differing tendencies with respect to the leakage current densities can be observed. However, a common feature of all measurements is a detectable more or less strong temperature influence on the leakage current conduction, but no systematic trends are observable which makes a precise allocation to the Poole-Frenkel or Schottky emission at this point not feasible. As for the single layer systems the leakage current conduction is probably caused by an overlay of different mechanisms with a strong influence of the temperature induced thermal excitation of trapped electrons or the electron transport across the potential barrier at the interface. For the generated ultra thin layers the width of the space charge region might exceed the full layer thickness and therefore an easy allocation of the responsible conduction mechanism is not possible at this point. Furthermore the complex interface structures are not understood in detail so far, causing a factor of uncertainty if the current conductions is mainly governed by interface or bulk charge carriers. Therefore the equations introduced in section 3.2.4 can not be transferred without restrictions and a precise calculation to identify the leakage current conduction mechanisms is not possible without further investigations.

It should be emphasized that *Si(111)* substrates exhibit an actually lower temperature dependency, which is with respect to a device stability of vital importance as low leakage current densities can be guaranteed over a wide temperature regime. The interlinked joule heating and increased leakage conduction do not enhance each other.

Independently from the final performance, it has been shown that bilayer and reverse bilayer gate stacks show contrary leakage current conduction behavior during temperature dependent measurements on n-*Si(111)*. While bilayer gate stacks exhibit untypical decreased leakage current densities for increasing processing temperature (s. figure 13.8.) on n-*Si(111)* substrates, the current density increases for the reverse bilayer gate stacks (s. figure 13.11.). Assuming, that TiO_2 behaves as a n-type and Nd_2O_3 as a p-type doped material, this might be explained by the different reaction or interaction of the p- and n-type charge carriers during negative biasing. For the bilayer samples, it might happen that the minority carriers, which are induced by the negative applied voltage, recombine with n-type TiO_2 charges and therefore an increase of the temperature may induce a faster compensation of leakage current, resulting in

finally lower measured leakage current densities. In case of the reverse bilayer, the negative voltage induces more minority carriers into the p-type Nd_2O_3 layer and an increase of the temperature causes a faster transfer/hopping of the charge carriers. The suggested mechanism is illustrated in figure 13.15.

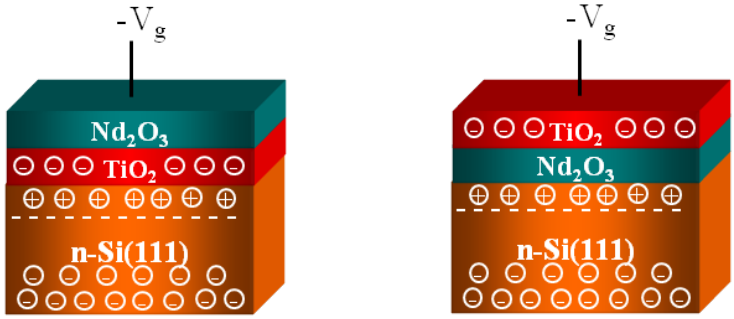


Figure 13.15.: Illustration of the charge carrier distribution within the bilayer ($TiO_2/Nd_2O_3/Si$) and reverse bilayer ($Nd_2O_3/TiO_2/Si$) samples during negative biasing.

14. Discussion & Conclusion

In the present thesis an innovative wet chemical, inorganic based thin film deposition technique has been introduced. The deposition techniques was optimized regarding ultra thin film thicknesses below 10 nm for an application in microelectronic devices. An associated high, defect free film quality in combination with excellent electrical performances is required. The introduced techniques is patented.

The deposition technique is primarily divided into three steps of preparation. Initially the substrates are cleaned and passivated against reoxidation by a wet chemical etching process, which leads to fully saturated hydrogen terminated surfaces. The cleaning is followed by the deposition of the precursor compound and finally the thermolytic formation of the REO.

The nitrate-hydrates of lanthanum and neodymium, $La(NO_3)_3 \times 6\ H_2O$ and $Nd(NO_3)_3 \times 6\ H_2O$, have been chosen from a developed precursor set of pure inorganic precursor materials in order to start a systematic investigation of the mechanism for the film formation by the invented wet chemical inorganic deposition process. The influence of differing lattice parameters of the substrate and the formed thin film, precursor decomposition temperature and molecule structure on the film formation from wet chemical deposition in incipiently state was investigated with respect to film thickness, roughness and the final electrical performance.

Substrates, which were investigated during the present thesis, are *Si(111)* that offers an atomically smooth and passivated hydrogen terminated surface after a specialized cleaning procedure. A high amount of dangling bonds is formed at elevated temperatures, which lead to detrimental electrical performances with conventional deposition techniques. Furthermore, *Si(100)* substrates have been tested, as *Si(100)* is the most common standard material in semiconductor industries for the production of microelectronic devices. The experiments have been extended to the alternative semiconductor substrates *Ge(100)* and *SiGe(111)*, as for future device built up, substrates besides *Si* might come into the focus of research due to their excellent electrical properties. Moreover, a substrate change opened the path to prove the reliability of the wet chemical

deposition technique for varying materials and therefore a broad applicability. For the wet chemical approach the film thickness has been controlled by the precursor solution concentration. The solvent selection was done under criteria of optimized wetting of the substrate. Different annealing temperatures have been tested in order to investigate the influence on the film roughness and the final electrical performance.

The different types of samples, which have been studied within the present thesis are summarized in figure 14.1.

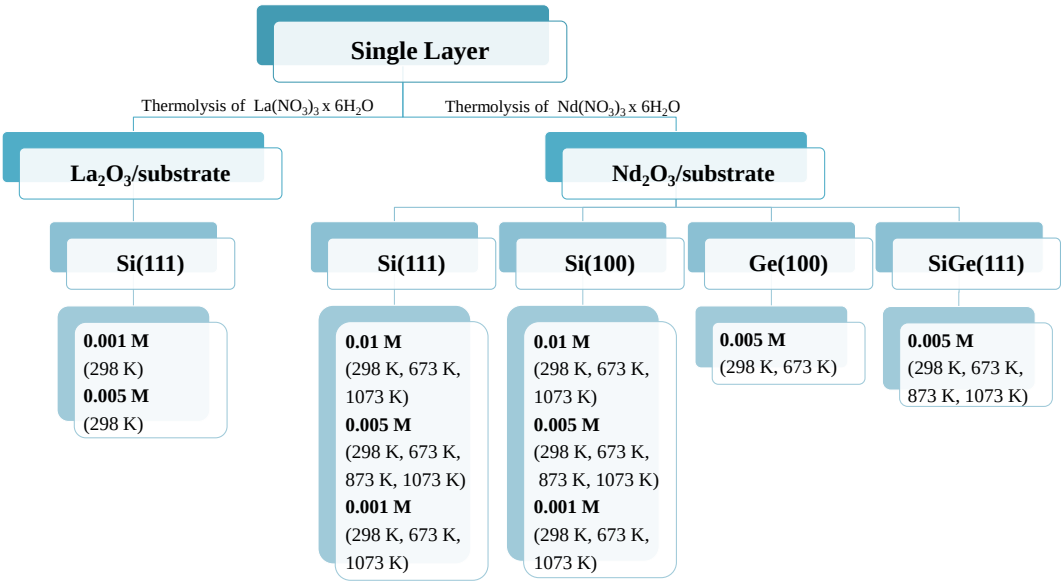


Figure 14.1.: Summary of the prepared single layer systems. Listed are the respective generated REO, substrate types, precursor solution concentrations used and annealing temperatures.

As multi layer oxide systems open the avenue to use high-κ materials as gate stack components, which are under stand alone conditions not thermodynamically stable in contact with the substrate or anyway not stable itself but show good to outstanding dielectric properties, in addition a bilayer gate stack tailoring was demonstrated. The wet chemical deposition technique was used for the REO (Nd_2O_3) and ALD with pure inorganic precursor compounds for a TiO_2 deposition. As TiO_2 offers high dielectric constants, but is anyways not thermodynamically stable in contact with Si, both possibilities of bilayer gate stacks, TiO_2 on top of the Nd_2O_3 and Nd_2O_3 on top of the TiO_2, have

been investigated. An overview of the types of bilayer samples can be found in figure 14.2.

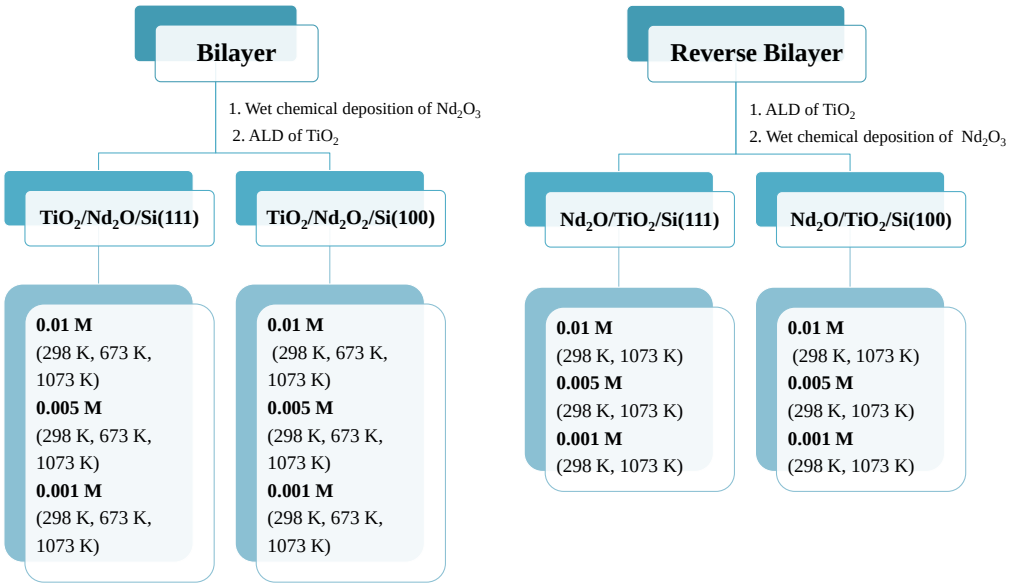


Figure 14.2.: Summary of the prepared bilayer and reverse systems. Listed are the respective substrate types, precursor solution concentrations used and annealing temperatures.

Annealing temperatures have been chosen according to expected crystallization processes within the generated films and thermal stability of the cleaned substrates.

Preliminary to the film deposition, composition and crystallography studies of the precursor powders, oxides and possible byproducts, during film formation, have been conducted, to obtain a detailed understanding of the compounds itself and further to collect reference data for the more complex film analysis. A complete analysis of the crystallographic and thermolytic characteristics of a manifold number of rare earth nitrates ($RE = La, Pr, Nd, Sm, Eu$) with different ligand types (H_2O, $CH(OCH_3)_3$, $C_4H_{10}O_2$, CH_3OH and C_4H_8O) has been summarized from previous project related work and as known from the literature. It has been shown that various requirements can be fulfilled, by choosing and combining the ligand and metal center of the complex anion systems. A database of tunable low decomposition temperatures depending on the RE center and the ligand has been illustrated, based on the work of M. Ahlers.[177] from the inorganic chemistry group of Prof. Dr. M. Wickleder.

An essential aspect is, that all final decomposition temperatures are below the temperature of the desorption of the passivating H-termination of the substrates used, which avoids unwanted interfacial surface reactions during thin film generation.

From the literature, XPS data for rare earth nitrates, are hardly available. Therefore, and for a reliable collection of reference data to analyze the complex rare earth compound film/substrate systems, detailed XPS studies of $Ln(OH)_3$, $Ln(NO_3)_3 \times 6H_2O$ and Ln_2O_3 (with $Ln = La$ and Nd) powders have been carried out in the present thesis. The purity of the powders could be confirmed by XRD analysis prior to the XPS measurements. Within the powder measurements, it was possible, by a precise peak fitting, to gather clear reference data for the *RE3d* and *O1s* signal of the precursors, the oxides and the eventually occurring hydroxide byproducts during a film deposition.

For the film generation based on literature known techniques, wet chemical etching procedures, using HF and NH_4F aqueous solutions, have been developed for the used substrate types, in order to remove the unwanted native formed oxide prior to the precursor deposition. The cleaning procedure leads to highly smooth and pure, hydrogen terminated, passivated surfaces. The successful implementation was proven by XPS analysis of the native oxidized and the cleaned surfaces, whereby the quality of the generated surface with respect to the roughness and stability is substrate type dependent. *Si(111)* substrates haven been shown to remain oxide free and exclusively smooth. *Si(100)* substrates are also passivated but show a higher roughness. Ge and Ge containing *SiGe(111)* substrates are less passivated as the reoxidation tendency is much higher.

Butanol has been chosen as solvent for precursor deposition, as it showed the most homogeneous wetting and an even evaporation. Under criteria of process compatibility and film quality the dip-coating deposition could be specified as most suitable technique from experiments with the dip-coat, drop-cast, liquid injection dosing into the UHV and spin coating. It can be implemented into device production, by a single immersion bath, exhibiting the best film quality. The oxide films are generated by the thermolysis of the precursors in N_2 flow or UHV, of the hydrate-nitrate precursors, deposited on the substrate. The temperatures for the thermolysis have been adjusted based on decomposition temperatures of the precursor powders, which have been analyzed by M. Ahlers.

The films have been characterized by SEM, AFM and STM regarding the precursor solution concentration and substrate dependent roughness. Associated with that, the adjustment of the solution concentration with respect to a preferred film formation towards an unwanted spontaneous nucleation from the solution has been investigated. Furthermore, the elementary composition of the precursor and oxide films as well as the influence on the underlying substrate has been analyzed by XPS. HRTEM imaging of selected samples allowed the determination of the film thickness, film and interfacial structure.

With respect to a preferred homogeneous film formation the precursor solution concentration could be limited by SEM images of the nucleation process.

AFM stability studies showed that all precursor films from the deposited nitrate show a significantly higher roughness than the films after decomposition and that the generated oxide films are with respect to the detected roughness stable under air exposure. It was found that the film roughness correlates directly but not linear with the roughness of the underlying substrate and for smooth substrates smooth oxide layers are formed, therefore the lowest roughness values have been detected for oxide films deposited on *Si(111)*. Annealing dependent experiments showed an increase of the film roughness for samples annealed at high temperatures, possibly caused by crystallization and, depending on the substrate type, interfacial oxide formation. Solution concentrations above the limit for homogeneous film formation exhibited a drastically increased film roughness. Thus, it has been shown that the limits of the deposition technique are given by the concentration dependent structure formation. The generated films showed a minimum RMS of 0.66 nm (17.8 % of the film thickness).

For semiconductor industries in the sub 22 nm node layer thickness below 10 nm of the REOs are in the point of interest, since the Equivalent Oxide Thickness (EOT) in this range reaches values, which allow a further miniaturization of MOSFET devices. In the present work it was demonstrated by HRTEM analysis that with the wet chemical inorganic dip-coating a maximum film thickness of 4.5 nm can be achieved for homogeneously formed, closed films, assuming that with respect to the film thickness the demand of the sub 22 nm node can be fulfilled by the wet chemical deposition technique. It was found that within the region of preferred film formation, the precursor solution concentration correlates linear with the film thickness. The upper limit could be identified as 0.01 M, which is the upper limit of the so called

Ostwald Miers region for crystallization, which is related to a spontaneous nucleation from solution. Butanolic precursor solutions of the $Nd(NO_3)_3 \times 6\ H_2O$ concentration lead to a maximum oxide film thickness of 4.5 nm for solution concentrations of 0.0096 M and a minimum demonstrated film thickness of 3.3 nm deposited from 0.001 M precursor solution. As the lower limit for a full coverage of the substrate, by i.e. a monolayer, was not reached with the 0.001 M precursor solutions, extension potential exists considering even thinner generated films. Moreover, from HRTEM imaging it was shown that the oxide films remain completely amorphous on the surface after precursor decomposition. According to the shown HRTEM images, no significant interfacial layer could be detected and a clear boundary zone between the substrate and the covering oxide was observable for *Si(111)* substrates. HRTEM imaging of *Si(100)* substrates covered with a bilayer oxide system (see below) exhibited a slight indication of an interfacial layer of $<$1 nm formed at the direct interface between the oxide and the underlying Si substrate. HRTEM analysis of the Ge and $SiGe$ substrates are planned in the future work. With respect to the electrical performance of the films the amorphous structure of the films has been discussed to be desirable as amorphous structures reduce the number of grain boundaries which may serve as high leakage path. With the amorphous films we overcome the problem of a lack of lattice matching and resulting cracked structure or increased strain within the deposited film. This is a major issues for conventionally crystallization growth based deposition techniques such as MBE or PVD. The solution based technique offers a wide application horizon whereby the scalability of the films is limited due to Ostwald Miers restrictions for crystallization processes.

Elementary analysis were done by XPS for *La*- and *Nd*-based films. In agreement with the reference data collected from the powder measurements the nitrate-hydrate prior and the oxides species after the thermolysis could clearly be identified according to the *O1s* and *RE3d* signals. This allowed the conclusion that after the deposition the precursor molecules form a salt like layer of the nitrate which decomposes to the oxide as aspired.

For all samples it was found that the passivation of the surface remains active during precursor deposition and no interaction with the substrate occurs. This lead to a possible explanation of the binding state of the precursor molecules on the surface in the initial phase after the deposition. Free hovering salt like layers are formed, which are not strongly bound to the underlying substrate.

The various substrate types exhibited each different behavior with respect to reoxidation tendencies during the precursor decomposition process. *Si(111)* as well as *Ge(100)* substrates did not show any indications of a reoxidation of the substrates whereas for *Si(100)* a slight and for *SiGe(111)* a strong reoxidation tendency was observed. Therefore, XPS analysis confirmed the data detected from the HRTEM as for *Si(111)* no indication of reoxidation, silicide or silicate formation can be detected while a slight interface reaction was observed for *Si(100)*.

It was possible to show that the generated films are carbon free within the detection limit of XPS and the organic solvent can be removed completely during the decomposition process. The formed films are stable up to a temperature of 1073 K, whereby above this limit the oxide transforms and a strong reoxidation of the substrate occurs. This is in agreement with the stability of the underlying substrate passivation as a desorption of the *H*-termination occurs above 810 K.

From the electrical characterization it has been firstly shown that films, generated from the new integrated inorganic dip-coating deposition technique, show excellent to average electrical behavior depending on the substrate type, the respective film thickness and annealing temperature.

C-V analysis enabled the determination of the dielectric constants of the deposited oxide films. Reasonable high κ values for all films deposited on *Si(111)* and *Si(100)* could be measured depending on the annealing temperature and the respective film thickness. It was demonstrated that annealing at different temperatures, influences the electrical performance of the films. Annealing up to 873 K obviously leads to improved electrical performances with respect to the C-V characteristics as higher dielectric constants could be observed. In agreement with the annealing dependent XPS studies, which indicate the formation of interfacial oxide or silicide structures and changes in the film stoichiometry for treatments above 1073 K, a degradation of the detected electrical performance can be observed independent of the sample. The degradation may be related to the compositional and structural changes and besides to a polycrystallization during annealing. The suspected crystallization process implies a required lattice matching of the substrate and the thin film, which is not given in the present case. Therefore strain is expected within the lattice. Worsened electrical performances are observed. Hysteresis behavior in

C-V analysis indicated high quality thin films with a low amount of interfacial traps and charges.

Different substrate orientations and dopings lead to a different leakage current density dependencies on the annealing processes, which might be related to changes in the oxygen stoichiometry and/or subsequently changed film densities. *Si(111)* substrates showed higher leakage current densities for samples annealed at higher temperatures whereas *Si(100)* exhibited a contrary behavior. Increased leakage current values of oxide films deposited on *Si(111)* after annealing might be explained by the above mentioned crystallization or interfacial layer formation but need to be investigated further in the future. For *Si(100)* higher annealing temperatures lead to an increase of the anyway formed interfacial SiO_x layer and therefore probably to a better lattice bridging and a simultaneously reduced leakage current density. Furthermore, the defect density should be reduced after annealing.

For the highly ordered and smooth *Si(111)* substrates leakage current density values within six orders of magnitude better than for the relatively rough *Si(100)* were observed.

In agreement with the elementary and roughness analysis *Si(111)* substrates showed the best performance and exhibited a κ value up to a maximum value of 12.3 which is more than three times higher than conventionally used SiO_2 ($\kappa = 3.9$) and a significantly low leakage current density of $2.47 \times 10^{-11} Acm^{-2}$. The analyzed leakage current densities are with respect to the calculated EOT values eleven orders of magnitudes lower than leakage currents for SiO_2 and still six orders of magnitude lower than detected values for alternative gate oxides deposited by ALD or MBE e.g. It is particularly important that with the new technique it was possible to show excellent electrical performances on *Si(111)*. Other techniques suffer from the high number of dangling bonds of the reconstructing surfaces at the processing temperatures. Therefore conventional techniques exhibit major draw backs such as bad interface qualities caused by lattice miss match and a high number of unsaturated dangling bonds, which lead to a promotion of the leakage current conduction and detrimental electrical performances. Therefore, with the unconventional, innovative technique we open the way to make *Si(111)* possible as a better wafer material for semiconductor industry and taking advantage of the atomically smooth, passivated surface which can not be achieved on *Si(100)* or *Si(110)* substrates.

The investigated electrical performances of the alternative materials are, with respect to the leakage current densities and relatively low κ values, rather average and similar to reported data from literature both for *Ge(100)* and *SiGe(111)* substrates. For the alternative substrates annealing at higher temperatures lead to improved electrical performances. Significantly better performances should be observed by tuning the annealing conditions to achieve a less oxygen rich atmosphere and therefore reduce the reoxidation of the substrate. Anyway, it has been shown that the invented technique is generally applicable for different types of substrates.

From temperature dependent I-V measurements, it was possible to achieve a first insight into the respective type of temperature induced leakage current conduction for certain selected samples. This is essential in order to achieve a precise understanding of the underlying effects for a future reduction of leakage current densities and device improvement. A required maximum of leakage current suppression is only possible by specific tailoring of the films with respect to a minimization of the effects, which are responsible for the respective leakage current conduction. For films deposited on *Si(111)* only an exceptional weak and non systematic dependence of the leakage current density and the operation temperature was observed. This leads to the conclusion that obviously non of the strongly temperature dependent mechanisms is dominant within the investigated temperature and electric field region. However, stable leakage current densities over varying operation temperatures are a great advantage as a stable device operation can be guaranteed even under high operating temperatures. Films deposited on *Si(100)*, *Ge(100)* and *SiGe(111)* showed systematic temperature dependent increased leakage current densities. It can be concluded from the shown analysis that for these samples the leakage current is mainly caused by minority carrier generation from interfacial states. In general, conduction mechanisms in pure oxides are mainly governed by intrinsic properties (e.g. intrinsic traps). Within the present thesis for the deposited films no precise assignment of Schottky or Poole-Frenkel was possible. The temperature dependency of the detected leakage currents obviously strongly depends on the respective system, operating temperature and applied electric field. A certain distinction was not possible as the film thicknesses of the analyzed systems are rather low and the standard equations to investigate the basic conduction mechanisms in insulating films are obviously not valid. Localized electric fields and incompletely formed space charge regions

may be formed resulting in a mixture of different dominating leakage current conduction mechanisms over increasing process temperatures.

It was shown from the electrical analysis that *Si(111)* obviously assumes as special role with respect to the wet chemical deposition as exclusively low leakage currents have been detected and different from all the other substrate types *Si(111)* samples exhibit a stable leakage current density under high operating temperatures. The origin of these differences is probably caused by the initial oxide anchoring on the surface, the chemical bond between oxide and substrate and therefore by the species responsible for the charge carrier transport. *Si(111)* showed the most stable H-passivation and exhibited atomically smooth passivated surfaces due to an etching stop at the <111> lattice plane. This is congruent with a completely suppressed reoxidation during the precursor deposition and decomposition process, which was not observable for all other substrate types as well as the detected significantly low roughness values.

Bilayer structures of Nd_2O_3 and TiO_2 on p-*Si(100)* and n-*Si(111)* deposited from the wet chemical dip-coat (Nd_2O_3) and ALD (TiO_2) ($TiO_2/Nd_2O_3/Si$) have been investigated at different annealing temperatures. It could be shown by AFM measurements that all bilayer structures are significantly rougher than the single layer structures on Si but annealing leads to decreased roughness values.

For the bilayer samples ($TiO_2/Nd_2O_3/Si$), a differing film thickness of the REO compared to the single layer samples, has been detected, which might be explained by a differing surface reaction mechanism. Therefore, detailed interface structure analysis are necessary in future work, to determine the specific influence of the TiO_2 top layer on the underlying REO, causing a decreased film thickness. From the analysis of the bilayer system it was possible to confirm an identical film thickness of the films deposited from the same precursor solution concentration on *Si(111)* and *Si(100)* substrates.

Electrical characterizations of the bilayer systems ($TiO_2/Nd_2O_3/Si$) deposited from different solution concentrations and annealed at varying temperatures, revealed good dielectric constants up to 2.5 times higher than conventionally used SiO_2 and leakage current values down to six orders of magnitude lower than SiO_2. It was demonstrated that a low amount of traps and charges is present within the films and the gate stacks are of high quality. The comparison

of high and low frequency measurements lead to the conclusion that no significant MIS structures are formed an *Si(111)* and a strong influence is observed on *Si(100)*. In general the trends of the changes in the electrical performance with the annealing temperature is comparable to the results achieved for the single layers even though the actual values of the leakage current density and κ are strongly different. The equal trends were expected as the electrical performance is besides the film quality mainly governed by the structure of the interface to the underlying substrates and this is generated under the same conditions for the single and bilayer samples by the wet chemical deposition.

Reverse bilayer systems ($Nd_2O_3/TiO_2/Si$) exhibit, as expected, worse electrical performances compared to the normal bilayer due to thermodynamic instability of the TiO_2 in direct contact with the Si substrates. Reverse bilayer systems exhibited leakage current characteristics contrary to all previously measured data as lower leakage current values were observed for annealed p-*Si(100)* substrates instead of *Si(111)*. This is caused by the initial anchoring of the gate stack on the substrate, which is mainly controlled by ALD instead of the wet chemical deposition technique and the initial interface structure is formed by a chemical reaction instead of the formation of a salt like layer. Since ALD is dependent on the available ordered surface sites, the role of the higher amount of dangling bonds comes into account and for *Si(111)* poorer electrical performances are observed compared to *Si(100)*.

From the differences to the single layer samples, it can be concluded that bilayer structures result in local compositional and structural inhomogeneities, causing increased trapping, which leads to lower κ values and increased leakage currents compared to single layer structures. Thus, bilayer systems open the path to use high-κ materials such as TiO_2 which are difficult to be used as gate dielectric on its own for Si-based transistors in direct contact with Si.

The achieved results from the electrical characterization are rather average compared to the results of the single layer and literature known conventionally deposited systems, but as the integrated wet chemical deposition mechanism is rather simple, the shown results are still excellent with respect to further tuning opportunities to improve the electrical performance of the bilayer systems.

To summarize, it was demonstrated that the invented wet chemical inorganic dip-coating technique opens a possible path for gate oxide deposition. The

deposited films show good to excellent electrical properties and a tunable film thickness and roughness. The inorganic precursors can be easily synthesized, are mostly non toxic and can be evaporated at low temperatures which overcomes the problems of conventional deposition techniques as availability of suitable precursors and high energy consumption. With the solution based, non UHV, wet chemical approach, we overcome the problems of highly time consuming processes as the reaction is not limited by the mean free path of the precursor molecules and the dip-coating system is rather easy to operate and it is possible to reduce the experimental effort to a minimum.

In addition to the energy and therefore cost issues the low precursor decomposition temperatures maintain the passivation of the substrate, which avoids an unwanted surface reaction and interfacial layer formation due to the low temperature regime. The final electrical performance limiting carbon impurities are one of the major issues for ALD deposition from complex organic molecules. The inorganic approach opens an avenue for carbon free film deposition. Crystallization issues as lattice mismatch and caused strain or inhomogeneities within the films are circumvented by the initially amorphous oxide films formed after the precursor thermolysis. With the easy and systematic precursor development, precursor design is possible with respect to specific requirements for corresponding applications. Due to the easy process integration the technique can be applied for virtually any types of substrates. In addition the simple experimental realization enables a material screening in preliminary state for new oxide components.

With the achieved electrical performances and detected film thicknesses we meet the requirements of the IRSC 2011. The low leakage current densities secure besides the required device stability a low power consumption and an optimum use of the applied voltage. The leakage current densities down to 10^{-11} Acm^{-2} enable the generated films to be possibly used in MOSFETs or even for low power or DRAM devices.

It has to be noted that, as depicted in the present thesis, the availability of the RE-ores and therefore the basic educts for precursor synthesis is recently politically limited due to a monopoly position of China. Thus, for an industrial mass production of REO thin films the disposability at reasonable prices is necessary to be ensured.

15. Outlook

Interface trap density (D_{it}) calculations as well as high speed C-V measurements to determine the types of traps and charges within the investigated oxide films will be shown based on the data of the present thesis in the work of M.M.V. Chong[242] for a further characterization of the generated dielectrics. Ongoing are Raman spectroscopy measurements to investigate the tensile/compressive stress within the films. A detailed study of the band structure will be possible by synchrotron X-ray Absorption (XAS) and X-ray Emission Spectroscopy (XES) analysis in collaboration with the group of Prof. M. Neumann (Physics Institute of the University of Osnabrück).

It appears from the presented results that HRTEM analysis of the alternative substrates Ge and $SiGe$ are required in order to achieve a more detailed understanding of the interface formation as it has been presented for Si substrates.

Further investigations of the leakage current conduction mechanisms with varying and especially low temperatures are necessary in order to achieve a detailed understanding of the dominating leakage current conduction mechanisms at certain temperatures and electric fields.

Due to the generated low film thicknesses crystallinity studies on annealed films are not trivial as conventional techniques such as laboratory XRD or ellipsometry reach their detection limits and elaborated HRTEM or synchrotron XRD studies are necessary in the future work. High resolution synchrotron XPS analysis are required to achieve a more detailed resolution of the detected signals and to tune the depth of the penetrating beam. For a more precise study of the film composition in the different thickness regions and at the interfaces, depth profiling via Time of Flight Secondary Ion Mass Spectroscopy (ToF-SIMS) is necessary. Density values have to be determined via Rutherford Back Scattering (RBS) and X-ray Reflectivity (XRR) measurements. Furthermore, experiments to investigate the oxygen stoichiometry are necessary to possibly explain the change in the leakage current density for the annealed and non annealed samples. The effect of different annealing conditions (flow gas, temperature, duration) on the electrical performance is of great

interest as for conventionally deposited oxide films a strong improvement of the properties can be achieved by tuning the annealing conditions.

For an actual integration of the shown system compatible gate electrodes for the tested oxides needs to be found for process integration as *Au*, which is scientifically validated but not suitable for industrial clean room applications due to the high reactivity with stored substrate materials and resulting impurities in the final manufactured devices.

Extensions to different compounds from the row of the rare earth elements are desirable, to confirm the applicability of the technique also for smaller ions and to investigate the influence of the lattice parameters of the precursors and oxides on the film formation and final film quality.

RE-elements with a different application potential than microelectronic devices are under investigation. Analogous to the films deposited from *La* and *Nd* experiments with *Eu* compounds are conducted. Thin films of *Eu* oxides are under a major focus of recent research due to the optical properties and a possible application for OLEDs i.a.

Exclusively low decomposition temperatures of approx. 400 K of *Sm* and *Sc* nitrate-precursor compounds, introduced within the developed precursor database, enable a future role to role deposition on flexible substrates (plastics) for flexible electronics, whereby the wet chemical dip coating is in demand, as conventional thin film deposition techniques reach their limits due to a lack of crystalline substrates, UHV incompatibility or required high process and substrate temperatures.

For catalytic applications thicker porous films, which can be generated from higher concentrated precursor solutions, due to a bubbly structure, caused by escaping gaseous precursor decomposition products, are of high interest due to a high surface/volume ratio.

Bibliography

[1] M. Schulz, *Nature* **1999**, *399*, 729–730.

[2] E. Gusev, E. Cartier, D. Buchanan, M. Gribelyuk, M. Copel, H. Okorn-Schmidt, C. D'Emic, *Microelectronic Engineering* **2001**, *59*, 341–349.

[3] J. Robertson, *Report of Progress in Physics* **2006**, *69*, 327–396.

[4] A. Laha, E. Bugiel, H. Osten, *Applied Physics Letters* **2006**, *88*, 1721071–1721073.

[5] J. Robertson, *The European Physical Journal - Applied Physics* **2004**, *28*, 265–291.

[6] V. Rozhkov, A. Y. Trusova, I. Berezhnoy, *Thin Solid Films* **1998**, *325*, 151.

[7] J. Kwo, M. Hong, B. Busch, D. Muller, Y. Chabal, *Journal of Crystal Growth* **2003**, *251*, 645–650.

[8] F. Giustino, A. Bongiorno, A. Pasquarello, *Applied Physics Letters* **2005**, *86(19)*, 192901 (3 pages).

[9] M. Leskelä, M. Ritala, *Thin Solid Films* **2002**, *409*, 138–146.

[10] G. Bonnet, M. Lachkar, J. Colson, J. Larpin, *Thin Solid Films* **1995**, *261(1-2)*, 31–36.

[11] M. Schumacher, P. Baumann, T. Seidel, *Chemical Vapor Deposition* **2006**, *12*, 99–108.

[12] A. F. Andreeva, *Powder Metallurgy and Metal Ceramics* **1998**, *37(1-2)*, 91–93.

[13] M. Singh, S. A. Shivashankar, *Journal of Crystal Growth* **2005**, *276*, 148–157.

[14] A. S. Ivanova, I. I. Bobrova, E. M. Moroz, V. Y. Kalinkin, *Kinetics and Catalysis* **1993**, *34(4)*, 758.

[15] S. Yunusov, B. M. A. Ivanova, V. Likholobov, V. Shur, *Journal of Molecular Catalysis* **1998**, *132(2-3)*, 263–265.

[16] G. Laukaitis, J. Dudonis, *Materials Science* **2005**, *11(1)*, 9–13.

[17] C. Ma, P. Briois, J. Böhlmark, F. Lapostolle, A. Billard, *Ionics* **2008**, *14*, 471–476.

[18] A. Fissel, H. J. Osten, E. Bugiel, *Journal of Vacuum Science Technology B* **2003**, *21*, 1765–1772.

[19] K. Siegbahn, C. Nordling, E. Sokolowski, *Physical Review* **1957**, *105*, 1676–1677.

[20] I. Lindau, P. Pianetta, S. Doniach, W. E. Spicer, *Nature* **1974**, *250*, 214–215.

[21] D. Briggs, M. P. Seah, *Practical Surface Analyses Volume 1: Auger and X-Ray Photoelectron Spectroscopy*, JOHN WILEY & SONS Ltd., **1990**.

[22] P. J. Cumpson, *Applied Surface Science* **2000**, *144-145*, 16–20.

[23] *Praktikumsskript: Fortgeschrittenen Praktikum SS 06, Versuch X-ray-Photoelectron-Spectroscopy*, Universität Oldenburg, Physikalische Chemie Al-Shamery, **2011**.

[24] T. Koopmans, *Physica (Elsevier)* **1934**, *1(1-6)*, 104–113.

[25] L. C. Feldman, J. W. Mayer, *Fundamentals of Surface and Thin Film Analysis*, Prentice Hall, **1986**.

[26] J. T. Grant, D. Briggs, *Surface Analysis by Auger and X-ray Photoelectron Spectroscopy*, Chichester: IM Publications, **2003**.

[27] W. C. Roentgen, *Eine neue art von Strahlen*, Verlag und Druck der Stahel'schen K. Hof- und Universitäts-Buch- und Kunsthandlung, **1895**.

[28] D. Bonnell, *Scanning Probe Microscopy and Spectroscopy and Theory, Techniques, and Applications*, WILEY-VCH Toronto, **2001**.

[29] R. Wiesendanger, *Scanning Probe Microscopy and Spectroscopy, Methods and Applications*, Cambride University Press, **1994**.

[30] G. Wedler, *Lehrbuch der Physikalischen Chemie, dritte durchgesehene Auflage*, VCH-Verlagsgesellschaft, Weinheim, **1987**.

[31] J. Tersoff, D. Hamann, *Physical Review Letters* **1983**, *50(25)*, 1998–2001.

[32] W. A. Hofer, A. S. Foster, A. L. Shluger, *Reviews of Modern Physics* **2003**, *75*, 1287–1327.

[33] *Praktikumsskript: Fortgeschrittenen Praktikum SS 06, Versuch Rasterkraftmikroskopie und Softlithografie*, Universität Oldenburg, Physikalische Chemie Al-Shamery, **2006**.

[34] G. Binnig, C. F. Quate, *Physical Review Letters* **1986**, *56*, 930–933.

[35] P. W. Hawkes, J. C. H. Spence, *Science of Microscopy*, Springer Science + Business Media, LLC, **2007**.

[36] R. Holze, *Surface and Interface Analysis, An Electrochemists Toolbox*, A. Castleman, J. Toennies, K. Yamanouchi, W. Zinth (Eds.), Springer-Verlag Berlin Heidelberg, **2009**.

[37] H.-U. Krotil, T. Stiftler, H. Waschipky, K. Weishaupt, S. Hild, O. Marti, *Surface and Interface Science* **1999**, *27(5-6)*, 336–340.

[38] G. Adachi, N. Imanaka, Z. Kang (Eds.), *Binary Rare Earth Oxides*, Kleuver Academic Publishers, Netherlands, **2004**.

[39] D. Foord, B. Freitag, C. Kübel, D. Tang, *Tecnai Advanced Material Science*, FEI Company, **2002**.

[40] J. Spence, *Experimental high-resolution electron microscopy*, Oxford University Press, New York, **1988**.

[41] *Lawrence Berkeley National Laboratory; National Center for Electron Microscopy*, **2011**.

[42] L. Flegler, *Elektronenmikroskopie. Grundlagen, Methoden, Anwendungen*, Spektrum Akademischer Verlag, **1995**.

[43] L. Reimer, *Transmission Electron Microscopy: Physics of Image Formation and Microanalysis 4th Edition*, Springer-Verlag Berlin Heidelberg New-York, **1997**.

[44] L. A. Giannuzzi, F. A. Stevie (Eds.), *Introduction to Focused Ion Beams; Instrumentation, Theory, Techniques and Practice*, Springer Science & Business Media LCC, **2005**.

[45] F. A. Stevie, C. B. Vartuli, L. A. Giannuzzi, *Surface and Interface Analysis* **2001**, *31*, 345–351.

[46] L. A. Giannuzzi, F. A. Stevie, *Micron* **1999**, *30*, 197–204.

[47] F. A. Stevie, T. C. Shane, P. Kahora, *Surface and Interface Analysis* **1995**, *23(2)*, 61–68.

[48] O. Marti, A. Plettl, *Vorlesungsskript: Physikalische Elektrotechnik und Messtechnik*, *Vol. 1*, Universität Ulm, **2007**.

[49] J. Goldstein, D. E. Newbury, D. C. Joy, C. E. Lyman, P. Echlin, E. Lifshin, L. Sawyer, J. Michael, *Scanning electron microscopy and X-ray microanalysis, Volume 1*, Springer, **2003**.

[50] L. V. Azároff, R. Kaplow, N. Kato, R. J. Weiss, A. J. C. Wilson, R. A. Young, *X-ray diffraction*, McGraw-Hill, **1974**.

[51] L. Spieß, R. Schwarzer, H. Behnken, G. Teichert, *Moderne Röntgenbeugung, Röntgendiffraktometrie für Materialwissenschaftler, Physiker und Chemiker*, Teubner Verlag, **2005**.

[52] C. R. Brundle, C. A. Evans, S. Wilson, *Encoclopedia of Materials Characterization*, Butterworth-Heinemann Ltd., **1992**.

[53] B. E. Warren, *X-Ray Diffraction*, Addison-Wesley Reading, **1969**.

[54] B. D. Cullity, *Elements of X-Ray Diffraction*, Addison-Wesley, Reading, **1978**.

[55] L. Schwartz, J. Cohea, *Diffraction from Materials*, Springer Verlag Berlin, **1987**.

[56] *http://www.nobelprize.org/nobel_prizes/physics/laureates/1915/*, **16.11.2011 10.13 h**.

[57] K. Kopitzky, P. Herzog, *Einführung in die Festkörperphysik*, Teubner Verlag Wiesbaden, **2002**.

[58] S. M. Sze, *Physics of Semiconductor Devices, 2nd Edition*, John Wiley & Sons, Inc., **1981**.

[59] B. V. Zeghbroeck, *Principles of Electronic Devices*, http://ece-www.colorado.edu/ bart/book/, **2011**.

[60] K. Harutunian, R. F. Pierret (Eds.), *Semiconductor Device Fundamentals*, Addison-Wesley Publishing Company Inc., **1996**.

[61] B. E. Deal, M. Sklar, A. S. Grove, E. H. Snow, *Journal of the Electrochemical Society 1* **1967**, *14*, 266.

[62] J. R. Ligenza, *Journal of Physical Chemistry* **1961**, *65*, 2011–2014.

[63] D. Kahng, *Technical memorandum issued by Bell Labs* **1961**.

[64] C. Chaneliere, J. L. Autran, R. Devine, B. Balland, *Material Science and Engineering R* **1998**, *22(6)*, 269–322.

[65] A. Paskaleva, M. Lemberger, E. Atanassova, A. Bauer, *Journal of Vacuum Science and Technology B* **2011**, *29(1)*, 01AA031–01AA0310.

[66] S. M. Sze, K. K. Ng, *Physics of Semicondcutor Devices, 3rd Edition*, John Wiley & Sons, Inc., **2007**.

[67] R. Perera, A. Ikeda, R. Hattori, Y. Kuroki, *Microelectronic Engineering* **2003**, *65*, 357–370.

[68] S. Aritome, R. Shirota, G. Hemink, T. Endoh, F. Masuoka, *Proceedings in IEEE* **1993**, *81(5)*, 776–788.

[69] E. Rosenbaum, L. F. Register, *IEEE Trans.Electron Devices* **1997**, *44(2)*, 317–323.

[70] S.-I. Takagi, N. Yasuda, A. Torium, *IEEE Journal Solid-State Circuits* **1999**, *46(2)*, 348–354.

[71] M. Volmer, *Zur Kinetik der Phasenbildung und der Elektrodenreaktionen*, Akademische Verlagsgesellschaft Geest & Portig K.-G., **1983**.

[72] M. A. Larson, *Solute clustering and secondary nucleation in Advances in Industrial Crystallization*, Butterworth-Heinemann Ltd., **1991**.

[73] W. Kleber, *Einführung in die Kristallographie, 18. Auflage*, Verlag Technik GmbH Berlin, **1998**.

[74] W. Bardsley, D. T. J. Hurle, J. B. Mullin (Eds.), *Crystal Growth: A Tutorial Approach*, North-Holland Publishing Company, Amsterdam New York, **1979**.

[75] S. Neve, *Doktorarbeit: Zur chemischen Badabscheidung von Zinkverbindungen für Cadmiumfreie Chalkopyritsolarzellen*, Freie Universität Berlin, **2001**.

[76] C. T. Campbell, *Surface Science Reports* **1997**, *27(1-3)*, 1–111.

[77] S. Spiga, C. Wiemer, G. Scarel, G. Seguini, M. Fanciulli, A. Zenkevich, Y. Lebedinskii, *Springer Series in Advanced Microelectronics* **2007**, *27*, 181–209.

[78] J. S. Suehle, *6th International Symposium on Plasma-Induced Damage* **2001**, 90.

[79] R. M. Wallace, D. Wilk, *Critical Reviews in Solid State and Material Sciences* **2003**, *28*, 231–245.

[80] P. N. Mehrotra, V. Chandrashekar, C. N. R. Rao, E. C. Subbarao, *Transactions of the Faraday Society* **1966**, *62*, 3586–3590.

[81] X. Yu, C. Zhu, H. Hu, A. Chin, M. Li, B. Cho, D. Kwong, M. Y. P. Foo, *Electron Dev. Lett* **2003**, *24*, 63.

[82] Y. Nakamura, I. Asano, M. Hiratani, T. Saito, H. goto, *VLSI Tech. Dig.* **2001**, 39.

[83] R. Chau, *Gate Dielectric scaling for High-Performance CMOS from SiO_2/Poly Si to high-κ Metal-Gate*, Talk, **2003**.

[84] S.-H. Lo, D. Buchanan, Y. Taur, W. Wang, *IEEE Electron Device Letters* **1997**, *18(5)*, 209–211.

[85] T. Ishikawa, D. Kodama, Y. Matsui, M. Hiratani, T. Furusawa, D. Hisamoto, *IEDM Tech. Dig.* **2002**, 940.

[86] H. Hang, C. X. Zhu, X. F. Yu, A. Chin, M. F. Li, B. J. Cho, D. L. Kwong, P. D. Foo, M. B. Yu, X. Y. Liu, J. Winkler, *Electron Dev.ice Letters* **2003**, *24*, 60.

[87] Y. K. Jeong, S. K. Won, D. J. Kwon, M. W. Song, W. H. Kim, M. H. Park, J. H. J. ang H. S. Oh, H. K. Kang, K. P. Suh, *VLSI Tech. Dig.* **2004**, 222.

[88] Y. L. Tu, H. L. Lin, L. L. Chao, D. Wu, C. S. Tsai, C. Wang, C. F. Huang, C. H. Lin, J. Sun, *VLSI Tech. Dig.* **2003**, 79.

[89] G. D. Wilk, R. M. Wallace, *Applied Physics Letters* **1999**, *74-76*, 2854–2856.

[90] T. Busani, R. Devine, *ECS Transactions* **2006**, *1(5)*, 331–340.

[91] E. Riedel, *Anorganische Chemie*, de Gruyter Berlin New York, **2002**.

[92] N. Kaltosoyannis, P. Scott, *The 4 f elements*, Oxford Chemistry Primers, Oxford, **1999**.

[93] *Kostbare Raritäten mit hohem Risikofaktor*, Financial Times Deutschland, **12.05.2012 Online**.

[94] K. Bradsher, *China Tightens Grip on Rare Minerals*, New York Times, **31.08.2009**.

[95] *EU und Vereinigte Staaten verklagen China, http://www.faz.net/aktuell/wirtschaft/wirtschaftspolitik/seltene-erden-eu-und-vereinigte -staaten-verklagen-china-11682578.html*, Frankfurter Allgemeine Zeitung NET, **18.04.2012 11.25 h**.

[96] G. D. Wilk, R. M. Wallace, J. M. Anthony, *Journal of Applied Physics* **2001**, *89(10)*, 5243–5275.

[97] K. Hubbard, D. Schlom, *Journal of Materials Research* **1996**, *11(11)*, 2757–2776.

[98] I. Barin, O. Knacke, *Thermochemical Properties of Inorganic Substances*, Springer-Verlag Berlin, **1973**.

[99] I. Barin, O. Knacke, *Thermochemical Properties of Inorganic Substances, Supplement*, Springer-Verlag Berlin, **1977**.

[100] U. S. B. of Mines Bulletin 672 (Ed.), *Thermodynamic Properties of Elements and Oxides*, U.S. Government Printing Office, Washington D.C., **1982**.

[101] L. Z. Pauling, *Zeitschrift für Krystallografie* **1928**, *69*, 415–459.

[102] W. C. Koehler, E. O. Wollan, *Acta Crystallographica* **1953**, *6*, 741–742.

[103] L. Eyring, *Handbook on the Physics and Chemistry of Rare Earths, Vol.3*, North-Holland: Amsterdam, **1979**.

[104] G. Adachi, N. Imanaka, *Chemical Reviews* **1998**, *98*, 1479–1514.

[105] H. Müller-Buschbaum, H. G. Schnering, *Zeitschrift für anorganische und allgemeine Chemie* **1965**, *340(5-6)*, 232–245.

[106] H. Müller-Buschbaum, *Zeitschrift für anorganische und allgemeine Chemie* **1966**, *343(1-2)*, 6–10.

[107] M. Foëx, J. P. Traverse, *Rev. Int. Hautes Temp. Re´fract.* **1966**, *3*, 429.

[108] I. M. Iskandarova, A. A. Knizhnik, I. V. Belov, E. A. Rykova, A. A. Bagatur'yants, S. Y. Umanskii, B. V. Potapkin, M. W. Stoker, *Russian Journal of Physical Chemistry B* **2007**, *1(2)*, 102–112.

[109] G. Koster, B. L. Kropman, J. H. M. G. Rijnders, H. A. D. Blank, H. Rogalla, *Applied Physics Letters* **1998**, *73*, 2920–2922.

[110] A. Fissel, Z. Elassar, O. Kirfel, *Journal of Applied Physics* **2006**, *99*, 0741051–0741056.

[111] A. C. Jones, H. C. Aspinall, P. R. Chalker, R. J. Potter, *Materials Science and Engineering B* **2005**, *118*, 97–104.

[112] T. Suntola, J. Antson, *Patent: US 4,058,430,*, **1977**.

[113] M. Putkonen, T. Sajavaara, L. N. und Juhani Keinonen, *Analytical and Bioanalytical Chemistry* **2005**, *382(8)*, 1791–1799.

[114] L. Niinistö, J. Päiväsaari, J. Niinistö, M. Putkonen, M. Nieminen, *Physica Status Solidi A* **2004**, *201*, 1443–1452.

[115] M. Leskelä, M. Ritala, *Angewandte Chemie Int. Edition* **2003**, *42*, 5548.

[116] M. Knez, K. Nielsch, L. Niinistö, *Advanced Materials* **2007**, *19*, 3425–3438.

[117] T. Blanquart, J. Niinistö, M. Heikkilä, T. Sajavaara, K. Kukli, E. Puukilainen, C. Xu, W. Hunks, M. Ritala, M. Leskelä, *Chemistry of Materials* **2012**, *24 (6)*, 975–980.

[118] R. A. Fischer (Ed.), *Precursor chemistry of advanced materials: CVD, ALD and nanoparticles*, Springer Berlin Heidelberg New York, **2005**.

[119] M. Leskelä, M. Kemell, K. Kukli, V. Pore, E. Santala, M. Ritala, J. Lu, *Materials Science and Engineering C* **2007**, *27*, 1504–1508.

[120] L. K. Tan, M. A. S. Chong, H. Gao, *Journal of Physical Chemistry C* **2008**, *112*, 69–73.

[121] L. K. Tan, H. Gao, Y. Zong, W. Knoll, *Journal of Physical Chemistry C* **2008**, *112*, 17576–17580.

[122] *http://nobelprize.org/nobel_prizes/physics/laureates/1956/*, **20.05.2011 10.06 h**.

[123] D. P. Brunco, B. D. Jaeger, G. Eneman, J. Mitard, G. Hellings, A. Satta, V. Terzieva, L. Souriau, F. E. Leys, G. Pourtois, M. Houssa, G. Winderick, E. Vrancken, S. Sioncke, K. Opsomer, G. Nicholas, M. Caymax, A. Stesmans, J. V. Steenbergen, P. W. Mertens, M. Meuris, M. M. Heynsa, *Journal of the Electrochemical Society* **2008**, *155(7)*, H552–H561.

[124] G. Mavrou, S. F. Galata, A. Sotiropoulos, P. Tsipas, Y. Panayiotatos, A. Dimoulas, E. K. Evangelou, J. Seo, C. Dieker, *Microelectronic Engineering* **2007**, *84*, 2324–2327.

[125] A. Dimoulas, Y. Panayiotatos, A. Sotiropoulos, P. Tsipas, D. Brunco, G. Nicholas, J. V. Steenbergen, F. Bellenger, M. Houssa, M. Caymax, M. Meuris, *Solid State Electronics* **2007**, *51*, 1508–1514.

[126] E. Evangelou, G. Mavrou, A. Dimoulas, N. Konofaos, *Solid State Electronics* **2007**, *51*, 164–169.

[127] G. Mavrou, S. Galata, P. Tsipas, A. Sotiropoulos, Y. Panayiotatos, A. Dimoulas, E. K. Evangelou, J. W. Seo, C. Dieker, *Journal of Applied Physics* **2008**, *103*, 014506–014515.

[128] U. Leist, *Doktorarbeit: Untersuchung zur Adsorption und Photochemie von Wasser an geordneten Eisenoxid-Filmen als Modellsystem von Elementarprozessen der Atmosphärenchemie an Staubpartikeln*, University of Oldenburg, **2002**.

[129] S. Neuendorf, *Doktorarbeit: Röntgenphotoelektronenspektroskopische und infrarotspektroskopische Untersuchungen an Platin-Cobalt-Oberflächenlegierungen*, University of Oldenburg, **2007**.

[130] K. Jousten (Ed.), *Wutz Handbuch Vakuumtechnik 10. Auflage*, Vieweg+Teubner, **2010**.

[131] A. Winkler, *Doktorarbeit: Untersuchung der Deposit-Substrat Wechselwirkungen und des Oxidationsverhaltens von Nanopartikeln auf einem oxidischen Träger am Beispiel der Systeme $Ni/Al_{10}O_{13}/NiAl(110)$ und $Ge/Al_{10}O_{13}/NiAl(110)$*, University of Oldenburg, **2005**.

[132] D. A. Shirley, *Physical Review B* **1972**, *5*, 4709–4717.

[133] R. Hesse, *Doktorarbeit: Verbesserung der qualitativen und quantitativen Analyse von Photoelektronenspektren und deren Verifizierung mittels mathematisch-numerischer Verfahren-Entwicklung und Test einer Bearbeitungs- und Analyse-Software*, Universität Leipzig, **2006**.

[134] Casa Software Ltd, *CasaXPS*, **2006**.

[135] B. V. Crist, *Journal of Surface Analaysis* **1998**, *4(3)*, 428–434.

[136] M. Ahlf, *Diplomarbeit: Die Abscheidung Dünner Selten-Erd-Oxid Schichten zur Anwendung in der Halbleiterindustrie*, University of Oldenburg, **2008**.

[137] H. Schnars, *Doktorarbeit: Die Abscheidung und Zersetzung von Selten-Erd-Precursorn auf der H-terminierten Si(111)- und der SiO_2-Oberfläche*, University of Oldenburg, **2009**.

[138] S. Middleman, A. Hochberg, *Process Engineering Analysis in Semiconductor Device Fabrication*, McGraw-Hill, **1993**.

[139] M. N. Ali, M. A. Garciaa, T. Parsons-Moss, H. Nitsche, *Nature Protocols* **2010**, *5*, 1440–1446.

[140] M. H. Zoellner, *Diplomarbeit: Seltenerdoxidschichten für Anwendungen in der Halbleiterindustrie*, University of Oldenburg, **2009**.

[141] M. N. Rahaman, *Ceramic Processing*, CRC Press, **2006**.

[142] A. Opitz, *Dissertation: Nanotribologische Untersuchungen von ultradünnen Wasserfilmen auf hydrophoben und hydrophilen Siliziumoberflächen*, TU Ilmenau, **2003**.

[143] *http://gestis.itrust.de/nxt/gateway.dll?f=templates&fn=default.htm &vid=gestisdeu:sdbdeu*, **04.04.2012 12.19h**.

[144] G. Benson, V. Lam, *Journal of Colloid and Interface Science* **1972**, *38(2)*, 294–301.

[145] G. Smith, L. Sorg, *Journal of Physical Chemistry* **1941**, *45*, 671–681.

[146] A. Campbell, E. Kartzmark, S. Anand, *Canadian Journalof Chemistry* **1968**, *46*, 2399–2407.

[147] D. Ramkumar, A. Kudchadker, *Journal of Chemical and Engineering Data* **1989**, *34(4)*, 463–465.

[148] J. Shewmaker, C. Vogler, E. Washburn, *Journal of Physical Chemistry* **1954**, *58*, 945–948.

[149] C. Kittel, *Einführung in die Festkörperphysik*, Oldenbourg München Wien, **1999**.

[150] W. Mönch, *Semiconductor Surfaces and Interfaces 3rd. edition*, Springer, **2001**.

[151] J. E. Griffith, G. P. Kochanski, *Critical Reviews in Solid State and Material Sciences* **1990**, *16(4)*, 255–289.

[152] Q. Liu, R. Hoffmann, *Journal of the American Chemical Society* **1995**, *117*, 4082.

[153] M. Rohlfing, P. Krüger, J. Pollmann, *Physical Review B* **1995**, *52(19)*, 13753–13756.

[154] D. J. Chadi, *Physical Review Letters* **1979**, *43(1)*, 43–47.

[155] K. Takayanagi, Y. Tanishiro, *Physical Review* **1986**, *34*, 1034–1040.

[156] K. Takayanagi, Y. Tanishiro, M. Takahashi, S. Takahashi, *Journal of Vacuum Science & Technology A: Vacuum Surface Films. 3* **1985**, *3*, 1502–1506.

[157] G. Binnig, H. Rohrer, C. Gerber, E. Weibel, *Physical Review Letters* **1983**, *50(2)*, 120–126.

[158] N. W. Ashcroft, N. D. Mermin, *Solid State Physics*, *Vol. 45-47*, Saunders College Publishing, **1976**.

[159] E. A. Wood, *Journal of Applied Physics* **1964**, *35*, 1306–1312.

[160] *Basic Crystallographic Definitions and Properties of Si, SiGe and Ge*, Verginia Semiconductor Inc., **2002**.

[161] G. Pietsch, *Applied Physics A* **1995**, *60*, 347–363.

[162] Virginia Semiconductor Inc., **2003**.

[163] G. Higashi, R. Becker, Y. J. Chabal, A. Becker, *Applied Physics Letters* **1991**, *58(15)*, 1656–1658.

[164] W. Kern, D. A. Puotinen, *RCA Reviews* **1970**, *31*, 187–206.

[165] G. W. Trucks, K. Raghavachari, G. S. Higashi, Y. J. Chabal, *Physical Review Letters* **1990**, *65(4)*, 504–507.

[166] H. Ubara, T. Imura, A. Hiraki, *Solid State Community* **1984**, *50(7)*, 673–675.

[167] D. Gräf, M. Grundner, R. Schulz, *Journal of Vacuum Science and Technology A* **1989**, *7(3)*, 808–814.

[168] G. Pietsch, U. Köhler, M. Henzler, *Journal of Applied Physics* **1993**, *73(10)*, 4797–4807.

[169] *http://www.microchemicals.eu/technische-infos/silizium_ aetzen.pdf*, **27.03.2008 10.08h**.

[170] P. Allongue, V. Kieling, H. Gerischer, *Electrochimica Acta* **1995**, *40(10)*, 1353–1360.

[171] S. Sun, Y. Sun, Z. Liu, D.-I. Lee, S. Peterson, P. Pianetta, *Applied Physics Letters* **2006**, *88*, 0219031–0219034.

[172] S. Gan, I. Li, T. Nguyen, H. Qi, R. Hicks, M. Yang, *Surface Science* **1998**, *395*, 69–74.

[173] K. Prabhakarana, T. Ogino, R. Hull, J. Bean, L. Peticolas, *Surface Science* **1994**, *316*, L1031–L1033.

[174] B. Onsia, T. Conard, S. de Gendt, M. M. Heyns, I. Hoflijk, P. W. Mertens, M. Meuris, G. Raskin, S. Sioncke, I. Teerlinck, A. Theuwis, J. V. Steenbergen, C. Vinckier, *Solid State Phenomena* **2005**, *103-104*, 27–30.

[175] J. C. Bean, *Layered Structures, Epitaxy and Interfaces Vol. 37*, J. M. Gibson, L. R. Dawson (Eds.), Materials Research Society Pittsburgh, **1985**.

[176] M. Brezeanu, L. Patron, O. Carp, I. Mindru, N. L. Petre, *Patent: RO 97-9701140 19970619*, **1999**.

[177] M. Ahlers, *Doktorarbeit: Neuartige Precursor zur Abscheidung von Selten-Erd-Oxiden*, University of Oldenburg, **2010**.

[178] M. Ahlers, *Diplomarbeit: Solvate von Nitraten und Perchloraten des Lanthans, Praseodyms und Neodyms: Synthese, Struktur und thermischer Abbau*, University of Oldenburg, **2007**.

[179] A. H. M. Gamal, B. A. A. Balboul, *Colloids and Surfaces A: Physicochem. Eng. Aspects* **2001**, *181*, 19–29.

[180] A. Kraus, M. Hanbücken, T. Koshikawa, H. Neddermeyer, *Analytical and Bioanalytical Chemistry* **2002**, *374(4)*, 688–694.

[181] K. Mironov, A. Popov, V. Vorobéva, Z. Grankina, *Russian Journal of Inorganic Chemistry* **1971**, *16*, 1474–1476.

[182] W. Wendlandt, J. Bear, *Journal of Inorganic and Nuclear Chemistry* **1960**, *12(3-4)*, 276–280.

[183] B. Hàjek, E. Helečková, *Sb. Vys. Sk. Chem.-Technol. Praze, Anorg. Chem. Technol.* **1980**, *B25*, 97.

[184] J.-C. Bünzli, J.-R. Yersin, *Inorganica Chimica Acta* **1984**, *94(6)*, 301–308.

[185] M. Niemeyer, *Zeitschrift für anorganische und allgemeine Chemie* **2006**, *632(8-9)*, 1449–1456.

[186] C. Hu, H. Liu, W. D. Y. Zhang, G. Bao, C. L. Z. L. Wang, *Advanced Materials* **2007**, *19*, 470–474.

[187] M. Bäumer, D. Cappus, H. Kuhlenbeck, H.-J. Freund, G. Wilhelmi, A. B. amd H. Neddermeyer, *Surface Science* **1991**, *253*, 116–128.

[188] B. Eriksson, L. Larsson, L. Niinistö, J. Valkonen, *Inorganic Chemistry* **1980**, *19 (5)*, 1207–1210.

[189] G. Bealla, W. Milligana, H. A. Wolcottb, *Journal of Inorganic and Nuclear Chemistry* **1977**, *39(1)*, 65–70.

[190] D. Rogers, N. J. Taylor, G. E. Toogood, *Acta Crystallographica Section C* **1983**, *39*, 939–941.

[191] N. Hirosaki, S. Ogata, C. Kocer, *Journal of Alloys and Compounds* **2003**, *351(1-2)*, 31–41.

[192] K. Tatsumi, M. Tsutsui, G. Beall, D. Mullica, W. Milligan, *Journal of Electron Spectroscopy and Related Phenomena* **1979**, *16*, 113–118.

[193] S. Suzuki, T. Ishii, T. Sagawa, *Journal of Physical Society Japan* **1974**, *37*, 1334–1340.

[194] O. Gunnarson, K. Schönhammer, *Physical Reviews* **1983**, *B28*, 4315–4341.

[195] S. Imada, T. Jo, *Physica Scripta* **1990**, *41*, 115–119.

[196] L. Schlapbach, H. Scherrer, *Solid State Communications* **1982**, *41(12)*, 893–897.

[197] Y. Uwamino, Y. Ishizuka, H. Yamatera, *Journal of Electron Spectroscopy and Related Phenomena* **1984**, *34(69)*, 67–78.

[198] V. I. Nefedov, D. Gati, B. Dyhurinskii, N. Sergushin, Y. Salyn, *Russian Journal of Inorganic Chemistry* **1975**, *20*, 2307–2314.

[199] R. P. Vasquez, *Journal of Electron Spectroscopy and Related Phenomena* **1991**, *56(3)*, 217–240.

[200] C. Abreu, M. Cristóbal, X. Nóvoa, G. Pena, M. Pérez, C. Serra, *Electrochimica Acta* **2004**, *49*, 3057–3065.

[201] J. F. Moulder, W. F. Stickle, P. E. Sobol, K. D. Bonhen, *Handbook of X-ray Photoelectron Spectroscopy*, J. Chastain, R. C. K. Jr. (Eds.), Physical Electronics Inc. (Minesota), **1995**.

[202] D. D. Sarma, C. N. R. Rao, *Journal of Electron Spectroscopy Related Phenomena* **1980**, *20*, 25–45.

[203] B. C. Hsu, C. C. Chen, S. W. Lee, C. W. Liu, *IEEE Transactions on Electron Devices* **2002**, *49(12)*, 2204–2208.

[204] W. Hebenstreit, J. Redinger, Z. Horozova, M. Schmid, R. Podloucky, P. Varga, *Surface Science* **1999**, *424*, L321–L328.

[205] M. Wagner, T. Heeg, J. S. amd St. Lenk, S. Mantl, C. Zhao, M. Caymax, S. D. Gendt, *Applied Physics Letters* **2006**, *88*, 172901–172904.

[206] M. Wagner, T. Heeg, J. Schubert, C. Zhao, O. Richard, M. Caymax, V. Afanasév, S. Mantl, *Solid-State Electronics* **2006**, *50(1)*, 58–62.

[207] F. Himpsel, F. McFreely, A. Taleb-Ibrahimi, *Physical Review B* **1988**, *38*, 6084–6096.

[208] G. Hollinger, *Applications of Surface Science* **1981**, *8*, 318–336.

[209] K. Kishi, S. Ikeda, *Bulletin of the Chemical Society of Japan* **1973**, *46*, 341–345.

[210] P. Schulze, S. Shaffer, R. Hance, D. Utley, *Journal of Vacuum Science and Technology A* **1982**, *1(1)*, 97–99.

[211] D. Y. Zemlyanov, E. Savinova, A. Scheybal, K. Doblhofer, R. Schlogl, *Surface Science* **1998**, *418(2)*, 441–456.

[212] M. Krisch, R. D'Auria, M. Brown, D. Tobias, J. Hemminger, M. Ammann, D. E. Starr, H. Bluhm, *Journal of Physical Chemistry C* **2007**, *111*, 13497–13509.

[213] A. Namiki, K. Tanimoto, T. Nakamura, N. Ohtake, S. Suzaki, *Surface Science* **1989**, *222*, 530–554.

[214] J. R. Engstrom, D. J. Bonser, T. Engel, *Surface Science* **1992**, *268*, 238–264.

[215] V. Nefedov, E.K, Zhumadilov, L. Baer, *Zh. Neorg. Khim* **1978**, *23*, 2113.

[216] H. Ono, T. Katsumata, *Applied Physics Letters* **2001**, *78(13)*, 1832–1834.

[217] W. S. J.F. Moulder, P. Sobol, K. Bomben, *Handbook of X-Ray-Photoelectron Spectroscopy, Perkin-Elmer Corporation-Physical Electronics Division*, Eden Prairie (USA), **1992**.

[218] T. Yamamoto, Y. Izumi, H. Hasimoto, M. Oosawa, Y. Sugita, *Japan* **2006**, *45*, 6196–6202.

[219] G. Hollinger, P. Kumurdjian, J. M. Mackowski, P. Pertrosa, L. Porte, T. M. Duc, *Journal of Electron Spectroscopy Related Phenomena* **1974**, *5*, 237–245.

[220] C. D. Wagner, D. a. Zatko, R. H. Raymond, *Analytical Chemistry* **1980**, *52*, 1445–1451.

[221] D. Nataraj, *Crystal Research and Technology* **1999**, *34(7)*, 867–872.

[222] A. Laha, H. J. Osten, A. Fissel, *Applied Physics Letters* **2006**, *89*, 1435141–1435141.

[223] J. Jiang, O. Awadelkarim, D.-O. Lee, P. Roman, J. Ruzyllo, *Solid-State Electronics* **2002**, *46*, 1991–1995.

[224] T. Busani, R. A. B. Devine, *Journal of Applied Physics* **2004**, *96*, 6642.

[225] T. Busani, R. Devine, *Journal of Applied Physics* **2005**, *98*, 0441021–0441025.

[226] I. Bunget, M. Popescu, *Physics of Solid Dielectrics*, Elesevier New York, **1984**.

[227] T.-M. Pan, T.-Y. Yu, *Semiconductor Science and Technology* **2009**, *24*, 1–8.

[228] J. Dabrowski, H. J. Muessig, *Silicon Surfaces and Formation of Interfaces*, World Scientific Singapore, **2000**.

[229] F. F. Fang, A. B. Fowler, *Physical Review* **1968**, *169*, 619–631.

[230] A. Ohwada, H. Maeda, K. Tanaka, *Japanese Journal of Applied Physics* **1969**, *8*, 629–630.

[231] M. Yang, M. Ieong, L. Shi, K. Chan, V. Chan, A. Chou, E. Gusev, K. Jenkins, D. Boyed, Y. Ninomiya, D. Pendleton, Y. Supris, D. Heenan, J. Ott, K. Guarini, C. D'Emic, M. Cobb, P. Mooney, B. To, N. Rovedo, J. Benedict, R. Mo, H. Ng, *Tech. Dig. IEDM* **2003**, 453.

[232] Y. Kim, A. Kuriyama, I. Ueda, S. Ohmi, K. Tsutsui, H. Iwai, *European Solid-State Device Research 2003 33rd Conference on ESSDERC* **2003**, *1*, 569–572.

[233] S. Guha, E. Cartier, N. Bojarczuk, J. Bruley, L. Gignac, J. Kranasinski, *Journal of Applied Physics* **2001**, *90(1)*, 512–514.

[234] A. Stesmans, *Journal of Applied Physics* **2000**, *88*, 489–498.

[235] C. O. Chui, S. Ramanathan, B. B. T. P. C. McIntyre, K. C. Saraswat, *IEEE Electron Device Letters* **2002**, *23*, 473–475.

[236] S. Schamm-Chardon, L. Lamagna, C. Wiemer, S. Baldovino, M. Peregoand, M. Fanciulli, *to be published.*

[237] S. Schamm-Chardon, P. Coulon, L. Lamagna, C. Wiemer, S. Baldovino, M. Fanciulli, *Microelectronic Engineering* **2011**, *88*, 419–422.

[238] X. Lu, N. W. Cheung, *Applied Physics Letters* **1996**, *69*, 1915–1918.

[239] M. M. V. Chong, *personal communication.*

[240] K. Kolanek, M. Tallarida, M. Michling, K. Karavaev, D. Schmeisser, *Physica Status Solidi C* **2011**, *8(4)*, 1287–1292.

[241] M. A. Henderson, *Surface Science* **1999**, *419*, 174–187.

[242] M. M. V. Chong, *to be published*, Nanyang Technological University, School of Materials Science and Engineering, **2013**.

[243] L. Bergmann, C. Schaefer, W. Raith, *Lehrbuch der Experimentalphysik, Bd. 6, Festkörper*, de Gruyter, **1992**.

[244] *http://de.wikipedia.org/wiki/Datei:Bandstruktur_-_indirekter_Band%C3%BCbergang.svg#filelinks*, **10.01.2012 13.25 h**.

[245] C. Weißmantel, C. Hamann, *Grundlagen der Festkörperphysik*, Wiley-VCH, **1999**.

List of Figures

2.1. Schematic XPS energy diagram. E_{kin} is the energy of the electrons at emission from the sample, E'_{kin} is the energy in access to the analyzer, E''_{kin} is the detected energy of the electrons at the detector (after[23]). 7
2.2. Primary and secondary electron excitation processes during interaction of matter with radiation. 9
2.3. Schematic XPS survey spectra to illustrate the different signals. 12
2.4. Assembly of a dual Mg/Al anode X-ray tube for XPS incident beam generation (after[23]). 14
2.5. Experimental setup of the different components for XPS. 15
2.6. Experimental STM system setup. 19
2.7. Atrractive and repulsive forces in dependency on the inter atmoic spacing between two atoms, Lennard Jones potential. . . 21
2.8. Alignment scheme and beam path inside the TEM column (a). Beam diagram in bright field (BF) mode (b). 27
2.9. Alignment of detectors for different electron/matter interactions to be determined. 29
2.10. Schematic illustration of a typical FIB column including the resulting ion beam and a detailed image of the LMIS. 32
2.11. Schematic XTEM specimen, lamella, manufacturing with FIB. . 34
2.12. Schematic demonstration of the diffraction, Bragg interference, of an incident beam on a periodically ordered crystal lattice (after[57]). 38
2.13. Construction of the Ewald circle. 39

3.1. Schematic cross section of a nMOS capacitor. V_G is supposed to be the gate voltage whereas V_B is the voltage at the back contact. 42
3.2. Charge distributions for a p-type substrate in accumulation, depletion and inversion operation mode of MOS devices (after[59]). 43
3.3. Nature and location of charge centers in thermally grown SiO_2-Si structures (after[60], ©1980 IEEE). 46

3.4. Electrical modeling of interfacial traps, as allowed electronic levels at the oxide-semicondcutor interface (a), filling of the interfacial levels under inversion(b), depletion (c) and accumulation (d) biasing in n-type devices (after[60]). 48
3.5. Cross section of a p-n junction, showing the respective depletion layers x_p and x_n in each region, with $\omega_{n(p)}$ as the width of the n-(p)type region. 51
3.6. p-n junction energy band diagrams for equilibrium, forward and reverse bias conditions (compare[60]). 52
3.7. Schematic illustration of a nMOSFET in saturation mode with respective applied voltages, the inversion and depletion layer regions which are formed during device operation are shown additionally. 55
3.8. Schematic illustration of a C-V/I-V measurement system. 59
3.9. C-V characteristics of a nMOS structure in dependence on the applied gate voltage V_G for high and low frequency measurements. 60
3.10. Charge fluctuation inside the nMOS capacitor under DC biasing conditions in accumulation, depletion and inversion (similar to[60]). 61
3.11. I-V curves for p- and n-type substrates. Shown are the linear scale for the ordinate in (a) and the typical logarithmic scale in (b). 63

4.1. Free Gibbs enthalpy of crystallization in dependency on the nuclei radius r (after[73]). 70
4.2. Saturation regions in solutions. 71
4.3. Heterogeneous crystallization process for substrate supported layer formation (compare[75]). 72
4.4. Contact angle in heterogeneous nucleus formation on dissimilar substrates. 73
4.5. Schematic illustration of different film growth types in dependency on the interface energy. 74
4.6. Possible interfacial structure formations from crystallization processes on dissimilar substrates. 74

5.1. Leakage currents vs. voltage for various thicknesses of SiO_2 layers (from[84]). 79

6.1. Photograph of the utilized UHV chamber for surface analysis. Shown are the analytical parts (green) and the constructional specifics (blue). 92
6.2. Sample holder with mounted sample within the chamber at room temperature (top), while heating (bottom) in front of the analyzer entrance slit (left), sample holder with approached Feulner cup snorkel of the mass spectrometer (middle) and left side view of the sample holder showing the Macor® contact slit (right). 93
6.3. Photograph of the sample holder with sample mounting. 94
6.4. Exchange module adjusted to the chamber (left) and with inserted sample holder prior to sample load (right). 95
6.5. *KEITHLEY 4200 SCS* and LCR meter for semiconductor analysis. 96
6.6. Sputter coater for back contact deposition (left) and high vacuum sputtering equipment for front electrode deposition (right). 97
6.7. RTA equipment with N_2 and O_2 annealing gas supply. 97
6.8. *Beneq TFS 200* operated with *Intouch Wonderware by Invensys software*. 98

7.1. Process flow of the deposition technique, surface cleaning (1.), precursor deposition (2.) and oxide formation (3.). 102
7.2. Schematic illustration of the different steps within the dip-coating process (similar to[141]). 105

8.1. Crystal structure of the diamond type crystal lattice. (see[149]) . 112
8.2. Reaction scheme of *H*-termination with *HF*. (after[165]) 116

9.1. Molecule structure of the *La* and *Nd* trinitrate-hexahydrate. . . 125
9.2. Dependency of the decomposition temperature of the RE-nitrate-solvates from the respective solvate and RE center. 126
9.3. DTA/TG-diagrams of $La(NO_3)_3(H_2O)_6$ (top) and $Nd(NO_3)_3(H_2O)_6$ (bottom). 127
9.4. XRD spectra of the precursor $La(NO_3)_3 \times 6\ H_2O$ (top) and the hydrolysis product $La(OH)_3$ (bottom) after thermolysis to La_2O_3 compared to measured[188] and simulated literature data[189].132
9.5. XRD spectra of the precursor $Nd(NO_3)_3 \times 6\ H_2O$ (top) and the thermolysis product Nd_2O_3 (bottom) compared to measured[190] and simulated literature data[191]. 133

9.6. Tendency of the electron affinity of the different binding partners. 135

9.7. Direction of chemical shifts of *RE3d* and *O1s* in dependency on the respective binding partners. 135

9.8. *La* based powder survey spectra measured with Mg-K_α for $La(OH)_3$ (top), La_2O_3 (middle) and $La(NO_3)_3(H_2O)_6$ (bottom). 137

9.9. Detail spectra of the *La3d* signal measured with Mg-K_α from the *La* based nitrate-hydrate (black), oxide (red) and hydroxide (blue) powders. The peak fit parameters are shown in table 9.5. 138

9.10. *O1s* signal measured with Mg-K_α of the three *La* based powders (nitrate (black, bottom), oxide (red, middle), hydroxide (blue, top). Included are the peak fits, which are utilized for precise analysis. 141

9.11. *Nd* based powder survey spectra measured with Al-K_α for $Nd(OH)_3$ (top), Nd_2O_3 (middle) and $Nd(NO_3)_3(H_2O)_6$ (bottom). 144

9.12. Detail *Nd3d* spectra of the *Nd* based hydroxide, oxide and nitrate powder measured with Al-K_α, showing the binding energy shift tendency (a), fitted $Nd3d_{5/2}$ signal, shown are the specific peaks and energy difference (ΔE) of the nitrate, oxide and hydroxide powder (b) of the main peak ($Nd3d_{5/2}$) and the respective satellite. 145

9.13. *O1s* signal of the three *Nd*-based powders measured with Al-K_α. Included are the detailed peak fits. 147

10.1. SEM images of droppy and brittle structures deposited from 0.5 M $Nd(NO_3)_3 \times 6H_2O$ butanolic precursor solution on *H-Si(111)*. The images are taken with 1.3 nA beam current and 30 kV acceleration voltage. 153

10.2. Series dilution from 0.5 M to 0.1 M of the *Nd* precursor in 1-butanol. 154

10.3. SEM images of *Si(111)* samples coated with 0.01 M $Nd(NO_3)_3 \times 6H_2O$ precursor solution in 1-butanol. Homogeneously spread structures from nucleation centers are obvious. The images are taken with 0.88 nA beam current and 10 kV acceleration voltage. 154

10.4. SEM images of *Si(111)* samples coated with 0.0096 M $Nd(NO_3)_3 \times 6H_2O$. Changes are obvious from comparison with the 0.01 M samples as no spots can be observed anymore. The beam current was set to 0.88 nA and the acceleration voltage to 10 kV. . 155

10.5. SEM images of *Si(100)* (left) and *Si(111)* (right) substrates coated with 0.01 M $Nd(NO_3)_3 \times 6H_2O$ butanolic solution showing significant differences in deposition structures. 156

10.6. STM images of films deposited from 0.001 M $La(NO_3)_3 \times 6H_2O$ butanolic precursor solution on *H-Si(111)*, exhibiting a RMS of 0.736 nm 158

10.7. Roughness studies using AFM tapping mode on bare cleaned *H-Si(111)* and *H-Si(100)*. Showing RMS values of 0.45 nm (*H-Si(111)*) and 1.36 nm (*H-Si(100)*). 159

10.8. AFM images taken in tapping mode and RMS values for oxide films after precursor thermolysis deposited from 0.001 M (top), 0.005 M (middle) and 0.01 M (bottom), $Nd(NO_3)_3 \times 6H_2O$ butanolic precursor solution on *H-Si(100)* (left) and *H-Si(111) (right)* substrates (*H-Si(111)*: x = 0.2 μm/div and z = 50 nm/div; *H-Si(100)*: x = 0.5 μm/div and z = 100 nm/div).161

10.9. AFM 3D and 1D images (tapping mode) of the films deposited from 0.01 M butanolic $Nd(NO_3)_3 \times 6H_2O$ precursor solution after deposition (top), decomposition (middle) and after 72 h of air exposure (bottom) on *H-Si(111)* (x = 0.2 μm/div and z = 50 nm/div). 163

10.10AFM 3D and 1D images (tapping mode) of the films, deposited from 0.005 M butanolic $Nd(NO_3)_3 \times 6H_2O$ precursor solution after deposition (top), decomposition (middle) and after 72 h of air exposure (bottom) on *H-Si(111)* (x = 0.2 μm/div and z = 50 nm/div). 164

10.11AFM 3D and 1D images (tapping mode) of the films, deposited from 0.001 M butanolic $Nd(NO_3)_3 \times 6H_2O$ precursor solution on *H-Si(111)* after deposition (top), decomposition (middle) and after 72 h of air exposure (bottom) (x = 0.2 μm/div and z = 50 nm/div). 165

10.12Dependency of the film roughness on the $Nd(NO_3)_3 \times 6H_2O$ butanolic precursor solution, concentration and the step of the process. Shown are the determined roughness values from AFM analysis in tapping mode of samples after deposition (precursor film, black), after decomposition (oxide film from thermolysis, red) and after 72 h of air exposure (blue) on *Si(111)*. Additionally the roughness of the cleaned bare substrate is given for comparison reasons. 166

10.13Annealing dependent roughness measured with AFM in tapping mode of films, deposited from 0.005 M butanolic $Nd(NO_3)_3 \times 6H_2O$ precursor solution on *H-Si(111)*. 168

10.14HRTEM images of the oxide film from precursor thermolysis, deposited from 0.0096 M $Nd(NO_3)_3 \times 6H_2O$ butanolic precursor solution on *H-Si(111)*. 169

10.15HRTEM images of the oxide film from precursor thermolysis, deposited from 0.005 M $Nd(NO_3)_3 \times 6H_2O$ butanolic precursor solution on *H-Si(111)*. 169

10.16HRTEM images of the oxide film from precursor thermolysis, deposited from 0.001 M $Nd(NO_3)_3 \times 6H_2O$ butanolic precursor solution on *H-Si(111)*. 170

10.17HRTEM images of films deposited from 0.0096 M, 0.005 M and 0.001 M $Nd(NO_3)_3 \times 6H_2O$ butanolic precursor solution. 170

10.18Film thickness plotted vs. the $Nd(NO_3)_3 \times 6H_2O$ butanolic precursor solution concentration. 171

10.19AFM images of the *Ge* substrates coated with oxide films, deposited from 0.005 M butanolic $Nd(NO_3)_3 \times 6H_2O$ precursor solution. Shown are the topography and RMS for oxide films after thermolysis and annealed at 673 K. Two different sample spots are illustrated each due to a large variety in the roughness (with x = 0.2 μm/div and z = 100 nm/div). 173

10.20AFM images of the *SiGe(111)* substrates, coated with oxide films, deposited from 0.005 M butanolic $Nd(NO_3)_3 \times 6H_2O$ precursor solution. The illustration shows topography and RMS for oxide films after thermolysis, at 873 K and 1073 K annealed samples. 175

10.21 Concentration dependent mechanistic regions for preferred film formation (white), spontaneous nucleation (red) and transition from stable film formation to under saturation, which is not determined precisely and therefore shown in crossed lines. 179

11.1. Survey spectra measured with Mg-K_α of the native oxidized surface, the H-terminated samples, La-based precursor film and oxide film from thermolysis deposited from 0.005 M butanolic $La(NO_3)_3 \times 6H_2O$ precursor solution on *Si(111)*. 187

11.2. *Si2p* (left) and *O1s* (right) spectra measured with Mg-K_α of the native oxidized the H-terminated samples, La-based precursor film and oxide film from thermolysis deposited from 0.005 M butanolic $La(NO_3)_3 \times 6H_2O$ precursor solution on *H-Si(111)*. . 188

11.3. *C1s* signal of the La-based precursor films and oxide films from thermolysis deposited from 0.005 M butanolic $La(NO_3)_3 \times 6H_2O$ precursor solution on *Si(111)* measured with Mg-K_α. 194

11.4. *La3d* signal of the precursor film and the oxide film from thermolysis deposited from 0.005 M butanolic $La(NO_3)_3 \times 6H_2O$ precursor solution on *Si(111)* measured with Mg-K_α. Marked are the peak maxima and the peak width. 195

11.5. Influence of the heating temperature on the interface formation respectively the influence on the Si substrate of the films deposited from 0.005 M butanolic $La(NO_3)_3 \times 6H_2O$ precursor solution on *Si(111)*, measured with Mg-K_α. Shown are the *Si2p* and *O1s* signal. 198

11.6. Survey spectra measured with Mg- and Al-K_α of the native oxidized surface, the H-terminated samples, precursor film and oxide film from thermolysis deposited from 0.005 M butanolic $Nd(NO_3)_3 \times 6H_2O$ precursor solution on *Si(111)*. 201

11.7. Survey spectra measured with Mg-K_α and Al-K_α of the native oxidized surface, the H-terminated samples, precursor film and oxide film from thermolysis deposited from 0.005 M butanolic $Nd(NO_3)_3 \times 6H_2O$ precursor solution on *Si(100)*. 202

11.8. *Nd3d* signal of the precursor film and the oxide film from thermolysis deposited from 0.005 M butanolic $Nd(NO_3)_3 \times 6H_2O$ precursor solution on *Si(111)* measured with Al-K_α. Notably is the overlap with the OKLL signal. Marked are the peak maxima and the peak width. 203

11.9. *Nd3d* signal of the precursor and oxide film from thermolysis deposited from 0.005 M butanolic $Nd(NO_3)_3 \times 6H_2O$ precursor solution on *Si(100)* measured with Mg-K_α. Marked are the peak maxima and the peak width. 204

11.10*Si2p* spectra measured with Mg-K_α of the native oxidized surface, the *H*-terminated samples, *Nd*-based precursor film and oxide film from thermolysis deposited from 0.005 M butanolic $Nd(NO_3)_3 \times 6H_2O$ precursor solution on *Si(111)* and *Si(100)*. . 206

11.11*O1s* spectra measured with Al-K_α of the native oxidized surface, the *H*-terminated samples, *Nd*-based precursor film and oxide film from thermolysis deposited from 0.005 M butanolic $Nd(NO_3)_3 \times 6H_2O$ precursor solution on *Si(111)* (left) and *Si(100)* (right). 210

11.12Survey spectra measured with Mg-K_α of the native oxidized surface, the *H*-terminated samples, precursor film and oxide film from thermolysis deposited from 0.005 M butanolic $Nd(NO_3)_3 \times 6H_2O$ precursor solution on *Ge(100)*. 214

11.13*Nd3d* signal of the precursor and oxide film from thermolysis deposited from 0.005 M butanolic $Nd(NO_3)_3 \times 6H_2O$ precursor solution on *Ge(100)* measured with Mg-K_α. Marked are the peak maxima and the peak width. 215

11.14*Ge3d* and *O1s* spectra measured with Mg-K_α (*O1s*) and Al-K_α (*Ge3d*) of the native oxidized surface, the *H*-terminated samples, *Nd*-based precursor film and oxide film from thermolysis deposited from 0.005 M butanolic $Nd(NO_3)_3 \times 6H_2O$ precursor solution on *Ge(100)*. 217

11.15Survey spectra measured with Mg-K_α of the native oxidized surface, the *H*-terminated samples, precursor film and oxide film from thermolysis, deposited from 0.005 M butanolic $Nd(NO_3)_3 \times 6H_2O$ precursor solution on *SiGe(111)*. 222

11.16 *Nd3d* signal of the *Nd*-based precursor and oxide film from thermolysis, deposited from 0.005 M butanolic $Nd(NO_3)_3 \times 6H_2O$ precursor solution on *SiGe(111)*, measured with Mg-K_α. Marked are the peak maxima and the peak width. 223

11.17 *Si2p*(a) and and *Ge3ds* (b) detail spectra measured with Al-K_α of the native oxidized, *H*-terminated *SiGe(111)* surfaces and the respective *Nd*-based precursor films and oxide films from thermolysis deposited from 0.005 M butanolic $Nd(NO_3)_3 \times 6H_2O$ precursor solution. 224

11.18 *O1s* detail spectra measured with Mg-K_α of the native oxidized, *H*-terminated *SiGe(111)* surfaces and the respective *Nd*-based precursor films and oxide films from thermolysis deposited from 0.005 M butanolic $Nd(NO_3)_3 \times 6H_2O$ precursor solution. 229

12.1. Schematic MOS capacitor built by electrode deposition (size ratios are not in agreement with real samples) (left), photograph of the sputtering mask (middle), SEM image of the deposited electrodes confirming a diameter of 270 μm (right). 238

12.2. C-V curves measured at 100 kHz (left) and 1 MHz (right) of the Nd_2O_3 films on n-*Si(111)*, generated from 0.01 M $Nd(NO_3) \times 6H_2O$ butanolic precursor solution. Shown are the analyses of the oxide from precursor thermolysis, at 673 K and 1073 K annealed samples. 240

12.3. C-V curves measured at 100 kHz (left) and 1 MHz (right) of the Nd_2O_3 films on n-*Si(111)*, generated from 0.005 M $Nd(NO_3) \times 6H_2O$ butanolic precursor solution. Shown are the analyses of the oxide from precursor thermolysis, at 673 K, 873 K and 1073 K annealed samples. 240

12.4. C-V curves measured at 100 kHz (left) and 1 MHz (right) of the Nd_2O_3 films on n-*Si(111)*, generated from 0.001 M $Nd(NO_3) \times 6H_2O$ butanolic precursor solution. Shown are the analyses of the oxide from precursor thermolysis, at 673 K and 1073 K annealed samples. 241

12.5. C-V curves measured at 100 kHz (left) and 1 MHz (right) of the Nd_2O_3 films on p-*Si(100)*, generated from 0.01 M $Nd(NO_3) \times 6H_2O$ butanolic precursor solution. Shown are the analyses of the oxide from precursor thermolysis, at 673 K and 1073 K annealed samples. 244
12.6. C-V curves measured at 100 kHz (left) and 1 MHz (right) of the Nd_2O_3 films on p-*Si(100)*, generated from 0.005 M $Nd(NO_3) \times 6H_2O$ butanolic precursor solution. Shown are the analyses of the oxide from precursor thermolysis, at 673 K, 873 K and 1073 K annealed samples. 244
12.7. C-V curves measured at 100 kHz (left) and 1 MHz (right) of the Nd_2O_3 films on p-*Si(100)*, generated from 0.001 M $Nd(NO_3) \times 6H_2O$ butanolic precursor solution. Shown are the analyses of the oxide from precursor thermolysis, at 673 K and 1073 K annealed samples. 245
12.8. I-V curves of the films deposited on n-*Si(111)* from 0.01 M $Nd(NO_3) \times 6H_2O$ butanolic precursor solution. Shown are curves of the oxide from precursor thermolysis, at 673 K and 1073 K annealed samples. Multiple curve shapes of the samples annealed at 1073 K have been detected. 247
12.9. I-V curves of the films deposited on n-*Si(111)* from 0.005 M $Nd(NO_3) \times 6H_2O$ butanolic precursor solution. Shown are curves of the oxide from precursor thermolysis, at 673 K, 873 K and 1073 K annealed samples. 248
12.10I-V curves of the films deposited on n-*Si(111)* from 0.001 M $Nd(NO_3) \times 6H_2O$ butanolic precursor solution. Shown are curves of the oxide from precursor thermolysis, at 673 K and 1073 K annealed samples. 248
12.11I-V curves of the films deposited on p-*Si(100)* from 0.01 M $Nd(NO_3) \times 6H_2O$ butanolic precursor solution. Shown are curves of the oxide from precursor thermolysis, at 673 K and 1073 K annealed samples. 250
12.12I-V curves of the films deposited on p-*Si(100)* from 0.005 M $Nd(NO_3) \times 6H_2O$ butanolic precursor solution. Shown are curves of the oxide from precursor thermolysis, at 673 K, 873 K and 1073 K annealed samples. 251

12.13I-V curves of the films deposited on p-*Si(100)* from 0.001 M $Nd(NO_3) \times 6H_2O$ butanolic precursor solution. Shown are curves of the oxide from precursor thermolysis, at 673 K and 1073 K annealed samples. 251

12.14Temperature dependent I-V measurements of Nd_2O_3 films, deposited from 0.005 M $Nd(NO_3) \times 6H_2O$ butanolic precursor solution on n-*Si(111)*, for different annealing temperatures. . . . 254

12.15Temperature dependent I-V measurements of films deposited from 0.005 M $Nd(NO_3) \times 6H_2O$ butanolic precursor solution on p-*Si(100)* for the samples annealed at different temperatures measured from 298 K to 398 K. 256

12.16ln(J/E) vs. $E^{1/2}$ plots over increasing temperatures of the Nd_2O_3 layers deposited from 0.005 M butanolic $Nd(NO_3)_3 \times 6H_2O$ precursor solution on p-*Si(100)* substrates (from thermolysis, annealed at 673 K/873 K and 1073 K). Shown are the data over the full measured electric field region. 257

12.17ln(J/E) vs. $E^{1/2}$ plots over increasing temperatures of the Nd_2O_3 layers deposited from 0.005 M butanolic $Nd(NO_3)_3 \times 6H_2O$ precursor solution on p-*Si(100)* substrates (from thermolysis, annealed at 673 K/873 K and 1073 K). Shown are the data under linearity conditions at high electric field. 258

12.18Leakage current density values for the films deposited on n-*Si(111)* and p-*Si(100)* from different $Nd(NO_3) \times 6H_2O$ butanolic precursor solution concentrations plotted vs. the annealing temperature. 264

12.19Leakage current density vs. EOT for the deposited Nd_2O_3 films and SiO_2. 268

12.20Measured C-V curves of the samples deposited from 0.005 M $Nd(NO_3) \times 6H_2O$ butanolic precursor solution on n-*Ge(100)* at 100 kHz and 1 MHz. 271

12.21Temperature dependent I-V curves of the samples deposited from 0.005 M $Nd(NO_3) \times 6H_2O$ butanolic precursor solution on n-*Ge(100)*. Shown are the oxide films from thermolysis (left) and at 673 K annealed samples (right). 272

12.22ln(J/E) vs. $E^{1/2}$ plots over increasing temperatures of the Nd_2O_3 layers deposited from 0.005 M butanolic $Nd(NO_3)_3 \times 6H_2O$ precursor solution on n-*Ge(100)* substrates (from thermolysis and annealed at 673 K). Shown are the data over the full measured electric field region. 273

12.23C-V curves of the films deposited from 0.005 M $Nd(NO_3) \times 6H_2O$ butanolic precursor solution on p-*SiGe(111)*. Shown are data of the oxide from precursor thermolysis, at 673 K, 873 K and 1073 K annealed samples. 274

12.24Temperature dependent I-V measurements for the films deposited from 0.005 M $Nd(NO_3) \times 6H_2O$ butanolic precursor solution on p-*SiGe(111)*. The oxide film from precursor thermolysis, after annealing at 673 K, 873 K and 1073 K has been investigated. . . 276

12.25ln(J/E) vs. $E^{1/2}$ plots over increasing temperatures of the Nd_2O_3 layers deposited from 0.005 M butanolic $Nd(NO_3)_3 \times 6H_2O$ precursor solution on p-*SiGe(111)* substrates (annealed at 673 K and 1073 K). Shown are the data over the full measured electric field region. 277

13.1. Schematic ALD process to deposit TiO_2 on *Si* surfaces. $TiCl_4$ has been used as metal and H_2O as oxygen source. 282

13.2. AFM images of TiO_2/N_2O_3 bilayer films deposited from 0.005 M butanolic $Nd(NO_3)_3 \times 6H_2O$ precursor solution and 50 cycles of ALD on *H-Si(111)* and *H-Si(100)*, oxides as deposited, annealed at 673 K/1073 K (tapping mode, x = 0.2 μm/div and z = 50 nm/div). 284

13.3. HRTEM images of TiO_2/N_2O_3 bilayer films deposited from 0.005 M butanolic $Nd(NO_3)_3 \times 6H_2O$ precursor solution and 50 cycles of ALD on *H-Si(111)* (top) and *H-Si(100)* (bottom). (images are taken by Global Foundries®Singapore) 285

13.4. EDX scan of the bilayer thin film on *Si(111)* deposited from 0.005 M $Nd(NO_3)_3 \times 6H_2O$ butanolic precursor solution and 50 cycles of ALD, confirming the oxide film to contain *Ti* and *Nd*. . 287

13.5. C-V curves of the bilayer films ($TiO_2/Nd_2O_3/Si$) deposited on H-terminated *n-Si(111)* from 0.01 M (top), 0.005 M (middle) and 0.001 M (bottom) $Nd(NO_3)_3 \times 6H_2O$ butanolic precursor solution and ALD-TiO_2 (50 cycles). Shown are the results of bilayer oxide films as deposited and annealed at 673 K/1073 K measured with 100 kHz (left) and 1 MHz (right). 289

13.6. C-V curves of the bilayer films ($TiO_2/Nd_2O_3/Si$) deposited on H-terminated p-*Si(100)* from 0.01 M (top), 0.005 M (middle) and 0.001 M (bottom) $Nd(NO_3)_3 \times 6H_2O$ butanolic precursor solution and ALD-TiO_2 (50 cycles). Shown are the results of bilayer oxide films as deposited and annealed at 673 K/1073 K measured with 100 kHz (left) and 1 MHz (right). 291

13.7. I-V curves of the bilayer samples ($TiO_2/Nd_2O_3/Si$) generated from ALD-TiO_2 and wet chemical deposition from 0.001 M/0.005 M/0.01 M $Nd(NO_3)_3 \times 6H_2O$ butanolic precursor solution on n-*Si(111)* (left) and p-*Si(100)* (right). 294

13.8. Temperature dependent I-V curves of the bilayer ($TiO_2/Nd_2O_3/Si$) system deposited from 0.005 M $Nd(NO_3)_3 \times 6H_2O$ butanolic precursor solution and ALD of TiO_2. The samples are the oxides as deposited and after annealing at 673/1073 K on n-*Si(111)* (left) and p-*Si(100)* (right). 296

13.9. C-V curves of the reverse bilayers Nd_2O_3/TiO_2 deposited on n-*Si(111)* for films deposited from 0.001 M, 0.005 M and 0.01 M $Nd(NO_3)_3 \times 6H_2O$ butanolic precursor solution and ALD of TiO_2 (50 cycles). Shown are data of the oxide films as deposited and annealed at 1073 K. 298

13.10. C-V curves of the reverse bilayers Nd_2O_3/TiO_2 deposited on p-*Si(100)* for films deposited from 0.001 M, 0.005 M and 0.01 M $Nd(NO_3)_3 \times 6H_2O$ butanolic precursor solution and ALD of TiO_2 (50 cycles). Shown are data of the oxide films as deposited and annealed at 1073 K. 300

13.11. I-V curves of the reverse bilayers films ($Nd_2O_3/TiO_2/Si$) generated from ALD of TiO_2 (50 cycles) and wet chemically deposited Nd_2O_3 from 0.001 M/0.005 M/0.01 M $Nd(NO_3)_3 \times 6H_2O$ butanolic precursor solution on n-*Si(111)* (left) and p-*Si(100)* (right). 303

13.12Temperature dependent I-V curves of the reverse bilayer films ($Nd_2O_3/TiO_2/Si$) generated from ALD TiO_2 and wet chemical deposited Nd_2O_3 from 0.005 M $Nd(NO_3)_3 \times 6H_2O$ butanolic precursor solution on n-*Si(111)* (left) and p-*Si(100)* (right) (as deposited and annealed at 1073 K). 305

13.13Dependency of the leakage current density on the solution concentration of the *Nd*-based solution and the respective annealing temperature. Shown are bilayer ($TiO_2/Nd_2O_3/Si$) (top) and reverse bilayer ($Nd_2O_3/TiO_2/Si$) (bottom) samples deposited from 0.01 M, 0.005 M and 0.001 M $Nd(NO_3)_3 \times 6H_2O$ butanolic precursor solution and ALD generation of TiO_2 (50 cycles), after deposition, annealing at 673 K and 1073 K. 311

13.14κ values and leakage current densities in dependency on the respective EOT values for the generated bilayer ($TiO_2/Nd_2O_3/Si$) and reverse bilayer ($Nd_2O_3/TiO_2/Si$) gate stacks on *H-Si(111)* and *H-Si(100)*. 312

13.15Illustration of the charge carrier distribution within the bilayer ($TiO_2/Nd_2O_3/Si$) and reverse bilayer ($Nd_2O_3/TiO_2/Si$) samples during negative biasing. 314

14.1. Summary of the prepared single layer systems. Listed are the respective generated REO, substrate types, precursor solution concentrations used and annealing temperatures. 316

14.2. Summary of the prepared bilayer and reverse systems. Listed are the respective substrate types, precursor solution concentrations used and annealing temperatures. 317

A.1. Part I: FIB-TEM lamella preparation 372

A.2. Part II: FIB-TEM lamella preparation 373

B.1. Semiconductors in the Periodic Table of Elements. Within the group of semiconductors covalent bondings are dominant. To the right of the semiconductors are non-conductors with predominant van der Waals bondings and to the left elements with prevalent metallic bondings (after[243]). 376

B.2. Electron transition from valence to conduction band in direct and indirect semiconductors. In indirect semiconductors, a change of $\vec{k}$ is necessary for excitation with a minimum energy difference between valence and conduction band (after[244]). 377
B.3. Simplified band structures and lattice structure scheme of intrinsic, p- and n-type semiconductors (after[59] and[91]). 379
B.4. Carrier recombination processes (after[59]). 386

E.1. XPS survey scan of the internal chamber standard, indicating a high fluorine impurity. The spectra is measured with Al-K_α. Spectrum shown with courtesy of Jörg Stöver 393

F.1. Capacitance densities detected of the 10 nm thick TiO_2 films deposited from ALD on n-*Si(111)* (left) and p-*Si(100)* (right). Shown are the curves of the oxides films after deposition, annealing at 673 k/873 K/1073 K measured at 100 kHz and 1 MHz.395
F.2. Leakage Current densities detected from 298 K to 398 K of the 10 nm thick TiO_2 films deposited from ALD on n-*Si(111)* (left) and p-*Si(100)* (right). Shown are the curves of the oxides films after deposition and annealing at 673 K/873 K. 397

List of Tables

2.1. High energy X-ray satellite lines.[21] 16

5.1. Alternative materials as high-κ replacement, κ values, band gaps and crystal structures.[79] [78] [80] 78

5.2. Thermodynamically stable and therefore interesting RE candidates for SiO_2 replacement and the respective ΔG_{1000} values. . . 84

5.3. Lattice parameters of the "low temperature modifications" of the lanthanide sesquioxides.[104] 85

6.1. Measurement parameters for XPS analysis. 99

7.1. Results of the wetting experiments of different solvents on the *H-Si(111)* surface and the tabulated surface tension values γ, vapor pressures p_v and dipole moments p of the solvents at room temperature. 107

9.1. Thermal decomposition temperatures in K of $RE(NO_3)_3(H_2O)_6$ with RE=La, Nd[178]. 128

9.2. Available lattice parameters of the ligand-metal combinations. All lattice spacings are given in pm. 129

9.3. Percentage difference of the lattice parameters of the $Ln(NO_3)_3\times 6H_2O$ ($Ln = La$ and Nd) to the Si and Ge substrates. 130

9.4. Electronegativities of the involved elements.[91] 134

9.5. Peak fit parameters and peak positions in eV for the *La3d* powder spectra of the nitrate, oxide and hydroxide. 139

9.6. Peak fit parameters and peak positions in eV for the *O1s* powder spectra of the *La* nitrate, oxide and hydroxide. 142

9.7. Peak fit parameters and peak positions in eV for the $Nd3d_{5/2}$ powder spectra of the nitrate, oxide and hydroxide. 146

9.8. Peak fit parameters and peak positions in eV for the *O1s* powder spectra of the *Nd*-based nitrate-hydrate, oxide and hydroxide. . 148

9.9. Summary of the collected XPS data showing the characteristic peak positions and distances in eV for the RE-nitrates, oxides and hydroxides (RE = *La, Nd*). 150

10.1. RMS and z-ranges in nm of the films illustrated in figure 10.8. and respective deviations between the two substrate types. . . . 161

10.2. RMS values and z-ranges in nm, extracted from AFM measurements in tapping mode, for the films deposited from 0.001 M, 0.005 M and 0.01 M butanolic $Nd(NO_3)_3 \times 6H_2O$ precursor solution on *Si(111)* directly after precursor deposition, after decomposition to the oxide and after 72 h of air exposure. 166

10.3. RMS values of AFM tapping mode measurements and z-ranges in nm for the films deposited on *H-Ge(100)* from 0.005 M butanolic $Nd(NO_3)_3 \times 6H_2O$ precursor solution, of the oxide films from thermolysis, after 873 K and 1073 K anneal. 174

10.4. RMS values of AFM imaging in tapping mode and z-ranges in nm for the oxide films deposited on *SiGe(111)* from 0.005 M butanolic $Nd(NO_3)_3 \times 6H_2O$ precursor solution after thermolysis, after 873 K and 1073 K anneal. 176

10.5. Percentage of the measured roughness values of the oxide films on *Si(111)*, related to the respective film thickness. 180

10.6. Percentage of the measured roughness values of the oxide films on *Si(100)*, related to the respective film thickness. 181

11.1. Peak fit parameters and peak positions in eV for the *Si2p* signal of the native oxidized, *H*-terminated as well as *La*-based precursor films and oxide films from thermolysis deposited from 0.005 M butanolic $La(NO_3)_3 \times 6H_2O$ precursor solution on the *Si(111)* substrates. 189

11.2. Peak fit parameters and peak positions in eV for the *O1s* signal of the native oxidized, *H*-terminated as well as *La*-based precursor films and oxide films from thermolysis deposited from 0.005 M butanolic $La(NO_3)_3 \times 6H_2O$ precursor solution on the *Si(111)* substrates. 190

11.3. Peak fit parameters and peak positions in eV for the *Si2p* signal of the *Nd*-based films on *Si(111)* substrates. 207

11.4. Peak fit parameters and peak positions in eV for the *Si2p* signal of the *Nd*-based films on *Si(100)* substrates. 208
11.5. Peak fit parameters and peak positions in eV for the *O1s* signal of the *Nd*-based films on *Si(111)* substrates. 211
11.6. Peak fit parameters and peak positions in eV for the *O1s* signal of the *Nd*-based films *Si(100)* substrates. 212
11.7. Peak fit parameters and peak positions in eV for the *Ge3d* signal of the *Nd*-based films on *Ge(100)* substrates measured with Al-K_α. 218
11.8. Peak fit parameters and peak positions in eV for the *O1s* signal of the *Nd*-based films on *Ge(100)* substrates. 220
11.9. Peak fit parameters and peak positions in eV for the *Si2p* signal of the *Nd*-based films on *SiGe(111)* substrates. 225
11.10Peak fit parameters and peak positions in eV for the *Ge3d* signal of the *SiGe(111)* substrates measured with Al-K_α 227
11.11Peak fit parameters and peak positions in eV for the *O1s* signal of the *Nd*-based films on *SiGe(111)* substrates. 230

12.1. Summary of the extracted capacitance density values from the C-V measurements, calculated κ and EOT values for the Nd_2O_3/n-*Si(111)* samples. 242
12.2. Summary of the extracted capacitance density values, calculated κ and EOT values for the Nd_2O_3/*Si(100)* samples. 246
12.3. Off state leakage current densities measured at -1 V for the Nd_2O_3 films deposited on n-*Si(111)*. 249
12.4. Off state leakage current densities measured at -1 V for the the Nd_2O_3 films deposited on p-*Si(100)*. 252
12.5. Calculated β factors in $V^{1/2}cm^{1/2}$ from theory and determined from data of the 0.005 M $Nd(NO_3) \times 6H_2O$ butanolic precursor solution on p-*Si(100)* for the samples annealed at different temperatures measured from 298 K to 398 K. 259
12.6. Summary of the calculated EOT values and respective leakage current densities for the Nd_2O_3/n-*Si(111)* and Nd_2O_3/p-*Si(100)* samples. 266
12.7. Leakage current densities of alternative gate dielectrics from literature at EOT 1.5 nm and the detected minimum from the wet chemical deposited Nd_2O_3 film. 267

12.8. Capacitance density in accumulation, κ and EOT values for Nd_2O_3 deposited from 0.005 M $Nd(NO_3) \times 6H_2O$ butanolic precursor solution on n-*Ge(100)*. 272
12.9. Capacitance density in accumulation, κ and EOT values for Nd_2O_3 deposited from 0.005 M $Nd(NO_3) \times 6H_2O$ butanolic precursor solution on p-*SiGe(111)*. 275
12.10Calculated β factors in $V^{1/2}cm^{1/2}$ from theory and determined data of the 0.005 M $Nd(NO_3) \times 6H_2O$ butanolic precursor solution on p-*SiGe(111)* for the samples annealed at different temperatures measured from 298 K to 398 K. 278

13.1. RMS roughness values and z-ranges in nm of the oxide films illustrated in figure 13.2. and respective deviations between the substrate types. 284
13.2. Capacitance densities measured at 100 kHz and the calculated κ and EOT values of the bilayer samples ($TiO_2/Nd_2O_3/Si$) deposited from ALD and 0.01 M, 0.005 M and 0.001 M $Nd(NO_3)_3 \times 6H_2O$ butanolic precursor solution on n-*Si(111)* and p-*Si(100)* (oxides as deposited, annealed at 673 K and 1073 K). 293
13.3. Leakage current densities measured from the bilayer system ($TiO_2/Nd_2O_3/Si$) deposited on n-*Si(111)* and p-*Si(100)*. 295
13.4. Capacitance densities measured at 100 kHz and the calculated κ and EOT values of the reverse bilayer samples deposited from 50 cycles of ALD (TiO_2) and 0.01 M, 0.005 M and 0.001 M $Nd(NO_3)_3 \times 6H_2O$ butanolic precursor solution (as deposited and annealed at 1073 K). 301
13.5. Leakage current densities measured from the reverse bilayer ($Nd_2O_3/TiO_2/Si$) system deposited on n-*Si(111)* and p-*Si(100)*. 304
13.6. Percentage of the measured roughness values of the oxide films related to the respective film thickness. 308

C.1. Specifications of the *n-Si(111)* substrates. 389
C.2. Specifications of the *n-Ge(100)* substrates. 389

D.1. List of used chemicals for wet chemical etching to prepare oxide free H-terminated surfaces. 391

F.1. Summary of the extracted capacitance density values, calculated and EOT for the TiO_2 10 nm single layer samples on n-*Si(111)* and p-*Si(100)* substrates. 396
F.2. Off state leakage current densities in Acm^{-2} of the TiO_2 single layer system deposited by ALD (150 cycles $\approx$ 150 nm) on n-*Si(111)* and p-*Si(100)* 398

A. Description of lamella preparation

Adjustment of Sample

- Load sample, fix the screw below the sample inside the chamber
- mode "high vacuum", pump the chamber
- home stage
- adjust the z-shift of the sample close to the 15 mm marker
- switch the e- and i-beam on by pushing the button wake up
- focus the sample with 10 kV acceleration voltage and 0.88 nA beam cur beam current, correct the astigmatism
- choose a part of the sample, zoom in until size line is 10 μm in maximum expansion, focus again
- adjust the sample in eucentric z-position to e- and i- beam (tilting between 0° and 52°, push “link z to forward”
- new focus with 13 nA

Platinum-Pattern Deposition

- e-beam induced *(for surface protection)*
  - sample tilt 0°
  - insert and heat up *Pt*-needle
  - Pt-deposition, pattern *rectangle* (20×1.5×20 μm), Beam alignment(10 kV, 13 nA; rel. int. dia. 150% Pt dep; Beam: Electron)
  - control focus
  - start *Pt*-deposition
  - retract injection needle

- i-beam induced *(causes surface damages)*
  - sample tilt 52°
  - screen shot; focus sample with 30 kV/0.3 nA, e-beam pattern visible as big as possible
  - insert *Pt*-needle
  - *Pt*-deposition above e-beam deposited layer, pattern: *rectangel* (20×1.5×3.5 μm), Beam alignment (10 kV, 13 nA; rel. int. dia. 150%, application: *Pt* dep; Beam: Ion)
  - start *Pt*-deposition
  - retract and cool down injection needle

Cutting Lamella with i-beam

- Step profile
  - new focus at 5 nA; *Attention: only two screen shots!*
  - cut step structure on both sides of the *Pt*-layer. Start at bottom side. Pattern *regular cross section* ($16 \times 8 \times 4$ μm), Beam alignment (30 kV, 5 nA; rel. int. dia. 150% application: *Si*, Beam: Ion)
- Lamella thinning
  - New focus at 3 nA beam current (only screen shots!)
  - Pattern *cleaning cross section* ($10 \times estimated \times 4$ μm), sample tilt 53.5° for thinning below *Pt*-layer and 51.5° for thinning above due to Gaussian profile of ion-beam
  - while constantly decreasing the beam current to approx. 0.1 nA thin lamella until thickness of 1 μm
  - tilt to 0°
  - lamella cut by arranging three rectangle pattern u-shaped leaving two material connections (approx. 1 μm) on top of the lamella to the bulk material. Control the progress with back scattered detector at run time. Stop progress when beam penetrates the lamella.
  - tilt to 52°

  - proceed thinning to lamella thickness below 100 nm; pattern *cleaning cross section* ($6 \times$ *estimated* $\times$ 4 μm) continuously decreasing beam current

- Cutting off lamella
  - Placing two rectangle pattern to delete the bridging material between bulk and prepared lamella. Using lowest beam current as possible (< 0.1 nA) and smallest expansion of patterns. Monitoring the progress with BSD.

- Sample transfer
  - tilt to 0°
  - vent the chamber with N_2

ex-situ lift out

- transfer of the sample into light microscope (magnification 20×) with micro manipulation equipment
- locate lamella on the sample
- increase the magnification (50×)
- insertion of micro manipulation quartz needle
- approach the needle head to the lamella until the lamella adheres to the needle, lift up
- position the TEM-grid (most suitable carbon and carbon/Formvar®) at the corner of the sample, moving with x-, y-shift below the needle head with the adhered lamella, lift the needle down
- cast off the lamella from the needle by carefully shaking the needle, placing the lamella on the film of the grid, retract the manipulation needle
- move grid into the transport box carefully

The different steps are illustrated with SEM images in figure A.1. and A.2.

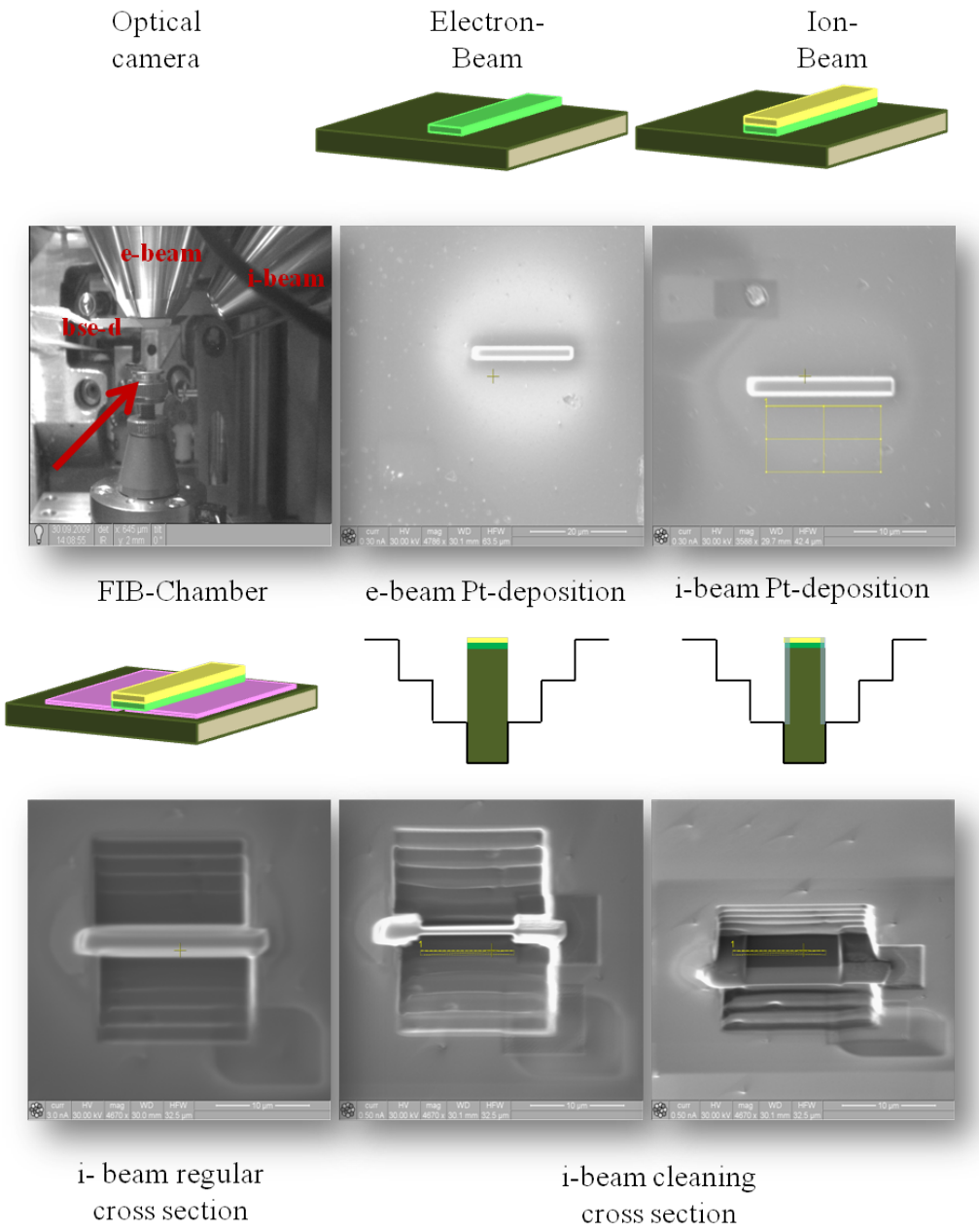


Figure A.1.: Part I: FIB-TEM lamella preparation

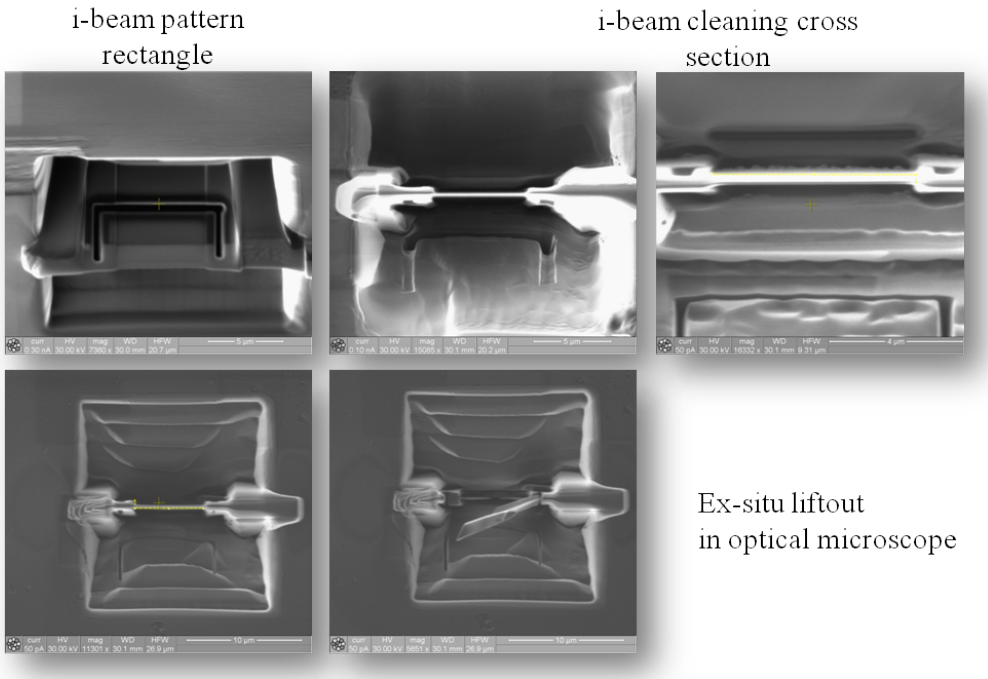


Figure A.2.: Part II: FIB-TEM lamella preparation

B. Fundamentals of Semiconductors

Semiconductors in general are materials with electrical conductivities between that of a conductor and an insulator. The most important properties of semiconductors are, according to Weissmantel[245], the characteristic strongly impurity dependent conductivities, negative temperature coefficients as well as large band gaps up to 3 eV. Semiconductors show insulating characteristics at low temperatures and they are conductive at room temperature. With respect to the conduction properties, semiconductors can be explained with the so called band model. Due to the narrow ordered atoms within the crystal lattice, the outer electrons can not be attributed to specific discrete energy levels. Approximately broad energy regions are created by the periodical order of atoms. The broad energy regions, bands, can be occupied by electrons. Most important are the valence band, which hosts the valence electrons and the conduction band, which is the lowest energy band of unoccupied states.

Semiconductors have characteristic band gaps between the valence and conduction band. They have characteristic properties due to their particular band structure and the resulting electrical conduction. Within the band gap, the density of states is equal to zero and therefore no permitted states are existent within the gap. Electrical conduction in semiconductors results from excitation of electrons by temperature or light. Semiconducting materials can be elements, compounds or alloys in different crystal structures. Elementary semiconductors are C (diamond, E_{Gap} = 5.47 eV), Si (E_{Gap} = 1,10 eV), Ge (E_{Gap} = 0.67 eV) and α-Sn (E_{Gap} = 0.08 eV). The energy of the band gap typically decreases with increasing atomic number at room temperature. Binary semiconductors are known from IV-IV, III-V, II-VI or IV-VI main group element combinations, which are shown in figure B.1.

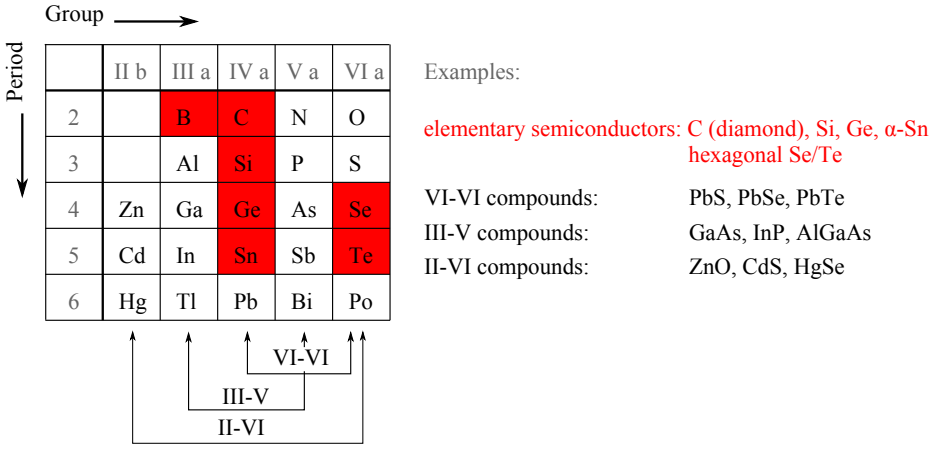


Figure B.1.: Semiconductors in the Periodic Table of Elements. Within the group of semiconductors covalent bondings are dominant. To the right of the semiconductors are non-conductors with predominant van der Waals bondings and to the left elements with prevalent metallic bondings (after[243]).

Semiconductors, notably single crystalline Si, are particular important in microelectronic industries since more than 95 % of all available semiconductor components like chips, transistors or solar cells are made from single crystalline Si. The characteristics of pure semiconductors, specifically the size of the band gaps and therefore the conductivity, can be tuned by insertion of donor or acceptor molecules within the semiconductor lattice structure. Pure semiconductors show intrinsic conduction, whereas increased extrinsic conduction can be observed from impurity containing semiconducting materials. The specific value of the conductivity is temperature dependent and increases with rising temperatures contrary to pure metals. The increase in electrical conductivity can be explained by enhanced promotion of electrons through the band gap due to temperature dependent higher electron mobility.

Conduction Mechanism and Energy Band Model

As the electrical properties in semiconductors are based on the partial unoccupied valence and conduction band, it is sufficient to consider only those two bands in the energy band model for a representative elucidation.

Direct and Indirect Semiconduction In general, semiconductors can be divided by their conduction mechanisms into direct and indirect semiconductors. The different characteristics can be explained by the examination of the band structure in k-space. The charge carriers in semiconductors can be described by matter waves with a quasi momentum ($\vec{k}$) and therefore the properties of the particles are defined by their energy level as well as their velocity (momentum).

Figure B.2. shows the excitation of electrons from valence to conduction bands in direct and indirect semiconduction.

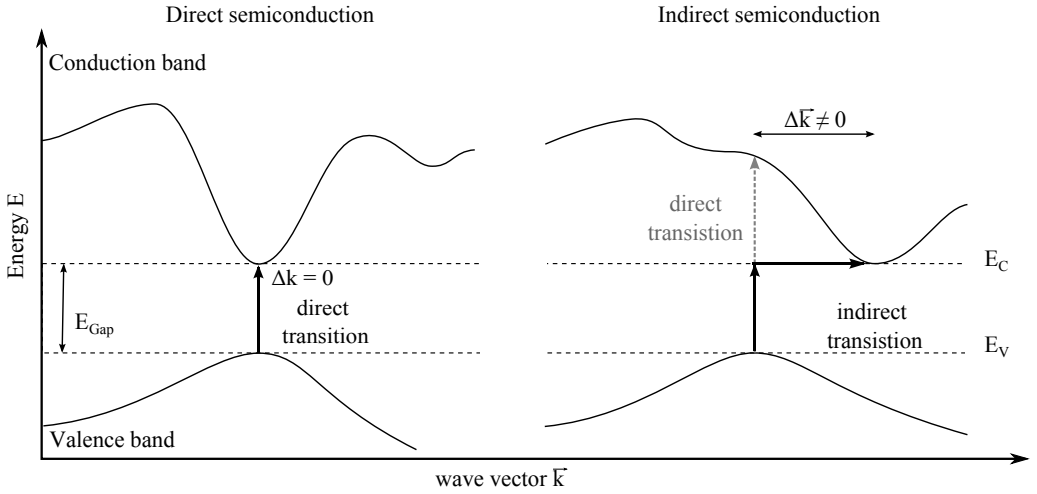


Figure B.2.: Electron transition from valence to conduction band in direct and indirect semiconductors. In indirect semiconductors, a change of $\vec{k}$ is necessary for excitation with a minimum energy difference between valence and conduction band (after[244]).

The conduction and valence band edge are not identical for every momentum, thus the electron excitation from valence to conduction band is most probable from the maximum of the valence band to the minimum of the conduction band. In direct semiconductors the quasi momentum of the valence band maximum and the conduction band minimum is equal, therefore a direct excitation of the conducting electrons from the valence to the conduction band is possible by an energy change, whereas the momentum keeps constant. In indirect semiconductors, a diverging quasi momentum of the minimum and maximum of the valence and conduction band leads to a required change in momentum, beside the change in energy to realize an excitation from valence to conduction

band. The change in the momentum can be implemented by phonons. Recombination processes of electrons and holes in direct semiconductors lead to an emission of photons with respective energies. In indirect semiconductors, recombination processes result in a generation of lattice oscillations. Therefore direct and indirect semiconductors can be differed by absorption experiments.

In figure B.2. it is assumed that the band gap energy E_{Gap} results from the difference in energy from the highest energy state existent in the valence band and the lowest in the conduction band. Even though the E_{Gap} might equal in both cases the amount of energy, which is required for an excitation from the valence to the conduction band might differ due to differences in the wave vector.

Intrinsic and Extrinsic Semiconduction In pure semiconductors, the intrinsic conduction is based on an occupied valence band, whereas the conduction band is empty at the absolute zero point. The valence and conduction band are divided by the band gap. With increasing temperature, electrons in the valence and conduction band are thermally excited and the electrical conductivity can be measured due to increased electron mobility and subsequent switching of electrons between the valence and conduction band. Mobilized electrons from the conduction band as well as the newly formed electron holes in the valence band contribute to the electrical conductivity.

In compound semiconductors, the stoichiometric defect of a component acts like an impurity. If donor or acceptor atoms within the lattice are positioned selectively. The process is called doping. Dopants which provide extra conduction electrons to the conduction band are donor atoms. If atoms with a lower number of electrons than the host material are implanted, they are denoted as acceptor atoms. In both cases, the entire crystal remains neutral since the accepted and donated electrons persist in the crystal collective. The implanted donors, like As in Si atoms, create an excess of negative carrier charges (n-type), therefore those compounds are termed as n-type semiconductors. Accordingly semiconductors with implanted acceptor atoms and a resulting excess of positive charges, like In in Si, are termed as p-type semiconductors. The electron excess or deficit leads to quantum mechanically permitted states within the "intrinsic band gap", in n-type semiconductors close to the conduction band (donor level) and in p-type close to the valence band (acceptor level), resulting in modified positions for electron hole interactions for conduct-

ing mechanisms and therefore so called intrinsic conduction. The thus tunable size and structure of the band gap strongly influences the electrical properties and can be determined in detail by optical absorption experiments.[149]

Figure B.3. shows schematically the differences in intrinsic, n- and p-type semiconductors.

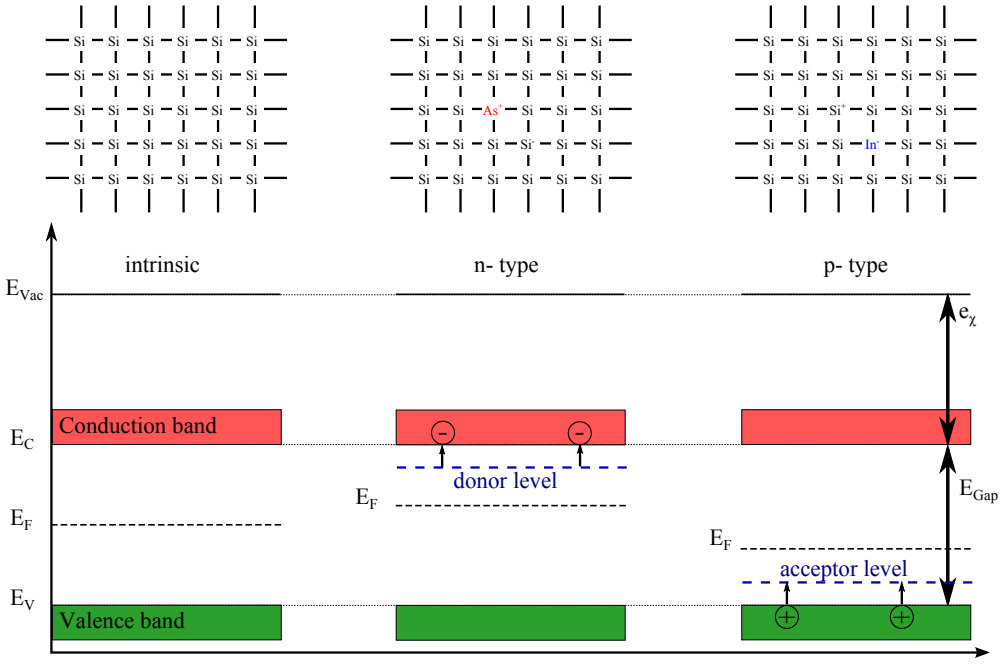


Figure B.3.: Simplified band structures and lattice structure scheme of intrinsic, p- and n-type semiconductors (after[59] and[91]).

Where E_V is the energy of the valence band, E_F the Fermi energy, E_C the energy of the conduction band and E_{Vac} the energy of the Vacuum as in XPS. E_{Gap} specifies the band gap between valence and conduction band and e_χ the electron affinity.

Equations of Motion: Electrons and Holes

The equations of motion and the dynamic characteristics of electrons and holes in semiconductors are essential to explain conduction mechanisms in semiconductors.

To explain the motion of electrons within the energy band, the motion of a wave packet in an outer electric field has to be elucidated. In compliance with

Newtons second law, the electron within the crystal is influenced by forces from the crystal lattice as well as outer forces. Within the crystal, $\hbar\frac{d\vec{k}}{dt}$ is equal to the outer force on the electron:

$$\hbar\frac{d\vec{k}}{dt} = \vec{F} \tag{B.1}$$

$\hbar\vec{k}$: quasi momentum of the electron

The force $\vec{F}$ in equation B.1 includes the Lorentz force affecting an electron in a magnetic field $\vec{B}$, assessing that the field is not as strong to destroy the band structure. Therefore, the equation of motion for electrons with the group velocity $\vec{v}$ and a constant magnetic field $\vec{B}$ is given by:

$$\hbar\frac{d\vec{k}}{dt} = -e\vec{v} \times \vec{B} \tag{B.2}$$

The group velocity can be written as:

$$\vec{v_g} = \frac{1}{\hbar}\nabla_{\vec{k}} \in (\vec{k}) \tag{B.3}$$

where $\in$ is the wave function of the energy and $\vec{k}$ the specific wave vector.

And it follows:

$$\frac{d\vec{k}}{dt} = -\frac{e}{\hbar^2}\nabla_{\vec{k}} \in \times\vec{B} \tag{B.4}$$

Concluding that the motion of an electron within the $\vec{k}$ space is perpendicular to the direction of the energy gradient $\in$ and therefore the electron moves within a plane of constant energy.

The second main aspect influencing the conduction in semiconductors are the characteristics of the unoccupied levels within occupied bands, the holes. Holes which are influenced by an electric or magnetic field behave like positive charge carriers.

From the symmetry of the Brillouin zone[1] (BZ), it can be followed that the wave vector of the occupied band $\vec{k}$ is zero:

$$\sum \vec{k} = \vec{k_e} + \vec{k_h} = 0 \tag{B.5}$$

$\vec{k_e}$: wave vector of the electron
$\vec{k_h}$: wave vector of the hole

The BZ has inversion symmetry. If the level is occupied by electrons, it can be concluded that all pairs of $\vec{k}$ and - $\vec{k}$ are occupied under full occupied conditions and the complete wave vector is zero. If one electron in the state of wave vector $\vec{k_e}$ is missing, the complete wave vector of the whole system is -$\vec{k_e}$. -$\vec{k_e}$ is denoted as the wave vector of the hole or the complete wave vector of the band with a missing electron.

The energy of the hole ($\in_h$) can be determined by the energy of the missing electron ($\in_e$):

$$\in_h (\vec{k_h}) = \in_e (\vec{k_e}) \tag{B.6}$$

The energy $\in$ of the upper valence edge is supposed to be zero. Therefore the energy of the hole is the higher, the deeper the level where the electron was removed from is. The velocity of the hole is equal to the velocity of the removed electron. The mass of the electrons and hole can be explained by the concept of effective masses. Based on the dispersion relationship, the energy can be written as $\in = \frac{\hbar^2}{2m}k^2$ and therefore the dispersion $\frac{d^2\in}{dk^2} = \frac{\hbar^2}{m}$ is given by the reciprocal mass of the free electron. For electrons within periodical potentials, a significant change in the dispersion of $\in \vec{k}$ close to the band edge occurs based on a strong interaction of the electron with the crystal lattice and a resulting different dynamic. Therefore the effective mass needs to be introduced by deviating the group velocity v_g:

$$\frac{dv_g}{dt} = \frac{1}{\hbar}\frac{d^2 \in}{dkdt} = \frac{1}{\hbar}\frac{d^2 \in}{dk^2}\frac{dk}{dt} \tag{B.7}$$

[1]The Brillouin zone is a geometric construction (primitive Wiegner-Seitz cell) of the reciprocal crystal lattice in momentum space. It is a demonstrative geometric interpretation of the diffraction conditions, based on the fact that particle waves are reflected by the Bragg layers. In solid state physics, the crystal momentum $\hbar\vec{k}$ of a particle or quasi particle is indicated by the vector in reciprocal space. A quasi particle with a defined $\vec{k_1}$ behaves exactly like one with a defined $\vec{k_2}$, which can be differed from each other by a reciprocal lattice vector $\vec{K}$. Therefore it is only necessary to determine the crystal momenta within the first Brillouin zone to gain information about crystal momentum dependent parameters.

with $\hbar$k = F (s. eq. B.2)

$$\frac{dv_g}{dt} = \left(\frac{1}{\hbar}\frac{d^2 \in}{dk^2}\right) F \Rightarrow F = \frac{\hbar}{d^2 \in /dk^2}\frac{dv_g}{dt} \tag{B.8}$$

with $m_e^{eff} = \frac{\hbar}{d^2 \in /dk^2}$ as the effective mass of the electron. Equation B.8 is the Newtonian law of movement, including the effective mass. The effective mass of the electron hole (m_h^{eff}) can be derived from the effective mass of the electron:

$$\in_h (\vec{k}_h) = - \in_e (\vec{k}_e) \Rightarrow m_h^{eff} = -m_e^{eff} \tag{B.9}$$

The movement equation of the electron hole can be written as

$$\hbar\vec{k_h} = e(\vec{E} + \vec{v_g} \times \vec{B}) \tag{B.10}$$

$\vec{E}$: electric field

The existence or incidence of effective masses is based on the wave character of the electrons. The effective mass can be different at different positions within the crystal depending on the Bragg interaction of electron waves within a crystal lattice. It can be determined by cyclotron resonance experiments. Including the effective mass takes into account that the electron is effected by a periodic potential. A detailed derivation of the properties of holes and electrons in semiconductors can be found in[149].

Density of States and Charge Carrier Distribution

The occupancy of an energy level E with electrons and holes can be described based on the the Fermi Dirac distribution function, which provides the probability of occupancy of energy levels by Fermions and therefore electrons. Fermions are half-integer spin particles, which obey the Pauli exclusion principle. After the Pauli exclusion principle, only one Fermion can occupy a single quantum state. Therefore Fermions fill the available states in an energy band from the lower to the higher energy levels. At 0 K, the energy levels are filled up to the Fermi level. With increasing temperature, the transition between occupied and unoccupied states increases gradually.[30] A system is

characterized by its temperature T and its Fermi energy E_F and the Fermi Dirac function is given by:

$$f(E) = 1 + e^{\frac{E-E_F}{kT}} \tag{B.11}$$

For impurity containing compounds, the acceptor and donor level properties need to be taken into account. To calculate the density of charge carriers in semiconductors, the number of states which are available in every energy level are required to be known. The number of electrons at each energy can be obtained by multiplying the number of states with the probability that a state is occupied by an electron. Due to a high, material and size dependent number of energy levels, the number of states is usually calculated per unit energy and per unit volume.

The density of states is equal to the density per unit volume and energy of the number of solutions to Schrödinger's equation. A semiconductor can be modeled as an infinite quantum well, which is set to zero, and where electrons with an effective mass move freely. Since the density of states per unit volume is independent on the actual shape and size of the semiconductor, the semiconducting materials can assumed to be a cube with the side length L. The Schrödinger equation for each space direction x, y, z is given by:

$$\Psi = A\sin(k_i, i) + B\cos(k_i, i) \; with \; i = x, y, z \tag{B.12}$$

where k_x is the space component in x direction etc. and A and B are factors to be determined.

By fixing the boundary conditions and solving the equation B.12, taking into account the three space direction and two possible spin solutions, the density per unit energy can be obtained as:

$$\frac{dN}{dE} = \frac{dN}{dk}\frac{dk}{dE} = \left(\frac{L}{\pi}\right)^3 \pi k^2 \frac{dk}{dE} \tag{B.13}$$

Including the connection between the kinetic Energy E of a particle with the mass, m^{eff} and the wave number k:

$$E(k) = \frac{\hbar^2 k^2}{2m^{eff}}, \; with \; \frac{dk}{dE} = \frac{m^{eff}}{\hbar^2 k} \; and \; k = \frac{\sqrt{2m^{eff}E}}{\hbar} \tag{B.14}$$

Therefore the density of states per unit volume and unit energy, g(E), becomes:

$$g(E) = \frac{1}{L^3}\frac{dN}{dE} = \frac{8\pi\sqrt{2}}{h^3} m^{eff\ 3/2}\sqrt{E}\ for\ E \geq 0 \tag{B.15}$$

$g(E) = 0$ for negative energies as well as for the bottom of the well. Applied to electrons in semiconductors, the minimum of energy of the electron is the energy at the bottom of the conduction band (E_C) and therefore the density of states for electrons is given by:

$$g_C(E) = \frac{8\pi\sqrt{2}}{h^3} m^{eff\ 3/2}\sqrt{E - E_C}\ for\ E \geq E_C \tag{B.16}$$

$$g_C(E) = 0,\ forE < E_C \tag{B.17}$$

From the respective distribution function eq. B.11 and the density of states (eq. B.16) the energy dependent electron (n) and hole (p) density for impurity free semiconductors can be calculated after:

$$n(E) = g_C(E)f(E) = \frac{8\pi\sqrt{2}}{h^3} m_e^{3/2}\sqrt{E - E_C}\frac{1}{1 + e^{\frac{E-E_F}{kT}}} \tag{B.18}$$

$$p(E) = g_V(E)(1 - f(E)) = \frac{8\pi\sqrt{2}}{h^3} m_h^{3/2}\sqrt{E_V - E}\frac{1}{1 + e^{\frac{E_F-E}{kT}}} \tag{B.19}$$

By approaching the Fermi distribution with a Boltzmann distribution, the effective density of states N_C and N_V can be introduced for the valence and conduction band. The integration of equations B.18 and B.19 leads to equations B.20 and B.21 to calculate the number of charge carriers per volume unit:

$$\begin{aligned} n_0 = \int_{E_C}^{\infty} g_C(E)f(E)dE &\approx \int_{E_C}^{\infty} \frac{8\pi\sqrt{2}}{h^3} m_e^{3/2}\sqrt{E - E_C}e^{\frac{E-E_F}{kT}}dE \\ &= N_C(T)e^{\frac{E_F-E_C}{kT}} \end{aligned} \tag{B.20}$$

$$\begin{aligned} p_0 = \int_{-\infty}^{E_V} g_V(E)(1 - f(E))dE &\approx \int_{-\infty}^{E_V} \frac{8\pi\sqrt{2}}{h^3} m_h^{3/2}\sqrt{E_V - E}e^{\frac{E_F-E}{kT}}dE \\ &= N_V(T)e^{\frac{E_V-E_F}{kT}} \end{aligned} \tag{B.21}$$

The intrinsic carrier density (geometric average of electron and hole density) is given by:

$$n_i = \sqrt{N_C N_V}e^{-\frac{E_G}{2kT}} \tag{B.22}$$

The insertion of the intrinsic Fermi energy, E_i, allows to avail the intrinsic values as references for the density and position of the Fermi level:

$$n_0 = n_i e^{\frac{E_F - E_i}{kT}} \Rightarrow E_F = E_i + kT \ln \frac{n_0}{n_i} \tag{B.23}$$

$$p_0 = n_i e^{\frac{E_i - E_F}{kT}} \Rightarrow E_F = E_i + kTln\frac{p_0}{n_i} \tag{B.24}$$

Based on the neutrality constraints, the electron and hole densities for doped semiconductors can be calculated after:

$$n_0 + N_A^- = p_0 + N_D^+ \tag{B.25}$$

$$\Rightarrow n_0 = \frac{N_D^+ - N_A^-}{2} + \sqrt{\frac{(N_D^+ - N_A^-)^2}{4} + n_i^2} \tag{B.26}$$

$$p_0 = \frac{N_A^- - N_D^+}{2} + \sqrt{\frac{(N_D^+ - N_A^-)^2}{4} + n_i^2} \tag{B.27}$$

With N_A and N_D as densities of the ionized doping atoms (acceptor, donor).

Carrier Transport, Recombination and Generation

The motion of free charge carriers in semiconductors is based on two characteristic motion types. The motion of charge carriers due to an electric field caused by an external applied voltage is referred as carrier drift, whereas motion caused by a carrier density gradient from regions with low density to regions with high density is called carrier diffusion. Any motion of the free charge carriers in a semiconductor leads to a current. The total current in a semiconductor equals the sum of the diffusion and drift current.

Carrier diffusion can be implemented by a variation of doping densities as well as thermal gradients within the material. Carrier drift and diffusion are mechanisms which are strongly dependent on each other, since they both effect the same particles and scattering mechanisms.

In recombination processes, electrons and holes annihilate each other in one or multi step transactions whereupon electrons occupy the empty states (holes). The energy difference between the initial and final state is released as radiation or energy transitioning, non radiating processes (phonons), where the difference in energy is passed to other phonons or generates an Auger electron. During recombination processes both, the electron as well as the hole, can disappear.

According to a simple model of recombination the recombination generation rate is proportional to the excess carrier density and no net recombination occurs in thermal equilibrium of the carrier density and can be applied for minority carriers [2] in a "quasi neutral" semiconductor.

In *steady state recombinations*, an equal number of electrons and holes is involved. The recombination rate of the majority carriers is limited by the excess minority carrier density, since the recombination rate is limited by them.

Figure B.4. shows schematically the three different types of recombination. Each process is reversible.

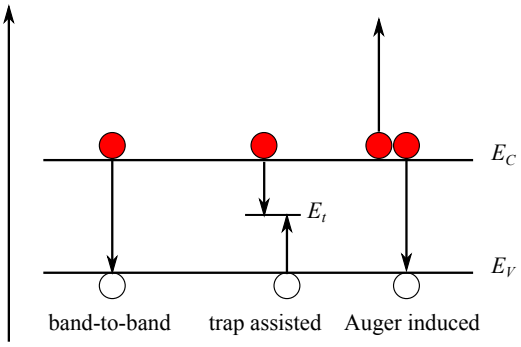


Figure B.4.: Carrier recombination processes (after[59]).

A typically radiative transition in semiconductors with direct band gaps is the *band-to-band recombination*, where the electron moves from the initial conduction band state into the empty state within the valence band. The process depends on the density of electrons and holes and the rate is expected to be proportional to the product of n- and p-type charge carriers. The recombination rate is equal to the generation rate in thermal equilibrium.

The two step *trap assisted recombination* occurs when an electron drops into a "trap", which is an additional energy level within the band gap caused by implanted atoms or structural defects, followed by the movement into an empty state within the valence band. Trap assisted recombination is also called Shockley-Read-Hall (SRH) recombination.

[2] In semiconductors charge carriers are divided into majority and minority charge carriers. Majority are the more abundant species (in n-type semiconductors holes in p-type electrons) and they are primarily responsible for the current transport. The less abundant species are referred to as minority charge carriers

In *Auger recombination*, the electron and hole recombine like in band-to-band recombination, but the energy difference is transfered to another electron or hole. The recombination rate is different to band-to-band recombination due to a third involved particle.

Since the surface and interface properties of semiconductors significantly influence the properties of the semiconductor, surface recombination processes need to be taken into account. Surfaces and interfaces exhibit a large number of recombination centers, on the one hand due to a large number of electrically activated states caused by termination of the semiconductor crystal and on the other hand due to a high impurity amount resulting from device fabrication. The recombination on surfaces is caused by a 2D density of traps.

The different charge carriers can also be generated without an associated recombination process. By illuminating the semiconductor with incoming photons, the excitation of electrons from lower to higher energy levels is induced. If an electron is removed from the valence band and added to the conduction band, an electron-hole pair is generated. The energy of the incident photon needs to be larger than the band gap energy. The photon is absorbed in this process and the photon energy is transfered to the electron-hole pair as kinetic energy. Electron-hole pairs can also be generated by high energy electron or particle beams if the beam energy is much larger than the band gap energy, so that a multiple number of electrons can be generated. The gradually loss of energy of the particle is used for nuclear based particle counters. Both mechanisms are referred to as *ionization processes*. The third generation process in semiconductors is *impact ionization*, caused by an electron/hole with a much larger/smaller energy than the conduction/valence band edge and where the released energy generates an electron-hole pair by a band to band transition with a following avalanche multiplication effect.

C. Data of Used Substrates

For the investigation in the present thesis *n-Si(111)* wafer of *Siegert Consulting* have been used. A detailed description of the specification is given below in table C.

Table C.1.: Specifications of the *n-Si(111)* substrates.

Designation:	4-Inch SSP Si-Wafer
Material/Growth:	*Si*/CZ
Diameter:	100 $\pm$2 mm
Type and doping:	*N/Ph*
Orientation:	111
Orientation tolerance:	$\pm 0.5^{\circ}$
Resistivity:	0.15 - 0.20 Ohm-cm
Thickness:	505 - 545 μm
TTV:	$< 10\mu$m
BOW:	$< 30\mu$m
Roughness:	$<$ 15 Å

The second substrate type used were *n-Ge(100)* wafer of $PHOTONIK^{h\nu}$ Singapore. The respective specifications as given by the supplier are summarized in table C.

Table C.2.: Specifications of the *n-Ge(100)* substrates.

Designation:	2-Inch Ge-Wafer
Type and doping:	*N/Ph*
Orientation:	100
Resistivity:	6 - 8 Ohm

The data of the *p-Si(100)* and *n-SiGe(111)* substrates have not been available until the publishing date. The *Ge* implementation into pure *Si* wafers has been realized by Global Foundries Singapore. A *Ge* amount 17 % has been specified.

D. List of Chemicals

Table D.1.: List of used chemicals for wet chemical etching to prepare oxide free H-terminated surfaces.

Chemical	**Manufacturer**
Acetone p.a. C_3H_6O	Fluka
Ammonium fluoride NH_4F 40 % aqueous solution semiconductor grade VLSI PURANAL	Honeywell Speciality Chemicals Seelze GmbH
Ammonium sulfite $(NH_4)_2SO_3$ 35 % solution for synthesis	Merck
Hydrogen fluoride HF 5 % aqueous solution	Honeywell Speciality Chemicals Seelze GmbH
Hydrogen fluoride HF 40 % aqueous solution	Honeywell Speciality Chemicals Seelze GmbH
Hydrofluoric acid HF 46 wt.% in H_2O	Sigma-Aldrich
Sulfuric acid H_2SO_4 Analytical reagent grade >95 %	Fischer Scientific
Hydrogen peroxide H_2O_2 30 % solution	Honeywell Speciality Chemicals Seelze GmbH

E. XPS of Internal Chamber Standard

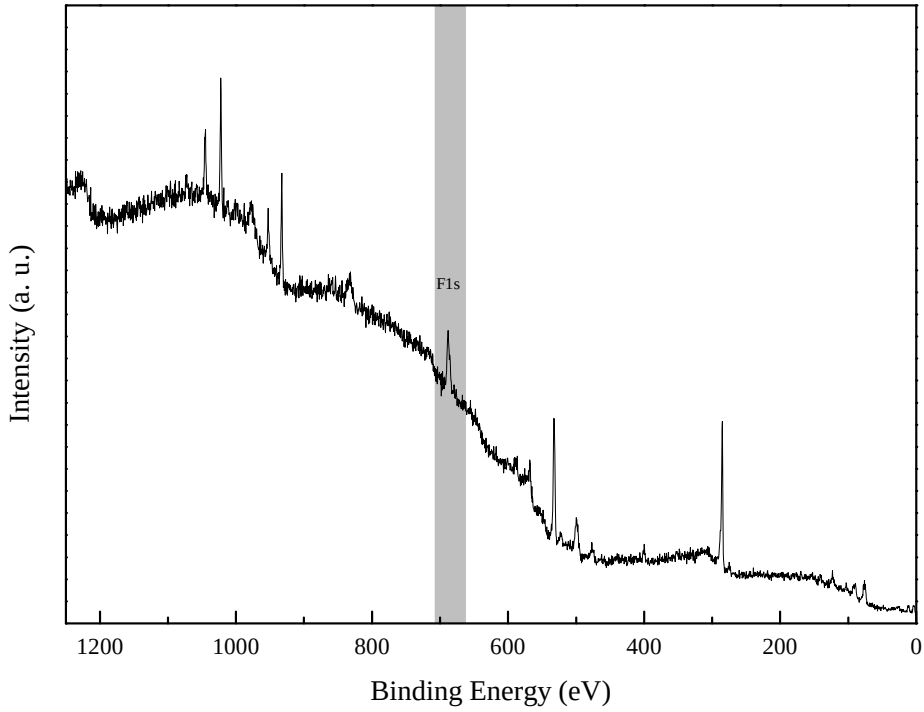


Figure E.1.: XPS survey scan of the internal chamber standard, indicating a high fluorine impurity. The spectra is measured with Al-K_α. Spectrum shown with courtesy of Jörg Stöver

F. Electrical Characterization of TiO_2 Single Layers

In the following section the electrical performance of TiO_2 on *Si(111)* and *Si(100)* is illustrated showing the results of the I-V and C-V measurements.

F.1. C-V characteristics

The results of the C-V measurements detected from the 10 nm TiO_2 film on n-*Si(111)* and p-*Si(100)* are shown in figure F.1.

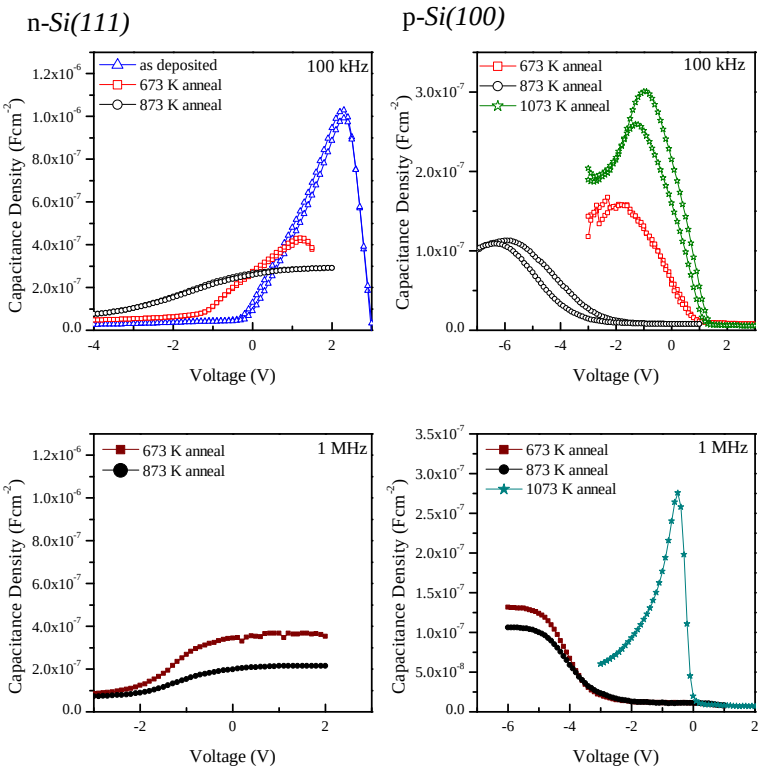


Figure F.1.: Capacitance densities detected of the 10 nm thick TiO_2 films deposited from ALD on n-*Si(111)* (left) and p-*Si(100)* (right). Shown are the curves of the oxides films after deposition, annealing at 673 k/873 K/1073 K measured at 100 kHz and 1 MHz.

The extracted capacitance densities in accumulation are listed in table F.1

Table F.1.: Summary of the extracted capacitance density values, calculated and EOT for the TiO_2 10 nm single layer samples on n-*Si(111)* and p-*Si(100)* substrates.

	n-*Si(111)*			p-*Si(100)*		
Sample	Cap. (Fcm^{-2})	κ	EOT (nm)	Cap. (Fcm^{-2})	κ	EOT (nm)
as dep.	1.03×10^{-6}	11.6	3.4	-	-	-
673 K	4.18×10^{-7}	4.7	8.3	1.67×10^{-7}	1.9	20.7
873 K	2.91×10^{-7}	2.5	15.8	1.12×10^{-7}	1.3	30.6
1073 K	-	-	-	2.59×10^{-7}	2.9	13.3

F.2. I-V Characteristics

The I-V curves detected over varying temperatures of the samples annealed at different temperatures are illustrated in the following.

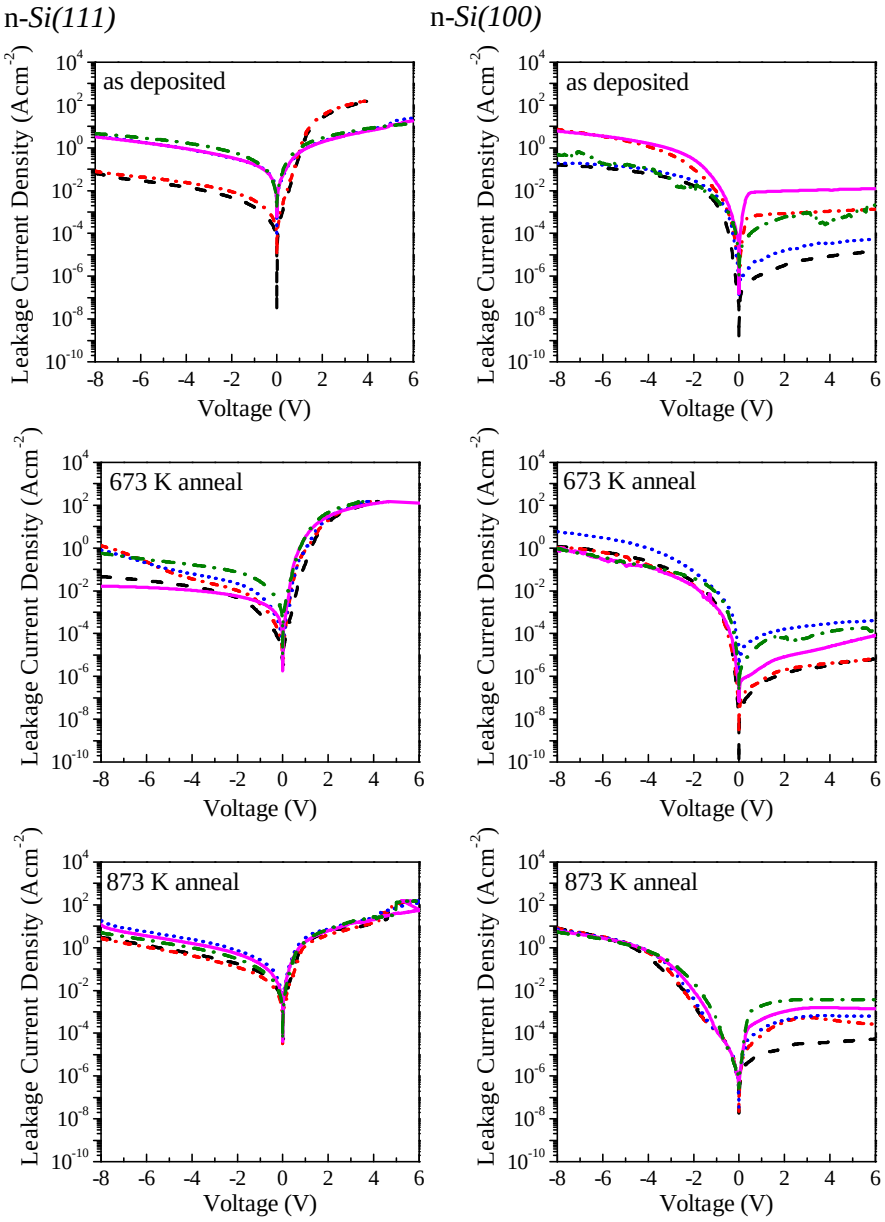


Figure F.2.: Leakage Current densities detected from 298 K to 398 K of the 10 nm thick TiO_2 films deposited from ALD on n-*Si(111)* (left) and p-*Si(100)* (right). Shown are the curves of the oxides films after deposition and annealing at 673 K/873 K.

The leakage current densities values are summarized in table F.2.

Table F.2.: Off state leakage current densities in Acm^{-2} of the TiO_2 single layer system deposited by ALD (150 cycles $\approx$ 150 nm) on n-*Si(111)* and p-*Si(100)*

Leakage current (Acm^{-2})	**As dep.**	**673 K**	**873 K**
n-*Si(111)*			
298 K	1.68×10^{-3}	8.41×10^{-4}	7.09×10^{-2}
323 K	3.43×10^{-3}	2.54×10^{-3}	4.62×10^{-2}
348 K	1.66×10^{-1}	5.91×10^{-3}	2.61×10^{-1}
373 K	1.67×10^{-1}	2.86×10^{-3}	1.74×10^{-1}
398 K	2.47×10^{-3}	2.71×10^{-2}	9.76×10^{-2}
p-*Si(100)*			
298 K	1.18×10^{-6}	4.87×10^{-7}	1.23×10^{-5}
323 K	7.29×10^{-4}	6.73×10^{-7}	8.81×10^{-2}
348 K	5.89×10^{-6}	8.25×10^{-5}	1.63×10^{-4}
373 K	8.78×10^{-3}	2.75×10^{-6}	4.45×10^{-4}
398 K	2.22×10^{-4}	3.66×10^{-5}	1.96×10^{-3}

G. Bilayer in Series Calculations

$$\frac{1}{C_{total}} = \frac{t_{Nd_2O_3}}{\kappa_{Nd_2O_3}\epsilon_0 A} + \frac{t_{TiO_2}}{\kappa_{TiO_2}\epsilon_0 A} \tag{G.1}$$

$$\frac{1}{C_{total}} - \frac{t_{TiO_2}}{\kappa_{TiO_2}\epsilon_0 A} = \frac{t_{Nd_2O_3}}{\kappa_{Nd_2O_3}\epsilon_0 A} \tag{G.2}$$

$$\left(\frac{1}{C_{total}} - \frac{t_{TiO_2}}{\kappa_{TiO_2}\epsilon_0 A}\right) \cdot \frac{\epsilon_0 A}{t_{Nd_2O_3}} = \frac{1}{\kappa_{Nd_2O_3}} \tag{G.3}$$

$$\frac{t_{Nd_2O_3}}{\left(\frac{1}{C_{total}} - \frac{t_{TiO_2}}{\kappa_{TiO_2}\epsilon_0 A}\right)\epsilon_0 A} = \kappa_{Nd_2O_3} \tag{G.4}$$

$$\frac{t_{Nd_2O_3}}{\left(\frac{\epsilon_0 A}{C_{total}} - \frac{t_{TiO_2}\epsilon_0 A}{\kappa_{TiO_2}\epsilon_0 A}\right)\epsilon_0 A} = \kappa_{Nd_2O_3} \tag{G.5}$$

$$\frac{t_{Nd_2O_3}}{\left(\frac{\epsilon_0 A - \kappa_{TiO_2} - t_{TiO_2} C_{total}}{C_{total}\kappa_{TiO_2}}\right)} = \kappa_{Nd_2O_3} \tag{G.6}$$

$$\frac{t_{Nd_2O_3} C_{total}\kappa_{TiO_2}}{\epsilon_0\kappa_{TiO_2} - t_{TiO_2} C_{total}} = \kappa_{Nd_2O_3} \tag{G.7}$$

(G.8)

Further information about the calculations of the total capacitance of two dielectrics in series can be found e.g. in[96].

Curriculum Vitae

Personal Details

Name:	Maraike Ahlf
Birthday, -place:	24.01.1984, Hamburg, Germany
Nationality:	German

Education

07/90-06/94	Primary School, Grundschule Potsdamer Straße, Hamburg
07/94-06/03	Grammar School, Gymnasium Rahlstedt, Hamburg - Degree: Abitur (grade: 1.7) (General qualification for university entrance)

Scientific Education/Academic Record

10/03-09/05	Diploma Study of Chemistry at the University of Hamburg - Degree: Prediploma (grade: excellent)
10/05-06/08	Diploma Study of Chemistry at the University of Oldenburg Physical-, Inorganic-, Technical-Chemistry, Business Administration: Human Resource Management Diploma Thesis in Physical Chemistry: *Die Abscheidung dünner Selten-Erd-Oxid Schichten zur Anwendung in der Halbleiterindustrie* - Degree: Diploma (grade: excellent)
since 07/08	PhD Candidate at the University of Oldenburg Physical Chemistry, Surface Science - Degree: Dr. rer. nat (approx. 10/2012)
since 01/10	Graduate Studies Science and Technology - Interface Science
08/10-07/11	Visiting Scholar at the Nanyang Technological University Singapore, School of Materials Science and Engineering, Singapore

Professional Experience

07/08-/09/12 Scientific fellow at the Institute for Pure and Applied Chemistry of the University of Oldenburg (Al-Shamery Group)

Scholarships and Awards

Heinz-Neumüller Stiftung: Begabtenförderung (6 Month)

German Academic Exchange Service (DAAD): PhD Overseas full time Scholarship South East Asia (12 Month)

Fonds of Chemical Industries (FCI): PhD Scholarship (24 Month)

Participation of the Marie Curie Summer School: Highlights in Microtechnology, Summer School and final Conference, **2008/2009**, Neuchâtel, Switzerland and Besanşon, France

Student participation of the 59th Meeting of Nobel Laureates dedicated to Chemistry, **2009**, Lindau, Germany

Nano4Woman: Nanoarts 3rd place, **2009**, Hanau, Germany

Nonuniversitary/Volontary Activities

since 04/09 Commission for Studies and Education, University of Oldenburg

05/07-05/09 Honorary work in the council of a student hostel, chairwoman

11/01-12/09 Shop assistant at Arko GmbH; Hamburg and Oldenburg

10/00-09/01 Warehouse assistant at Phoenix Pharmahandel & Co. KG; Hamburg

Scientific Work

Patent

1. Hanno Schnars, Katharina Al-Shamery, Mathias Wickleder; Mareike Ahlers, Maraike Ahlf; *Method for producing metal oxide layers*; **2009/2011**, PCT/EP2009/057855, US2011/0175207

Paper

1. *Ultra thin bilayer films by solution based chemical deposition for advanced gate stacks*; Maraike Ahlf, Meng Meng Vanessa Chong, Mareike Ahlers, Alfred Iing Yoong Tok, Mathias Wickleder, Pooi See Lee, Katharina Al-Shamery, **submitted**
2. *Wet chemical based deposition of Nd_2O_3 thin films from inorganic precursor materials*; Maraike Ahlf, Mareike Ahlers, Hanno Schnars, Mathias Wickleder, Pooi See Lee, Katharina Al-Shamery, **to be published**
3. *Electrical behavior and leakage current conduction mechanism of a Nd_2O_3/TiO_2 bilayer gate stack on Si(111) and Si(100)*; Meng Meng Vanessa Chong, Maraike Ahlf, Mareike Ahlers, Alfred Iing Yoong Tok, Mathias Wickleder, Pooi See Lee, Katharina Al-Shamery, **submitted**
4. *Electrical behavior and leakage current conduction of wet chemically processed high performance Nd_2O_3 ultra thin layers*; Maraike Ahlf, Meng Meng Vanessa Chong, Mareike Ahlers, Alfred Iing Yoong Tok, Mathias Wickleder, Pooi See Lee, Katharina Al-Shamery, **submitted**
5. *Substrate dependent bath deposition of alternative gate oxide materials - an XPS study*; Maraike Ahlf, Meng Meng Vanessa Chong, Mareike Ahlers, Alfred Iing Yoong Tok, Mathias Wickleder, Pooi See Lee, Katharina Al-Shamery, **submitted**

Talks

1.	03/12	*High quality REO thin films from wet chemical deposition*; DPG Spring Meeting **2012**, Condensed Matters, Berlin, Germany
2.	06/11	*Charge Trapping and Current-conduction Mechanism Studies on Rare Earth Oxide Films and Structures*, ICMAT **2011**, Singapore

3.	06/11	*New Approach to Deposit Rare Earth Oxide Thin Films*; ICMAT **2011**, Singapore
4.	05/10	*New approach to deposit Rare Earth Oxide ultra thin films for microelectronic devices*; Maraike Ahlf, Mareike Ahlers, Marvin H. Zöllner, Mathias Wickleder, Katharina Al-Shamery, Bunsentagung **2010**, Bielefeld, Germany
5.	03/10	*Rare Earth Oxide ultra thin films*; Maraike Ahlf, Mareike Ahlers, Marvin H. Zöllner, Mathias Wickleder, Katharina Al-Shamery, DPG Spring Meeting **2010**, Condensed Matters, Regensburg, Germany
6.	07/09	*Rare earth oxides for MOSFET gates*; Highlights in Micro Technology, Final Conference **2009**, Neuchâtel, Switzerland
7.	03/09	*The deposition of rare earth oxide ultra thin films with inorganic precursors - a new simplified deposition process*; DPG Spring Meeting **2009**, Condensed Matters, Dresden, Germany
8.	07/08	*The deposition of rare earth oxide thin films with inorganic precursors*; 2nd German-Danish Meeting on Interface Related Phenomena **2008**, Sønderborg, Denmark

Poster

1.	08/2011	*Current Conduction Mechanism of Radically New Deposited Rare-Earth-Oxide Thin Films on Si(111)*; Maraike Ahlf, Meng Meng Vanessa Chong, Mareike Ahlers, Alfred Iing Yoong Tok, Mathias Wickleder, Pooi See Lee, Katharina Al-Shamery, ECOSS **2011**, Wroczlaw, Poland
2.	04/2010	*Rare Earth Oxide films*; Maraike Ahlf, Mareike Ahlers, Mathias Wickleder, Katharina Al-Shamery, Center of Interface Science, From the witches cauldrons of material science, **2010**, Goslar, Germany
3	07/2009	*Deposition of Rare Earth Oxide Films*; Maraike Ahlf, Mareike Ahlers, Marvin H. Zöllner, Katharina Al-Shamery, Mathias Wickleder, 3rd German-Danish Meeting on Interface related Phenomena, **2009**, Papenburg, Germany
4.	05/09	*The deposition of rare earth oxide thin films with inorganic precursors on silicon surfaces*; Bunsentagung **2009**, Cologne, Germany

5. 04/09 *The Deposition of rare earth oxide films for MOSFET applications, Center of Interface Science*; From the witches cauldrons in materials science, **2009**, Goslar, Germany
6. 09/08 *$La(NO_3)_3$ based designer precursors for deposition of ultra thin La_2O_3 films on semiconductor surfaces*; Mareike Ahlers , Mathias Wickleder , Maraike Ahlf, Hanno Schnars, Katharina Al-Shamery, GdCh Fachgruppe Festkörperchemie und Materialforschung, 14. Vortragstagung, **2008**, Bayreuth, Germany
7. 06/08 *Growth of rare earth oxides on silicon wafers by liquid injection precursor deposition*; Hanno Schnars, Maraike Ahlf, Frauke Gerlach, Katharina Al-Shamery, Mathias Wickleder, 15th Workshop on Dielectrics in Microelectronics, **2008**, Bad Saarow (Berlin), Germany

Summer Schools & Workshops

11/10 *Workshop on Atomic Layer Deposition (ALD) and Its Applications*, A*STAR Institute of Material Research and Engineering (IMRE), **2010**, Singapore

08/09 *Nanoscaled Oxides - Big Opportunities in Small Structures*, Wilhelm and Else Heraeus Physics School, **2009**, Bad Honnef, Germany

07/09 *Highlights in Microtechnology*, Final Conference, **2009**, Neuchâtel, Switzerland

06/09 *59th Meeting of Nobel Laureates dedicated to Chemistry*, **2009**, Lindau, Germany

06/08 *Highlights in Microtechnology*, Summer School, **2008**, Neuchâtel, Switzerland and Besançon, France

03/08 *VDI Seminar in Vakuumtechnology*, **2008**, Düsseldorf, Germany

Statement of Authorship - Selbstständigkeitserklärung

I hereby certify that this dissertation has been composed by myself, and describes my own work. All references and verbatim extracts have been quoted, and all sources of information have been specifically acknowledged. The present thesis has not been accepted in any previous application for a degree.

Hiermit versichere ich, dass ich die vorliegende Dissertation selbständig verfasst, alle benutzten Quellen und Hilfsmittel vollständig angegeben und die Stellen der Arbeit, die anderen Werken im Sinn entnommen sind, in jedem Fall als Entlehnung kenntlich gemacht habe. Die vorliegende schriftliche Arbeit hat weder in Teilen noch in Gänze einer anderen wissenschaftlichen Hochschule zur Begutachtung in einem anderen Promotionsverfahren vorgelegen.



Maraike Ahlf, Oldenburg (Oldb)